DOE/ER-0313/19

Fusion Materials

Semiannual Progress Report for Period Ending December 31, 1995

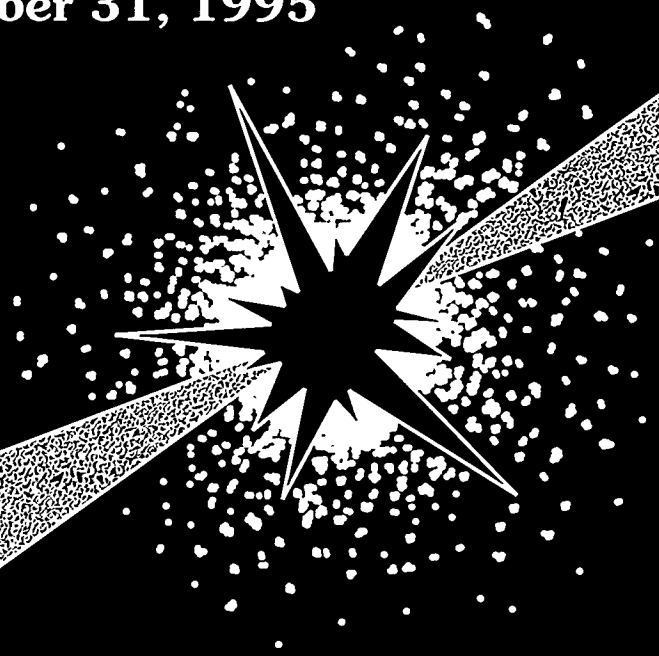

U. S. Department of Energy
Office of Fusion Energy

DOE/ER-0313/19
Distribution
Categories
UC-423, -424

FUSION MATERIALS
SEMIANNUAL PROGRESS REPORT
FOR THE PERIOD ENDING
DECEMBER 31, 1995

Prepared for
DOE Office of Fusion Energy
(AT 15 05 01 0)

DATE PUBLISHED: APRIL 1995

Prepared for
OAK RIDGE NATIONAL LABORATORY
Oak Ridge, Tennessee 37831
Managed by
Lockheed Martin Energy Research Corp.
for the
U.S. DEPARTMENT OF ENERGY
under Contract DE-AC05-96OR22464

FOREWORD

This is the nineteenth in a series of semiannual technical progress reports on fusion materials. This report combines the full spectrum of research and development activities on both metallic and non-metallic materials with primary emphasis on the effects of the neutronic and chemical environment on the properties and performance of materials for in-vessel components. This effort forms one element of the materials program being conducted in support of the Magnetic Fusion Energy Program of the U.S. Department of Energy. The other major element of the program is concerned with the interactions between reactor materials and the plasma and is reported separately.

The Fusion Materials Program is a national effort involving several national laboratories, universities, and industries. A large fraction of this work, particularly in relation to fission reactor experiments, is carried out collaboratively with our partners in Japan, Russia, and the European Union. The purpose of this series of reports is to provide a working technical record for the use of the program participants, and to provide a means of communicating the efforts of materials scientists to the rest of the fusion community, both nationally and worldwide.

This report has been compiled and edited under the guidance of A. F. Rowcliffe by Gabrielle Burn, Oak Ridge National Laboratory. Their efforts, and the efforts of the many persons who made technical contributions, are gratefully acknowledged.

F. W. Wiffen
Division of Advanced Physics
and Technology

Reports previously listed in this series are as follows:

DOE/ER-0313/1	Period ending September 30, 1986
DOE/ER-0313/2	Period ending March 31, 1987
DOE/ER-0313/3	Period ending September 30, 1987
DOE/ER-0313/4	Period ending March 31, 1988
DOE/ER-0313/5	Period ending September 30, 1988
DOE/ER-0313/6	Period ending March 31, 1989
DOE/ER-0313/7	Period ending September 30, 1989
DOE/ER-0313/8	Period ending March 31, 1990
DOE/ER-0313/9	Period ending September 30, 1990
DOE/ER-0313/10	Period ending March 31, 1991
DOE/ER-0313/11	Period ending September 30, 1991
DOE/ER-0313/12	Period ending March 31, 1992
DOE/ER-0313/13	Period ending September 30, 1992
DOE/ER-0313/14	Period ending March 31, 1993
DOE/ER-0313/15	Period ending September 30, 1993
DOE/ER-0313/16	Period ending March 31, 1994
DOE/ER-0313/17	Period ending September 30, 1994
DOE/ER-0313/18	Period ending March 31, 1995
DOE/ER-0313/100	Technical Evaluation of the Technology of Vanadium Alloys for Use as Blanket Structural Materials in Fusion Power Systems

CONTENTS

Both the fusion and light water reactor program require the use of subsize specimens to obtain sufficient irradiation data on neutron-induced embrittlement of ferritic steels. While the development of fusion-relevant size effects correlations can proceed analytically, it is more cost-effective at this time to use data currently being obtained on embrittlement of pressure vessel steels to test and expand the correlations developed earlier using fusion-relevant steels.

Dynamic finite element modeling of the fracture behavior of fatigue-precracked Charpy specimens was performed to determine the effect of single variable changes in ligament size, width, span, and thickness on the upper shelf energy. A method based on tensile fracture-strain was used for modeling crack initiation and propagation. It was found that the upper shelf energy of precracked specimens (USE_p) is proportional to b^n, where b is ligament size and n varies from about 1.6 for subsize to 1.9 for full size specimens. The USE_p was found to be proportional to width according to W^{25}. The dependence on thickness was found to be linear for all cases studied. Some of the data from the FEM analysis were compared with experimental data and were found to be in reasonable agreement.

Specimen fabrication is underway for an irradiation screening experiment planned to start in January 1996 in the SM-2 reactor in Dimitrovgrad, Russia. The purpose of the experiment is to evaluate the effects of neutron irradiation at ITER-relevant temperatures on the bond integrity and performance of Cu/SS and Be/Cu joints, as well as to further investigate the base metal properties of irradiated copper alloys. Specimens from each of the four ITER parties (U.S., EU, Japan, and RF) will be irradiated to a dose of ~0.2 dpa at two different temperatures, 150 and 300°C. The specimens will consist of Cu/SS and Be/Cu joints in several different geometries, as well as a large number of specimens from the base materials. Fracture toughness data on base metal and Cu/SS bonded specimens will be obtained from specimens supplied by the U.S. Due to a lack of material, the Be/Cu specimens supplied by the U.S. will only be irradiated as TEM disks.

Postirradiation electrical resistivity and tensile measurements have been completed on pure copper and copper alloy sheet tensile specimens irradiated in the SM-2 reactor to doses of ~0.5 to 5 dpa and temperatures between ~80 and 400°C. Considerable radiation hardening and accompanying embrittlement was observed in all of the specimens at irradiation temperatures below 200°C. The radiation-induced electrical conductivity degradation consisted of two main components: solid transmutation effects and radiation damage (defect cluster and particle dissolution) effects. The radiation damage component was nearly

1.0 VANADIUM ALLOYS

DEVELOPMENT OF LASER WELDING TECHNIQUES FOR VANADIUM ALLOYS*

R. V. Strain, K. H. Leong, and D. L. Smith

OBJECTIVE

Techniques for joining vanadium alloys, and possibly vanadium, to steel will be required for the construction of fusion devices. The primary objective of this program is to develop laser welding techniques for vanadium alloys, particularly for the manufacture of test specimens of welded materials.

SUMMARY

Laser welding is potentially advantageous because of its flexibility and the reduced amount of material affected by the weld. Lasers do not require a vacuum (as do electron beam welders) and the welds they produce have high depth-to-width ratios. Scoping tests with a small pulsed 50 J YAG laser indicated that lasers could produce successful welds in vanadium alloy (V-5%Cr-5%Ti) sheet (1 mm thick) when the fusion zone was isolated from air. The pulsed laser required an isolating chamber filled with inert gas to produce welds that did not contain cracks and showed only minor hardness increases. Following the initial scoping tests, a series of tests were performed with a 6 kW continuous CO_2 laser. Successful bead-on-plate welds were made on V-4%Cr-4%Ti and V-5%Cr-5%Ti alloys to depths of about 4 mm with this laser.

EXPERIMENTAL PROGRAM

Because of the potential advantageous of laser welding, it is important to include laser-welded samples in the materials testing program for vanadium alloys, and laser welding tests on vanadium alloys were begun in late 1994. Initial scoping tests with a small pulsed laser were performed to determine the environment required to make successful welds and the depth-of-penetration capability of this welder. These tests indicated that successful welding of a V-5%Cr-5%Ti alloy would require protection of the molten metal from contamination by interstitial elements (primarily oxygen). Some initial tests have been performed with a 6 kW continuous CO_2 laser and an argon purge to protect the weld. Successful bead-on-plate welds have been made on 1 mm-thick sheet and 4 mm-thick plates. Modification of the purge-stream configuration and adjustment of the welding parameters will be pursued as methods of optimizing these welds. The use of a 1600 W pulsed YAG laser will also be evaluated for making these welds.

RESULTS

Weld beads were generated during initial scoping tests with a 50 J pulsed YAG laser by overlapping individual spot welds. Welds made in air with the aid of an argon purge to protect the welds resulted in welds that contained cracks. However, a crack-free weld was made by placing the sample in a glass chamber filled with argon. In this case, metal vaporized during the individual shots coated the glass and significantly reduced the penetration depth near the end of the bead. These results showed that laser welding was feasible, but that protection of the weld from interstitial impurities was necessary.

Previous experience of the operators of the 6 kW continuous laser indicated that successful welds could probably be made on vanadium alloys by using inert gas purges, which would avoid the complications associated with enclosing the work piece. Initial weld trials have shown that bead-on-plate welds could be obtained to depths of about 4 mm with a power of 5.5 kW and a speed of 4.5 cm/s. Argon at a flow rate of 100 cfh was distributed through a diffuser nozzle aimed just behind the laser beam on the upper surface of the work piece. The rapid solidification rate in these welds resulted in a fine, highly elongated grain structure, as shown in Fig. 1. Results of microhardness measurements (Fig. 2) show an increase from about 180 dph in the bulk material to about 230 dph in the fusion zone.

---

*Work supported by U.S. Department of Energy, Office of Fusion Energy Research, under Contract W-31-109-Eng-38.

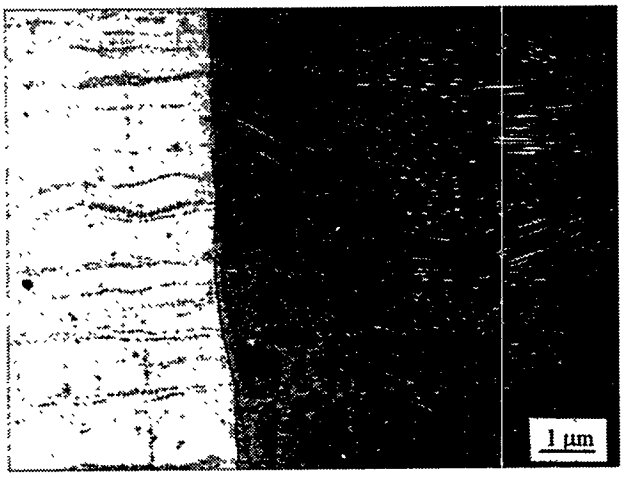

Fig. 1. Microstructure of Laser Weld and Base Material; 100X.

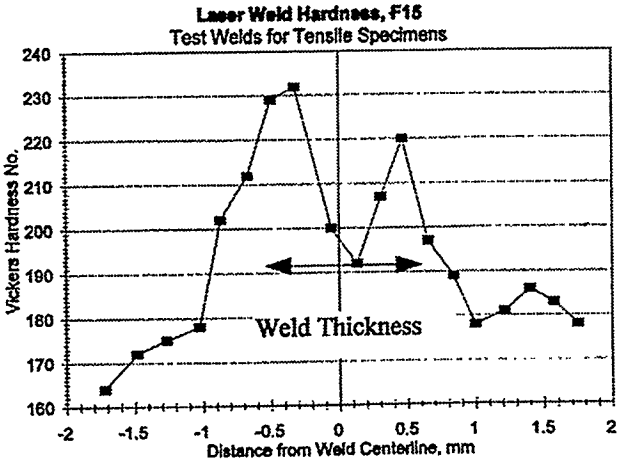

Fig. 2. Microhardness Measurements on Laser Weld and Base Material.

Results of Charpy impact testing on V-4%Cr-4%Ti alloy samples fabricated with the weld located transversely at the notch showed good ductility at 100°C, but poor ductility at -25°C. Only three welded samples were available for testing so no additional data were obtained on the as-welded samples. The third sample was heat treated under vacuum at 1000°C for 1 h and then tested. Charpy testing showed that this sample had good ductility at -25°C. A preliminary interpretation of these results is that the reduction in ductility resulted from the welding. If oxygen contamination were the cause of the reduction in ductility, the annealing operation may have caused the oxygen to precipitate from the matrix in the form of titanium oxides.

FUTURE ACTIVITIES

The next step in the development of laser welding techniques is to evaluate the performance of a 1600 W YAG laser in welding the vanadium alloys. Both improved purging techniques and inert gas enclosures will be included as methods to reduce or eliminate oxygen contamination. Efforts will be made to optimize the power and speeds used to weld 1- and 4-mm-thick material. The effectiveness of changing the welding and cover gas parameters will be measured by mechanical testing, as well as by microstructural and microchemical characterization of samples. Post-welding heat treating will be studied if it is needed to obtain material properties in the weld that are comparable to those in the bulk material.

PRODUCTION AND FABRICATION OF VANADIUM ALLOYS FOR THE RADIATIVE DIVERTOR PROGRAM OF DIII–D – W. R. Johnson, J. P. Smith, and R. D. Stambaugh (General Atomics)

SUMMARY

V-4Cr-4Ti alloy has been recently selected for use in the manufacture of a portion of the DIII–D Radiative Divertor modification, as part of an overall DIII–D vanadium alloy deployment effort developed by General Atomics (GA) in conjunction with the Argonne and Oak Ridge National Laboratories (ANL and ORNL). The goal of this work is to produce a production-scale heat of the alloy and fabricate it into product forms for the manufacture of a portion of the Radiative Divertor (RD) for the DIII–D tokamak, to develop the fabrication technology for manufacture of the vanadium alloy Radiative Divertor components, and to determine the effects of typical tokamak environments on the behavior of the vanadium alloy. The production of a ~1300-kg heat of V-4Cr-4Ti alloy is currently in progress at Teledyne Wah Chang of Albany, Oregon (TWCA) to provide sufficient material for applicable product forms. Two unalloyed vanadium ingots for the alloy have already been produced by electron beam melting of raw processed vanadium. Chemical compositions of one ingot and a portion of the second were acceptable, and Charpy V-Notch (CVN) impact tests performed on processed ingot samples indicated ductile behavior. Material from these ingots are currently being blended with chromium and titanium additions, and will be vacuum-arc remelted into a V-4Cr-4Ti alloy ingot and converted into product forms suitable for components of the DIII–D RD structure. Several joining methods selected for specific applications in fabrication of the RD components are being investigated, and preliminary trials have been successful in the joining of V-alloy to itself by both resistance and inertial welding processes and to Inconel 625 by inertial welding.

PROGRESS AND STATUS

1. Introduction

General Atomics (GA), along with the Argonne and Oak Ridge National Laboratories (ANL and ORNL), has developed a plan for the utilization of vanadium alloys in the DIII–D tokamak which will culminate in the fabrication, installation, and operation of a vanadium alloy structure in the DIII–D Radiative Divertor (RD) modification.[1,2] The use of a vanadium alloy will provide a meaningful step towards developing advanced materials for fusion power applications by 1) demonstrating the in-service behavior of a vanadium alloy in a typical tokamak environment, and 2) developing knowledge and experience on the design, processing, and fabrication of full-scale vanadium alloy components.

The program consists of three phases: first, small vanadium alloy coupons is being exposed in DIII–D at positions in the vessel floor and behind the existing divertor structure; second, a small vanadium alloy component will be operated in conjunction with the existing divertor, and third, during the forthcoming RD modification, in 1998 a portion of the upper section of the new double-null, slotted divertor will be fabricated from vanadium alloy product forms. A major portion of the program is research and development to support fabrication and resolve key issues related to environmental effects. The execution of the plan is a joint effort by GA, the DIII–D Program, and Department of Energy (DOE) Material Program participants, primarily ANL and ORNL.

On the basis of excellent properties that have been determined for both laboratory-scale and production-scale heats, V-4Cr-4Ti alloy has been identified as the most promising vanadium-based candidate alloy for application in fusion reactor structural components,[3,4] and has been selected for procurement in product forms applicable for the manufacture of a portion of the DIII–D RD modification.

The alloy has been, and is currently being exposed in DIII–D during various stages of DIII–D operation to assess the effects of a typical tokamak environment on the behavior of the alloy. Procurement of product forms (sheet and rod) of the alloy has also been initiated, and a ~1300-kg V-4Cr-4Ti alloy ingot is currently in processing at TWCA to provide applicable product forms for the manufacture of a portion of the upper section of the DIII–D radiative divertor. In addition, fabrication studies are in progress to develop joining methods applicable to manufacture of the vanadium alloy RD components.

2. PHASE 1: Specimen and Coupon Exposures and Analysis

In March of 1995, minature Charpy V-notch (CVN) impact and tensile specimens of V-4Cr-4Ti alloy from a large production-scale heat fabricated for ANL by TWCA (500-kg, Heat ID#832665)[4] were installed in DIII–D in positions behind the divertor baffle. These specimens were scheduled for long-term exposure (~1 year). ANL supplied the samples, and GA provided the design and fabrication of the hardware for retaining the samples. The specimen environment was monitored (i.e., thermocouples, residual gas analyzer, and pressure gauges) during various stages of DIII–D operation (e.g., baking, discharge cleaning, boronization, plasma discharges, etc.). Comparison of specimen and vessel thermocouple readings indicate that the specimens closely followed (within ~5°C) the outer vessel wall temperature (i.e., the inner wall of the outer toroidal surface of the vessel). These samples were removed during the January 1996 DIII–D vent, having experienced numerous thermal cycles up to temperatures of ~350°C as well as exposure to trace amounts (10^{-9}–10^{-6} atm) of potentially embrittling impurities (e.g., H_2, O_2, H_2O, N_2, B, CO, CO_2, and a number of hydrocarbons). GA is currently analyzing the environmental data while ANL is performing an evaluation of the specimens. These data will be used to provide a preliminary assessment of the effects of a tokamak environment on the behavior of the alloy. During the January 1996 vent, additional V-4Cr-4Ti alloy CVN and tensile specimens were installed in the DIII–D specimen holder, and will be exposed (and monitored) until the next DIII–D vent.

In parallel, other V-4Cr-4Ti alloy (Heat ID #832665) samples were exposed in a position in the DIII–D vessel floor utilizing the DIII–D Divertor Material Exposure System (DiMES). Utilization of the DiMES allows for an exposure of a material without waiting for a vent to retrieve samples. A V-4Cr-4Ti alloy disc was exposed during the initial baking and cleaning of DIII–D after the February 1995 vent, as a post-vent baking cycle representing what is expected to be the most potentially severe environmental condition for the vanadium alloy specimen. During the exposure the disc was monitored using an infrared camera (temperature), RGA, and pressure gauges. It was removed soon after the bake/clean was completed having experienced temperatures and exposure to trace amounts of impurities typical of bakeout conditions. The disc is currently being evaluated at ANL to quantify any possible impurity(s) pickup. Additional exposures of five (5) miniature V-4Cr-4Ti alloy CVN specimens to a similar baking cycle were performed in July 1995, and are also currently under evaluation at ANL. Other DiMES exposures are planned to evaluate the effects of other DIII–D environmental conditions (e.g., discharge cleaning, boronization, etc.).

3. PHASE 2: Small Component Exposure

A second step in the DIII–D Vanadium Plan is to install a small V-4Cr-4Ti alloy component in DIII–D which will operate in conjunction with the existing DIII–D Advanced Divertor. This component will be a single radiatively-cooled divertor plate or a small representative water-cooled component which will be operated in series with the primary water-cooled divertor panels. The component will be installed during an upcoming DIII–D vent, exposed for some period of operation, and then removed. Samples from the component will be excised by GA, and GA, ANL, and ORNL will perform metallurgical analyses and property measurements on the excised materials. A decision as to the specific component has not been made at this time.

4. PHASE 3: Radiative Divertor Program

The final step in the deployment of a vanadium alloy in DIII–D is the design, manufacture, and installation of a portion of the upper half of the RD structure using V-4Cr-4Ti alloy, with the other portions being fabricated from Inconel 625. The V-4Cr-4Ti alloy structure will contain toroidally-continuous, water-cooled structural panels with inertially-cooled graphite tiles mechanically attached to their surfaces by welded studs. The panels will be water cooled during machine operation, experiencing a maximum temperature of ~60°C. During post-vent clean-up, hot air will replace the water in the coolant channels of the structure, and the structure (along with the DIII–D vessel) will be baked to ~400°C. The panels will be supported from the vacuum vessel by Inconel 718 supports which will provide the required strength for reacting disruption loads and the flexibility for withstanding differential thermal growth during baking. Due to the lower electrical resistivity of the V-4Cr-4Ti alloy as compared to Inconel 625, the toroidal current flow during disruption will be approximately 4 times larger. The design of the panels and supports will be modified to react the larger loads.[1]

The panels will be made in segments and fabricated of sandwich construction from two 4.76 mm sheets, each containing a 1.5 mm deep coolant channel milled into its side. Resistance seam welding is the primary candidate process being considered for joining the panel edges and creating a leak tight seal. Electron beam welding may be used in addition to resistance seam welding as a process for ensuring the leak tightness of the water-cooled panels. Electron beam welding is being considered for making the water connections (V-4Cr-4Ti alloy tubing) to the panels with inertial welding as a possible backup. Inertial welding is the primary candidate process being considered for joining studs to the panels for graphite tile attachment, and for making V-4Cr-4Ti alloy to Inconel 625 bi-metallic joints for effecting in-vessel gas tungsten arc (GTA) field welds to Inconel 625 water supply tubes.

4.1 Fabrication of Product Forms For The Radiative Divertor

The production campaign for the V-4Cr-4Ti alloy product forms consists of electron beam melting of unalloyed vanadium ingot materials, alloying with high purity Cr and Ti and vacuum-arc melting (two times) of a large-scale (~1300-kg) V-4Cr-4Ti alloy ingot, extrusion of the alloyed vanadium ingot into rectangular bars, and subsequent conversion by rolling (and drawing) and heat treatments into 4.76 mm thick sheet and 10.16 mm diameter rod product forms. The specification for the alloy was developed by GA with input from ANL and ORNL. Particular attention was given to the control of impurities to meet the immediate goals for the RD program and also future goals for further deployment of vanadium alloys in advanced fusion systems including the minimization of Nb, Mo, and Ag for low neutron activation; the optimization of Si (400–1000 ppm) to suppress neutron-induced swelling; and the limiting of O, N, C, Cu, S, P, Cl, Ca, K, Mg, Na, and B to avoid grain boundary segregation and precipitation of embrittling phases.[4] The final specification of unalloyed vanadium and alloyed vanadium ingot chemistries for the V-4Cr-4Ti alloy procurement is listed in Table 1.

Processing of the V-4Cr-4Ti alloy by TWCA was initiated in September 1994. The raw vanadium for the unalloyed vanadium ingots for the alloy, in the form of ~100-kg lots was prepared from high purity vanadium oxide by the aluminothermic process. Chemical analysis of the ~30 lots processed, although deemed not specifically precise with respect to predicting the composition of subsequent ingots, revealed substantial variation in their chemical compositions. Several key chemical attributes were noted as follows: 1) all of the lots were out of specification limits with respect to Si (400–1000 wppm), containing only 100–200 wppm, a variation often observed in processed raw vanadium due to the varying Si levels typically found in the starting material (vanadium oxide); 2) all of the lots contained <50 wppm Mo (within specification limits); 3) approximately half of the lots contained <50 wppm Nb, with the other half containing substantially more Nb (several hundred wppm); and 4) lot-averaged values for Fe and S were slightly greater than specifications limits. Variations in other elements were also noted with most elements being within specification limits for all of the lots. Rather than process additional raw vanadium in the hopes of increasing the Si to within specification levels (400–1000 wppm), and delay the production of the V-4Cr-4Ti alloy, or make Si additions to the vanadium during processing of the alloyed vanadium ingot, and run the risk of producing unwanted Si segregation in the alloy, the low-Si raw vanadium lots were accepted for further processing.

Lots of raw vanadium were then selected into two groups by TWCA in collaboration with GA based on their overall chemistries with respect to meeting all of the specification requirements, and two 395 mm diameter vanadium ingots were processed by electron beam melting. Chemical analysis of the resulting ingots indicated that both ingots were generally within specification limits for all elements except primarily for Nb (See Table 1). One ingot (~900-kg) had a Nb level of which averaged ~40 wppm and another larger ingot (~2200-kg) had a Nb level of several hundred wppm. Samples (~0.5 in. × ~0.5 in. × ~1.5 in.) were excised from the surfaces of the low-Nb ingot and the higher-Nb ingot portion at their mid-lengths for mechanical property measurements to confirm their purity (and microstructure). These samples were subsequently processed by cold rolling and annealing at ORNL, and were then machined into CVN specimens and tested at ANL at –196°C and above to evaluate their toughness (ductility), a property which is extremely sensitive to impurities in vanadium. Both ingot materials exhibited ductile behavior and had impact toughness (ductility) values similar to that obtained by ANL for the pure vanadium ingot material for the 500-kg V-4Cr-4Ti alloy heat.[5] Since the blending of the low-Nb ingot with a portion of the higher-Nb ingot was expected to result in only a doubling of the final Nb level, from ~40 wppm to ~90 wppm Nb, and this increase was not expected to compromise the properties of the alloy for its intended application, a decision was made to blend the ingot materials to produce the ~1300-kg of the alloy.

TABLE 1
CHEMICAL COMPOSITION GOALS FOR V-4Cr-4Ti ALLOY
AND CHEMISTRIES OF VANADIUM INGOTS

	Content, parts/million by weight (ppm)*			
Element	Specification For Unalloyed Vanadium Ingot	Unalloyed Vanadium Ingot [Heat ID #820645] (Average of 3 Measurements)	Unalloyed Vanadium Ingot [Heat ID #820642] (Average of 3 Measurements)	Specification For Alloyed Vanadium (V-4Cr-4Ti) Ingot
Cr	–	-	-	4±0.5 wt %
Ti	–	-	-	4±0.5 wt %
Si	400–1000	173	197	400–1000
H	<10	<3	<3	<10
O	<400	313	213	<400
N	<200	113	153	<200
C	<200	24	25	<200
Al	<200	243	167	<200
Fe	<300	147	135	<300
Cu	<50	<50	<50	<50
Mo	<50†	<50	<50	<50†
Nb	<20†	40	226	<20†
Cl	<3	‡	‡	<3
Ga	<10	<5	<5	<10
Ca	<1†	<10[d]	<25[d]	<1†
Na	<1†	<5[d]	<5[d]	<1†
K	<1†	<5[d]	<5[d]	<1†
Mg	<1†	<10[d]	<10[d]	<1†
P	<30	<30	<30	<30
S	<30	<10	<10	<30
B	<5	<5	<5	<5
Ag	<1	<5[d]	<5[d]	<1
V	balance	balance	balance	balance

*Unless otherwise specified in weight %.

†Desired values — <5 ppm Mo, <1 ppm Nb, <1 ppm total Ca+Na+K+Mg.

‡Not analyzed.

#Request initiated to TWCA for re-analysis to higher sensitivity level

During February 1996, consolidation of the two vanadium ingot materials with each other was initiated at TWCA, to be followed by addition of high purity Cr and Ti (double vacuum-melted Ti), and alloying by vacuum arc melting (twice) of the V-4Cr-4Ti alloy ingot.

4.2 Manufacturing Technology Development

As manufacturing development is a major focus of this project a significant amount of research and development is being performed in this area. The RD structure will require many metal/metal joints, and joining development is therefore a key area of study. In addition to the welding development work on vanadium alloys being conducted at ANL and ORNL (laser, electron beam, GTA, etc.) to support this program, GA is investigating several different joining processes which are attractive for fabrication of RD components including resistance seam, electrodischarge (stud), inertial, and electron beam welding. The scope of the GA joining development efforts has been limited by the availability of material, some of which has been purchased from TWCA (V-5Cr-5Ti; Heat ID #932394) and some of which has been supplied by ANL (V-5Cr-5Ti alloy; Heat ID #832394 and V-4Cr-4Ti alloy; Heat ID #832665). Support is also being provided by ANL and ORNL in the development of basic engineering design properties.

Resistance Welding Studies

Resistance seam welding is planned to form the closure weld in the RD water-cooled structural panels. Industrial companies with seam welding experience have been contacted and resistance spot welding trials are currently being performed by one of these vendors (K-T Aerofab of El Cajon, CA).

Resistance welding trials (in air) were initially performed on sandwiches of 1 mm pure and alloyed vanadium sheet by B-J Enterprizes of Albany, Oregon. Weld nuggets were formed and microhardness measurements on a sectioned sample showed very little increase (<10%) in hardness in the weld or heat-affected zones (HAZ) over the parent metal.

Thicker sheet material (3.81 mm) of V-4Cr-4Ti was obtained from ANL and resistance spot weld trials (12 trials) were initiated at the local vendor. Although some diffusion bonding (up to ~80% of the interface regions directly under the weld electrodes) was obtained between sheet sandwich samples, no weld nuggets were observed. A second set of trials (4 trials) using different weld parameters (i.e., slightly higher current inputs) were made over several of the original spots from the first trials. Diffusion bonding was observed to a greater extent (~95%), yielding strengths of greater than 135 MPa using crude shear strength tests, but still no weld nuggets were developed. A third set of trials (8 trials) was performed with similar V-4Cr-4Ti alloy sheet material using weld parameter data obtained from the literature for carbon steel which were found to have similar strength and resistivity to V-4Cr-4Ti. These trials were successful, with metallography of sectioned samples indicating good diffusion bonds for the lowest current trials, good weld nuggets with no porosity for intermediate current levels, and weld nuggets with some porosity (single central pores) for the highest current levels. Weld nuggets for the best trials were ~7 mm in diameter, and microhardness measurements showed less than ~10% increase in hardness in the weld and HAZs over that of the parent metal. Additional spot weld trials are now in planning using material similar in thickness to that to be used for the RD water-cooled panels (4.76 mm). V-5Cr-5Ti alloy sheet material, 6.35 mm in thickness, was supplied by ANL, and has recently been cold rolled by ORNL to this thickness for these trials.

Inertial Welding Studies

Inertial welding to join a vanadium alloy (V-5Cr-5Ti alloy) to itself, and to stainless steel and Inconel 625, have been investigated. A vendor with experience in joining pure vanadium to Monel was located (Interface Welding of Carson, CA) and preliminary welding trials have been completed. Inertial welding trials on V-5Cr-5Ti alloy to itself (19.05 mm diameter disc to 9.52 mm diameter rod) were successful. Metallography showed complete bonding with no indications of porosity or cracking. Microhardness measurements showed only slight increases in hardness in the weld and HAZs. Tensile pull tests were performed on three weld trial specimens at room temperature, and all three samples failed in the threaded grip area of the V-5Cr-5Ti alloy rod (at ~520 MPa stress) well away from the weld areas. Torque tests were also performed on two additional samples to measure the capability of the joint to withstand torsion loads as would be experienced in a stud-to-plate joint. Again, failures occurred in the V-5Cr-5Ti alloy threaded sections away from the weld joints. Trials to join stainless steel (19.05 mm diameter disc) to V-5Cr-5Ti alloy (9.52 mm diameter rod) did not achieve complete bonding, but results indicated that development of such bi-metallic joints could be enhanced by decreasing the diameter of the stainless steel part and enhancing its forgability relative to that of the softer vanadium alloy. Joining trials were continued on Inconel 625 (12.7 mm diameter rod) to V-5Cr-5Ti alloy

(9.52 mm diameter rod) in order to be more relevant to the planned DIII–D effort. Additional trials using similar size V-5Cr-5Ti alloy rod (9.52 mm diameter) and smaller diameter (6.35 mm diameter) Inconel 625 rod to match the forgabilities of the two materials were successful. Metallography showed complete bonding with no porosity or cracking. Tensile pull tests were performed on three weld trial samples. Two samples failed in the Inconel 625 section well away from the weld area (at ~930 MPa stress) and one sample failed at the approximate weld interface, but at a stress level of ~760 MPa. Additional inertial weld trials are now being planned to fabricate bi-metallic tube joints.

Stud Welding Studies

Stud welding trials utilizing the drawn arc method were performed between vanadium alloy (V-5Cr-5Ti) stud (9.6 mm diameter) and plate (3.8 mm thickness) materials. A representative from the stud welding equipment manufacturer (TRW Nelson Stud Welding Division of Walnut, CA) assisted in the trials. A range of welding parameters were used without success. The weld materials would not stay in the weld area, blowing out from the sides. Cracking was also observed (audible) during cool down of the materials. Visible bonding never exceeded ~50%, and for many of the trials achieved much less than this value. A second set of trials was performed with a different stud geometry, but were also unsuccessful. These failures, and the successes achieved in the vanadium alloy inertial weld trials, prompted the investigation of portable friction welding as a process for the attachment of studs. Preliminary V-5Cr-5Ti alloy stud-to-plate, portable friction welding trials were performed at RamStud Inc. of Smyrna, GA, and substantial bonding was achieved. Evaluation of these trials is currently in progress.

Electron Beam Welding Studies

Preliminary electron beam welding trials have also been initiated at GA. Initial weld parameters were obtained from ORNL personnel and weld penetration tests were performed using 6.35 mm thick V-5Cr-5Ti alloy plate acquired from ANL. Initial metallography was performed on these weld penetration trial samples to establish specific weld parameters for creating a lap weld of two 3.85 mm thick vanadium alloy sheet materials (V-5Cr-5Ti alloy to V-4Cr-4Ti alloy). A lap weld of the materials was created and metallurgically examined. Good weld penetration was obtained with no indications of cracking. Microhardness measurements showed less than ~10% increase in hardness. Tensile and shear specimens are planned to evaluate the strength of the welds.

CONCLUSIONS

A program for utilizing vanadium alloys in DIII-D has been developed, and production of material for this program has started. Two vanadium ingots have been electron beam melted as base materials for a ~1300-kg V-4Cr-4Ti alloy ingot. Chemical analyses of one ingot (900-kg) and a portion (~400-kg) of another larger (~2200-kg) ingot, Charpy V-notch impact test results on material excised from both ingots were found to be satisfactory to continue the processing of the V-4Cr-4Ti alloy. Preliminary successes were achieved in developing similar metal weldments of vanadium alloys by resistance spot and inertial welding methods, and in producing vanadium alloy/Inconel 625 dissimilar metal weldments by inertial welding.

ACKNOWLEDGMENTS

This is a report of work supported by the U.S. Department of Energy under Contract Nos. DE-AC03-89ER51114 and General Atomics under IR&D funding. The authors are appreciative of the efforts of both ANL and ORNL in supporting this program. General Atomics would also like to recognize TWCA for contributing data and information regarding the processing of the vanadium alloy, and for reviewing this manuscript.

REFERENCES

[1]J. P. Smith, W. R. Johnson, R. D. Stambaugh, P. W. Trester, D. Smith, and E. Bloom, "Vanadium Alloys For The Radiative Divertor Program of DIII–D," to be published in Proc. of the 16th IEEE/NPSS Symposium on Fusion Engineering, Champlain, Illinois, September 30 through October 5, 1995.

[2]J. P. Smith, W. R. Johnson, R. D. Stambaugh, P. W. Trester, D. Smith, and E. Bloom, "Utilization of Vanadium Alloys In The DIII–D Radiative Divertor Program," to be published in Proc. of the Seventh International Conference on Fusion Reactor Materials (ICFRM-7), Obninsk, Russia, September 25–29, 1995.

[3]D. L. Smith, H. M. Chung, B. A. Loomis, H. Matsui, S. Votinov, and W. Van Witzenburg, "Development of Vanadium-Base Alloys For Fusion First-Wall-Blanket Applications," Fusion Engineering and Design, Vol. 29 (1995), pp. 399–410.

[4]H. M. Chung, H.--C. Tsai, D. L. Smith, R. Peterson, C. Curtis, C. Wojcik, and R. Kinney, "Fabrication of 500-kg Heat of V-4Cr-4Ti," Fusion Reactor Materials Semiannual Progress Report, DOE/ER-0313/17, Oak Ridge National Laboratory, Oak Ridge Tennessee (1994), pp. 178–187.

[5]Private communication with H. M. Chung, ANL, on January 25, 1996; work not yet published.

PHYSICAL PROPERTIES OF O- AND N-CONTAINING V-Cr-Ti ALLOYS*

J.-H. Park, D. Kupperman, E. T. Park, and G. Dragel (Argonne National Laboratory)

SUMMARY

Incorporation of O in the surface of V-Ti-Cr alloys has been investigated in controlled environments at 550-750°C, and tests were performed to determine the physical properties of V-Cr-Ti-O solid solutions. The amount of O in the alloys has been determined by weight–change measurements. Microhardness was used to determine O depth profiles of the alloys. X-ray diffraction indicated a phase transformation from body-centered-cubic (bcc) to tetragonal in the lattice that was highly stressed because of O incorporation. Back–scattered–electron images and electron–energy–dispersive spectra revealed Cr depletion near alloy grain boundaries. Elastic modulus and Vickers hardness increased in O-enriched V-Cr-Ti alloys. Hardening of the alloys results from O atoms on face-centered interstitial sites in the bcc sublattice and the formation of very fine coherent oxide particles. Oxygen or N diffusion occurs via the interstitial sublattice of bcc V-base alloys and is accompanied by the formation of homogeneous oxide or nitride phases via internal oxidation or nitridation. The O,N–enriched surface region exhibited the extraordinarily high Vickers hardness of ≈18 GPa (1800 kg/mm^2), a value that is typical of oxides, nitrides, or carbides, or that is obtainable by ion–beam irradiation of metals.

INTRODUCTION

Several V–base alloys exhibit good high–temperature creep strength, low ductile–to–brittle transition temperatures, and high resistance to neutron irradiation damage.[1] However, thermomechanical processing to produce alloys in plate, sheet, and tubular form requires high–temperature annealing in vacuum or inert gas environments. Contamination of the processing environment by trace levels of O_2, N_2, H_2O, CO_2, etc., leads to formation of a hard ceramiclike near-surface region on the alloys. In some applications, surface modification by controlled addition of O, N, or C, with and without the formation of ceramic compounds within the substrate, could be desirable. Modification of the surface region of V–base alloys by diffusion of O, N, or C into the interstitial sublattice has been investigated under conditions in which V-O, V-N, or V-C ceramic compounds do not form at the alloy/gas interface. Most of these compounds have melting points greater than (VN, 2320°C) or comparable to (VO_2 and V_2O_3) that of the alloys (≈1910°C), except for the low–melting V_2O_5 (690°C) phase. Formation of V_2O_5 must be avoided in all thermomechanical and surface-modifying processes. The hardness and elastic modulus of V-Cr-Ti-O solid solutions have been investigated.

EXPERIMENTAL PROCEDURE

Several experimental methods were used to explore the relationship between O and/or N and the physical properties of V-Cr-Ti alloys, namely (a) surface O charging of the alloys, followed by evaluations by optical metallography, transmission– and scanning–electron microscopy (TEM and SEM); (b) X-ray diffraction, energy–dispersive electron spectroscopy (EDS), secondary–ion mass spectroscopy (SIMS), and microhardness tests; and (c) elastic modulus measurements.

Oxygen and/or N charging of the near–surface region of V-4Cr-4Ti. Oxygen and/or N charging of the near–surface region of the alloy was carried out in flowing 99.999% Ar and/or N_2 that contained ≤5 ppm O_2, ≤ 5 ppm H_2O, and a total impurity content of ≤20 ppm, at 550-1030°C for 17-96 h. Oxygen and N pickup by the alloys was determined by weight-change measurements.

X-ray diffraction and related studies. The surface of O-charged samples (25 x 25 x 1 mm) was subjected to X-ray diffration to investigate the relationship between hardness and O content of the materials. To determine X-ray parameters as a function of depth, the specimen surface was polished with a diamond paste. Secondary–ion mass spectroscopy studies were performed on cross sections of O-charged regions of the specimens. Vickers hardness was used to determined the depth of O or N diffusion into the alloys. TEM of O–enriched regions was performed to confirm the presence of a small cluster phase in this region.

---

*Work supported by U.S. Department of Energy, Office of Fusion Energy Research, under Contract W-31-109-Eng-38.

Elastic modulus measurements. Elastic modulus measurements were performed by a simple pulse-echo technique on O-charged small samples (25 x 25 x 1 mm). Because of relatively low attenuation, 15 MHz elastic waves were used.

RESULTS AND DISCUSSION

Oxygen and/or Nitrogen Charging of Near–Surface Region of V-4Cr-4Ti

When V or V–base alloys (e.g., V-Cr, V-Ti, V-Cr-Ti, or V-Cr-Al) oxidize in high–O environments, the low–melting V_2O_5 phase forms via outward diffusion of cations, even in the presence of O–active elements such as Y, Si, Al, etc.[2,3] It is well known that O can be incorporated into the interstitial sublattice of bcc V and its alloys.[4] In the bcc lattice of V-Cr-Ti, O can occupy interstitial sites within the lattice up to several atomic percent. Weight gain of V–4Cr–4Ti specimens was determined after 70–h exposures to flowing high–purity Ar and N_2 (99.999%) that contained O as an impurity. At temperatures of 500-1030°C, the rate of O pickup by the alloy was greater than that of N. This could indicate that the energy of interaction between Ti in the alloy and O is greater than that between Ti in the alloy and N. Also, the atomic size of N is larger than that of O. Diffusion coefficients of O and N in V indicate that O diffuses 10-1800 times faster than N. The activation energies of O and N (plus traces of O as impurity) uptake by the alloy are 0.83 and 0.65 eV, respectively.

Analysis of a back–scattered–electron image from the cross section of an O-charged specimen revealed that the dark area indicates elements with low atomic numbers, i.e., the O–enriched area. Localized enrichment of O occurs in the grains and near grain boundaries. From EDS analysis, areas enriched with O and Ti contain less Cr. However, localized Cr depletion did not occur during O charging at ≤670°C. Based on metallographic information and weight gain data, the depth of the O–charged layer can be controlled by exposure temperature and time in a flowing Ar atmosphere. Oxygen concentration in the near–surface layer was calculated from weight gain, surface area, and thickness of the hardened region; it ranged from 250 ppm (as–received) to ≈2–3%, depending on position within the layer and exposure conditions.

Microhardness Tests on O, N*-Charged V Alloys

Hardness profiles across the O–charged region and at ≥200 μm below the surface of V-4Cr-4Ti specimens were obtained after exposure to flowing Ar at several temperatures. Hardness at the interior of the specimen charged with O at 550°C is higher than that of the as–received specimen. Presumably, O penetration was greater at 550°C than at higher temperatures. An O-blocking mechanism could be involved at high temperatures; for example, local Ti migration or Cr depletion was detected by EDS analysis near grain boundaries. If Ti migrates to grain boundaries or to the surface via cation diffusion, residual O in the alloy will follow Ti, and, as a result, enrichment of O near grain boundaries or at the surface will occur. Because hardness is directly related to O concentration in the alloy, the amount of O pickup by the alloy in the near–surface region in relation to the exposure temperature increases in the order 615-685>703>750>550°C.

X-Ray Diffraction Studies

To determine whether the hardening mechanism involves primarily occupation of interstitial sites by O or formation of small particles of V-O, Ti-O, or V-Ti-O, TEM and X-ray diffraction were performed on the near–surface region of an O-charged V-5Cr-5Ti specimen that was exposed to pure Ar for 21 h at 650°C.

Figure 1 is a TEM photomicrograph of a surface that reveals small particles of coherent oxide. The TEM study supports a hardening mechanism whereby O and/or N lead to internal oxidation or nitridation at elevated temperatures. Coefficients of thermal expansion (CTE) of dilute solid solutions of O in V-O,

*We expect O and a very small amount of N contamination in the system. SIMS analysis indicated only contamination, but measured microhardness was very high.

Ti-O, or V-Ti-O are probably not much higher than those of V and the alloys, ≈9.2 x10^{-6}/K. However, the CTEs of small coherent particles of oxide, nitride, oxynitride, or carboxynitride present in the alloy at high temperatures are probably lower than those of the alloy matrix, and, during cooling from high temperatures, stresses develop that are due to the difference in CTE of the coherent particles and the matrix. This effect seems to be more significant in V-base alloys than in other alloy systems, e.g., Ni–base alloys.[5] X-ray peaks that tend to broaden because of strain that originates from small particles in the alloy (Fig. 3) provide evidence that hardening occurs by incorporation of interstitial impurities.

Figure 1.
TEM photomicrograph of O-charged region of V-5Cr-5Ti after exposure to Ar for 21 h at 650°C.

However, hardening can also be explained by an alternative mechanism. When O or N is incorporated into an alloy by a solid–state diffusion process at elevated temperatures and the alloy is cooled, impurities can become trapped in interstitial positions. The X-ray spectrum from this specimen did not show significant broadening; only the X–ray lattice parameter of the bcc structure increased. Based on the Vickers hardness versus O–charged depth of the near–surface region at various temperatures, we can write the following equation:

$$\text{Log } K_c = 2.77 - 1615/T \text{ (K)} \qquad (\mu m/h^{1/2}),$$

where K_c is the rate constant for the O-affected depth $x = K_c t^{1/2}$.

Figure 2 shows the X-ray diffraction spectrum from the surface of a specimen after ≈20 μm of the O-charged layer was removed by polishing, and the d-spacing of the (110) and (200) planes as a function of depth. The results indicate that the variation of interstitial O in the alloy with depth can be directly related to the average strain distribution with position. In general, all d-spacings decreased with depth. However, as mentioned previously, if Ti migrates from the bulk to grain boundaries or to the surface, then residual bulk O follows Ti, and enrichment of O near grain boundaries or the surface occurs. The X-ray lattice parameter could also increase because of vacancy formation (Fig. 2).

X-ray diffraction profiles in Fig. 3, from the near–surface region of an O-charged sample, reveal phase transformation from a bcc to a tetragonal phase. Oxygen charging at low temperatures produces more separation of the ratio of the a/c spacing in the lattice. It is possible that the high–purity Ar maintains a constant O partial pressure (pO_2) over the range of temperatures and stabilizes the tetragonal phase in the alloy. Lower temperatures should increase the thermodynamic stability of this phase, and less relaxation (diffusion) should occur. Therefore, the difference in a/c is larger (produces more distortion) at low temperatures. During heating, stress relaxes at the free surface and if the tetragonal phase is present within bulk regions of the bcc lattice, it could generate active diffusion/reactive sites during thermal cycling.

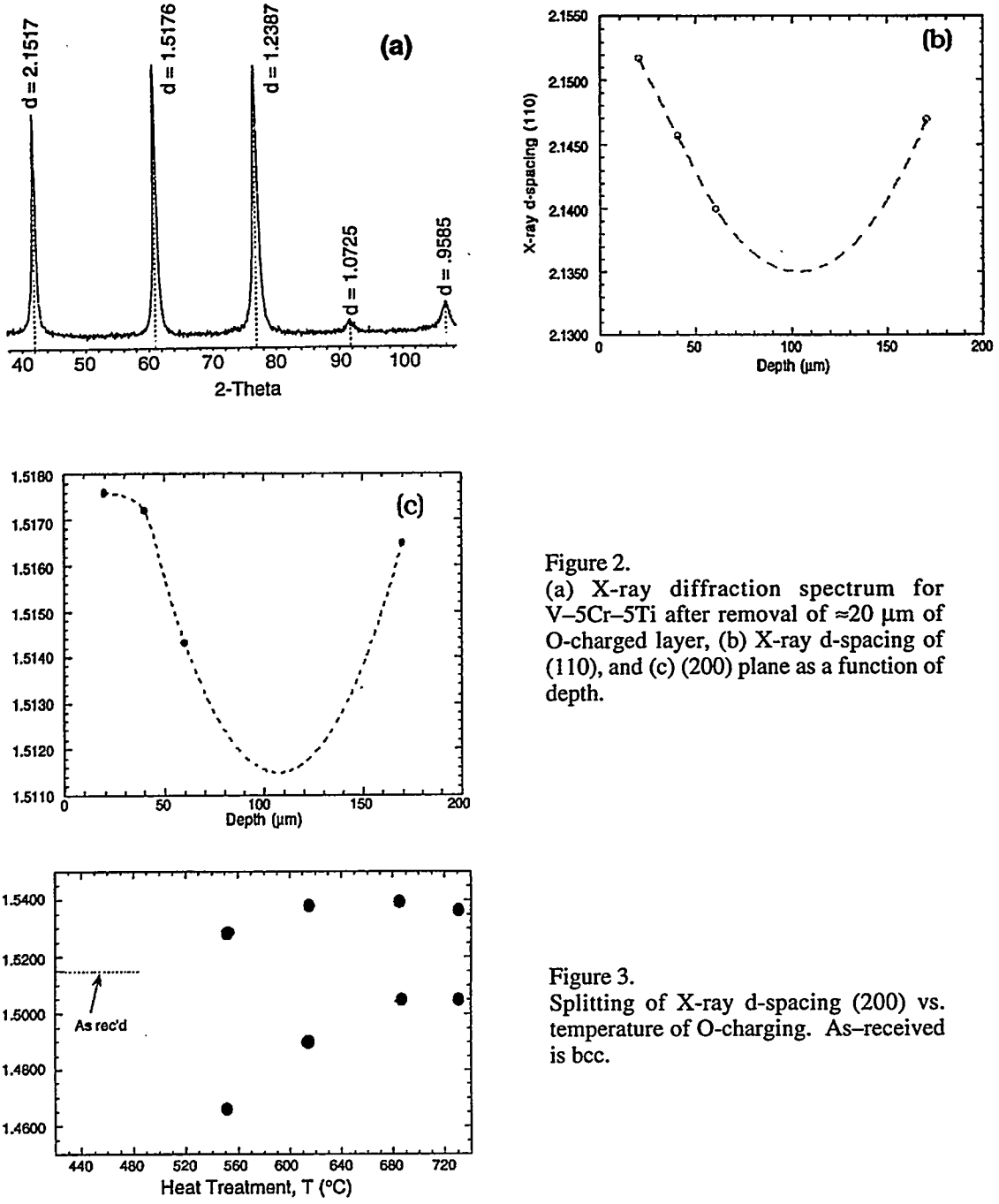

Figure 2.
(a) X-ray diffraction spectrum for V–5Cr–5Ti after removal of ≈20 μm of O-charged layer, (b) X-ray d-spacing of (110), and (c) (200) plane as a function of depth.

Figure 3.
Splitting of X-ray d-spacing (200) vs. temperature of O-charging. As–received is bcc.

Elastic Modulus Measurements on O-Charged Specimen

A relationship between hardness and impurity concentration in the V-Cr-Ti was developed from the results of TEM, SEM, X-ray diffraction, and hardness measurements. Elastic modulus measurements were performed on O– and O,N-charged samples at room temperature. Because of the relatively low attenuation of V–base alloys, 15 MHz elastic waves were applied. The results are shown in Fig. 4, and the data are replotted in Fig. 5 in terms of the change in elastic modulus with the amount of either O or O, N in the V-4Cr-4Ti samples.

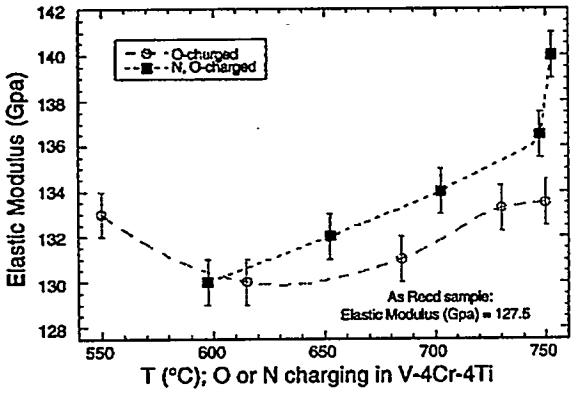

Figure 4.
Room-temperature elastic modulus of V-4Cr-4Ti vs. temperature of O or N charging.

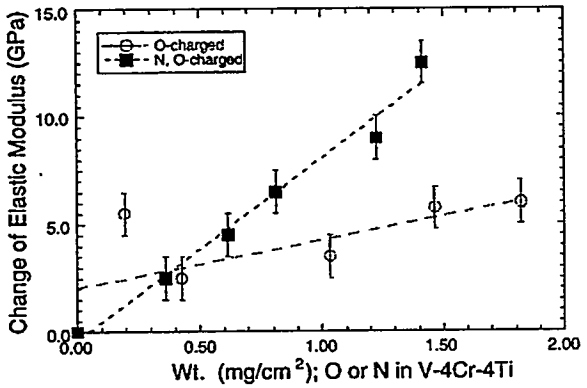

Figure 5.
Change in elastic modulus of V-4Cr-4Ti vs. weight gain during either O or O, N charging.

CONCLUSIONS

Incorporation of O and N in the surface of V-Ti-Cr alloys produced a high degree of hardening in the alloys. X-ray diffraction indicated a phase transformation from body–centered–cubic (bcc) to tetragonal phase and a highly stressed lattice because of O and N incorporation. O and N atoms occupied face-centered interstitial sites and sites between corners in the bcc sublattice. Elastic modulus and Vickers hardness also increased in O– and N-enriched V-Cr-Ti alloys.

REFERENCES

[1] R. F. Mattas, B. A. Loomis, and D. L. Smith, *Vanadium Alloys for Fusion Reactor Applications,* JOM, **44**(8), 26 (1992).

[2] J. K. Keller and D. L. Douglass, *The High-Temperature Oxidation Behavior of Vanadium-Aluminum Alloys*, Oxid. Met. **36**(5/6) 439-464 (1991).

[3] J.-H. Park, Unpublished results at Argonne National Laboratory (1994).

[4] A. U. Seybolt and H. T. Sumsion, *Vanadium-Oxygen Solid Solutions*, J. Metals Trans. AIME, 292-299 (1953).

[5] J.-H. Park and J. Gazda, *Vanadium-Oxygen and Vanadium-Nitrogen Solid Solutions*, 188th Electrochemical Society Meeting, ECS Oct. 8-13, 1995, Chicago, IL.

TENSILE PROPERTIES OF V–(4–5)Cr–(4–5)Ti ALLOYS* H. M. Chung, L. Nowicki, D. Busch, and D. L. Smith (Argonne National Laboratory)

OBJECTIVE

The objective of this work is to provide a data base on the baseline tensile properties of nonirradiated V-(4–5)Cr-(4–5)Ti alloys, including a 500–kg production heat of V–4Cr–4Ti.

SUMMARY

The current focus of the U.S. program of research on V–base alloys is on V-(4-5)Cr-(4-5)Ti that contains 500–1000 wppm Si. In this paper, we present experimental results on baseline tensile properties of two laboratory–scale heats of this alloy and of a 500–kg production heat of V–4Cr–4Ti (Heat 832665) that were measured at 23–700°C. Both the production– and laboratory–scale heats of the reference alloy V–4Cr–4Ti exhibited excellent tensile properties at temperatures up to ≈650°C.

INTRODUCTION

A recently reported comprehensive data base on tensile strength and ductility of several major alloys of the V–Cr–5Ti system includes a 30–kg laboratory heat (BL–47) of the reference alloy V–4Cr–4Ti that has been known to exhibit excellent properties after irradiation with and without He generation.[1] Subsequently, a 500–kg production heat of V–4Cr–4Ti (Heat 832665) and a 15–kg laboratory heat of V–5Cr–5Ti (Heat T87) were fabricated successfully. Excellent impact properties of these new heats have been reported recently.[2–5] This report presents results of tensile tests on the three heats.

MATERIALS AND PROCEDURES

The chemical composition of the three heats of V–(4–5)Cr–(4–5)Ti used in this study is given in Table 1. In the table, electron–beam–melted raw V Heat 820630 was used to melt the ingots of both V–4Cr–4Ti Heat 832665 and V–5Cr–5Ti Heat T87. Final forms of the extruded products were 3.8–, 1.0–, and 0.3–mm–thick plates and sheets. Tensile specimens were machined from 0.7–1.0–mm–thick sheets so that the rolling direction of the sheet was parallel to the uniaxial loading direction.

Table 1. Composition of three heats of V–(4–5)Cr–(4–5)Ti

	Alloy Composition	Impurity Concentration (wt. ppm)			
Heat ID	(wt.%)	O	N	C	Si
820630	V	200	62	75	780
BL-47	V–4.1Cr–4.3Ti	350	220	200	870
832665	V–3.8Cr–3.9Ti	310	85	80	783
T87	V–4.9Cr–5.1Ti	380	89	109	545

Typically, the machined and polished specimens were annealed at 1000°C for 1 h in a high–quality vacuum before testing. This annealing condition has been found to produce optimal impact properties in the two new heats T87 and 832665[2–4] and it produced an ≈70% recrystallized structure in Charpy–impact specimens. The only secondary phase in the as–annealed specimen was a Ti(O,N,C) precipitate, ≈300–500 nm in size, which is normally observed in Ti–containing vanadium alloys with O+N+C > 400 wppm. The gauge cross section of each polished specimen was measured individually. Tensile tests were conducted at 23–700°C at a strain rate of 1.1×10^{-3} s^{-1}. High–temperature tests were conducted in a quartz cylinder that was evacuated and continuously flushed with flowing Ar. Specimen temperature was

* Work supported by U.S. Department of Energy, Office of Fusion Energy Research, under Contract W-31-109-Eng-38.

monitored with two thermocouples spot–welded on the gauge section. Reduction in area was determined from magnified SEM images of the fracture surface that was photographed perpendicular to the tensile axis.

RESULTS AND DISCUSSION

Yield strength, ultimate tensile strength, uniform elongation, total elongation, and reduction in area are shown in Figs. 1–5, respectively. Note that yield strength of the alloys was nearly constant between 200 and 700°C. Ultimate strength appears to be slightly lower at ≈250–300°C than at <200°C or >300°C. At 700°C, the yield and ultimate tensile strengths decreased only slightly.

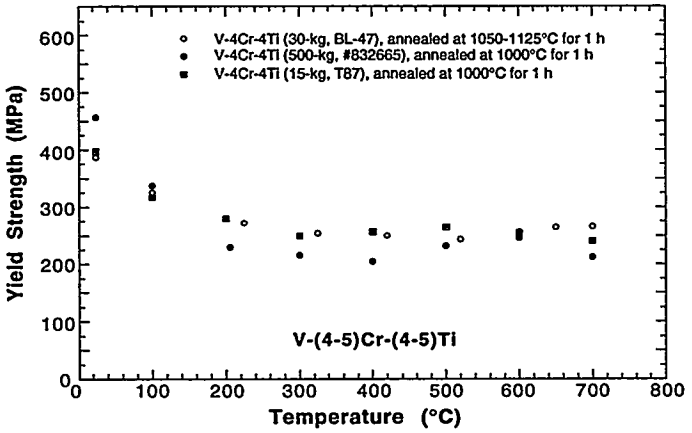

Fig. 1.
Yield strength of three heats of nonirradiated V-(4–5)Cr-(4–5)Ti alloys at 23–700°C.

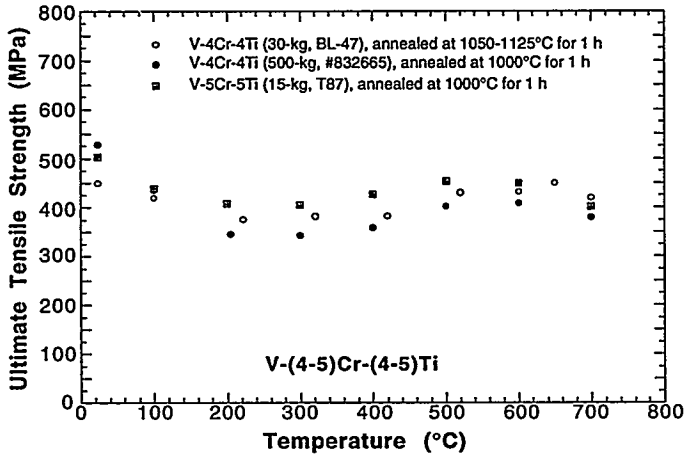

Fig. 2.
Ultimate tensile strength of three heats of nonirradiated V-(4–5)Cr-(4–5)Ti alloys at 23–700°C.

At all test temperatures in the previous studies, yield and ultimate strength of V–Cr–(4–5)Ti increased monotonically for increased chromium content, indicating the predominant effect of Cr on the tensile strength of the alloy system.[1] The results shown in Figs. 1 and 2 appear to be consistent with the findings of the previous studies, that is, for similar annealing conditions, the strength of T87 (V–4.9Cr–5.1Ti) was higher than that of 832665 (V–3.8Cr–3.9Ti). Tensile specimens of BL–47 (V–4.1Cr–4.3Ti) were annealed at temperatures somewhat higher than those of 832665. Note that the strength of BL–47 is slightly higher than that of 832665. It is not clear if this is because of the higher annealing temperature or the higher combined content of Cr and Ti (i.e., 8.4 vs. 7.7 wt.%) of BL–47.

The yield strength of V–Cr–Ti alloys at room temperature and 420–600°C could be correlated well with combined content of Cr and Ti, as shown in Fig. 6. The strength of the two new heats of V–(4–5)Cr–(4–5)Ti alloys is also consistent with the correlation shown in Fig. 6. The excessive alloying addition of Cr

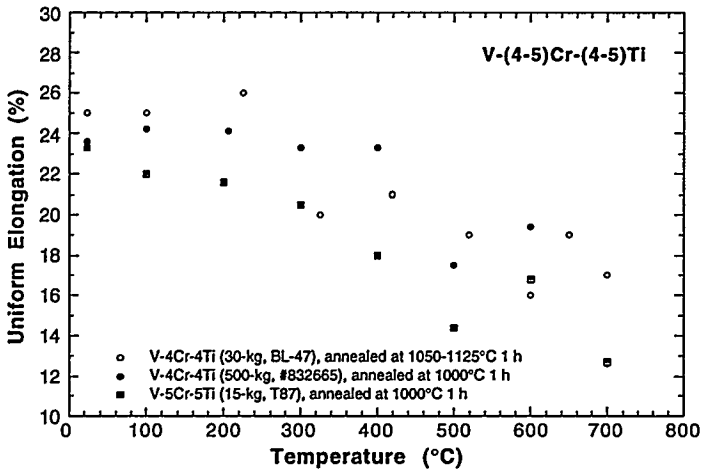

Fig. 3.
Uniform elongation of three heats of nonirradiated V-(4–5)Cr-(4–5)Ti alloys at 23–700°C.

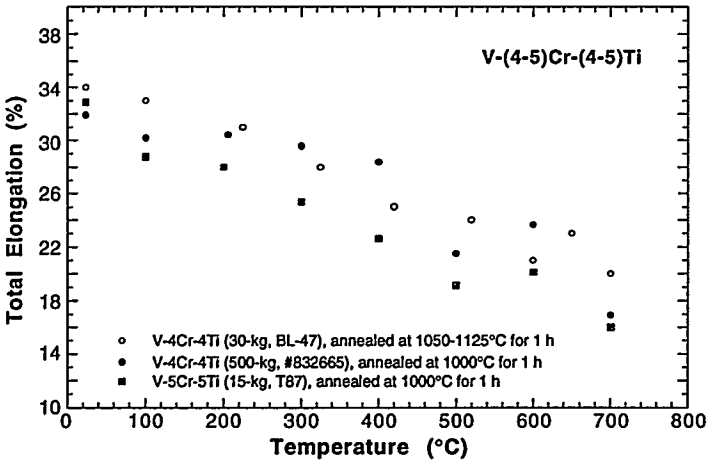

Fig. 4.
Total elongation of three heats of nonirradiated V-(4–5)Cr-(4–5)Ti alloys at 23–700°C.

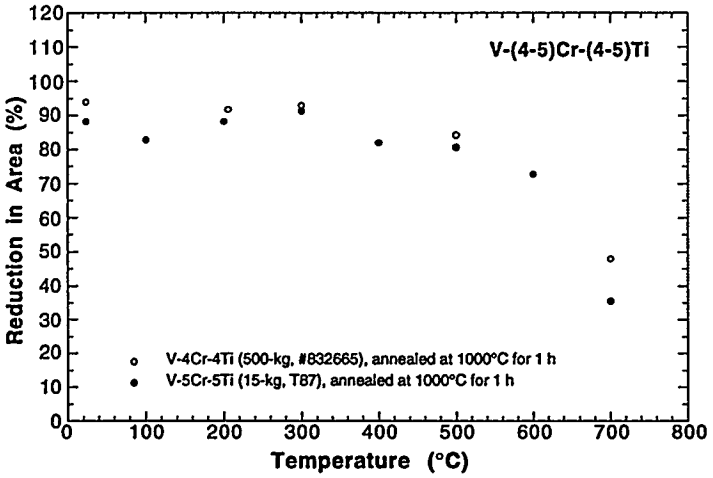

Fig. 5.
Reduction in area of V-4Cr-4Ti and V-5Cr-5Ti alloys at 23–700°C.

(≥6 wt.%) is undesirable from the standpoint of irradiation–induced degradation of material toughness. Likewise, excessive addition of titanium (≥9 wt.%) is believed to be undesirable from the standpoint of higher ductile–brittle transition temperature and, probably, thermal creep.

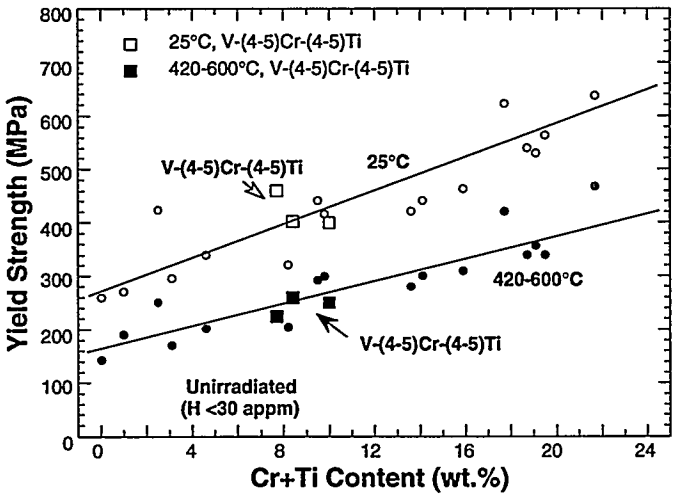

Fig. 6.
Yield strength of non–irradiated V, V–Ti, V–Cr–Ti, and V–Ti–Si alloys at 25°C and 420–600°C as function of combined Cr and Ti content.

Within the limits of data scattering, uniform and total elongation of the laboratory and production heats of V–4Cr–4Ti (Figs. 3 and 4) is similar at 20–700°C, i.e., 15–26 and 20–34%, respectively. However, uniform (12–23%) and total (16–35%) elongation of the laboratory heat of V–5Cr–5Ti is somewhat lower than that of V–4Cr–4Ti for the similar temperature range. Uniform and total elongation decreases monotonically with increasing temperature.

Reflecting the high elongation, reduction in area (Fig. 5) of the production heat of V–4Cr–4Ti and the laboratory heat of V–5Cr–5Ti was significantly large, i.e., ≈80% at 20–600°C. However, reduction in area decreased significantly to <40% at 700°C.

CONCLUSIONS

1. Baseline tensile properties of one production– and two laboratory–scale heats of V–(4–5)Cr–(4–5)Ti alloy were determined at 23–700°C. Yield strength of the alloys was nearly constant at 200–280 MPa at 200–700°C, whereas ultimate strength (330–530 MPa) was slightly lower at ≈200–250°C than at <150°C or >350°C. Yield strength of the V–(4–5)Cr–(4–5)Ti alloys at room–temperature and 420–600°C was consistent with a previously developed correlation between yield strength and the combined content of Cr and Ti of the V–(0–15)Cr–(0–20)Ti alloys.

2. Uniform and total elongation of the laboratory and production heats of V–4Cr–4Ti was similar, i.e., 15–26 and 20–34%, respectively. However, uniform (12–23%) and total (16–35%) elongation of the laboratory heat of V–5Cr–5Ti was somewhat lower than that of V–4Cr–4Ti. Uniform and total elongation decreased monotonically with increasing temperature.

3. Reduction in area of the production heat of V–4Cr–4Ti and the laboratory heat of V–5Cr–5Ti was significantly large, i.e., ≈80% at 20–600°C. However, reduction in area decreased significantly to <40% at 700°C.

4. The reference alloy V–4Cr–4Ti, identified as the most promising candidate alloy for a fusion reactor first–wall structure on the basis of its excellent resistance to irradiation–induced embrittlement, swelling, creep, and microstructural evolution, exhibited excellent baseline tensile properties at temperatures up to ≈650°C. The ratio of uniform to total elongation of the alloy remained constant at ≈0.8 regardless of test temperature, whereas the ratio of yield to ultimate tensile strength decreased monotonically from ≈0.9 at room temperature to ≈0.6 at 700°C, indicating more pronounced work hardening of the alloy at higher temperatures.

REFERENCES

1. B. A. Loomis, H. M. Chung, and D. L. Smith, "Baseline Tensile Properties of V–4Cr–4Ti Alloys," U.S. Contribution to 1994 ITER Summary Report, Task T12: Compatibility and Irradiation Testing of Vanadium Alloys, ANL/FPP/TM–287, ITER/US/95/IV MAT 10, Compiler, D. L. Smith, Argonne National Laboratory, 1995, pp. 79–85.
2. H. M. Chung, L. Nowicki, and D. L. Smith, "Effect of Annealing on Impact Properties of Production–Scale Heat of V–4Cr–4Ti," in: Fusion Reactor Materials Semiannual Progress Report for Period Ending March 31, 1995, DOE/ER-0313/18, U.S. Department of Energy, Office of Fusion Energy, July 1995, pp. 273–278.
3. H. M. Chung, L. Nowicki, and D. L. Smith, "Impact Properties of Precracked V–4Cr–4Ti Charpy Specimens," ibid., pp. 253–258.
4. H. M. Chung, L. Nowicki, and D. L. Smith, "Fabrication and Impact Properties of Laboratory–Scale Heat of V–5Cr–5Ti," ibid., pp. 259–264.
5. M. L. Grossbeck, D. J. Alexander, J. J. Henry, Jr., W. S. Eatherly, and L. T. Gibson, "Characterization of V–4Cr–4Ti Heat 832665," ibid., pp. 183–186.

Effect of Heat Treatment on Precipitation in V-5Cr-5Ti heat BL63 - **D. S. Gelles and Huaxin Li, (Pacific Northwest National Laboratory)***

OBJECTIVE

The objective of this work is to explain changes in mechanical properties of V-5Cr-5Ti heat BL63 due to variations in heat treatment.

SUMMARY

The microstructures of V-5Cr-5Ti heat BL63 are compared following heat treatments at 1125C for 1 h and 1125C for 1 h followed by 890C for 24 h. Following the 890C treatment, precipitate density was increased due to the presence of a moderate density of highly elongated particles. Microchemical analysis showed that these particles often contained both Ti and V, some particles showed minor amounts of Si, S and P, but it was also possible to show that these precipitates were enriched in O rather than C or N. Following the 1125C heat treatment, only Si was found as a minor impurity in large particles, but S could be identified at grain boundaries, which were coated with a fine distribution of precipitates. The embrittlement observed is ascribed to a combination of interstitial solid solution hardening and grain boundary embrittlement, with interstitial hardening likely the dominant factor.

PROGRESS AND STATUS

Introduction

It has been shown that some heats of V-5Cr-5Ti are sensitive to heat treatment variations.[1-4] The effects can be large. For example, heat treatment of material from Teledyne heat # 832394 (ANL code BL63) at 1125C/1 h (HT1), gives fracture toughness less than 70 kJ/m^2 when tested at 25C (due to brittle failure), and the ductile to brittle transition temperature (DBTT) as determined by testing 1/3 size Charpy impact specimens is about room temperature.[4] Properties can be recovered by a treatment of 890C/24 h (HT2).[3] The reasons for this behavior are not completely understood. Sulfur concentrations on grain boundaries were found to be higher, by a factor of six, and precipitate concentrations appeared to be decreased for the 1125/1 h treatment.[4]

The purpose of this effort was to examine precipitate structures in BL63 in more detail following HT1 and HT1+HT2 using transmission electron microscopy (TEM) and analytical electron microscopy.

Experimental Procedure

Mechanical properties specimens given HT1 and HT1+HT2, as described in references 3 and 4, were sectioned with a slow speed saw, and sections were punched to provide TEM disks 3 mm in diameter by 0.25 mm thick. Samples were thinned in a commercial twin jet polishing apparatus using a solution of 5% sulfuric acid in methanol operating at 40 V and -20C with a moderate pump speed.

Specimens were examined both in a JEOL 1200EX electron microscope operating at 120 KeV (to provide microstructural information) and a JEOL 2010F electron microscope operating at 200 KeV (to

*Pacific Northwest National Laboratory is operated for the U.S. Department of Energy by Battelle under Contract DE-AC06-76RLO 1830.

provide microchemical information). Precipitates were attacked more slowly than the grain matrix during electopolishing, making it possible to restrict precipitate composition spectra to particles hanging over the edge of the thin foil, reducing the effect of the surrounding matrix. Beam conditions on the 2010F provide an electron probe approximately 1 nm in diameter for compositional analysis.

Results

Precipitate Distributions

The microstructures of the two specimen conditions revealed differences in precipitate structures. HT1 produced generally clean microstructures, with a very low density of large precipitates, often associated with grain boundaries and triple points. However, unusual contrast was observed on some grain boundaries, indicative of fine precipitation. The HT1+HT2 condition contained a higher density of precipitate particles, generally decorating grain boundaries, but also in groups in the matrix. Particles in the matrix were generally rod shaped, but at grain boundaries they were more globular forming complex particle arrays. As precipitation is generally coarser following heat treatment at higher temperatures, it is possible that the fine precipitate found at grain boundaries following HT1 had formed during slow furnace cooling.

Examples of these structures are provided in Figure 1. Figures 1a and b provide low magnification examples of grain boundary structures in V-5Cr-5Ti heat BL63 following heat treatment at 1125C for 1 h and furnace cooled (HT1). Figure 1c shows particles at a grain boundary in a specimen of the same material heat treated for a further 24 h at 890C and then furnace cooled (HT1+HT2). Figures 1d, e, and f give examples of precipitate structures at higher magnification, showing the fine grain boundary structure following HT1 in Figure 1d, the coarser grain boundary structure following HT1+HT2 in Figure 1e and precipitation in the matrix following HT1+HT2 in Figure 1f.

Therefore, HT1+HT2 provides a microstructure with a higher density of second phase particles, probably at a higher volume fraction. However, the precipitate density actually on grain boundaries may be similar for the two conditions because a fine distribution of particles is found on boundaries following HT1.

Precipitate Compositions

Compositional spectra were obtained for precipitates extending over the edge of foils prepared with large perforations, to provide information on a large number of particles. Approximately eight precipitate particles were analyzed for condition HT1 and 30 for HT1+HT2. In addition, seven grain boundary areas were analyzed in condition HT1. In both cases, particles were found for each of three composition ranges, 1) high Ti with V, 2) approximately equal levels of Ti and V, and 3) high V with Ti. In both conditions, the high Ti case (1) was the most frequently observed. The statistical details are provided in Table 1. However, significant differences could be identified between the two conditions with regard to S, P, Si and O. Also of note were two flakes of material, found on the HT1 condition, that showed unusually high S content.

Table 1. Number of Precipitate Particles Examined with Observed Minor Elements noted

Treatment	# V rich	# (V,Ti)	# Ti rich
HT1	2 showing low Si, S	1 showing low Si, S	5 showing Si
HT1+HT2	9 showing O, C, Si, P, and S	5 showing C, O	17 showing O, Si, P, and S

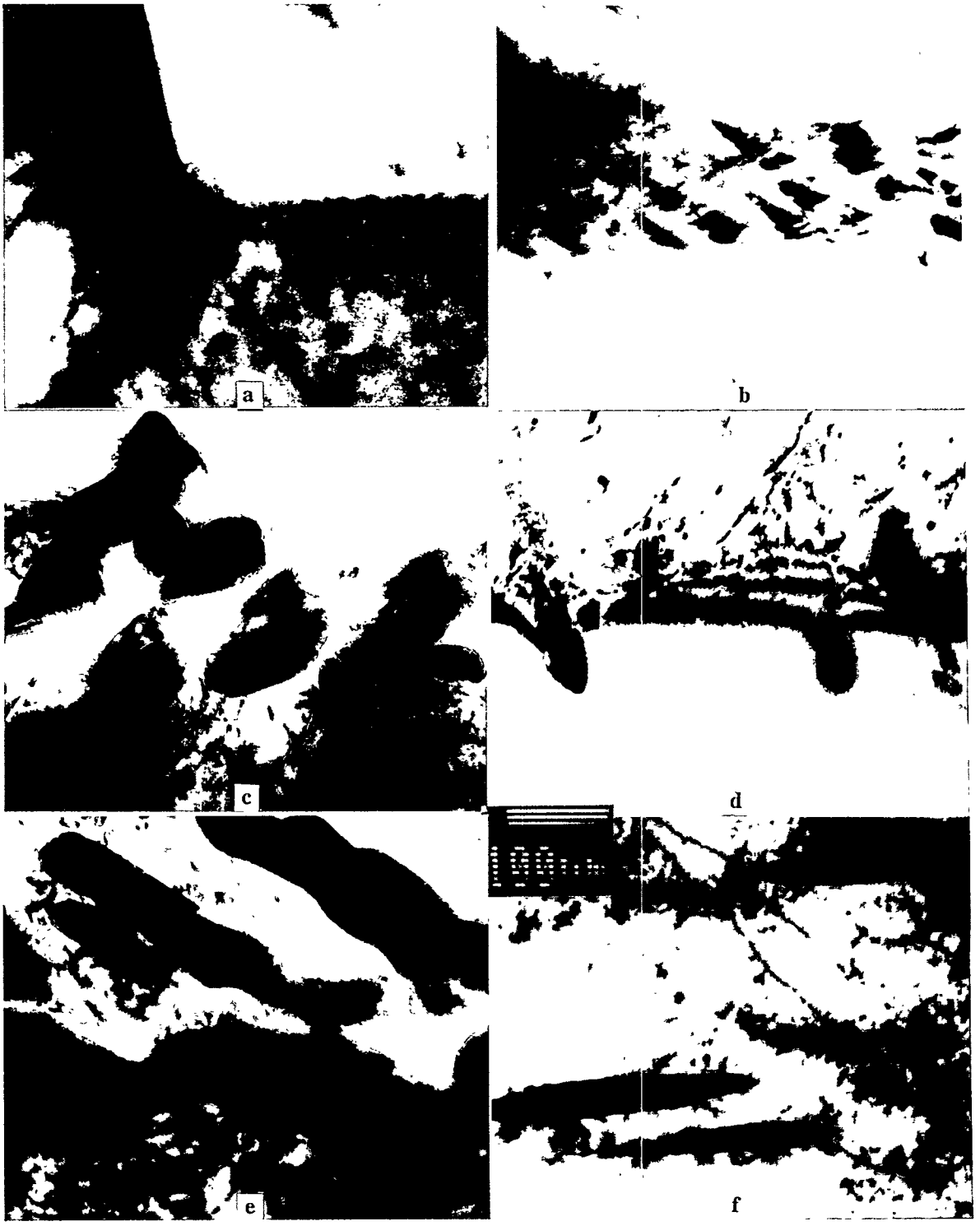

Figure 1. Precipitate structures in V-5Cr-5Ti HT1, (a), (b), and (d), and in HT1+HT2, (c), (e), and (f).

Examples of x-ray spectra for representative particles from each condition are provided in Figure 2 along with a matrix spectrum for the HT1+HT2 condition. Figures 2 a through d are from the HT1 condition and 2 e through h are from the HT1+HT2 condition. Figure 2h, showing a typical matrix spectum, should be examined first. It displays peaks typical of a material high in V, with low levels of Ti and Cr, but the V-K_b peak overlaps the Cr-K_a. The V-L and Ti-L peaks can be identified in the low energy range at 0.5 and 0.25 KeV, respectively. These L peaks provide a basis for comparison with light elements C, N, and O, which overlap this region, in effect providing information on the efficiency of the x-ray detecting system for light elements. Figure 2a shows the spectrum for a particle that contained high V levels in condition HT1. A strong C peak is indicated, but it should be noted that this peak grew relative to the other peaks during acquisition, indicating that it was largely due to C contamination, and therefore conclusions regarding C must be taken with care. Figures 2b and c show particles containing approximately equal levels of V and Ti, and high Ti, respectively. Of particular note is the fact that the peak at 0.5 KeV is larger in both cases than that in Figure 2h, indicating the presence of O. Figure 2d shows an example of a spectrum taken of a grain boundary region, which indicates the presence of S, by the peak at 2.3 Kev.

Figures 2e, 2f, and 2g show similar features for precipitates with high V, with approximately equal levels of V and Ti, and with high Ti, respectively. Three features are of particular note. The C contamination was not a problem with this specimen, so C peaks are often absent. Oxygen is indicated in all precipitates, and the O levels are significantly higher than in the HT1 spectra. Also, evidence of Si, P, and S can be found in several particles, particularly in the case of Figure 2g for the high Ti containing particle where a strong S peak can be seen at 2.3 KeV.

These results demonstrate that heat treatment at 890°C for 24 h results in higher O, S, P, and perhaps Si levels in precipitate particles, compared to the situation following heat treatment at 1125°C for 1 h. The concentration of these elements left in solid solution would therefore be significantly higher following the high temperature treatment. The results also confirm that S is found in grain boundary regions following the high temperature heat treatment, and this S may be in the form of thin layers, as indicated by the flake material identified with high sulfur.

Discussion

The present work provides two possible explanations for the observed embrittlement and reduction of toughness arising from heat treatment of V-5Cr-5Ti heat BL63 at 1125°C for 1 h: interstitial hardening and grain boundary embrittlement during furnace cooling.

We find that recovery of ductility and toughness properties is achieved by concurrent precipitation of (Ti,V)O. This removes not only Ti from solid solution, but also significant amounts of O. Precipitation would generally increase strength and reduce ductility, but the particle spacing is quite large, so the major effect is expected to occur from interstitial hardening or lack thereof. Precipitates also incorporate significant amounts of P and S, apparently reducing the concentrations in solid solution and at grain boundaries. Therefore, precipitation is expected to not only reduce interstitial hardening, but also the level of S at grain boundaries.

We also find that precipitation does develop on grain boundaries following the 1125°C treatment. The precipitate is at high density and in the form of fine particles directly associated with the boundary. As noted, it is expected that such precipitation formed on cooling rather than at temperature, in part because a much coarser structure is expected at higher temperature, but also because it is shown that a strong tendency exists to form such structures at somewhat lower temperatures, and a slow cooling process such as furnace cooling would allow such precipitates to form, but to a less extent than for a long time at temperature.

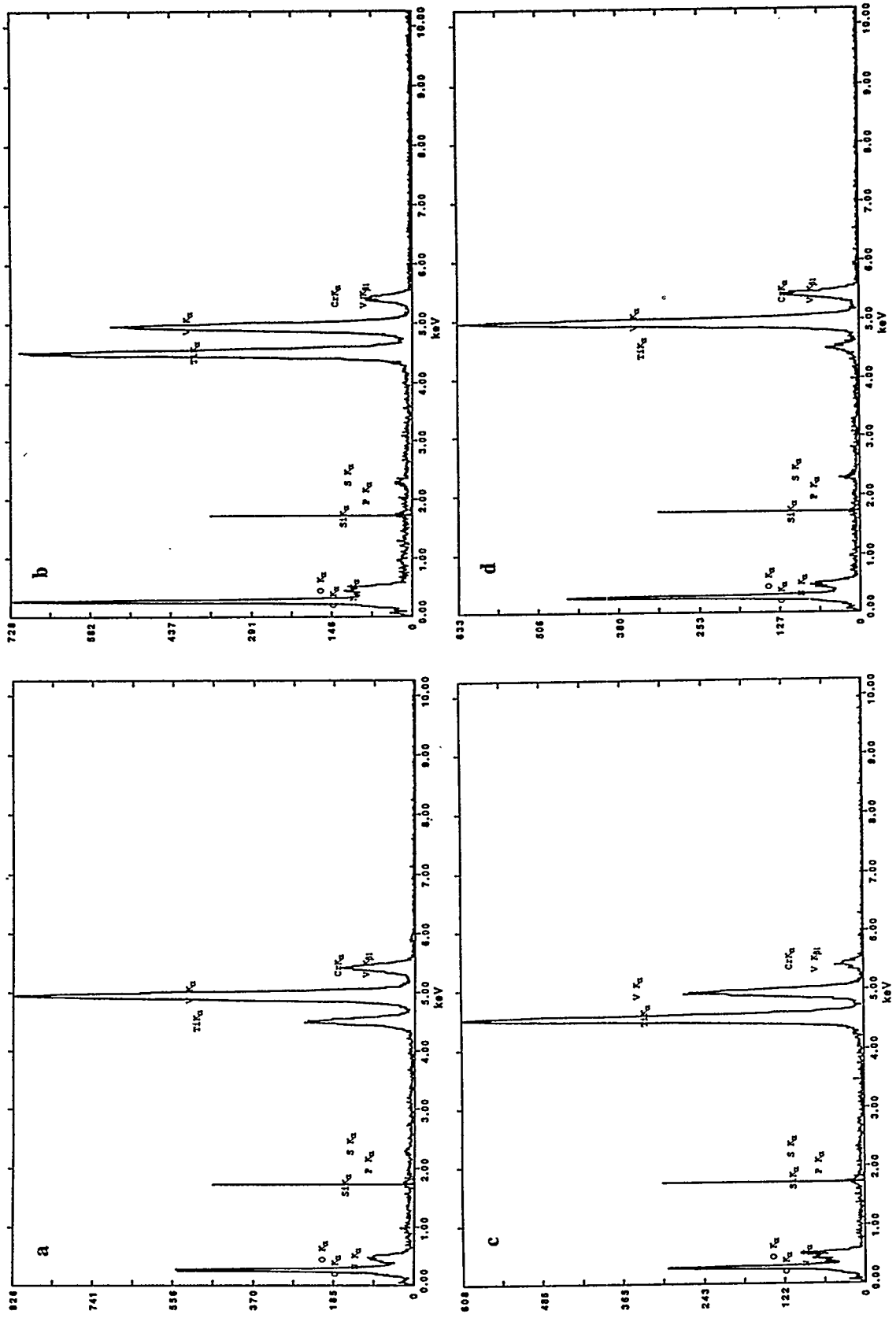

Figure 2. X-ray Spectra for a specimen with HT1 in (a), (b), (c), and (d). Continued on Next Page.

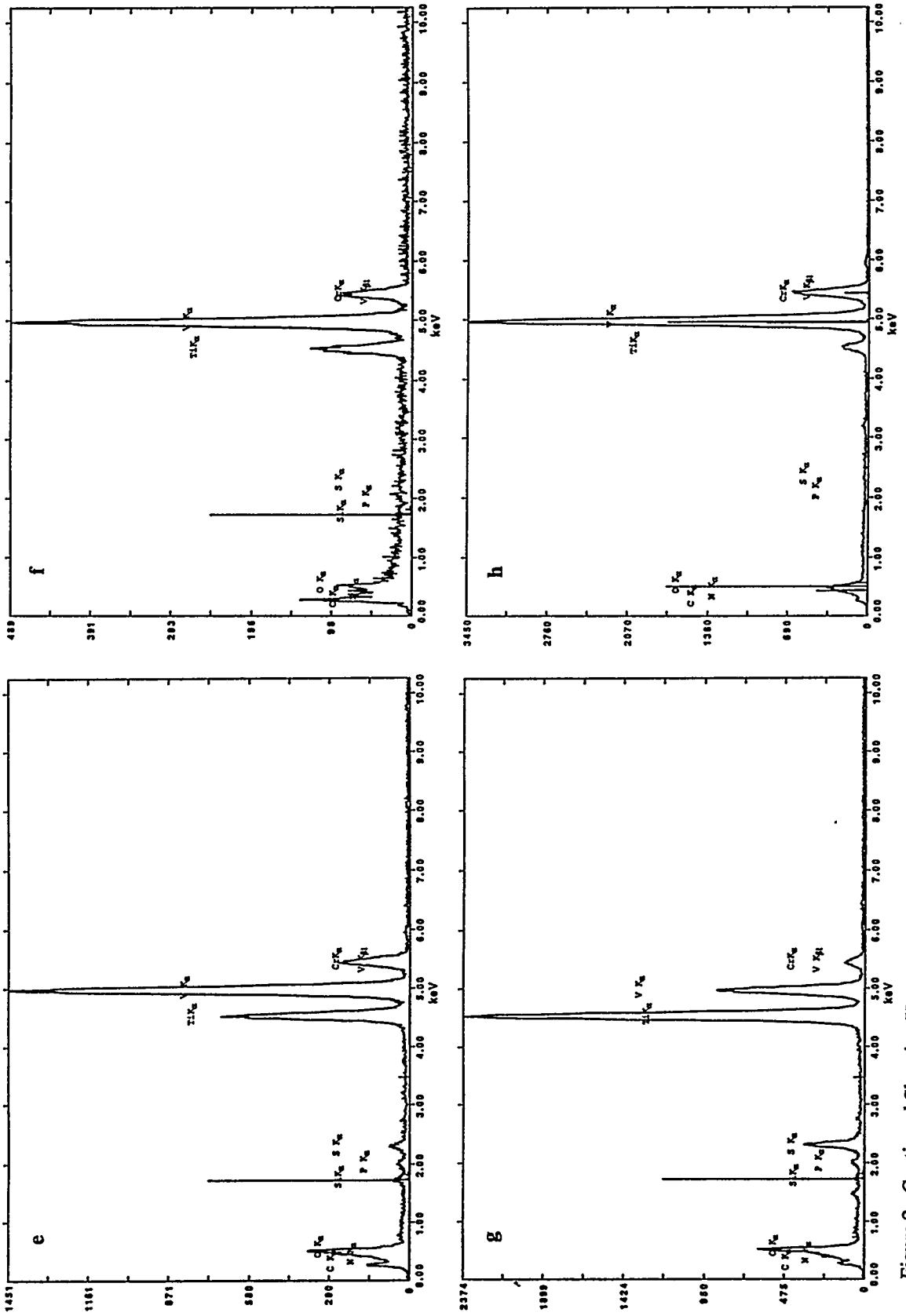

Figure 2. Continued Showing X-ray Spectra for a specimen with HT1+HT2 in (e), (f), (g), and (h).

The question can then be asked, which of these processes is more important? It can be noted that failure as a result of embrittlement consisted of both brittle transgranular cleavage and failure at grain boundaries. Therefore, both grain boundary embrittlement and hardening play a role because the failure mode changed from dimple rupture to transgranular cleavage. As interstitial hardening can explain both cleavage and intergranular features whereas grain boundary embrittlement cannot, it is anticipated that precipitation of (Ti,V)O is the more important process because it reduces the levels of interstitial O available for solid solution hardening.

CONCLUSIONS

The microstructures of two conditions of V-5Cr-5Ti heat BL63 have been compared to explain the embrittlement arising from heat treatment at 1125°C for 1 h (HT1) and the recovery of ductility and toughness from heat treatment at 890°C for 24 h (HT1+HT2). Differences in precipitation are found between the two conditions such that more precipitation, consisting of (Ti,V)O and containing Si, P and S, develops at 890°C and a high density of fine precipitates is found on grain boundaries following heat treatment at 1125°C. This grain boundary precipitation is believed to develop during furnace cooling. Enhanced sulfur concentrations are confirmed following the 1125°C heat treatment. The embrittlement is ascribed to a combination of interstitial solid solution hardening and grain boundary embrittlement, with interstitial hardening likely the dominant factor.

FUTURE WORK

This effort will continue as further specimens are available.

REFERENCES

1. H. M. Chung, J. Gazda, L. J. Nowicki, J. E. Sanecki and D. L. Smith, DOE/ER-0313/15, 207.
2. M. L. Grossbeck, A. F. Rowcliffe and D. J. Alexander, DOE/ER-0313/16, 244.
3. H. Li, M. L. Hamilton and R. H. Jones, DOE/ER-0313/17, 165.
4. H. Li, M. L. Hamilton and R. H. Jones, DOE/ER-0313/18, 215.

KINETICS OF RECOVERY AND RECRYSTALLIZATION OF THE LARGE HEAT OF V-4Cr-4Ti

— A. N. Gubbi , A. F. Rowcliffe, W. S. Eatherly and L. T. Gibson
(Oak Ridge National Laboratory)

OBJECTIVE

The purpose of this research is to evaluate the kinetics of recovery and recrystallization, and to develop a suitable model to explain the mechanistics of recrystallization of vanadium alloys.

SUMMARY

A series of slow cycle and rapid cycle anneals was carried out on the large heat of V-4Cr-4Ti alloy (heat 832665). Also, a differential scanning calorimetry (DSC) study was initiated on the samples of the same alloy. The recovery and recrystallization phenomena of V-4Cr-4Ti in slow cycle annealing were quite different from that observed in rapid cycle annealing. The large driving force for recrystallization due to rapid heating resulted in the first nuclei appearing after only 1 min at 1000°C. There was a two-stage hardness reduction; the first stage involved recovery due to cell formation and annihilation of dislocations, and second stage was associated with the growth of recrystallization nuclei. This is consistent with results obtained from the DSC in which there was a broad exothermic peak from ~200° to 800°C due to recovery followed by a sharp exotherm associated with recrystallization. The activation energy for recrystallization for V-4Cr-4Ti, which was determined as 576 ± 75, kJ/mole is significantly higher than that for pure V, and is thought to be related to Ti and Cr in solid solution.

INTRODUCTION

Vanadium alloys with Cr and Ti contents ranging from 3 to 6 wt. % have been proposed as possible candidate materials for the first wall/blanket structure in a demonstration reactor.[1-4] More recently, it was concluded by researchers in the U.S.[5] that a V-4Cr-4Ti alloy has an optimum combination of creep and fracture properties, and resistance to irradiation-induced swelling and embrittlement. Using plate material from a 500 kg heat of V-4Cr-4Ti prepared by Teledyne Wah Chang (TWCA), Albany, Oregon, the U.S. fusion materials program is engaged in a broad study of physical and mechanical properties, gaseous and liquid metal compatibility, insulating coatings, and irradiation performance. The work reported here was undertaken to provide an understanding of recovery, recrystallization, and precipitation behavior in support of efforts to further improve strength and creep properties and swelling resistance.

EXPERIMENTAL PROCEDURE

Specimens for TEM and optical metallography were prepared from the 500 kg heat of V-4Cr-4Ti using 1.02-mm-thick sheet supplied by TWCA in a ~40% cold-worked condition. Three types of annealing study were carried out to investigate recovery, recrystallization and precipitation kinetics.

(a) Slow cycle annealing: Conventional heat treatments were carried out in a tungsten element furnace with a vacuum better than 1×10^{-6} torr ($<10^{-4}$ Pa). Temperatures ranged from 900° to 1100°C for times ranging from 1 to 4 hours. The time to reach temperature and the time for subsequent cool-down was approximately 120 minutes.

(b) Rapid cycle annealing: Specimens were encapsulated in quartz tubes under a vacuum of $\sim 10^{-5}$ torr (10^{-3} Pa) and annealed in an induction heating system capable of reaching a temperature of 1200°C in 60 to 80 seconds with a temperature control of ± 5°C. A thermocouple was fixed in contact with the quartz tube. The rapid cycle annealing was carried out at 1000°C for times from 60 s to 3600 s. Following the anneal, the quartz capsule was quenched into ice-cold water to produce a cool-down time of 1 to 2 seconds.

(c) Differential scanning calorimetry: This was carried out in a Stanton-Redcroft apparatus using 5 mm diameter disks prepared from the ~1.0 mm thick sheet. Heat flow measurements were obtained with

heating rates of 0.167 to 0.667°C/s for temperatures up to 1300°C. Three disks were used in each anneal cycle to increase the heat release rate. The same mass of fully annealed material was used as a reference. These anneals were carried out in an atmosphere of high purity flowing argon.

RESULTS

Slow cycle annealing

The microstructure of as-rolled plate consisted of elongated grains and precipitate particles, primarily titanium oxycarbonitrides, which were aligned into stringers during the initial hot working operations. The initial hardness was 200 ± 5 DPH. Hardness is plotted as a function of time for various temperatures in Fig. 1. After 1 hour at 900°C, sub-grains ~1 μm diameter developed within the original elongated grain structure. With increasing annealing time the residual dislocation density within the sub-grains continued to decrease and after 4 hours a few recrystallized grain nuclei could be detected. No additional precipitation at grain boundaries or within the sub-grains could be detected for 1- and 4-h anneals at 900°C.

At 950°C the hardness dropped rapidly to ~155 DPH after only 1 hour at temperature (Fig. 1). New recrystallized grains appeared and it was estimated that at this point the material was approximately 10% recrystallized (Fig. 2). After 4 hours, the hardness dropped to its minimum value of ~145 DPH, with recrystallization about 30 to 40% complete. The remaining un-recrystallized regions consisted of well developed sub-grains with a low dislocation density; no additional precipitation could be detected following any of the treatments at 950°C.

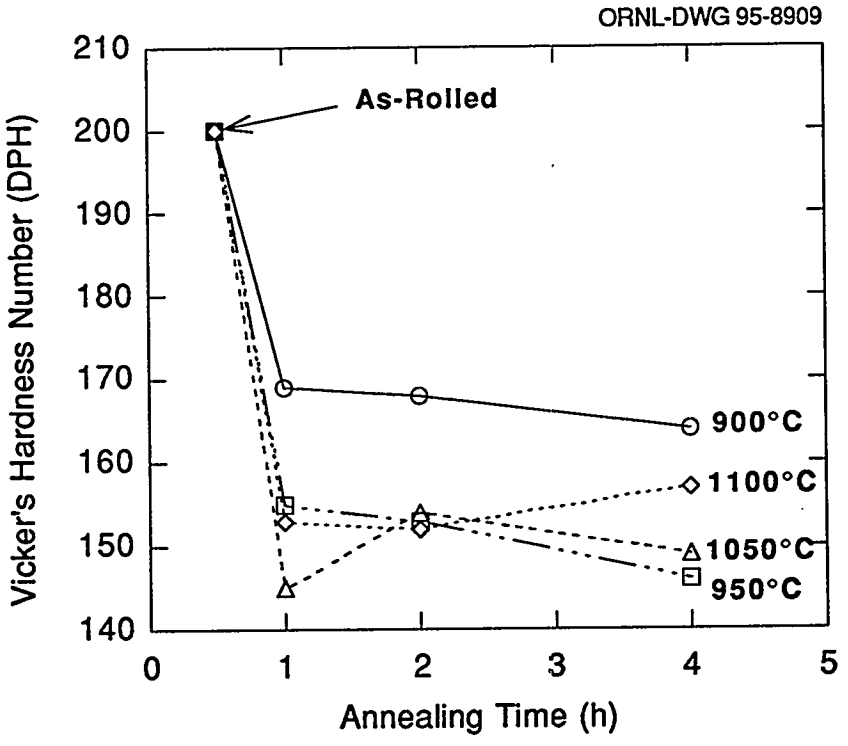

Figure 1. Microhardness as a function of annealing time for various temperatures for V-4Cr-4Ti

ORNL-DWG 95-8910

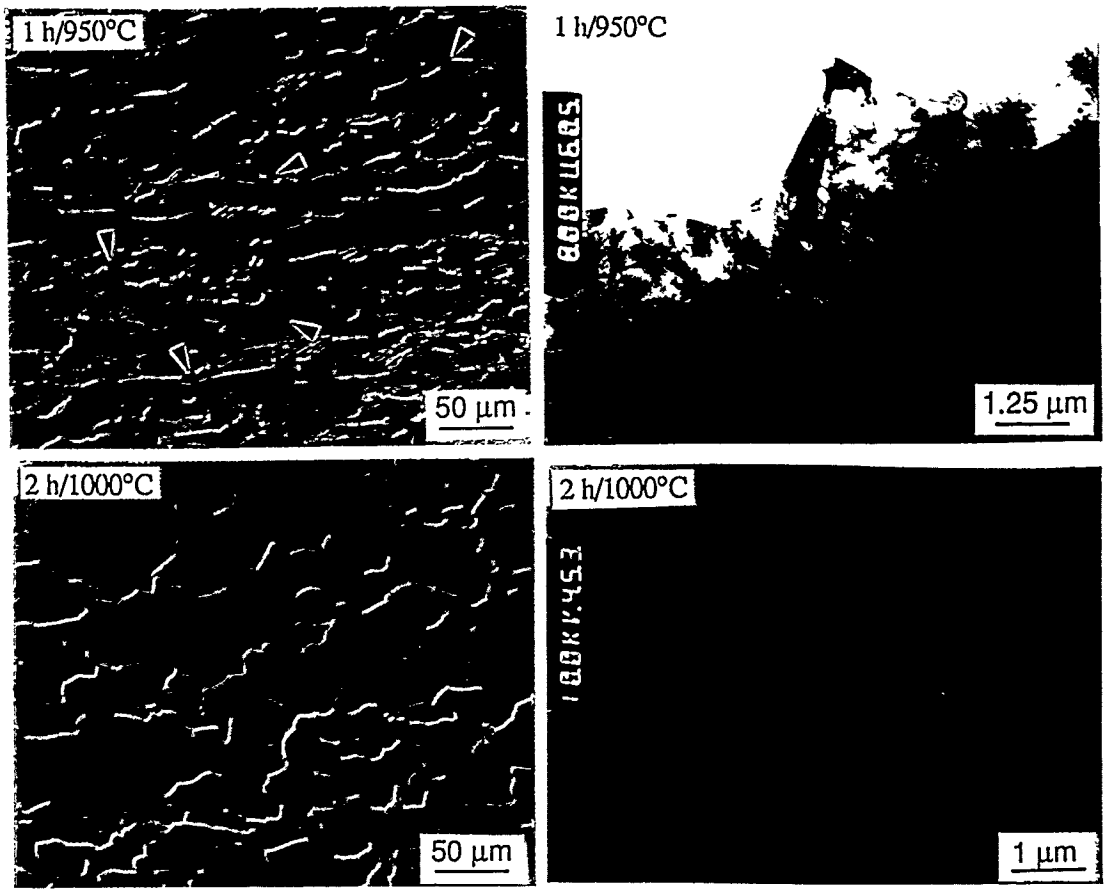

Figure 2. Optical and TEM microstructures at 950° and 1000°C for the large heat of V-4Cr-4Ti. The arrow heads indicate nuclei appearing at pre-existing grain boundaries.

Recrystallization occurred rapidly at 1000°C and was complete after 2 hours (Fig. 2); all sub-grains were consumed, leaving a low density of individual dislocations. After annealing, many of the new grain boundaries contained small titanium oxycarbonitride particles which had precipitated during the cool-down from 1000°C.

After a 1 h anneal at 1050°C, recrystallization was complete; the microstructure consisted primarily of new equiaxed grains interspersed with larger grains which retained their original elongated shape. The latter were probably old grains which had undergone complete recovery without being swept by new migrating grain boundaries. New grain boundaries contained a dispersion of fine (0.06 to 0.2 µ) titanium oxycarbonitride particles. At 1100°C, recrystallization occurred rapidly followed by development of a bi-modal grain structure. Grain growth was restricted in the vicinity of the bands of coarse oxycarbonitrides produced
during the initial stages of processing. After annealing for 4 hours, the hardness was significantly higher than after annealing for 2 hours, probably due to some pick-up of interstitial elements from the furnace atmosphere.

Rapid cycle annealing

Figure 3 shows the variation in hardness with annealing times for samples rapidly heated to 1000°C and quenched after holding for the time shown. Hardness dropped rapidly in the first 2 minutes from 200 DPH to ~180 DPH. During the next 8 minutes at 1000°C, very little change in hardness occurred. This period was followed by further softening until, after 1 hour at temperature, the minimum hardness value of ~150 DPH was approached. Optical metallography and TEM examination showed that the initial rapid drop in

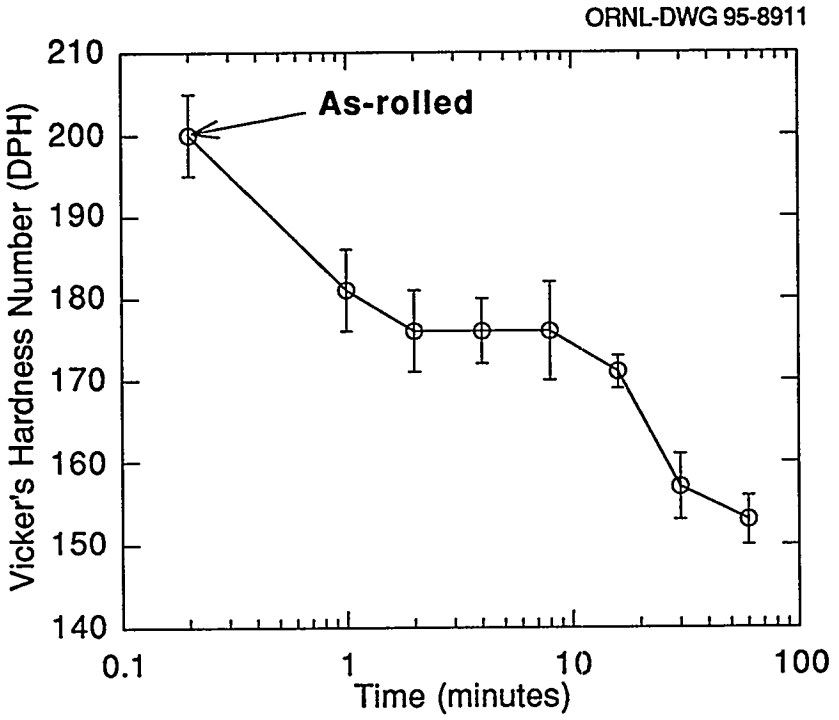

Figure 3. Microhardness as a function of annealing time for V-4Cr-4Ti

hardness during the first minute was entirely due to recovery of the cold worked dislocation structure into a system of cells which still contained a fairly high dislocation density. However, a small number of randomly occurring subrains (1 to 2 μm diameter) were almost completely free of dislocations and it is believed that these are the nuclei for recrystallization. During the 480 to 600-s period where the hardness remains fairly constant, the sub-grain structure became better developed and the number of recrystallization nuclei increased. The subsequent period of decreasing hardness with annealing time was associated with the rapid growth of the recrystallization nuclei, which expanded to consume the remaining sub-structure.

Differential scanning calorimetry

Differential scanning calorimetry has been widely used to provide kinetic information on solid state reactions such as recovery, recrystallization, precipitation and dissolution, and radiation damage annealing[6-14]. The technique measures the difference between the heat flow required to heat the material under investigation and a thermally inert reference material. Both materials are heated at a constant rate and

the changes in heat flow due to endothermic or exothermic reactions are recorded until the reaction is complete. Kinetic parameters are obtained by plotting the peak temperature as a function of heating rate. The relationship between the heating rate ß and the peak temperature T_p is given by

$$ß = A \exp\left(-\frac{Q}{RT_p}\right)$$

where A is a transformation function and Q is the activation energy[13] which can be determined from a plot of Ln (ß) as a function of reciprocal of T_p [9].

In the present study, calorimetric measurements were carried out on the 40% cold-worked material using fully annealed samples as a reference. Heating rates ranged from 10 to 40°C per min. A typical thermogram determined for a heating rate of 20°C/min is shown in Fig. 4. A broad region of exothermic behavior with several subsidiary peaks occurs over the approximate range from 200 to 800°C. A second, more sharply defined exotherm, that is associated with recrystallization, begins at around 900°C. Gaussian curves were fitted to the recrystallization exotherms and first derivatives were obtained to determine the peak temperatures for a series of heating rates. A plot of Ln (ß) versus the reciprocal of the peak temperature is shown in Fig. 5.

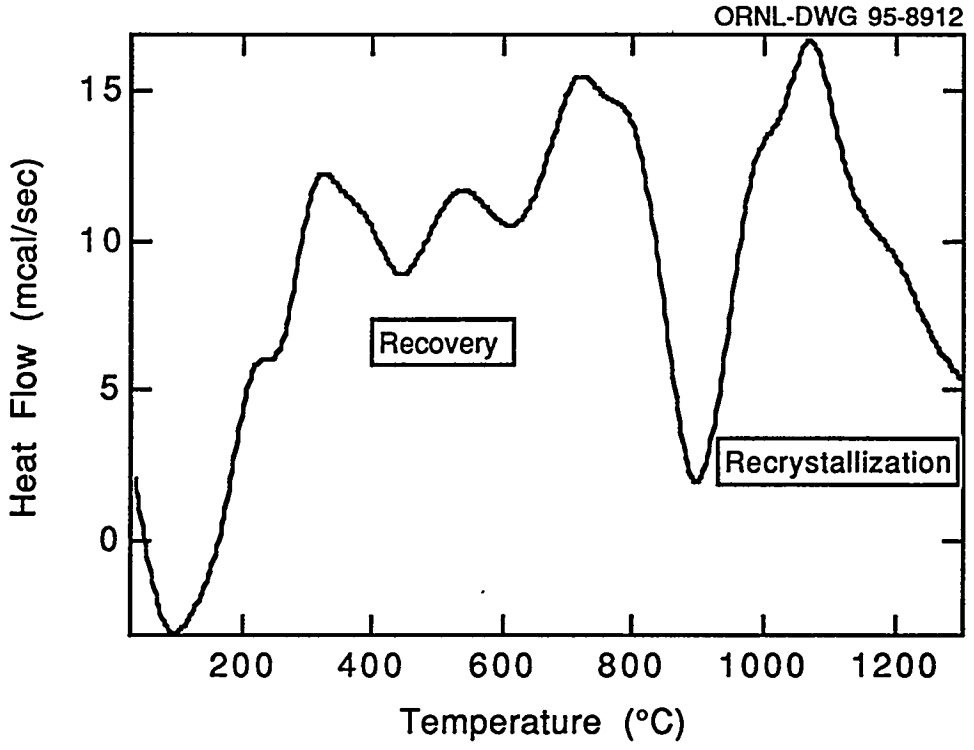

Figure 4. DSC thermogram obtained for a heating rate of 20°C/min for V-4Cr-4Ti

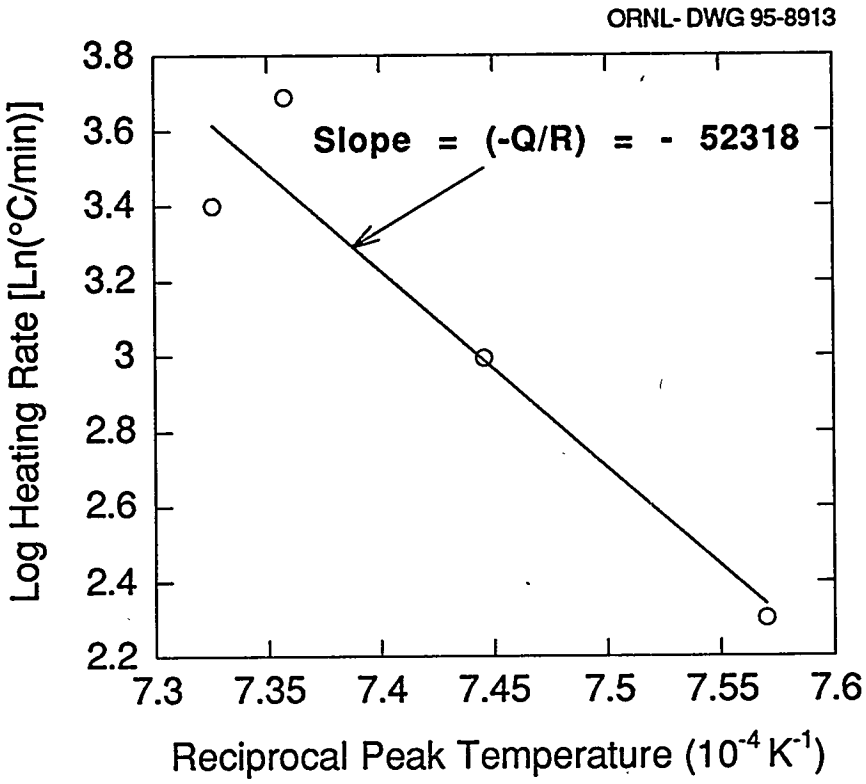

Figure 5. Log heating rate as a function of reciprocal peak temperature of recrystallization

DISCUSSION

The slow heating and cooling cycles are typically used during heat treatment of specimens for mechanical property testing and irradiation experiments, or during fabrication of components. It is not possible to define a unique recrystallization temperature. The extent of recrystallization in any given heat treatment is strongly dependent upon the initial level of deformation and upon the temperature at which that deformation was carried out. It also depends upon the heating and cooling rate and upon the time at temperature. The slow cycle annealing study of the V-4Cr-4Ti alloy in 40% cold-worked condition showed that annealing for 1 hour produces recovery and subgrain formation at 900°C, partial recrystallization at 1000°C, full recrystallization at 1050°C, and significant grain growth at 1100°C. It is critically important to specify heat treatments in terms of the microstructures produced rather than simply quoting the time at temperature. It has been shown in companion studies[15] that Charpy impact properties depend upon microstructure, as well as upon the distribution and concentration of interstitial elements; the resistance to transgranular cleavage at low temperatures is greater when the microstructure contains a high proportion of recovered subgrains.

The rapid cycle annealing (in which the annealing temperature is reached in ~30 to 40 s gives a better definition of the kinetics of recovery and recrystallization. Because of the rapid heating rate there is a large driving force for the formation of recrystallization nuclei, and the first nuclei are detected after only 1 minute at 1000°C. Following the initial hardness reduction due to dislocation recovery, there is a period during which further nuclei develop, unaccompanied by any significant change in hardness. This is

followed by a second stage of hardness reduction associated with the rapid growth of recrystallization nuclei.

The differential scanning calorimetry measurements show an exothermic recovery process beginning in the vicinity of 200°C. A hardness recovery process at ~200°C in 85% CW V-4Cr-4Ti was reported by Loomis, et al[16], followed by several minima and maxima in hardness with increasing annealing temperature. The low temperature maxima was tentatively ascribed to the diffusion of carbon, oxygen, hydrogen, and nitrogen to dislocations and the low temperature recovery was ascribed to evolution of hydrogen, and/or removal of oxygen, nitrogen and carbon from solid solution. The interstitial species are highly mobile at these temperatures[17] and the strong interaction between interstitials and dislocations is evidenced by the strain-aging phenomena at ~100°C described by Edington, et al.[18]. Thus, the broad exothermic recovery region between 200 and 800°C (Fig. 4) probably encompasses contributions from several processes, including segregation of interstitial elements to dislocations, annihilation of vacancies, and the climb and annihilation of dislocations. The second, more well defined exothermic peak is ascribed to recrystallization. This is consistent with the observation from the rapid cycle anneal of two fairly distinct stages of hardness recovery separated by a recrystallization incubation period where very little hardness recovery occurs.

From the plot of Fig. 5, the activation energy for recrystallization is determined to be 576 ± 75 kJ/mole. This value is significantly greater than the value of 397 kJ/mole reported by Loria et al[19] for recrystallization in pure V, and the activation energy of 309 kJ/mole for self-diffusion in V single crystals reported by Pelleg[20]. The higher value determined here is thought to be related to the presence of Ti and Cr in solid solution, although some influence of un-dissolved titanium oxycarbonitrides is possible.

CONCLUSIONS

The recovery and recrystallization phenomena of V-4Cr-4Ti in slow cycle annealing are quite different from that observed in rapid cycle annealing. The large driving force for recrystallization due to rapid heating results in first nuclei appearing after only 1 min at 1000°C. There is a two-stage hardness reduction; the first stage involves recovery due to cell formation and annihilation of dislocations, and second stage is associated with the growth of recrystallization nuclei. This is consistent with results obtained from the differential scanning calorimetry in which there is a broad exothermic peak from ~200° to 800°C due to recovery followed by a sharp exotherm associated with recrystallization. The activation energy for recrystallization for V-4Cr-4Ti, which is determined as 576 ± 75, kJ/mole is significantly higher than that for pure V, and is thought to be related to Ti and Cr in solid solution.

ACKNOWLEDGMENT

This research is sponsored by the Office of Fusion Energy, U. S. Department of Energy, under contract DE-AC05-84OR21400 with Lockheed Martin. We thank W. D. Porter for doing DSC analysis. This research was supported in part by an appointment (ANG) to the Oak Ridge National Laboratory Postdoctoral Research Associates Program administered jointly by the Oak Ridge National Laboratory and the Oak Ridge Institute for Science and Education.

REFERENCES

[1] B. A. Loomis and D. L. Smith, J. Nucl. Matls., 179-181 (1991), pp 783-786.

[2] B. A. Loomis, D. L. Smith, and F. A Garner, J. Nucl. Matls., 179-181 (1991), pp 771-776.

[3] H. M. Chung and D. L. Smith, J. Nucl. Matls., 191-194 (1992), pp 942-947.

[4] B. A. Loomis, L. J. Nowicki, J. Gazda, and D. L. Smith, Fusion Reactor Materials Semiannual Progress Report, DOE/ER-0313/14, March 31, 1993, pp 318-325.

[5] B. A. Loomis, H. M. Chung, L. J. Nowicki, and D. L. Smith, J. Nucl. Matls., 212-215 (1994), pp 799-803.

[6] A. Lucci and M. Tamanini, Thermochim. Acta, 13 (1975) pp 147-163.

[7] W. H. Hildegrandt, Metall. Trans.A, Vol. 10A, August 1979, pp 1045-1048.

[8] C. García Cordovilla and E. Louis, Scripta. Met., Vol. 18, 1984, pp 549-553.

[9] K. H. Schönborn and F. Haessner, Thermochim. Acta, 86 (1985), pp 305-320.

[10] J. Lendvai, G. Honyek, A. Juhàsz and I. Kovàcs, Scripta. Met., Vol. 19, 1985, pp 943-946.

[11] C. García Cordovilla and E. Louis, J. Mat. Sci., 21, 1986, pp 971-979.

[12] J. M. Howe, Metall. Trans.A, Vol. 17A, April 1986, pp 593-605.

[13] A. Varschavsky, J. Mat. Sci., 26, 1991, pp 3603-3612.

[14] Mustafa Cigdem, Z. Meallkd., 84, 1993, 10, pp 725-728.

[15] A. N. Gubbi, A. F. Rowcliffe, D. J. Alexander, M. L. Grossbeck & W. S. Eatherly, Fusion Reactor Materials Semiannual Progress Report, DOE/ER-0313/18, March 31, 1995, 203-214.

[16] H. M. Chung, H.-C. Tsai, D. L. Smith, R. Peterson, C. Curtis, C. Wojcik, and R. Kinney, Fusion Reactor Materials Semiannual Progress Report, DOE/ER-0313/17, September 30, 1994, 178-182.

[17] R. W. Powers and Margaret V. Doyle, Acta Metall., Vol. 6, October 1958, pp 643-646.

[18] J. W. Edington, T. C. Lindley, and R. E. Smallman, Acta Metall., Vol. 12, September 1964, pp 1025-1031.

[19] R. E. Gold, D. L. Harrod, R. L. Ammon, P. W. Buckman, Jr., and R. C. Svedberg, Final Report on Technical Assessment of Vanadium Alloys for Fusion Reactor Applications, Westinghouse Electric Corporation, April 1978.

[20] J. Pelleg, Phil. Mag., Vol. 29, 1974, pp 383-393.

EFFECT OF Cr AND TI CONTENTS ON THE RECOVERY, RECRYSTALLIZATION, AND MECHANICAL PROPERTIES OF VANADIUM ALLOYS — A. N. Gubbi, A. F. Rowcliffe, D. J. Alexander, M. L. Grossbeck, W. S. Eatherly and L. T. Gibson (Oak Ridge National Laboratory)

OBJECTIVE

The aim of this work is to examine the effect of varying Cr and Ti contents on the recovery and recrystallization, and mechanical properties like yield stress, tensile strength and impact properties of small heats of vanadium alloys.

SUMMARY

A series of vacuum-anneals at temperatures from 900° to 100°C for 1 to 4 h was carried out on small heats of vanadium alloys with Cr and Ti contents ranging from 3 to 6 wt.%. The alloys examined in this work were V-3Cr-3Ti, V-4Cr-4Ti-Si, V-5Cr-5Ti, V-6Cr-3Ti and V-6Cr-6Ti. Optical microscopy, TEM and microhardness testing were conducted. Variation in Cr and Ti over the range 3 to 6 wt.% had no discernible effect on recovery/recrystallization behavior. The hardness of both recovered and recrystallized structures increased with total (Cr + Ti) content. In order to study the effect of Cr and Ti content on mechanical properties, Charpy impact testing and tensile testing were carried out on small heats of compositional variants. The V-4Cr-4Ti-Si alloy, in a fully recrystallized condition, exhibited a high level of resistance to cleavage failure with a DBTT at ~—190°C. The alloys containing higher concentrations of Cr and Ti, in a fully recrystallized condition, exhibited a DBTT at around —100°C, whereas the V-3Cr-3Ti alloy failed by pure ductile shear at liquid nitrogen temperature without any ductile-to-brittle transition. Tensile testing was conducted on SS-3 tensile specimens punched from 0.762-mm-thick plates of V-3Cr-3Ti and V-6Cr-6Ti. The tests were done in air at room temperature at strain rates ranging from 10^{-3} to 2 x 10^{-1}/s. For V-6Cr-6Ti, both the 0.2% yield stress (YS) and the ultimate tensile strength (UTS) were higher than those for V-3Cr-3Ti at all strain rates. Both YS and UTS showed a similar trend of incremental increase with strain rate for the two alloys. In the same token, both alloys exhibited an identical behavior of almost no change in uniform and total elongation up to a strain rate of 10^{-1}/s and a decrease with further increase in strain rate.

INTRODUCTION

In the early stages of the program on the development of alloys for fusion reactor applications, vanadium alloys with 3 to 6 wt.% Cr and Ti were investigated.[1-4] This composition range was subsequently narrowed down to vanadium alloys with 4 wt.% each of Cr and Ti based on the thermal creep properties, low DBTT under Charpy impact testing, resistance to swelling, and also resistance to helium- and irradiation-induced embrittlement exhibited by a laboratory-scale heat of this alloy.[5] A production-scale heat (~500-kg, heat 832665) of V-4Cr-4Ti alloy has been fabricated by Teledyne Wah Chang, Albany, Oregon (TWCA) recently. Impact data have been reported from the testing conducted on the samples machined from a warm-worked plate[6] as well as from an annealed plate.[7] Also, recovery and recrystallization behavior of this heat has been documented.[8] The present study reports the results from recovery and recrystallization study, and impact and tensile testing of the small heats of compositional variants with Ti and Cr contents ranging from 3 to 6 wt.%. These alloys will give the window for permissible ranges of Cr and Ti concentrations for consistent properties.

EXPERIMENTAL PROCEDURE

A small heat of (~15-kg melt) V-5Cr-5Ti (heat T87) was produced by Teledyne Wah Chang as per the specifications supplied by Argonne National Laboratory. Four small heats (each ~15-kg melt), V-3Cr-3Ti (heat T91), V-4Cr-4Ti-Si (heat T89), V-6Cr-3Ti (heat T92), and V-6Cr-6Ti (heat T90) were fabricated according to the specifications set by Oak Ridge National Laboratory. The samples for the recovery and recrystallization study were obtained from the rolled plates (~1.02-mm thick) of small heats. The

V-5Cr-5Ti alloy had a cold work level of approximately 40%[10] whereas the other small heats had a cold work of approximately 49%. The chemical compositions of the small heats of compositional variants have been presented elsewhere.[8]. Heat treatments were carried out on samples (for both optical metallography and TEM analysis) from 900° to 1100°C for 1 to 4 h in a vacuum better than 1×10^{-6} torr ($<10^{-4}$ Pa). Optical metallography, microhardness testing, and TEM analysis were carried out to understand the effect of temperature-time on the recovery and recrystallization of vanadium alloys.

One-third-size blunt-notch Charpy specimens (3.33 x 3.33 x 25.4 mm), with a notch that was 0.51 mm deep, with a root radius of 0.08 mm and an included angle of 30°, were obtained by electrodischarge machining from 3.81-mm-thick plates which were in a 40% warm-rolled (400°C) condition. All the specimens were oriented such that the crack could propagate parallel to the rolling direction. The machined Charpy samples were annealed at temperatures from 950° to 1050°C for 2 h in a vacuum better than 1×10^{-6} torr ($<10^{-4}$ Pa). Impact testing was carried out in a semiautomated pendulum-type impact testing system modified for subsize specimens.[9] Test temperatures employed were from –196° to 100°C with low temperatures being achieved by using liquid nitrogen. The results from the testing were fitted with a hyperbolic tangent function for determining the DBTT and upper-shelf energy. The lower-shelf energy was fixed at 0.2 J. The midpoint between the upper- and lower-shelf energy levels was considered as the DBTT. Fractography was done using a scanning electron microscope on the fracture surfaces obtained after the impact testing.

Tensile specimens (SS-3s) with a gauge length of 7.62 mm and a gauge width of 1.52 mm were punched from the as-received sheets. The punched samples were recrystallized by annealing for 2 h at 1000°C in a vacuum better than 1×10^{-6} torr ($<10^{-4}$ Pa). Tensile testing was carried out in air at room temperature at strain rates ranging from 1.1×10^{-3} to 2.2×10^{-1}/s.

RESULTS AND DISCUSSION

RECOVERY AND RECRYSTALLIZATION

The complete results from the recovery and recrystallization study on the compositional variants have been presented earlier.[8] No significant difference in recovery and recrystallization kinetics was observed among the five alloys examined. A major drop in hardness due to recovery by annihilation of dislocations and cell formation leading to nucleation of some new grains was observed for 900°C anneals. At 950°C, recrystallization proceeds from 20-30% after 1 h to 70-80% complete after 2 h. The recrystallization was almost fully complete for 1000°C anneals after 1-2 h. The grain growth was observed in all five alloys for anneals at 1050°C.

Figure 1 shows a plot of microhardness as a function of (Cr + Ti) content for alloys in a recovered (900°C) condition and in a fully recrystallized (1050°C) condition. The increasing dependence of hardness of V alloys on Cr and Ti concentration has been reported by Loomis et al.[11] and the data reported here follow the same trend. In the present data, however, there does seem to be a significant incremental step in hardness values when the combined Cr + Ti concentration exceeds ~9 wt.%. The 3Cr-3Ti, 4Cr-4Ti, and 6Cr-3Ti alloys have a minimum hardness in the range 130 to 142 DPH, whereas minimum hardness for the 5Cr-5Ti and 6Cr-6Ti alloys falls in the range 160 to 165 DPH.

IMPACT TESTING

A full report on the impact testing and fracture behavior of the compositional variants has been published earlier.[7] The 6Cr-3Ti alloy was tested with the following microstructures: recovered structure with small amount of recrystallization (after 2-h anneal at 950°C), a partially recrystallized structure (after 2-h anneal at 1000°C), and a fully recrystallized structure (after 2-h anneal at 1050°C). All the three microstructures showed a typical ductile-to-brittle transition behavior with a decrease in impact test temperature. The DBTT ranged from around –175°C for the recovered structure to around –75°C for the fully recrystallized structure which indicates that the final microstructure has a significant influence on the impact behavior.

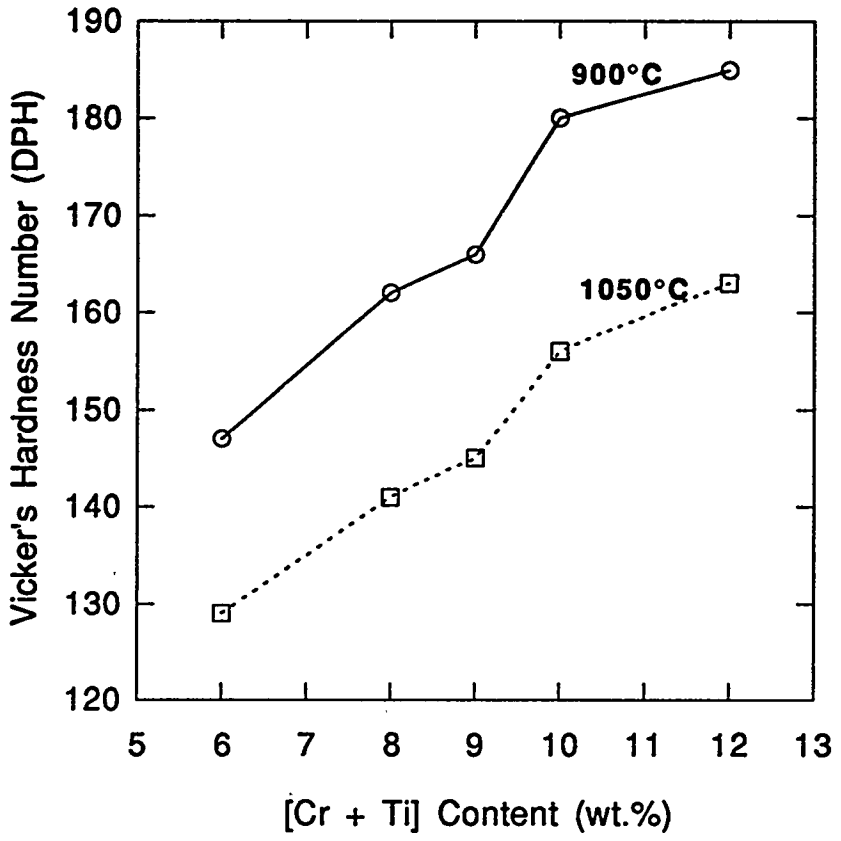

Figure 1. Variation of Hardness with (Cr + Ti) content
(All 2-h anneals)

Figure 2 shows the results from the Charpy impact testing with absorbed energy as a function of test temperature for V-5Cr-5Ti (heat T87), V-3Cr-3Ti (heat T91), V-4Cr-4Ti-Si (heat T89), V-6Cr-3Ti (heat T92), and V-6Cr-6Ti (heat T90). All the alloys were annealed at 1000°C for 2 h to produce an almost fully recrystallized microstructure. The impact results shown in Fig. 2 can be placed into two groups: one group containing alloys with lower (Cr + Ti) contents, i.e. V-3Cr-3Ti and V-4Cr-4Ti-Si, and the other group having alloys with higher (Cr + Ti) contents, i.e. V-5Cr-5Ti, V-6Cr-3Ti, and V-6Cr-6Ti. The lower (Cr + Ti)-containing alloys exhibit excellent impact behavior with V-4Cr-4Ti-Si showing DBTT of around −175°C. The V-3Cr-3Ti alloy did not show any ductile-to-brittle transition and remained quite ductile even at −196°C with shelf energy around 12 J. The higher (Cr + Ti)-containing alloys, V-5Cr-5Ti, V-6Cr-3Ti, and V-6Cr-6Ti all had a DBTT of ~ −120°C. The only difference among these alloys is in the upper shelf energy with that for V-6Cr-3Ti being around 15 J and V-5Cr-5Ti and V-6Cr-6Ti having around 11 J. In a companion article,[8] it was reported that the microhardness of the same alloys studied in the present work was grouped in a similar fashion. In the fully recrystallized conditions, the lower (Cr + Ti)-containing alloys had lower microhardness values (130-140 DPH) compared to the higher (Cr + Ti)-containing alloys which possessed higher hardness values (155-160 DPH). Thus, the results of the impact testing in conjunction with the results from recovery and recrystallization study[8] indicate that there is an incremental change in the physical and mechanical properties when the combined (Cr + Ti) content exceeds ~8 wt %.

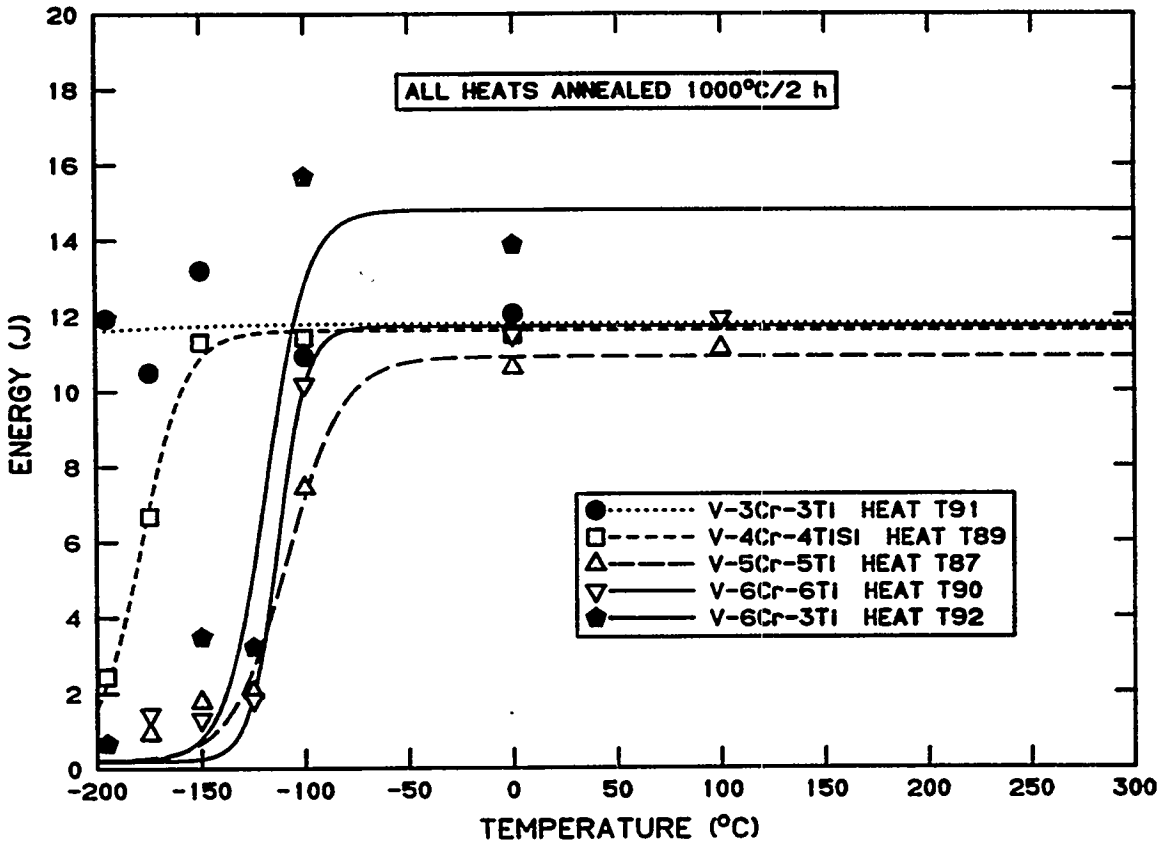

Figure 2. Third-size Charpy impact data for the Compositional Variants.

TENSILE TESTING

Figure 3 shows the variation of 0.2% yield stress (YS) with strain rate and Figure 4 shows the variation of ultimate tensile strength (UTS) with strain rate for the 3Cr-3Ti and 6Cr-6Ti alloys. Both alloys exhibited a general trend of incremental increase in YS and UTS with strain rate which is in line with the observed results for many metals. There is a marked difference in the YS and UTS of 3Cr-3Ti with those of 6Cr-6Ti for all strain rates tested. The V-6Cr-6Ti alloy was much stronger both at 0.2% strain and in UTS compared to the V-3Cr-3Ti alloy. It is useful to recall here the results of the microhardness testing from an earlier study[8] which showed that in both the recovered and fully recrystallized states, 6Cr-6Ti was much harder (160-185 DPH) than 3Cr-3Ti (130-140 DPH), see Fig. 1. Hence, the results of tensile testing in the present study in conjunction with the previous microhardness results reveal that the V-6Cr-6Ti alloy is an intrinsically stronger alloy (possibly due mainly to solid solution strengthening from higher Cr and Ti contents) compared to the V-3Cr-3Ti alloy. This strength difference may help explain the difference in the impact behavior (strain rate of ~10^3/s) observed in the previous study[7] between the V-6Cr-6Ti and V-3Cr-3Ti alloys. The V-3Cr-3Ti alloy did not show any ductile-to-brittle transition behavior whereas the V-6Cr-6Ti alloy showed a higher DBTT (compared to lower [Cr + Ti]-containing alloys) of around –120°C with both alloys exhibiting identical upper shelf energy of around 12 J, see Fig. 2.

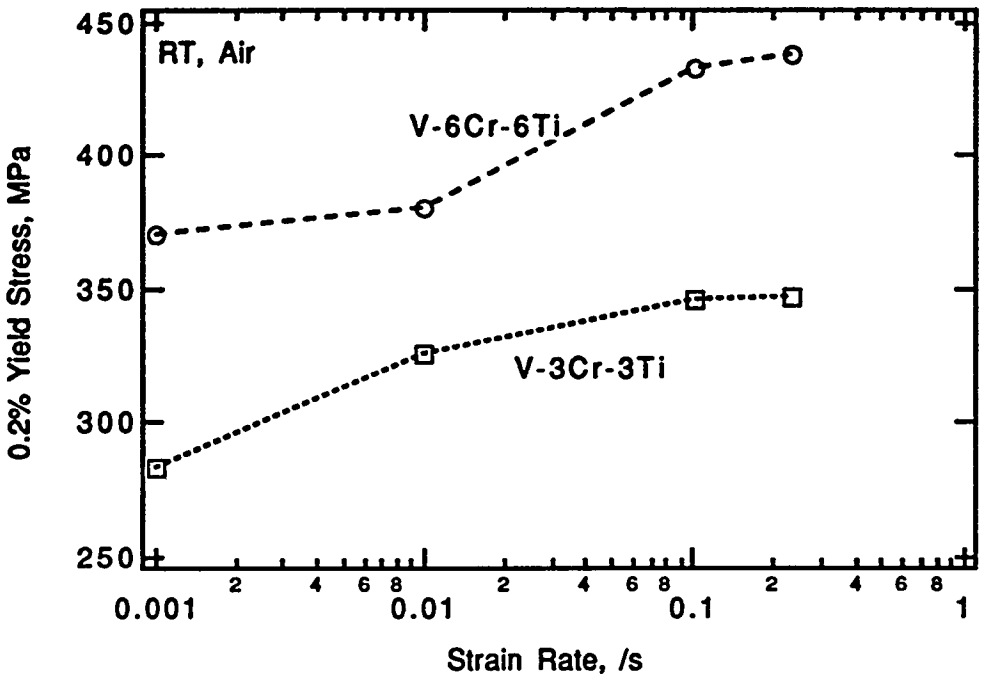

Figure 3. Variation of Yield Stress with Strain Rate for V-3Cr-3Ti and V-6Cr-6Ti.

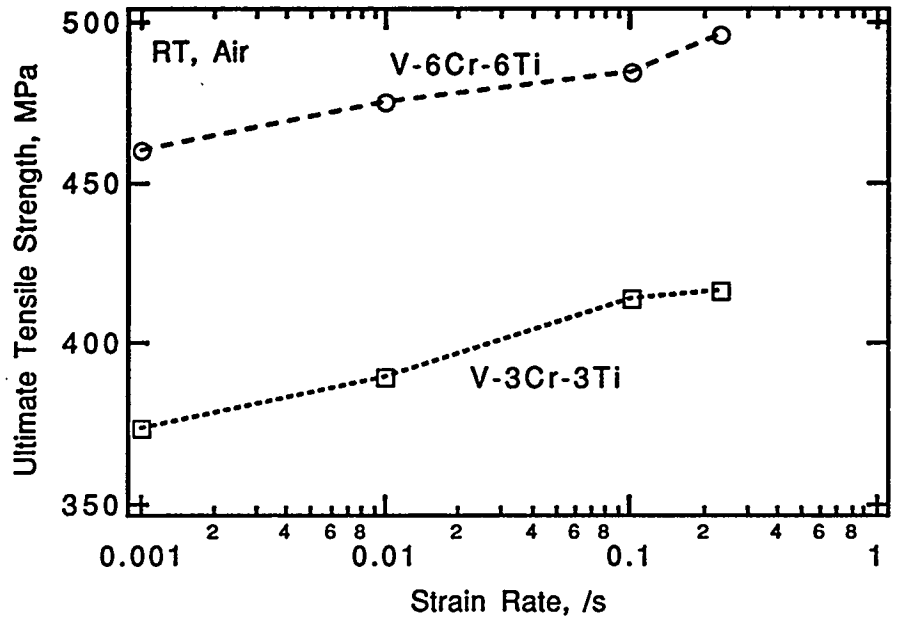

Figure 4. Variation of UTS with Strain Rate for V-3Cr-3Ti and V-6Cr-6Ti.

Figure 5 shows the variation of uniform elongation with strain rate for the 3Cr-3Ti and 6Cr-6Ti alloys. Both showed identical behavior with ductility exhibiting no change for strain rates up to 1×10^{-1}/s and a decrease for higher strain rate.

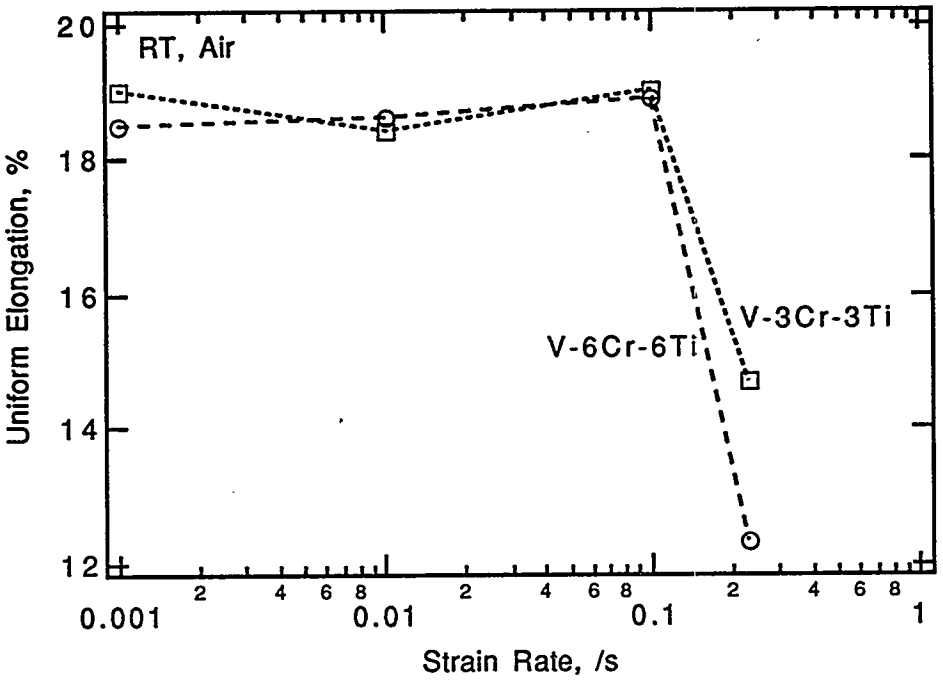

Figure 5. Uniform Elongation as a function of Strain Rate for V-3Cr-3Ti and V-6Cr-6Ti.

CONCLUSIONS

(1) Variations in Cr and Ti over the range 3 to 6 wt.% have no discernible effects on recovery and recrystallization kinetics; the hardness of both recovered and recrystallized structures increases with total (Cr + Ti) content.

(2) In a fully recrystallized microstructural condition, the Charpy impact properties of the compositional variants fall into two groups. Alloys containing a combined (Cr + Ti) content in excess of ~8 wt.% exhibit a DBTT of —120°C. Alloy containing 3Cr3Ti and 4Cr4Ti showed better resistance to cleavage fracture at low temperatures.

(3) The 0.2% yield stress and UTS, in general, increase with increase in strain rate for both 3Cr-3Ti and 6Cr-6Ti alloys. The V-6Cr-6Ti alloy was much stronger both at 0.2% strain and in UTS compared to the V-3Cr-3Ti alloy. The results of tensile testing in the present study in conjunction with the previous microhardness results reveal that the V-6Cr-6Ti alloy is an intrinsically stronger alloy (possibly due mainly to solid solution strengthening from higher Cr and Ti contents) compared to the V-3Cr-3Ti alloy.

ACKNOWLEDGMENT

This research is sponsored by the Office of Fusion Energy, U. S. Department of Energy, under contract DE-AC05-84OR21400 with Lockheed Martin. We thank W. D. Porter for doing DSC analysis. This research was supported in part by an appointment (ANG) to the Oak Ridge National Laboratory Postdoctoral Research Associates Program administered jointly by the Oak Ridge National Laboratory and the Oak Ridge Institute for Science and Education.

REFERENCES

[1] B. A. Loomis and D. L. Smith, J. Nucl. Matls., 179-181 (1991), pp 783-786.

[2] B. A. Loomis, D. L. Smith, and F. A Garner, J. Nucl. Matls., 179-181 (1991), pp 771-776.

[3] H. M. Chung and D. L. Smith, J. Nucl. Matls., 191-194 (1992), pp 942-947.

[4] B. A. Loomis, L. J. Nowicki, J. Gazda, and D. L. Smith, Fusion Reactor Materials Semiannual Progress Report, DOE/ER-0313/14, March 31, 1993, pp 318-325.

[5] B. A. Loomis, H. M. Chung, L. J. Nowicki, and D. L. Smith, J. Nucl. Matls., 212-215 (1994), pp 799-803.

[6] H. M. Chung, L. Nowicki, J. Gazda, and D. L. Smith, Fusion Reactor Materials Semiannual Progress Report, DOE/ER-0313/17, September 30, 1994.

[7] A. N. Gubbi, A. F. Rowcliffe, D. J. Alexander, M. L. Grossbeck, and W. S. Eatherly - Impact Testing and Fracture Behavior of Vanadium Alloys - Fusion Reactor Materials Semiannual Progress Report, DOE/ER-0313/18, March 31, 1995, pp 203-213.

[8] A. N. Gubbi, A. F. Rowcliffe, and W. S. Eatherly - Recovery and Recrystallization Study on Vanadium Alloys - Fusion Reactor Materials Semiannual Progress Report, DOE/ER-0313/18, March 31, 1995, pp 187-201.

[9] M. L. Grossbeck, A. F. Rowcliffe, and D. J. Alexander, Fusion Reactor Materials Semiannual Progress Report, DOE/ER-0313/16, March 31, 1994, pp 244-257.

[10] H. M. Chung, H.-C. Tsai, D. L. Smith, R. Peterson, C. Curtis, C. Wojcik, and R. Kinney, Fusion Reactor Materials Semiannual Progress Report, DOE/ER-0313/17, September 30, 1994.

[11] B. A. Loomis, J. Gazda, L. J. Nowicki, and D. L. Smith, Fusion Reactor Materials Semiannual Progress Report, DOE/ER-0313/13, September 30, 1992, pp 217-221.

Effect of Specimen Size on the Fracture Toughness of V-4Cr-4Ti - R. J. Kurtz (Pacific Northwest National Laboratory)*, Huaxin Li (Associated Western Universities-Northwest Division), and R. H. Jones (Pacific Northwest National Laboratory)*

OBJECTIVE

The purpose of this research is to characterize the effect of specimen dimensions on the fracture toughness of a low activation vanadium alloy.

SUMMARY

J-R curves were generated using the single specimen unload-compliance technique on four specimens of V-4Cr-4Ti to determine the effect of specimen dimensions on the fracture behavior. Ductile crack initiation and growth was observed in the 6.35 mm thick specimens but not in the 12.70 mm thick specimens. The J-R curves determined from these tests were not valid per ASTM validity criteria so quantitative measures of the resistance to ductile crack initiation and growth were not obtained. These data suggest that standard fracture toughness tests performed with small-scale DCT specimens may also not be valid.

PROGRESS AND STATUS

Introduction

Development of vanadium alloys for the first-wall and blanket structures of fusion power systems requires detailed information on the fracture properties in both the unirradiated and irradiated conditions. Irradiation volumes for typical neutron sources limit the in-plane dimensions of fracture toughness specimens to a few millimeters. Small-scale disk compact tension (DCT) specimens are being used [1,2] to determine the fracture toughness of irradiated V-4Cr-4Ti. A recent study [3] of the mixed-mode (I/III) fracture toughness behavior of V-5Cr-5Ti (Heat BL-63) annealed at 1125 °C for one hour and tested at room temperature (RT) and 100 °C indicated the mode I toughness was about 60 kJ/m^2 and 470 kJ/m^2, respectively. ASTM validity requirements were satisfied for the RT tests, but not for the 100 °C tests. Recent developments in vanadium alloy processing indicate the unirradiated fracture toughness will be high at RT and above. Tensile test data on unirradiated and irradiated V-4Cr-4Ti specimens [4-5] suggest that room temperature mechanical properties of unirradiated material are similar to irradiated material at about 600 °C. Thus, measurements of the fracture toughness of unirradiated V-4Cr-4Ti at room temperature will provide insight as to the validity of elevated temperature toughness measurements using small-scale DCT specimens of irradiated material. A study of the effect of in-plane and thickness dimensions on the mode I J-R curve behavior of unirradiated V-4Cr-4Ti was performed to aid the development and interpretation of results from small-scale specimens used in irradiation experiments.

Experimental Procedure

The material used in this study was V-4Cr-4Ti (Heat #832665) produced by Teledyne Wah Chang. Material fabrication details have been reported previously [6]. The material was annealed by the manufacturer for 2 hours at 1050 °C in a vacuum better than about 1.3 x 10^{-3} Pa. Compact tension test specimens in the T-L orientation were machined from 6.35 and 12.7 mm thick plates. All specimens were heat treated at 180 °C for 2 hours following machining to remove hydrogen. Table

*Operated for the U. S. Department of Energy by Battelle Memorial Institute under Contract DE-AC06-76RLO 1830.

1 gives the pertinent specimen dimensions employed in this study.

Table 1. Compact Tension Specimen Dimensions for J-R Curve Testing

Specimen ID	Width, mm	Thickness, mm	Side Groove Depth, %	Net Thickness, mm
V95 T1-2	50.80	12.70	None	12.70
V95 T2-1	50.80	6.35	10	5.08
V95 S1-2	30.48	12.70	10	10.16
V95 S2-1	30.48	6.35	10	5.08

J-R curves were generated by the single specimen unload-compliance test procedure. All tests were performed in laboratory air at 25 °C. Specimens were fatigue cracked before and after J-testing to mark the extent of ductile crack growth.

Results

Plots of the J-R curves for the 6.35 mm thick specimens are shown in Figures 1 and 2. Figure 1 presents results for the 30.48 mm wide specimen and Figure 2 gives the results for the 50 80 mm specimen. The results for the two specimens are similar. Figures 1 and 2 show J-values approaching 1500 kJ/m^2 for both specimens. ASTM validity criteria for J_{max} and Δa_{max} were violated for these tests so critical J-values for crack extension were not computed from the data.

The test results for the 12.70 mm thick specimens showed no ductile crack initiation and growth occurred. Inspection of the fracture surfaces after the test confirmed this finding. Normally the fracture toughness should decrease with increasing thickness until plane-strain conditions are reached. Under plane-strain conditions the fracture toughness will not depend on specimen thickness and therefore, constitutes a fundamental material property. The present tests were not conducted under plane-strain conditions. Thus, the fracture toughness would be expected to decrease with increasing thickness. The lack of ductile crack extension for the 12.70 mm thick samples suggests the toughness of these specimens is higher than for the thinner samples. This result is contrary to expectation.

Discussion

Elastic-plastic fracture mechanics using the J-integral is based on the concept of J dominance, where the stress and strain states near the crack tip are established by the J-level. The applicability of the J-integral is limited to high constraint crack geometries. For J to be the relevant fracture mechanics parameter controlling ductile crack initiation in the region of intense plastic deformation near the crack tip must be small relative to certain specimen dimensions such as the thickness and uncracked ligament. ASTM test procedure E 1152-87 [7] describes a standard method for determining valid J-R curves for metallic materials. This standard puts limits on the J-level and amount of ductile crack extension permitted for a measured J-R curve to be considered valid. The maximum J-integral capacity for a particular specimen is given by the smaller of:

$$J_{max} = b\sigma_Y/20, \text{ or}$$

$$J_{max} = B\sigma_Y/20$$

where σ_Y is the material flow stress (i.e., the average of the 0.2% offset tensile yield strength and the ultimate tensile strength), and B is the specimen thickness. The maximum crack extension, Δa_{max},

capacity for a specimen is given by:

$$\Delta a_{max} = 0.1 b_o$$

where b_o is the size of the initial uncracked ligament. Table 2 gives the maximum J-integral and crack extension capacities for the specimens used in this study compared to the standard DCT specimens used in irradiation experiments. The RT value of σ_Y used to generate Table 2 was 420 MPa [4]. Note the J-integral capacity of the DCT specimens is limited by their small in-plane dimensions, but the specimens used in this study are limited by their thickness dimensions. Clearly the results presented in Figures 1 and 2 are not valid J-R curves per ASTM criteria.

Thus, a critical J-value (J_{Ic}) for ductile crack initiation can not be determined from these curves. Larger test specimens or alternative analysis techniques such as those recently advanced by Edsinger, et. al. [8] may be needed to obtain valid estimates of the fracture toughness of V-4Cr-4Ti over the temperature range of interest in a fusion power system.

Table 2. Maximum J-Integral Measurement Capacities for Various Specimen Geometries

Specimen ID	J_{max}, kJ/m^2*	J_{max}, kJ/m^2**	Δa_{max}, mm
V95 T1-2	267	533	2.54
V95 T2-1	133	533	2.54
V95 S1-2	267	320	1.53
V95 S2-1	133	320	1.53
DCT-A***	75	50	0.24
DCT-B***	123	83	0.39

*Based on thickness dimension.
**Based on uncracked ligament dimension.
***Standard Fusion Materials Program DCT specimens.

CONCLUSIONS

The RT fracture toughness of V-4Cr-4Ti (Heat 832665) is very high. ASTM validity criteria for J-R curve determination were not satisfied for any of the specimens tested. These results suggest that standard fracture toughness tests performed with small-scale DCT specimens may also not meet ASTM criteria. No ductile crack extension was observed for the 12.70 mm thick specimens. This suggests the toughness of the 12.70 mm thick specimens is greater than the 6.35 mm specimens which is contrary to expectation since thicker specimens should exhibit higher constraint.

FUTURE WORK

Alternative fracture toughness measurement techniques will be investigated to determine applicability to fusion power system materials, components and structures.

REFERENCES

1. D. J. Alexander, "Fracture Toughness Measurements with Subsize Disk Compact Specimens," in Small Specimen Test Techniques Applied to Nuclear Reactor Vessel Thermal Annealing and Plant Life Extension, ASTM STP 1204, W. R. Corwin, F. M. Hagag, and W. L. Server, Eds., American Society for Testing and Materials, Philadelphia, 1993, pp. 130-142.

2. C. M. Elliott, M. Enmark, G. E. Lucas, G. R. Odette and A. Rowcliffe, "Development of Disc Compact Tension Specimens and Test Techniques for HFIR Irradiations," Journal of Nuclear Materials, 179-181, 1991, pp. 434-437.

3. H. Li, M. L. Hamilton, and R. H. Jones, "Effect of Heat Treatment on Microstructure and Fracture Toughness of a V-5Cr-5Ti Alloy," Fusion Materials Semiannual Progress Report for Period Ending September 30, 1994, DOE/ER-0313/17, pp. 165-177.

4. B. L. Loomis, L. J. Nowicki, and D. L. Smith, "Tensile Properties of Vanadium and Vanadium-Base Alloys," Fusion Materials Semiannual Progress Report for the Period Ending March 31, 1991, DOE/ER-0313/10, pp. 145-155.

5. H. M. Chung, L. J. Nowicki, D. E. Busch, and D. L. Smith, "Ductile-Brittle Transition Behavior of V-4Cr-4Ti Irradiated in the Dynamic Helium Charging Experiment," Fusion Materials Semiannual Progress Report for the Period Ending September 30, 1994, DOE/ER-0313/17, pp. 205-210.

6. H.M. Chung, H.-C. Tsai, D. L. Smith, R. Peterson, C. Curtis, C. Wojcik, and R. Kinney, "Fabrication of 500-kg Heat of V-4Cr-4Ti," Fusion Materials Semiannual Progress Report for Period Ending September 30, 1994, DOE/ER-0313/17, pp. 178-182.

7. "E 1152-87 Standard Test Method for Determining J-R Curves," Annual Book of ASTM Standards, Vol. 03.01, pp. 763-773.

8. K. Edsinger, G. R. Odette, and G. E. Lucas, "The Use of Confocal Microscopy and Fracture Reconstruction to Obtain Structurally-Relevant Fracture Parameters," in Proceedings of the IEA International Symposium on Miniaturized Specimens for Testing of Irradiated Materials, Julich, Germany, September 22 - 23, 1994.

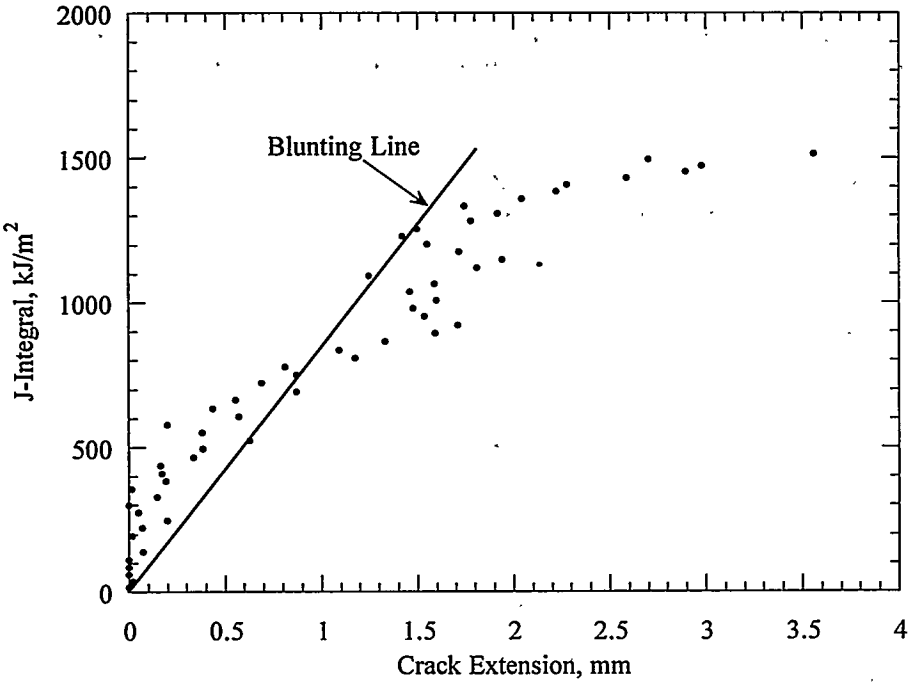

Figure 1. J-R Curve for Specimen V95 S2-1

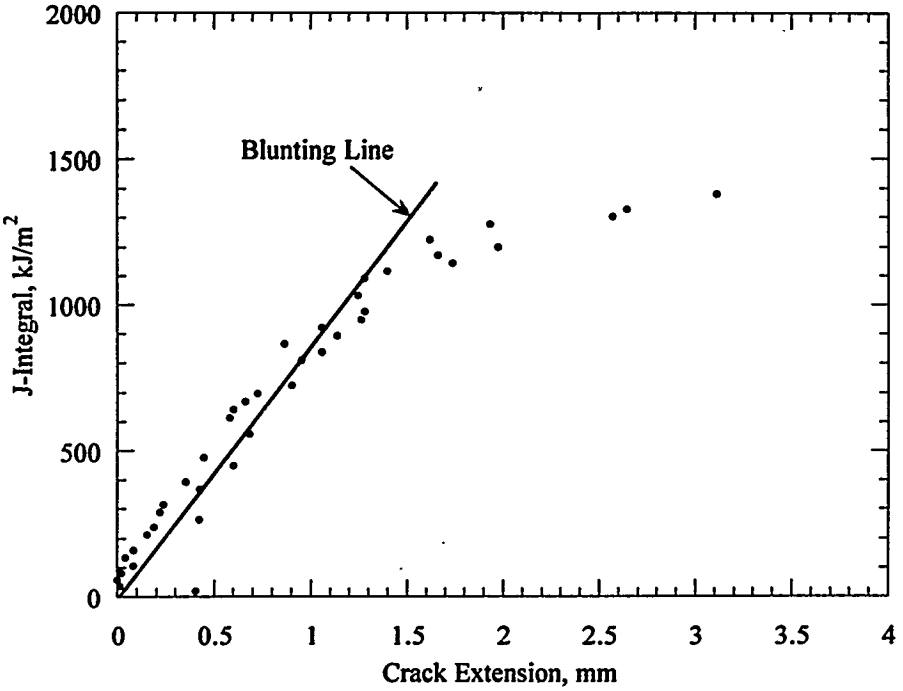

Figure 2 J-R Curve for Specimen V95 T2-1

EFFECT OF OXYGEN AND OXIDATION ON TENSILE BEHAVIOR OF V-5Cr-5Ti*

K. Natesan and W. K. Soppet (Argonne National Laboratory)

OBJECTIVE

The objectives of this task are to (a) evaluate the oxygen uptake of V-Cr-Ti alloys as a function of temperature and oxygen partial pressure in the exposure environment, (b) examine the microstructural characteristics of oxide scales and oxygen entrapped at the grain boundaries in the substrate alloys, (c) evaluate the influence of oxygen uptake on the tensile properties of the alloys at room and elevated temperatures, (d) evaluate oxidation kinetics of the alloys with aluminum-enriched surface layers, and (e) determine the effect of oxygen uptake on the tensile behavior of the alloys.

SUMMARY

Oxidation studies were conducted on V-5Cr-5Ti alloy specimens in an air environment to evaluate the oxygen uptake behavior of the alloy as a function of temperature and exposure time. The oxidation rates calculated from parabolic kinetic measurements of thermogravimetric testing and confirmed by microscopic analyses of cross sections of exposed specimens were 5, 17, and 27 μm per year after exposure at 300, 400, and 500°C, respectively. Uniaxial tensile tests were conducted at room temperature and at 500°C on preoxidized specimens of the alloy to examine the effects of oxidation and oxygen migration on tensile strength and ductility. Microstructural characteristics of several of the tested specimens were determined by electron optics techniques. Correlations were developed between tensile strength and ductility of the oxidized alloy and microstructural characteristics such as oxide thickness, depth of hardened layer, depth of intergranular fracture zone, and transverse crack length.

EXPERIMENTAL PROGRAM

The heat of vanadium alloy selected for the study had a nominal composition of V-5 wt.%Cr -5 wt.%Ti and was designated as BL-63. A sheet material of the alloy was annealed for 1 h at 1050°C prior to its use in oxidation and tensile testing. Coupon specimens measuring ≈15 x 7.5 x 1 mm were used for the oxidation studies. Oxidation experiments were conducted in air in a thermogravimetric test apparatus. The test temperatures ranged between 300 and 650°C.

Tensile specimens were fabricated according to ASTM specifications and had a gauge length of ≈19 mm and a gauge width of ≈4.5 mm. The grain size of the specimens was ≈32 μm. The specimens were preoxidized in air at 500°C for 24, 250, 600, 1000, and 2060 h prior to tensile testing in air at 500°C. Similar specimens preoxidized up to 1000 h at 500°C in air were also tensile tested at room temperature. As-annealed (control) specimens were tensile tested on an Instron machine at constant crosshead speeds between 0.0005 and 0.2 cm/min. These speeds correspond to initial strain rates in the range of 4.4×10^{-6} to 1.8×10^{-3} s^{-1}. The preoxidized specimens were tested at a strain rate of 1.8×10^{-4} s^{-1}. The test temperature was maintained within 2°C in all tests performed in air at 500°C. The specimens were loaded by means of pins that pass through holes in the grips and enlarged end sections of the specimen, thus minimizing misalignment. Total elongation was measured with a vernier caliper and by using load/elongation chart records. The fracture surfaces and longitudinal and axial cross sections of tested specimens were examined by scanning electron microscopy (SEM). In addition, Vickers hardness was measured on several of the tested specimens. Coupon specimens of the alloy that were oxidized with the tensile specimens were analyzed for bulk oxygen content by a vacuum-fusion technique.

RESULTS AND DISCUSSION

Oxidation Behavior

Oxidation of the alloy followed parabolic kinetics with time. Detailed SEM analysis (with both energy-dispersive and wavelength-dispersive analysis) of the oxidized samples showed that the outer layer was predominantly vanadium-rich oxide and the inner layer was (V,Ti) oxide. Further, X-ray diffraction of the

*Work supported by U.S. Department of Energy, Office of Fusion Energy Research, under Contract W-31-109-Eng-38.

oxides showed the outer oxide to be V_2O_5; no nitrogen or nitride phases were detected. The thickness of the oxide scale of the specimens calculated from a parabolic rate equation was in good agreement with the values determined by microscopy. The results were discussed in earlier reports (1, 2). Secondary ion mass spectrometry is presently used to obtain depth profiles for oxygen in the tested specimens.

Effect of Oxidation on Tensile Properties

To evaluate the effect of oxide scale formation and oxygen penetration into the substrate alloy, tensile behavior of the alloy was examined as a function of oxygen ingress and oxide scale formation. Specimens were exposed to air for 24-2060 h in air at 500°C and then tensile tested in air at either room temperature or 500°C at a strain rate of 1.8×10^{-4} s^{-1}.

Figure 1 shows the engineering stress/engineering strain curves at 500°C for specimens after oxidation for several exposure times up to 2060 h. Stress/strain behavior of the alloy is virtually unaffected by 24 h exposure in air at 500°C. As exposure time increases to 250 h, alloy strength increases, with some loss in tensile ductility. In the exposure period of 250-1000 h, the alloy essentially has the same ultimate tensile strength but with reductions in tensile ductility from 0.21 at 24 h exposure to 0.14 at 1000 h exposure. Further exposure of the alloy to air at 500°C causes loss of strength and tensile ductility, as evidenced by the stress/strain curve for the specimen preoxidized for 2060 h.

Figure 2 shows engineering stress/engineering strain curves obtained at room temperature for specimens after oxidation for several exposure times up to 1000 h. A significant increase in tensile strength of the alloy is seen after 24 h of oxidation. The rupture strain of the specimen decreased from ≈0.32 to 0.265 after 24 h of oxidation at 500°C. However, the effect of oxidation on ductility was more severe as oxidation time increased to 260 h and beyond. The rupture strain values were, respectively 0.07, 0.032, and 0.032 after 260, 600, and 1000 h of oxidation. Figures 3 and 4 show the variations in maximum engineering stress and rupture strain as a function of preoxidation time in air at 500°C for tests conducted at room temperature and 500°C.

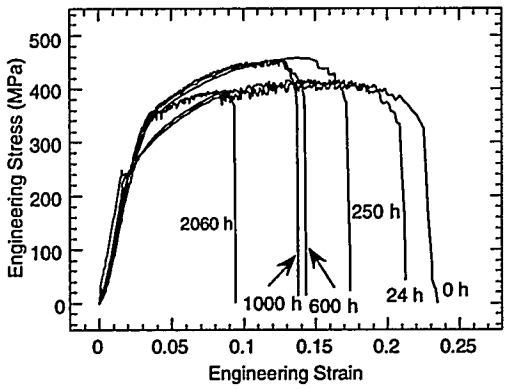

Figure 1. Effect of preoxidation at 500°C on stress-strain behavior of V-5Cr-5Ti alloy tested at 500°C in air at a strain rate of 1.75×10^{-4} s^{-1}.

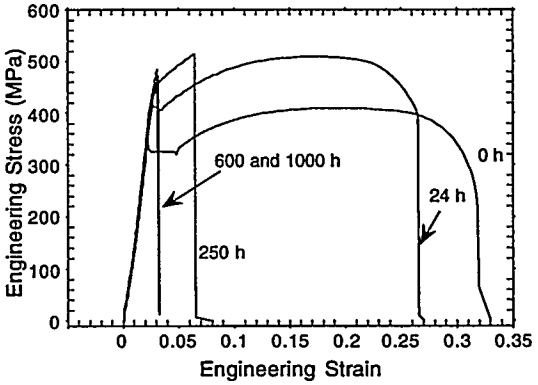

Figure 2. Effect of preoxidation at 500°C on stress-strain behavior of V-5Cr-5Ti alloy tested at room temperature in air at a strain rate of 1.75×10^{-4} s^{-1}.

Microstructural Observations

Axial cross sections of several tested specimens were examined by SEM. Figure 5 shows specimen sections tested in as-annealed condition and after oxidation for 24, 250, 1000, and 2060 h in air at 500°C. The photomicrographs show that as oxidation time increases, both the cracks in the transverse direction and the crack spacing in the axial direction increase. Furthermore, as oxidation time increases, the specimen undergoes little necking of the gauge section during the tensile test. It is evident, especially from specimens exposed for 1000 and 2060 h, that fracture occurred by propagation of an axial crack and that because the core of the alloy was somewhat ductile, the crack- propagation direction in the core region was at an angle of ≈45°.

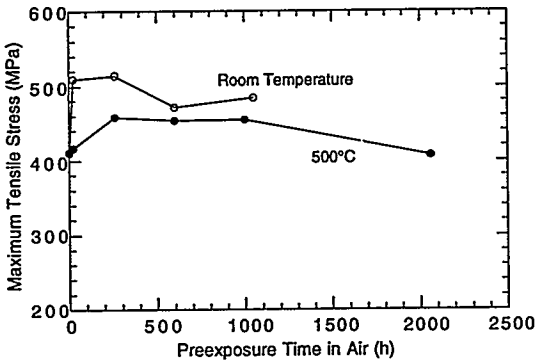

Figure 3. Maximum tensile stress as a function of preexposure time in air for specimens of V-5Cr-5Ti alloy tested in air.

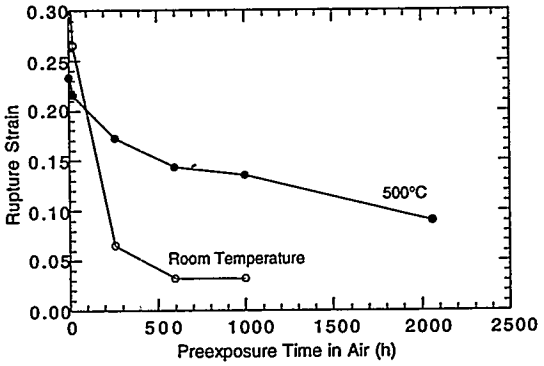

Figure 4. Rupture strain as a function of pre–exposure time in air for specimens of V-5Cr-5Ti alloy tested in air.

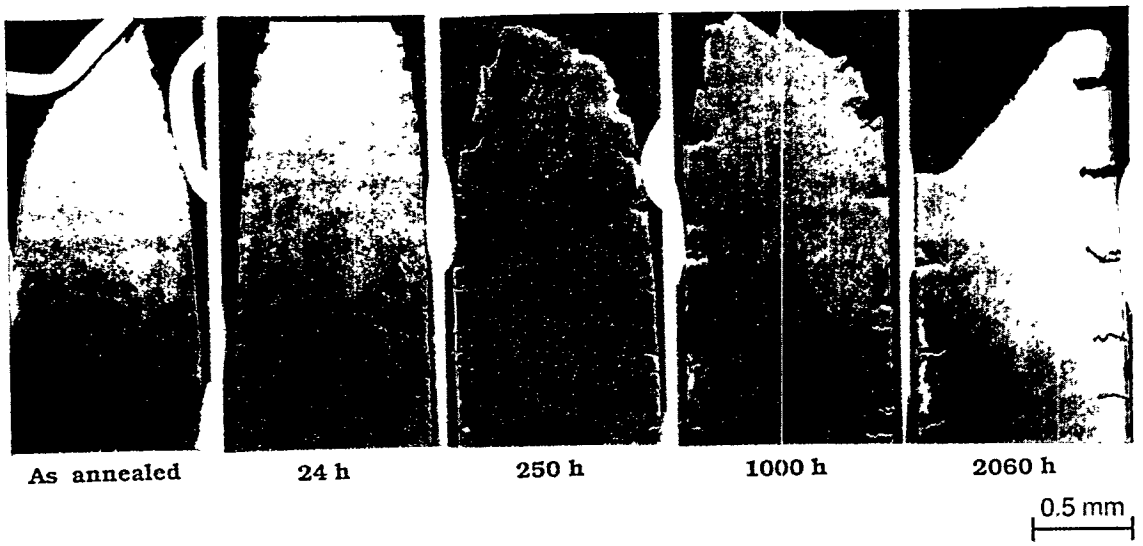

Figure 5. Scanning electron photomicrographs of axial sections of V-5Cr-5Ti specimens tensile tested at 500°C in as-annealed condition and after oxidation in air at 500°C for several exposure times

Figure 6 shows photomicrographs of as-annealed and preoxidized specimens tested at room temperature. The as-annealed specimen exhibited significant necking prior to fracture. The specimen preoxidized for 24 h exhibited numerous cracks, but less necking than in the as-annealed specimen. The specimen preoxidized for 260 h exhibited several small cracks but virtually no necking prior to fracture. The specimens preoxidized for 600 and 1000 h showed no surface cracks but were fully embrittled.

Table 1 lists the calculated and measured thickness of oxide layers, depths of hardened layers (from Vickers hardness measurements), thickness of intergranular fracture zones, and transverse crack lengths for specimens as-annealed, preoxidized, and tensile tested at room temperature and 500°C. The data in Table 1 show that the oxide layer is fairly thin even after exposure to air at 500°C for 2060 h. However, oxygen diffusion into the substrate alloy and its enrichment in the surface regions of the specimens alter the fracture mode, changing it from ductile to cleavage. Furthermore, the thickness of the intergranular fracture zone is in good agreement with the crack lengths measured in the transverse direction. The difference in the intergranular fracture zone thickness and the crack length can be attributed to a subsurface oxygen-enriched layer that is not fully brittle. The results also indicate a threshold oxygen concentration in the alloy for embrittlement to ensue, and this is presently being investigated.

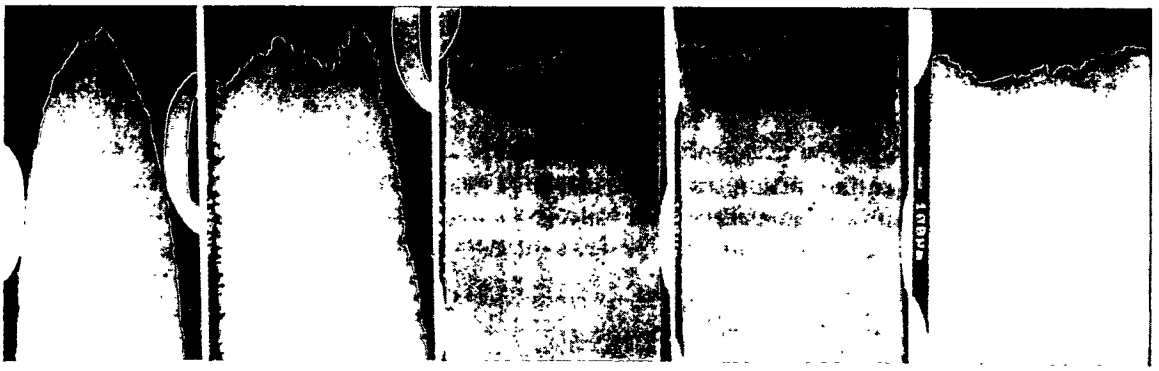

Figure 6. Scanning electron photomicrographs of axial sections of V-5Cr-5Ti specimens tensile tested at room temperature in as-annealed condition and after oxidation in air at 500°C for several exposure time

Table 1. Oxidation, hardness, and fracture data for V-5Cr-5Ti alloy

Exposure time (h)	Calculated oxide thickness[a] (μm)	Measured oxide thickness (μm)	Depth of hardened layer after exposure at 500°C (μm)	Intergranular-fracture zone (μm)		Measured crack length (μm)		Rupture strain	
				RT[b]	500°C	RT[b]	500°C	RT[b]	500°C
0	0	0	0	0	0	0	10	0.322	0.233
24	1.4	1.2	<25	c	25	24	22	0.265	0.215
250[d]	4.6	5.0	45	>500	65	e	50	0.065	0.172
600	7.1	7.1	68	>500	100	e	90	0.032	0.143
1000[d]	9.1	9.0	80	>500	120	e	110	0.032	0.135
2060	13.1	14.0	120	NT[f]	165	NT[f]	160	NT[f]	0.090

[a]Values were calculated with an equation developed from a parabolic fit of all the oxidation data .
[b]RT=room temperature.
[c]Fracture is partially ductile and no transition is noted from ductile to brittle fracture.
[d]Exposure times were 260 and 1050 h for the samples tested at room temperature.
[e]Specimen fully embrittled.
[f]NT=not tested.

Additional exposures as a function of oxygen partial pressure in the exposure environment, as well as tensile tests at other temperatures on oxidized specimens, are underway to establish alloy performance in an oxygen-containing environment.

REFERENCES

1. K. Natesan and W. K. Soppet, "Effect of Oxidation on Tensile Behavior of V-Cr-Ti Alloys," Fusion Reactor Materials Progress Report for the Period Ending March 31, 1995, Argonne National Laboratory.

2. K. Natesan and W. K. Soppet, "Effect of Oxidation on Tensile Behavior of a V-Cr-Ti Alloy," Proc. 2nd Intl. Conf. Heat Resistant Materials, Gatlinburg, TN, Sept. 11-14, 1995, ASM International, p. 375 (1995).

CHEMICAL AND MECHANICAL INTERACTIONS OF INTERSTITIALS WITH VANADIUM ALLOYS-J. R. DiStefano, L. D. Chitwood and J. H. DeVan*, Oak Ridge National Laboratory, P.O. Box 2008, Oak Ridge, TN 37831-6157

OBJECTIVE

Liquid lithium contained by a vanadium alloy structure is the favored concept for an advanced breeding blanket for certain fusion reactor concepts. The objective of this task is to determine the kinetics of reactions of vanadium alloys with hydrogen and oxygen as a function of alloy composition and microstructure, and to determine their effects on mechanical properties.

SUMMARY

Oxidation studies of V-4Cr-4Ti were conducted in air and reduced oxygen partial pressures (10^{-4}, 10^{-5} and 10^{-6} Torr). Reaction rates were determined by weight change measurements and chemical analyses. Mechanical properties after the exposures were determined by room temperature tensile tests.

In air at 400 and 500°C, oxide films form on the surface. Initially, rates are high but decrease with time reaching similar values to those found in oxygen partial pressures of 10^{-4}, 10^{-5} and 10^{-6} Torr. At 400°C, oxygen pick-up followed a logarithmic function of time and was confined to regions near the surface. Little change in room temperature tensile properties were noted for oxygen increases up to 1500 ppm. Thermal cycling specimens from 400°C to room temperature up to 14 times had no apparent effect on oxidation rate or tensile properties. At 500°C, oxygen pick-up appeared to follow a parabolic relation with time. Rates were ~10 times those at 400°C and correspondingly larger oxygen increases occurred when compared with the 400°C tests after similar time periods. This resulted in a significant decrease in total elongation after 240 h.

At reduced oxygen partial pressures, rates were measured for times ≤100 h. Data are relatively sparse but generally show a slightly higher initial rate before slowing down. At 400°C increases to ~200 ppm oxygen were found with no effect on room temperature elongation. At 500°C increases in oxygen of ~2400 ppm after 50 h/10^{-5} Torr resulted in a decrease of around 25% in room temperature elongation. By comparison, exposure to air at 500°C for 12 h caused nearly the same results.

Results and Discussion

Air The oxidation of V-4Cr-4Ti has been studied in air at 400 and 500°C. As was previously done with V-5Cr-5Ti, we are continuing to use small tensile specimens (SS-3), nominally 0.76 mm thick with 1.5 mm x 7.6 mm gage sections that were stamped from sheet.

Cyclic oxidation behavior of annealed material (1050°C) was determined by repeatedly heating samples to 400°C for 24 h and then cooling to room temperature (1 cycle). Weight changes and room temperature tensile properties after exposure for 1 - 14 cycles (24 - 337 h) are shown in Table 1. The weight change data best fit a logarithmic time dependence:

---

* Consultant

$$\Delta W\ (mg/cm^2) = 1.1 \times 10^{-1} \log t\ (h) - 5.27 \times 10^{-2},$$

an indication that chemisorption of oxygen or electric-field-induced transport of electrons or ions across the oxide film may be rate limiting. The weight change data in Table 1 show considerable scatter; therefore, in a separate experiment, a single specimen was given 9 cycles in air while its weight was continuously monitored in a microbalance system. In this case a slightly different logarithmic function fit the data:

$$\Delta W\ (mg/cm^2) = 0.8 \times 10^{-1} \log t\ (h) - 3.3 \times 10^{-2},$$

Table 1. Results of Cyclic Oxidation of V-4Cr-4Ti at 400°C in Air

Spec. No.	Time (h)	Cycles	Weight Change mg/cm^2	Rate $mg/cm^2/h$	Room Temp. Tensile Y.S. (MPa)	U.T.S. (MPa)	Elong. (%)
WE-43	24	1	.085	3.5×10^{-3}	363	449	30.8
WE-44	48	2	.135	2.8×10^{-3}	350	441	31
WE-45	72	3	.165	2.3×10^{-3}	347	446	31
WE-46	96	4	.215	2.2×10^{-3}	352	441	28.8
WE-47	120	5	.205	1.7×10^{-3}	350	445	30.7
WE-48	144	6	.185	1.3×10^{-3}	354	445	29.5
WE-49	169	7	.160	9.5×10^{-4}	339	438	32
WE-50	193	8	.265	1.4×10^{-3}	359	458	28.6
WE-51	217	9	.205	9.5 x 10-4	357	451	29.3
WE-52	265	11	.190	7.2×10^{-4}	368	467	26.8
WE-53	289	12	.190	6.6×10^{-4}	357	452	26.0
WE-54	313	13	.200	6.4×10^{-4}	356	452	28.8
WE-55	337	14	.280	8.3×10^{-4}	361	452	28.7
WE-58	577	None	.270	4.7×10^{-4}	358	458	27.8

Even though oxygen increases up to 1500 ppm occurred, room temperature tensile properties were essentially unchanged by the exposures to air at 400°C. Total elongation averaged 29.3% with a standard deviation of only 1.7%. An oxide scale was observed on the surface to a thickness of < 2 μm (0.1 mil). The specimens also showed a hardness increase immediately below the scale, an indication of internal oxidation. However, the depth of the increase was limited to ~ 10μm, further confirmation that bulk properties should not have been affected.

The non-cyclic oxidation of V-4Cr-4Ti was measured in air at 500°C for times to 240 h as shown in Table 2. Based on a parabolic rate law, the parabolic rate constant was found to be 4.8×10^{-3} (mg^2/cm^4 h). At this temperature, oxygen increases were higher than at 400°C reaching 6080 ppm after 240 h. Room temperature elongation decreased with increasing oxygen pick-up and was 8.9% after 240 h.

Table 2. Results of Oxidation of V-4Cr-4Ti at 500°C in Air

	Time (h)	Temp. (°C)	ΔW (ppm)	Y.S. (MPa)	U.T.S. (MPa)	Elong. (%)	Rate $mg/cm^2/h$
Air	12	500	2118	374	469	24.8	3.1×10^{-2}
Air	48	500	2871	402	504	18.1	1.1×10^{-2}
Air	72	500	3796	392	483	13.1	9.4×10^{-3}
Air	95	500	4373	381	477	15.3	8.2×10^{-3}
Air	240	500	6080	382	456	8.9	4.5×10^{-3}

Reduced Oxygen Pressure The oxidation of V-4Cr-4Ti was also measured at 400 and 500°C at reduced oxygen pressures of 10^{-4} and 10^{-5} Torr. Results are summarized in Table 3. If we compare oxidation rates under these conditions with those previously measured in air or at $Po_2 = 1 \times 10^{-6}$ Torr, discussed below (Table 4), it is interesting to note that after long times there is little difference. In air an oxide film forms on the specimen at both 400 and 500°C, although it is significantly thicker at 500°C. Overall the oxidation rate in air at 500°C was about a factor of 10 higher than at 400°C. However, the rate during the first 120 h of exposure at 400°C was about the same as during the last 135 h at 500°C. In low pressure oxygen, oxide films are not visually or microscopically apparent and the rates of oxygen uptake do not change dramatically with time. Although the limited data at reduced pressures do not yet allow reporting a rate law dependence, the data at 500°C at 10^{-4} and 10^{-5} Torr are not inconsistent with parabolic behavior, which indicates a thermal diffusion process. Since the rate in air is initially much higher, than after longer times, it appears that formation and growth of the oxide film is a factor. However, it is not readily apparent why long-term rates in air are essentially the same as those at reduced pressures where measurable oxide films do not form.

In other experiments, V-4Cr-4Ti was exposed to oxygen at 1×10^{-6} Torr at either 400 or 500°C, without and without a pre-oxidation in air at the same temperature, respectively. Results are summarized in Table 5.

Based on weight changes at 10^{-6} Torr and 500°C, pre-oxidation in air at 500°C appeared to prevent further oxidation during the subsequent low-pressure exposure for times to 100 h. Furthermore, total elongation was slightly higher with pre-oxidation than without.

At 400°C, pre-oxidation in air at 400°C was not as effective, probably because the oxide film formed during the air exposure was very thin or was not continuous after 24 h. Even so, as had been the case at 500°C, no serious loss in ductility was observed.

Table 3. Oxidation of V-4Cr-4Ti at Low Oxygen Partial Pressures

Sample No.	Conditions	Wt. Change (mg)	Rate $mg/cm^2/h$	Y.S. (MPa)	U.T.S. (MPa)	Elong. %
	1×10^{-4} Torr O_2/400°C					
WE69	10h	.06	3.1×10^{-3}	358	441	35.5
70	25h	.04	8.4×10^{-4}	350	444	34.0
71	50h	.07	7.4×10^{-4}	359	458	34.0
	1×10^{-5} Torr O_2 /400°C					
WE72	25	.03	6.3×10^{-4}	353	436	34.0
73	50	.03	3.2×10^{-4}	355	445	35.7
74	100	.07	3.7×10^{-4}	359	452	33.3
	1×10^{-4} Torr O_2/500°C					
WE75	10	.15	7.9×10^{-3}	348	451	33.8
76	26	.31	6.3×10^{-3}	364	470	28.7
77	50	.45	4.7×10^{-3}	366	480	30.0
	1×10^{-5} Torr O_2/500°C					
WE34	25	.38	8×10^{-3}	343	454	30.0
35	50	.59	6.2×10^{-3}	337	455	25.3
36	100	.79	4.2×10^{-3}	344	458	24.7

Table 4. Oxidation Rates of V-4Cr-4Ti

PO_2 Torr	Rate ($mg/cm^2/h$) 400°C	500°C
Air	$5\text{-}35 \times 10^{-4}$	$5\text{-}30 \times 10^{-3}$
1×10^{-4}	$7\text{-}32 \times 10^{-4}$	$5\text{-}8 \times 10^{-3}$
1×10^{-5}	$3\text{-}6 \times 10^{-4}$	$4\text{-}8 \times 10^{-3}$
1×10^{-6}	7×10^{-4}	$3\text{-}8 \times 10^{-3}$

Table 5. Effects of Pre-Oxidation in Air

Pre-Oxidation		Oxidation					Room Temperature Tensile Properties[a]		
Pre-Oxidation Treatment	Weight Change (ppm)	Oxygen Pressure (Torr)	Time (h)	Temp. (°C)	Weight Change (ppm)	($mg/cm^2/h$)	Y.S. (MPa)	U.T.S. (MPa)	Total Elong. (%)
None	____	1×10^{-6}	48	500	1375	.005	353	449	21.5
24h/500°C	2106	1×10^{-6}	48	500	-29	-.0001	366	460	23.8
12h/500°C	2118	-----	-----	-----	-----	-----	374[b]	469[b]	24.8[b]
12h/500°C	2210	1×10^{-6}	48	500	-86	-.0003	358	451	23.3
24h/400°C	467	-----	-----	-----	-----	-----	359	476	25
24h/400°C	311	1×10^{-6}	48	400	198	.0007	363	482	21.1

a. Samples heat treated 100h/500°C in vacuum following oxidation except where noted.
b. Sample not heat treated following pre-oxidation.

Work in Progress

Experiments to determine the oxidation of the reference V-4Cr-4Ti alloy at low oxygen partial pressures are continuing to develop rate equations for the uptake of oxygen as a function of temperature and oxygen pressure. Samples from these experiments are also being used to evaluate the effect of oxygen uptake on the mechanical properties of the alloy. Large-grained material may be more susceptible to embrittlement by oxygen and, therefore, the effect of grain size is also being studied.

SOLUBILITY OF HYDROGEN IN V-4Cr-4Ti AND LITHIUM* J.-H. Park, G. Dragel, R. A. Erck, and D. L. Smith (Argonne National Laboratory) and R. E. Buxbaum (Michigan State University)

SUMMARY

The solubility of hydrogen in V-4Cr-4Ti and liquid lithium was determined at 400–675°C and a hydrogen pressure of 9.09×10^{-4} torr (1.21×10^{-1} Pa). Hydrogen concentration in both materials decreased as temperature increased, and the ratio of the hydrogen concentration in liquid lithium and V-4Cr-4Ti (hydrogen distribution ratio R) increased with temperature, e.g., R was ≈17 at 400°C and ≈80 at 700°C. Desorption of hydrogen from V-4Cr-4Ti is a thermally activated process and the activation energy of the desorption rate is 0.405 eV.

INTRODUCTION

The ion density in fusion reactor designs is $1.2 \times 10^{20} \cdot m^{-3}$, which corresponds to a hydrogen pressure of $\approx 10^{-5}$ torr at room temperature. Interaction between hydrogen and first–wall components in a fusion reactor is not likely to produce hydrogen embrittlement of structural materials because the partial pressure of hydrogen in the system is low. However, it is important to determine the solubility of hydrogen in vanadium and liquid lithium and its rate of transport in these materials to optimize the design of a liquid–metal–cooled blanket in a fusion reactor. DeVan et al.[1] measured the solubility of hydrogen in V-5Cr-5Ti at hydrogen pressures of $6 \times 10^{-4} - 3 \times 10^{-2}$ torr by equilibration, followed by fast and slow cooling of specimens that were then analyzed for hydrogen. Cooling rate was found to be an important parameter; the concentration of hydrogen in slow–cooled specimens was higher by factors of 4–7 than that in specimens that were subjected to a fast cooling rate.

EXPERIMENTAL PROCEDURES

Several small tabular specimens of V-4Cr-4Ti (1.0 x 12.7 x 75 mm and ≈10 g, and 1.0 x 4.0 x 75 mm and ≈3.4 g) were used in the hydrogen solubility/desorption rate studies. Similar studies were performed on liquid lithium (≈1.3 g) in a V-7.5Cr-15Ti tube (7.5 mm diameter, 0.4 mm wall thickness, with a mass of 6.829 g) that was sealed with V-20Ti end plugs (7 mm long, with a combined mass of 2.313 g) by tungsten–inert–gas welding in a helium environment. The sealed cells were heated in a vacuum at 700°C for 24 h to check for leakage of lithium; no leaks occurred. The outside surface of each capsule was sputter–coated with palladium.

Several experimental parameters, such as the volume of the vacuum chamber and steady–state flow rate of hydrogen as a function of pressure, were determined for the apparatus. Hydrogen pressure measured with an ionization gauge (IG) was lower by a factor of 0.44 than the actual pressure. The relationship between hydrogen flow rate and pressure in Fig. 1 is linear to $\approx 10^{-6}$ torr, and the data could be extrapolated with confidence to the 10^{-7} torr range.

The specimens were heated in a tantalum tube furnace (178 mm long, 12.7 mm diameter, 0.5 mm thick), which was installed horizontally in the vacuum chamber. The furnace could be heated to 850°C within 7 min by an AC current of ≈125 A. Pure hydrogen was admitted to the system by diffusion through a palladium membrane, and a steady–state pressure of 9.09×10^{-4} torr (IG = 4.0×10^{-4} torr) was maintained by a partially open turbo gate. After attaining the steady state, the pressure was monitored as a function of time with the turbo gate fully open to obtain hydrogen flow rate as a function of pressure in Fig. 1. The solubility of hydrogen in the samples was obtained from these data and by integration of the hydrogen evolution rate as a function of time. However, before measurements could be performed, sources of hydrogen in the system, such as the furnace, chamber, current supplying system, etc., had to be quantified relative to hydrogen contained in the specimens for which experimental data on hydrogen solubility (X_H) and desorption rate (J_H) were obtained. For the transport experiments, net flux of hydrogen from the samples can be written as

*Work supported by U.S. Department of Energy, Office of Fusion Energy Research, under Contract W-31-109-Eng-38.

$$J = J_{H,\,total} - J_{H,system} \quad (1)$$

where J is the net hydrogen desorption rate of the specimens and $J_{H,system}$ is the hydrogen desorption rate of the system, e.g., from the tantalum furnace, chamber wall, etc. The concentration of hydrogen in the specimens was obtained by integrating J between time limits 0 and ∞, i.e.,

$$X_H = \int J(t)\,dt. \quad (2)$$

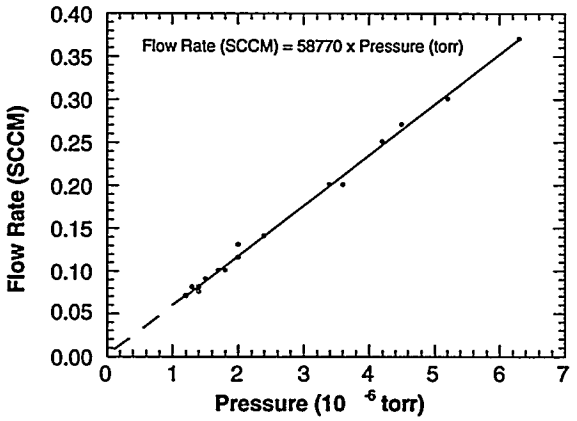

Figure. 1.
Hydrogen flow rate vs. pressure with turbo gate open.

In each experiment, the specimens attain an equilibrium hydrogen concentration at a given temperature. Then, the hydrogen partial pressure in the chamber is lowered by opening the turbo gate for 120 s, during which time most of the hydrogen desorbes at a system pressure of $\approx 10^{-6}$ torr. The remaining hydrogen in the specimens (and the tantalum furnace) desorbs as the furnace is heated to 860°C by an AC current of ≈125 A. Figures 2 and 3 are typical plots of temperature and pressure versus time, respectively. Figure 4 shows the amount of hydrogen released from 10 and 32.5 g of the alloy as a function of time during the desorption phase of the experiment. This amount was obtained by integrating hydrogen flux as a function of time. By comparing the results from two tests on specimens of different mass, we can be obtain the net amount of hydrogen released by V-4Cr-4Ti. The difference in the amount of hydrogen released from the two sets of specimens is constant after 8.5 min (Fig. 4); however, the initial values are ≈1 cm^3 for a hydrogen pressure of 9.09×10^{-4} torr in the chamber. These results indicate that the relative experimental error may increase if this method is used with higher initial hydrogen pressures. Hydrogen solubility in liquid lithium was obtained in a similar manner.

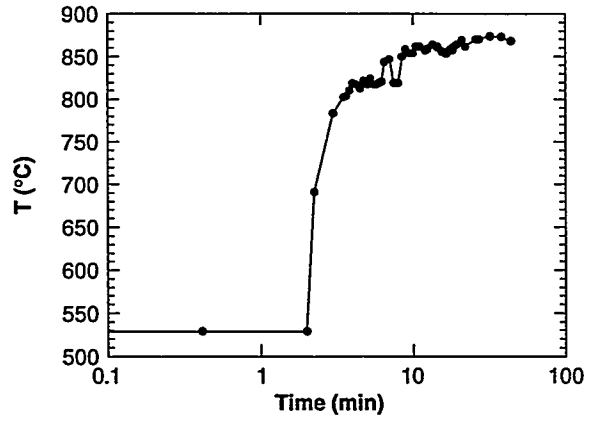

Figure 2.
Furnace temperature vs. time during isothermal and high–heating–rate conditions produced by AC current of 125 A.

Figure 5 shows the effect of temperature on the hydrogen concentration in lithium and V–(4,5)Cr–(4,5)Ti from this investigation and from Ref. 1, along with the predicted dependence on hydrogen in pure vanadium and lithium based on the data in Ref. 2, at a hydrogen pressure of 9.09×10^{-4} torr. Hydrogen concentrations in V–4Cr–4Ti are lower by two orders of magnitude than in pure vanadium. These results were used to calculate the ratio of the hydrogen concentration in lithium and vanadium and V-4Cr-4Ti, i.e., the distribution ratio as a function of temperature, as shown in Fig. 6. The ratios based on our experimental

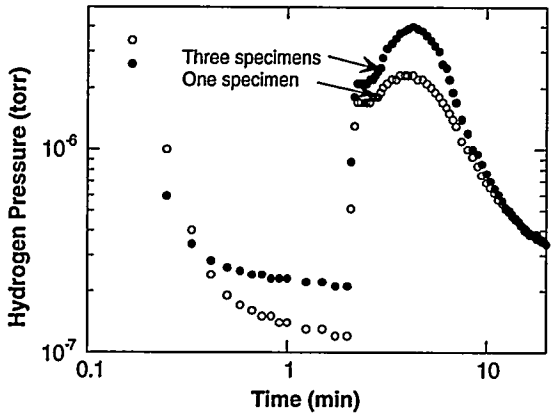

Figure 3.
Typical hydrogen pressure–vs.–time plot for 10 and 23.5 g of V-4Cr-4Ti.

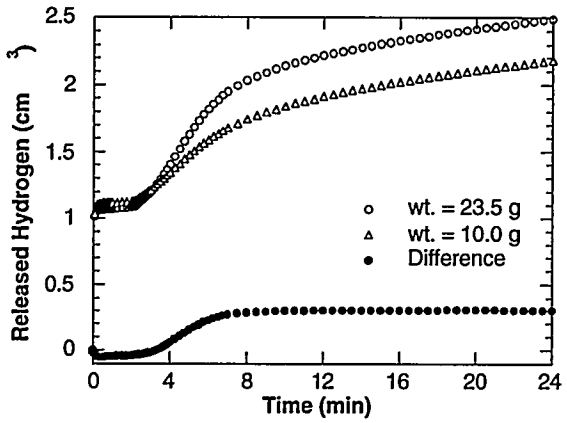

Figure 4.
Amount of hydrogen released vs. time during desorption, from integration of hydrogen flux as a function of time.

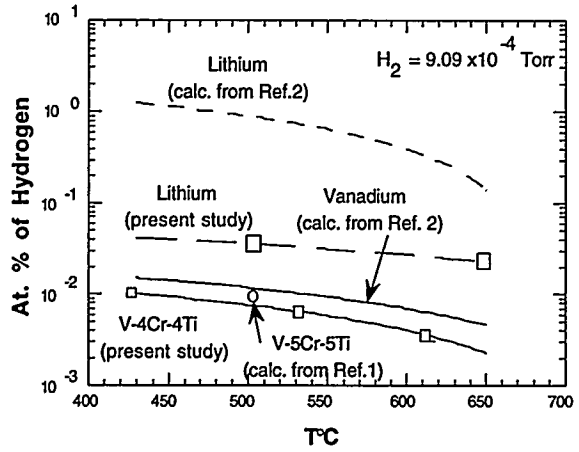

Figure 5.
Atom fraction of hydrogen in lithium, vanadium, and V-4Cr-4Ti vs. temperature at hydrogen pressure of 9.09 x 10^{-4} torr.

data increase as temperature increases from ≈17 at 400°C to ≈80 at 700°C. Distribution ratios based on hydrogen solubility data in lithium from Ref. 2 are also shown in the figure; they are higher by a factor of >10 than the present results and the values decrease as temperature increases.

The hydrogen desorption rate for V–4Cr–4Ti specimens, obtained from pressure–vs.–time plots (e.g., Fig. 3), is shown as function of reciprocal temperature in Fig. 7. Desorption of hydrogen from V-4Cr-4Ti is a thermally activated process with an activation energy of 0.405 eV.

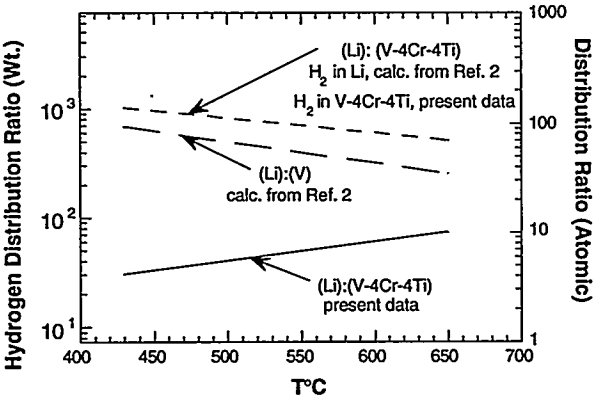

Figure 6.
Calculated hydrogen distribution ratio between (a) lithium and V-4Cr-4Ti, from this study; (b) lithium and vanadium, based on data in Ref. 2; and (c) lithium and V–4Cr–4Ti, based on data for lithium in Ref. 2 and experimental data for the vanadium alloy from this study.

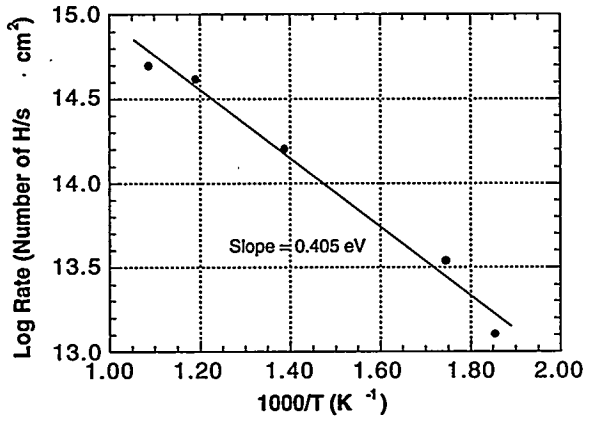

Figure 7.
Hydrogen desorption rate for V–4Cr–4Ti vs. reciprocal temperature at hydrogen pressure of 9.09×10^{-4} torr.

CONCLUSIONS

Hydrogen solubility and desorption rate information for V-4Cr-4Ti and liquid lithium were obtained as a function of temperature at a hydrogen pressure of 9.09×10^{-4} torr. Hydrogen distribution ratios between the vanadium alloy and liquid lithium have been determined at 400-700°C at this hydrogen pressure.

ACKNOWLEDGMENTS

The authors appreciate interaction with Dr. W. J. Shack on numerical calculations and thank C. Konicek for welding the lithium–containing capsules.

REFERENCES

[1] J. H. DeVan, J. R. DiStefano, and J. W. Hendricks, *Chemical and mechanical interactions of interstitial in V-5%Cr-5%Ti,* in Fusion Materials Semiannual Progress Report for Period Ending March 31, 1994, DOE/ER-0313/16, pp. 240-243 (1994).

[2] K. Natesan and D. L. Smith, *Effectiveness of tritium removal from a CTR lithium blanket by cold trapping secondary liquid metals Na, K, and NaK,* Nucl. Technol. **22**, 138-150 (1974).

HYDROGEN UPTAKE IN VANADIUM FIRST WALL STRUCTURES

E. P. Simonen and R. H. Jones, (Pacific Northwest National Laboratory[a])
Richland, WA 99352

OBJECTIVE

To evaluate hydrogen isotope concentrations in layered vanabium structures.

SUMMARY

Evaluation of hydrogen sources and transport are needed to assess the mechanical integrity of V structures. Two sources include implantation and transmutation. The proposed coatings for the DEMO and ITER first wall strongly influence retention of hydrogen isotopes. Upper limit calculations of hydrogen inventory were based on recycling to the plasma and an impermeable coolant-side coating. Hydrogen isotope concentrations in V approaching 1,000 appm may be achieved.

TECHNICAL PROGRESS

Background

Vanadium is being considered as a first wall structural material due to its many advantages including low activation and potential for resistance to high temperature and high dose irradiation. A critical issue for the use of V is its compatibility with hydrogen. Hydrogen is known to affect the mechanical behavior of refractory metals such as V. Two key sources of hydrogen are from plasma implantation fluxes and from transmutations. Because of incompatibility of V with the plasma and MHD compatibility with the Li coolant, coatings have been proposed for use on both the plasma surface and the coolant surface. Be is proposed on the plasma side to minimize problems associated with sputtered surface atoms. An insulating coating is proposed on the coolant side to minimize MHD pumping losses in the liquid Li coolant. These coatings affect the inventory of hydrogen during first wall exposure.

In this study, the permeation model DIFFUSE[1] has been used to evaluate the potential build up of hydrogen in V as a function of temperature and irradiation fluence.[2] DEMO and ITER relevant conditions are examined and effects of boundary condition assumptions are described.

Hydrogen Uptake Considerations

A schematic of the multilayer first wall structure assumed in the present analysis is shown in Figure 1. A 1 mm Be layer is assumed on the plasma side and an impermeable barrier is assumed on the coolant side. The Be and V diffusivities and solubilities are assumed as given in the DIFFUSE code.[1,3] The down-stream insulating barrier is accounted for by assuming a zero flux boundary condition across the barrier. A temperature gradient of 200°C was used in the calculations such that the plasma interface was 200°C higher than the coolant interface.

---

[a]Pacific Northwest National Laboratory is operated for the U.S. Department of Energy by Battelle Memorial Institute under Contract DE-AC06-76RLO 1830.

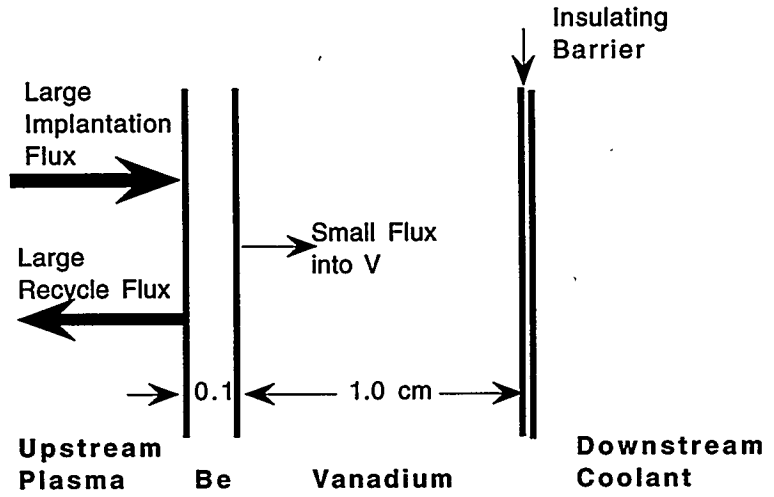

Figure 1. A schematic of hydrogen isotope uptake by implantation. Most of the implanted hydrogen is recycled to the plasma because of the shallow depth of implantation. Transmutation produced hydrogen isotopes (not shown) are generated throughout the structure based on local elemental compositions, neutron spectra, and cross-section for nuclear reactions.

The implanted tritium concentration profile was calculated from the TRIM code[4] and an energy of 100 eV for implantation into Be. An implantation flux of 10^{16} ions/cm^2 was assumed to be representative of the ITER first wall. The concentration of tritium at the surface was assumed to be zero, that is the recycle flux was diffusion controlled in contrast to surface recombination controlled.

The down stream insulating barrier was assumed to have a high permeation resistance. Insulators are known to possess high permeation resistance,[5] however, there is evidence that radiation can significantly enhance migration of hydrogen in insulators.[6] The possibility of a significant loss in permeation resistance during irradiation was evaluated by considering a variable permeation reduction factor compared to V. Because Li is considered as a coolant and because Li has a high affinity for hydrogen, the coolant boundary condition did not require consideration of hydrogen uptake from the coolant to the V structure.

Transmutation rates were calculated from the STARFIRE first wall spectrum[7,8] and for an alloy composition of V- 4 Ti - 4 Cr and for pure Be. The total production of hydrogen isotopes was calculated to be 18.7 appm/dpa for the V alloy and 3.7 appm/dpa for Be.

Calculations of Hydrogen Uptake

The calculated concentration profiles of hydrogen uptake in the multilayered structure are shown in Figures 2 and 3 for the mechanisms of implantation and transmutation, respectively.

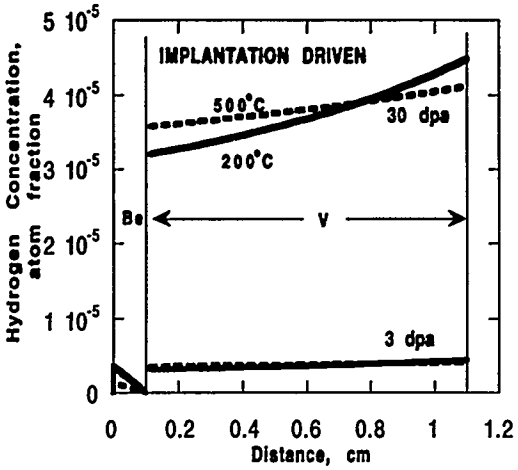

Figure 2. Implantation driven uptake of hydrogen isotopes. Profiles are shown at coolant temperatures of 200°C (solid) and at 500°C (dashed). The upper curves are at 30 dpa, whereas the lower curves are at 3 dpa. The profiles in Be are at steady state and do not change with dose.

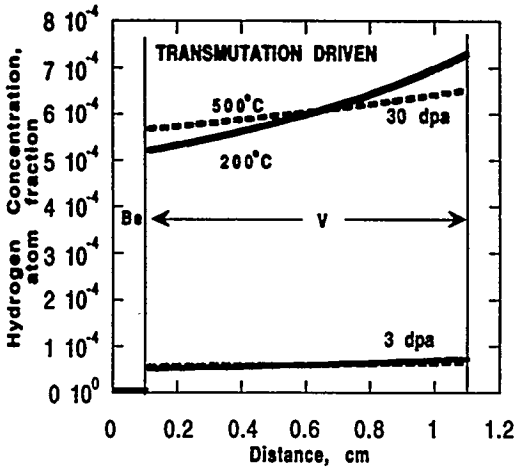

Figure 3. Transmutation driven uptake of hydrogen isotopes. Profiles are shown at coolant temperatures of 200°C (solid) and at 500°C (dashed). The upper curves are at 30 dpa, whereas the lower curves are at 3 dpa. The profiles in Be are at steady state and do not change with dose.

Coolant temperatures of 200°C and 500°C were assumed at 3 and 30 dpa based on a dpa rate of 3 x 10^{-7} dpa/s. The hydrogen isotope concentration achieves levels of about 40 appm from implantation and about 600 appm from transmutation. The concentration profile in V is caused by the assumed temperature gradient. Vanadium is an exothermic absorber of hydrogen and therefore exhibits a lesser solubility in the hotter plasma-side region. Increasing the coolant temperature from 200°C to 500°C does not change the average hydrogen isotope concentration in the V layer but does change the concentration profile slightly. The dose dependence of the maximum hydrogen concentration is shown in Figure 4 for both uptake mechanisms. A linear dose dependence is indicated.

Effects of Uncertainty in Assumed Parameters

Uncertainty in this analysis lies mainly in the assumed material characteristics of Be, V and the insulating layer. In addition, the material parameters are based on measured characteristics of unirradiated materials, whereas hydrogen uptake will occur in irradiated materials.

The depth of implanted hydrogen isotopes into Be controls the fraction of ions that are recycled to the plasma or permeated into the underlying V. The linear dose dependence seen in Figure 4 indicates that the incubation time to achieve a steady state concentration in the Be is short compared to the lifetime of a first wall. The low solubility in Be compared to V results in a near zero hydrogen isotope concentration in the Be at the Be/V interface. At steady state, the permeation flux is equal to the implantation flux multiplied by the ratio of the implantation depth to the Be layer thickness. Therefore, the implantation flux is inversely proportional to the Be layer thickness. Reducing the Be layer thickness by a factor of two increases the permeation flux to the V by a factor of two.

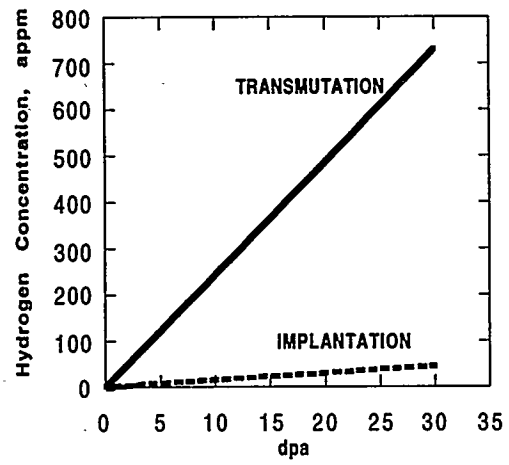

Figure 4. The dose dependence of the maximum hydrogen isotope concentration for both implantation driven and transmutation driven mechanisms.

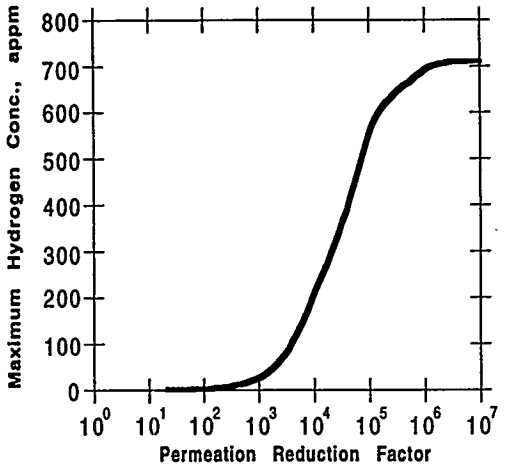

Figure 5. The dependence of the maximum hydrogen isotope concentration on the assumed permeation reduction factor in the last 1 mm of V at the coolant interface.

The effect of surface recombination limits on the recycle flux was examined. Control by bulk diffusion implies that formation of molecular hydrogen on the surface from recombination of atomic hydrogen is fast and does not influence the releases rate of hydrogen from the Be coating. If recombination where found to be a limiting factor, the fraction of hydrogen taken up by the V would be greater than indicated in this analysis. As expected for endothermic hydrogen absorbers, like Be, the recombination influence was not found to be significant for the recombination parameters included in the DIFFUSE code.

Permeation and solubility measurements of hydrogen in V have revealed conflicting results because of the sensitivity of hydrogen absorption to surface condition of the V sample.[9] Careful control of the V surface condition has revealed that hydrogen absorption in V is exothermic and that diffusion is rapid even at room temperature. The present calculations are not influenced by the surface condition because each surface is coated with either Be or an insulating layer. Furthermore, the uptake mechanism does not involve absorption at a surface. For implantation the ions are implanted through the surface and for transmutations the hydrogen isotopes are created internally. Therefore, the present analysis is not subject to the known uncertainties associated with permeation measurements in V.

An assumed high permeation resistance for the insulating barrier may be influenced by radiation-induced hydrogen diffusion and permeation. Enhanced diffusion of hydrogen in insulators is associated with ionization states that promote migration. Effects of radiation on hydrogen transport in insulators at DEMO and ITER relevant temperatures have not been established. Therefore, the effect of variation in the assumed permeation resistance of the coolant barrier on the calculated hydrogen isotope concentration was calculated and is shown in Figure 5. For these transmutation-induced calculations, the last (coolant-side) 1 mm of V was assumed to have a reduced permeation rate defined by a permeation reduction factor. It is necessary to reduce the

permeation by a factor of 1000 to obtain significant concentrations of hydrogen isotopes in the V layer. A permeation reduction factor of 10^6 is equivalent to a perfect permeation resistance for the coolant barrier. Therefore to ensure that only insignificant levels of hydrogen accumulate in V, it is necessary to establish that the insulating barrier have permeation rate fast enough to allow flow of hydrogen isotopes to the coolant. The barrier permeation rate must not be less than three orders of magnitude of the V permeation rate.

FUTURE WORK

No future work is planned.

REFERENCES

1. M. I. Baskes, DIFFUSE 83, SAND 83-8231, Sandia National Laboratories, Albuquerque, NM, USA, 1983.

2. Simonen E. P., J. L. Brimhall and R. H. Jones, 1993, "Consideration of Tritium and Hydrogen Distributions in Layered Structures for ITER," in Fusion Reactor Materials Semiannual Progress Report DOE/ER-0313/15.

3. M. I. Baskes, A. E. Pontau, and K. L. Wilson, J. of Nucl. Mater., 122&123, 1511 (1984).

4. J. F. Ziegler, J. P. Biersack and U. Littmark, "The Stopping and Range of Ions in Solids," Pergamon Press, New York, New York.

5. G. W. Hollenberg, E. P. Simonen, G. Kalinin, and A. Terlain, Fusion Engineering and Design 28 (1995) 190-208.

6. Y. Chen, M.M. Abraham and L. C. Templeton, J. Am. Ceram. Soc., 60 (1977)101-104.

7. F. A. Garner and L. R. Greenwood, Materials Transactions, JIM, Vol. 34, No. 11 (1993), pp. 985-998. references includes above Starfire reference.

8. F. A. Garner, L. R. Greenwood and F. M. Mann: Fusion Reactor Materials Semiannual Progress Report, DOE/ER-0313/13, (1992), p. 42. Starfire reference

9. J. L. Brimhall, E. P. Simonen and R. H. Jones, 1994, "Data Base on Permeation, Diffusion, and Concentration of Hydrogen Isotopes in Fusion Reactor Materials," in Fusion Reactor Materials Semiannual Progress Report DOE/ER-0313/16 also PNL-SA-24872.

CORROSION OF V AND V-BASE ALLOYS IN HIGH-TEMPERATURE WATER*

I. M. Purdy, P. T. Toben, and T. F. Kassner (Argonne National Laboratory)

SUMMARY

Corrosion tests of nonalloyed V, V–5Cr–5Ti, and V–15Cr–5Ti were conducted in high-purity deoxygenated water at 230°C for up to ≈4500 h. The effects of Cr concentration in the alloy and temperature on the corrosion behavior were determined from weight-change measurements and microstructural observations. An expression was obtained for the kinetics of corrosion as a function of Cr content of the alloy and temperature.

INTRODUCTION

Vanadium–base alloys are being considered for the first–wall/blanket structure in fusion reactors that employ a liquid–metal cooling system. Because reference alloys that contain 4–5% Cr and Ti exhibit excellent mechanical properties after neutron irradiation,[1] their use in reactor designs with an aqueous coolant is also of interest. For this application, the alloy should resist corrosion and possible embrittlement by uptake of corrosion–product H. In this study, corrosion tests were conducted on pure V, V–5Cr–5Ti, and V–15Cr–5Ti in high-purity deoxygenated water at 230°C.

EXPERIMENTAL PROCEDURE

Details of the experimental procedures are described in Ref. 2. Tabular specimens were cut from thin sheets of material whose compositions are given in Table 1. Approximate dimensions of the pure V, V–5Cr–5Ti, and V–15Cr–5Ti specimens (in mm) are 28 x 15 x 0.6, 20 x 8 x 1, and 10 x 10 x 1.5, respectively. Specimens were annealed in vacuo at 1055°C for 1 h. Vickers microhardness values (25–g load) before and after annealing were 186 vs. 121, 237 vs. 195, and 254 vs. 195, for pure V and the 5Cr and 15Cr alloys, respectively. V–15Cr–5Ti specimens are from the same heat used in a previous corrosion investigation at 288°C.[3] Corrosion tests were conducted on duplicate specimens of each alloy, i.e., two sets of six specimens were prepared for each alloy so that one set (two specimens) could be removed from the autoclave for metallographic evaluation and H analysis at ≈1–month intervals over an ≈6–month period. During each time interval, all specimens were removed from the autoclave and weighed. Consequently, six measurements were obtained for each alloy and its duplicate after ≈1 month of exposure, five measurements after 2 months of exposure, etc. Corrosion tests on pure V were conducted for up to ≈3 months. The surface area of each specimen was measured by an image analysis technique. Tests were conducted in a refreshed Hastelloy C276 (62%Ni-16%Cr-16%Mo) autoclave system at 230°C (±2°C) with ≈100 psi overpressure (above saturation) to maintain liquid–phase water. Dissolved-oxygen concentration of inlet water was maintained at <12 ppb. Weight changes of the specimens were determined to ±1 μg.

Table 1. Composition of V and V-base alloys

		Composition (wt.%)		Impurity Concentration (wt. ppm)												
Alloy	Heat ID	Cr	Ti	O	N	C	H	Si	Al	Fe	Mo	Nb	Cu	S	P	Ca
V	820630	<0.01	<0.005	200	62	75	3	780	100	230	410	<50	<50	10	<30	–
5Cr–5Ti	T87	4.9	5.3	460	18	210	9	300	200	600	400	<100	<100	90	10	50
15Cr–5Ti	L–1	12.8	5.0	830	50	370	4	300	100	800	200	<100	100	40	<10	80

RESULTS

Weight loss versus time of exposure for pure V and the two alloys is shown in Fig. 1. The data were fitted to the expression $W = A \cdot t^n$, where W is the weight loss in $g \cdot m^{-2}$, t is the exposure time in hours, and A and n are empirical fitting parameters. The values of n in the power-law expression range from ≈1.0 for

*Work supported by U.S. Department of Energy, Office of Fusion Energy Research, under Contract W-31-109-Eng-38.

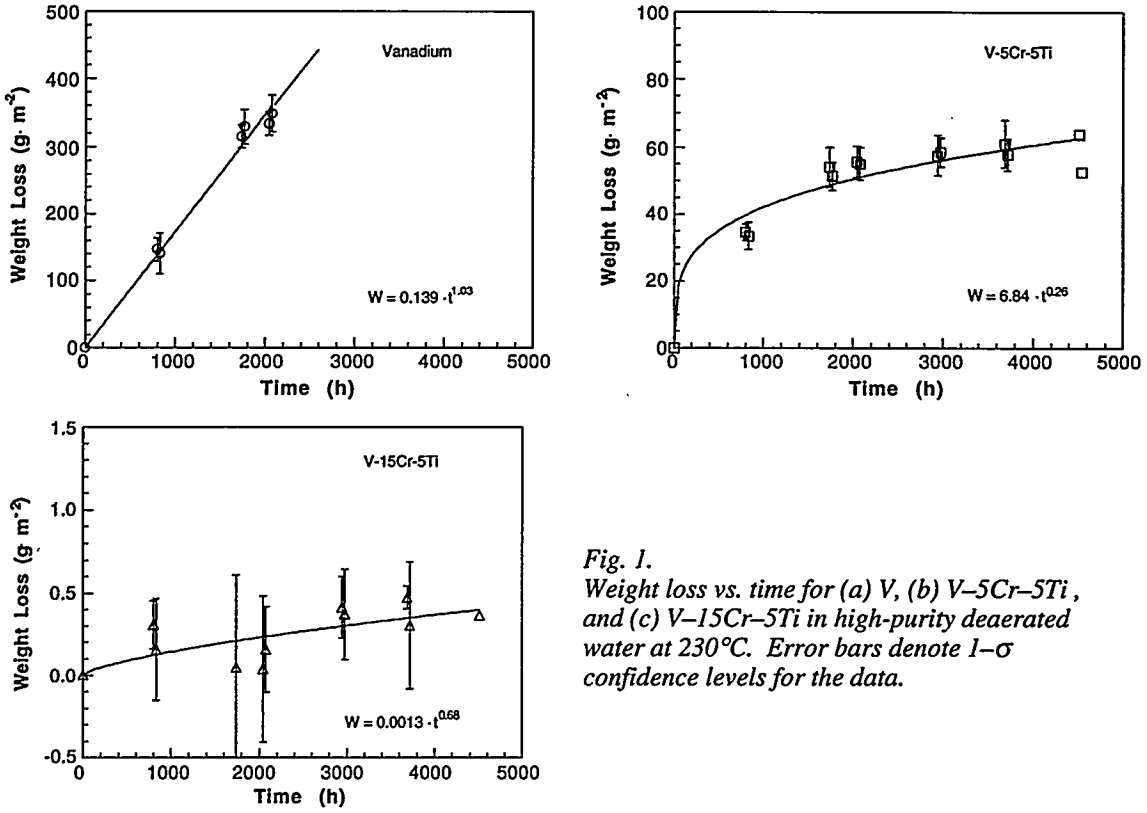

Fig. 1.
Weight loss vs. time for (a) V, (b) V–5Cr–5Ti, and (c) V–15Cr–5Ti in high-purity deaerated water at 230°C. Error bars denote 1–σ confidence levels for the data.

pure V to ≈0.3 for the V–5Cr–5Ti alloy. Exposure time in the figures was adjusted slightly to delineate data from the two sets of specimens. Measured weight loss for V–15Cr–5Ti was very small when compared with pure V and V–5Cr–5Ti, as indicated by the different ordinate scales on the figures. The effect of Cr concentration on weight loss at ≈2000 h is shown in Fig. 2. Corrosion decreases according to an exponential dependence on Cr concentration in the alloys.

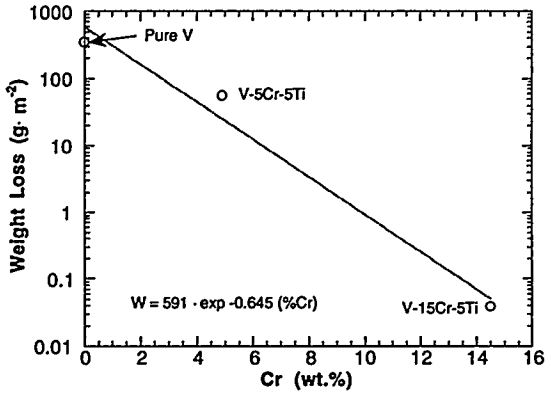

Fig. 2.
Effect of Cr concentration on weight loss of V–Cr–5Ti at 2046 h in high-purity deaerated water at 230°C

The effect of temperature on the corrosion rate of V–15Cr–5Ti at ≈2000 h is shown in Fig. 3, based on results from this work at 230°C and a previous investigation at 288°C.[3] Loss in thickness in μm/yr is also denoted on the figure. The results indicate that the corrosion rate of this alloy decreases rapidly with temperature, i.e., the activation energy is ≈40 kcal/mol.

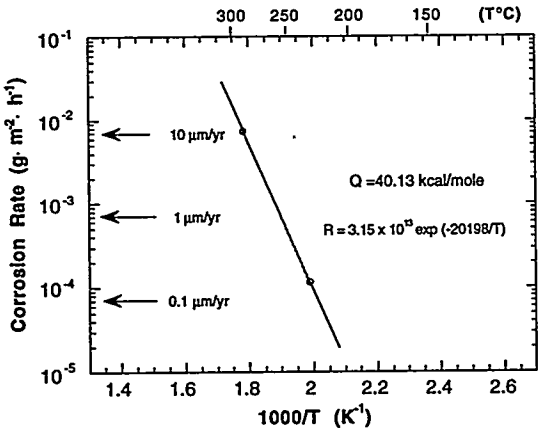

Fig. 3.
Effect of temperature on corrosion rate of V–15Cr–5Ti in high-purity deaerated water at ≈2000 h

Parameters for corrosion weight loss of the materials at 230°C are given in Table 2 along with calculated loss in weight at 2000 h and loss in thickness at 1 yr (8760 h), based on these parameters and an average alloy density of ≈6.16 g·cm^{-3}. The table also includes results for V–15Cr–5Ti in water that contained ≈30, 190, and 4000 ppb dissolved oxygen at 288°C, from Ref. 3.

Table 2. Best–fit parameters in relationship $W = A \cdot t^n$ for V and V–base alloys, and calculated loss in weight (W) and thickness (L) at 2000 and 8760 h (1 yr), respectively, in high–purity deaerated water

Material	Temp. (°C)	Oxygen (ppb)	A (g·m^{-2})	n	W at 2000 h (g·m^{-2})	L at 1 yr (µm)
V	230	12	0.139	1.03	349.0	259.0
V–5Cr–5Ti	230	12	6.835	0.26	49.3	11.8
V–15Cr–5Ti	230	12	1.31×10^{-3}	0.68	0.23	0.10
V–15Cr–5Ti[a]	288	30	3.41×10^{-3}	1.10	14.6	12.0
V–15Cr–5Ti[a]	288	190	2.84×10^{-2}	0.67	4.62	2.0
V–15Cr–5Ti[a]	288	4000	6.19×10^{-3}	0.91	6.25	24.0

[a]Data from Ref. 3.

Figure 4 shows the dependence of calculated loss in thickness at 1 yr on Cr concentration, based on the parameters in Table 2 and the relationships in Fig. 1. Loss in thickness at one year also exhibits an exponential dependence on Cr concentration in V–Cr–5Ti alloys, and is consistent with experimental data for ≈2000 h, shown in Fig. 2. If the temperature dependence of the corrosion of V–Cr–5Ti alloys is the same as that of V–15Cr–5Ti in Fig. 3, the results in Figs. 2 and 3 can be used to develop an expression for loss in thickness L of V–Cr–5Ti alloys as a function of temperature in high–purity deoxygenated water at any time, e.g., 1 yr, as follows:

$$d\ln L = \frac{\partial}{\partial}\frac{\ln L}{T}\bigg|_{Cr} dT + \frac{\partial}{\partial}\frac{\ln L}{X_{Cr}}\bigg|_{T} dX_{Cr}, \tag{1}$$

where the partial derivatives were evaluated from results in Figs. 3 and 4 and are given by

$$\frac{\partial}{\partial}\frac{\ln L}{T}\bigg|_{Cr} = -\frac{20196}{T^2} \tag{2}$$

$$\frac{\partial}{\partial}\frac{\ln L}{X_{Cr}}\bigg|_{T} = -0.534. \tag{3}$$

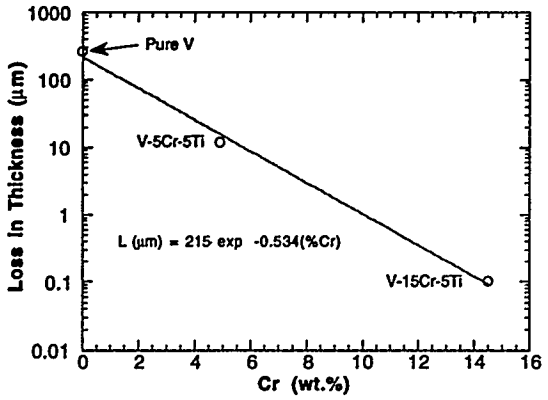

Fig. 4.
Effect of Cr concentration on loss of thickness of V–Cr–5Ti alloys in high-purity, deaerated water at 230°C for 8760 h (1 yr), based on parameters in Table 2

When Eqs. 2 and 3 are inserted into Eq. 1, the expression (Eq. 4) can be integrated between the limits

$$\int_{0.1}^{L} d\ln L = -\int_{503}^{T} \frac{20196}{T^2}\,dT - \int_{15}^{X} 0.534\,dX \tag{4}$$

to yield the loss in thickness (μm) at 1 yr (Eq. 5).

$$\ln L = 45.814 - \frac{20196}{T} - 0.534\,(X_{Cr}). \tag{5}$$

Because corrosion of each material follows a different rate law, i.e., a linear law for pure V and a ≈0.3 power dependence on time for V–5Cr–5Ti, Eq. 5 is only valid for the time that was selected, viz., 1 yr. Nevertheless, this expression enables one to assess the effects of temperature and Cr concentration on corrosion in the context of alloy selection and operating temperature. A corrosion allowance of ≈20 μm/yr may be acceptable for the first–wall of a fusion reactor.[4] In Fig. 5, the estimates of the corrosion of V–Cr–5Ti alloys at 1 yr from Eq. 5 are presented with values obtained from Table 2 for the three materials at 230 and 288°C. Equation 5 provides a reasonable representation of corrosion behavior; however, experimental data at other temperatures and for other alloy compositions are not available to assess the validity of the expression.

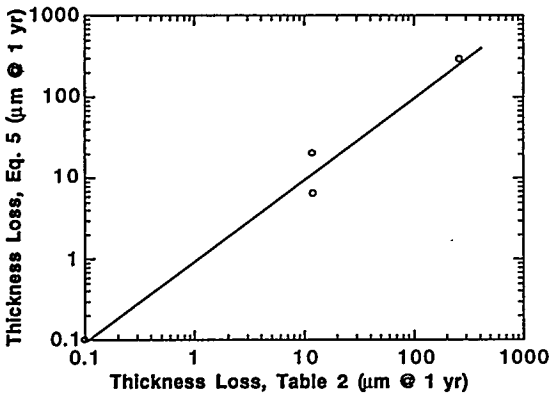

Fig. 5.
Loss of thickness of V–Cr–5Ti alloys in high-purity deaerated water at 1 yr, from Eq. 5 and parameters in Table 2

Specimens were analyzed to determine uptake of corrosion–product H by the materials during long–term exposure to high–temperature water. Table 3 shows that H pickup by V and the alloys was minimal in these experiments, which suggests that H embrittlement from this source of H should not be a concern.

Table 3. Hydrogen (ppm) in V, V–5Cr–5Ti, and V–15Cr–5Ti after exposure to water at 230°C

	Exposure Time (h)			
Material	0	799	2046	4508
V	3	37.5	56.5	–
V–5Cr–5Ti	9	–	14.6	22.5
V–15Cr–5Ti	4	–	2.9	3.0

Metallographic sections of the specimens were prepared and examined by scanning electron microscopy (SEM). The photomicrographs indicate an adherent ≈30–μm–thick corrosion-product film on V specimens for exposure times ≥1700 h. Films on V–5Cr–5Ti were ≈8 μm thick for all of the exposure times; those on V–15Cr–5Ti were much thinner (<1 μm). Figure 6 show the corrosion–product layer on V–5Cr–5Ti specimens after ≈3 and 6 months of exposure to water at 230°C. Although film thickness did not increase with exposure time, slight intergranular oxidation is evident after ≈3 and 6 months. Detachment of the film from the metal in Fig. 6 occurred during specimen preparation. Because film thicknesses were small, characterization by X-ray diffraction was not attempted. However, X–ray diffraction powder patterns in a previous study[3] indicated that the corrosion product on V–15Cr–5Ti contained V, Cr, and Ti. X–ray peaks were consistent with tetragonal and/or orthorombic forms of $Cr_{0.1}V_{0.9}O_2$. TiO_2 and TiV_2O_6 were also identified.

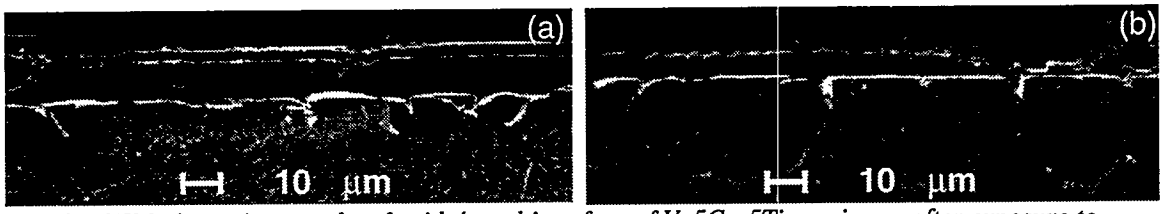

Fig. 6. SEM photomicrographs of oxide/metal interface of V–5Cr–5Ti specimens after exposure to high–purity deaerated water at 230°C for (a) 2046 and (b) 4508 h

CONCLUSIONS

Vanadium and V–Cr–Ti alloys that contained Cr and Ti undergo weight loss and thinning during exposure to high–purity deoxygenated water at temperatures ≤288°C. Corrosion resistance of V–Cr–5Ti alloys increases with Cr concentration in the alloy. Pickup of H liberated by the corrosion reaction was minimal during the ≈6–month corrosion test; which suggests that H embrittlement due to corrosion should not be a concern. An expression was developed for loss of thickness as a function of temperature and Cr content of the alloy. If V–base alloys are considered for structural applications in a fusion reactor with an aqueous coolant, the influence of water velocity on corrosion behavior should be investigated.

REFERENCES

[1] R. F. Mattas, B. A. Loomis, and D. L. Smith, *Vanadium Alloys for Fusion Reactor Applications, JOM,* **44**(8), (1992) 26.

[2] I. M. Purdy, *Assessment of Niobium-Base Alloys for Structural Applications in the ITER Divertor,* Fusion Reactor Materials Semiannual Report for Period Ending March 31, 1993, DOE/ER-0313/14, Oak Ridge National Laboratory, p. 294 (July 1993).

[3] D. R. Diercks and D. L. Smith, *Corrosion Behavior of Vanadium–Base Alloys in Pressurized Water,* J. Nucl. Mater., **141–143** (1986) 617–621.

[4] D. L. Smith, R. F. Mattas, and M. C. Billone, "Fusion Reactor Materials," Chapt. 10, in *Nuclear Materials*, ed. B. R. T. Frost, Vol. 10B of Material Science and Technology, eds. R. W. Cahn, P. Haases, and E. J. Kramer, VCH Publishers (New York) 1994, pp. 243-340.

CaO INSULATOR AND Be INTERMETALLIC COATINGS ON V-BASE ALLOYS FOR LIQUID-LITHIUM FUSION BLANKET APPLICATIONS*

J.-H. Park and T. F. Kassner (Argonne National Laboratory)

SUMMARY

The objective of this study is to develop (a) stable CaO insulator coatings at the liquid-Li/structural-material interface, with emphasis on electrically insulating coatings that prevent adverse MHD-generated currents from passing through the V–alloy wall, and (b) stable Be-V intermetallic coatings for first–wall components that face the plasma. Electrically insulating and corrosion-resistant coatings are required at the liquid–Li/structural interface in fusion first-wall/blanket applications. The electrical resistance of CaO coatings produced on oxygen–enriched surface layers of V-5%Cr-5%Ti by exposing the alloy to liquid Li that contained 0.5-85 wt.% dissolved Ca was measured as a function of time at temperatures between 250 and 600°C. Crack–free Be_2V intermetallic coatings were also produced by exposing V–alloys to liquid Li that contained Be as a solute. These techniques can be applied to various shapes (e.g., inside/outside of tubes, complex geometrical shapes) because the coatings are formed by liquid-phase reactions.

INTRODUCTION

In the design of liquid–metal cooling systems for fusion–reactor blanket applications, major concerns are corrosion resistance of structural materials and the magnetohydrodynamic (MHD) force and its subsequent influence on thermal hydraulics. When the system is cooled by a liquid metal, an electrically insulating layer (e.g., CaO) is required on piping surfaces in contact with the coolant [1,2]. Because plasma–facing components are subjected to high operating temperatures and heat loads, they must exhibit high thermal conductivity and resistance to thermal shock, thermal erosion, and radiation damage [3,4]. Graphite, binary–element ceramics, refractory metals, and low–atomic–number elements, e.g., Be and B, have been considered for these applications [5]. Figure 1 depicts a V–alloy first wall with Be and CaO surface coatings that are capable of being formed on various shapes by exposure to liquid Li under controlled conditions. The coatings could also improve general corrosion resistance and act as a diffusion barrier for deuterium and tritium. This paper describes methods to fabricate both electrically insulating CaO and Be-V intermetallic coatings on V-alloys, which are being considered for the first wall/blanket in fusion reactors.

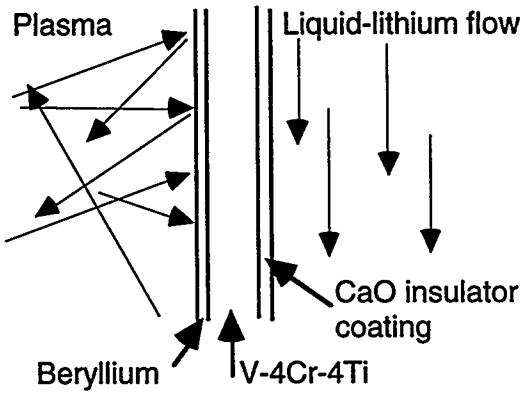

Fig. 1. Schematic diagram of first wall in a fusion reactor

*Work supported by U.S. Department of Energy, Office of Fusion Energy Research, under Contract W-31-109-Eng-38.

CaO Coating on V–Alloys in Liquid Li

According to previous studies [6,7], several ceramic materials that are thermodynamically stable in Li exhibit poor compatibility with the liquid metal because of thermodynamically unstable impurities that form at grain boundaries during fabrication. For example, sintered AlN disintegrated in liquid Li, but exhibited compatibility when yttrium, which acts as an oxygen getter and stabilizes the material (Y/Y_2O_3), was added before sintering [6]. Three types of experiments have been conducted to develop electrical insulator coatings for use in liquid Li: (a) in-situ fabrication of intermetallic layers for subsequent conversion to electrically insulating layers by oxidation, (b) reaction of an oxygen–rich surface layer in a V–base alloy with Ca dissolved in liquid Li to produce a ceramic insulator coating (CaO) on the material, and (c) in-situ electrical resistance measurements of insulator coatings on V-alloys as a function of time and temperature in Li. To fabricate a CaO coating on the alloy substrate, oxygen concentration in the near–surface region in V and Ca in liquid Li must be controlled. Oxygen can be incorporated into the interstitial sublattice in body-centered-cubic (bcc) V and its alloys. Thus, O that is present in the alloy (as a reactant) has a higher affinity for a solute (such as Ca dissolved in Li) than do the alloy elements. In the bcc lattice of a V-Cr-Ti alloy, O can occupy interstitial sites within a lattice up to several atomic percent. Samples of V-5%Cr-5%Ti were heat treated in flowing Ar at 670°C to charge the near–surface region of the alloy with O. The samples were then immersed in Ca-bearing liquid Li for ≈96 h at 420°C to investigate the formation of CaO.

In addition to thermodynamic stability in liquid Li and adherence of the coating to the V alloy under thermal cycling conditions, the in–situ self–healing behavior of defects (such as cracks in the coating) in liquid–Li environments is also an important consideration. Because the coefficient of thermal expansion of CaO is higher than that of V (12×10^{-6} vs. 9.2×10^{-6}/K), a CaO layer that forms in–situ on a V–5%Cr–5%Ti alloy will be subjected to tensile stress during cooling. Microcracks have been observed in CaO coatings after cooling of coated specimens to room temperature. Regions with diameters of ≈30–40 μm and crack widths of ≈2000 Å covered most of the CaO surface, which suggests that the cracks originate from a mismatch of thermal expansion coefficients during cooling, i.e., they are "crazing cracks." However, adhesion of the CaO film to the V–5%Cr–5%Ti substrate appeared to be quite good. Preliminary studies have been conducted to explore the self–healing properties of CaO coatings under temperature cycling [8]. Self–healing of CaO was investigated at temperatures between 300 and 740°C. At 300°C, self–healing did not occur in a 10–h period; at ≥360°C, cracks appeared to heal (e.g., at 450°C, resistivity was restored to its initial value within several hours, and at 500°C in <1 h). When a CaO coating was subjected to compressive stress by increasing the temperature in a similar manner, no appreciable cracking was detected.

Be Coating on V-5%Cr-5%Ti

Beryllium forms intermetallic phases with many elements [9,10] including, Cr, Ti, and V. Consequently, this property can be potentially useful in forming Be intermetallic coatings on V-Cr-Ti alloys. According to the Be-V binary phase diagram, $Be_{12}V$ and Be_2V intermetallic phases are present. Similarly, Cr and Ti form $CrBe_2$ and $CrBe_{12}$, and $TiBe_2$, $TiBe_3$, Ti_2Be_{12}, and $TiBe_{17}$, respectively. Beryllium intermetallic coatings can form on structural alloys during exposure in a liquid–metal environment that contains Be as a solute element. In a liquid-Li environment, in contrast to vapor–phase deposition processes, contamination of the alloy surface by oxygen and other contaminants during the coating process does not occur and no other phases form at the Li/alloy substrate. Only dissolved Be at a relatively low concentration in Li reacts with the V alloy. The Be_2V intermetallic phase on the surface of a V-5%Cr–5%Ti specimen and a Be depth profile obtained by secondary–ion mass spectroscopy are shown in Fig. 2. The photomicrographs reveal good bonding and no cracks because the layer formed by inward diffusion of Be into V and then by a solid-state reaction to form the Be_2V phase. In general, it is difficult to prepare crack–free Be coatings by conventional methods.

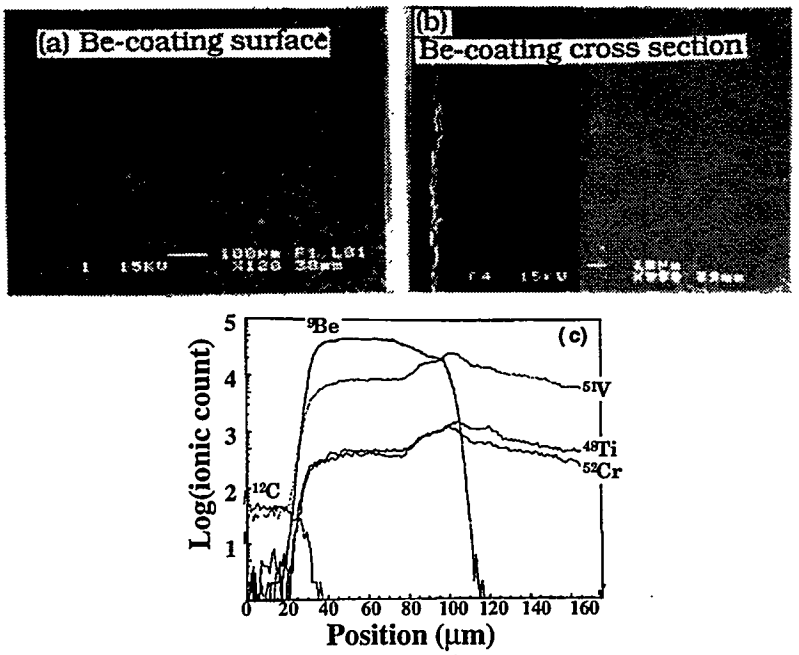

Fig. 2. (a, b) Be_2V intermetallic phase on V-5%Cr-5%Ti surface and cross section, and (c) Be depth profile obtained by secondary–ion mass spectroscopy

Be/V-Alloys/CaO/Li

Beryllium is used extensively for plasma–facing components in the design of the International Thermonuclear Experimental Reactor (ITER) because of the high fluxes of energetic particles and heat from the plasma [11,12]. Deuterium and tritium atoms from the plasma are implanted in the first wall, and neutron irradiation causes proton production within the materials by n,p reactions. The materials and material combinations (i.e., a layered structure, Fig. 1) influence hydrogen isotope recycling from the inner surface of the first wall to the plasma, as well as the magnitude of the hydrogen inventory in and permeation through the first–wall structure to the liquid–Li blanket/coolant [13,14]. Computer codes have been developed to assess the magnitude of hydrogen inventory, permeation, and recycling in the first wall because of (a) possible radiological hazards associated with tritium and (b) embrittlement of the structure by hydrogen isotopes [12–14].

Many factors contribute to transport and retention of hydrogen, namely, rates of release of hydrogen isotopes from the plasma–facing surface to the vacuum vessel, diffusivities and solubilities of hydrogen, densities of neutron–damage–induced traps, and thermodynamic distribution of hydrogen among the different materials in the blanket/structure. Radiation damage and diffusion/desorption behavior of tritium from irradiated Be have been reviewed [15,16]. Operating conditions such as duration of burn and recovery times, temperatures, and duty cycle also influence tritium inventory. Estimates of tritium inventory in the first–wall and permeation through the wall to the Li coolants (e.g., Fig. 1) vary over a wide range, depending on whether optimistic or pessimistic assumptions are invoked for the rate coefficient for recombination and release of hydrogen species back to the plasma, as well as effects of surface films thereon, neutron–induced trapping versus nontrapping of hydrogen in the structural materials, and presence or absence of a diffusion barrier (e.g., CaO) at the V–alloy/Li interface [11,13,14]. To reduce the uncertainty in these estimates, we are obtaining hydrogen solubility and permeability data in V-4%Cr-4%Ti in liquid Li, and in liquid Li-Ca alloys with and without CaO coatings [17].

CONCLUSIONS

Based on results of liquid–Li compatibility tests, information on the thermodynamic stability of ceramic materials in Li, and phase diagram considerations, we have developed methods for in-situ fabrication of CaO insulator and Be–intermetallic coatings on V–base alloys in a liquid-Li environment. Crack–free Be_2V intermetallic coatings and highly insulating CaO coatings were produced on a V-5%Cr–5%Ti alloy. The coating processes are facilitated in liquid Li because surface contamination by O or oxide films is virtually eliminated and the processes produce homogeneous coatings on various surface shapes through control of exposure time, temperature, and composition of the liquid metal. Additional work is underway to improve the mechanical stability of the coatings during thermal cycling and to establish the mechanisms for self-healing of the coatings.

ACKNOWLEDGMENTS

K. Rhode of The McCrone Group, Westmont, IL, and B. Tani of the Argonne Analytical Chemistry Laboratory provided analyses of the phases. G. Dragel assisted in the liquid-Li experimental work.

REFERENCES

[1] C. C. Baker et al., *Tokamak Power System Studies FY 1985*, Argonne National Laboratory Report ANL/FPP-85-2 (1985).

[2] T. Kammash, *Fusion Reactor Physics*, Chapter 15, Ann Arbor Science Pub. Inc., Ann Arbor, MI (1975), pp. 405-439.

[3] R. F. Mattas, B. A. Loomis, and D. L. Smith, *Vanadium Alloys for Fusion Reactor Applications*, JOM, **44**(8) (1992) 26.

[4] D. L. Smith, MRS Bull. (July 1989), 48.

[5] H. E. Prebble, C. B. A. Forty, and G. J. Butterworth, J. Nucl. Mater., **191–194** (1992), 391–395.

[6] J.-H. Park, T. Domenico, G. Dragel, and R. W. Clark, *Development of Electrical Insulator Coatings for Fusion Power Applications,* Fusion Engineering and Design **27** (1995) 3-16.

[7] R. J. Lauf and J. H. DeVan, *Evaluation of Ceramic Insulator for Lithium Electrochemical Reduction Cells,* J. Electrochem. Soc., **139** (1992) 2087-2091.

[8] J.–H. Park and T. F. Kassner, *Formation and Self–Healing Behavior of CaO Insulator Coatings on aVanadium–Base Alloy in Liquid Lithium,* in Fusion Reactor Materials Semiannual Progress Report for the Period Ending March 31, 1995, DOE/ER–0313/18, pp. 339–345 (July 1995).

[9] M. Hansen, *Constitution of Binary Alloys,* McGraw-Hill, New York (1958).

[10] F. A. Shunk, *Constitution of Binary Alloys, Second Supplement,* McGraw-Hill, New York (1969).

[11] R. A. Causey and K. L. Wilson, *Tritium Inventory and Permeation in the ITER Beryllium*, J. Nucl. Mater., **212-215** (1994) 1436-1442.

[12] J. W. Davis, D. E. Driemeyer, J. R. Haines, and R. T. McGrath, *Engineering and Materials Issues in Designing a Cold–Gas Divertor*, J. Nucl. Mater., **212-215** (1994) 1353-1359.

[13] G. Gervasini and F. Reiter, *Hydrogen Isotopes Transport in Fusion Reactor First Wall Materials*, J. Nucl. Mater., **212-215** (1994) 1379-1383.

[14] P. L. Andrew and M. A. Pick, *Review of Tritium Retention in First–Wall Materials*, J. Nucl. Mater., **212-215** (1994) 111–117.

[15] D. S. Gelles, G. A. Sernyaev, M. Dalle Donne, and H. Kawamura, Radiation Effects in Berryllium Used for Plasma Protection, J. Nucl. Mater., **212-215** (1994) 29–38.

[16] D. L. Baldwin and M. C. Billone, *Diffusion/Desorption of Tritium from Irradiated Beryllium,* J. Nucl. Mater., **212-215** (1994) 948-953.

[17] J.-H. Park, D. L. Smith, and R. E. Buxbaum, to be published in Fusion Reactor Materials Semiannual Progress Report for the Period Ending June 30, 1996, DOE/ER–0313/20 (1996).

EFFECT OF DYNAMICALLY CHARGED HELIUM ON TENSILE PROPERTIES OF V–5Ti, V–4Cr–4Ti, AND V–3Ti–1Si*

H. M. Chung, B. A. Loomis, L. Nowicki, and D. L. Smith
(Argonne National Laboratory)

SUMMARY

In the Dynamic Helium Charging Experiment (DHCE), helium was produced uniformly in the specimen at linear rates of ≈0.4 to 4.2 appm He/dpa by the decay of tritium during irradiation to 18–31 dpa at 425–600°C in the lithium-filled DHCE capsules in the Fast Flux Test Facility. This report presents results of postirradiation tests of tensile properties of V–5Ti, V-4Cr-4Ti, V–3Ti–1Si. The effect of helium on tensile strength and ductility was insignificant after irradiation and testing at >420°C. Contrary to initial expectation, room–temperature ductility of DHCE specimens was higher than that of non–DHCE specimens, whereas strength was lower, indicating that different types of hardening centers are produced during DHCE and non–DHCE irradiation. In strong contrast to results of tritium–trick experiments, in which dense coalescence of helium bubbles is produced on grain boundaries in the absence of displacement damage, no intergranular fracture was observed in any tensile specimens irradiated in the DHCE.

INTRODUCTION

Recent attention in the development of vanadium alloys has focused on V-4Cr-4Ti for fusion reactor structural components because of its excellent mechanical and physical properties before and after neutron irradiation.[1,2] Similar to V–4Cr–4Ti, the V–5Ti and V–3Ti–1Si also exhibited excellent resistance to irradiation embrittlement under non–DHCE conditions (negligible helium generation).[2] However, one property of these alloys that is not well understood is the effect of helium; only initial results of tensile testing on V–4Cr–4Ti have been reported on the effects of simultaneous generation of helium and neutron displacement damage under fusion–relevant conditions (i.e., ≈5 appm He/dpa ratio), although the effect of helium on other vanadium alloys has been investigated by less–than–prototypical simulation techniques such as tritium-trick,[3,4] cyclotron-injection,[5] and boron-doping.[5,6] In the DHCE,[7,8] fusion–relevant helium–to–dpa damage ratio is closely simulated by utilizing slow transmutation of controlled amounts of ^{6}Li and a tritium–doped mother alloy immersed in $^{6}Li + {}^{7}Li$. This report presents results of postirradiation examination of mechanical properties of V–5Ti, V-4Cr-4Ti, and V–3Ti–1Si alloys, which have been reported to exhibit excellent resistance to displacement damage under non–DHCE irradiation.[2]

MATERIALS AND PROCEDURES

The elemental composition of the V–5Ti, V–4Cr–4Ti, and V–3Ti–1Si alloys, determined prior to irradiation, is given in Table 1. The alloy ingots, melted from low–chlorine titanium and high–purity vanadium by the multiple–vacuum–arc process, were typically extruded at 1150°C and annealed at 1050°C. Final forms of the product were 3.8–, 1.0–, and 0.3–mm–thick annealed plates and sheets. Tensile specimens with a gauge length of 7.62 mm and a gauge width of 1.52 mm were machined from 1.0–mm–thick sheets that had been annealed at ≈1050°C. The only secondary phase in the recrystallized specimen was Ti(O,N,C), which is normally observed in titanium–containing vanadium alloys with >400 wppm O+N+C. Tensile properties were measured at 23°C and at irradiation temperatures in flowing argon at a strain rate of 0.0011 s^{-1}. The thickness and gauge width of each specimen were measured individually after irradiation and before each tensile test.

The alloy specimens were irradiated in the Fast Flux Test Facility (FFTF) at 420, 520, and 600°C to neutron fluences (E > 0.1 MeV) ranging from 3.7×10^{22} n/cm^2 (≈18 displacements per atom, or dpa) to 6.4×10^{22} n/cm^2 (≈31 dpa). Helium in the alloy specimens was produced by transmutation of controlled amounts of ^{6}Li and predetermined amounts of tritium–doped vanadium mother alloy immersed in $^{6}Li + {}^{7}Li$.[7,8] Table 2 summarizes the irradiation temperature, weight of the mother alloy, fraction of ^{6}Li, and tritium and lithium inventory charged in each of the seven DHCE capsules before irradiation.

---

* Work upported by the U.S. Department of Energy, Office of Fusion Energy Research, under Contract W-31-109-Eng-38.

Table 1. Composition of vanadium–base alloys

	Nominal Composition	Impurity Composition (wppm)			
ANL ID	(wt.%)	O	N	C	Si
BL–45	V–2.5Ti–1Si	345	125	90	9900
BL–46	V–4.6Ti	305	53	85	160
BL–47	V–4.1Cr–4.3Ti	350	220	200	870

Table 3 summarizes actual postirradiation parameters determined from tensile and transmission electron microscopy disk specimens of the V–4Cr–4Ti alloy, i.e., fast neutron fluence, dose, and helium and tritium contents measured ≈20–25 days after the postirradiation tests. Helium and tritium content was determined by mass spectrometry at Rockwell International Inc., Canoga Park, CA. The tritium content was determined on the basis of an analysis of ^{3}He decay, measured on the same specimens ≈50 days apart.

Table 2. Summary of capsule–loading parameters of DHCE

Capsule ID No.	Irradiation Temp. (°C)	Total Weight (g)			Fraction of ^{6}Li (%)	Initial Tritium Charged[a]	
		Vanadium[a]	Specimen[b]	Lithium		(Ci)	(mmol)
4D1	425	1.5468	5.86	0.765	5.0	99	1.70
4D2	425	1.5536	5.38	0.765	4.5	70	1.20
5E2	425	1.5657	5.38	0.670	1.0	26	0.45
5D1	500	1.5727	5.77	0.938	6.5	73.5	1.26
5E1	500	1.5651	5.82	0.952	1.0	57	0.98
5C1	600	1.5656	5.82	0.808	8.0	16.4	0.28
5C2	600	1.5466	5.95	0.955	8.0	18	0.31

[a] Letter from C. E. Johnson to K. Pearce, April 23, 1991; 1 mmol = 58.3 Ci.
[b] Excluding tritium–charged mother alloy.

Table 3. Summary of irradiation parameters of Dynamic Helium Charging Experiment and helium and tritium contents measured in V–4Cr–4Ti specimens

Capsule ID No.	Irradiation Temp. (°C)	Fluence (E >0.1 MeV) (1022 n cm–2	Total Damage (dpa)	Calculated Helium (appm) to dpa Ratioa at EOI[b] (Assumed ka or k_W)[c] k_a=0.073 (k_W=0.01)	Measured Helium Content[d] (appm)	Actual Helium to dpa Ratio (appm/dpa)	Measured Tritium Content[e] (appm)
4D1	425	6.4	31	3.8	11.2–13.3	0.39	27
4D2	425	6.4	31	2.8	22.4–22.7	0.73	39
5E2	425	3.7	18	2.1	3.3–3.7	0.11	2
5D1	500	3.7	18	4.4	14.8–15.0	0.83	4.5
5E1	500	3.7	18	3.1	6.4–6.5	0.36	1.7
5C1	600	3.7	18	1.1	8.4–11.0	0.54	20
5C2	600	3.7	18	1.1	74.9–75.3	4.17	63

[a] L. R. Greenwood "Revised Calculations for the DHCE," April 30, 1993.
[b] Beginning of irradiation (BOI) May 27, 1991; end of irradiation (EOI) March 19, 1992; 203.3 effective full power days (EFPD), hot standby at ≈220°C until November 1992.
[c] Equilibrium ratio (k_a by atom, k_W by weight) of tritium in V alloy to that in surrounding liquid lithium.
[d] Measured June 1994.
[e] Measured August 1994.

RESULTS

Yield strength, ultimate tensile strength, uniform elongation, and total elongation, measured on tensile specimens of V–4Cr–4Ti irradiated at 425°C–600°C to 18–34 dpa in the DHCE (4–75 appm He, or helium generation rate of ≈0.4–4.2 appm He/dpa), are summarized in Fig. 1. For comparison, similar properties, measured on irradiated non–DHCE (<0.1 appm He) specimens, are also plotted as a function of irradiation temperature. Similar results from V–5Ti (9–20 appm He) and V–3Ti–1Si (6–36 appm He) are given in Figs. 2 and 3, respectively. In these figures, two groups of postirradiation tensile properties are given, i.e., those measured at the irradiation temperatures and those measured at 20–200°C.

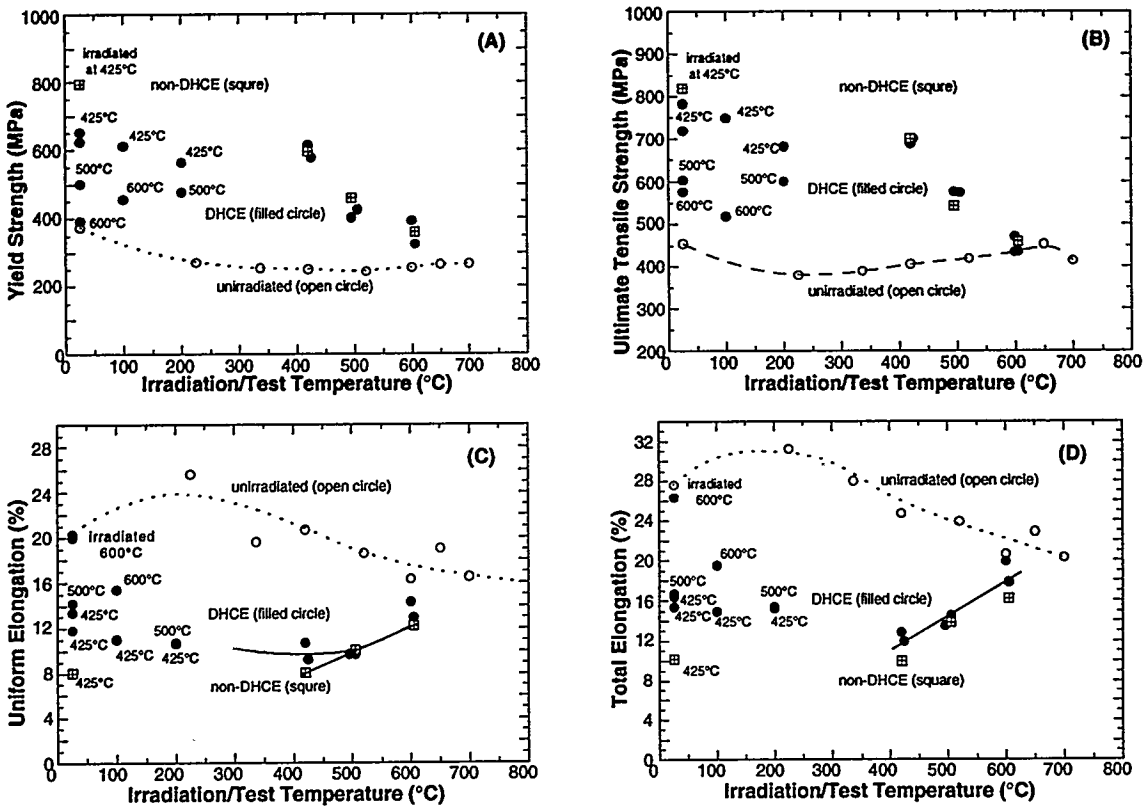

Fig. 1. Yield strength (A), ultimate tensile strength (B), uniform elongation (C), and total elongation (D) of V–4Cr–4Ti after irradiation at 420–600°C to 18–34 dpa in DHCE (0.4–4.2 appm He/dpa) and non–DHCE conventional irradiation (negligible helium generation).

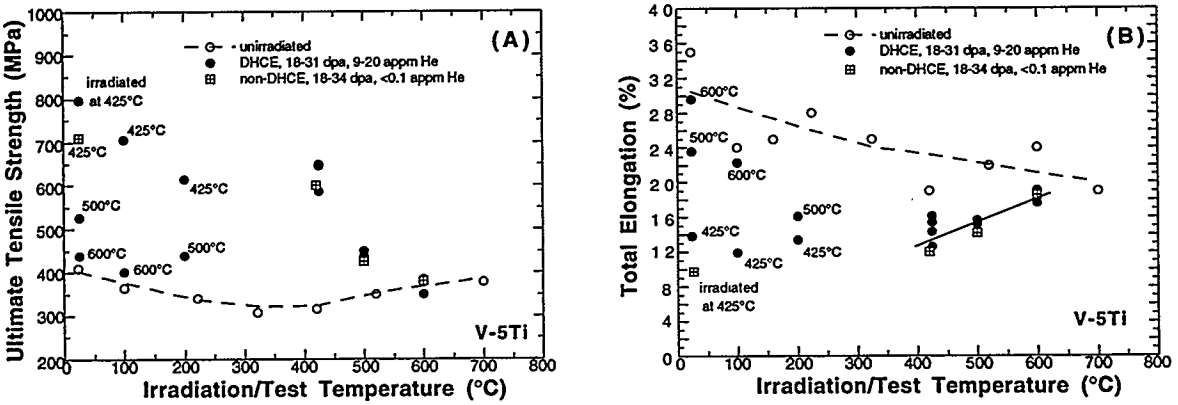

Fig. 2. Ultimate tensile strength (A) and total elongation (B) of V–5Ti after irradiation at 420–600°C to 18–34 dpa in DHCE (9–20 appm He) and non–DHCE conventional irradiation (<0.1 appm He).

After irradiation to ≈30 dpa in either a DHCE or a non–DHCE, ductilities of all three alloys remained significantly high, i.e., >9% uniform elongation and >12% total elongation. Tensile properties of DHCE specimens, measured at 425°C, 500°C, and 600°C (the same as the irradiation temperatures), were essentially the same as or slightly higher than those measured on non–DHCE specimens, showing that the effect of helium was insignificant. For all three alloys, ductility at 20–200°C of the DHCE specimens (irradiated at 425°C, 500°C, and 600°C) was higher than that of similar non–DHCE specimens, whereas

strength was lower. This was an unexpected finding. Initially, this finding was reported for V–4Cr–4Ti; the present confirmation of similar behavior in V–5Ti and V–3Ti–1Si provides a conclusive trend. Although the mechanisms leading to the higher ductility and lower strength of the DHCE specimens are not understood at this time, the consistent observations indicate that different types of hardening centers are produced during DHCEs and non–DHCEs.

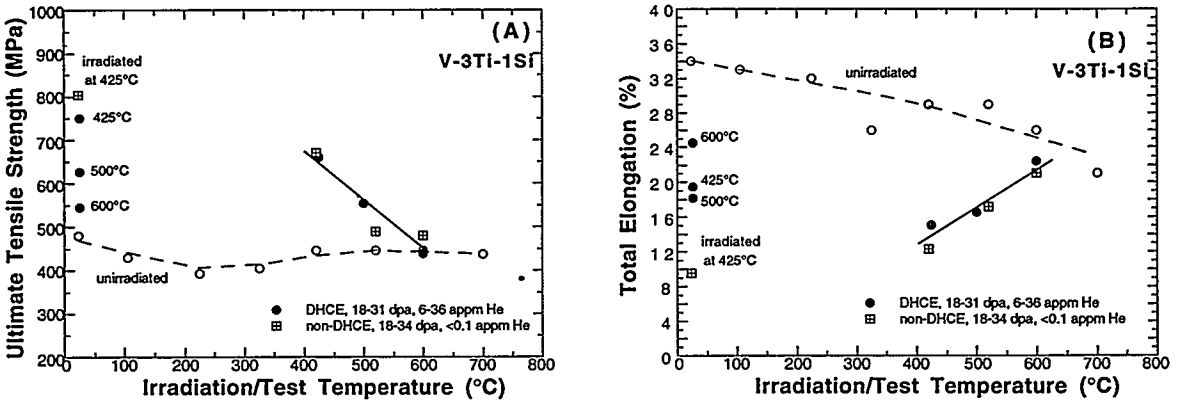

Fig. 3. Ultimate tensile strength (A) and total elongation (B) of V–3Ti–1Si after irradiation at 420–600°C to 18–34 dpa in DHCE (6–36 appm He) and non–DHCE conventional irradiation (<0.1 appm He).

The dependence of uniform and total elongation on irradiation and test temperature, is in sharp contrast to similar results obtained from specimens in which helium atoms were produced by the tritium–trick method. In the latter type experiments, total elongation measured at room temperature and at 700–800°C was significantly lower than that measured at 500–600°C, because of the strong susceptibility to intergranular cracking that is associated with extensive formation of grain–boundary helium bubbles.[4] However, no intergranular fracture surface morphology was observed in the tensile specimens of V–5Ti, V–4Cr–4Ti, and V–3Ti–1Si irradiated in the DHCE and tested at 25–600°C (including the V–4Cr–4Ti specimen irradiated in Capsule 5C2 at 600°C at a helium generation rate of 4.2 appm He/dpa), and no ductility degradation similar to that in tritium–trick experiments was observed. This is shown in Fig. 4, where the ratio of total strain in specimens with and without helium is plotted as a function of irradiation and test temperature for the DHCE and tritium–trick experiments.

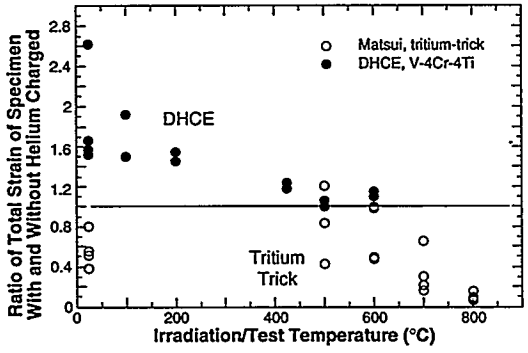

Fig. 4.
Ratio of total strain in specimens with and without helium as a function of irradiation and test temperature. Results obtained from tritium–trick experiment and DHCE are shown for comparison.

DISCUSSION

An important finding from the DHCE was that the actual (measured) amount of helium and tritium in V–5Ti, V–4Cr–4Ti, and V–3Ti–1Si specimens was significantly lower than previously calculated (see Table 3) on the basis of an assumed equilibrium ratio (k_W = 0.01, by weight) of tritium in the alloys to that in the liquid lithium (Table 2). In the case of V–4Cr–4Ti, except for specimens irradiated in Capsule 5C1 and 5C2 at 600°C, actual helium/dpa ratios (i.e., 0.36–0.83) were several times lower than those calculated

on the basis of an equilibrium ratio of $k_W = 0.01$ (i.e., 2.1–4.4). The helium generation rates in the specimens in Capsule 5C2 (≈4.2 appm He/dpa) were, however, close to the fusion–relevant rate of ≈5 appm He/dpa. The smaller helium/dpa rate, in particular for irradiation at ≈420°C, indicates that the level of hydrogen and tritium in the lithium–cooled V–4Cr–4Ti first–wall/blanket structure, and hence the effect of hydrogen and tritium on fracture toughness, will be significantly lower than previously assumed.

Helium microvoids were insignificant in all of the specimens that were irradiated at 500–600°C in the DHCE; only a few helium bubbles were observed at the interface between the grain matrix and some Ti(O,N,C) precipitates that are normally present in Ti–containing alloys. Even in V–4Cr–4Ti specimens that were irradiated at 600°C at the highest helium generation rate of ≈4.2 appm helium/dpa (Capsule 5C2), no microvoids could be detected in either grain matrix or grain boundaries.[9] For V–4Cr–4Ti specimens irradiated to 31 dpa at 425°C, low densities of diffuse helium bubbles were distributed more or less uniformly in a localized grain matrix and near a limited fraction of grain boundaries.

Although, in some of the V–5Ti and V–3Ti–1Si specimens irradiated at 425°C, more helium bubbles were observed in limited regions of grain boundaries than in grains, significant coalescence of helium bubbles, which is nearly continuous on grain boundaries in tritium–tricked specimens, was not observed. However, considering the relatively low helium generation rates measured in the specimens irradiated at ≈425°C, it is desirable to demonstrate the above finding for higher helium generation rates (e.g., 5–7 appm He/dpa) from a modified DHCE at 300–450°C. Neither partially nor fully intergranular failure was observed in any of the present specimens that were irradiated in the DHCE and subsequently tested in uniaxial tension at 20–600°C. These observations, consistent with the characteristics of the helium bubble distribution described above, are also in distinct contrast to the propensity for intergranular failure that is commonly observed in tritium–trick experiments.

For the three alloys, V–5Ti, V–4Cr–4Ti, and V–3Ti–1Si, the uniform and total elongations, determined from the tensile tests at 20–200°C on DHCE specimens, were significantly greater than similar elongations measured on specimens irradiated in either non–DHCE (Figs. 1–3) or tritium–trick experiments (Fig. 4). This is also consistent with the absence of continuous aggregation of helium bubbles on grain boundaries in the specimens irradiated in the DHCE. In addition, the observation indicates that different types of hardening centers are produced in the alloy during DHCE and non–DHCE irradiation at 425–600°C.

Although the nature of the hardening centers produced during DHCE is not understood at this time, we believe that helium atoms are involved. In a series of studies on thermal desorption of helium from unalloyed vanadium and V–5Ti irradiated with helium ions of various energy levels, van Veen et al.[10] and Buitenhuis et al.[11] concluded that helium–oxygen–vacancy and helium–nitrogen–vacancy (and probably helium–vacancy–carbon as well) complexes are formed in the irradiated material. These investigators further deduced that the complexes are stable at low temperatures (<230°C) but dissociate into helium atoms and oxygen–vacancy and nitrogen–vacancy complexes at 270–310°C, leading to a prominent helium desorption peak at ≈290°C that was observed consistently in their experiments. Desorption peaks at ≈770°C and ≈1250°C, observed only after irradiation with helium ion to higher doses, were attributed to clusters of helium atoms and helium bubbles, respectively. These clusters and bubbles of helium are believed to be unstable only at the high temperatures. During the degassing treatment in the present study in which DHCE specimens were heated to 400°C at a rate of ≈0.2°C/s, desorption peaks were observed consistently at ≈290°C, although helium desorption was not positively identified by mass spectroscopy, as done by van Veen et al.[10] and Buitenhuis et al.[11]

Based on these observations, it is likely that stable helium–vacancy–impurity complexes are also present in the specimens irradiated in DHCE during tensile tests at room temperature. In contrast, in specimens irradiated in non–DHCE under similar conditions, vacancies and impurities (such as oxygen, nitrogen, and carbon) are not expected to form complexes in the absence of appreciable helium atoms. Rather, the impurity atoms in solution and vacancies or vacancy clusters will be scattered more or less randomly in interstitial and vacancy sites, respectively. Dislocation motion would then be more difficult, and hence ductility would be lower in the non–DHCE than in the DHCE specimens; this seems to be in accordance with the results shown in Figs. 1–3.

CONCLUSIONS

1. Tensile ductilities of V–5Ti, V–4Cr–4Ti, and V–3Ti–1Si, irradiated to 18–31 dpa at 425°C to 600°C in the Dynamic Helium Charging Experiment (DHCE) at helium generation rates of 0.4–4.2 appm He/dpa, remained significantly high at 25–600°C, i.e., >9% uniform elongation and >12% total elongation. Tensile properties measured at >400°C were essentially the same as those measured on non–DHCE specimens (negligible helium), showing that the effects of helium were insignificant.

2. Postirradiation ductility of these alloys, measured at 20–200°C, was higher than that of similar non–DHCE specimens, whereas strength was lower. These observations indicate that different types of hardening centers are present at room temperature in the DHCE specimens (helium–vacancy–impurities complex, impurities being oxygen, nitrogen, and carbon) and in non–DHCE specimens (defects and defect clusters, impurities in interstitial sites).

3. Fracture morphology and the dependence of uniform and total elongation on irradiation and test temperature were in distinct contrast to similar results obtained from specimens in which helium atoms were produced by the tritium–trick method. Neither partial nor predominantly intergranular fracture was observed in tensile specimens irradiated in the DHCE and tested at 20–600°C.

ACKNOWLEDGMENTS

Successful completion of the Dynamic Helium Charging Experiment, a complex and difficult irradiation test, was possible only through many years of effort and contributions from many investigators in the U.S. and Japan: F. W. Wiffen, H. Matsui, K. Abe, C. E. Johnson, R. G. Clemmer, J. P. Kopasz, L. R. Greenwood, M. L. Hamilton, K. L. Pearce, R. Ermi, A. Ermi, H.–C. Tsai, R. V. Strain, and D. Donahue. The authors are grateful, in particular, to L. R. Greenwood and B. M. Oliver for their calculation and measurement, respectively, of helium and tritium content.

REFERENCES

[1] B. A. Loomis, L. Nowicki, and D. L. Smith, "Effect of Neutron Irradiation on Tensile Properties of V–Cr–Ti Alloys," in Fusion Reactor Materials, Semiannual Prog. Report, DOE/ER-0313/15, Oak Ridge National Laboratory, Oak Ridge, TN (1994), pp. 219–222.

[2] B. A. Loomis, H. M. Chung, L. Nowicki, and D. L. Smith, "Effects of Neutron Irradiation and Hydrogen on Ductile-Brittle Transition Temperatures of V–Cr–Ti Alloys," ibid., pp. 253–257.

[3] D. N. Braski, in Influence of Radiation on Material Properties, ASTM-STP 956 (1986), pp. 271-290.

[4] H. Matsui, M. Tanaka, M. Yamamoto, and M. Tada, J. Nucl. Mater. 191-194 (1992) 919.

[5] W. van Witzenburg and E. de Vries, in Effects of Radiation on Materials, ASTM-STP 1125 (1990).

[6] H. Kawanishi, Y. Arai, and S. Ishino, J. Nucl. Mater. 191-194 (1992) 933.

[7] D. L. Smith, H. Matsui, L. R. Greenwood, and B. A. Loomis, J. Nucl. Mater. 155-157 (1988) 1359.

[8] D. L. Smith, B. A. Loomis, H. Matsui, M. L. Hamilton, K. L. Pearce, J. P. Kopasz, C. E. Johnson, R. G. Clemmer, and L. R. Greenwood, in Fusion Reactor Materials, Semiannual Prog. Rep. DOE/ER-0313/10, Oak Ridge National Laboratory, Oak Ridge, TN (1991), p. 159.

[9] H. M. Chung, L. Nowicki, J. Gazda, and D. L. Smith, "Void Structure and Density Change of Vanadium–Base Alloys Irradiated in the Dynamically Helium Charging Experiment Helium," in Fusion Reactor Materials, Semiannual Prog. Rep. DOE/ER-0313/17, Oak Ridge National Laboratory, Oak Ridge, TN (1995), p. 211–218.

[10] A. van Veen, H. Eleveld, and M. Clement, J. Nucl. Mater., 212-215 (1994) 287.

[11] T. Buitenhuis, A. Fedorov, and A. van Veen, "Thermal Desorption Investigation of V–5Ti Alloy," IRI–131–94–005, Delft University of Technology, The Netherlands, 1994.

DENSITY DECREASE IN VANADIUM-BASE ALLOYS IRRADIATED IN THE DYNAMIC HELIUM CHARGING EXPERIMENT*

H. M. Chung, T. M. Galvin, and D. L. Smith (Argonne National Laboratory)

SUMMARY

Combined effects of dynamically charged helium and neutron damage on density decrease (swelling) of V–4Cr–4Ti, V–5Ti, V–3Ti–1Si, and V–8Cr–6Ti alloys have been determined after irradiation to 18–31 dpa at 425–600°C in the Dynamic Helium Charging Experiment (DHCE). To ensure better accuracy in density measurement, broken pieces of tensile specimens ≈10 times heavier than a transmission electron microscopy (TEM) disk were used. Density decreases of the four alloys irradiated in the DHCE were <0.5%. This small change seems to be consistent with the negligible number density of microcavities characterized by TEM. Most of the dynamically produced helium atoms seem to have been trapped in the grain matrix without significant cavity nucleation or growth.

INTRODUCTION

Recent attention in the development of vanadium–base alloys for application in fusion reactor first–wall and blanket structure has focused on the findings of excellent impact toughness of V–4Cr–4Ti[1,2] and V–5Cr–5Ti[3] and virtual immunity of V-4Cr-4Ti, V–5Ti, and V–3Ti–1Si to embrittlement by fast neutron displacement damage.[4] Excellent resistance of these alloys to neutron–irradiation–induced (negligible helium generation) swelling has also been reported.[5] One unresolved issue in the performance of these alloys, however, has been the effect of fusion–relevant simultaneous generation of helium and neutron damage (at a ratio of 4–5 appm helium/displacement per atom [dpa]) on swelling (i.e., density decrease). In the unique DHCE,[6] the fusion–relevant helium–to–dpa ratio is simulated realistically by utilizing transmutation of controlled amounts of ^{6}Li and a predetermined amount of tritium–doped mother alloy immersed in $^{6}Li + ^{7}Li$. This report describes results of density measurements on V–4Cr–4Ti, V–5Ti, V–3Ti–1Si, and V–8Cr–6Ti alloys irradiated to 18–31 dpa at 425–600°C in the DHCE. The results were compared to similar data obtained from non–DHCE specimens (negligible helium generation) irradiated to 18–34 dpa at 420–600°C. Earlier measurements of density change that utilized small (≈10 mg) TEM disks indicated significant data scattering.[5,7] Therefore, heavier (70–110 mg) broken pieces of tensile specimens were used in this study to determine density decrease more accurately.

MATERIALS AND PROCEDURES

The elemental compositions of the V–4Cr–4Ti, V–5Ti, V–3Ti–1Si, and V–8Cr–6Ti are given Table 1. Tensile specimens, 0.7–1.0 mm thick, were polished and annealed at 1050–1125°C in high vacuum. Microstructures of V–4Cr–4Ti, characterized before and after irradiation in a non–DHCE (negligible helium generation) and a DHCE (0.4–4.2 appm helium/dpa), have been described elsewhere.[7] The only secondary phase in the as–annealed specimens was Ti(O,N,C), 200–500 nm in size, which is normally observed in titanium–containing vanadium alloys with O+N+C > 400 wppm. After irradiation in a non–DHCE or a DHCE, Ti_5Si_3 precipitates <20 nm in size were observed in high density.

Table 1. Composition of vanadium–base alloys

ANL ID	Nominal Composition (wt.%)	Impurity Composition (wppm) O	N	C	Si	S	P	Nb	Mo
BL-47	V–4.1Cr–4.3Ti	350	220	200	870	20	<40	<100	<100
BL-46	V–4.6Ti	305	53	85	160	10	<100	<100	–
BL-45	V–2.5Ti–1.0Si	345	125	90	9900	30	–	200	140
BL-49	V–7.9Cr–5.7Ti	400	150	127	360	20	–	<100	170

Sheet tensile specimens were irradiated in the Fast Flux Test Facility (FFTF) Cycle 12 Materials Open Test Assembly (MOTA) 2B at 420, 500, and 600°C to neutron fluences (E > 0.1 MeV) ranging from 3.7 x 10^{22}

* Work upported by the U.S. Department of Energy, Office of Fusion Energy Research, under Contract W-31-109-Eng-38.

n/cm^2 (≈18 dpa) to 6.4 x 10^{23} n/cm^2 (≈31 dpa). Counterpart tensile specimens were also irradiated to similar fluence at similar temperatures in non–DHCE (negligible helium generation) capsules in the MOTA–2B. Helium in the DHCE specimens was produced by utilizing transmutation of controlled amounts of ^{6}Li and a predetermined amount of tritium–doped vanadium mother alloy immersed in ^{6}Li + ^{7}Li. Table 2 summarizes the actual postirradiation parameters determined from tensile and disk specimens of the V–4Cr–4Ti alloy, i.e., fast neutron fluence, dose, and helium and tritium content measured shortly after the postirradiation tests. Helium and tritium were determined by mass spectrometry at Rockwell International Inc., Canoga Park, CA.

Table 2. Summary of irradiation parameters of Dynamic Helium Charging Experiment and helium and tritium content of V–4Cr–4Ti specimens

Capsule ID No.	Irradiation Temp. (°C)	Fluence (E >0.1 MeV) (10^{22} n cm^{-2})	Total Damage (dpa)	Calculated Helium (appm) to dpa Ratio[a] at EOI[b] (Assumed k_a or k_W)[c] k_a=0.073 (k_W=0.01)	Measured Helium Content[d] (appm)	Actual Helium to dpa Ratio (appm/dpa)	Measured Tritium Content[e] (appm)
4D1	425	6.4	31	3.8	11.2–13.3	0.39	27
4D2	425	6.4	31	2.8	22.4–22.7	0.73	39
5E2	425	3.7	18	2.1	3.3–3.7	0.11	2
5D1	500	3.7	18	4.4	14.8–15.0	0.83	4.5
5E1	500	3.7	18	3.1	6.4–6.5	0.36	1.7
5C1	600	3.7	18	1.1	8.4–11.0	0.54	20
5C2	600	3.7	18	1.1	74.9–75.3	4.17	63

[a] L. R. Greenwood "Revised Calculations for the DHCE," April 30, 1993.
[b] Beginning of irradiation (BOI) May 27, 1991; end of irradiation (EOI) March 19, 1992; 203.3 effective full power days (EFPD), hot standby at ≈220°C until November 1992.
[c] Equilibrium ratio (k_a by atom, k_W by weight) of tritium in V alloy to that in the surrounding liquid Li.
[d] Measured June 1994.
[e] Measured August 1994.

Density decrease (swelling) was determined from weight of nonirradiated and irradiated (DHCE and non–DHCE) specimens, measured in air and in research–grade CCl_4. A typical specimen (70–110 mg in air) was a piece of the shoulder region of a 1.0–mm–thick tensile specimen, cut after a tensile test in an inert atmosphere at the same temperature as the irradiation temperature or at 20–200°C.[8]

RESULTS AND DISCUSSION

Density could be determined more accurately by measurements on broken tensile specimens than on 0.3–mm thick, ≈10–mg TEM disks. This is shown in Fig. 1, in which data scattering of baseline density of nonirradiated tensile and disk specimens of V–4Cr–4Ti is presented. The uncertainty limit of the density measured on tensile specimens is significantly smaller than that measured on small TEM disks.

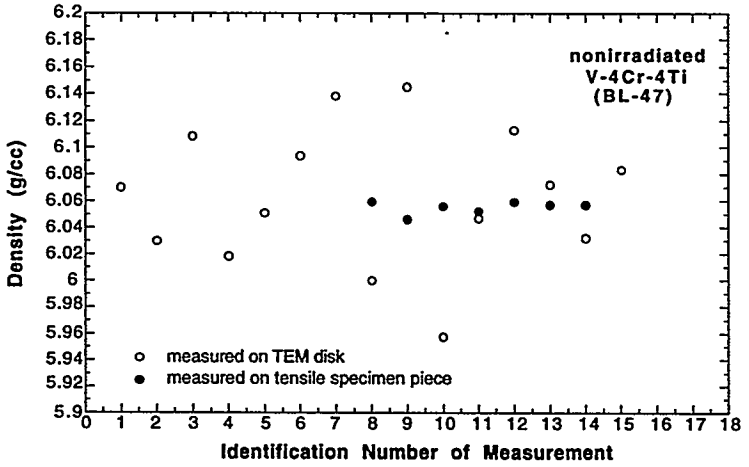

Figure 1. Densities obtained from ≈10–mg TEM disks in weight) and ≈70–110–mg broken tensile specimens of nonirradiated V–4Cr–4Ti, showing significantly more accurate data from tensile specimens.

The decrease in density for V–4Cr–4Ti, V–5Ti, V–3Ti–1Si, and V–8Cr–6Ti is given in Figs. 2–5, respectively. For comparison, density changes determined under similar irradiation conditions in a non–DHCE are shown in Figs. 2–4.

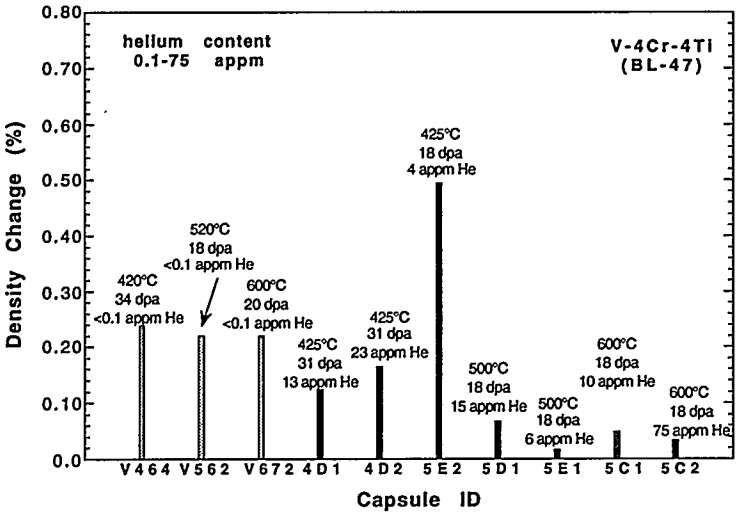

Figure 2.
Density changes of V–4Cr–4Ti (BL–47) after irradiation to 18–34 dpa at 420–600°C in the DHCE (0.4–4.2 appm He/dpa) (dark bars) and in a non–DHCE (negligible helium) (light bars). Each bar represents the average of densities measured on three separate pieces of broken tensile specimens.

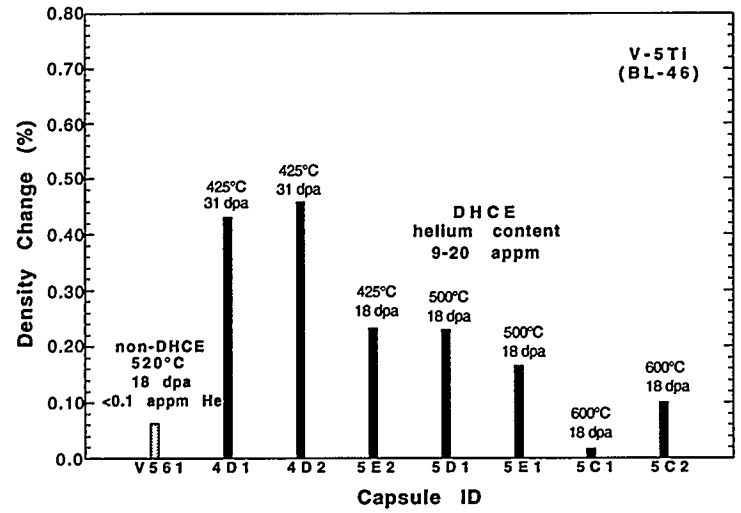

Figure 3.
Density changes of V–5Ti (BL–46) after irradiation to 18–31 dpa at 425–600°C in the DHCE (9–20 appm He) (dark bars) and in a non–DHCE (negligible helium) (light bars). Each bar represents the average of densities measured on three separate pieces of broken tensile specimens.

Density changes measured for the non–DHCE and DHCE specimens of the reference alloy V–4Cr–4Ti were low (<0.5 %). This small density change seems to be consistent with the negligible density of voids or helium bubbles in the DHCE specimens of the alloy. At least for helium generation rates in the range of 0.4–4.2 appm He/dpa, there was no evidence of a significant effect of dynamically charged helium on density change (Fig. 2); the reference alloy V–4Cr–4Ti seems to be inherently resistant to swelling under the present conditions of the DHCE and non–DHCE, indicating that swelling of the alloy under fusion reactor conditions is also low.

Although helium generation was rather low (<1.1 appm He/dpa), density changes measured for the DHCE specimens of V–5Ti, V–3Ti–1Si, and V–8Cr–6Ti were also low (<0.5%), regardless of irradiation temperature and dose. There are indications that density changes measured for V–5Ti and V–3Ti–1Si irradiated at 425°C (to ≈31 dpa) are somewhat higher than those measured for specimens irradiated at 500–600°C (to ≈18 dpa).

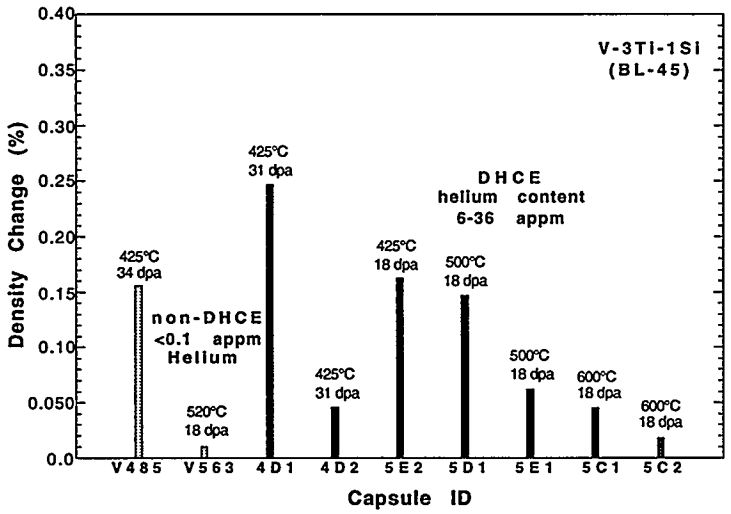

Figure 4.
Density changes of V–3Ti–1Si (BL–45) after irradiation to 18–34 dpa at 425–600°C in the DHCE (6–36 appm helium) (dark bars) and in a non–DHCE (negligible helium) (light bars). Each bar represents the average of densities measured on three separate pieces of broken tensile specimens.

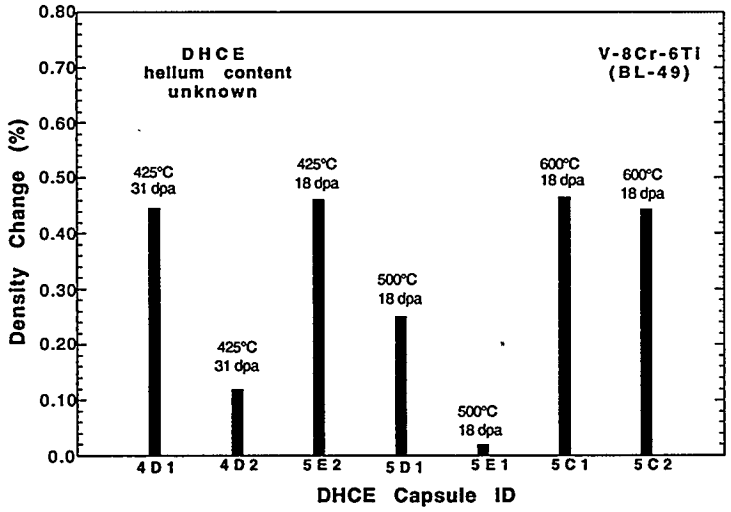

Figure 5.
Density changes of V–8Cr–6Ti (BL–49) after irradiation to 18–34 dpa at 420–600°C in the DHCE (helium content unknown). Each bar represents the average of densities measured on three separate pieces of broken tensile specimens.

CONCLUSIONS

1. For the reference alloy V–4Cr–4Ti irradiated to ≈18–31 dpa at 425–600°C in the Dynamic Helium Charging Experiment (DHCE) with helium generation rates of ≈0.4–4.2 appm He/dpa, density decrease (swelling) was low (<0.5%). Density changes measured for the DHCE and non–DHCE (negligible helium generation) specimens were similar, showing insignificant effect of dynamically charged helium. The reference alloy seems to be inherently resistant to swelling under the present conditions of the DHCE (helium and dpa damage) and non–DHCE (dpa damage only), indicating that swelling of the alloy under fusion reactor conditions is also low.

2. Although the dynamic helium generation rate was low (<1.1 appm He/dpa), density changes measured for the DHCE specimens of V–5Ti, V–3Ti–1Si, and V–8Cr–6Ti were also low (<0.5%), regardless of the irradiation temperature (420–600°C) and dose (18–31 dpa).

3. Density change can be determined significantly more accurately with heavier tensile specimens than with small TEM disks.

REFERENCES

[1] H. M. Chung, L. Nowicki, and D. L. Smith, "Effect of Annealing on Impact Properties of Production–Scale Heat of V–4Cr–4Ti," in: Fusion Reactor Materials Semiannual Progress Report for Period Ending March 31, 1995, DOE/ER-0313/18, U.S. Dept. of Energy, Office of Fusion Energy, July 1995, pp. 273–278.

[2] H. M. Chung, L. Nowicki, and D. L. Smith, "Impact Properties of Precracked V–4Cr–4Ti Charpy Specimens," ibid., pp. 253–258.

[3] H. M. Chung, L. Nowicki, D. Busch, and D. L. Smith, "Fabrication and Impact Properties of Laboratory–Scale Heat of V–5Cr–5Ti," ibid., pp. 259–264.

[4] B. A. Loomis, H. M. Chung, L. J. Nowicki, and D. L. Smith, "Effects of Neutron Irradiation and Hydrogen on Ductile-Brittle Transition Temperatures of V–Cr–Ti Alloys," J. Nucl. Mater. 212–215 (1994) 799–803.

[5] H. M. Chung, B. A. Loomis, and D. L. Smith, "Effect of Irradiation Damage and Helium on Swelling and Structure of Vanadium–Base Alloys," J. Nucl. Mater. 212–215 (1994) 804–812.

[6] D. L. Smith, H. Matsui, L. R. Greenwood, and B. A. Loomis, J. Nucl. Mater. 155-157 (1988) 1359.

[7] H. M. Chung, B. A. Loomis, H. Tsai, L. Nowicki, J. Gazda, and D. L. Smith, "Swelling and Structure of Vanadium Alloys Irradiated in the Dynamic Helium Charging Experiment," in Fusion Reactor Materials, Semiannual. Prog. Report, DOE/ER-0313/16, Oak Ridge National Laboratory, Oak Ridge, TN (1994), p. 204–211.

[8] H. M. Chung, B. A. Loomis, L. Nowicki, and D. L. Smith, "Effect of Dynamically Charged Helium on Tensile Properties of V–5Ti, V–4Cr–4Ti, and V–3Ti–1Si," in this report.

MICROSTRUCTURAL EVOLUTION OF V-4Cr-4Ti DURING ION IRRADIATION AT 200°C*

J. Gazda and M. Meshii (Northwestern University), and B. A. Loomis and H. M. Chung (Argonne National Laboratory)

OBJECTIVE

The objective of this study is to simulate microstructures produced by irradiation with fusion-energy neutrons in the reference vanadium alloy V-4Cr-4Ti at a relatively low temperature (200°C) utilizing ion irradiation of bulk specimens to understand the concomitant microstructural evolution of the alloy.

SUMMARY

The results of a transmission electron microscopy (TEM) investigation of the microstructural evolution of V-4Cr-4Ti (Heat #832665) that was irradiated with 4.5 MeV $^{58}Ni^{++}$ ions at 200°C are presented. Dose effects were investigated for fluences ranging from 0.5 to 5 dpa. When the irradiation dose was increased, the relative number density of black dots and dislocation loops was nearly constant and accompanied by an increase in the size of the defects. Cavity formation was not observed in any of the specimens, indicating high resistance of the alloy to void swelling at the low temperature of the experiments.

INTRODUCTION

Vanadium-base alloys are the most promising candidate low-activation materials for application in first-wall structures of magnetic fusion reactors. Recently, the V-4Cr-4Ti alloy was identified as a material that exhibited the optimal combination of mechanical and physical properties.[1,2] The virtual immunity to embrittlement and excellent resistance to swelling of several V-Cr-Ti, V-Ti, and V-Ti-Si alloys have been reported previously under both ion and neutron irradiation in the temperature range of 420 - 600°C.[3-6] However, data on the performance of the alloy in the low to moderate temperature range (<400°C) is limited. Confirmation of minimal swelling and demonstration of resistance to embrittlement by displacement damage and helium in this temperature range are particularly important issues.

The customary method for determining the irradiation performance of fusion candidate materials, i.e., tests utilizing fast fission neutrons (E > 0.1 MeV), is now much more difficult to conduct because of reactor shutdowns. Therefore, in this study, we chose an alternative approach to evaluate the irradiation-induced microstructural evolution of vanadium-base alloys at moderate-to-low temperatures. The approach is based on extrapolation of results from ion irradiation experiments. Work consisted of series of ion irradiations at 200°C to obtain doses of 0.5, 2, and 5 dpa in the maximum-damage region of bulk specimens. Microstructural changes in the production-scale (500 kg) heat of V-4Cr-4Ti alloy were generated by $^{58}Ni^{++}$ ion beams produced in the Tandem Ion Accelerator/High Voltage Electron Microscope Facility located at Argonne National Laboratory (ANL). Conventional transmission electron microscopy (TEM) was used to identify the type and number density of produced defects.

MATERIAL AND PROCEDURES

Fabrication of the V-4Cr-4Ti alloy (Heat ID 832665) is described in detail elsewhere.[7] The composition of the extruded plate that was used for the present specimens is given in Table 1. Procedures for preparing of the specimens are described in the previous report,[8] with one modification: discs were ground to a thickness of ≈125 μm before the polishing and annealing steps. The ion irradiations were performed at the Tandem Accelerator facility operated by the ANL Materials Science Division. Beams of 4.5 MeV $5^{8}Ni^{++}$ ions were produced by the 2-MV NEC ion accelerator, while the vacuum in the ion chamber used for the irradiations was maintained at 1×10^{-6} Pa. Irradiation temperature was 200 ± 2°C. The procedure for final preparation of foils for TEM observations is described in Ref. 8. Microstructure observations were conducted with a

* Work supported by U.S. Department of Energy, Office of Fusion Energy Research, under Contract W-31-109-Eng-38.

Philips CM30 transmission electron microscope. Number density and dislocation loop size were measured from bright field images obtained with $\mathbf{g} = (200)$ and $\mathbf{g} = (0\bar{1}1)$ diffraction vectors near the [011] foil orientation. Dislocation loop size was measured from prints with a Zeiss particle size analyzer/counter.

Table 1. Composition of production heat of V-4Cr-4Ti alloy [a]

Heat ID	ANL ID	Cr	Ti	Cu	Si	O	N	C	S	P	Ca	Cl	B
832665	BL-71	3.8	3.9	<50	783	310	85	80	<10	<30	<10	<2	<5

[a] Cr and Ti in wt.%, impurities in wppm.

RESULTS AND DISCUSSION

After irradiation up to 5 dpa at 200°C, the microstructure consisted of "black dot" defects (BD) and dislocation loops. Line dislocations were not observed in any of the specimens at this temperature and in this dose range. Two types of dislocation Burgers vectors, a_o<100> and $a_o/2$<111>, were found to coexist in all of the specimens. The combined number density of defects and dislocations was compared among specimens that had received different irradiation doses. These comparisons are presented in Fig. 1. The plots given in Fig. 1 are based on the relative number density of defects that resulted from counting visible defects in photomicrographs with $\mathbf{g} = (0\bar{1}1)$. The diffraction conditions in foils with such orientation allow only for visibility of 1/2 of the total number of $a_o/2$<111> type loops, and 2/3 of the total number of a_o<100> type loops in the body centererd cubic vanadium alloys. However, because the evidence for formation of equal numbers of each type of loop was not obtained, these proportions cannot be easily applied to the numbers obtained from the measurements. Therefore, relative numbers obtained under consistent diffraction conditions are quoted.

Examples of typical microstructures of specimens irradiated to 0.5, 2, and 5 dpa at 200°C are shown in Fig. 1. At 0.5 dpa, the microstructure is dominated by BDs, with only a limited number of dislocation

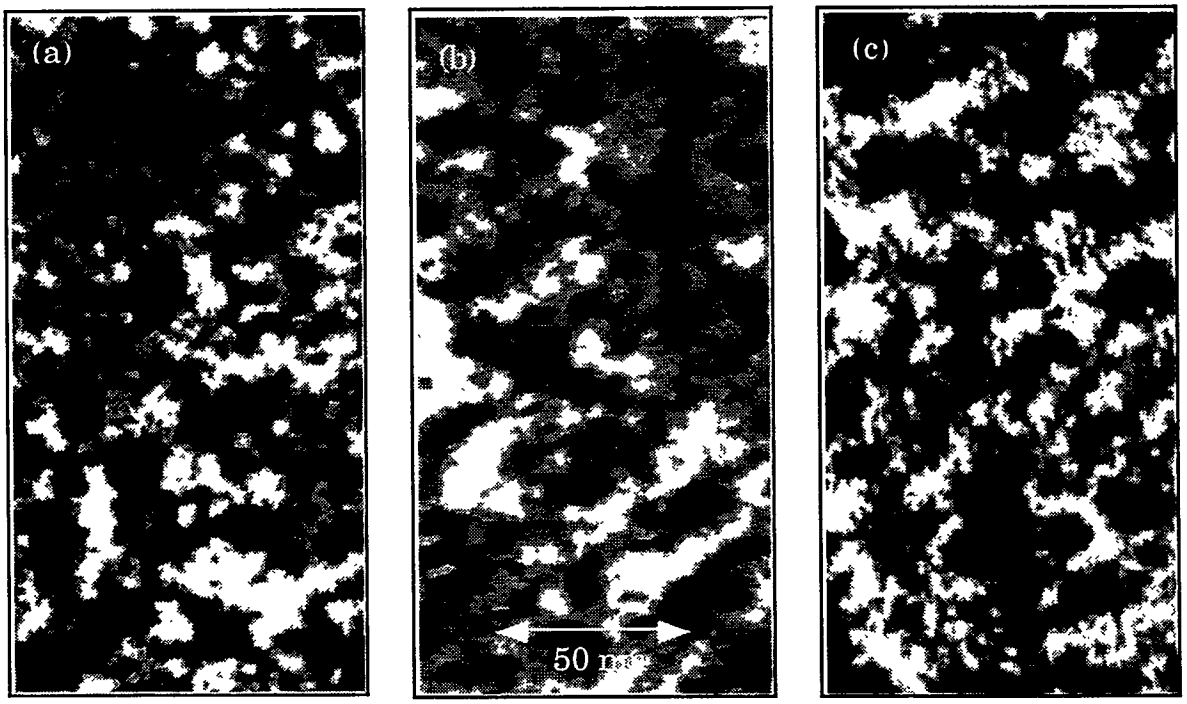

Figure 1. Microstructure of V-4Cr-4Ti alloy after $^{58}Ni^{++}$ ion irradiation at 200°C to: (a) 0.5, (b) 2, and (c) 5 dpa. Kinematical two-beam conditions $\mathbf{g} = (0\text{-}11)$, near [011] foil orientation.

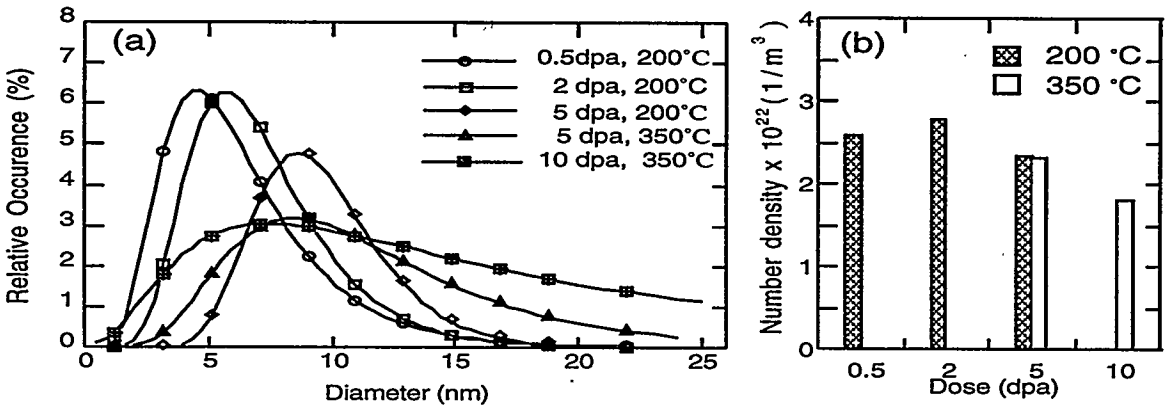

Figure 2. Evolution of microstructure of V-4Cr-4Ti under ion irradiation at 200°C and 350°C: (a) distribution of BDs and loop diameters; (b) relative number density of loops and BDs.

loops resolvable, their diameters reaching at most 20 nm. Similar features were observed in specimens irradiated to 2 dpa, but the number of resolvable loops increased. After 5 dpa, the loops became the prevailing feature of the microstructure, with their diameters reaching up to 50 nm. However, a significant number of BDs still remained after this damage dose. Figure 2a gives the observed distribution of BDs and loop diameter sizes. At all doses, the combined number density of BDs and loops remained approximately the same, as shown in Fig. 2b. The microstructure at 200°C was compared with one described in Ref. 8 that was obtained after 4.5 MeV $^{58}Ni^{++}$ ion irradiation to 5 and 10 dpa at 350°C. The number density of defect was approximately the same, whereas specimens irradiated to 10 dpa also showed formation of dislocation segments not observed at 200°C.

The data indicate early formation of a high density of defect clusters that act as point defect sinks during continuing irradiation. Growth of dislocation loops is sustained by production of freely migrating point defects from the remains of cascades. The other defect sinks present in the specimens include grain boundaries and interfaces between the matrix and Ti(CNO) thermal precipitates formed during fabrication of the alloy. The high density of sinks shortens the diffusion paths of point defects and efficiently removes them from solution. Dislocation segments in specimens irradiated to 10 dpa at 350°C could be explained by unfolding of dislocation loops when they reach a larger size.

Cavity formation was not observed in any of the specimens, including those irradiated to 5 dpa. In a previous investigation[8] with 4.5 MeV $^{58}Ni^{++}$ ion irradiation at 350°C to ~5 and ~10 dpa, cavity formation was also not observed. Likewise, a similar heat of V4Cr4Ti (BL47) was reported[6] to be resistant to cavity formation during fast neutron irradiation at ~420°C. Thus, the alloys of V-4Cr-4Ti composition appear to be resistant to void swelling, even at low temperatures, down to 200°C.

CONCLUSIONS

1. Consistent with the results from void swelling characterization of V-4Cr-4Ti (Heat 832655) irradiated at 350°C to ~10 dpa by $^{58}Ni^{++}$ ions and V-4Cr-4Ti (Heat BL-47) irradiated at ~420°C to ~34 dpa by fast neutrons (E > 0.1 MeV), no cavities were observed in V-4Cr-4Ti (Heat 832655) specimens irradiated by $^{58}Ni^{++}$ ions at 200°C to ~5 dpa. This indicates that the alloy class is resistant to void swelling at low temperatures, down to 200°C.

2. After irradiation with 4.5 MeV $^{58}Ni^{++}$ at 200°C: a) the predominant features of microstructure were small (<50 nm) dislocation loops and "black dot" defects; b) the size of dislocation loops increased with irradiation dose, whereas the combined number density of black dots and dislocation loops remained constant up to a fluence of 5 dpa. These findings indicate early formation of a large density

of defect clusters that act as point defect sinks and grow into dislocation loops during continuing irradiation.

3. The size and combined defect and loop number density after ion irradiation at 200°C were similar to those resulting from ion irradiation at 350°C.

REFERENCES

1. H. M. Chung, B. A. Loomis, and D. L. Smith, "Properties of V-4Cr-4Ti for application as fusion reactor structural components," Fusion Eng. Des. **29** (1995), pp. 455-464.

2. D. L. Smith, B. A. Loomis, and H. M. Chung, Plasma Devices and Operations **3**, 1994, pp. 167-179.

3. D. N. Braski, "The effect of neutron irradiation on vanadium alloys," J. Nucl. Mater. **141-143** (1986) 1125-1131.

4. B. A. Loomis and D. L. Smith, "Response of un-irradiated and neutron-irradiated vanadium alloys to charpy-impact loading," J. Nucl. Mater. **179-181** (1991) 783-786.

5. H. M. Chung, B. A. Loomis, L. J. Nowicki, J. Gazda, and D. L. Smith, "Irradiation-induced density change and microstructural evolution of vanadium-base alloys," in Fusion Reactor Materials, Semiannual Progress Report, DOE/ER-0313/15, Oak Ridge National Laboratory, Oak Ridge TN, pp. 223-231, September 1993.

6. H. M. Chung, L. J. Nowicki, J. Gazda, and D. L. Smith, "Void structure and density change of vanadium-base alloys irradiated in the dynamic helium charging experiment," in Fusion Reactor Materials, Semiannual Progress Report for Period Ending September 30, 1994, DOE/ER-0313/17 , Oak Ridge National Laboratory, Oak Ridge, TN, pp. 211-218, September 1994.

7. H. M. Chung, H. C. Tsai, D. L. Smith, R. Peterson, C. Curtis, C. Wojcik, and R. Kinney, "Fabrication of 500-kg heat of V-4Cr-4Ti," ibid., pp. 178-182.

8. J. Gazda, M. Meshii, B. A. Loomis, and H. M. Chung, "Microstructural evolution of V-4Cr-4Ti during dual-ion irradiation at 350°C," in Fusion Reactor Materials, Semiannual Progress Report for Period Ending March 31, 1995, DOE/ER-0313/18, Oak Ridge National Laboratory, Oak Ridge TN, pp. 243-246, March 1995.

UNUSUAL RESPONSE OF THE BINARY V-2Si ALLOY TO NEUTRON IRRADIATION IN FFTF AT 430-600C - S. Ohnuki, H. Kinoshita (Hokkaido University), F. A. Garner (Pacific Northwest National Laboratory) and H. Takahaski (Hokkaido University)

To be published in J. Nuclear Materials, 1996 proceedings of ICFRM-7

Abstract

When V-2Si was irradiated in FFTF at 430, 500 and 600C to doses as high as 80 dpa, a very unusual swelling response was observed in which the swelling appeared to saturate rather quickly at ~35% at 430 and 540C, but approached this swelling same level much more slowly at 600C.

Microstructural examination revealed that a peculiar form of microstructural self-organization had occurred that is linked to the saturation behavior. Each individual grain was observed to have subdivided into cells surrounded by relatively void-free walls of V_3Si. The cells contain very little silicon inside their boundaries and develop average sizes that increase with increasing irradiation temperature. These cell walls enclose regions of very high swelling with strong gradients in void size and density in the vicinity of the cell walls. At lower irradiation temperatures the cell size does not appear to change with increasing displacement level, mirroring the early saturation observed in the swelling at these temperatures.

The possible causes of this phenomenon are discussed as well as the implications of these findings on the swelling behavior of other high swelling vanadium binary alloys.

[1] Operated for the US Department of Energy by Battelle Memorial Institute under Contract DE-AC06-76RLO 1830.

TRANSMUTATION-INDUCED EMBRITTLEMENT OF V-Ti-Ni AND V-Ni ALLOYS IN HFIR - S. Ohnuki, H. Takahashi (Hokkaido University), F. A. Garner (Pacific Northwest National Laboratory), J. E. Pawel (Oak Ridge National Laboratory), K. Shiba, and A. Hishinuma (Japan Atomic Energy Research Institute)

To be published in J. Nuclear Materials, 1996 proceedings of ICFRM-7

Extended Abstract

Vanadium, V-1Ni, V-10Ti and V-10Ti-1Ni (at%) were irradiated in HFIR to doses ranging from 18 to 30 dpa and temperatures between 300 and 600C. Since the irradiation was conducted in a highly thermalized neutron spectrum without shielding against thermal neutrons, significant levels of chromium (15-22%) were formed by transmutation. The addition of such large chromium levels strongly elevated the ductile to brittle transition temperature. At higher irradiation temperatures radiation-induced segregation of transmutant Cr and solute Ti at specimen surfaces leads to strong increases in the density of the alloy. The resultant shrinkage, possibly compounded by thermal cycling, leads to cracks developing at all intersections of grain boundaries with the specimen surface. This causes specimens irradiated at 500C or below to often fail during retrieval from the reactor, as well as during electropolishing and other handling operations. At 600C, the cracking and embrittlement processes are so severe that only a fine dust, composed mostly of individual grains or chunks of grains, was found in the irradiation capsule.

[1] Operated for the US Department of Energy by Battellle Memorial Institute under Contract CE-AC-06-76RLO 1830.

2.0 SILICON CARBIDE COMPOSITE MATERIALS

STATUS OF SILICON CARBIDE COMPOSITES FOR FUSION -- L. L. Snead (Oak Ridge National Laboratory), R. H. Jones (Pacific Northwest Laboratory), A. Kohyama (Kyoto University), and P. Fenici (JRC-Ispra)

Presented at the Seventh International Conference on Fusion Reactor Materials, Obninsk, Russia, September 25-29, 1995, and to be published in the Journal of Nuclear Materials, 1996

Extended Abstract

Silicon carbide composites are currently being investigated as potential fusion energy structural materials in the United States, the European Community, and Japan. This paper, which was presented as an invited oral at the ICFRM-7 conference, gives an overview of some of the recent issues regarding the use of this low activation material, including the radiation performance of present day materials and the direction towards the development of radiation hardened SiC composites. Specific topics that were explored in some detail include:

1. SiC as a Low Activation Material

   The question of the true activity of a commercially available SiC-based composite which is used in the first wall and blanket region of a fusion power system is discussed. The effect of the metallic impurity level present in the composite is discussed along with the production of Al-26. It is shown that impurity levels are quite variable and can most likely be controlled. The production of Al-26 is shown to be highly dependent on the position in the machine due to the high energy cross-section thresholds involved. Calculations[1] show that for SiC used away from the first wall, the Al-26, and the associated activity is of no consequence.

2. Helium and Hydrogen Production

   The production of helium and hydrogen are also a function of the incident neutron energy. The helium production ratio is shown to be approximately 130 atoms/dpa at the first wall falling to about 30 atoms/dpa in a typical end of blanket region. This can be compared to a fairly uniform helium production in Type 316 stainless steel of ~20 appm.

3. Dimensional Stability and Amorphization

   The regimes of dimensional stability are discussed and recent work on the temperature threshold for amorphization of SiC reviewed. It is shown that the amorphization threshold is dependent not only on the irradiation temperature but also on the irradiating ion species. The absence of amorphization in neutron irradiated SiC may be due to a spectrum induced threshold temperature shift.

4. Thermal Conductivity

   The thermal conductivity for both chemically vapor deposited SiC and SiC composites are presented. It is seen that the thermal conductivity quickly degrades to some fraction of its initial value, and that this fraction is largely dependent on the irradiation temperature. It is speculated that large improvement from the relatively low thermal conductivity of current day materials can be made and that, for the expected use temperatures of these materials, a saturation reduction in thermal conductivity on the order of 50% can be expected.

5. Irradiation Stability of Present-Day Composites

   Available data on the radiation resistance of Ceramic Grade Nicalon fiber composites are reviewed; the degradation mechanism of the composite is attributed to densification of the Nicalon fiber. Radiation data on improved fibers are presented and discussed and a general direction for the future research is discussed.

[1]H. L. Heinisch, "Activation of Silicon Carbide in Fusion Energy Systems," to be published in Fusion Reactor Materials Semiannual Report. DOE/ER-0313/19 (1995).

Review of Data on Irradiation Creep of Monolithic SiC - F. A. Garner, G. E. Youngblood and M. L. Hamilton (Pacific Northwest National Laboratory)

Summary

An effort is now underway to design an irradiation creep experiment involving SiC composites and SiC fibers. In order to successfully design such an experiment, it is necessary to review and assess the available data for monolithic SiC to establish the possible bounds of creep behavior for the composite. The data available show that monolithic SiC will indeed creep at a higher rate under irradiation compared to that of thermal creep, and surprisingly, it will do so in a temperature-dependent manner that is typical of metals.

Introduction

At the outset of the SiC development program it was not obvious that irradiation creep would indeed occur in such a non-metal. The published irradiation creep data on monolithic SiC were acquired by General Atomics as part of the High Temperature Gas Reactor Base Program. Although limited, the data are quite revealing.

In the first set of experiments[1], oriented graphite substrates measuring about 6 x 1 x 1 mm were overcoated with pyrolytic SiC and then irradiated in the ETR reactor (ORNL) at 640 and 900°C to exposures of 3.2 and 3.8 x 10^{21} nvt (E>0.18 MeV) respectively. Irradiation-induced expansion of the graphite substrate put the SiC in tension. Very rough estimates of the steady state creep constant K were inferred from the resultant strain and the presence or absence of cracks. A linear creep equation, $\varepsilon=K\sigma\gamma$, was developed where ε is the strain, σ is the stress and γ is the neutron fluence.

For irradiation at 650°C a creep constant K on the order of 2 x 10^{-37} (Pa-n/m^2)$^{-1}$ was estimated. At 900°C an upper limit of 4 x 10^{-37} (Pa-n/m^2)$^{-1}$ was inferred. These values are two orders of magnitude lower than those found in pyrolytic carbons. Due to the nature of this test, these estimates must be considered to be very rough, however. It is quite possible that plastic strain may have occurred or that some chemical interaction may have occurred between the SiC and graphite.

While the first set of experiments provides at least an upper bound to the creep behavior, the second set of experiments appears to be much more useful. In an unpublished beta-SiC experiment by Price (that was reviewed briefly in ref. 2), strips of pyrolytic beta-SiC measuring about 6 x 1 x 0.1 mm were bent to about half their fracture strain in four-point straining fixtures and irradiated in the ETR reactor at 780, 950 and 1130°C. The specimens were in three starting conditions, having been vapor deposited at 1400, 1750 and 1800°C to produce grain sizes of 1, 5, and 10 microns, respectively.

The strips were removed from their fixtures after irradiation and their residual curvature was measured. Using a method developed to study thermal creep on the same type of specimens[3], it was possible to derive creep coefficients. The insensitivity of the fractional strain relaxation to the initial elastic strain confirmed that the creep rate was linearly proportional to stress.

The steady-state irradiation creep constant K, calculated from the strain relaxation assuming a linear creep law, is shown in Fig. 1 as a function of irradiation temperature. For some specimens irradiated at the highest temperature, relaxation was almost complete and only a lower limit for the creep constant could be

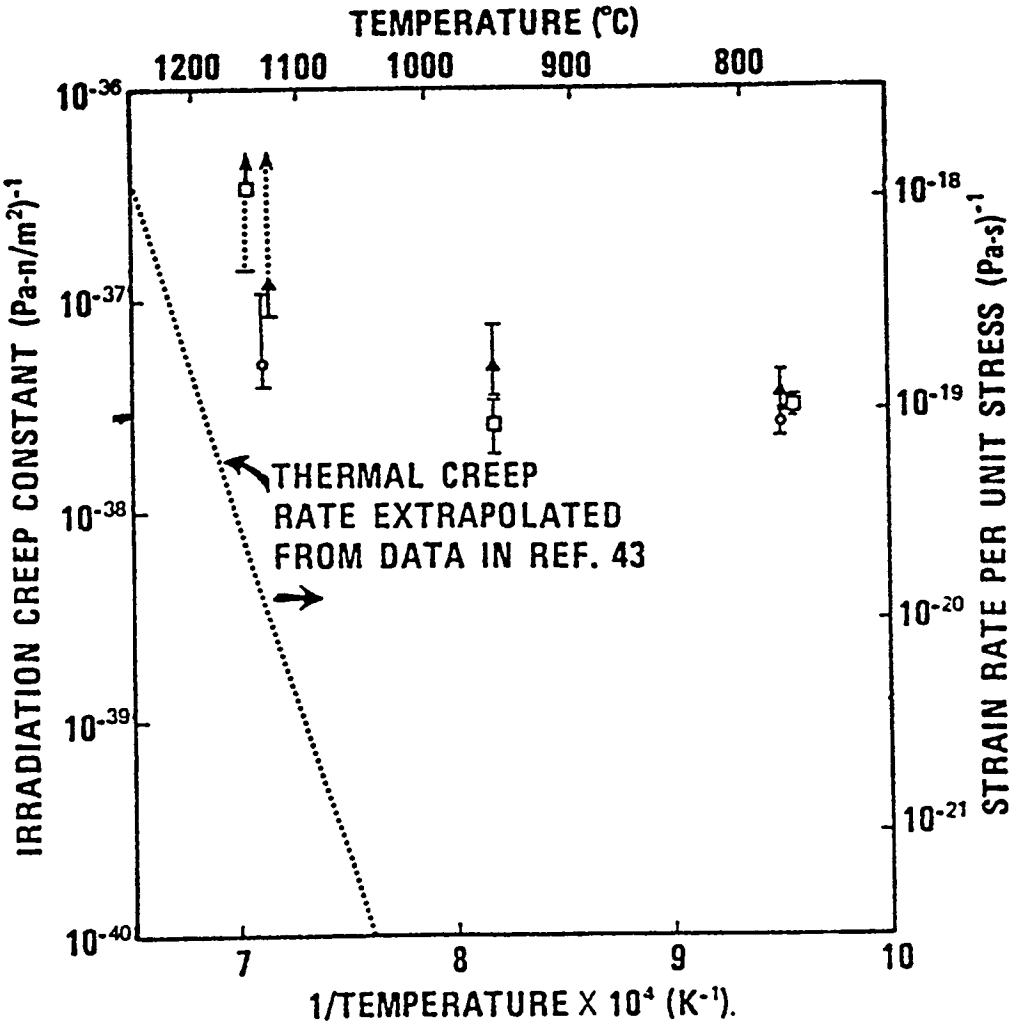

SYMBOL	DEPOSITION TEMP (K)	APPROX GRAIN SIZE (μm)
○	1673	1
▲	2023	5
□	2073	10

Fig. 1. Irradiation creep constant and strain rate for pyrolytic β-SiC strips restrained in bending as a function of irradiation temperature.[2]

established. The right scale in Fig. 1 shows the approximate creep rate per unit time, and the dashed line indicates the calculated thermal creep rate extrapolated from data in Ref. 2. The irradiation creep data are subject to substantial errors because of uncertainty and fluctuations in the temperatures of 100 to 150°C and the neglect of transient creep in the analysis.

Several conclusions can be drawn from these data, however.

1) The creep rate is enhanced by irradiation at all temperatures compared to that developed by thermal creep alone. The creep rates are significantly smaller than those measured in the first set of experiments, however.

2) Surprisingly, the creep behavior below ~1050°C is very nearly independent of temperature, as would be expected by analogy with the sink-dominated regime of metals. Above ~1050°C the creep behavior is directly analogous to that of thermal-dominated behavior in metals.

3) In the thermally dominated regime above ~1050°C there is a tendency of the creep rate to increase with initial grain size, especially as the irradiation temperature increases.

It is instructive to examine the creep rate in the temperature-insensitive regime and compare it to that of typical metals. This rate is roughly 3×10^{-38} (Pa-n/m^2)$^{-1}$. If we assume that roughly ~5 dpa were produced per 10^{26} n m^{-2} (E > 0.18 MeV), we obtain $K \sim 0.6 \times 10^{-6}$ MPa^{-1} dpa^{-1}, which is close to that of typical metals at ~1×10^{-6} MPa^{-1} dpa^{-1}. Since the details of the spectrum are not known and thus the true dpa conversion is also not known, this must be considered only a rough agreement. However, it does indicate that the creep behavior of SiC has many similarities to that of metals and alloys.

References

1. R. J. Price, in "HTGR Base Program Quarterly Progress Report for the Period Ending August 31, 1967," GA-8200, p. 91, General Atomic Division of General Dynamics (1967).

2. R. J. Price, Nuclear Technology 35 (1977) 320.

3. . D. Gulden and C. F. Driscoll, "Creep of Chemically Vapor-deposited β-SiC With an Analysis of Creep in Bending", GA-10366, General Atomic Company (1971).

MICROSTRUCTURAL EFFECTS OF NEUTRON IRRADIATION ON SIC-BASED FIBERS -

G. E. Youngblood and R. H. Jones (Pacific Northwest National Laboratory)* and
A. Hasegawa (Tohoku University, Japan)

OBJECTIVE

The objective of this task is to examine the irradiation effects on advanced SiC-type fibers.

SUMMARY

For extreme irradiation conditions, 43 dpa at temperatures of ≈ 1000°C, Hi Nicalon SiC fiber exhibits a much higher degree of microstructural stability than Nicalon CG fiber.

Introduction

Monolithic silicon carbide (SiC), and more recently SiC fiber reinforced SiC composites (SiC_f/SiC), have been examined for fusion reactor applications because of their intrinsically low afterheat and residual activation as well as their promising high temperature performance [1-3]. In particular, SiC_f/SiC is attractive as a structural material because its strength, toughness and strain-to-failure properties can be improved over that of monolithic SiC. Monolithic SiC itself has exhibited attractive dimensional stability in a high energy neutron environment, especially in the high temperature range of 800 to 1000°C [4]. However, available commercial SiC-based fibers have exhibited serious degradation for these same irradiation conditions. For instance, the observed shrinkage of irradiated Nicalon CG™ fiber was thought to be primarily responsible for the concurrent mechanical property degradation in irradiated SiC_f/SiC composites made with this fiber [4].

To determine the reason for the dimensional instability of the irradiated Nicalon fiber and, in general, whether the irradiation performance of SiC-based fibers can be improved, a microstructural analysis by TEM was carried out for two different Nicalon SiC fiber types, CG and Hi Nicalon.

Although the production of both Nicalon fibers starts from a polycarbosilane precursor fiber, subsequent processing routes yield a much lower oxygen content in the Hi Nicalon (0.5 wt. %) as compared to the Nicalon CG (11.7 wt. %). The resulting microstructure of Nicalon CG was reported to consist of ß-SiC grains of about 2 nm size surrounded by an amorphous Si-C-O phase and some turbostratic free carbon [6]. Likewise, the microstructure of Hi Nicalon was more crystalline because the ß-SiC grains were closer to 5 nm size, the turbostratic carbon layers were more organized and the amorphous Si-C-O phase was no longer observable. The chemical composition and microstructures which result from the different fiber processing routes lead to the slightly higher density and tensile modulus exhibited by Hi Nicalon as compared to Nicalon CG, while the tensile strength and elongation are slightly lower.

*Pacific Northwest Laboratory is operated for the U. S. Department of Energy by Battelle Memorial Institute under Contract DE-AC06-76RLO 1830.

Fiber Characterization

Typical properties of the two examined Nicalon fiber types, both manufactured by Nippon Carbon Co., appear in Table 1.

Table 1. Typical Properties of Nicalon CG and Hi Nicalon [5].

Properties		**Nicalon CG**	**Hi Nicalon**
Fiber diameter	(um)	14	14
Density	(g/cm^3)	2.55	2.74
Tensile strength	(GPa)	3.0	2.8
Tensile modulus	(GPa)	220	270
Elongation	(%)	1.4	1.0
Chemical composition	Si (wt %)	56.6	62.4
	C	31.7	37.1
	O	11.7	0.5
	C/Si (atomic)	1.31	1.39
Crystallite grain size	(nm)	<2	5-10
Amorphous matrix		Si-C-O someurbostraticC	turbostratic C

Snead, et al, reported on the neutron radiation effects on these two SiC-based fibers for relatively low doses (1-3 dpa) at temperatures <500°C [7]. They attributed the observed structural degradation in Nicalon CG fibers to the presence of the Si-C-O amorphous phase, whereas the performance of Hi Nicalon fibers was much better, resembling somewhat the behavior of monolithic SiC. Youngblood, et al, also reported that the dimensional stability of a more crystalline SiC-type fiber was much improved compared to that of Nicalon CG after neutron irradiation at 430°C to a relatively high dose of 26 dpa [8]. They also observed that any shrinkage in SiC-based fibers due to the irradiation had occurred by the time doses less than 5 dpa had been attained. In contrast, axial shrinkage of carbon fibers, irradiated together with the SiC-based fibers, was much greater (up to 60%) and did not saturate as a function of dose, while in the diametral direction the carbon fibers continually swelled. The latter observation is connected to the fundamental nature of radiation damage in the anisotropic graphite structure, i.e., shrinkage in the crystallographic â direction with concurrent growth in the c direction [9]. Since both Nicalon CG and especially Hi Nicalon contain a significant turbostratic intergrain carbon phase, the irradiation performance of graphite fibers is relevant.

Experimental

Small bundles (6.35 cm long) of Nicalon CG and Hi Nicalon fibers were irradiated at 1000°C in the EBR-II reactor to a high dose of 43 dpa. These irradiation conditions represent a most severe exposure expected for a fusion reactor design; exposure conditions for which SiC structures would be preferable to metal structures. Both Nicalon fiber types were expected to be thermally stable at temperatures around 1000°C based on short term exposures during strength retention [5], grain growth [9], and creep resistance [10] tests. However, to separate from irradiation effects the possible effects of long term exposure of the fibers to high temperature alone, control samples of each fiber type were held at 1000°C in a helium atmosphere for 165 days, which approximately duplicated the thermal exposure of the irradiated fibers.

Changes in fiber length, density and tensile strength will be analyzed at a later time. The emphasis of this report is the analysis of the microstructural changes induced by either (1) the thermal heat treatment without irradiation (HT) or (2) the high temperature, high dose neutron irradiation (HTHD).

Microstructural observations of the as received (AR), the HT and the HTHD fibers were carried out by TEM (JEOL-2000FX) at 200 kV. Specimen preparation consisted of fixing a few individual fibers to a thin molybdenum washer and ion milling the fibers with 5 keV argon ions to perforation through their centers. The remaining sides of the perforated fiber retained the fiber shape.

Results and Discussion

Representative TEM micrographs of both unirradiated and irradiated Nicalon CG and Hi Nicalon fibers are shown in Figures 1 (a-c) and 2 (a-c), respectively. Figure 1-a is a dark field image of the HT Nicalon CG fiber. The TEM micrograph shows an extremely fine grain structure with crystallite sizes below 2 nm. The accompanying selected area diffraction (SAD) pattern is a series of fuzzy concentric rings which indicates an amorphous state. The SAD pattern for the AR fiber was identical. The micrograph, which was taken along the first bright inner ring of the SAD, is representative of both unirradiated cases. The corresponding bright field image (not shown) indicated no apparent diffraction contrast. The microstructure of the HT Nicalon CG appeared to be stable for the long time exposure of 165 days at 1000°C in an inert atmosphere. Microstructural changes observed are due to the irradiation conditions, not to the thermal conditions alone.

Figures 1-b and 1-c are images of a HTHD Nicalon CG specimen in dark and bright field, respectively. Some small bright spots are now observed superimposed on the diffraction rings of the accompanying SAD. The micrographs show grain growth with some grains exceeding 5 nm. Small black spots also are now observed in Figure 1-c. These black spots are attributed to the same grains seen as bright spots in Figure 1-b. It is readily apparent that the irradiation conditions (43 dpa at 1000°C) induced considerable grain growth and crystallization in Nicalon CG.

Figure 2-a is a dark field image of the heat treated (HT) Hi Nicalon fiber. Again, no differences were observable between the micrographs or their SAD patterns for the AR and HT fibers, thus the HT micrographs as presented are representative of the AR state as well. As expected, the microstructure of the Hi Nicalon fiber was stable at the 1000°C thermal exposure alone. However, in Hi Nicalon some of the ß-SiC grain sizes are 10 nm in size, which is much larger than observed for any of the SiC grains in Nicalon CG. Also, the accompanying SAD ring pattern now shows the appearance of some well defined spots due to a somewhat greater degree of crystallinity in Hi Nicalon as compared to Nicalon CG. These microstructural observations are in line with observations by others for unirradiated fibers of each type [5,6,9] and support the physical property differences reported for Nicalon CG and Hi Nicalon as given in Table 1.

Dark and bright field images of a HTHD Hi Nicalon specimen are shown in Figures 2-b and 2-c, respectively. In contrast to the microstructural effects observed for HTHD Nicalon CG, relatively little change in the grain size was observed for HTHD Hi Nicalon. This observation is supported by the accompanying SAD pattern for the irradiated fiber shown in Figure 2-b, which is very similar to the SAD pattern shown in Figure 2-a for the unirradiated fiber. Nevertheless, the ring patterns indicate the existence of an amorphous or nanocrystalline structure as well.

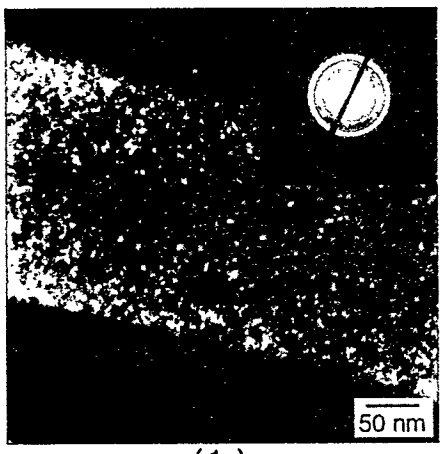

(1a)

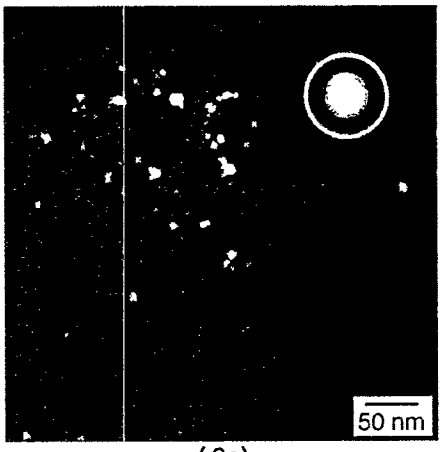

(2a)

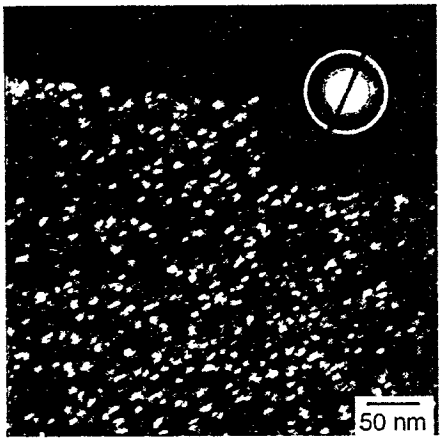

(1b)

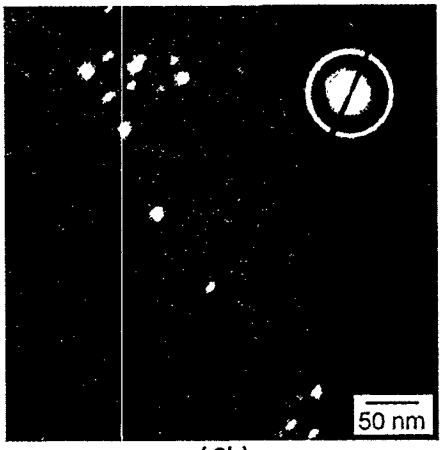

(2b)

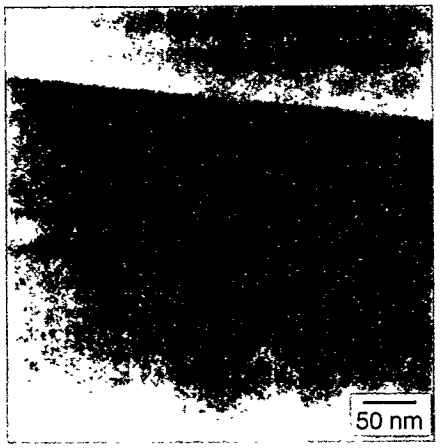

(1c)

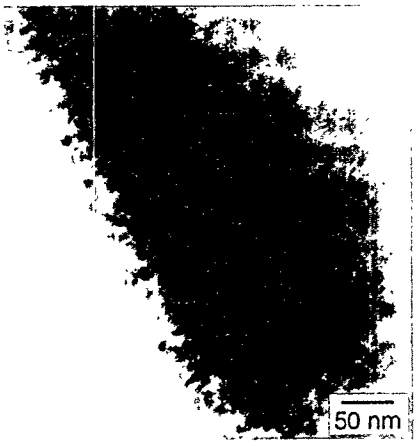

(2c)

Figure 1(a-c) Nicalon CG. **(a)** TEM dark field and SAD of heat-treated (1010°C, 4000 hr in He) fiber, **(b)** dark field and SAD and **(c)** bright field of irradiated (43 dpa, 1000°C) fiber.

Figure 2(a-c) Hi Nicalon. **(a)** TEM dark field and SAD of heat-treated (1010°C, 4000 hr in He) fiber, **(b)** dark field and SAD and **(c)** bright field of irradiated (43 dpa, 1000°C) fiber. Bright ring in the SADs indicates the SiC {111} reflection ring.

Unfortunately, microstructural evidence for the presence of the turbostratic carbon intergrain layers, known to occur in both of these SiC fiber types with excess carbon, was not observed in this work. However, as observed previously for graphitic fiber [8], the effect of irradiation on the carbon intergrain layers would be expected to be detrimental.

Conclusions

Even for the extreme irradiation conditions examined in this work (43 dpa at ≈ 1000°C), the Hi Nicalon fiber shows a much higher degree of microstructural stability than the Nicalon CG fiber. It is expected that the physical properties of the Hi Nicalon also should exhibit enhanced irradiation performance, and if used in SiC_f/SiC composite, should lead to improved irradiation performance of the composite. Future development of a more stoichiometric SiC fiber without the carbon intergrain layers holds even more promise for producing a radiation tolerant fiber and, therefore, should be more appropriate for use in the fabrication of SiC_f/SiC composite for fusion applications.

Future Work

The length, density and strength change analysis of unirradiated and irradiated Nicalon CG and Hi Nicalon SiC fibers will be completed. These same two fiber types, as well as six other advanced SiC fiber types, have been irradiated in the COBRA 1A2 series (EBR II, 80 dpa at 800°C). Postirradiation analysis of all these fibers will soon commence. Future irradiations of Hi Nicalon fiber and Super Nicalon, a near stoichiometric SiC fiber type, will take place in HFIR (Jupiter P3-3, 10 dpa at 500°C) commencing in April, 1996, and analysis should be completed in early 1997.

Acknowledgments

This work was supported by the Office of Fusion Energy of the U. S. DOE under contract DE-AC06-76RLO 1830 with Battelle Memorial Institute and Jupiter (Japan-USA Program of Irradiation Testing for Fusion Energy Research).

References

1. L. H. Rovner and G. R. Hopkins, "Ceramic Materials for Fusion," *Nucl. Technol.* **29(3)**, 274-302 (1976).

2. G. R. Hopkins and J. Chin, "SiC Matrix/SiC fiber Composite: A High-Heat Flux, Low Activation, Structural Material," *J. Nucl. Mater.* **141-143**, 148-151 (1986).

3. Russell H. Jones, Charles H. Henager, Jr. and Glenn W. Hollenberg, "Composites for Fusion Applications," *J. Nucl. Mater.* **191-194**, 75-83 (1992).

4. G. W. Hollenberg, C. H. Henager, Jr., G. E. Youngblood, D. J. Trimble, S. A. Simonson, G. A. Newsome and E. Lewis, "The Effect of Irradiation on the Stability and Properties of Monolithic SiC and SiC_f/SiC Composites up to 25 dpa," *J. Nucl. Mater.* **219**, 70-86 (1995).

5. Hiroshi Ichikawa, Kiyohito Okamura and Tadao Seguchi, "Oxygen-Free Ceramic Fibers from Organosilicon Precursors and E-Beam Curing," pp. 65-74 in High-Temperature Ceramic-Matrix Composites II, Ceramic Transactions vol. 58, edited by A. G. Evans and R. Naslain, The American Ceramic Society, Westerville, Ohio (1995).

6. A. R. Bunsell, M. H. Berger and N. Hochet, "Structural and Mechanical Characterisation of Some Alumina and SiC Based Fibres," pp. 85-94 in Ref. 5.

7. L. L. Snead, M. Osborne and K. L. More, "Effects of Radiation on SiC-Based Nicalon Fibers," *J. Mater. Res.* **10(3)**, 736-747 (1995).

8. G. E. Youngblood, D. J. Senor and G. W. Hollenberg, "Dimensional Stability of Neutron Irradiated Carbon and SiC-Based Fibers at High Doses," Fusion Materials Semiannual Progress Report for Period Ending March 31, 1995, U. S. Department of Energy publication DOE/ER-0313/18.

9. Ya. I. Shtrombakh, B. A. Gurovich, P. A. Platonov and V. M. Alekseev, "Radiation damage of Graphite and Carbon-Graphite Materials," J. Nucl. Mater. 225, 273-301 (1995).

10. G. Chollon, R. Bodet, R. Pailler and X. Bourrat, "Structure and Thermal Evolution of SiC-Based fibers with Low Oxygen Content," pp. 305-310 in Ref. 5.

IMPROVEMENT OF THE THERMAL CONDUCTIVITY OF SIC_F/SIC COMPOSITE - G. E. Youngblood (Pacific Northwest Laboratory)* and W. Kowbel (MER Corporation, Tucson AZ)

OBJECTIVE

The objective of this work is to examine SiC composites fabricated by various processing methods designed to improve their thermal conductivity. Specifically, it is desired to increase the thermal conductivity of these composites to meet requirements for potential fusion reactor applications.

SUMMARY

Two methods, high temperature annealing and doping, were examined for improving the thermal conductivity of simulated CVI/ß-SiC matrix material. For instance, a two hour 1500°C anneal led to the increase of the room temperature (RT) thermal conductivity from 38 to 59 W/mK. Be-doping was even more effective in causing the thermal conductivity to increase with RT conductivity values up to 160 W/mK attained. To further optimize the thermal conductivity, hot-pressed SiC materials with carefully controlled amounts of Be- and B_4C-doping were investigated. Although a small improvement ($\approx$ 8%) was achieved with 2.0 wt% Be-doping, the effort to refine the amount of doping needed was largely unsuccessful. Apparently, hot-pressing SiC introduced numerous substructural stacking faults which effectively scattered phonons in the intermediate temperature range and nullified the benefits of doping. Nevertheless, Be- and B_4C-doping and/or thermal treatments appear to be promising strategies to achieve the goal of eventually improving the thermal conductivity of SiC_f/SiC composite.

PROGRESS AND STATUS

Introduction

Silicon carbide (SiC) has been considered as a structural material for fusion applications because of its low neutron activation and after heat and its stability at high temperature during irradiation as well as its outstanding mechanical properties.[1-3] To provide improved strength and toughness, continuous fiber reinforced SiC composites (SiC_f/SiC), being developed primarily for advanced aerospace applications, also are now being examined for fusion reactor applications.[4-7] Such composites typically are fabricated with about 40% by volume fiber reinforcement, while the matrix can be fabricated by either chemical vapor infiltration (CVI) or polymer infiltration and pyrolysis (PIP). The higher strengths as well as the improvement in toughness and strain-to-failure originate from a somewhat "weaker" interphase, generally either pyrolytic carbon or porous SiC, that is applied as a thin coating to the fiber bundles or fabric layups prior to the matrix infiltration. Under load the weak interphase (or a weak interface) deflects matrix cracks and the fibers tend to debond from the matrix, thus allowing transfer of the load to the inherently stronger fiber bundles.[8]

Unfortunately, while the thermomechanical properties of SiC_f/SiC can be improved over that of monolithic SiC, the thermal conductivity is significantly reduced. For instance, a high density, high purity SiC made by chemical vapor deposition (CVD) generally will have a RT thermal conductivity value >300 W/mK,[9] while through-the-thickness conductivities of SiC_f/SiC(CVI) have been observed to be <10 W/mK.[7] Generally, the thermal conductivity of SiC_f/SiC(PIP) has been observed to be even less

*Pacific Northwest Laboratory is operated for the U. S. Department of Energy by Battelle Memorial Institute under Contract DE-AC06-76RLO 1830.

with values of 2-4 W/mK typical. Although porosity in the composite can account for some of this observed reduction in thermal conductivity, reasonable porosity correction factors cannot account for the observed factor of 30 or greater reduction. Moreover, upon neutron irradiation to doses above a few dpa, the composite's thermal conductivity is substantially reduced even further due to accumulation of point defects.[7]

In a conceptual design study of the thermal performance of a fusion reactor with a SiC_f/SiC first wall of thickness 3 mm, efficient steady operation could be maintained if the thermal conductivity of the SiC_f/SiC exceeded 7 W/mK.[10] For the high thermal efficiency required for a fusion reactor diverter, the thermal conductivity would have to exceed 70 W/mK.[10] Obviously SiC_f/SiC with a thermal conductivity much below 10 W/mK will greatly limit potential applications of these materials.

Recent studies have shown that in the direction perpendicular to the fiber planes in 2D plane weave SiC_f/SiC, the SiC fibers themselves contribute very little to the thermal conductivity of the composite.[11] The weakly bonded fiber structures, necessary for optimized mechanical properties in SiC_f/SiC, apparently act as an insulating phase, while heat transport takes place primarily through the matrix phase. Thus, differences in thermal conductivity between types of SiC_f/SiC will depend upon the morphology and substructure of the matrix as well as the degree of crystallinity and purity of the matrix, but probably will depend little on the type of SiC fiber used. **Importantly, significant improvement in the matrix conductivity does appear to be attainable by optimizing processing parameters to control purity and structure of the matrix.**

Takeda showed that SiC hot-pressed to full density while using 1-2% BeO or other Be-compounds as sintering aids exhibited RT thermal conductivities up to 270 W/mK.[12] While examining the effect of thermal treatments, Collins *et al.* showed that the thermal conductivity of high purity CVD/SiC could be improved by increasing the deposition temperature from 1300 to 1350°C.[13] They attributed this improvement to an increase in the grain size attained by use of a higher processing temperature. Using these concepts, researchers at MER Corporation (Tucson AZ), under an SBIR grant from DOE/Fusion Energy, currently are examining the potential for improving the thermal conductivity of ß-SiC matrix material by doping and by thermal treatments.[14]

MER researchers have simulated CVI/ß-SiC matrix material by vapor depositing a thick layer of ß-SiC (no fiber preform) onto a graphite substrate while utilizing deposition conditions typical for CVI, i.e., they used a gas mixture of methyltrichlorosilane (MTS) and hydrogen and a deposition temperature of 1150°C. Kinetic constraints for the CVI process with a fiber preform limit deposition temperatures to 1150°C, much below the 1300 to 1450°C range normally used for fabricating dense, high purity ß-SiC by CVD. MER also has fabricated simulated Be-doped CVI/ß-SiC matrix material by mixing a very low level of $BeBr_2$ vapor with the MTS/hydrogen mixture to codeposit the Be simultaneously with the SiC, a process amenable to scale up.

Without the Be-doping, a CVI/ß-SiC sample deposited at 1150°C had a density of 2.6 g/cc (81% T.D.) and a RT thermal conductivity of 38 W/mK. By annealing the undoped CVI/ß-SiC deposit for two hours at 1500°C in helium, a 50% increase in the thermal conductivity was induced.[14] Until recently, SiC_f/SiC composites have been limited to exposure temperatures below about 1200°C due to thermal instability of available first generation SiC fibers (such as Nicalon CG). Therefore, heat treatments to improve the thermal conductivity of SiC_f/SiC were not feasible. Advanced fibers now becoming available, like Hi-Nicalon or MER CVR/SiC, are thermally stable up to 1500°C, so 1500°C now represents a practical high

temperature limit for SiC_f/SiC containing these advanced fibers. Finally, a CVI/ß-SiC deposit fabricated with Be-doping exhibited an even greater enhancement of the thermal conductivity; a very promising RT value of 160 W/mK was attained![14]

To optimize the thermal conductivity of CVI/ß-SiC even further, MER researchers set about fabricating SiC with precisely controlled levels of Be- or B_4C-doping. Since it was difficult to control the exact amount of Be additive by the vapor codeposition process, conventional hot-pressing was employed to more precisely control the doping levels. The measurement and analysis of the thermal transport properties of these materials, i.e., hot-pressed Be- and B_4C-doped SiC fabricated by MER, are the subjects of this report.

Experimental Procedure

Therefore, dense (>97% TD) SiC plates were fabricated by hot-pressing at 2050°C. Appropriate amounts of SiC powders were mixed with Be or B_4C powders to attain precise doping levels of 0, 0.25, 0.50, 1.0 and 2.0 wt% Be-doping or 0, 1.0 and 2.0 wt% B_4C-doping.

The thermal transport properties of these materials were characterized by measuring the thermal diffusivity by the laser flash technique over a 300 to 1200°C temperature range. In this technique, described else-where,[11] four or more separate shots were made at each temperature to give an average thermal diffusivity value with a typical uncertainty of ± 5%. For comparison, diffusivity measurements also were made on six different fully dense, high purity CVD/ß-SiC samples (obtained from Morton International) and on a commercially available SiC_f/SiC(CVI) composite (obtained from Dupont) with a two-dimensional (2D) plain weave fiber architecture. Microstructural and phase details currently are being analyzed by TEM (and HRTEM), optical and XRD methods.

Results and Discussion

In Figure 1(a-b), the measured thermal diffusivity values as a function of temperature for the hot-pressed SiC doped with (1a) 0-2 wt% Be or (1b) B_4C are shown together with similar data for the reference material, monolithic CVD/ß-SiC, and for the 2D SiC_f/SiC(CVI) composite. For analysis, the data are shown replotted as the reciprocal thermal diffusivity in Figure 2(a-b). In this figure the straight lines through the data points for each composition were determined by least squares regression. The curved lines shown in Figure 1(a-b) are included for guidance only.

The thermal diffusivity (α) is a derived quantity given by $\alpha = k/\rho C_p$, where k is the thermal conductivity, ρ is the bulk density and C_p is the specific heat at constant pressure. A useful expression relating the lattice thermal conductivity to an effective phonon mean free path (l_{eff}) is $k = (1/3)Cvl_{eff}$ where now C is the specific heat per unit volume and v is the lattice wave velocity (usually taken as the sound velocity).[15] If the expressions for thermal diffusivity and conductivity are combined, and noting that $\rho C_p = C$, one gets:

$$\alpha = (1/3)v\, l_{eff} \qquad (1).$$

Since v is only slightly dependent on temperature, the temperature dependence of α directly reflects the temperature dependence of l_{eff}. For analysis purposes, the reciprocal diffusivity ($1/\alpha$) provides a convenient way to separate the contributions of various phonon scattering processes. The reciprocal of Eq. (1) becomes:

$$1/\alpha = (3/v)\Sigma_i (1/l_i) \qquad (2),$$

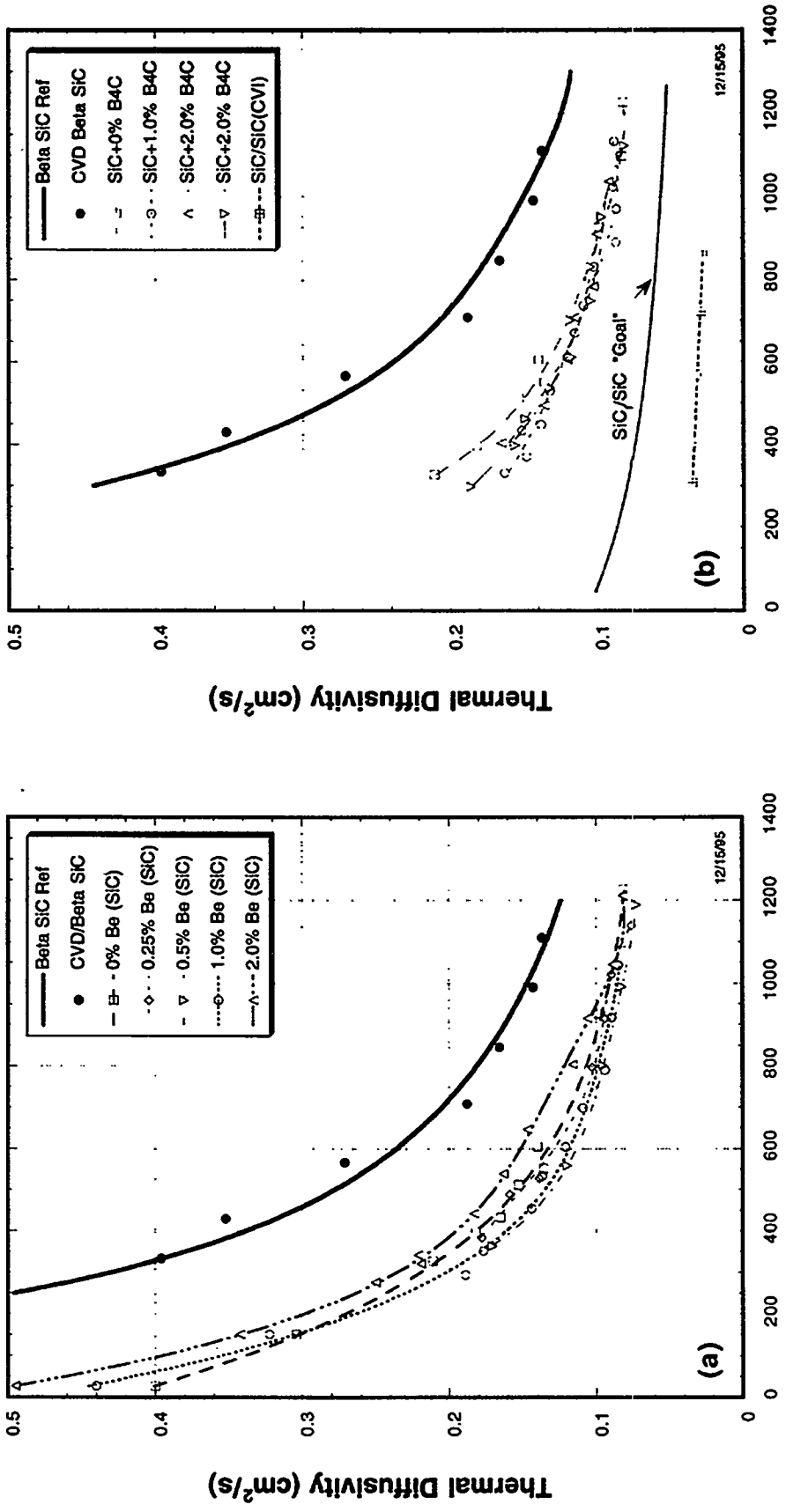

Figure 1(a-b) Comparison of the measured thermal diffusivity of CVD/β-SiC and hot-pressed SiC doped with 0-2 wt%. **(a)** Be or **(b)** B_4C. Also shown in (1b) are measured values for a commercial 2D SiC_f/SiC (CVI) composite and calculated "goal" values for potential fusion reactor applications of this type composite.

R95120149.2

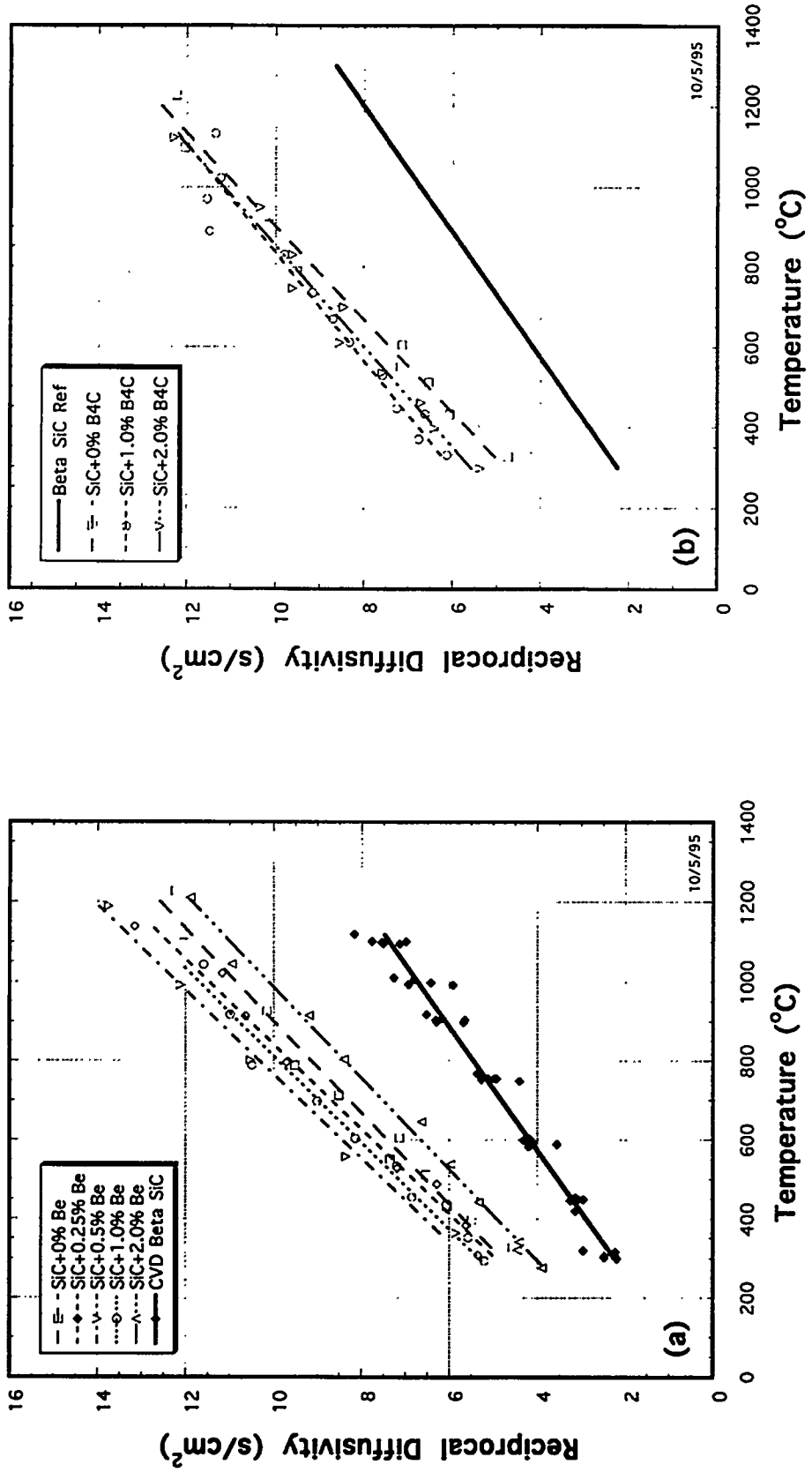

Figure 2(a-b) Reciprocal thermal diffusivity as a function of temperature for hot-pressed SiC doped with 0-2 wt%. **(a)** Be or **(b)** B_4C. The corresponding plot for the CVD/β-SiC reference material also is given.

R95120149.3

where $1/l_{eff}$ is composed additively of contributions from each process type (i), i.e., scattering by intrinsic phonon-phonon interactions and by extrinsic impurity, irradiation produced point defects, dislocations, substructural faults, etc. Equation (2) assumes that the scattering processes are independent of each other.

In Figures 2(a-b), the $1/\alpha$ data are fit approximately by a linear relation of the form a + bT over the 300 to 1200°C temperature range for the hot-pressed Be- and B_4C-doped SiC as well as for the Morton CVD/ß-SiC. The effect of a very small amount of Be-doping is to lower α (raise $1/\alpha$) initially by 13% for 0.5 wt% Be, afterwhich α increases for additional doping up to +8% for 2.0 wt% Be. Apparently, in the Be-doped samples some small amount of Be goes into solution and scatters phonons as impurity point defects. Further Be-doping, however, reduces the phonon scattering. The RT α(k) value for the 2 wt% Be-doped SiC, the hot-pressed material exhibiting the highest α, was 0.50 cm^2/s (102 W/mK). The latter value is somewhat below the 160 W/mK achieved for CVI/ß-SiC. The calculated mean free path at RT, using a value of 1.26×10^4 m/s for v in Eq. (1), would be about 12 nm.

In Figure 3, a TEM micrograph of the hot-pressed SiC with 2 wt% Be-doping shows numerous stacking faults within the SiC grains of size ≈ 5 μm. The stacking faults appear to have a mean spacing of from 10 to 100 nm, which is of the order of the calculated mean free path in this material. The close agreement between the calculated l_{eff} and the observed fault spacing suggests that in ß-SiC substructural faults may effectively scatter phonons even up into the intermediate temperature range and, therefore, they may have a significant influence on the magnitude of the thermal conductivity in the range of interest to fusion energy.

It is also observed in Figure 2(a) that the slopes for the hot-pressed Be-doped (and undoped) SiC are similar (the straight lines are approximately parallel), but are somewhat steeper than the slope for the CVD/ß-SiC. Again, this is probably caused by the different temperature dependence of phonon scattering from substructural faults which are likely to be more prevalent in the hot-pressed SiC than in the CVD/ß-SiC.

CONCLUSIONS

In general, the dramatic improvement expected in k for Be- or B_4C-doped SiC was not achieved in these hot-pressed specimens. Even though the doping contents could be controlled and the porosity removed by hot-pressing, this type fabrication did not provide the desired improvement in the thermal conductivity. Apparently, hot-pressing introduces numerous faults into the SiC microstructure so that this process does not simulate the relatively stress-free fabrication of CVI/ß-SiC material. Nevertheless, Be-doping and thermal treatments appear to be promising strategies to achieve the goal of eventually improving the thermal conductivity of SiC_f/SiC.

FUTURE WORK

Further efforts to optimize and control the Be-doping in simulated CVI/ß-SiC matrix will be carried out. However, future fabrication will preferably utilize the lower temperature, CVD-type deposition process. Also, examination of simulated ß-SiC matrix material made using PIP-type processing with doping and thermal treatments will be initiated. MER will continue to carry out the fabrication development and structural analysis, while PNNL will carry out the thermal transport analysis.

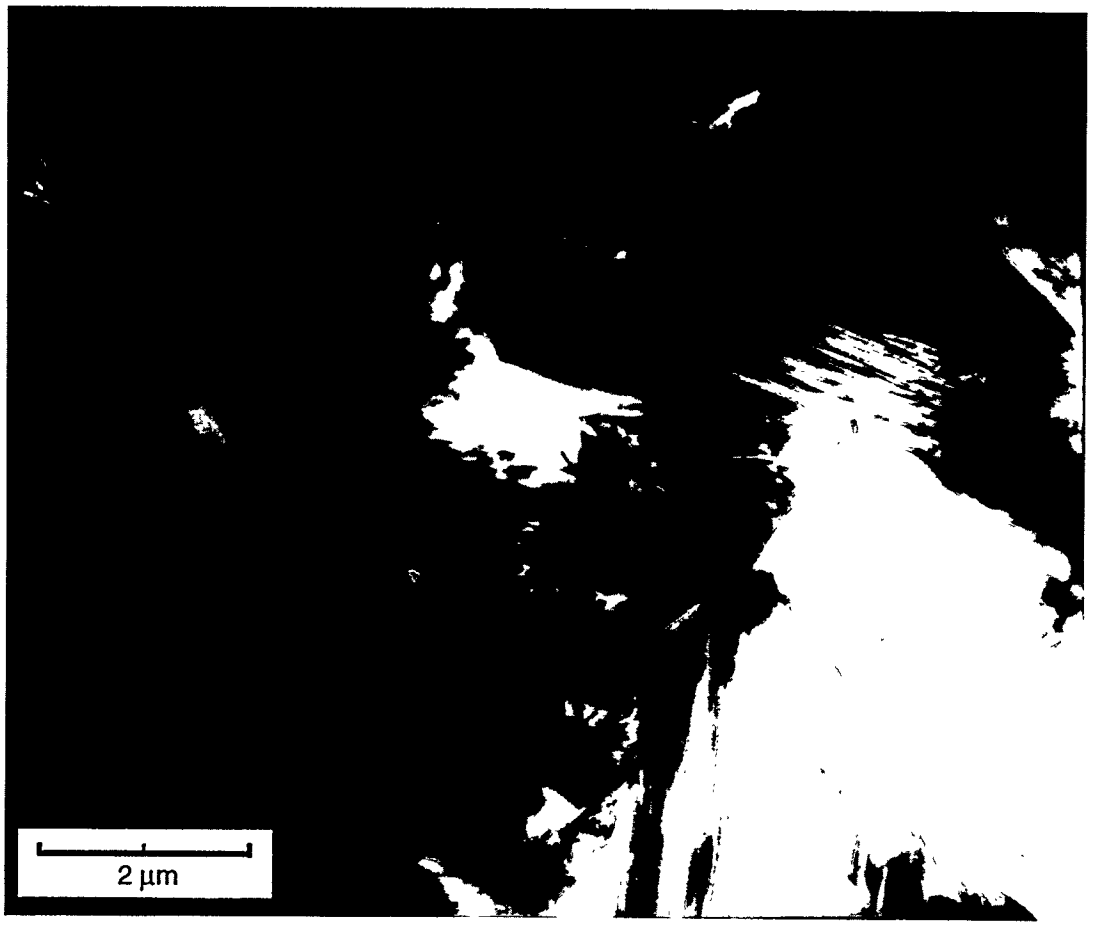

Figure 3 TEM micrograph of hot-pressed SiC with 2.0 wt% Be-doping showing numerous stacking faults.

REFERENCES

1. L. H. Rovner and G. R. Hopkins, "Ceramic Materials for Fusion," Nuclear Technology **29**, 274-302 (1976).

2. J. C. Corelli, J. Hoole, J. Lazzaro and C. W. Lee, "Mechanical, Thermal and Microstructural Properties of Neutron-Irradiated SiC," J. Am. Ceram. Soc. **66**(7), 529-37 (1983).

3. G. R. Hopkins, R. J. Price and P. W. Trester, "Radiation Effects on Structural Ceramics in Fusion," Fusion Technology **10**, 719-27 (1986).

4. G. R. Hopkins and J. Chin, "SiC Matrix/SiC Fiber Composite: A High-Heat Flux, Low Activation Structural Material," J. Nucl. Mater. **141-143**, 148-51 (1986).

5. Russell H. Jones, Charles H. Henager, Jr. and Glenn W. Hollenberg, "Composites for Fusion Applications," J. Nucl. Mater. **191-194**, 75-83 (1992).

6. Lance L. Snead, "Development of Silicon Carbide Composites for Fusion," Fusion Technology **24**, 65-82 (1993).

7. G. W. Hollenberg, C. H. Henager, Jr., G. E. Youngblood, D. J. Trimble, S. A. Simonson, G. A. Newsome and E. Lewis, "The Effect of Irradiation on the Stability and Properties of Monolithic SiC and SiC_f/SiC Composites up to 25 dpa," J. Nucl. Mater. **219**, 70-86 (1995).

8. H. C. Cao, E. Bischoff, O. Sbaizero, Manfred Ruhle, Anthony G. Evans, David B. Marshall and J. J. Brennan, "Effect of Interfaces on the Properties of Fiber-Reinforced Ceramics," J. Am. Ceram. Soc. **73**(6), 1691-99 (1990).

9. M. A. Pickering and W. Haigis, "CVD- Scaled Up for Commercial Production of Bulk SiC," Ceramic Bulletin **72**(3), 74-77 (1993).

10. Clement Wong (of General Atomics, San Diego, CA), "Thermal Conductivity of SiC and SiC-Composites and Design Implications," presented at SiC/SiC Workshop held in Richland, WA April 18-19, 1995.

11. D. J. Senor, G. E. Youngblood and C. E. Moore, "Thermal Conductivity of Neutron Irradiated SiC-Based Composites and Monolithic Ceramics," Interim Report (unpublished), Pacific Northwest Laboratory, Richland WA, June 1995.

12. Yukio Takeda, "Development of High Thermal Conductive SiC Ceramics," Ceramic Bulletin **67**(12), 1961-63 (1988).

13. A. K. Collins, M. A. Pickering and R. L. Taylor, "Grain Size Dependence of the Thermal Conductivity of Polycrystalline Chemical Vapor Deposited ß-SiC at Low Temperatures," J. Appl. Phys. **68**(12), 6510-12 (1990).

14. W. Kowbel, F. Gao, J. C. Withers and G. E. Youngblood, "Beryllium Doping and Thermal Annealing Effects on Thermal Properties of CVI-SiC," accepted for publication in Journal of Materials Synthesis and Processing, July 1995.

15. Y. S. Touloukian, R. W. Powell, C. Y. Ho and P. G. Klemens, Eds. "Thermophysical Properties of Matter, Vol. 2: Thermal Conductivity - Nonmetallic Solids," IFI/Plenum, New York, 1970.

THE MONOTONIC AND FATIGUE BEHAVIOR OF CFCCs – N. Miriyala, P. K. Liaw, and C. J. McHargue (University of Tennessee) and L. L. Snead (Oak Ridge National Laboratory).

OBJECTIVE

To develop a fundamental understanding of the fabric orientation effects on the monotonic and fatigue behavior of Nicalon/Al_2O_3 and Nicalon/SiC composites.

SUMMARY

Flexure tests were performed to study the fabric orientation effects on the monotonic and fatigue behavior of two commercially available continuous fiber reinforced ceramic composites (CFCCs), namely, (i) Nicalon fiber fabric reinforced alumina (Al_2O_3) matrix composite fabricated by a direct molten metal oxidation (DIMOX) process and (ii) Nicalon fiber fabric reinforced silicon carbide (SiC) matrix composite fabricated by an isothermal chemical vapor infiltration (ICVI) process. The fabric orientation effects on the monotonic and fatigue behavior were strong in the Nicalon/Al_2O_3 composite, while they were relatively weak in the Nicalon/SiC composite.

PROGRESS AND STATUS

Introduction

As structural materials, monolithic (unreinforced) ceramics inherently suffer from two important reliability issues; high sensitivity to processing and service generated flaws (low fracture toughness) and the inability to tolerate stress overloads without catastrophic failure. Although whisker reinforcement enhances toughness, it does not remove the possibility of catastrophic failure, a problem that severely restricts the use of whisker-toughened ceramics in aerospace engines. Continuous fiber reinforced ceramic matrix composites (CFCCs), on the other hand, can provide significant toughness increases along with the ability to fail in a non-catastrophic manner similar to a metal [1, 2].

Woven fiber fabric reinforcement of the matrix has been a popular choice of process engineers attempting to develop CFCCs with improved toughness. Although most of the advanced CFCCs developed to date are 2-D reinforced, the effect of fabric orientation on their mechanical behavior has received scarce attention of the material testing community. Hence, it has been decided to investigate the effects of fabric orientation on the monotonic and fatigue performance of two of the advanced CFCCs, namely, (i) Nicalon fiber fabric reinforced alumina (Al_2O_3) matrix composite fabricated by a direct molten metal oxidation (DIMOX) process and (ii) Nicalon fiber fabric reinforced silicon carbide (SiC) matrix composite fabricated by an isothermal chemical vapor infiltration (ICVI) process. Flexural specimens were performed to obtain the stress-strain curves and fatigue stress-life (S-N) curves for both composites. In addition, the progression of damage during cyclic loading was assessed by measuring the "effective modulus" of the composite at regular intervals of the fatigue tests. Fracture surfaces of both composites were examined under a scanning electron microscope to gain an insight into the damage mechanisms operative under static and cyclic loadings.

Experimental Details

Materials

The Nicalon fiber fabric reinforced alumina (Al_2O_3) matrix composite, fabricated by a direct molten metal oxidation (DIMOX) process, was donated by Lanxide Corporation. The as-received material was in the form of plate, approximately 150 × 150 × 3.2 mm. A 12-harness satin woven Nicalon fabric in a 0/90 sequence was used as the preform in this composite. The fabric preform was given a duplex coating of boron nitride (BN) and silicon carbide (SiC) via chemical vapor deposition (CVD). While BN acts as the interlayer between the fiber and the matrix, the overlaying SiC coating protects the fiber and the BN interlayer during

matrix infiltration. The BN coating thickness was approximately 0.2 to 0.5 μm, while the SiC coating thickness varied from 3 to 4 μm. The duplex-coated preform was then placed in contact with molten aluminum at 900 to 1100°C in air. The matrix in the composite was formed by the growth of alpha alumina, starting from the alloy/preform interface. The nominal fiber volume percent in the composite was approximately 35.

The Nicalon fiber fabric reinforced silicon carbide (SiC) matrix composite, fabricated by an isothermal chemical vapor infiltration (ICVI) process, was donated by AlliedSignal Corporation. The as-received material was in the form of two plates, approximately 200 × 150 × 2.4 mm, manufactured by DuPont Corporation. A 2-D braided Nicalon fabric was used as the preform, which was first given an interfacial coating of carbon (approximately 0.4 to 0.5 μm) by a CVD process, prior to the infiltration of SiC matrix. The SiC matrix was infiltrated by the decomposition of methyltrichlorosilane, in the presence of hydrogen, at 1100 to 1200°C. The nominal fiber volume percent in the composite was approximately 40.

Flexure testing

Flexure bars were machined from the composite plates using diamond tooling. The ASTM Standard C 1161 configuration requires the specimens to be 50 mm long, 4 mm wide and 3 mm thick. However, in order to objectively study the effects of fabric orientation on the mechanical behavior of the two composites, flexural bars of squared cross-section were fabricated. The flexural bars of the Nicalon/Al_2O_3 composite used in the present investigation were 50 × 3 × 3 mm, while the Nicalon/SiC composite specimens were only 50 × 2 × 2 mm. The four-point bend monotonic and fatigue tests were performed on a MTS servohydraulic system, equipped with a graphite heating element furnace, that can be used to conduct elevated-temperature tests, up to 2000°C in vacuum or argon. To date, all the mechanical tests were performed at room temperature.

The monotonic tests were conducted under displacement control at a cross-head displacement rate of 0.5 mm/min. The midspan deflection of the specimen was monitored using a deflection gage made of SiC. The fatigue tests were conducted under load control. All the tests were conducted using a sinusoidal wave form at a test frequency of 5 Hz. The R-ratio (minimum load/maximum load) was 0.1 in all the cases. At periodic intervals during the fatigue tests, the load and midspan deflection values for two consecutive load cycles were recorded. Two hundred pairs of load and deflection values were recorded each time the data was captured. The fatigue run-out was one million cycles, which corresponds to approximately 56 hours of testing.

During the monotonic and fatigue tests, loads were applied to the specimens either parallel or perpendicular to the fabric plies. Accordingly, the specimen configurations were referred to as edge-on and transverse, depending on whether the load was parallel or perpendicular to the fabric plies, respectively (Figure 1).

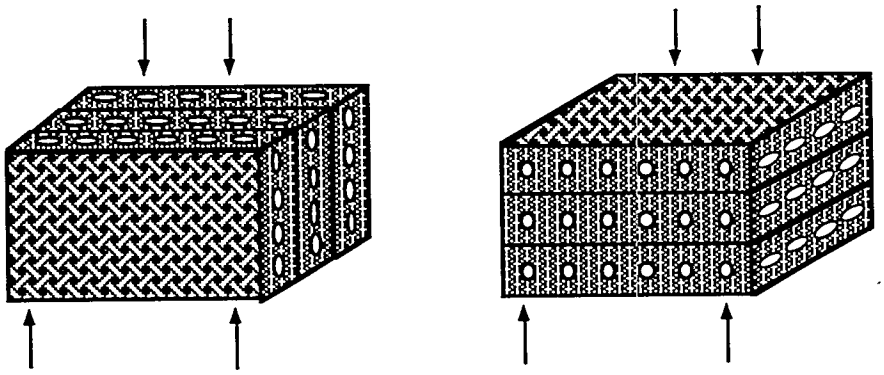

Figure 1. Geometries for testing Nicalon fabric reinforced ceramic matrix composites: (a) edge-on and (b) transverse.

Fractography

The composite fracture surfaces were examined under a Hitachi S-800 Scanning Electron Microscope (SEM), at the High Temperature Materials Laboratory (HTML) of the Oak Ridge National Laboratory (ORNL). An excitation voltage of 5 KeV was used to illuminate the electron beam on fracture surfaces. The images were directly captured onto a Macintosh personal computer using Adobe Photoshop software (version 2.5). The digital images were then processed using a public domain NIH Image software (version 1.57). The Image program was used to select areas of interest in the computer-captured images and enhance the "picture quality."

Results and Discussion

Monotonic Behavior

For the Nicalon/Al_2O_3 composite, significant differences were observed in the stress-strain curves for the two specimen configurations investigated (Figure 2). In the edge-on orientation, the ultimate flexural strength was 503 ± 11 MPa, while the strength was only 341 ± 9 MPa in the transverse orientation. However, the proportional limit was 70 MPa for both configurations, indicating that the proportional limit is an intrinsic property of the material and is independent of fabric orientation. This trend is consistent with the trends observed by Liaw [3] and Chawla et al. [4, 5] in Nicalon/SiC and Nextel/SiC composites. Also, the flexural proportional limit observed in the present investigation, 70 MPa, is comparable to the tensile proportional limit of 60 MPa reported by Fareed et al. [6]. From Figure 2, it can be seen that the strain to failure and the area under the stress-strain curve are higher for the edge-on orientation than the transverse orientation, which indicates that the edge-on orientation is tougher than the transverse orientation. It is a well known fact that the 2-D composites suffer from poor interlaminar strength. As a result, the fabric plies can slide with respect to each other in the transverse orientation, while the relative movement is not permitted in the edge-on orientation. Fractography revealed that multiple cracking (Figure 3) and interfacial debonding were observed in the composite. Interlaminar cracking was observed in the transverse specimens, while it was not observed in the edge-on specimens.

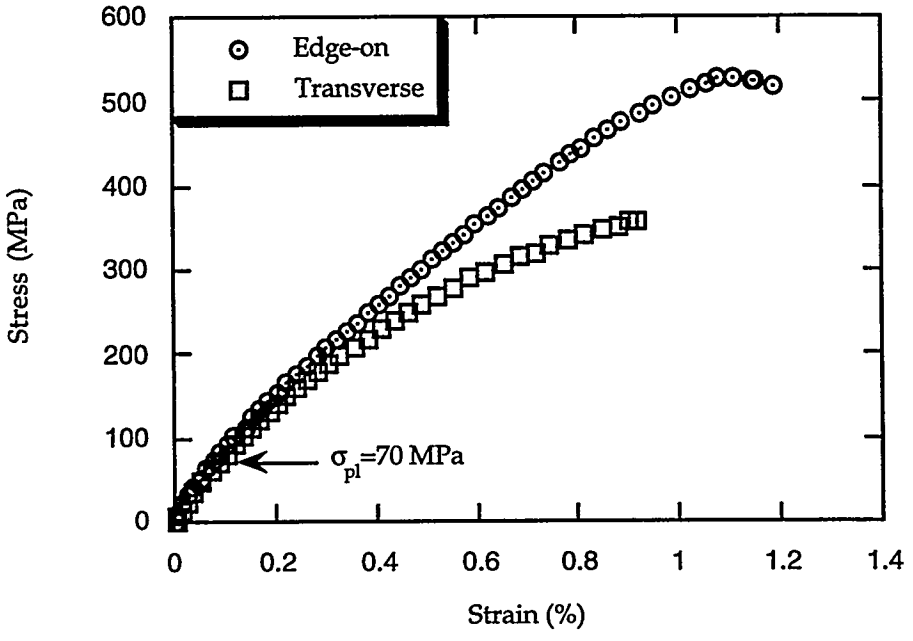

Figure 2. Stress-strain curves in the edge-on and transverse orientation for the Nicalon/Alumina composite.

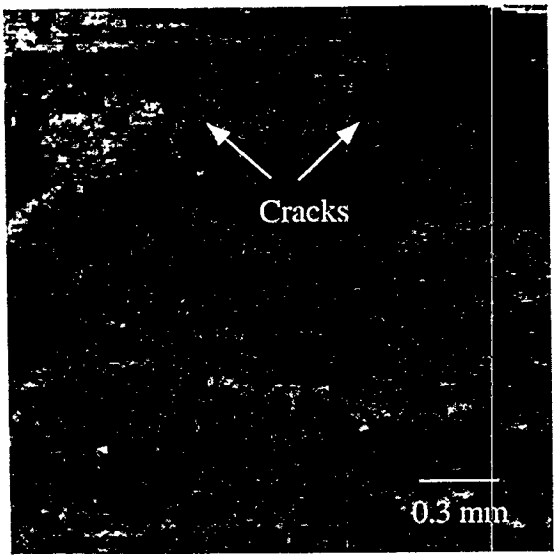

Figure 3. Multiple cracks on the tensile surface of a Nicalon/Alumina flexural specimen.

Interestingly, the interlaminar cracks did not propagate along the interface between two fabric plies. Instead, cracks were formed by the linkup of debonded interfaces within a fabric ply [7]. Fiber pullout, which contributes to composite toughness, was evident in specimens tested in both orientations (Figure 4).

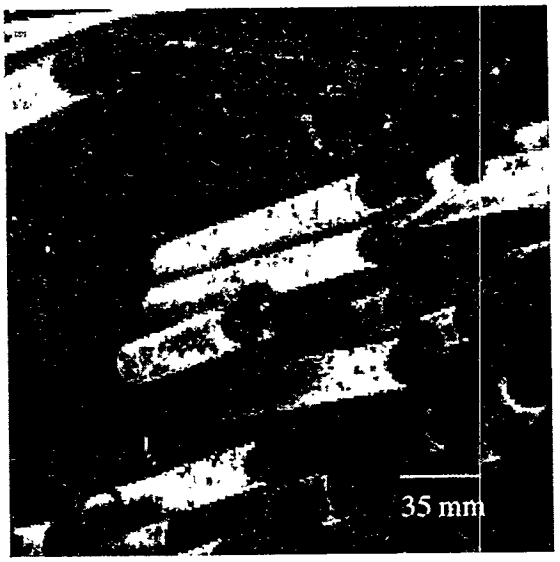

Figure 4. Fiber pullout, indicative of toughness in the edge-on orientation of the Nicalon/Alumina composite.

For the Nicalon/SiC composite, a significant scatter in ultimate strength values was observed in both edge-on and transverse orientations. The flexural strength in the edge-on orientation was 234 ± 27 MPa, while the strength was 241 ± 23 MPa in the transverse orientation. The large scatter in the strength values can be attributed to the variation in the density of the samples (2.38 to 2.64 g/cm^3). The flexural stress-strain curves for the Nicalon/SiC composites are presented in Figure 5. Although the average flexural strength is about 7 MPa higher in the transverse orientation than in the edge-on orientation, it is worth noting that this

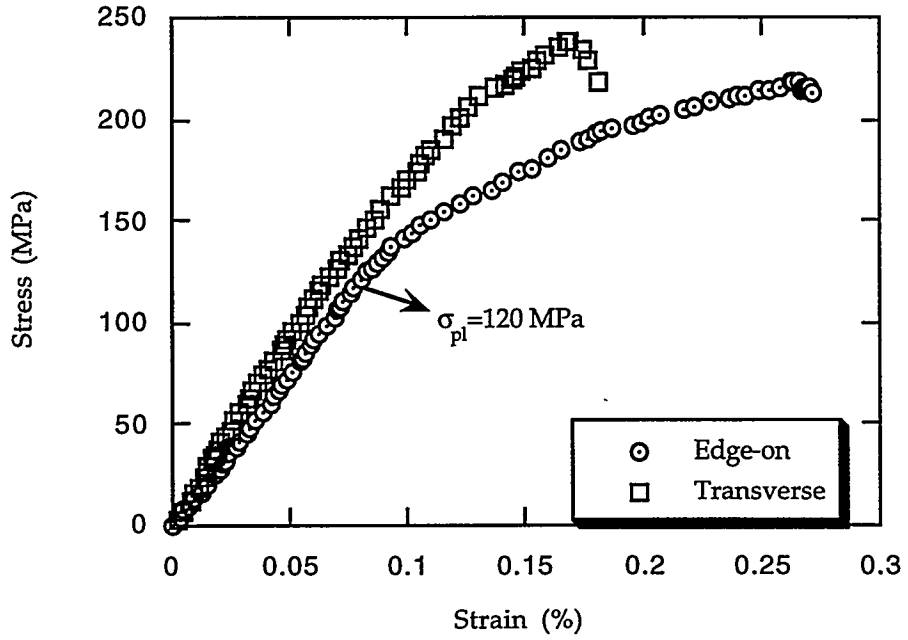

Figure 5. Stress-strain curves in the edge-on and transverse orientation for the Nicalon/SiC composite.

value is within the scatter band for the strength in both orientations. Therefore, it can be said that the strength of the composite is essentially unaffected by the orientation of fabric plies to the applied load in this composite, which is in contrast with that observed for the Nicalon/Al_2O_3 composite used in the present study. However, the proportional limit in both orientations was 120 MPa, similar to the trend observed in the Nicalon/Al_2O_3 composite. The strain to failure and the area under the stress-strain curve are higher in the edge-on orientation than in the transverse orientation, similar to the trend found in the Nicalon/Al_2O_3 composite. While multiple matrix cracking and fiber pullout were observed in the samples tested in both orientations, interlaminar cracking was observed only in the samples tested in the transverse orientation [7].

Fatigue Behavior

The stress versus number of cycles (S-N) curves for the Nicalon/Al_2O_3 composite in the edge-on and transverse orientations are shown in Figure 6. The endurance limit (the stress at which the material survives 1 million cycles) in the edge-on orientation was 318 MPa, which is about 65 % of the monotonic flexural strength. In contrast, the endurance limit in the transverse orientation was 257 MPa, which is about 75% of the monotonic strength. Thus, it appears that cyclic loading reduces the load bearing capacity of the composite in the edge-on orientation, more than it does in the transverse orientation. The proportional limit for both orientations was 70 MPa. At stresses above the proportional limit, extensive matrix cracking occurs in CFCCs. The specimens tested in the edge-on orientation were subjected to a higher level of fatigue stresses than the specimens tested in the transverse orientation (Figure 6). Hence, it could be expected that the degradation in material strength due to matrix cracking was much higher in the edge-on orientation than in the transverse orientation.

The progressive damage in the composite can be *qualitatively* monitored using the slope of the linear portion in the load versus midspan deflection traces recorded at periodic intervals. The slope at any point during the fatigue test can be normalized with respect to the slope for the first cycle and plotted against the number of cycles. The normalized slope is known as the effective slope. However, it must be emphasized

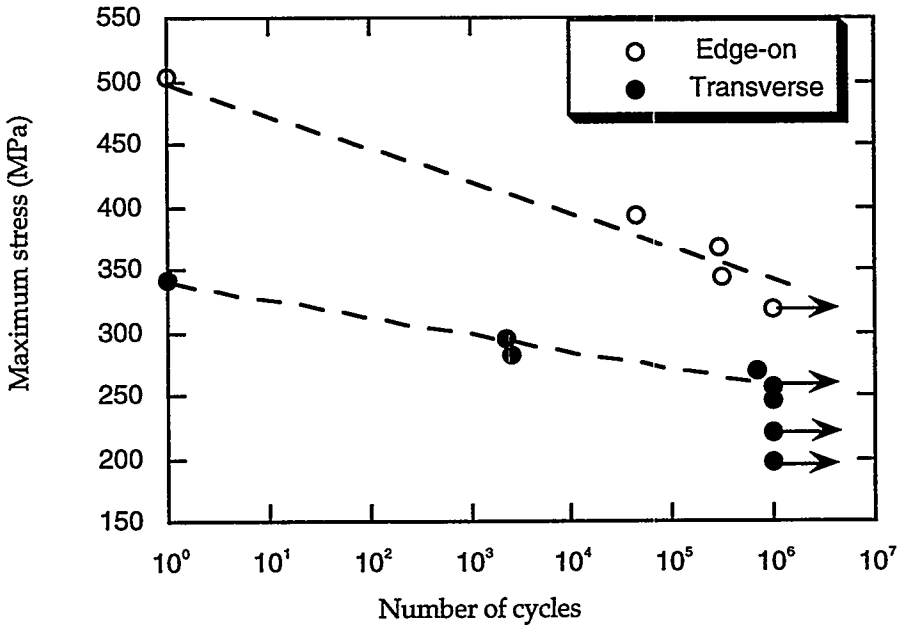

Figure 6. Stress versus life curves for the Nicalon/Alumina composite in the edge-on and transverse orientations.

that the normalized slope values do not readily translate into normalized modulus values. The effective modulus values are plotted against the number of cycles for the Nicalon/Al_2O_3 composite in Figures 7 and 8. It can seen from these figures that the effective modulus values continued to drop rapidly with increased cycling in the edge-on orientation, while the drop in the effective modulus values with cycling was more gradual for the specimens tested in the transverse orientation. However, at present, the reasons for the shapes of the curves observed are not apparent. It is hoped that *in situ* microscopy of the specimens, which will be performed shortly, might provide an insight into the damage in the material and hence help understand the stress versus life and effective modulus trends observed upon cyclic loading.

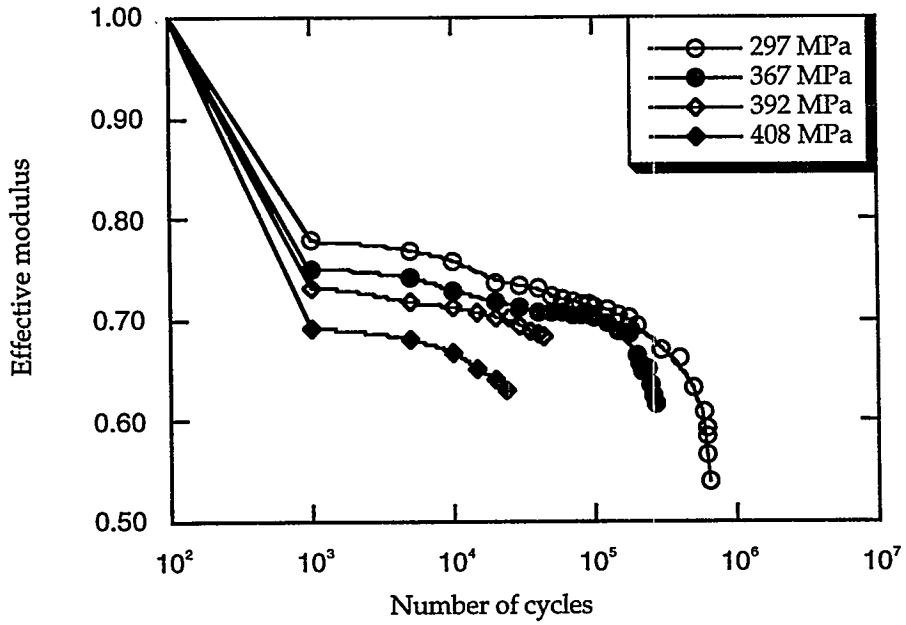

Figure 7. The reduction in effective modulus due to fatigue in the edge-on orientation of the Nicalon/Alumina composite.

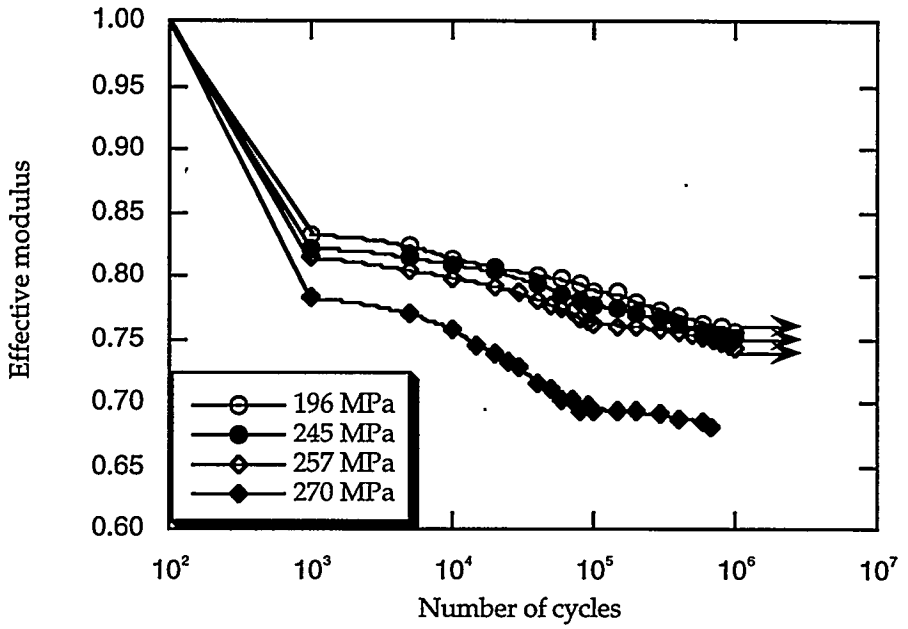

Figure 8. The reduction in effective modulus due to fatigue in the transverse orientation of the Nicalon/Alumina composite.

The S-N curves for the Nicalon/SiC composite in the edge-on and transverse orientations are shown in Figures 9. It is apparent that, in contrast to the Nicalon/Al_2O_3 composite, the endurance limit seems to be slightly higher in the transverse orientation than in the edge-on orientation. For the edge-on orientation, while specimens tested at a maximum stress of 207 MPa (which corresponds to 88% of the average monotonic ultimate strength) survived almost 1 million cycles, those attempted to be tested at a maximum stress 214 MPa failed before the maximum load could be applied. It must be mentioned here that there is a large scatter in monotonic ultimate strength values (234 ± 27 MPa) in the edge-on orientation. A stress value of 207 MPa is within this scatter band. Therefore, it can be postulated that the strength degradation due to cyclic loading is marginal in this composite. In the transverse orientation, the Nicalon/SiC specimens survived 1 million cycles at a maximum stress of 223 MPa, which corresponds to approximately 92 % of the average monotonic strength. The composite specimens survived > 10^5 cycles at a maximum stress of 231 MPa, which is approximately 96% of the average monotonic ultimate strength. A stress value of 223 MPa is within the scatter band for the monotonic strength values (241 ± 23 MPa). Hence, it can be deduced that the strength degradation due to cyclic loading is rather small in the transverse orientation as well. The effective modulus values for the edge-on and transverse orientations are plotted against the number of cycles in Figures 10 and 11, respectively. It can be seen that the effective modulus values decreased only marginally, after the initial drop, in the specimens that survived 1 million cycles, while the values dropped considerably for the samples that failed in less than a million cycles. It is interesting to note that higher monotonic strength translated into higher fatigue strength, with regard to fabric orientation, in both composites. This behavior is similar to that observed in metallic materials. Fractography revealed that a significant amount of repeated interfacial sliding was operative in the Nicalon/SiC composite specimens subjected to fatigue loading (Figure 12). While this phenomenon suggests that significant damage was induced at the fiber/matrix interface upon cyclic loading, surprisingly, however, the S-N curves indicate that strength degradation due to fatigue loading was only marginal in both edge-on and transverse orientations. In view of the small differences in the monotonic and endurance limit values in the edge-on and transverse orientations, it can be hypothesized that the fabric orientation effects are not strong in the Nicalon/SiC composite.

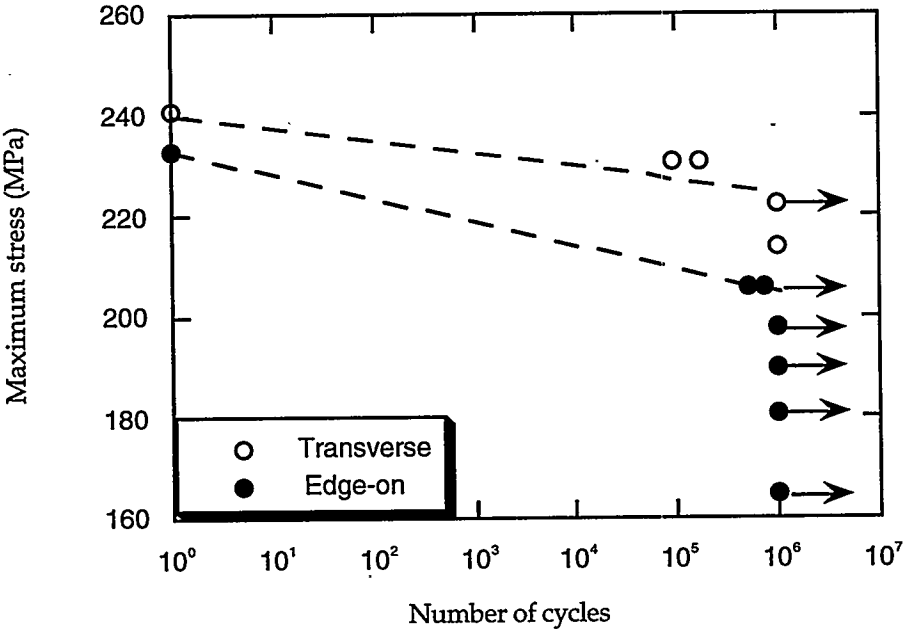

Figure 9. Stress versus life curves for the Nicalon/SiC composite in the edge-on and transverse orientations.

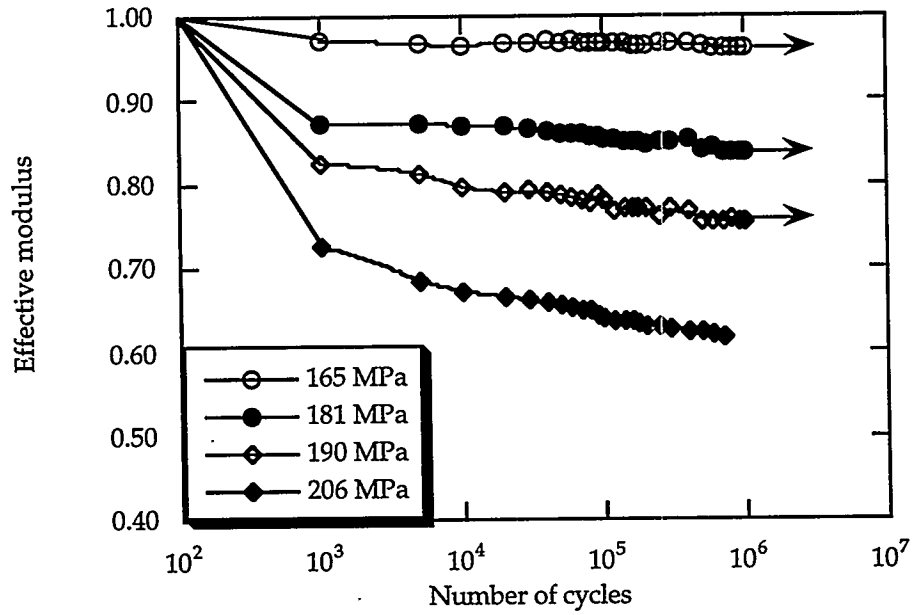

Figure 10. The reduction in effective modulus due to fatigue in the edge-on orientation of the Nicalon/SiC composite.

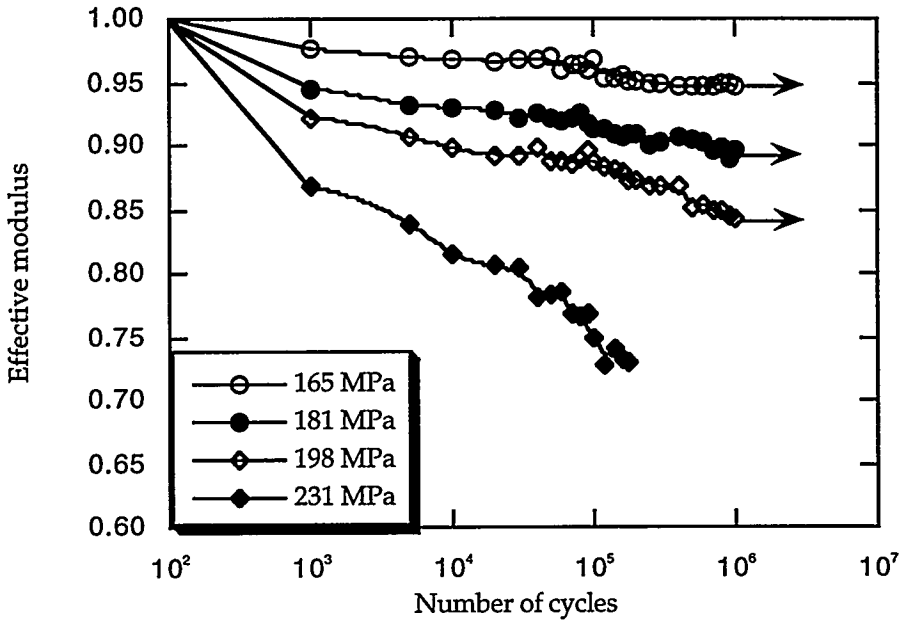

Figure 11. The reduction in effective modulus due to fatigue in the transverse orientation of the Nicalon/SiC composite.

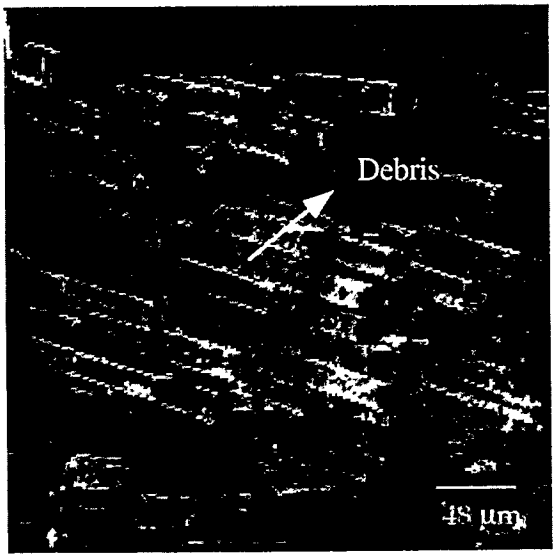

Figure12. Debris left by repeated interfacial sliding in the Nicalon/SiC composite.

CONCLUSIONS

The monotonic and fatigue behavior of the Nicalon/Alumina composite seems to be strongly influenced by the orientation of fabric plies to the applied loads, while the orientation effects seem to be only marginal for the Nicalon/SiC composite. In the Nicalon/Alumina composite, the monotonic and fatigue strengths were higher in the edge-on orientation than in the transverse orientation. In the Nicalon/SiC composite, the opposite trend was observed, i.e., the monotonic and fatigue strengths were higher in the transverse than in the edge-on orientation. However, in both composites higher monotonic strength translated into higher fatigue strength. This trend is identical to that observed for metallic materials.

FUTURE WORK

All the experiments to date have been conducted at room temperature. The modulus reduction plots indicated some interesting trends in damage accumulation upon cyclic loading in the Nicalon/Alumina and Nicalon/SiC composites. However, an understanding of progressive damage has not been achieved yet. Well polished flexural bars will be *in situ* monitored for damage development in the next few months. Elevated-temperature tests will also be performed to study the monotonic and fatigue behavior of the two CFCCs used in the present investigation, with particular regard to fabric orientation effects. In addition, the influence of span-to-thickness ratio, on the monotonic and fatigue behavior of both composites, will be evaluated. After an understanding of the damage mechanisms that operate in the two composites is developed, an attempt will be made to use finite element method (FEM) analysis to help explain some of the experimental results.

ACKNOWLEDGMENTS

This work is supported by the Department of Energy under contract No. Martin Marietta 11X-SL261V to the University of Tennessee. We are grateful to Drs. Arthur Rowcliffe and Everett Bloom of ORNL for their understanding and support. Thanks are due to Dr. Ali Fareed of Lanxide Corporation and Dr. Jeff Armstrong of AlliedSignal Corporation for providing the composite materials used in the present study. We would like to acknowledge Ted Long, Greg Jones, Doug Fielden, and Mike Ensor for their help in setting up the flexural test system and fabrication of the composite specimens.

REFERENCES

1. J. A. Dicarlo, Adv. Mater. Proc. (June 1989) 41.

2. R. W. Rice, Ceram. Eng. Sci. Proc. **2** (1981) 661.

3. P. K. Liaw, JOM (October 1995) 38.

4. N. Chawla, M. S. Thesis, University of Tennessee, Knoxville, 1994.

5. N. Chawla, P. K. Liaw, E. Lara-Curzio, R. A. Lowden, and M. K. Ferber, in **High Performance Composites - Commonalty of Phenomena**, K. K. Chawla, P. K. Liaw and S. G. Fishman (eds.), TMS, Warrendale, PA (1994) 291.

6. A. S. Fareed, D. J. Landini, T. A. Johnson, A. N. Patel, and P. A. Craig, paper EM92-216, SME, Dearborn, MI, 1992.

7. N. Miriyala, Doctoral Dissertation Proposal, The University of Tennessee, 1995.

3.0 FERRITIC/MARTENSITIC STEELS

Fatigue Performance and Cyclic Softening of F82H, a Ferritic-Martensitic Steel - J. F. Stubbins, (University of Illinois, Urbana) and D. S. Gelles, (Pacific Northwest National Laboratory)*

OBJECTIVE

The objective of this work is to provide mechanical properties data for the IEA reduced activation heat of martensitic steel.

SUMMARY

The room temperature fatigue performance of F82H has been examined. The fatigue life was determined in a series of strain-controlled tests where the stress level was monitored as a function of the number of accrued cycles. Fatigue lives in the range of 10^3 to 10^6 cycles to failure were examined. The fatigue performance was found to be controlled primarily by the elastic strain range over most of the range of fatigue lives examined. Only at low fatigue lives did the plastic strain range contribute to the response. However, when the significant plastic strain did contribute, the material showed a tendency to cyclically soften. That is, the load carrying capability of the material degrades with accumulated fatigue cycles. The overall fatigue performance of the F82H alloy was found to be similar to other advanced martensitic steels, but lower than more common low alloy steels which posses lower yield strengths.

PROGRESS AND STATUS

Introduction

Ferritic steels are of high interest for application as structural materials in advance fusion systems. These materials have exhibited an ability to resist the effects of irradiation to very high doses at irradiation temperatures above about 400°C.[1] They are very resistant to void swelling and loss of fracture resistance as tested both by fracture toughness and by Charpy impact tests after doses as high as 200 dpa. The irradiation performance at lower temperatures is also good, though the materials is somewhat more prone to the loss of ductility through the irradiation-induced embrittlement process.

The structural and irradiation performance of the ferritic-martensitic class of these alloys (e.g. mod 9Cr 1Mo and HT-9) have particularly appealing properties which are largely based on the relatively complicated microstructure obtained through alloying and heat treatment. This class of alloys has particularly good strength properties with adequate ductility.[2,3] Much of this performance is based on high dislocation densities and a fine, well dispersed precipitation distribution. These alloys, however, are prone to softening during cyclic loading.[4-7]

Based on the success of other ferritic-martensitic alloys, the F82H alloy was developed to take account of the advances in understanding of the compositional and microstructural features which would optimize alloy performance for fusion structural materials applications. The present work is an examination of the room temperature fatigue response of this alloy with particular attention to the tendency for cyclic softening.

---

*Pacific Northwest National Laboratory is operated for the U.S. Department of Energy by Battelle under Contract DE-AC06-76RLO 1830.

Experimental Procedures

Specimens of F82H ferritic-martensitic steel for fatigue testing were fabricated from a 8 mm plate. The plate composition is (wt.%) 7.71Cr-2.1W-0.18V-0.04Ta-0.096C-0.003P-0.003S. The specimens were taken both parallel and perpendicular to the rolling direction. Specimen dimensions were based on a subsize specimen geometry for widely used irradiation exposure. This specimen has a 3.1 mm gauge diameter and a 6.32 mm uniform gauge length. This specimen geometry has been shown in other studies to provide reliable fatigue response, though the fatigue lives and the relative values of the elastic and plastic strain ranges may be somewhat different than standard ASTM specimen dimensions with gauge diameters of greater than or equal to 6.35 mm (0.25 in.) and uniform gauge lengths of 25.4 mm (1 in.).[8-10] In particular, the smaller specimen size may result in slightly lower fatigue lives than the standard specimens under fixed fatigue testing conditions.

Fatigue tests were performed on a closed-loop servo-hydraulic mechanical loading stand. The test were run under strain range control such that the total strain range was held constant over the duration of the test. The stress required to maintained the applied strain range was monitored as a function of the number of loading cycles. All tests were performed at room temperature in air.

Results

The number of cycles to failure, N_f, is plotted against half the total strain range, $\Delta\varepsilon_{tot}/2$, in Figure 1. In addition, contributions of the elastic strain range, $\Delta\varepsilon_{elastic}/2$, and the plastic strain range, $\Delta\varepsilon_{plastic}/2$, are shown in the figure. The value plotted were taken from the hysteresis loop response at half the failure life. The figure indicates that, over the range of lives studied, the elastic strain was the dominant portion of the total strain range. The plastic strain was significant only for the test conditions which resulted in the lowest fatigue lives. From the data, it is apparent that the fatigue transition life, that is the point where the elastic and plastic strain ranges are equivalent, $\Delta\varepsilon_{elastic} = \Delta\varepsilon_{plastic}$, occurs at fatigue lives of around 10^3 cycles to failure. The transition life is usually assume to delineate the low cycle fatigue (LCF) behavior where the plastic strain dominates and the high cycle fatigue (HCF) life where the elastic response dominates.

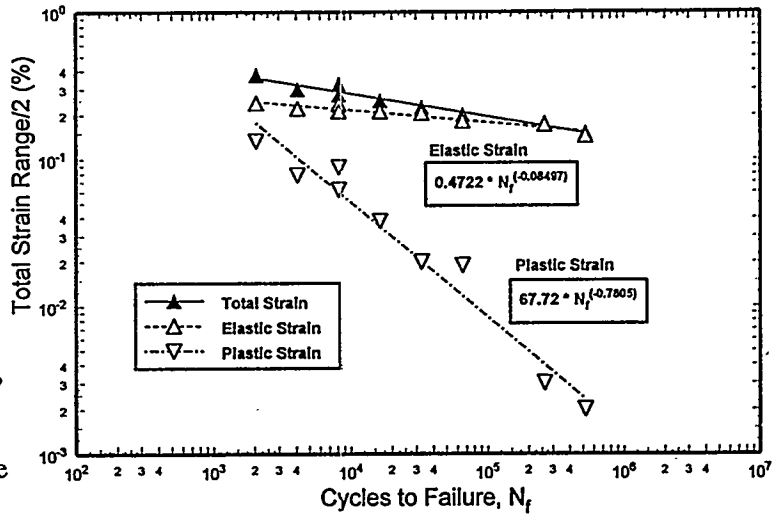

Figure 1 Strain - life plot indicating the relative contributions of the elastic and plastic strain range to the failure life. The equations for the elastic and plastic strain ranges are indicated.

The fatigue response can be well represented by the well known strain-life equation:

$$\Delta\varepsilon_{tot}/2 = \sigma_f/E\,(N_f)^b + \varepsilon_f\,(N_f)^c = 0.47\,(N_f)^{-0.085} + 67.7\,(N_f)^{-0.78}$$

where E is the elastic modulus, σ_f is the fatigue strength coefficient, and ε_f is the fatigue strain coefficient. The values of the exponents b = - 0.085 and c = - 0.78 are within typical ranges, though the value for c is somewhat higher than "universal" values of -0.5 proposed by Coffin or -0.6 proposed by Manson, and typical values on comparable alloys of around -0.55 (see below). In the present work, the plastic strain ranges were typically small, resulting is some degree of uncertainty in the precise

value.

Figure 2 shows the stress response versus the number of accrued fatigue cycles. The maximum stress or stress amplitude, required to attain the fixed strain level is plotted over the duration of the fatigue life. For the tests at the lowest fatigue lives, that is, the largest plastic strain ranges, there is a clear indication of cyclic softening, particularly following the initial loading cycle. This drop in strength is an indication of loss in load carrying capability following extended cycling. The cyclic softening behavior is not apparent at the lower strain ranges where the plastic strain becomes a vanishing small fraction of the total strain. In those cases, the stress response is virtually unaffected by the accrued numbers of loading cycles.

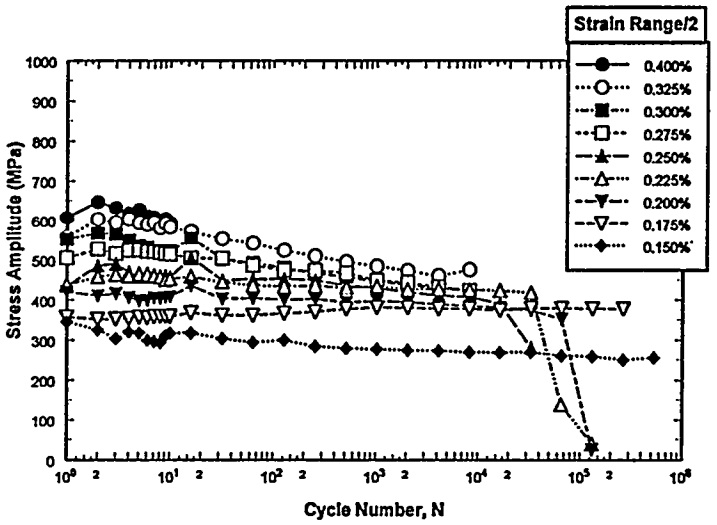

Figure 2 The stress amplitudes at each strain range is shown as a function of the number of applied fatigue cycles.

Discussion

Fatigue Life

The room temperature fatigue performance of the F82H alloy is similar to that reported for the modified 9Cr 1MoVNb alloy class.[2] The strain range vs. fatigue life response for the F82H alloy is compared to the median room temperature fatigue lives and the average 550 C fatigue trend curve of the mod 9Cr 1MoVNb alloy [1b] in Figure 3. The room temperature response for the two alloys is similar. The slightly lower lives of the F82H may, in part, be due to specimen size effects. However, the points plotted for room temperature fatigue response of the mod 9Cr 1MoVNb alloy class is representative of the midpoint lives.

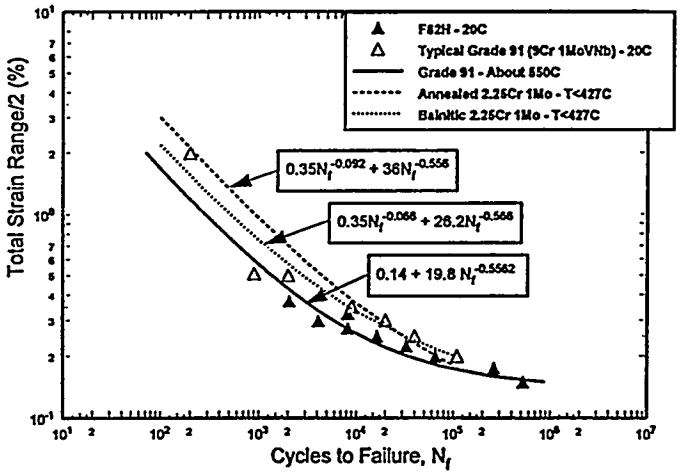

Figure 3 The fatigue life trend curves are compared for the present F82H materials with fatigue response values for mod 9Cr 1MoNbV steel and annealed or bainitic 2.25Cr 1Mo steels.

The fatigue life attributes of the 2.25Cr 1Mo in both the annealed condition and in the bainitic (normalized or normalized and tempered) condition[11] are also indicated in Figure 3. Both the annealed and bainitic forms show superior fatigue life to F82H and to the 9Cr 1MoVNb class of materials. This trend is typical in the low cycle fatigue regime where lower strength and higher ductility provide better LCF resistance.

It is noteworthy that while the fatigue performance of the mod 9Cr1MoVNb alloy class is indicated to

have a fatigue endurance limit around a strain range of $\Delta\varepsilon_{tot}/2 = 0.14\%$, the F82H and the 2.25Cr 1Mo alloys provide no indication of such a limit over the range of conditions tested.

Cyclic Softening

The tendency for cyclic softening is associated primarily with the plastic strain range. Since the elastic strain dominates over most of the conditions tested here (see Figure 1), the full effect of cyclic softening is not evident. The degree of softening in the materials conditions tested at strain levels at and above $\Delta\varepsilon_{tot}/2 \geq 0.250\%$ are shown in Figure 4 and compared to the cyclic softening phenomenon found in bainitic 2.25Cr 1Mo steels.[12] Figure 4 contains a plot of the experimentally determined cyclic softening response of the bainitic 2.25Cr 1 Mo material tested at 565 C.[12] Trend lines for two strain ranges, $\Delta\varepsilon_{tot}/2 = 0.500$ and 0.250 %, are shown. The similarity in the softening slopes should be noted despite the relatively large differences in the stress levels to produce similar levels of strain. This cyclic softening behavior has been shown to have a dramatic effect on the strength properties of these steels, particularly at elevated temperature. In particular, the creep strength of the bainitic 2.25Cr 1Mo steel was drastically reduced subsequent to only a few cycles of fatigue loading.[13]

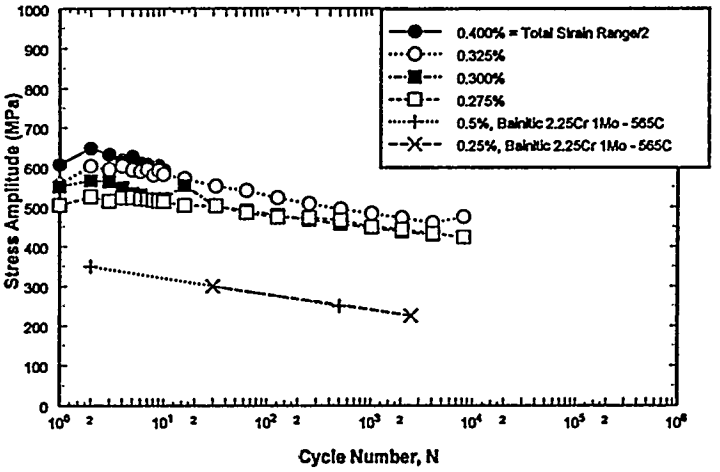

Figure 4 Comparison of cyclic softening trends for F82H at room temperature and 2.25Cr 1Mo steel in the bainitic form at 565 C.

Other Effects

It was noted that specimens were obtained both perpendicular and parallel to the rolling direction in the present F82H material. The fatigue response, however, seems not to be affected by the orientation with respect to the rolling direction. The data for the strain - life response are re-plotted in Figure 5. There is no apparent difference in the fatigue lives or the relative contributions of the elastic and plastic strain response with specimen orientation. This is an indication of the uniformity of the as rolled microstructure.

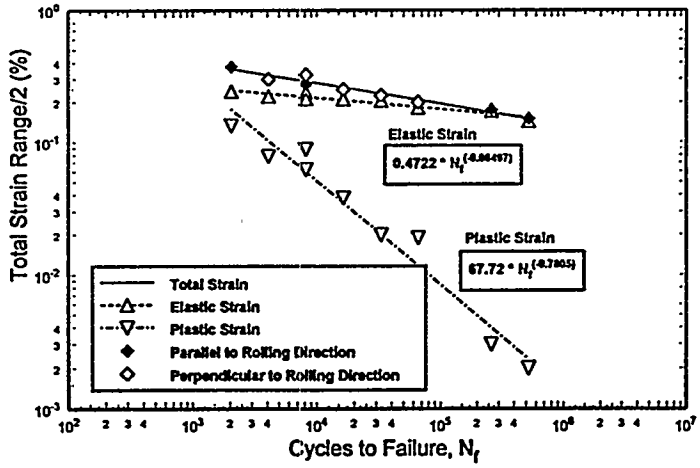

Figure 5 The effect of specimen orientation with respect to rolling direction is indicated. The elastic and plastic strain range symbols are associated with the total strain range symbol directly above them.

The potential influence of specimen size on fatigue life and cyclic stress response has been mention above. It is useful to note that in most cases where sub-sized specimens have been employed, the differences in fatigue

performance compared to standard size specimens is small, but does tend to result in the same or slightly lower lives at fixed fatigue conditions , i.e., fixed strain ranges.

CONCLUSIONS

The room temperature fatigue response of F82H has been examined in a number of strain controlled cyclic loading tests. The following conclusions can be drawn from the results of those tests.

1. The fatigue performance of the F82H is dominated by the elastic strain range over most of the useful fatigue life regime. The fatigue transition life is at or below one thousand cycles.

2. At low lives where the plastic strain contributes most, the alloy is prone to softening with cycling, that is cyclic softening. This effect is evident by the constantly dropping stress levels which are required to maintain a fixed strain level. This loss of load carrying capability has serious consequences for design requirements.

3. The fatigue response is close to other advanced ferritic - martensitic alloys such as the mod 9Cr 1Mo steels.

ACKNOWLEDGMENTS

The authors would like to express their appreciation to Dr. S. Raghuraman for his help in running the mechanical properties tests.

FUTURE WORK

This effort will be continued, to include microstructural explanations for fatigue softening.

REFERENCES

1. D. S. Gelles, J. Nucl. Mater., 212-215 (1994) 719.
2. Wareing and Tavassoli, "Assessment of martensitic steels for advanced fusion reactors," EEC-ITER draft report (1994)
3. D. J. Alexander, J. Pawel. M. Grossbeck and A. Rowcliffe, "Fracture Toughness of Irradiated Candidate Materials for ITER First Wall/Blanket Structures," DOE/ER-0313/16 (1994) 173.
4. J. F. Stubbins, B. A. Kschinka and D. L. Marriott, J. Nucl. Mater., 141-143 (1986) 55.
5. P. Marme, J. Nucl. Mater., 212-215 (1994) 594.
6. R. Lindau and A Moslang, J. Nucl. Mater., 212-215 (1994) 599.
7. H-J. Chang, J-J. Kai and C-H. Tsai, J. Nucl. Mater., 212-215 (1994) 574.
8. A. Singhal, et al., J. Nucl. Mater., 212-215 (1994) 1307.
9. K. Leedy, et al., this conference
10. K. C. Liu and M. Grossbeck, ASTM STP 888 (1986) 276.
11. S. J. Sanderson et al. "Comparison of low-cycle fatigue data of 2.25Cr-1Mo steel," Rep. EUR-8501 (1983).
12. F. A. Leckie, D. L. Marriott, J. F. Stubbins, J. L. Handrock, and B. A. Kschinka, "Development of a Design Methodology for High-Temperature Cyclic Application of Materials which Experience Cyclic Softening." ORNL/SUB/85-55904/01, UILU ENG-88-4011 (August 1987).
13. R. W. Swindeman, MPC-21, ASME (1984) 31.

IMPACT BEHAVIOR OF REDUCED-ACTIVATION STEELS IRRADIATED TO 24 DPA -- R. L. Klueh and D. J. Alexander (Oak Ridge National Laboratory)

Journal of Nuclear Materials

Publication: Summer, 1996

EXTENDED ABSTRACT

Charpy impact properties of eight reduced-activation Cr-W ferritic steels were determined after irradiation to ≈21-24 dpa in the Fast Flux Test Facility (FFTF) at 365°C. Chromium concentrations in the eight steels ranged from 2.25 to 12wt% Cr (steels contained ≈0.1% C). The 2 1/4Cr steels contained variations of tungsten and vanadium, and the steels with 5, 9, and 12% Cr, contained a combination of 2% W and 0.25% V. A 9Cr steel with 2% W, 0.25% V, and 0.07% Ta was also irradiated. The steels had previously been irradiated at 365°C in FFTF to ≈6-8 and ≈15-17 dpa. Irradiation caused an increase in the DBTT and decrease in the USE, but there was little further change in the DBTT from that observed after the 15-17 dpa irradiation, indicating that the shift had essentially saturated with fluence.

The microstructures of the 2 1/4Cr steels were bainite with various amounts of polygonal ferrite, depending on the tungsten present in the steel. The two 9Cr steels and the 5Cr steel were 100% martensite, and the 12Cr-2WV steel was martensite with ≈25% δ-ferrite. The properties of the steels with 100% martensite were superior to those of the steels with the duplex structures of bainite and ferrite or martensite and ferrite. Indications are that the properties of the 2 1/4Cr bainitic steel with tungsten and vanadium, which is the 2 1/4Cr steel with the most irradiation resistance, would be improved if it were 100% bainite.

The 9Cr steels were least affected by irradiation, with the 9Cr-2WVTa showing only a 21°C increase in DBTT after ≈22.5 dpa. The 9Cr-2WVTa steel was the only steel that showed a slight increase in the shift with increasing fluence. This 21°C shift was an increase from shifts of 4 and 14°C in previous irradiations at 365°C to ≈6.4 and ≈15.4 dpa, respectively. Despite the slight increase over the previous irradiations, 21°C is one of the lowest shifts in DBTT for this type of steel irradiated to these conditions, and it compares with a 52°C shift for the 9Cr-2WV, which had the second lowest shift. The advantage for the 9Cr-2WVTa over the 9Cr-2WV is further enhanced by the much lower DBTT of the 9Cr-2WVTa before irradiation.

The results are encouraging because they indicate that the effect of irradiation on toughness can be favorably affected by changing composition and microstructure.

CHARPY IMPACT TEST RESULTS FOR LOW ACTIVATION FERRITIC ALLOYS IRRADIATED TO 30 DPA - L. E. Schubert, M. L. Hamilton, and D. S. Gelles (Pacific Northwest National Laboratory)

OBJECTIVE

The objective of this work is to evaluate the effects of neutron irradiation in low activation ferritic alloys, primarily by examining the shift of the ductile to brittle transition temperature (DBTT) and the reduction of the upper shelf energy (USE) in miniature Charpy V-notch (CVN) specimens.

SUMMARY

Miniature specimens of six low activation ferritic alloys have been impact tested following irradiation at 370°C to 30 dpa. Comparison of the results with those of control specimens and specimens irradiated to 10 dpa indicates that degradation in the impact behavior appears to have saturated by ~10 dpa in at least four of these alloys. The 7.5Cr-2W alloy referred to as GA3X appears most promising for further consideration as a candidate structural material in fusion reactor applications, although the 9Cr-1V alloy may also warrant further investigation.

PROGRESS AND STATUS

Introduction

A previous report[1] described results of post-irradiation CVN tests on six low activation ferritic alloys which were irradiated in the FFTF MOTA 1C experiment at 370°C to approximately 10 dpa. This document reports results of CVN impact tests on identical specimens irradiated in FFTF through the MOTA 1E experiment to ~30 dpa at a temperature of 370°C. The alloys under investigation have been designated as series L0 (7.5Cr-2W), L3 (2Cr-1V), L5 (9Cr-1V), L7 (12Cr-6Mn-1V), L8 (9Cr-1W), and L9 (12Cr-6Mn-1W). The 7.5Cr-2W alloy (L0) is referred to as GA3X.

Experimental Procedure

The specimens utilized were about one third the size of the ASTM standard CVN specimen.[2] The specimens were fatigue precracked before irradiation. The impact tests were conducted inside a hot cell using a remotely operated vertical drop tower.[3] The drop assembly included an 8.9 kN load cell fitted with a modified striking tup. The tip radius was 4 mm, half of that used for standard size specimen tests. The tup was also relatively long and narrow to allow for passage of the tup and the specimen pieces through the 18 mm gap between the support anvils without binding. The 1 mm radius at the tip of each anvil results in a 20 mm unsupported span before impact. A rigid, opaque flag, mounted to the drop assembly, passed through an infrared detector immediately prior to impact. Precisely measuring the time of passage of the flag allowed the velocity, and thus the kinetic energy, to be precisely calculated for each test; the velocity at impact was ~2.1 m/sec^2 for these tests.

Specimen temperature control was accomplished in a ceramic enclosure adjacent to the anvils.[4] A pneumatic ram moved the specimen from the temperature chamber to the test position. Elevated temperatures were achieved by passing low voltage electric current (AC) through the specimen. Temperatures below ambient were achieved by flowing nitrogen gas chilled to ~-196°C over the

specimen. The flow rate was adjusted to obtain different specimen temperatures. Specimens typically reach the test temperature in 10-20 minutes and are allowed to stabilize at temperature for three minutes prior to test initiation. The time interval from the specimen exit from the chamber to impact is approximately two seconds. If positioning is not completed properly, or if the time interval exceeds three seconds, the impact test is not performed, the specimen is returned to the temperature chamber, and the heating/cooling cycle is repeated. The highest temperature at which tests were performed was 300°C due to limitations of the test system.

Static load cell calibration was accomplished with NIST-traceable calibrated dead weights in a static, compressive load configuration. To verify the validity of the calibration, specimens of the strain rate insensitive aluminum alloy 6061-T651 were tested in a static loading configuration as well as in the impact loading configuration.

The signal from the load cell was recorded with a digital oscilloscope during each test. Typical test resolution was 2 μs and 50 μV with the impact and fracture event comprising ~2500 points. The millivolt versus time values were saved to floppy disk and transferred to a desk top computer for analysis, where these data were converted to load versus displacement utilizing the established calibration factor and the velocity at impact calculated for each test. The area under the load/displacement trace is the apparent energy, E_a, which is calculated by numerical integration and subsequently corrected for deceleration during the impact loading. The corrected fracture energy is E_d, determined as $E_d = E_a(1 - E_a/4E_o)$ where E_o is the kinetic energy at impact;[5] this determination of E_d is exact.

Results

Tests were conducted on each alloy over a range of temperatures in order to establish full DBTT curves. The data are plotted in Figures 1-6 with the data obtained earlier at 10 dpa. Virtually no additional shift in the DBTT curve was observed between 10 and 30 dpa for the L0 (7.5Cr-2W), L3 (2Cr-1V), L8 (9Cr-1W) and L9 (12Cr-6Mn-1W) alloys. The shift in DBTT with irradiation for these alloys had evidently saturated by 10 dpa. Of these four alloys, the only one that retained a DBTT below room temperature was L0 (7.5Cr-2W), for which alloy the DBTT of the unirradiated material was also very close to that of the material irradiated to 10 dpa and to 30 dpa. The L3 (2Cr-1V), L8 (9Cr-1W), and L9 (12Cr-6Mn-1W) alloys exhibited DBTTs well above room temperature as well as large irradiation-induced shifts in DBTT. The DBTT increased ~30°C between 10 and 30 dpa for the L7 (12Cr-6Mn-1V) alloy, and actually appeared to decrease by ~30°C between 10 and 30 dpa for the L5 (9Cr-1V) alloy. Thus L0 (7.5Cr-2W) and L5 (9Cr-1V) are the only alloys that appear to warrant continued interest on the basis of DBTT, although the DBTT values obtained on these one-third size specimens are most likely lower than those that would be obtained on full size specimens.

While the L5 (9Cr-1V) alloy exhibits some shift in DBTT with irradiation, the USE appears to remain unchanged and at a moderately high level (for precracked, one-third size specimens). The USE of the L0 (7.5Cr-2W) alloy decreased ~40% with irradiation to 10 dpa, but the drop has apparently saturated by then since no additional decrease was observed with continued irradiation to 30 dpa. The USE of both alloys is comparable in the irradiated condition. Thus both the L0 (7.5Cr-2W) and L5 (9Cr-1V) alloys appear to warrant further consideration, although the L0 (7.5Cr-2W) alloy is the only one with a DBTT that remains below room temperature.

Discussion

A few comments are in order about the earlier data obtained on both unirradiated controls and

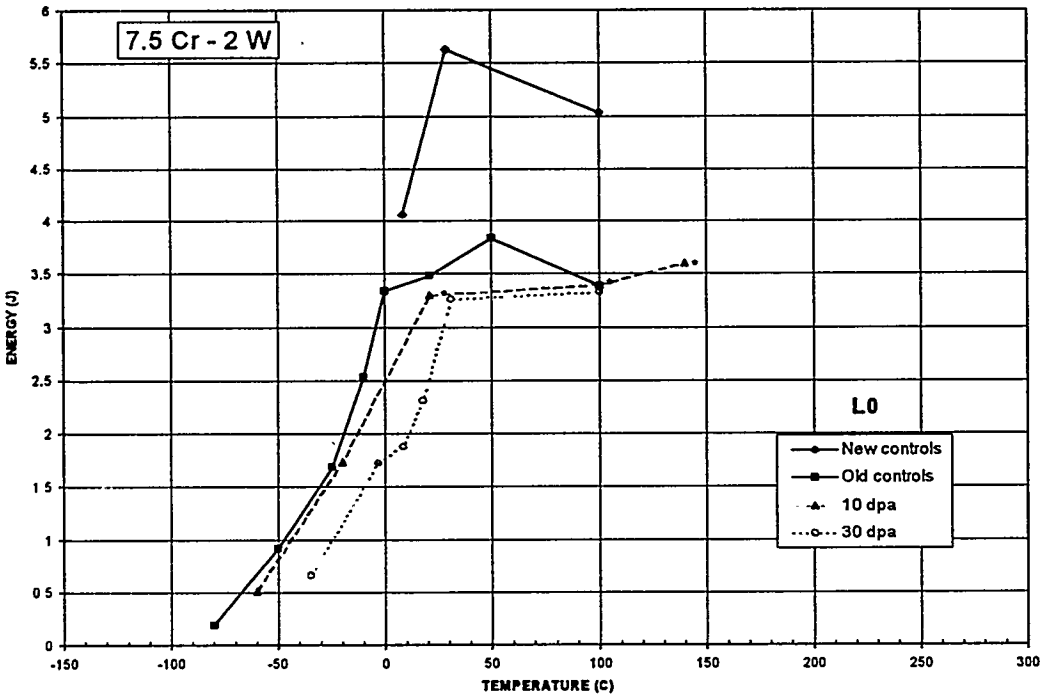

Figure 1. Charpy impact data obtained on precracked, one-third size specimens of the ferritic alloy GA3X (7.5Cr-2W) [series L0]. Asterisked points indicate reevaluated oscilloscope traces, as described in text.

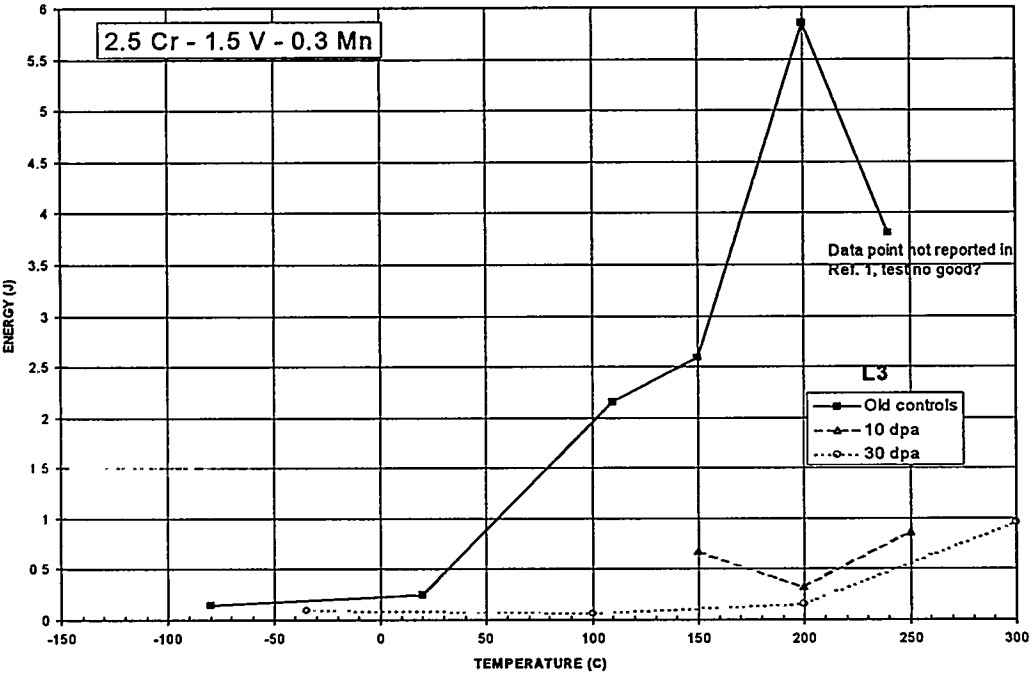

Figure 2. Charpy impact data obtained on precracked, one-third size specimens of the ferritic alloy 2Cr-1V [series L3].

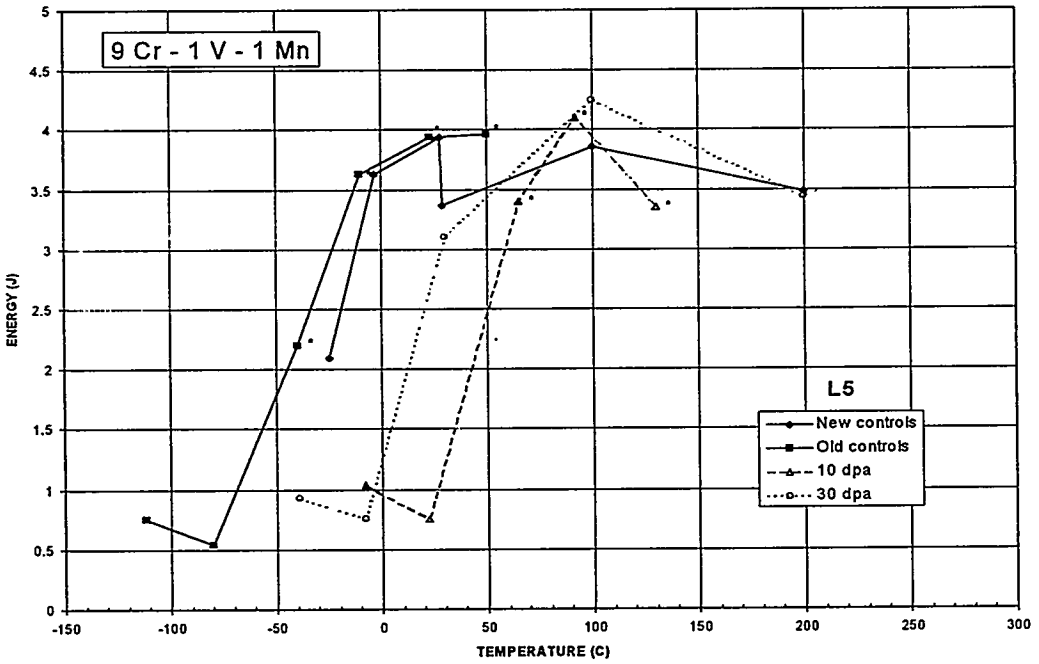

Figure 3. Charpy impact data obtained on precracked, one-third size specimens of the ferritic alloy 9Cr-1V [series L5]. Asterisked points indicate reevaluated oscilloscope traces, as described in text.

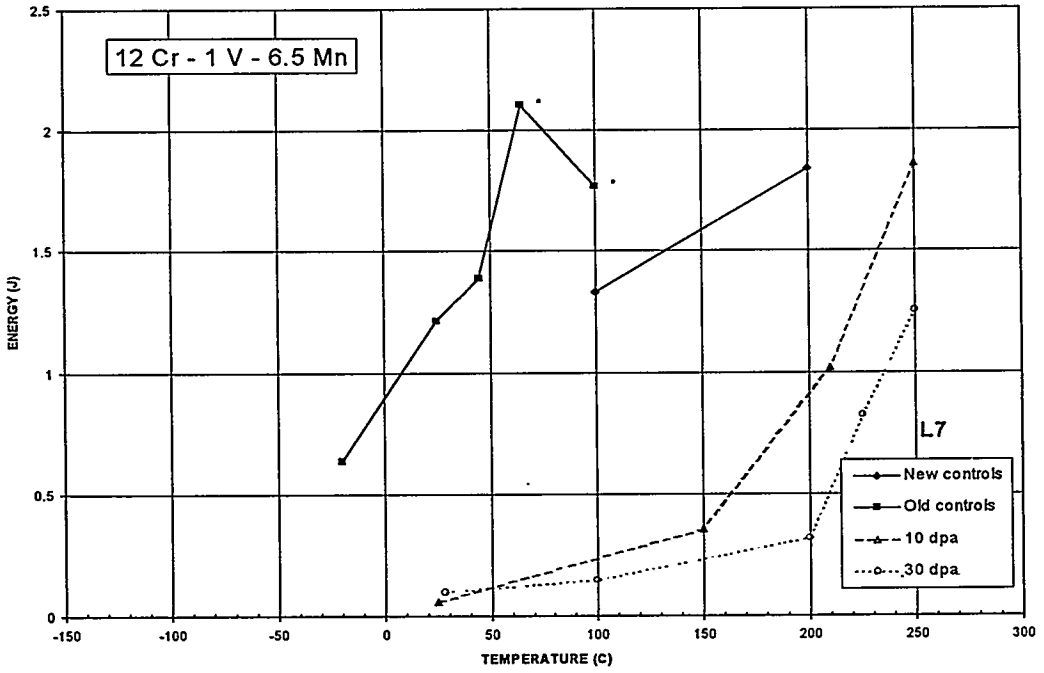

Figure 4. Charpy impact data obtained on precracked, one-third size specimens of the ferritic alloy 12Cr-6Mn-1V [series L7]. Asterisked points indicate reevaluated oscilloscope traces, as described in text.

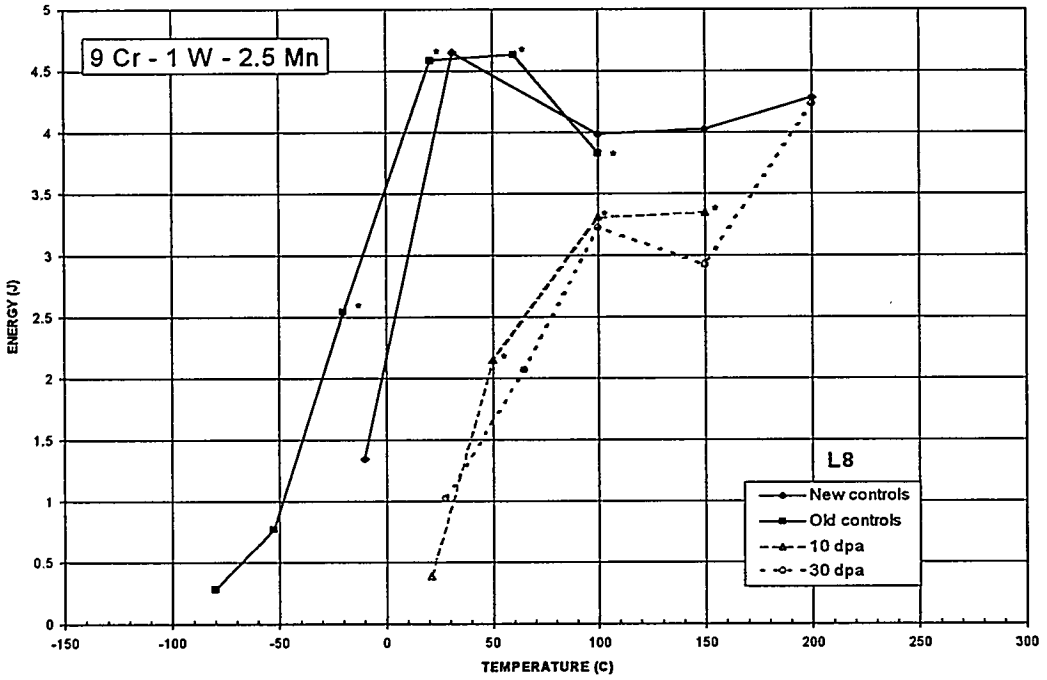

Figure 5. Charpy impact data obtained on precracked, one-third size specimens of the ferritic alloy 9Cr-1W [series L8]. Asterisked points indicate reevaluated oscilloscope traces, as described in text.

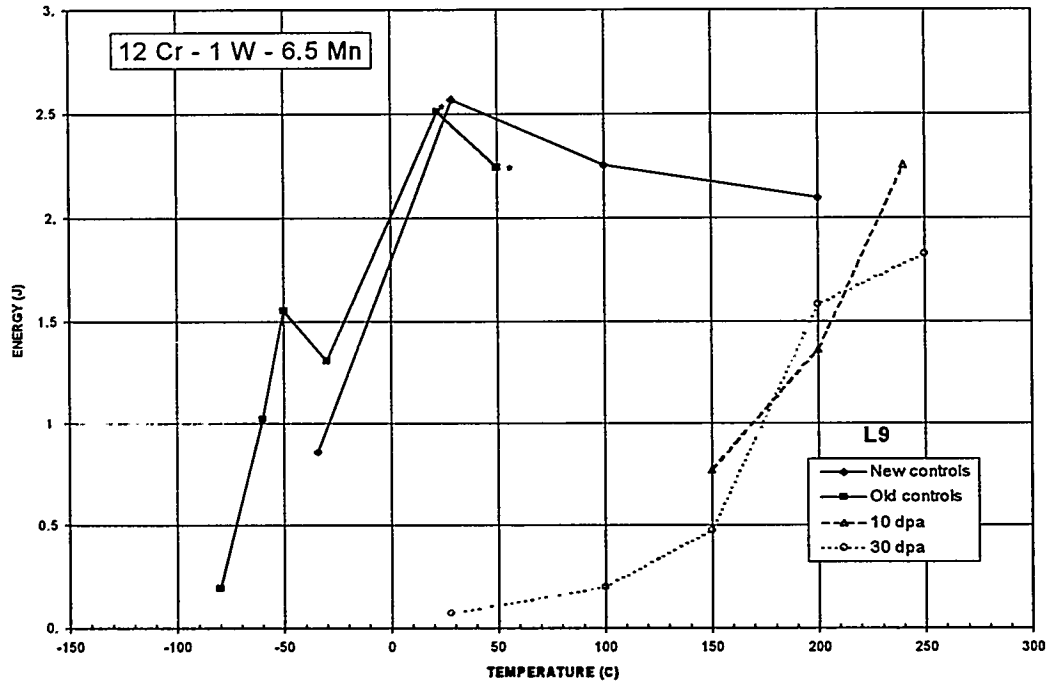

Figure 6. Charpy impact data obtained on precracked, one-third size specimens of the ferritic alloy 12Cr-6Mn-1W [series L9]. Asterisked points indicate reevaluated oscilloscope traces, as described in text.

specimens irradiated to 10 dpa. Both the earlier control data and the data obtained at 10 dpa that are shown in these figures have been reevaluated to reflect the fact that for temperatures at or above the DBTT, full oscilloscope traces were not obtained. A number of new control tests were performed to support the reevaluation. The reevaluation of the incomplete traces generated for the earlier controls was accomplished using a desktop computer by overlaying the traces from the old and new control tests, calculating what fraction of the total energy had been expended in the new test at the point where the old trace ended, and increasing the energy obtained from the old trace by the inverse of that fraction. Despite the fact that ~10 years elapsed between the times the old and new control data were obtained, it is believed that this technique is reasonable due to the incredible similarity in the traces that were overlaid (see Figure 7). None of the floppy disks containing the traces for the earlier L0 (7.5Cr-2W) control specimens were located, and no new control tests were performed on the L3 (2Cr-1V) alloy because no precracked control specimens were available; the energies of the old L3 and L0 control tests were therefore corrected by the average correction factor from the other unirradiated tests. Fairly good agreement between the old and new control data are evident in the majority of the plots, with the exception of alloys L0 (7.5Cr-2W), where the subjective correction factor was clearly too small, and L3 (2Cr-1V), where no new control data were available.

The same type of technique was applied to the incomplete traces generated at 10 dpa, although more judgement was necessary since no additional specimens at 10 dpa were available for testing. The

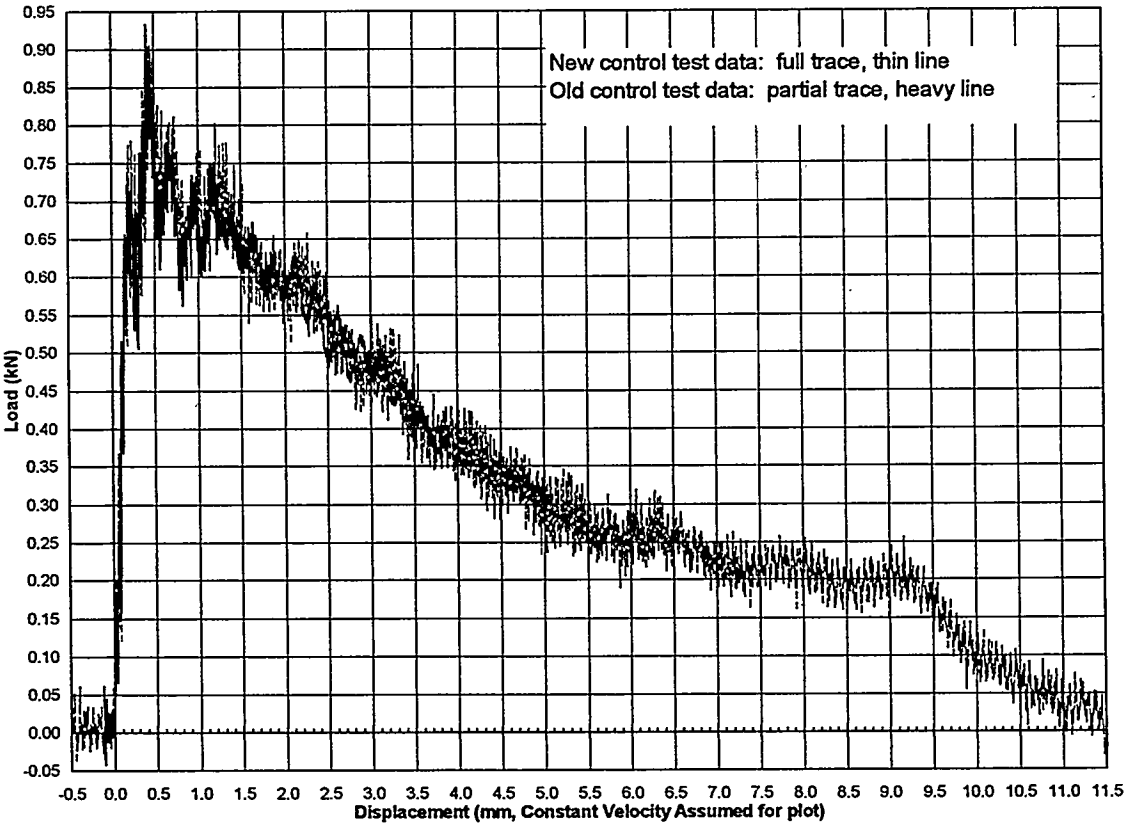

Figure 7. Comparison of oscilloscope traces for an old and a new test performed on unirradiated control specimens of alloy series L5 (9Cr-1V) at ~-10°C, illustrating the similarity in the traces.

oscilloscope traces from the specimens at 10 dpa were typically compared to traces produced at 30 dpa to determine the fraction by which they should be increased, although the 30 dpa was not necessarily obtained at the same temperature as the 10 dpa trace.

Conclusion

Impact tests were performed on a number of ferritic alloys irradiated at 370°C to 30 dpa. The impact behavior of the L0 (7.5Cr-2W) alloy (GA3X) is clearly superior to that of the others, although that of the L5 (9Cr-1V) alloy was also fairly good. On the basis of the impact data, both alloys appear to warrant further consideration as potential structural materials in fusion reactors.

Future Work

Scanning electron microscopy will be performed on fracture surfaces from the specimens tested in this work to determine the fracture mode. Additional impact testing will be performed on similar one-third size specimens irradiated under different conditions of temperature and neutron exposure.

REFERENCES

1. N. S. Cannon, W. L. Hu, and D. S. Gelles, "Charpy Impact Test Results for Low Activation Ferritic Alloys," p. 119 in Fusion Reactor Materials Semiannual Progress Report for the Period Ending March 31, 1987, DOE/ER-0313/2, U.S. DOE, Office of Fusion Energy.

2. "Standard Test Method for Notched Bar Impact Testing of Metallic Materials," Designation: E 23, The American Society for Testing and Materials.

3. W. L. Hu and N. F. Panayotou, "Miniature Charpy Specimen Test Device Development and Impact Test Results for the Ferritic Alloy HT9," p. 235 in Alloy Development for Irradiation Performance Semiannual Progress Report for the Period Ending September 30, 1981, DOE/ER-0045/7, U.S. DOE, Office of Fusion Energy.

4. W. L. Hu, "Miniature Charpy Impact Test Results for Irradiated Ferritic Alloys," p. 255 in Alloy Development for Irradiation Performance Semiannual Progress Report for the Period Ending September 30, 1982, DOE/ER-0045/9, U.S. DOE, Office of Fusion Energy.

5. L. E. Schubert, "Effects of Specimen Size Reduction on the Transition Curve of the Charpy V-Notch Impact Test," Master of Science Thesis, Nuclear Engineering, A. S. Kumar--Advisor, University of Missouri-Rolla, May 1995.

IRRADIATION CREEP AND VOID SWELLING OF TWO LMR HEATS OF HT9 AT ~400C AND 165 dpa - M. B. Toloczko (University of California at Santa Barbara) and F. A. Garner (Pacific Northwest National Laboratory)

To be published in J. Nuclear Materials, 1996 proceedings of ICFRM-7

Extended Abstract

Two nominally identical heats of HT9 ferritic-martensitic steel were produced, fabricated into pressurized tubes, and then irradiated in FFTF, using identical procedures. After reaching 165 dpa at ~400C, small differences in strains associated with both phase-related changes in lattice parameter and void swelling were observed in comparing the two heats. The creep strains, while different, exhibited the same functional relationship to the swelling behavior. The derived creep coefficients, the one associated with creep in the absence of swelling and the one directly responsive to swelling, were essentially identical for the two heats. Even more significantly, the creep coefficients for this bcc ferritic-martensitic steel appear to be very similar and possibly identical to those routinely derived from creep experiments on fcc austenitic steels.

[1] Operated for the US Department of Energy by Battelle Memorial Institute under contract DE-AC06-76RLO 1830.

LOW-CHROMIUM REDUCED-ACTIVATION FERRITIC STEELS FOR FUSION -- R. L. Klueh, D. J. Alexander, and E. A. Kenik (Oak Ridge National Laboratory)

Journal of Nuclear Materials

Publication Date: December 1995

EXTENDED ABSTRACT

Development of reduced-activation ferritic steels has concentrated on high-chromium (8-10 wt.% Cr) steels. However, there are advantages for a low-chromium steel, and initial ORNL studies on reduced-activation steels were on compositions with 2.25 to 12% Cr. Those studies showed an Fe-2.25Cr-2W-0.25V-0.1C (2 1/4Cr-2WV) steel to have the highest strength of the steels studied. Although this steel had the best strength, Charpy impact properties were inferior to those of an Fe-9Cr-2W-0.25V-0.07Ta-0.1C (9Cr-2WVTa) and an Fe-2.25Cr-2W-0.1C (2 1/4Cr-2W) steel. Therefore, further development of the low-chromium Cr-W steels was required.

Microstructural studies indicated the superior impact properties of 2 1/4Cr-2W relative to 2 1/4Cr-2WV were due to the type of bainite formed in the two steels. The 2 1/4Cr-2WV contained granular bainite, and the 2 1/4Cr-2W contained acicular bainite. Based on these and previous observations, it was concluded that the difference in microstructure was due to cooling rate, with the acicular bainite being formed by the faster cooling rate. It was concluded that acicular bainite formation should also be promoted by increasing the hardenability.

A small amount of boron (0.005%) is known to improve hardenability, and a 2 1/4Cr-2WVB steel with 0.005% B had improved Charpy properties over 2 1/4Cr steels without boron. A combination of 0.005% B and 0.07% Ta (2 1/4Cr-2WVTaB) gave Charpy properties comparable to those of 2 1/4Cr-2WVB. Thus, improving hardenability improved impact toughness. Chromium will also increase hardenability, and a chromium addition to obtain 2.6Cr-2WVTa and 2.6Cr-2WVTaB steels gave Charpy properties better than those of 9Cr-2WVTa after tempering at both 700 and 750°C.

Previous work showed that the 9Cr-2WVTa steel had properties comparable or better than those for 9Cr-1MoVNb and 12Cr-1MoVW steels, the conventional Cr-Mo steels that were considered for fusion applications. The present results therefore indicate that the low-chromium steels also have properties that exceed those for 9Cr-1MoVNb and 12Cr-1MoVW.

These results indicate that it is possible to develop low-chromium reduced-activation ferritic steels that have tensile and impact properties as good or better than those of high-chromium (7-9% Cr) steels. Further improvement of properties should be possible by optimizing the composition.

DEVELOPMENT OF OXIDE DISPERSION STRENGTHENED FERRITIC STEELS FOR FUSION -

D.K. Mukhopadhyay, C. Suryanarayana, F.H. Froes (University of Idaho) and
D. S. Gelles (Pacific Northwest Laboratory)[a]

OBJECTIVE

The objective of this research is to develop low-activation oxide dispersion strengthened fully ferritic steels for first wall applications in a fusion reactor.

SUMMARY

Seven ODS steels, Fe-(5-13.5)Cr-2W-0.5Ti-0.25 Y_2O_3 (in weight percent) were manufactured using the mechanical alloying process. Only the composition Fe-13.5Cr-2W-0.5Ti-0.25Y_2O_3 showed no austenite formation at any temperature using differential thermal analysis and hence was selected as an experimental alloy for the present investigation. Milled powders were consolidated by hot isostatic pressing and hot swaging. Electron microscopy studies indicated high material homogeneity. The hardness of the as-swaged specimen was 65 R_c. Annealing of the as-swaged material at 800°C, 900°C, 1000°C, 1100°C and 1200°C showed a minor decrease in the hardness.

PROGRESS AND STATUS

Introduction

The oxide dispersion strengthened (ODS) ferritic steel called MA 957,[1] produced by mechanical alloying, has received international consideration for fuel cladding applications in liquid metal fast breeder reactors.[2] The alloy shows excellent long term microstructural stability in irradiation environments[3] and is expected to retain superb high temperature strength. This MA 957 alloy has the composition Fe-14Cr-1Ti-0.25Mo-0.25Y_2O_3. The microstructure consists of a metal matrix with uniformly distributed Y_2O_3 dispersoids on the order of 5 nm in diameter. It also contains a highly elongated subgrain structure which is introduced by thermo-mechanical processing. Based on the performance demonstrated to date, this technology should be considered for first wall applications of a fusion reactor.

Therefore, an effort has been initiated[4-5] to consider the use of mechanically alloyed ODS alloys for fusion by altering the alloy composition to be in line with low activation criteria. The objective of the present investigation was to continue that development by optimizing the composition and determining the creep response of the ODS alloy. The alloy composition selected was Fe-13.5Cr-2W-0.5Ti-0.25Y_2O_3.

Experimental Procedure

The starting powder compositions and the maximum mesh sizes are shown in Table 1. A Spex 8000 shaker mill was used for the mechanical alloying. The alloy was optimized by studying the phase transformations of the powders which are mechanically alloyed and then annealed at 1000°C for 1 h, using a Perkin-Elmer DTA 7 differential thermal analyzer (DTA). The optimization of the

---

[a]Operated for the U.S. Department of Energy by Battelle Memorial Institute under Contract DE-AC06-76RLO 1830.

composition was achieved by studying seven ODS steels, Fe-(5, 9, 10, 11, 12, 13, 13.5) Cr-2W-0.5Ti-$0.25Y_2O_3$, produced by mechanical alloying. The milled powders were also characterized in a Siemens D 5000 X-ray powder diffractometer to understand the structural evolution during milling. Low carbon steel tubing with 1" ID x 0.14" wall thickness x 13" overall length was used for HIP canning. The cans were pumped down to 20 millitorr and then baked at 400°C for 30h and heat crimped before HIPPing. The hot isostatic pressing was then carried out on at 950°C and 210 MPa by IMT Inc., Andover, MA. The outside diameter of the HIPPed billets (including the can) was 7/8".

After soaking at 950°C for 1 h following HIPPing the billets were hot swaged in a hot swaging unit. The outer diameter of the hot swaged materials was 1/2". The cans were opened after hot swaging. The inner diameter of the ODS material was found to be 5/16".

Hardness measurements of the ODS compacts were done in a Tukon hardness tester. Thin foils were made from the compact and characterized in JEOL 1010 and 2010 F transmission electron microscopes (TEM).

The chemical assay of the milled powders was done by Crucible Research, Pittsburgh, PA.

Table 1: Powder specifications

Powders	Size (mesh)	Compositions
Fe	-325	99.4% pure
Fe-Cr master alloy	-200	Fe-73.53 wt.% Cr
Fe-Ti master alloy	-100	Fe-40.53 wt.% Ti
W	-200	99.9% pure
Y_2O_3	-325	99.9% pure

Results

1. Alloy Optimization

The x-ray diffraction patterns of all the seven alloys indicated the presence of only the α-Fe solid solution after 10 h of milling. Figure 1 shows the x-ray diffraction patterns of the Fe-13.5Cr-2W-0.5Ti-$0.25Y_2O_3$ (ODS 13.5Cr) powder as a function of milling time. All seven ODS steel powders produced by mechanical alloying were annealed at 1000°C for 1 h prior to the phase transformation studies in a DTA. The DTA plots of the ODS steel powders for 5, 13 and 13.5 Cr milled for 10 h (Figure 2) indicates no austenite transformation only in the ODS 13.5 Cr steel. The amount of interstitial elements in the ODS 13.5 Cr steel powder milled for 10 h was obtained by chemical analysis and was given as follows:

carbon : 0.055 oxygen : 0.855 nitrogen : 0.284

2. Characterization

Metallographic sections of the as-swaged material in both the transverse and longitudinal directions were prepared and the results are shown in Figure 3. The micrograph reveals the elongated grain structure in the longitudinal direction. No porosity was observed in the material. A calculation of the bulk density from the machined dimensions showed the material to be 100% dense. The hardness of the as-swaged material was measured to be 65 R_c. The TEM micrograph in Figure 4 shows the

elongated grain structure and also the presence of very fine dispersoids of sizes less than 10 nm in the ferrite matrix.
The as-swaged material was annealed at 800°C, 900°C, 1000°, 1100°C and 1200°C for 1 h in order to examine the change in the hardness with annealing temperature. A plot of hardness versus annealing temperature in Figure 5 showed a slight decrease in the hardness value with an increase in the annealing temperature. The plot in Figure 5 clearly indicates that the hardness remains very high even following a 1200°C anneal.

Discussion

1. Homogeneity of the α-Fe Solid Solution

X-ray diffraction of the as mixed powders showed only reflections of Fe and W. The Cr and Fe reflections superimpose since their lattice parameters are very close. The amounts of Fe-Ti and Y_2O_3 powders were so small that they could not be detected in the x-ray pattern of the as-mixed powder. X-ray diffraction of the powder milled for 10 h showed the presence of only α-Fe, with a lattice parameter of 2.89 Å (calculated from the (110) reflection). The disappearance of W reflections and the increase in lattice parameter from 2.86 Å to 2.89 Å demonstrates that W was in solid solution following mechanical alloying. The chemical analysis of the powder obtained from the analytical TEM matches with the targeted composition.

The variations in composition studied covered 5-13.5 Cr. It can be noted that in the pure Fe-Cr system the austenite loop ends at a composition of 12.7 Cr. The presence of 2% W and 0.5% Ti in the α-Fe solid solution should further suppress the austenite loop to about 10.75 Cr (calculated from chromium equivalent formula[6]) and hence the transformation to austenite should not be observed in the alloys with Cr > 10.75 %. However, the austenite formation was observed by DTA in the ODS (11, 12, 13) Cr alloys. The presence of nitrogen and carbon which act as austenite stabilizers are probably responsible for the austenite transformations in ODS (11, 12, and 13) Cr alloys.

2. Microstructural Stability

The as-swaged material shows an elongated microstructure both in optical and transmission electron microscopy typical of hot worked ferritic ODS alloys. Analytical microscopy also indicated high homogeneity in the material. The hardness of the swaged material was very high due to the high dislocation density in the material. High hardness value was retained after 1 h exposure of the as-swaged material at 1200°C indicating a high thermal stability of the microstructure. Therefore, we can anticipate excellent high temperature creep response.

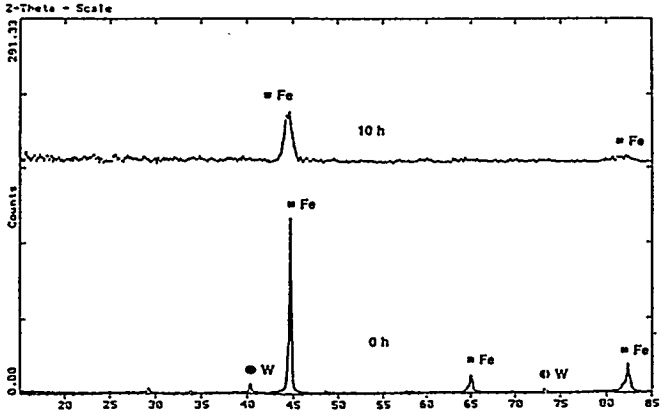

Figure 1: X-ray diffraction patterns of the ODS-13.5Cr powder as a function of milling time.

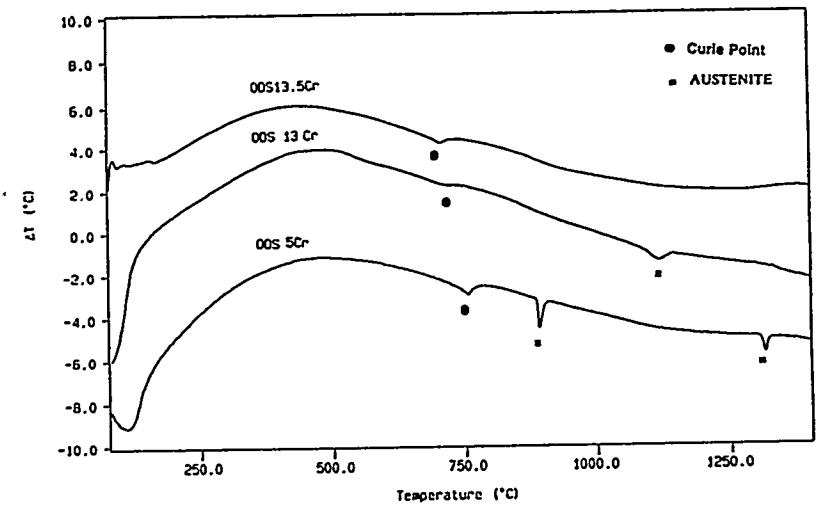

Figure 2: DTA plots of the ODS-5, 13 and 13.5 Cr powders milled for 10 h showing no austenite transformation only in ODS-13.5 Cr.

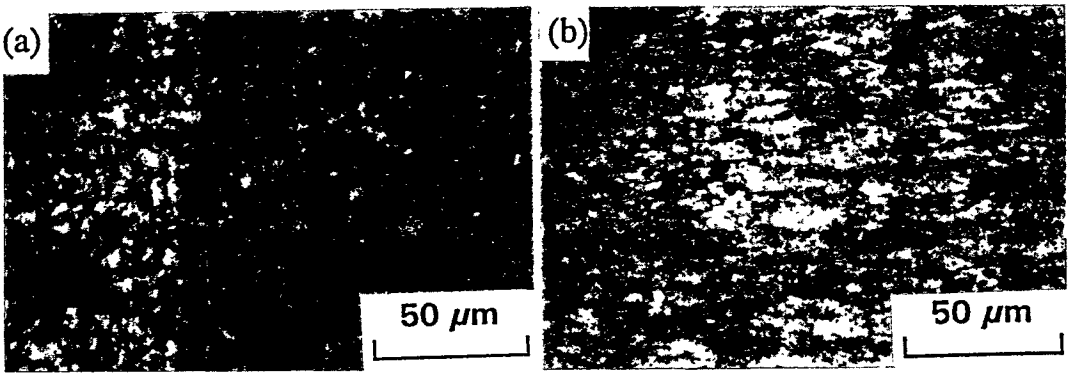

Figure 3: Polished and etched (Vilella's reagent) sections of as-swaged ODS-13.5 Cr material are shown in (a) transverse (b) longitudinal directions.

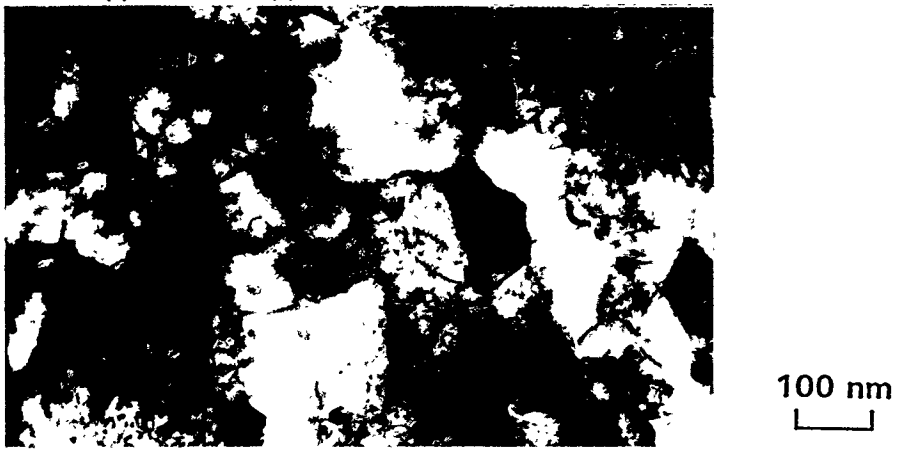

Figure 4: A TEM micrograph showing the elongated grains in the longitudinal direction of the ODS-13.5Cr as-swaged material.

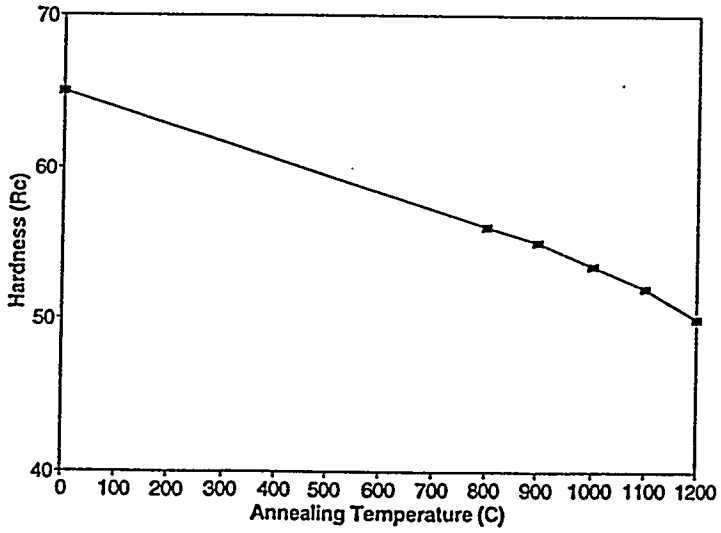

Figure 5: A plot of hardness versus annealing temperature (one hour anneals) indicating a slight decrease in the hardness with temperature.

CONCLUSIONS

A low-activation grade ODS ferritic steel has been optimized (Fe-13.5Cr-2W-0.5Ti-0.25Y_2O_3) and successfully manufactured by mechanical alloying. High material homogeneity was observed by electron microscopic study. Hardness remains very high even following a 1200°C annealing treatment indicating a highly stable microstructure.

FUTURE WORK

Thermal creep testing of the ODS-13.5Cr alloy is planned for the next reporting period. A transmission electron microscopy study will also be carried out on the crept material.

ACKNOWLEDGEMENTS

The authors would like to thank Mr. John Hebeisen, Vice President, Marketing & Sales, IMT Inc., Andover, MA and Mr. C.F. Yolton of Crucible Research, Pittsburgh, PA respectively for HIPPing and oxygen, carbon, nitrogen analysis of the ODS steel powders. One of the authors, D.K. Mukhopadhyay, would like to acknowledge the financial support of a Pacific Northwest National Laboratory Research fellowship.

REFERENCES

1. J.J. Fischer, U.S. Patent 4,075,010 (February 21, 1978).
2. D.S. Gelles, ISIJ Intl. 30 (1990) 905.
3. D.S. Gelles, DOE/ER-0313/16 (1994) 146.
4. A.N. Niemi, M.G. McKimpson and D.S. Gelles, DOE/ER-0313/6, (1989) 187.
5. A.N. Niemi, M.G. McKimpson and D.S. Gelles, DOE/ER-0313/8, (1990) 177.
6. F.B. Pickering, Physical Metallurgy and the Design of Steels, Applied Science Publishers Ltd., Essex, UK, 1978.

DYNAMIC FINITE ELEMENT MODELING OF THE EFFECTS OF SIZE ON THE UPPER SHELF ENERGY OF FERRITIC STEELS - S. E. Sidener, A. S. Kumar, (University of Missouri), L. E. Schubert, M. L. Hamilton, (Pacific Northwest National Laboratory), and S. T. Rosinski (Electric Power Research Institute)

SUMMARY

Both the fusion and light water reactor programs require the use of subsize specimens to obtain sufficient irradiation data on neutron-induced embrittlement of ferritic steels. While the development of fusion-relevant size effects correlations can proceed analytically, it is more cost-effective at this time to use data currently being obtained on embrittlement of pressure vessel steels to test and expand the correlations developed earlier using fusion-relevant steels.

Dynamic finite element modeling of the fracture behavior of fatigue-precracked Charpy specimens was performed to determine the effect of single variable changes in ligament size, width, span, and thickness on the upper shelf energy. A method based on tensile fracture-strain was used for modeling crack initiation and propagation. It was found that the upper shelf energy of precracked specimens (USE_p) is proportional to b^n, where b is ligament size and n varies from about 1.6 for subsize to 1.9 for full size specimens. The USE_p was found to be proportional to width according to $W^{2.5}$. The dependence on span was found to be nonlinear. The dependence on thickness was found to be linear for all cases studied. Some of the data from the FEM analysis were compared with experimental data and were found to be in reasonable agreement.

PROGRESS AND STATUS

Introduction

Subsize Charpy V-notch specimens have been proposed as a reasonable alternative to the ASTM standard full size Charpy specimens for the surveillance of nuclear reactor pressure vessels (RPV). The choice of subsize Charpy specimens would permit the placement of a sufficiently large number of specimens near the RPV for the purpose of monitoring its embrittlement throughout its lifetime. For example, if third size specimens were to be used, twenty seven specimens could be placed in the same volume as a single full size Charpy specimen. The choice of subsize specimens would not only increase the number of surveillance specimens that could be placed near the RPV, but it would also increase the uniformity of temperature and neutron fluence among the surveillance specimens. Furthermore, broken halves of irradiated full size specimens can be machined to fabricate subsize specimens which can be reinserted into the vessel for continued surveillance at higher fluences.

The choice of subsize surveillance specimens necessitates the development of methodologies for the prediction of the upper shelf energy of full size Charpy V-notch specimens based on subsize data. Numerous investigations have been carried out in the past to develop such methodologies [1-18] . These methodologies, however, are not applicable at all ductility levels of irradiated RPV materials. As the upper shelf energy (USE) diminishes from a high value (~200 J) to a low value (<100 J), three different methodologies have been found to be successful in correlating the USE of full and subsize specimens in different regimes of ductility.

The simplest of these methodologies is applicable at high ductility levels (USE >200 J). In this technique, normalized USE is defined as the ratio of the measured value and a normalization factor Bb^2 [1,2] or $(Bb)^{3/2}$ [3,4], often referred to as the fracture volume. The normalized values of USE are

equal for full and subsize Charpy specimens [1-4,7]. It is important to note that the normalization factor is independent of the span and the notch geometry, including the notch angle, notch depth, and the notch root radius. It is believed that blunting of the crack tip during macro-crack initiation and crack propagation makes the effects of span and notch geometry on USE minimal.

A little more complicated situation arises when the USE falls below 100 J. RPVs during the latter half of their life are expected to attain such low values of USE. Kumar and coworkers [5,6,8-10] have shown that the USE normalized by a factor equal to $(Bb^2)/(S^*K_t')$ is equal for full and subsize specimens. Here S is span and K_t' is a modified stress concentration factor. K_t' is equal to the product of the elastic stress concentration factor at the notch root (K_t), and the plastic constraint (Q) [19]. Q is equal to $(1 + \pi/2 - \theta/2)$, where θ is the notch angle in radians. It is to be noted that at the low value of USE the blunting of the crack tip is relatively small and the effects of span and the stress concentration factor on crack initiation and propagation are significant.

For medium USE materials (USE ~ 150 J), there does not appear to be a clear consensus on the choice of a single normalization factor. For some materials, the normalization factor of Louden et al. [7] works well, while for some other materials, the normalization factors used by Corwin et al. [1,2] and Lucas et al. [5,6] work well [8].

Kumar et al. [15] have recently developed a methodology to correlate the USE of full size and subsize specimens for medium USE materials. This methodology is based on the partitioning of the USE into macro-crack initiation and crack propagation energies. The latter is approximated as the energy absorbed in the complete fracture of a specimen fatigue-precracked to half width (USE_p). The macro-crack initiation energy (ΔUSE) is approximated as the difference between the energy absorbed by a notched specimen USE and USE_p. The normalization factors for ΔUSE and USE_p were $(Bb^2)/(S^*K_t')$ and (Bb^2), respectively. The sums of the normalized values of ΔUSE and USE_p were found to be equal for full size and subsize specimens.

All of the size effects studies so far [1-18] have involved the use of specimens such that more than one variable (e.g. span, width, thickness, or notch geometry) changes from the full size to subsize specimens. Therefore, it is not possible to determine the dependence of USE on any of the geometry variables in an unambiguous manner.

The work presented in this paper was undertaken to elucidate the dependence of the upper shelf energy of precracked specimens (USE_p) on single variables such as ligament size, width, thickness, and span. Precracked specimens were chosen since the absence of the notch eliminates the dependence of USE on K_t, the stress concentration factor, which, by itself, is a complicated function of the specimen dimensions and the notch geometry. Dynamic finite element modeling (FEM) using the computer code ABAQUS Explicit of the fracture of full (1.000 x 1.000 x 5.400 cm), half (0.500 x 0.500 x 2.360 cm), medium (0.400 x 0.400 x 2.360 cm) and third size (0.333 x 0.333 x 2.360 cm) specimens was performed. The USE_p determined by FEM was compared with the experimental data. For the full size Charpy specimen, the span was 4.600 cm. For all subsize specimens, the span was 2.000 cm. In addition, one set of half size specimens (0.500 x 0.500 cm) with full length of 5.400 cm and full span of 4.600 cm was also examined. For all five specimen geometries, four different precrack depths, i.e., 30%, 40%, 50%, and 60% of the full width (W) of the corresponding specimen, were modeled. The experimental data for comparison were available for precrack depths that were 42%, 52% and 68% of W. A comparison was made between the experimental values and the best fit of the FEM data. A reasonable agreement was achieved in most cases. Having achieved the required confidence in the FEM analysis, a systematic study was performed to examine the dependence of USE_p on width (W), thickness (B), and span (S).

Experimental Procedure

The specimens used to obtain the experimental data were machined from A533B Plate 02 material. The material was obtained from Dr. R. K. Nanstad of Oak Ridge National Laboratory. The fatigue precracking and Charpy impact testing of the specimens were performed according to the procedures published earlier by Kumar et al. [15].

Model Development

All modeling of the Charpy specimens and impact testing was conducted using a dynamic explicit-integration finite element code, ABAQUS Explicit, from the HKS corporation [20]. Two HP 9000-715/75 workstations were used to run the code. Depending on specimen geometry and mesh refinement, a typical simulation of the Charpy impact test could take from 3 to 40 hours of CPU time.

Explicit dynamic analysis using ABAQUS

ABAQUS Explicit uses a dynamic analysis procedure which implements an explicit integration rule with the use of diagonal mass matrices [20]. The equations of motion are integrated using the explicit central difference integration rule:

$$\dot{J}^{i+\frac{1}{2}} = \dot{J}^{i-\frac{1}{2}} + \frac{\Delta t^{i+1} + \Delta t^{i}}{2} \ddot{J}i$$

$$J^{i+1} = J^{i} + \Delta t^{i+1} \dot{J}^{i+\frac{1}{2}}$$

The superscript (i) refers to the increment number. The central difference integration is explicit in that the kinematic state may be advanced using known values of $\dot{J}^{i-1/2}$ and $\ddot{J}^{i}$ from the previous increment. In order to increase computational efficiency, ABAQUS uses diagonal element mass matrices. The accelerations at the beginning of the increment may be computed by:

$$\ddot{J} = M^{-1} x \ (F^{i} - I^{i})$$

Where M is the diagonal lumped mass matrix, F is the applied load vector, and I is the internal force vector. The code integrates through time using many small stable time increments. The time incrementation scheme in ABAQUS is fully automatic and requires no user intervention. The use of small increments (directed by the stability limit) is advantageous in that it allows the solution to proceed without iterations and without requiring tangent stiffness matrices. The explicit procedure is ideally suited for analyzing high speed dynamic events like those found in Charpy impact testing.

Assuming that the stable time increment does not change drastically during the analysis, the cost in CPU time for an explicit dynamic analysis is related to the size of the mesh in the following manner:

$$Cost \propto N\frac{T}{\Delta t}$$

where N is the total number of elements in the mesh, T is the duration of the event, and t is the stable time increment size. The stable time increment decreases exponentially with decreasing element size. Therefore, the total CPU cost usually increases linearly with the number of elements in the model, and exponentially with the refinement of the mesh.

ABAQUS failure model

ABAQUS Explicit contains an elastic-plastic material model which allows the modeling of crack growth by deleting elements from the mesh. ABAQUS treats crack initiation and growth by calculating a space-averaged strain and then deleting elements in the mesh when any element reaches an input-defined plastic failure strain (ε_f^{pl}). In order for this deletion of elements to produce stable results, the stress state of the damaged element must be reduced to zero by the time of failure. ABAQUS accomplishes this by applying a damage level to the material prior to failure. This damage parameter is used to degrade the stress state as well as the elastic moduli. The damage value of any element is zero until the strain in the element exceeds a user-defined offset failure strain (ε_0^{pl}). The damage in an element can range from zero (no damage) to one (failed) and is calculated from the equivalent plastic strain as follows:

$$DAMAGE = D = \frac{\varepsilon^{pl} - \varepsilon_0^{pl}}{\varepsilon_f^{pl} - \varepsilon_0^{pl}}$$

At each increment, the equivalent plastic strain (ε^{pl}) is obtained and damage is assessed using the above equation. Damage may not be removed from an element, and when the damage reaches a value of one, the element is deleted from the mesh and a crack is formed or extended.

User-defined material model

When modeling Charpy impact tests using the ABAQUS material failure model, a fundamental problem with the crack propagation is observed [21]. ABAQUS only determines the magnitude of plastic strain in an element relative to the failure criterion. This allows cracks to initiate and propagate under tensile or compressive constraints with identical failure criterion. In order to correct this problem, a user-defined Fortran subroutine is used to model the material constituent equations and hence model failure. This routine is called by ABAQUS instead of the normal material model. The routine uses the same mechanism for modeling crack initiation and propagation as the ABAQUS model with the exception of when the damage factor is incremented. A deviatoric stress given by

$$\sigma_{mean} = \frac{1}{3}(\sigma_{11} + \sigma_{22} + \sigma_{33})$$

is used to determine if an element is under tensile or compressive loading. If the value of σ_{mean} is positive then damage is allowed to increase in that increment. If σ_{mean} is negative or zero then no further damage can result. This user defined material failure model accurately models the fracture of a Charpy specimen under impact. The model has been tested and benchmarked against the ABAQUS Von Mises plasticity material model [21].

Benchmarking

In order to obtain confidence in both the elastic response of the user defined material failure model and the ABAQUS finite element model which included initial and boundary conditions, a simple, low-velocity bar impact was modeled. Because an analytical solution for the maximum deflection in a simple bar is easily obtained, comparison of analytical and ABAQUS results would allow benchmarking of the model.

The analytical solution for a full size unnotched specimen under 3-point elastic impact loading was developed using a conservation of energy approach. If gravitational forces on the striker and bar are neglected, the kinetic energy of the striker prior to impact can be related to the strain energy stored in the elastically bent specimen. The maximum center load-line displacement (CLLD) of the bar can be given as a function of striker velocity. From small-displacement elastic theory, the displacement as a function of static load is given by:

$$\Delta = \frac{PL^3}{48EI}$$

where E is Young's modulus of the material and I is the moment of inertia of the specimen. The energy balance equation is written as:

$$U_k = U_e$$

$$\frac{1}{2}mv^2 = \frac{1}{2}P\Delta_{max}$$

The above two equations are combined to give the maximum CLLD as a function of striker velocity,

$$\Delta_{max} = \sqrt{\frac{mv^2L^3}{48EI}}$$

The maximum displacement is linear with respect to striker velocity. The only assumptions used are that inertial effects in the bar are neglected, the striker is modeled as a rigid body, and the striker remains in contact with the specimen until maximum deflection is reached.

To simulate the elastic impact of a full size specimen, the striker was given a mass of 1 kg. The impact velocity of a rigid striker was varied from 10 cm/s to 150 cm/s and modeled using ABAQUS. A comparison of the results of maximum CLLD vs. striker impact velocity with the analytical elastic solution is given in Fig. 1. When the impact velocity reaches around 70 cm/s, the maximum stress in the bar at maximum CLLD exceeds the yield limit, thus moving into the plastic deformation regime. Before reaching this point, ABAQUS results agree with the elastic solution. As would be expected, the ABAQUS results diverge from the elastic solution as the impact velocity is increased beyond 70 cm/s.

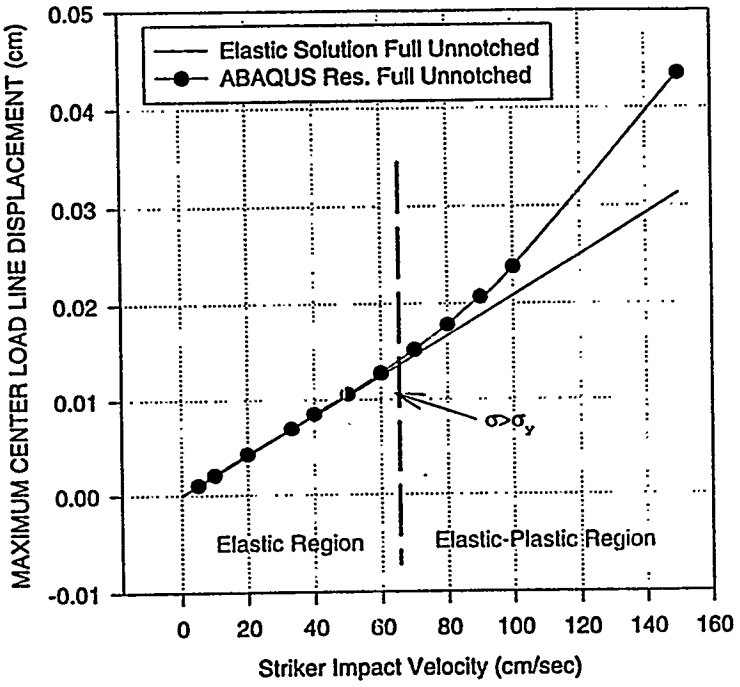

Fig. 1. Analytical Max. Load-Line Displacement Under Impact vs. ABAQUS Results

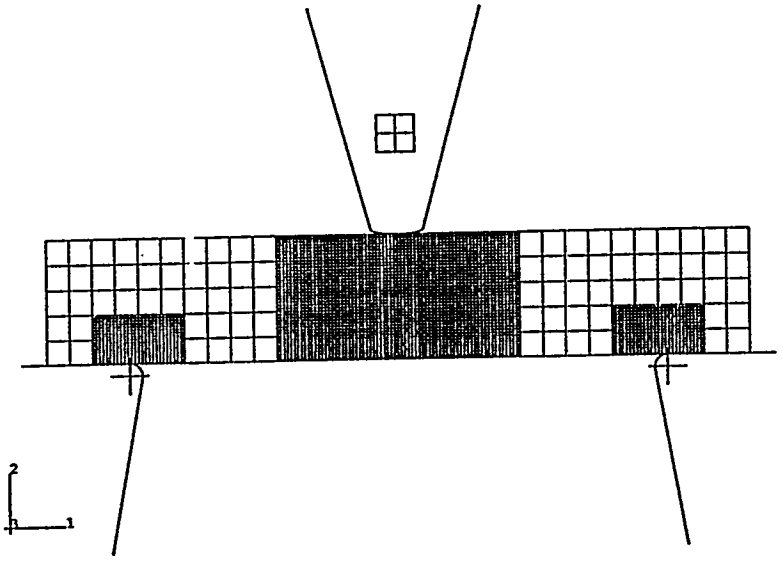

Fig. 2. 2D Finite Element Mesh

Charpy impact modeling

A dynamic finite element model of the Charpy impact test was run in which fracture initiation and propagation to complete failure were considered. Both 2D half-symmetry and 3D quarter-symmetry models of the striker, precracked Charpy specimens, and anvil were constructed using the codes IDEAS-SDRC and ABAQUS. Models for full (1.000 x 1.000 x 5.400 cm), half (0.500 x 0.500 x 2.360 cm), half-2xL (0.500 x 0.500 x 5.400 cm), medium (0.400 x 0.400 x 2.360 cm), and third (0.333 x 0.333 x 2.360 cm) size specimens have been made for several USE materials. A study of finite element mesh schemes and coarseness was used to develop a stable and reliable model of the Charpy impact test [21]. The striker and anvils were modeled using rigid bodies. An illustration of the mesh for a full size specimen is given in Fig. 2. An area (or volume for 3D) around the crack plane has been refined as well as an area around the anvils. In order to save computing cost, the elements in the extremities of the specimen were left relatively coarse. The effect on USE of not refining the entire specimen is negligible. It was found that if the Charpy impact was modeled using conventional impact energies (around 200 J), the computational time was excessive. In order to speed up the simulation and therefore save CPU time, a high energy impact on the order of 80,000 J was used. Fig. 3 illustrates the effect of increasing the impact energy on the USE of a third size, medium USE specimen. It can be seen that with a difference of only 8.5% in USE, a savings of 69 hours of CPU time on an HP9000-715/75 can be made.

The material properties for A533B Plate 02 were obtained from the EPRI report (NP-933) Nuclear Pressure Vessel Steel Data Base [22]. Ramberg-Osgood constants for a true stress-strain curve were obtained from Haggag [23]. An initial bilinear stress-strain relation for A533B with a failure strain of around 30% was made. This 30% failure strain was chosen with the knowledge that the local failure strain would be higher than the EPRI 2 in. gauge length failure strain (~24%). The offset failure strain was then chosen at 10% less than the failure strain. It was found that the model becomes unstable if the difference between offset and failure strain is less than 5%. The USE of a full size specimen (precracked to 40% width) calculated by ABAQUS was compared to the corresponding experimental value of 35.5 J. The failure and offset strains were then shifted to calibrate the ABAQUS model with experimental data. It was found that the failure strain needed to be increased to 50%. This calibrated medium-USE material stress-strain curve is shown in Fig. 4.

Results and discussion

Fig. 5 shows the upper shelf energy (USE_p) of full size precracked Charpy specimens as a function of ligament size. The ABAQUS FEM material stress-strain curve was calibrated at a ligament size of 0.4 cm. The USE_p for three more ligament sizes (0.5, 0.6 and 0.7 cm) was then calculated using ABAQUS. A curve of the form $USE_p = mb^n$ was fit through the four data points, where m and n are fitting parameters and b is the ligament size. The values of m and n were 202.0 and 1.90 for the best fit, with a correlation factor of 0.9992. It is worth noting that the value of n is quite close to 2. Fig. 5 also shows the experimentally obtained USE_p measurements for full size specimens with ligament sizes equal to 0.40, 0.48, and 0.64 cm. The scatter in the experimental data around the mean value is shown by a vertical band. The experimental data are in excellent agreement with the best fit curve.

Fig. 6 shows the calculated and experimental data for USE_p of half size specimens (0.500 x 0.500 x 2.360 cm). The best fit curve through the calculated data for USE_p of specimens with ligament sizes of 0.21, 0.26, 0.30, and 0.34 cm is represented by the equation $USE_p = 57.0b^{1.55}$. The first two experimental data points (b = 0.21 and 0.26 cm) are in reasonable agreement but the third is substantially far away from the curve. Additional experiments and ABAQUS calculations are in progress to ascertain the reasons for this discrepancy. The discrepancy is particularly puzzling since

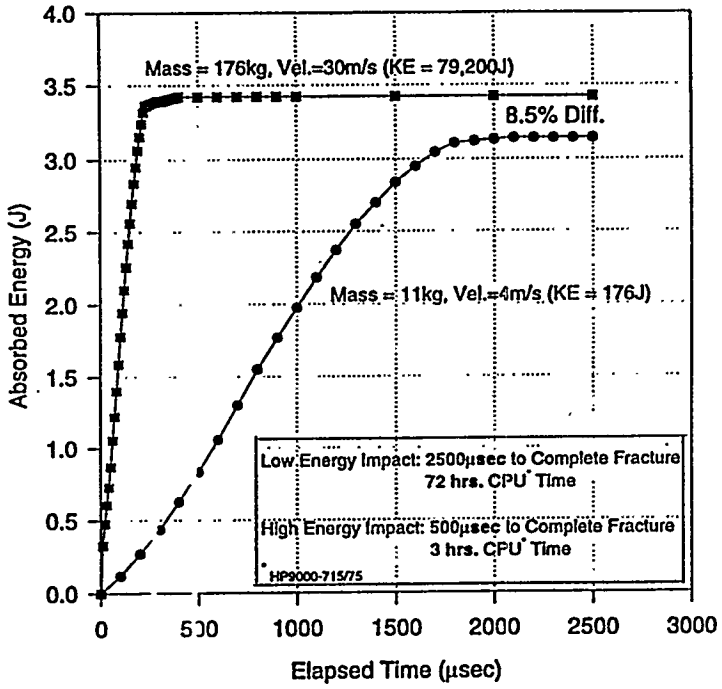

Fig. 3. Comparison of Low and High Energy Impact for 3D Third Size Medium USE Specimen (Precracked 50% W)

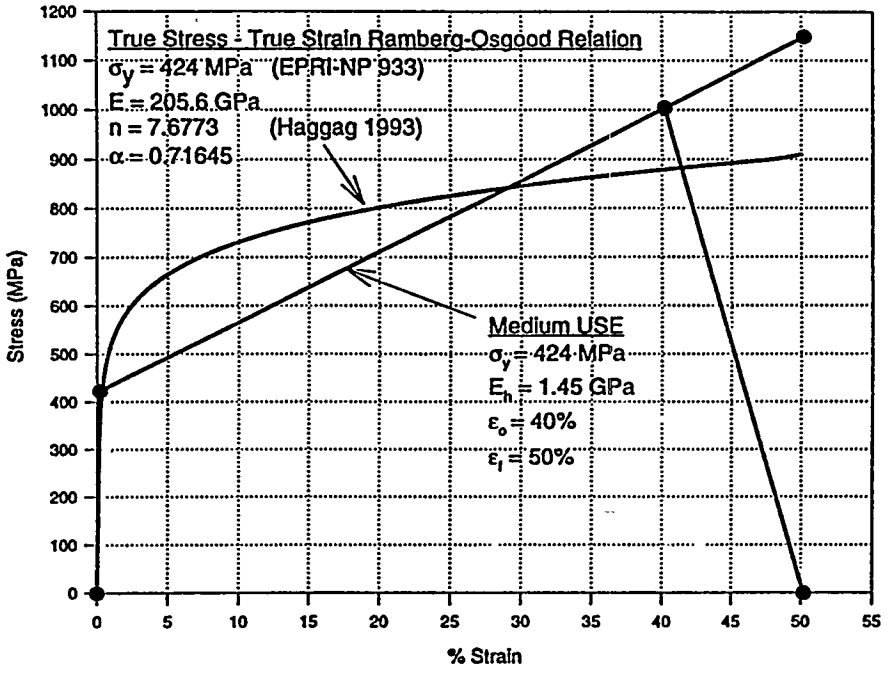

Fig. 4. Stress-Strain Curve of Medium USE for A533B Plate 02 Steel Used in ABAQUS

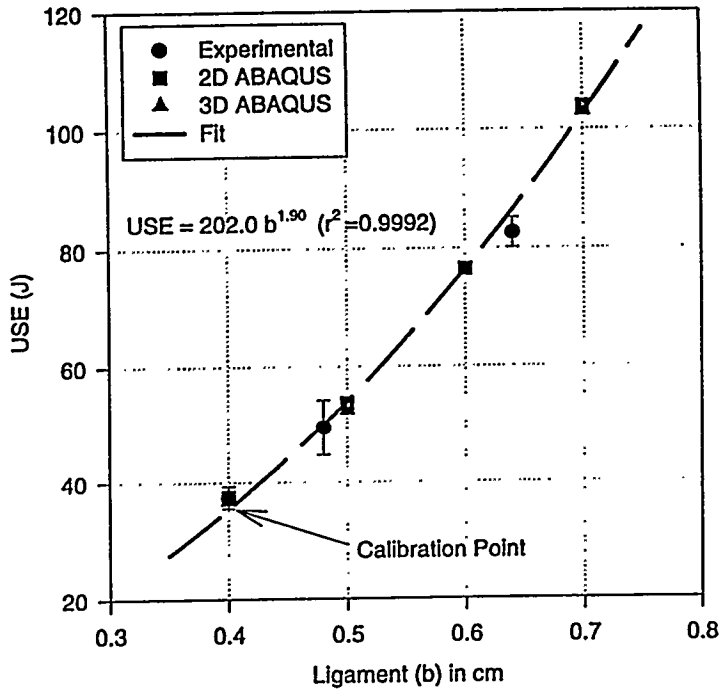

Fig. 5. USE vs. Ligament Size (b) for Full Size Medium USE Material

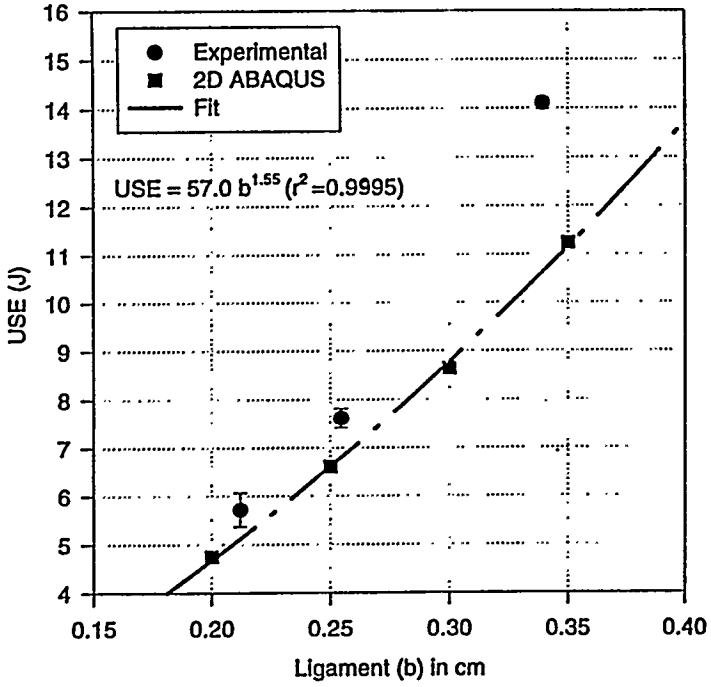

Fig. 6. USE vs. Ligament Size (b) for Half Size Medium USE Material

the ABAQUS calculations and experimental data are in excellent agreement for half size-2xL specimens (0.500 x 0.500 x 5.400 cm).

Fig. 7 shows the experimental and ABAQUS-calculated data for the half size full-length specimens. The calculated data can be best fit by the expression $USE_p = 59.5\ b^{1.53}$. Fig. 8 shows the USE_p data for medium size specimens (0.400 x 0.400 x 2.360 cm). Both calculated and experimental data are shown. The calculated data can be best fit by the expression $USE_p = 45.8b^{1.56}$. The experimental data are in reasonable agreement. However, the difference between experimental and calculated data appears to increase with decreasing ligament size. The dependence of the USE_p on ligament size has decreased to approximately the 3/2 power for the subsize specimens (0.500 x 0.500 cm and 0.400 x 0.400 cm) from the roughly square dependence for full size specimens. Fig. 9 shows the dependence of the USE_p of third size (0.333 x 0.333 x 2.360 cm) specimens on ligament size. The computed values can be best fit by the expression $USE_p = 44.8\ b^{1.66}$. The ligament size dependence of USE_p of third size specimens increased slightly from that of the half size specimens. The experimental values are consistently lower than the calculated data by about 5%.

From the foregoing analysis, it is quite clear that the ligament size dependence of full size and subsize specimens is not the same. There is a general tendency for the dependence to increase from an approximate value of 3/2 for subsize to about 2 for the full size specimens.

Having achieved good agreement between ABAQUS data and the experimental values, parametric studies were conducted to examine the width, span, and thickness dependence of USE_p using ABAQUS. The width (W) dependence of USE_p for full size specimens (50% precracked, b = 0.5 cm) is shown in Fig. 10. USE_p is proportional to $W^{2.51}$ for the ABAQUS calculated data.

The span dependence of the USE_p of full size specimens as shown in Fig. 11 is quite nonlinear. For specimens with spans ranging from 100% to 250% of standard full size specimens, the USE_p is almost independent of specimen size. However, USE_p rises steeply as the span decreases below 100% of the full size span. Under these conditions, it is difficult to assign a span dependence for USE_p.

The thickness (B) dependence of the full size USE_p has been found to be quite linear as shown in Fig. 12. In this figure, the thickness was allowed to vary between 30 and 120% of 1.0 cm (the full size standard thickness). This linear dependence is the reason why 2D and 3D calculations give results that are very close to each other, as shown in Fig. 5. A slight nonlinearity is seen, however, at lower values of thickness (~30%).

CONCLUSIONS

The following conclusions were made regarding the impact energy of medium ductility materials (notched USE ~ 150 J):

(1) Dynamic finite element modeling by ABAQUS can be performed to predict the USE_p of full size precracked specimens based on subsize data. The required inputs are the stress-strain curve and the fracture strain of the material. Subsize data will serve as the calibration point.

(2) Finite element modeling calculations of the USE_p were found to be in reasonable agreement with experimental data for full (1.000 x 1.000 x 5.400 cm), half (0.500 x 0.500 x 2.360 cm), half-2xL (0.500 x 0.500 x 5.400 cm), medium (0.400 x 0.4 00 x 2.360 cm) and third size (0.333 x 0.333 x 2.360 cm) specimens. The specimens were fatigue precracked so that ligament sizes (b) ranged from

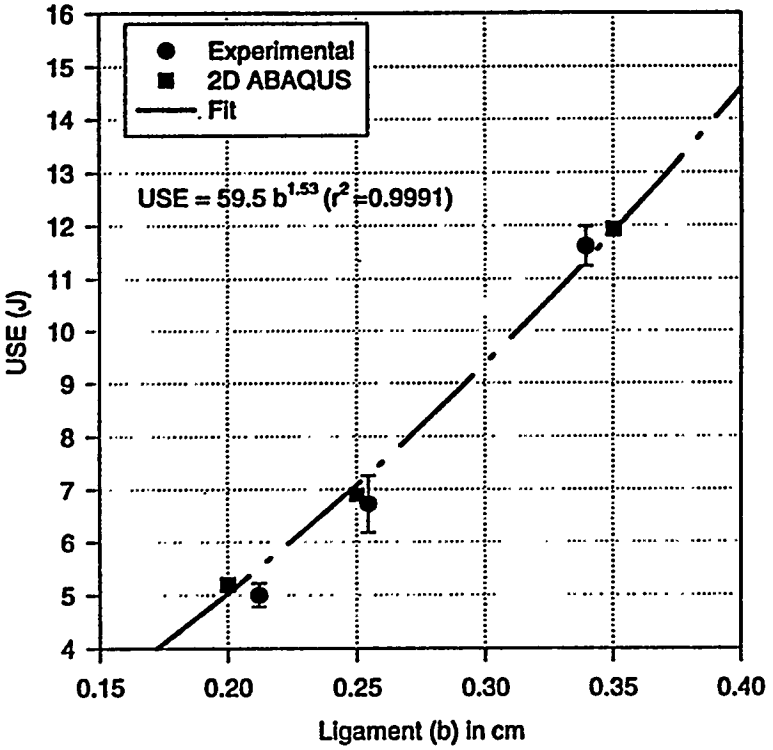

Fig. 7. USE vs. Ligament Size (b) for 2xL Half Size Medium USE Material

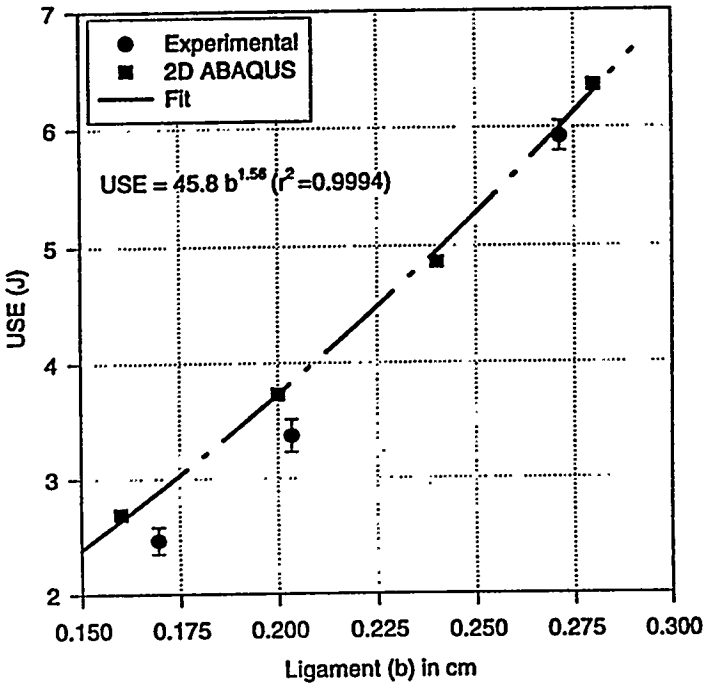

Fig. 8. USE vs. Ligament Size (b) for Medium Size Specimen Medium USE Material

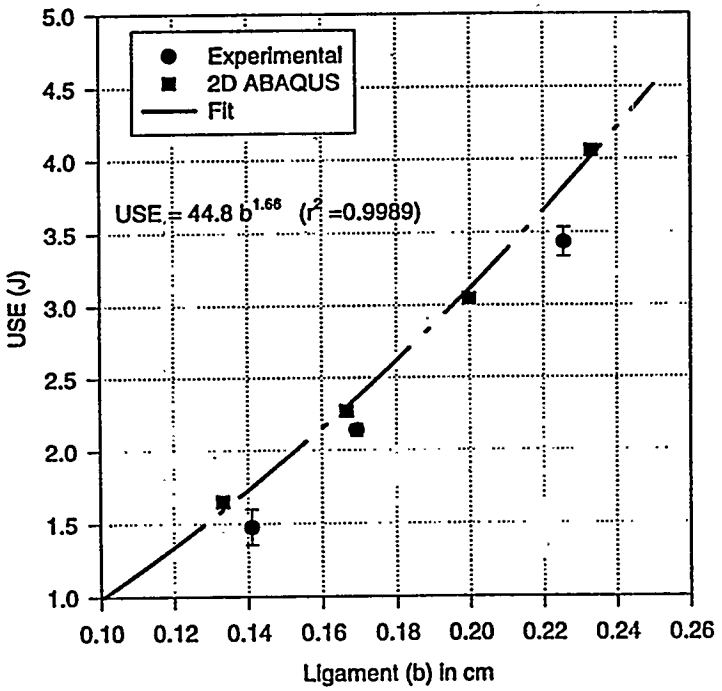

Fig. 9. USE vs. Ligament Size (b) for Third Size Medium USE Material

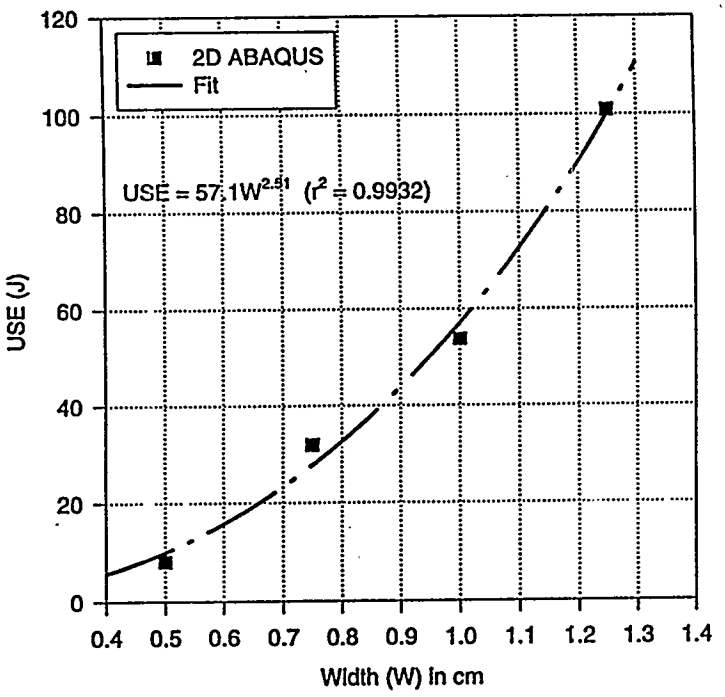

Fig. 10. USE vs. Width (W) for Full Size Medium USE Material 50% W Precracked

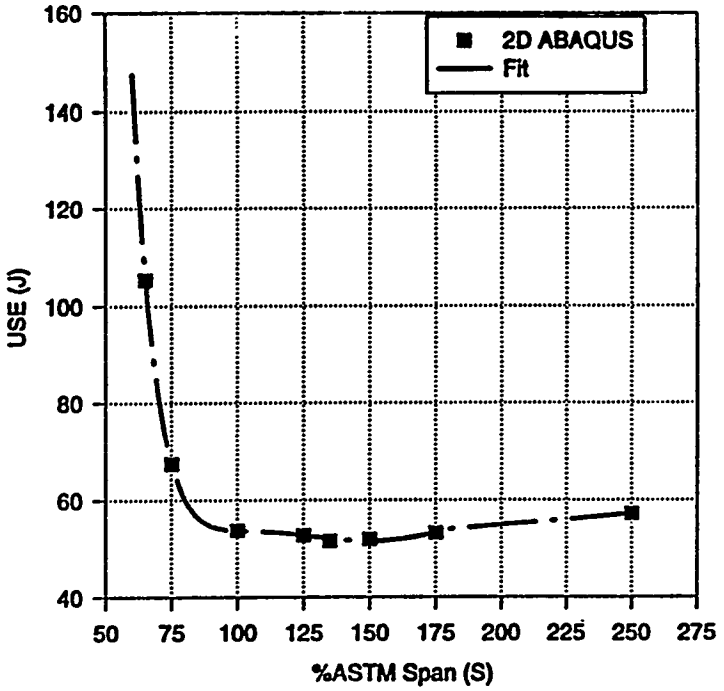

Fig. 11. USE vs. %ASTM Span (S) for Full Size Medium USE 50% W Precrack

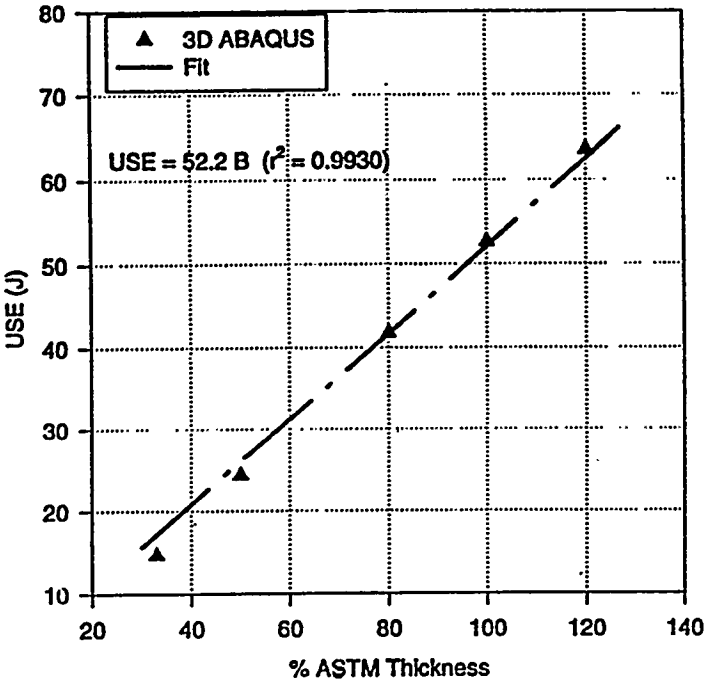

Fig. 12. USE vs. Thickness (B) for 3D Full Size Medium USE Material (Precracked 50% W)

40 to 70% of the width. The b dependence varied from about 3/2 for subsize specimens to 2 for full size specimens.

(3) USE_p for full size specimens varied with $W^{2.51}$ and varied linearly with thickness (B). USE_p increased steeply with decreasing span for spans less than 4.000 cm. Little span dependence was observed for spans larger than 4.000 cm.

Acknowledgment

This work was supported by the United States Department of Energy under contract DE-AC04-94AL85000 and also DE-AC06-76RLO 1830.

References

[1] W.R. Corwin, R.L. Klueh, and J.M. Vitek, J. Nucl. Mater.,Vols. 122 & 123, (1984), p. 343.

[2] W. R. Corwin and A. M. Hougland, The Use Small Scale Specimens for Testing Irradiated Material, ASTM STP 888, W. R. Corwin and G. E. Lucas, Eds., American Society of Testing and Materials, Philadelphia, 1986, p. 325.

[3] B. L. Ferguson, American Society for Metals. (ASM) Proceedings of American Institute of Mining, Metallurgical, and Petroleum Engineers, (AIME) Annual Meeting on "What Does the Charpy Test Really Tell Us?," Denver, CO, Feb. 1978, A.R. Rosenfield, et al., Eds., pp. 90-107.

[4] F. Abe, T. Noda, H. Araki, M. Okada, M. Narai, and H. Kayano, Journal of Nuclear Materials, Vol. 150, 1987, pp. 292-301.

[5] G. E. Lucas, G. R. Odette, J. W. Sheckherd, P. McConnell, and J. Perrin, The Use of Small-Scale Specimens for Testing Irradiated Material, ASTM STP 888, W. R. Corwin and G. E. Lucas, Eds., American Society for Testing and Materials for Testing and Materials, Philadelphia, 1986, p. 305.

[6] G. E. Lucas, G. R. Odette, J. W. Sheckherd, and M. R. Krishnadev, Fusion Technology, Vol. 10, 1986, p. 728.

[7] B. S. Louden, A.S. Kumar, F.A. Garner, M.L. Hamilton, and W. L. Hu, J. Nucl. Mater., Vols. 155 to 157, 1988, pp. 662-667.

[8] A. S. Kumar, F. A. Garner, and M. L. Hamilton, Effects of Radiation on Materials: 14th International Symposium (Volume II), ASTM STP 1046, N. H. Packan, R. E. Stoller, and A. S. Kumar, Eds., American Society for Testing and Materials, Philadelphia, 1990, pp. 487-495.

[9] S. T. Rosinski, A. S. Kumar, N. S. Cannon, and M. L. Hamilton, ASTM STP 1204, W. R. Corwin, W. L. Server, and F. M. Haggag, Eds., American Society for Testing and Materials, Philadelphia, 1993, pp. 405-416.

[10] A. S. Kumar, Cannon N. S., S. T. Rosinski, M. L. Hamilton, Effect of Radiation on Materials: 16th International Symposium, ASTM STP 1175, Arvind S. Kumar, David S.

Gelles, Randy K. Nanstad, and Edward A. Little, Editors, American Society for Testing and Materials, Philadelphia, 1993, pp. 147-155.

[11] H. Kayano, H. Kurishita, M. Narui, M. Yamazaki, Y. Suzuki, Journal of Nuclear Materials, Vols. 179-181, 1991, pp. 425-428.

[12] D.J. Alexander, and R.L. Klueh, "Specimen Size Effects in Charpy Impact Testing," ASTM STP 1072, John M. Holt, Ed., American Society for Testing & Materials, Philadelphia, 1990, p. 179.

[13] A.D. Amayev, V.I. Badanin, A.M. Kryukov, V.A. Nikolayev, M.F. Rogov, A. Sokolov, ASTM STP 1204, W. R. Corwin, W. L. Server, and F. M. Haggag, Eds., American Society for Testing and Materials, Philadelphia, 1993, pp. 424-439.

[14] H. Kurishita, H. Kayano, M. Narui, M. Yamazaki, Y. Kano, I. Shibahara, Materials Transactions, Vol. 34, 1993, pp. 1042-1052.

[15] A. S. Kumar, L.E. Schubert, M. L. Hamilton and N.S. Cannon, J. Nucl. Mater., Vols. 225 (1995)238.

[16] L.E. Schubert, A. S. Kumar, S.T. Rosinski and M. L. Hamilton, J. Nucl. Mater., Vols. 225 (1995)231.

[17] H. Kurishita, H. Kayano, M. Narui, M. Yamazaki, Journal of Nuclear Materials, Vols. 212-215 (1994) 1682-1687.

[18] H. Kurishita, H. Kayano, M. Narui, M. Yamazaki, Y. Kano, and I. Shibahara, Materials Transactions, JIM, Vol. 34, No. 11 (1993) 1042-1052.

[19] A. S. Tetelman, Fracture of Structure Materials, John Wiley & Sons, Ed., 1967, P. 295.

[20] Hibbit, Karlsson, & Sorensen, Inc., ABAQUS Explicit Users Manual Ver. 5.4, HKS 1995.

[21] S. E. Sidener, Dynamic Finite Element Analysis of Charpy Impact Tests for use in Nuclear Power Plant Life Extension, M.S. Thesis, University of Missouri-Rolla, December 1995.

[22] Nuclear Pressure Vessel Steel Data Base, Electric Power Research Institute Report Number-NP-933, December 1978.

[23] F.M. Haggag, In-Situ Measurements of Mechanical Properties Using Novel Automated Ball Indentation System, Small Specimen Test Techniques Applied to Nuclear Reactor Vessel Thermal Annealing and Plant Life Extension, ASTM STP 1204, W.R. Corwin, F.M. Haggag, and W.L. Server, Eds., American Society for Testing and Materials, Philadelphia, 1993, pp. 27-44.

4.0 COPPER ALLOYS AND HIGH HEAT FLUX MATERIALS

Status of ITER Task T213 Collaborative Irradiation Screening Experiment on Cu/SS Joints in the Russian Federation SM-2 Reactor - D.J. Edwards (PNNL), S.A. Fabritsiev (D.V. Efremov Institute, St. Petersburg, Russia), A.S. Pokrovsky (SRIAR, Dimitrovgrad, Russia), S.J. Zinkle (ORNL), R.F. Mattas (ANL), R.D. Watson (SNL)

OBJECTIVE

This report summarizes the current status of specimen fabrication and details of the U.S. participation in the planned irradiation experiment in the R.F. SM-2 reactor.

SUMMARY

Specimen fabrication is underway for an irradiation screening experiment planned to start in January 1996 in the SM-2 reactor in Dimitrovgrad, Russia. The purpose of the experiment is to evaluate the effects of neutron irradiation at ITER-relevant temperatures on the bond integrity and performance of Cu/SS and Be/Cu joints, as well as to further investigate the base metal properties of irradiated copper alloys. Specimens from each of the four ITER parties (U.S., E.U., Japan, and R.F.) will be irradiated to a dose of ~0.2 dpa at two different temperatures, 150 and 300°C. The specimens will consist of Cu/SS and Be/Cu joints in several different geometries, as well as a large number of specimens from the base materials. Fracture toughness data on base metal and Cu/SS bonded specimens will be obtained from specimens supplied by the US. Due to a lack of material, the Be/Cu specimens supplied by the US will only be irradiated as TEM disks.

INTRODUCTION

ITER has begun to investigate the possible methods by which the first wall and divertor assemblies can be fabricated to produce a viable structure of Be/Cu/SS. This work is being conducted under ITER Tasks T212 and T221, and is concerned primarily with the fabrication of large full scale panels produced by a variety of methods, including hot isostatic pressing (HIP), explosion bonding, and brazing. All four of the ITER home teams are involved in the production of these panels and joints. In the United States the production, nondestructive evaluation (NDE), and evaluation of the properties of the bonded panels are being pursued through a collaboration between DOE national laboratories, industry, and universities.

The effects of neutron irradiation on Cu/SS and Be/Cu joints has never been investigated to the knowledge of the authors, which causes serious concern since the fabrication method chosen to produce the panels may be strongly influenced by how the bonds perform under irradiation during ITER operation. To address this concern ITER Task T213 has been given the responsibility of irradiating specimens from the panels and joints produced under Tasks T212 and T221.

A series of low dose (≤0.3 dpa) irradiation screening experiments are being planned through 1997 to help evaluate the effects of neutron irradiation on the properties of joints produced by the methods mentioned earlier. Later experiments will irradiate joints deemed to be acceptable by the earlier evaluations, and at doses up to 3-5 dpa to investigate the irradiation effects at dose levels representative of the ITER Basic Physics Phase.

The first experiment is scheduled to start in January 1996, and will include specimens from each of the four home teams. Details of the irradiation conditions, choice of materials, and specimen geometries are discussed in the following sections.

IRRADIATION CONDITIONS

Specimens of each type of joint and material will be irradiated to ~0.2 dpa in two separate capsules. The two capsules will be irradiated in succession in the Channel 5 position of the SM-2 reactor core. The fast neutron fluence in this position is 3 x 10^{21}n/cm^2 (E>0.1 MeV), with a corresponding thermal neutron fluence of 3 x 10^{21}n/cm^2 (E<0.67 eV). The first capsule will be irradiated at a temperature of 150°C ±10°C, the second capsule at 300°C ±10°C. The capsules will be irradiated in a closed water loop (Channel 5), where the temperature of the water is controlled by varying the water pressure and flow rate of the water through the loop. The specimens will be enclosed in He-filled stainless steel subcapsules to protect them from the reactor coolant water.

The temperature of the specimens will determined indirectly by measuring the water temperature at various positions within the water loop. The ratio of capsule temperature to coolant temperature has been calibrated in previous experiments, so that the water temperature and pressure inside the closed loop can be varied to maintain the desired specimen temperature. Heat transfer analysis codes will then be used to calculate the temperature of the specimens. Gamma heating in this channel position is relatively low (10 W/gm), so the heating will occur by thermal transfer from the coolant water. The temperature inside the capsule will be passively monitored using materials with different melting temperatures to establish the temperature limits of the irradiation experiment. No Cd-shielding will be used in this experiment as the low irradiation dose will yield low levels of the transmutants nickel and zinc. Fast and thermal neutron fluence monitors will be used in this experiment to measure the dose.

STATUS OF SPECIMEN FABRICATION IN U.S.

1. Materials

The first panels of Cu/SS produced by ITER Task T212 were GlidCop™ Al15 bonded to 316L by two methods - explosive bonding and hot isostatic pressing (HIP). Although CuAl25, which is produced by SCM Metal Products, is considered to be the prime ITER candidate copper alloy, at the time the panels were produced (Fall 1994) only two panels of stress-relieved CuAl15 were available from SCM Metal Products. The small size of the two CuAl15 panels (0.64 cm x 25.4 cm x 106.7 cm, 1.27 cm x 50.8 cm x 121.9 cm) resulted in only a small section of each subsequent Al15/316L panel (5.08 cm x 20.3 cm) being made available for this first irradiation experiment; the remainder was used to evaluate the two bonding techniques. The composition of the starting materials is provided in Table 1.

The Be/Cu joints were supplied by Dr. R. Watson from Sandia National Laboratories. Four types of joints were to be included in the irradiation experiment, however, some of the materials did not survive the electrical discharge machining (EDM) into test specimens. Joints of electroplated copper to beryllium and explosively bonded beryllium to copper withstood the EDM specimen machining, but Be/Cu joints formed by inertia welding or brazing broke apart during the machining. For the available Be/Cu joints only TEM disks were fabricated due to the small size of the joints.

Because of the lack of available bonded material, base metal specimens from CuAl25 in the cross rolled and annealed condition (CR & A) and in the as-HIPped condition were included in the matrix. The two separate CuAl25 conditions were made from the same starting powder, LOX-80. This powder has been boron deoxidized to remove any free Cu_2O, and the powder was screened to below 80 mesh to narrow the size range of the starting powders. The screening eliminated or reduced the

Table 1 Composition of Materials (wt%)

CuAl15	99.65 Cu	0.15 Al	0.01 Fe	0.01 Pb	0.13 O	~250 ppm B	--------	--------
CuAl25*	99.65 Cu	0.25 Al	0.01 Fe	0.01 Pb	0.22 O	~250 ppm B	--------	--------
CuNiBe	99.5 Cu	0.5 Be	1.8 Ni	0.2 Al	0.2 Si	--------	--------	--------
Be/Cu	50.0 Be	50.0 Cu	--------	--------	--------	--------	--------	--------
316L	68.0 bal Fe	2.0 Mn	1.0 Si	17 Cr	12 Ni	0.045 P	0.03 S	0.03 C

* LOX -80 CuAl25 powder, ITER Grade 0 (IG0)

number of large copper powder particles that tended to have large particles of α-Al_2O_3 (~1μm) attached to their surfaces, thereby achieving a more uniform distribution of the small Al_2O_3 particles responsible for the properties of this alloy.

The as-HIPped plate was consolidated at ~14:1 reduction ratio at 980°C. No further thermomechanical treatments were given to the plate, simulating the condition of CuAl25 powder HIPped directly to stainless steel, which is one processing route being considered for the ITER first wall.

The cross-rolled and annealed CuAl25 is the result of improved thermomechanical processing that, in conjunction with the LOX-80 starting powder, yields better elongation up to temperatures as high as 350°C [1]. The extruded plate is given an additional warm rolling treatment perpendicular to the original extrusion direction, yielding approximately 60% reduction. The plate is then annealed at 1000°C for 1 hour to stress relieve the plate, producing strength levels closer to that of the as-extruded plate. The final properties of the cross-rolled and annealed plate at room temperature are: σ_{UTS}= 421 MPa, σ_{YS}= 331 MPa, ε_{total}= 27%, and an electrical conductivity 86% IACS. The properties of the as-HIPped plate are almost identical at room temperature. This composition and powder processing has been unofficially designated as ITER Grade 0 (IG0) by SCM Metals.

Two large plates of Brush Wellman's CuNiBe Hycon 3HP™ were purchased, one plate in the HT condition (fully hardened temper, 69% IACS, hardness R_B= 92) and the second in the AT condition (solution annealed and aged, 65% IACS, R_B= 92). Additional mechanical tests are planned to better establish the starting mechanical properties of the CuNiBe alloys. A small amount of Hycon 3HP overaged to produce a higher conductivity/lower strength condition was also included in the irradiation matrix on a limited basis. The conductivity of this material was 74% IACS, with a σ_{YS}= 633 MPa. In addition to the copper alloys, a limited number of specimens of the 316L stainless steel used to make the Cu/SS panels were included in the matrix.

2. Specimen Geometry

At the time the specimen matrix was set up, no data were available from the evaluations on the Cu/SS panels being performed under Task T212. Consequently, the choice of specimen geometries was made based on the necessity of testing in hot cells and using geometries considered somewhat standard for testing materials. Unfortunately, the small size of the Cu/SS panels (5.08 cm x 20.3 cm) restricted the type of specimens that could be included in the irradiation experiment. It was decided to use miniature bend bars (Fig. 1) to evaluate the fracture behavior of the Cu/SS interface, lap shear specimens (Fig. 2) of different overlaps to measure the shear strength of the interface, and butt tensile specimens (Fig. 3) to provide additional data on the interface properties. The complete matrix of specimens for the Cu/SS, Be/Cu joints, and base materials is provided in Tables 2 & 3, respectively.

Note that in Figure 1 the bend bar configuration was varied to change the orientation of the interface with respect to the notch. The idea was to observe the behavior of the crack as it approached the interface, to see whether it deflected away from the interface into the base material, or propagated across or along the interface. TEM disks were also included in the irradiation experiment, and are illustrated in Figure 4 for the base materials, Cu/SS, and the Cu/Be joints.

The bend bars for the Cu/SS specimens are too small to allow significant precracks to be grown into the specimen. Therefore the specimens were precracked a total of 0.76 mm as measured from the outside edge of the specimen (notch + crack length = 0.76 mm). Details of the precracking will be presented in a later report.

Table 2 Bonded Cu/SS matrix for RBT-10 Task T213 irradiation experiment. Specimens listed are for one irradiation temperature only.

	TEM Disks	Butt Tensile	Lap Tensile W = 1.5 mm	Lap Tensile W = 2mm	3-Point Bend Bars Angle/Notch entry 0	3-Point Bend Bars Angle/Notch entry 45/Cu	3-Point Bend Bars Angle/Notch entry 45/SS
GlidCop Al15/316L Explosively Bonded	5	4	4	4	2	2	2
GlidCop Al15/316L HIP	5	4	4	4	2	2	2
Be/Cu Explosion Bonded	5	----------	----------	----------	--------	--------	--------
Be/Cu Electroplated Cu	5	----------	----------	----------	--------	--------	--------
Total	20	8	8	8	4	4	4

Table 3 Base materials matrix for RBT-10 Task T213 irradiation experiment. Specimens listed are for one irradiation temperature only.

	TEM disks	STS Tensile	LTS Fatigue	Disk Compact Tension	3 Point Bend Bars
GlidCop Al25 CR & Annealed	5	4	6	2	2
GlidCop As-HIPped	5	4	----------	2	2
CuNiBe HT (CW & aged)	5	4	----------	2	2
CuNiBe AT (SA & aged)	5	4	6	2	2
CuNiBe High Cond. (74%IACS)	5	4	----------	----------	----------
316SS	5	4	----------	----------	----------
Total	30	24	12	8	8

Data on the fracture toughness of irradiated GlidCop CuAl25 and CuNiBe are almost nonexistent, so two types of fracture toughness specimens were included in this experiment. The bend bars and disk compact tension (DCT) specimens (Figs. 5 & 6) are based on geometries and sizes used in other parts of the U.S.
fusion program [2-4]. The bend bars and DCT specimens will be precracked according to ASTM Standard E399-90.

The STS tensile and LTS fatigue specimens shown in Figs. 7 & 8, respectively, are Russian specimen geometries that have been used in previous irradiation experiments.

All specimens included in the irradiation experiment are being laser engraved.

FUTURE WORK

The control specimens need to be engraved, and afterwards a fraction of them will be shipped to Russia for testing. Both the unirradiated and irradiated tensile and fatigue specimens will tested in Russia. Fracture toughness testing on the unirradiated control specimens will begin shortly, as well as characterization of the various materials and joints. Post-irradiation testing will commence six weeks after the specimens are removed from reactor to allow sufficient cooling times. U.S. fracture toughness specimens will be shipped to the United States for testing in existing facilities.

ACKNOWLEDGEMENTS

One of the authors (DJ Edwards) would like to thank M.L. Hamilton, D.J. Alexander, G.E. Lucas, and J.F. Stubbins for their advice and help on putting this experiment together.

REFERENCES

1. R.R. Solomon, A.V. Nadkarni, and J.D. Troxell, to be published in the Journal of Nuclear Materials as part of the Proceedings of the 7th International Conference on Fusion Reactor Materials, held in Obninsk, Russia, Sept. 25-29, 1995.

2. H. Tsai, R.V. Strain, A.G. Hins, H.M. Chung, L.J. Nowicki, and D.L. Smith, *Fusion Materials Semiannual Progress Report*, DOE/ER-0313/17, April 1995, pp. 8-14.

3. H. Tsai, R.V. Strain, I. Gomes, A.G. Hins, and D.L. Smith, *Fusion Materials Semiannual Progress Report*, DOE/ER-0313/18, July 1995, pp 81-84.

4. H. Tsai, R.V. Strain, A.G. Hins, H.M. Chung, L.J. Nowicki, and D.L. Smith, *Fusion Materials Semiannual Progress Report*, DOE/ER-0313/18, July 1995, pp 85-88.

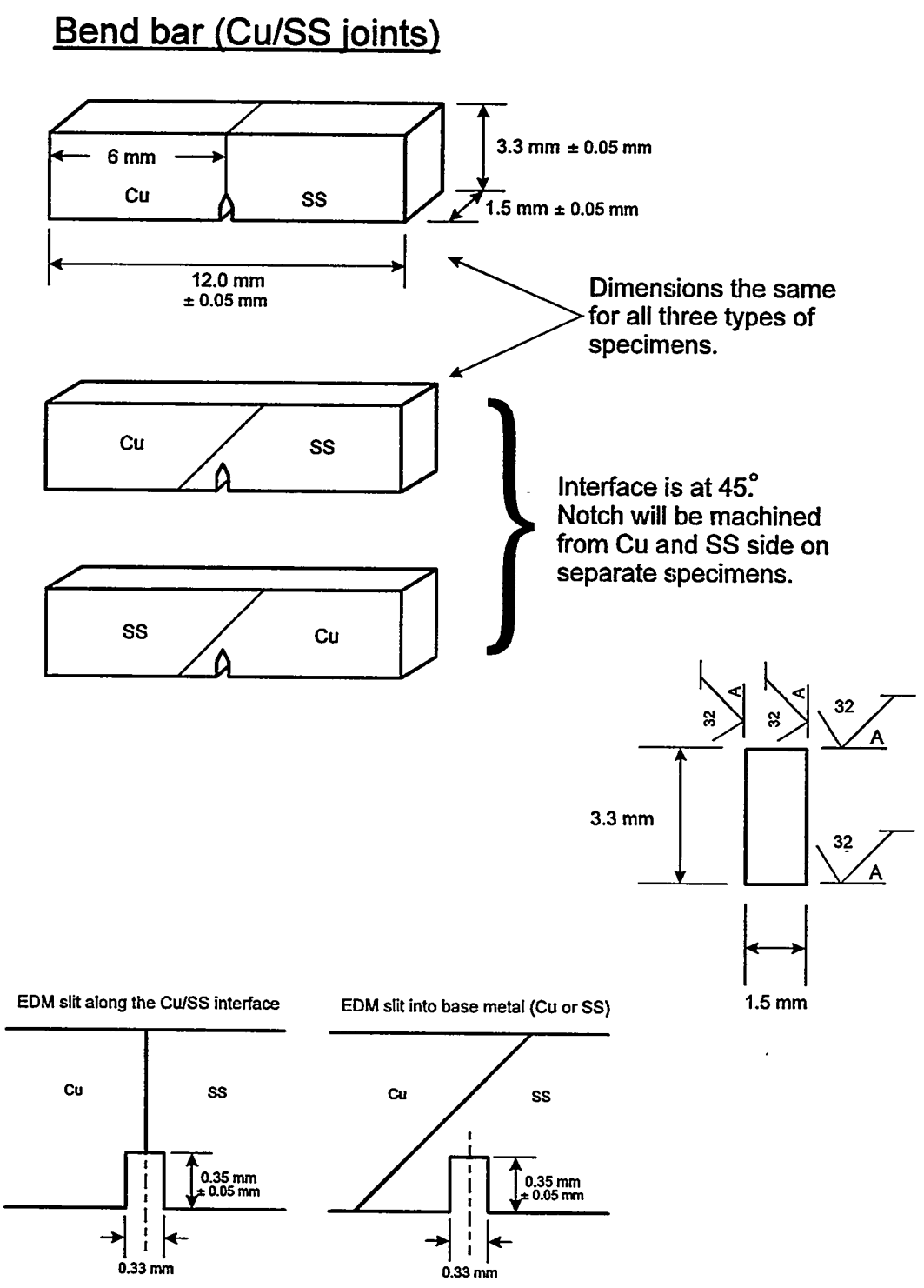

Figure 1 Bend bar configuration for the Cu/SS joints. Note the variation of the interface with respect to the notch.

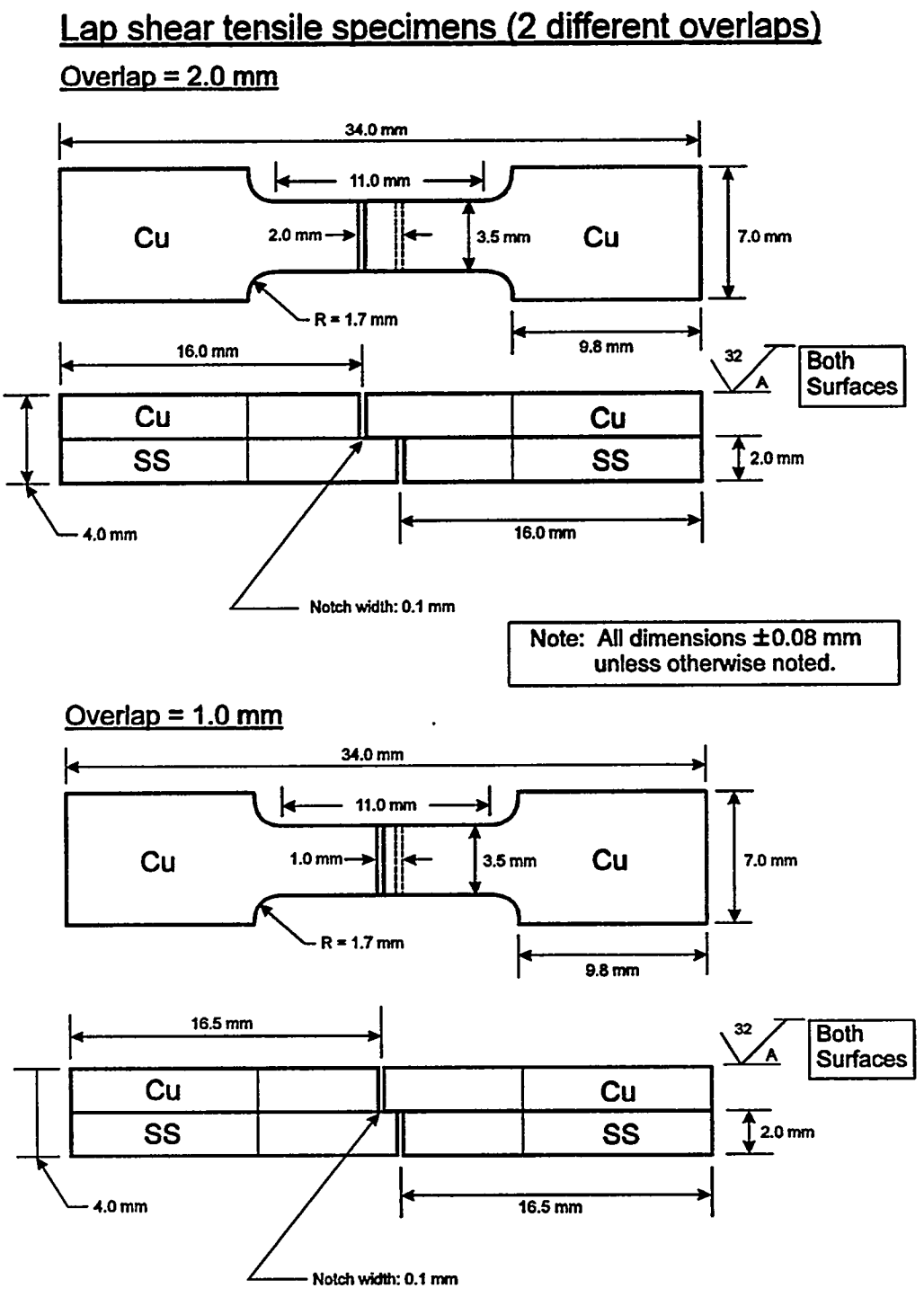

Figure 2 Lap shear geometry for testing the Cu/SS joints.

Tensile specimens for Cu/SS joints

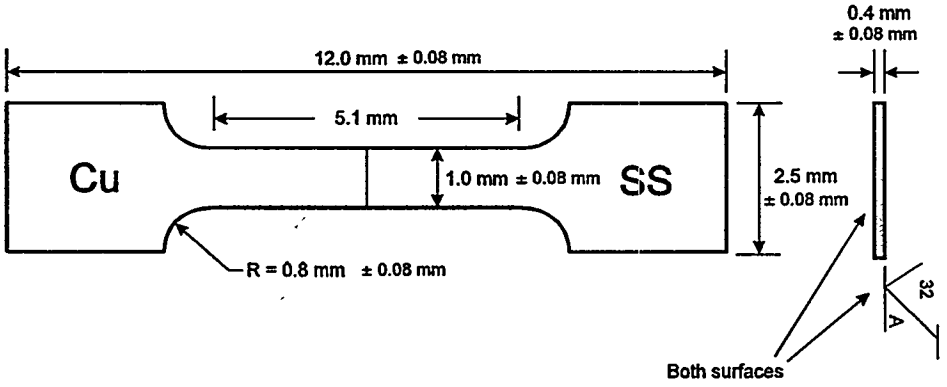

Figure 3 Butt tensile specimen geometry for the Cu/SS joints.

TEM Disks

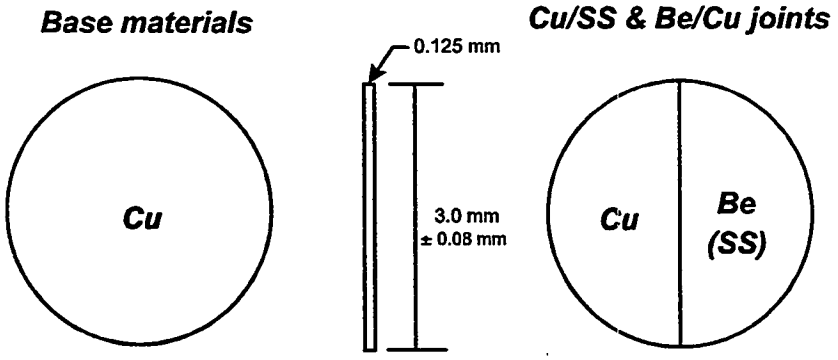

Figure 4 TEM disk geometry for the Cu/SS, Be/Cu, and base materials.

Bend bar (base material)

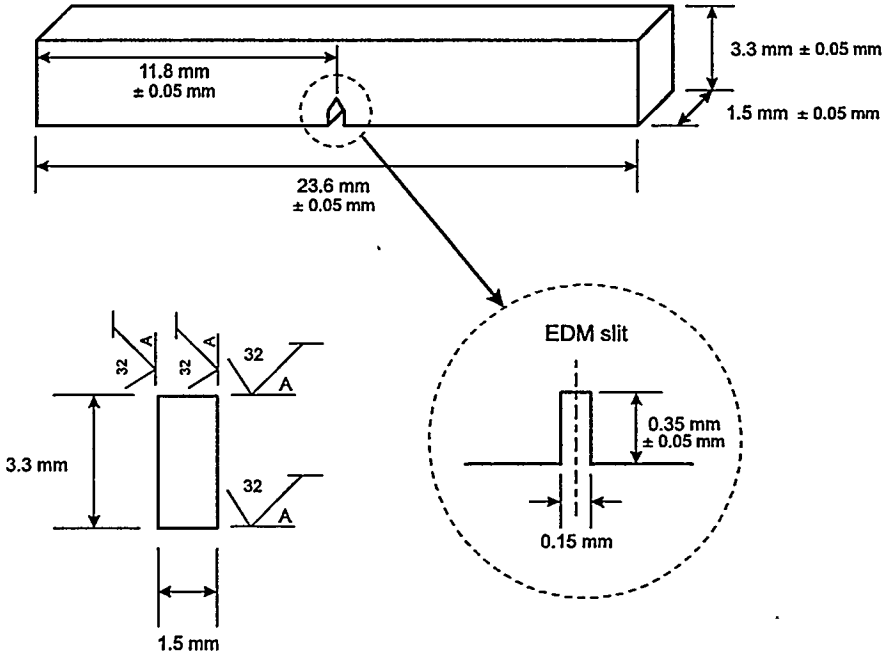

Figure 5 Bend bar for base materials. Based on ASTM standards, but scaled down proportionally in size for the irradiation experiment.

Disk compact tension specimens

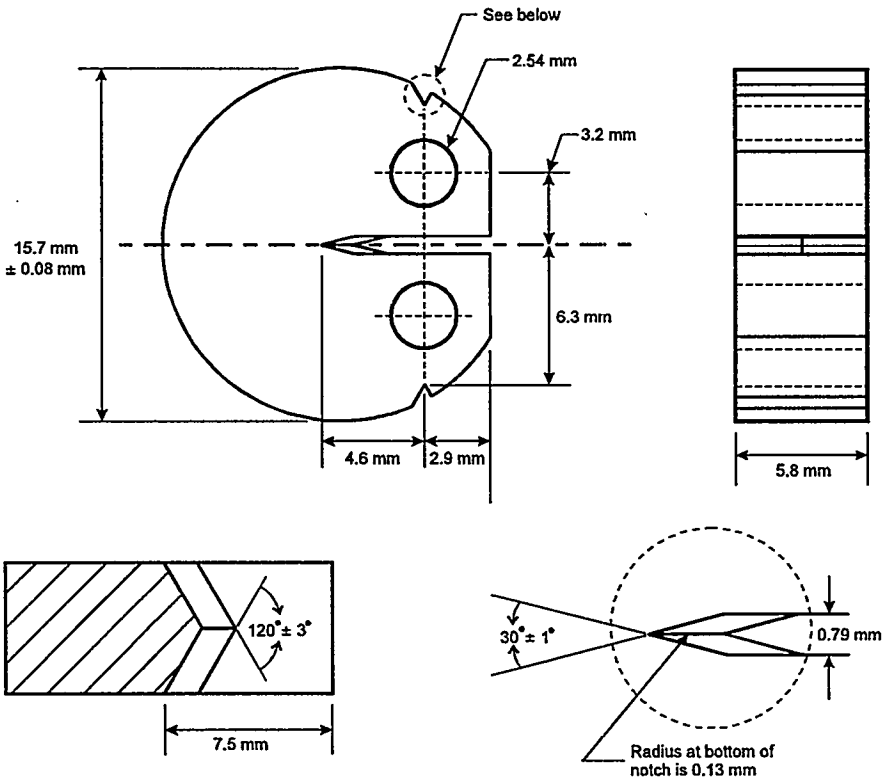

Notch for Clip Gage Attachment

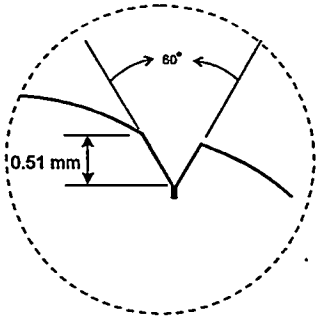

0.05 mm radius at bottom of notch

NOTES:

1. All dimensions in millimeters.
2. Tolerances are ±0.05 mm unless otherwise noted.
3. Clean machined specimens with acetone followed by alcohol in an ultrasonic bath.

Figure 6 Disk compact tension specimen geometry for the base materials.

STS specimen dimensions

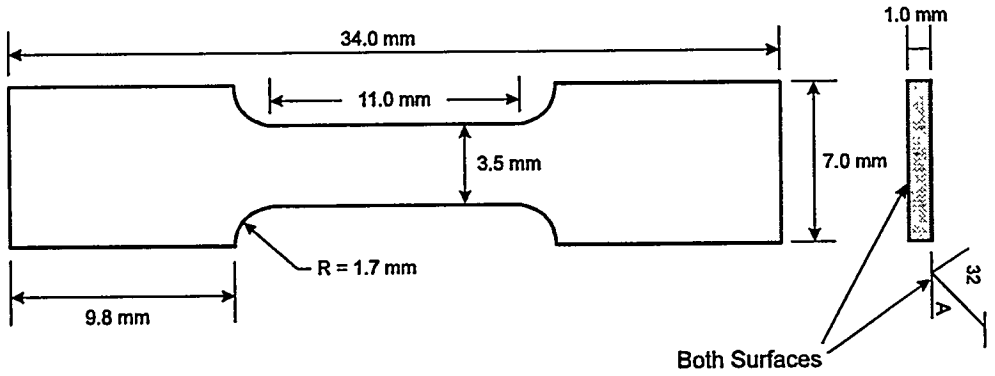

Figure 7 STS tensile specimen geometry for the base materials.

LTS fatigue specimen dimensions

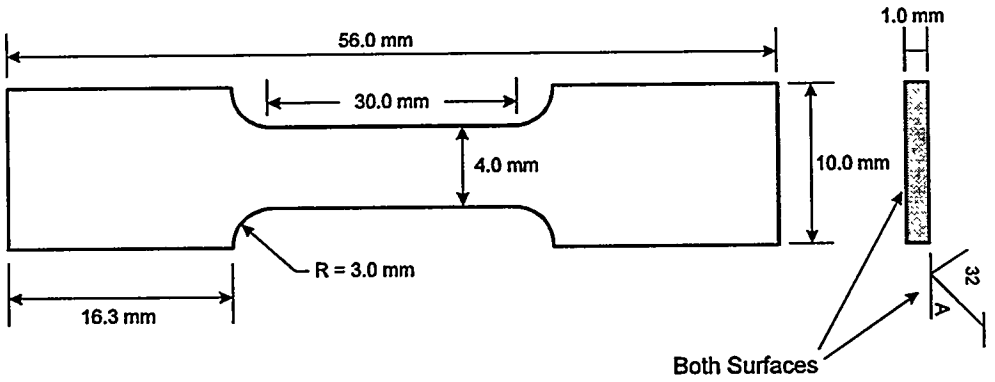

Figure 8 LTS bending fatigue specimen geometry for base materials.

TENSILE AND ELECTRICAL PROPERTIES OF COPPER ALLOYS IRRADIATED IN A FISSION REACTOR – S. A. Fabritsiev (D.V. Efremov Institute, St.Petersburg, Russia), A. S. Pokrovsky (Scientific Research Institute of Atomic Reactors, Dimitrovgrad, Russia), S. J. Zinkle and A. F. Rowcliffe (Oak Ridge National Laboratory), D. J. Edwards and F. A. Garner (Pacific Northwest National Laboratory), V. A. Sandakov (Scientific Research Institute of Atomic Reactors, Dimitrovgrad, Russia), B. N. Singh (Risø National Laboratory, Roskilde, Denmark) and V.R. Barabash. (ITER Joint Central Team, Garching, Germany)

OBJECTIVE

The objective of this report is to summarize the postirradiation tensile and electrical resistivity data on copper and copper alloys irradiated in the SM-2 reactor as part of a US-RF collaborative experiment. This study provides some of the data needed for the ITER research and development Task T213.

SUMMARY

Postirradiation electrical resistivity and tensile measurements have been completed on pure copper and copper alloy sheet tensile specimens irradiated in the SM-2 reactor to doses of ~0.5 to 5 dpa and temperatures between ~80 and 400°C. Considerable radiation hardening and accompanying embrittlement was observed in all of the specimens at irradiation temperatures below 200°C. The radiation-induced electrical conductivity degradation consisted of two main components: solid transmutation effects and radiation damage (defect cluster and particle dissolution) effects. The radiation damage component was nearly constant for the doses in this study, with a value of ~1.2 nΩ-m for pure copper and ~1.6 nΩ-m for dispersion strengthened copper irradiated at ~100°C. The solid transmutation component was proportional to the thermal neutron fluence, and became larger than the radiation damage component for fluences larger than ~5×10^{24} n/m^2. The radiation hardening and electrical conductivity degradation decreased with increasing irradiation temperature, and became negligible for temperatures above ~300°C.

PROGRESS AND STATUS

Introduction

This report summarizes in tabular form all of the tensile and electrical resistivity measurements that have been made on pure copper and copper alloy sheet tensile specimens irradiated in the SM-2 reactor as part of a U.S.-RF collaborative experiment. Information concerning the experimental details and some of the initial results have been presented in previous progress reports [1,2]. Two papers summarizing many of the results will be published in the proceedings of the 7th International Conference on Fusion Reactor Materials held in Obninsk, Russia, in September 1995 [3,4]. A paper on the high-temperature helium embrittlement behavior of copper and dispersion-strengthened copper alloys has also been prepared [5].

The materials were irradiated in the form of sheet tensile specimens and transmission electron microscopy disks for about 45 days in the Channel 4 and core positions of the water-cooled SM-2 reactor in Dimitrovgrad, Russia. Some of the specimens in the Channel 4 position were irradiated inside a 1.5 mm Cd shroud in order to reduce the thermal neutron flux. The irradiation produced damage levels of 0.5 to 1.6 dpa in the Channel 4 position, and 3.5 to 5 dpa in the Core position. Typical fast (E>0.1 MeV) and thermal neutron fluences were 1.4×10^{25}/m^2 and 0.9×10^{25} n/m^2, respectively in the unshielded regions of Channel 4, 1.4×10^{25}/m^2 and 0.2×10^{25} n/m^2, respectively in the Cd-shielded regions of Channel 4, and 7.2×10^{25}/m^2 and 1.0×10^{25} n/m^2, respectively in the Core positions. Specimens were irradiated at temperatures of ~100 and ~200°C in Channel 4, and ~100, ~240 and ~350°C in the Core.

Results and Discussion

Tables 1-11 summarize the tensile data obtained on the irradiated materials. All of the tensile measurements were performed in vacuum (~10^{-4} Pa) at a temperature close to the irradiation temperature. Most of the STS sheet tensile specimens had gage dimensions of 11 × 3.5 × 0.25 mm. Some of the STS specimens had a thickness of 0.5 mm. The LTS sheet tensile specimens had gage dimensions of 30 × 4 × 1 mm. The tensile tests were performed at a cross-head speed of ~1 mm/minute, which produced initial strain rates of 5.6×10^{-4}/s and 1.5×10^{-3}/s in the LTS and STS specimens, respectively.

Considerable radiation hardening was observed in all specimens at irradiation temperatures below 200°C. The irradiated yield strength in specimens strengthened by dispersoids or cold-working was comparable for the Cd-shielded and unshielded regions of Channel 4, indicating that these changes in neutron spectrum had a relatively minor effect [4]. In contrast, significantly higher levels of strength were observed in pure copper and Cu-B specimens irradiated in the unshielded regions of Channel 4 compared to Cd-shielded regions. By comparing the tensile results in Tables 1-11 with literature data, it is concluded that severe radiation embrittlement (uniform elongation <1%) occurs in copper alloys irradiated at temperatures ≤100°C for doses above ~0.01 to 0.1 dpa [3,4]. On the other hand, irradiation at temperatures above 150-180°C causes only moderate embrittlement for doses up to ~5 dpa.

The present tensile results demonstrate that low temperature radiation embrittlement may have a considerable impact on the use of high-strength copper alloys for ITER structural applications. Low temperature radiation embrittlement is found to be very sensitive to the irradiation temperature. For precipitation hardened and dispersion strengthened copper alloys, 150°C appears to be a critical temperature for manifestation of embrittlement. The high-strength alloys embrittle dramatically at irradiation temperatures below 150°C, with uniform and total elongations close to zero. The plastic flow at the deformation zone is unstable under these irradiation conditions. At irradiation temperatures above 150-180°C, the precipitation hardened and dispersion strengthened alloys have a satisfactory level of ductility, with irradiated elongations in the range of 50 to 90% of the unirradiated values. It is recommended that the minimum operating temperature for copper alloys intended for structural applications in fusion energy systems should be 180°C, unless uniform elongations <1% can be accomodated in the design.

Tables 12-20 summarize the unirradiated and irradiated room temperature electrical resistivity data. The electrical resistivity measurements were performed using standard 4-point probe techniques on the STS and LTS sheet tensile specimens (before and after irradiation) prior to postirradiation tensile testing. The accuracy in the resistivity measurements was ±0.3 nΩ-m (±0.03 μΩ-cm). The electrical resistivity data could be separated into two components, a solid transmutation component $\Delta\rho_{tr}$ which was proportional to thermal neutron fluence and a radiation defect component $\Delta\rho_{rd}$ which was nearly independent of dose at damage levels >0.5 dpa [4]. The saturation value for $\Delta\rho_{rd}$ was ~1.2 nΩ-m for pure copper and ~1.6 nΩ-m for the DS copper alloys irradiated at 100°C in positions with a fast-to-thermal neutron flux ratio of 5. Further discussion of the tensile and electrical properties obtained in this study are given in refs. 3,4.

The $\Delta\rho_{tr}$ component depends primarily on the thermal neutron flux. It is determined by the transmutation rate (mainly Ni and Zn solutes) and has a weak dependence on the fast neutron flux and irradiation temperature. The $\Delta\rho_{rd}$ component is determined mainly by the level of radiation damage (which approaches a saturation level during irradiation at low temperatures for damage levels above ~0.1 dpa), and reduces practically to zero as the irradiation temperature approaches 250°C. The increase in $\Delta\rho_{rd}$ correlates with the increase in yield strength, $\Delta\sigma_{Yirr}$, since both of these properties are determined by the density of defect clusters. A comparison of the dose dependence of $\Delta\rho_{rd}$ for samples irradiated with and without Cd shielding in Channel 4 indicates that irradiation with thermal neutrons results in an increase in $\Delta\rho_{rd}$ (i.e., defect density), probably because of some effect of Ni and Zn on dislocation loop formation and the development of defect complexes. The magnitude of $\Delta\rho_{rd}$ appears to be ~30% higher in the DS copper alloys compared to pure copper, most likely because of partial dissolution of the oxide particles. Transmission electron microscopy will be performed on the irradiated materials to provide further information about the effect of neutron spectrum on the microstructural evolution in pure copper and the copper alloys.

Since the electrical (and to a lesser extent, tensile) properties of copper alloys are influenced by the solid transmutation generation rate, fusion engineering data on irradiated copper alloys should preferably be obtained in facilities where the solid transmutation rate is comparable to the fusion condition. The Core position of the SM-2 reactor produces fusion-relevant solid transmutation rates in copper, but most other mixed spectrum reactors may require spectral tailoring to reduce the Ni and Zn transmutation rates to fusion-relevant levels [4].

Future Work

Transmission electron microscopy and immersion density measurements will be performed on the irradiated TEM disks. In addition, the microstructure of the strained gage regions of several broken tensile specimens will be examined by TEM to provide further insight into the mechanisms responsible for the poor work hardening behavior and low ductility of copper alloys irradiated at temperatures below 180°C. The He content of several irradiated TEM disks will be measured and compared to measurements performed in Russia as part of a round-robin testing program.

Acknowledgements

Research sponsored in part by the Office of Fusion Energy, U.S. Department of Energy under contracts DE-AC05-96OR22464 with Lockheed Martin Energy Research Corp and DE-AC06-76RLO 1830 with Battelle Memorial Institute.

REFERENCES

1. S. J. Zinkle, F. A. Garner, V. R. Barabash, S. A. Fabritsiev, and A. S. Pokrovsky, in Fusion Reactor Materials Semiann. Prog. Report for period ending March 31, 1993, DOE/ER-0313/14, pp. 347-351.

2. S. A. Fabritsiev, A. S. Pokrovsky, S. J. Zinkle, A. F. Rowcliffe, B. N. Singh, F. A. Garner, and D. J. Edwards, in Fusion Materials Semiann. Prog. Report for period ending Sept. 30, 1994, DOE/ER-0313/17, pp. 221-228.

3. S. A. Fabritsiev, A. S. Pokrovsky, S. J. Zinkle, and D. J. Edwards, "Low Temperature Embrittlement of Copper Alloys," 7th Intern. Conf. on Fusion Reactor Materials, Obninsk, Russia, proceedings to be published in J. Nucl. Mater.

4. S. A. Fabritsiev, A. S. Pokrovsky, S. J. Zinkle, A. F. Rowcliffe, D. J. Edwards, F. A. Garner, V. A. Sandakov, B. N. Singh and V. R. Barabash, "The Effect of Neutron Spectrum on The Mechanical and Physical Properties of Pure Copper and Copper Alloys," 7th Intern. Conf. on Fusion Reactor Materials, Obninsk, Russia, proceedings to be published in J. Nucl. Mater.

5. S. A. Fabritsiev, A. S. Pokrovsky, S. J. Zinkle, D. J. Edwards, V. P. Chakin and B. N. Singh, "High Temperature Radiation Embrittlement of Copper Alloys," to be submitted to J. Nucl. Mater. (1996).

Table 1. Tensile Properties of Copper and Cu Alloys Irradiated in the Lower Part of the SMT-1 Capsule (LTS geometry, Cd-shielded region)

Alloy, heat treatment	Capsule	Floor	Fluence (Φt), 10^{20} n/cm^2		T_{irr}, °C	T_{test}, °C	σ_y, MPa	σ_u, MPa	δun, %	δto, %
			E>0.1 MeV	E<0.68 eV						
Cu pure 350C, 1h	6	1	8.6	2.27	85	100	268	269	0.6	4.4
						400	75	113	10.6	24.0
Cu + B1 350C, 1h	5	1	12.1	2.27	85	100	381	394	0.25	0.6
						400	263	263	0.12	1.3
Cu + B2 350C, 1h	5	2	17.8	2.92	88	100	411	413	0.16	1.8
						400	316	322	0.33	2.3
MAGT-0.2 as wrought	6	2	12.7	2.92	88	100	538	544	0.3	0.6
						400	262	263	0.3	0.6
Cu 99.999% as wrought	3	2	15.3	2.93	88	100	350	388	0.42	1.9
Cu 99.999% 550°C, 2h	4	2	17.8	2.92	88	100	187	216	12.0	16.4
GlidCop Al15+B as wrought	1	2	17.8	2.92	88	100	385	391	0.38	0.5
GlidCop Al15 + B, induction brazed	2	2	12.7	2.92	88	100	322	322	0	0
						400	163	163	0.16	0.33
GlidCop Al25 (no B) as wrought	1	1	12.1	2.27	85	100	520	538	0.4	2.5
						400	195	200	0.58	7.3
GlidCop Al25+B as wrought	2	1	8.6	2.92	88	100	519	519	0.24	0.24
GlidCop Al25 (no B) 20% c. w.	3	1	10.3	2.27	85	100	458	469	0.41	3.9
						400	211	228	0.5	9.0
GlidCop Al25 + B 20% c. w.	4	1	12.1	2.27	85	100	420	447	0.5	0.67
						400	273	280	0.67	3.8

Table 2. Tensile properties of copper and Cu alloys irradiated in the upper part of the SMT-1 capsule (LTS geometry, unshielded region)

Alloy, heat treatment	Capsule	Floor	Fluence (Φt), 10^{21} n/cm^2		T_{irr}, °C	T_{test}, °C	σ_y MPa	σ_u MPa	δ_u %	δ_{tot} %
			E>0.1 MeV	E<0.68 eV						
Cu pure c. w.	3	1	1.85	1.4	88	100	444	44	0.2	1.5
						400	282	284	0.33	2.3
Cu pure 350C, 1h	5	3	1.3	0.97	85	100	302	319	0.5	3.5
	1	1	1.42	1.4	88	100	319	319	0.16	3.8
						400	119	124	9.1	20.0
Cu + B1 350C, 1h	2	3	1.3	0.97	85	100	418	419	0.3	2.4
						400	204	206	0.25	2.0
	2	1	2.27	1.4	88	100	393	413	0.33	2.7
Cu + B2 350C, 1h	1	3	0.82	0.97	85	100	494	497	0.1	1.0
						400	256	263	0.33	1.8
Cu + B1 c. w.	2	2	1.9	1.24	88	100	506	506	0.16	0.16
						400	193	200	0.9	4.0
Cu - Cr - Zr I	5	1	2.27	1.4	88	100	413	413	0.1	0.1
						400	348	350	0.25	0.5
Cu - Mo as wrought	1	2	1.2	1.24	88	100	199	206	0.33	1.4
						400	196	203	0.6	1.5
Cu - Be	4	2	1.2	1.24	88	100	550	575	3.0	5.0
						100	766	894	4.1	6.5
						400	516	663	5.7	6.0
MAGT-0.2 as wrought	4	1	1.42	1.4	88	100	549	550	0.3	0.6
						400	360	360	0.16	0.5
	4	3	0.82	0.97	85	100	519	519	0.1	0.1

Table 3. Tensile properties of copper and Cu alloys irradiated in the lower part of the SMT-1 capsule (STS geometry, Cd-shielded region)

Alloy, heat treatment	Capsule	Floor	Fluence (Φt), 10^{20} n/cm^2		T_{irr}, °C	T_{test}, °C	σ_y, MPa	σ_u, MPa	δ_{un}, %	δ_{tot}, %
			E>0.1 MeV	E<0.68 eV						
GlidCop AL25 + B as wrought	1	2	10.7	2.63	82	100	473	475	0.2	0.3
					82	100	474	485	0.8	0.8
Cu 99.999 ann 950°C 0.5 h	1	1	8	2.19	76	100	227	254	12.8	12.8
GlidCop Al25 (no B) as wrought	1	2	10.7	2.63	82	100	500	526	1.1	1.1
GlidCop Al25 (no B) 20% c.w.	2	2	15	2.63	82	100	515	526	0.7	0.7
Cu 99.999 ann 550°C	1	1	8	2.19	76	100	238	245	16.0	21.3
Cu 99.999, 80% c.w.	1	2	10.7	2.63	82	100	442	445	0.4	0.4
Cu pure c.w.	4	2	10.7	2.63	82	100	426	484	1.1	2.2
Cu pure ann. 350°C, 1 h	5	1	8	2.19	76	100	234	250	5.0	10.5
	5	1	8	2.19	76	100	241	250	8.5	8.5
	3	3	18.3	3.0	87	100	241	258	12.0	15.0
Cu + B2 c.w.	5	3	13.1	3.0	80	100	475	485	0.4	0.4
	5	3	17.1	3.0	80	100	457	473	0.6	0.6
Cu pure II c.w.	5	2	10.7	2.63	82	100	400	410	1.2	1.6
MAGT 0.2 as wrought	3	2	15	2.63	82	100	478	498	0.8	0.8
Cu 99.999 400°C 1h	1	1	8	2.19	76	100	217	254	13.7	14.3
GlidCop Al25 + B 20% c.w.	2	2	15	2.63	82	100	505	551	0.35	0.35
GlidCop Al15 + B as wrought	2	1	11.2	2.19	76	100	473	475	0.2	0.3
Cu+B1 c.w.	4	1	8	2.19	76	100	485	502	1.9	2.3

Table 4. Tensile properties of copper and Cu alloys irradiated in the upper part of the SMT-1 capsule (STS geometry, unshielded region)

Alloy, heat treatment	Capsule	Floor	Fluence (Φt), 10^{21} n/cm^2		T_{irr}, °C	T_{test}, °C	σ_y, MPa	σ_u, MPa	δ_{un}, %	δ_{tot}, %
			E>0.1 MeV	E<0.68 eV						
MAGT-0.2 as wrought	2	3	1.2	1.25	86	100	529	564	0.5	0.5
	2	2	1.36	1.36	89	100	548	564	0.2	0.2
Cu pure ann 350°C, 1hr	1	1	2.3	1.42	80	100	245	262	14.7	16.0
Cu + B3 as wrought	3	4	1.57	1.1	81	100	179	296	2.5	3.2
	1	2	2.17	1.36	89	100	197	376	2.7	4.6
Cu + B1 c.w.	4	3	1.2	1.25	80	100	388	403	2.4	3.4
Cu-Mo-B as wrought	1	3	1.91	1.25	86	100	633	695	1.1	5.6
	1	3	1.91	1.25	86	100	432	461	0.7	0.9
Cu + B2 c.w.	3	3	1.91	1.25	86	100	470	472	0.3	0.3
	3	2	2.17	1.36	89	100	430	469		
	3	2	2.17	1.36	89	100	412	412	0.1	0.1
Cu + B2 ann	4	1	1.45	1.42	93	100	317	329	0.65	2.0
					80	100	341	349	1.2	6.5
	4	5	0.73	0.9	75	100	308	317	1.0	4.3
	4	1	1.45	1.42	93	100	275	280	0.6	2.6
Cu pure II c.w.	9	4	0.99	1.1	81	100	482	488	0.2	0.3
Cu pure c.w.	2	1	1.45	1.42	93	100	398	402	0.3	0.45

Table 5. Tensile properties of copper and Cu alloys irradiated in the lower part of the SMT-2 capsule (LTS geometry, Cd-shielded region)

Alloy, heat treatment	Cap-sule	Floor	Fluence (Φt), 10^{20} n/cm^2		T_{irr}, °C	T_{test}, °C	σ_y, MPa	σ_u, MPa	δ_{un}, %	δ_{tot}, %
			E>0.1 MeV	E<0.68 eV						
Cu + B2 350C, 1h	5	1	12	2.66	196	200	233	240	0.3	3.2
MAGT-0.2 as wrought	5	2	17.9	3.4	196	200	235	242	1.3	2.7
	5	2	17.9	3.4	196	200	224	228	1.1	3.7
Cu 99.999% as wrought	3	2	14.9	3.4	196	200	126	155	19.7	23.0
Cu 99.999% 550C, 2h	4	2	14.9	3.4	196	200	104	144	12.7	17.8
GlidCop Al15 + B as wrought	2	1	10	2.66	176	200	244	255	0.7	7.8
GlidCop Al15 + B, ind. brazed	2	2	14.9	3.4	196	200	290	302	0.33	4.1
GlidCop Al25 (no B) as wrought	1	1	10	2.66	176	200	275	288	0.5	6.0
GlidCop Al25 + B as wrought	2	1	10	2.66	176	200	287	300	0.6	3.8
GlidCop Al25 (no B) 20% c. w.	3	1	10	2.66	176	200	338	350	0.5	4.0
GlidCop Al25 + B 20% c. w.	4	1	10	2.66	176	200	255	265	0.5	1.5

Table 6. Tensile properties of copper and Cu alloys irradiated in the upper part of the SMT-2 capsule (LTS geometry, unshielded region)

Alloy, heat treatment	Cap-sule	Floor	Fluence (Φt), 10^{21} n/cm^2		T_{irr}, °C	T_{test}, °C	σ_y, MPa	σ_u, MPa	δ_{un}, %	δ_{tot}, %
			E>0.1 MeV	E<0.68 eV						
Cu pure c. w.	2	1	2.65	1.64	207	200	79	118	27.0	30.3
Cu pure 350C, 1h	1	1	1.66	1.64	207	200	165	175	8.8	13.3
Cu + B1 350C, 1h	3	2	1.4	1.45	198	200	94	130	24.2	35.3
Cu + B2 350C, 1h	1	2	1.4	1.45	198	200	218	241	7.5	13.2
Cu + B1 c. w.	2	2	2.22	1.45	198	200	105	177	12.5	24.3
Cu - Cr - Zr I	2	3	1.52	1.13	180	200	305	318	0.1	2.8
Cu - Cr - Zr II	3	3	0.96	1.13	180	200	228	238	0.83	2.0
	3	3	0.96	1.13	180	200	200	200	1.0	1.0
Cu - Be	4	3	1.52	1.13	180	200	704	818	7.0	7.7
MAGT-0.2 as wrought	3	1	1.66	1.64	207	200	255	263	0.3	3.2
Cu-Si-Ni-Cr as wrought	1	3	0.96	1.13	180	200	560	583	0.5	1.2
MAGT-0.05 as wrought	4	2	2.22	1.45	198	200	92	162	18.5	27.2

Table 7. Tensile properties of copper and Cu alloys irradiated in the lower part of the SMT-2 capsule (STS geometry, Cd-shielded region)

Alloy, heat treatment	Cap-sule	Floor	Fluence (Φt), 10^{20} n/cm^2		T_{irr}, °C	T_{test}, °C	σ_y, MPa	σ_u, MPa	δ_{un}, %	δ_{tot}, %
			E>0.1 MeV	E<0.68 eV						
Cu pure II c.w.	7	3	21.4	3.51	178	200	134	148	26.7	27.0
Cu pure c.w.	7	3	21.4	3.51	178	200	203	214	9.2	11.7
Cu pure, as wrought	6	3	21.4	3.51	178	200	246	274	17.1	18
Cu-0.2 Al , as wrought	7	3	21.4	3.51	178	200	174	294	0.7	1.0
Cu-0.16Zr	6	3	21.4	3.51	178	200	270	277	0.5	0.6
Cu pure ann 350°C	8	3	21.4	3.51	178	200	164	175	5.0	6.3
Cu + B1 350°	8	3	21.4	3.51	178	200	175	186	6.4	8.4
GlidCop Al25 (no B) 20% c.w.	7	2	17.5	3.08	180	200	332	424	2.4	5.9
GlidCop Al25 + B 20% c.w.	7	2	17.5	3.08	180	200	388	432	1.6	3.4
GlidCop Al15 + B 70% c.w.	7	2	17.5	3.08	180	200	415	481	1.3	2.8
GlidCop Al15 as wrought	7	1	13.1	2.51	161	200	239	272	1.9	4.4
Cu 99.999, 80% c.w.	7	1	13.1	2.51	161	200	135	175	21.2	22.0
GlidCop Al25 + B, as wrought	6	2	14.5	3.08	180	200	262	311		
GlidCop Al15 + B, ind. braz.	7	1	13.1	2.56	161	200	275	275	0	0
Cu 99.999, 550°C, 2h	6	1	13.1	2.56	161	400	47	60	16.5	22.0
Cu + B1 c.w.	8	2	17.5	3.08	180	400	115	124	4.5	5.1
Cu + B1 c.w.	8	2	17.5	3.08	180	100	391	408	1.5	3.3
MAGT-0.2, as wrought	8	2	17.5	3.08	180	100	264	289	0.7	0.7

Table 8. Tensile properties of copper and Cu alloys irradiated in the upper part of the SMT-2 capsule (STS geometry, unshielded region)

Alloy, heat treatment	Cap-sule	Floor	Fluence (Φt), 10^{20} n/cm^2		T_{irr}, °C	T_{test}, °C	σ_y, MPa	σ_u, MPa	δ_{un}, %	δ_{tot}, %
			E>0.1 MeV	E<0.68 eV						
Cu + B3 as wrought	6	2	2.54	1.59	169	200	136	139	1.3	4.5
Cu pure ann 350° C	6	1	2.69	1.66	174	200	50	54	2.5	9.0
Cu pure c.w.	6	4	1.84	1.29	178	200	133	136	7.0	7.5
Cu + B1 ann 350°C	6	1	2.69	1.66	174	200	132	216	8.0	10.4
Cu + B1 c.w.	6	3	2.23	1.46	176	200	151	175	9.5	19.0
Cu + B2 c.w.	6	3	2.23	1.46	176	200			11.6	23.5
Cu pure spec. as wrought	6	5	1.36	1.05	159	200	229	231	19.6	20.0
MAGT-0.05 as wrought	6	5	1.36	1.05	159	200	103	130	3.7	5.9
Cu + B1 ann 350°C	6	1	2.69	1.66	174	400	73	88	4.1	5.1

Table 9. Tensile properties of copper and Cu alloys irradiated in the Core subcapsule #1 (100°C, STS geometry)

Alloy, heat treatment	Cap-sule	Floor	Fluence (Φt), 10^{20} n/cm^2		T_{irr}, °C	T_{test} °C	σ_y, MPa	σ_u, MPa	δ_{un}, %	δ_{tot}, %
			E>0.1 MeV	E<0.68 eV						
Cu + B3 as wrought	2	1	51	7.7	120	100	254	254	0.2	0.2
	2	15	54	8.0	90	100	410	415	0.2	0.2
MAGT-0.2 as wrought	1	1	51	7.7	120	100	386	386	0	0
Cu pure, ann 350°C 1h	1	1	51	7.7	120	100	187	253	19.5	20.7
Cu + B1 ann 350°C 1h	2	14	65	9.1	100	100	246	301	3.0	3.3
Cu + B2 ann 350°C 1h	2	16	47	7.0	80	100	313	349	1.3	1.5
Cu-Mo-B as wrought	2	15	54	8.0	90	100	452	498	0.25	0.5
GlidCop Al25 (no B) as wrought	1	16	44	7.0	80	100	511	541	0.5	0.65
GlidCop Al25 (no B) 20% c.w.	1	15	54	8.0	90	100	525	566	0.4	0.4
GlidCop Al25 + B 20% c.w.	1	15	54	8.0	90	100	482	482	0.1	0.1
GlidCop Al15 + B as wrought	1	14	65	9.1	90	100	289	333	0.3	0.3
Cu 99.999 80% c.w.	1	14	65	9.1	100	100	274	288	15.8	17.0
Cu 99.999 ann. 550°C 2h	1	14	65	9.1	100	100	198	258	9.5	12.5

Table 10. Tensile properties of copper and Cu alloys irradiated in the Core subcapsule #3 (240°C, STS geometry)

Alloy, heat treatment	Cap-sule	Floor	Fluence (Φt), 10^{20} n/cm^2		T_{irr}, °C	T_{test}, °C	σ_y, MPa	σ_u, MPa	δ_{un}, %	δ_{tot}, %
			E>0.1 MeV	E<0.68 eV						
MAGT-0.2 as wrought	3	2	74	8.4	265	250	341	366	3.3	3.3
Cu + B1 ann 350°C 1h	3	1	60	7.3	265	250	191	208	6.0	6.0
Cu pure, ann	3	3	78	8.7	260	250	154	187	16.5	17.8
Cu 99.999, 550°C 2h	3	14	52	6.6	230	250	145	180	17.8	20.0
GlidCop Al25 no B, 20% c.w.	3	13	64	7.6	230	250	276	324	2.0	5.1
Glidcop Al25 + B as wrought	3	12	77	8.6	240	250	317	361	0.9	1.1
GlidCop Al25 no B as wrought	3	12	77	8.6	240	250	350	426	1.5	3.4
Cu 99.999, 80% c.w.	3	14	52	6.6	230	250	221	244	17.7	23.2

Table 11. Tensile properties of copper and Cu alloys irradiated in the Core subcapsule #4 (350°C, STS geometry)

Alloy, heat treatment	Cap-sule	Floor	Fluence (Φt), 10^{20} n/cm^2		T_{irr}, °C	T_{test}, °C	σy, MPa	σu, MPa	δun, %	δtot, %
			E>0.1 MeV	E<0.68 eV						
MAGT-0.2 as wrought	4	1	60	7.3	400	350	188	203	2.7	4.0
Cu + B3 as wrought	4	14	52	6.6	350	350	94	97	1.0	1.5
Cu pure ann 350°C	4	1	60	7.3	400	350	203	244	8.9	13.5
GlidCop Al15 + B as wrought	4	13	64	7.6	350	350	142	164	3.8	6.3
GlidCop Al25 + B 20% c.w.	4	12	77	8.6	360	350	190	239	5.6	8.6
Cu 99.999, 80% c.w.	4	13	64	7.6	350	350	67	85	11.0	13.0
GlidCop Al25 no B 20% c.w.	4	12	77	8.6	360	350	194	224	6.3	16
Cu 99.999, 550°C 2h	4	13	64	7.6	360	350	110	130	9.6	13.8
GlidCop Al25 no B as wrought	4	2	74	8.4	400	350	155	196	3.3	4.8

Table 12. Electrical resistivity of copper and Cu alloys irradiated in the lower part of the SMT-1 capsule (LTS geometry, Cd-shielded region)

Alloy	Cap-sule	Floor	ρ_{nonirr} μΩ-cm	ρ_{irr} μΩ-cm	ρ_{irr}/ρ_{non} %	Φt_{fast}, 10^{21} n/cm^2 E>0.1MeV	Φt_{therm}, 10^{20} n/cm^2 E<0.68 eV	T_{irr}, °C
Cu, pure anneal 350°C, 1 h	6	1	1.676	1.882	12.0	0.86	2.27	85
Cu+B1 anneal 350°C, 1 h	5	1	1.728	2.001	15.8	1.21	2.27	85
Cu+B2 anneal 350°C, 1 h	5	2	1.767	1.971	11.6	1.78	2.92	88
MAGT 0.2 as wrought	6	2	2.071	2.268	9.5	1.27	2.92	88
GlidCop Al15+B 70% c. w.	1	2	1.886	2.115	12.1	1.78	2.92	88
GlidCop Al25+B 20% c. w.	4	1	1.965	2.194	11.6	1.21	2.27	85
GlidCop Al25+B as wrought	2	1	1.923	2.163	12.5	.0.86	2.27	88
Cu 99.999% as wrought	3	2	1.689	1.909	13.1	1.53	2.92	88
Cu 99.999% anneal 550°C, 2 h	4	2	1.686	1.894	12.2	1.78	2.92	88
GlidCop Al25 (no B) 20% c. w.	3	1	1.972	2.180	10.6	1.03	2.27	85
GlidCop Al15+B induct. brazed	2	2	2.027	2.249	11.0	1.27	2.92	88
GlidCop Al25 (no B) as wrought	1	1	1.948	2.178	11.8	1.21	2.27	88
GlidCop Al15+B as wrought	1	2	1.892	2.178	14.9	1.78	2.92	88

Table 13. Electrical resistivity of copper and Cu alloys irradiated in the upper part of the SMT-1 capsule (LTS geometry, unshielded region)

Alloy	Capsule	Floor	ρ_{nonirr} μΩ-cm	ρ_{irr} μΩ-cm	ρ_{irr}/ρ_{nonirr} %	Φt_{fast}, 10^{21} n/cm^2 E>0.1MeV	Φt_{therm}, 10^{21} n/cm^2 E<0.68 eV	T_{irr}, °C
Cu pure anneal 350°C, 1 h	1	1	1.683	2.281	33.2	1.42	1.4	88
Cu+B1 anneal 350°C, 1 h	2	1	1.720	2.350	36.7	2.27	1.4	88
Cu+B2 anneal 350°C, 1 h	1	3	1.775	2.146	20.9	0.82	0.97	85
MAGT 0.2 as wrought	4	1	2.059	2.643	28.4	1.42	1.4	88
Cu pure c. w.	3	1	1.741	2.339	34.3	1.85	1.4	88
Cu + Be	4	2	6.190	7.149	15.5	1.2	1.24	88
Cu-Mo as wrought	3	2	2.016	2.774	37.6	1.55	1.24	88
Cu + Cr + Zr	5	1	2.107	2.997	42.3	2.27	1.4	88
Cu + B1 c. w.	2	2	1.758	2.274	29.4	1.9	1.24	88

Table 14. Electrical resistivity of copper and Cu alloys irradiated in the lower part of the SMT-1 capsule (STS geometry, Cd-shielded region)

Alloy	Capsule	Floor	ρ_{nonirr} μΩ-cm	ρ_{irr} μΩ-cm	ρ_{irr}/ρ_{nonirr} %	Φt_{fast}, 10^{21} n/cm^2 E>0.1MeV	Φt_{therm}, 10^{20} n/cm^2 E<0.68 eV	T_{irr}, °C
Cu + B3 c.w.	3	1	1.942	2.111	8.7	1.12	2.19	76
Cu + B1 c.w.	4	1	1.858	2.046	10.1	0.8	2.19	76
Cu + B1 anneal	1	3	1.742	2.099	20.5	1.31	3.0	87
Cu + B2 anneal	2	3	1.719	2.085	21.3	1.83	3.0	87
Cu pure anneal	5	1	1.681	1.905	13.3	0.8	2.19	76
Cu pure II c.w.	5	2	1.779	1.989	11.8	1.07	2.63	82
Cu pure c.w.	4	2	1.751	1.969	12.5	1.07	2.63	82
Cu - Mo - B as wrought	4	3	1.915	2.179	13.8	1.31	3.0	87
MAGT-0.2 as wrought	3	2	2.043	2.282	11.7	1.5	2.63	82
Cu + B2 c. w.	5	3	1.801	2.108	17.0	1.31	3.0	87
GlidCop Al25 (no B) 20% c. w.	2	2	1.948	2.266	16.3	1.5	2.63	82
GlidCop Al25 (no B) as wrought	1	2	1.981	2.264	14.3	1.07	2.63	82
GlidCop Al25 + B as wrought	1	2	1.991	2.298	15.4	1.07	2.63	82
Cu 99.999% ann. 950°C, 0.5 h	1	1	1.699	1.918	12.9	0.8	2.19	76
Cu 99.999% anneal 400°C, 1 h	1	1	1.692	1.904	12.5	0.8	2.19	76
GlidCop Al15 + B as wrought	2	1	2.018	2.308	14.4	1.12	2.19	76
GlidCop Al15 + B ind. br.	2	1	2.243	2.435	8.5	1.12	2.19	76
GlidCop Al15 + B 70% c. w.	2	2	1.941	2.218	14.3	1.5	2.63	82
Cu 99.999% 80% c. w.	2	2	1.727	1.943	12.5	1.5	2.63	82
GlidCop Al25 (no B) 20% c. w.	2	2	1.933	2.203	13.9	1.5	2.63	82
Cu 99.999% ann. 550 °C, 2 h	1	1	1.686	1.880	11.5	0.8	2.19	76

Table 15. Electrical resistivity of copper and Cu alloys irradiated in the upper part of the SMT-1 capsule (STS geometry, unshielded region)

Alloy	Capsule	Floor	ρ_{nonirr} μΩ-cm	ρ_{irr} μΩ-cm	ρ_{irr}/ρ_{nonirr} %	Φt_{fast}, 10^{21} n/cm^2 E>0.1MeV	Φt_{therm}, 10^{21} n/cm^2 E<0.68 eV	T_{irr}, °C
Cu + B3 c. w.	1	2	1.911	2.500	30.8	2.17	1.36	89
Cu + B1 c. w.	4	3	1.819	2.359	29.7	1.2	1.25	86
Cu + B1 anneal	3	1	1.736	2.461	41.8	2.3	1.42	93
Cu + B2 anneal	1	1	1.762	2.455	39.3	2.3	1.42	93
Cu pure anneal	4	1	1.700	2.336	40.0	1.45	1.42	93
Cu pure II c. w.	2	4	1.776	2.287	28.7	0.99	1.1	81
Cu pure c. w.	2	1	1.750	2.434	39.1	1.45	1.42	93
Cu - Mo - B	1	4	2.026	2.579	27.3	1.57	1.1	81
MAGT-0.2 as wrought	2	3	2.048	2.692	31.4	1.2	1.25	86
Cu + B2 c. w.	3	2	1.789	2.412	34.8	2.17	1.36	89

Table 16. Electrical resistivity of copper and Cu alloys irradiated in the lower part of the SMT-2 capsule (STS geometry, Cd-shielded region)

Alloy	Cap-sule	Floor	ρ_{nonirr} μΩ-cm	ρ_{irr} μΩ-cm	ρ_{irr}/ρ_{nonirr} %	Φt_{fast}, 10^{21} n/cm^2 E>0.1MeV	Φt_{therm}, 10^{20} n/cm^2 E<0.68 eV	T_{irr}, °C
Cu + B1 c.w.	8	2	1.858	2.021	8.8	1.75	3.08	180
Cu + B1, 350°C anneal	8	3	1.742	1.998	14.7	2.14	3.51	178
Cu + B2, 350°C anneal	7	1	1.719	1.925	12.0	1.31	2.51	161
Cu pure II c.w.	7	3	1.779	1.934	8.7	2.14	3.51	178
Cu pure c.w.	7	3	1.751	1.909	9.0	2.14	3.51	178
Cu - Mo - B as wrought	7	3	1.915	2.217	15.8	2.14	3.51	178
MAGT-0.2 as wrought	8	2	2.043	2.186	7.0	1.75	3.08	180
Cu + B2 c. w.	7	1	1.801	1.988	10.4	1.31	2.51	161
GlidCop Al25 (no B) 20% c. w.	7	2	1.948	2.133	9.5	1.75	3.08	180
GlidCop Al25 (no B) as wrought	8	2	1.981	2.135	7.8	1.75	3.08	180
GlidCop Al25 + B as wrought	6	2	1.991	2.150	8.0	1.45	3.08	180
Cu 99.999% ann. 950°C, 0.5 h	7	1	1.699	1.852	9.0	1.31	2.51	161
GlidCop Al15 + B as wrought	7	1	2.018	2.246	11.3	1.31	2.51	161
GlidCop Al15 + B ind. br.	7	1	2.243	2.263	0.9	1.31	2.56	161
Cu 99.999% 80% c. w.	7	1	1.727	1.842	6.7	1.31	2.51	161
Cu 99.999% ann. 550°C, 2 h	6	1	1.686	1.829	8.5	1.31	2.56	161

Table 17. Electrical resistivity of copper and Cu alloys irradiated in the upper part of the SMT-2 capsule (STS geometry, unshielded region)

Alloy	Cap-sule	Floor	ρ_{nonirr} μΩ-cm	ρ_{irr} μΩ-cm	ρ_{irr}/ρ_{nonirr} %	Φt_{fast}, 10^{21} n/cm^2 E>0.1MeV	Φt_{therm}, 10^{21} n/cm^2 E<0.68 eV	T_{irr}, °C
Cu + B1 c. w.	6	3	1.819	2.304	26.7	2.23	1.46	176
MAGT-0.2 as wrought	6	6	2.048	2.429	18.6	1.74	1.2	178
Cu + B2 c. w.	6	3	1.789	2.311	29.2	2.23	1.46	176

Table 18. Electrical resistivity of copper and Cu alloys irradiated in the Core subcapsules #1 and #2 (STS geometry, 100°C)

Alloy	Capsule	Floor	ρ_{nonirr}	$\Delta\rho_{irr}$	Φt_{fast}, (E>0.1 MeV)	Φt_{therm}, (E<0.68 eV)	T_{irr},
			μΩ-cm	μΩ-cm	10^{21} n/cm^2	10^{20} n/cm^2	°C
GlidCop Al25 no B as wrought	3-1	16	2.074	0.446	4.7	7.0	80
GlidCop Al25 + B as wrought	3-1	16	2.074	0.575	4.4	7.0	80
GlidCop Al15 + B as wrought	3-1	14	2.099	0.604	6.5	9.1	100
GlidCop Al15 + B ind. brazed	3-1	16	2.338	0.355	4.4	7.0	80
Cu pure ann.	3-1	1	1.761	0.341	5.1	7.7	120
Cu 99.999 550 °C, 2h	3-1	14	1.735	0.382	6.5	9.1	100
Cu 99.999 80% c.w.	3-1	14	1.767	0.415	6.5	9.1	100
Cu + B2 ann. 350 °C	3-2	14	1.801	0.46	6.5	9.1	100
Cu + B2 ann. 350 °C	3-2	16	1.801	0.281	4.4	7	80
Cu + B1 ann	3-2	14	1.817	0.519	6.5	9.1	100
Cu + B1 ann	3-2	16	1.817	0.393	4.4	7.0	80
Cu + B3 c.w.	3-2	15	1.959	0.326	5.4	8.0	90
Cu + B3 c.w.	3-2	1	1.959	0.417	5.1	7.7	120
Cu-Mo-B as wrought	3-2	1	1.960	0.419	5.1	7.7	120
MAGT-0.2	3-1	1	2.1	0.406	5.11	7.7	120

Table 19. Electrical resistivity of copper and Cu alloys irradiated in the Core subcapsule #3 (STS geometry, 240°C)

Alloy	Capsule	Floor	ρ_{nonirr}	$\Delta\rho_{irr}$	Φt_{fast}, (E>0.1 MeV)	Φt_{therm}, (E<0.68 eV)	T_{irr},
			μΩ-cm	μΩ-cm	10^{21} n/cm^2	10^{20} n/cm^2	°C
GlidCop Al25, no B, 20% c.w.	3-3	13	2.01	0.416	6.4	7.6	230
GlidCop Al25, no B, as wrought	3-3	12	2.017	0.362	7.7	8.6	240
GlidCop Al15 + B ind. brazed	3-3	12	2.109	0.463	7.7	8.6	240
GlidCop Al25 + B as wrought	3-3	12	2.074	0.498	7.7	8.6	240
GlidCop Al15 + B as wrought	3-3	14	2.147	0.4	7.8	8.7	260
Cu pure annealed	3-3	2	1.742	0.335	7.4	8.4	265
Cu 99.999 550 °C	3-3	14	1.759	0.297	5.2	6.6	230
Cu 99.999 80% c.w.	3-3	14	1.786	0.274	5.2	6.6	230
Cu 99.999 80% c.w.	3-3	13	1.786	0.281	6.4	7.6	230
Cu + B 1 annealed	3-3	1	1.8	0.397	6.0	7.3	265
Cu + B 2 annealed	3-3	1	1.810	0.340	6.0	7.3	265
MAGT-0.2	3-3	2	2.1	0.356	7.4	8.4	265

Table 20. Electrical resistivity of copper and Cu alloys irradiated in the Core subcapsule #4 (STS geometry, 350°C)

Alloy	Capsule	Floor	ρ_{nonirr}	$\Delta\rho_{irr}$	Φt_{fast}, (E>0.1 MeV)	Φt_{therm}, (E<0.68 eV)	T_{irr},
			μΩ-cm	μΩ-cm	10^{21} n/cm^2	10^{20} n/cm^2	°C
GlidCop Al25 no B 20% cw	3-4	12	2.056	0.181	7.7	8.6	360
GlidCop Al15 + B ind.brazed	3-4	2	2.088	0.273	7.4	8.4	400
GlidCop Al25 + B as wrought	3-4	2	2.110	0.302	7.4	8.4	400
GlidCop Al15 + B as wrought	3-4	13	2.19	0.21	6.4	7.6	350
Cu pure ann.	3-4	3	1.730	0.174	7.8	8.7	390
Cu 99.999 550 °C	3-4	12	1.735	0.239	7.7	8.6	360
Cu 99.999 80% c.w.	3-4	13	1.797	0.124	6.4	7.6	350
Cu-Mo-B as wrought	3-4	14	1.984	0.076	5.2	6.6	350
Cu-Mo-B as wrought	3-4	14	1.974	0.233	5.2	6.6	350
MAGT-0.2	3-4	1	2.098	0.169	6.0	7.3	400

FRACTURE TOUGHNESS AND FATIGUE CRACK GROWTH OF OXIDE-DISPERSION STRENGTHENED COPPER

D. J. Alexander and B. G. Gieseke, Oak Ridge National Laboratory

OBJECTIVE

The fracture toughness and fatigue crack growth behavior of oxide-dispersion strengthened copper alloys were examined. These alloys are candidate materials for first wall and divertor structural applications. The fracture behavior of these materials must be characterized to determine their suitability.

SUMMARY

The fracture toughness and fatigue crack growth behavior of copper dispersion strengthened with aluminum oxide (0.15 wt % Al) was examined. In the unirradiated condition, the fracture toughness was about 45 kJ/m^2 (73 MPa$\sqrt{m}$) at room temperature, but decreased significantly to only 3 kJ/m^2 (20 MPa$\sqrt{m}$) at 250°C. After irradiation at approximately 250°C to about 2.5 displacements per atom (dpa), the toughness at room temperature was about 19 kJ/m^2 (48 MPa$\sqrt{m}$), and at 250°C the toughness was very low, about 1 kJ/m^2 (12 MPa$\sqrt{m}$). The fatigue crack growth rate of the unirradiated material at room temperature is similar to other candidate structural alloys such as V-4Cr-4Ti and 316L stainless steel. The fracture properties of this material at higher temperatures and in controlled environments need further investigation, in both irradiated and unirradiated conditions.

PROGRESS AND STATUS

Introduction

High-strength copper alloys with high thermal conductivity are attractive candidates for some structural applications in ITER. One of these alloys is GLIDCOP AL-15, a commercially available dispersion-strengthened copper alloy with 0.15 wt % Al that has been internally oxidized to produce small Al_2O_3 particles in a copper matrix. However, there is very little information about the fracture behavior of these alloys, in particular the fracture toughness and fatigue crack growth resistance. A recent review of copper-based alloys [1] pointed out the need for additional data in these areas. Some preliminary testing was conducted to determine the fracture toughness before and after irradiation, and the fatigue crack growth rate in the unirradiated condition.

Experimental Procedure

Specimens were fabricated from an as-wrought plate measuring 165 mm wide by 12.7 mm thick by ~ 3 m long that was produced by SCM Metals for the ORNL Fusion Energy Division in 1987 [2]. This plate had been warm worked during the consolidation of the -20 mesh powder. The plate was then extruded at about 820°C with an extrusion ratio of 25:1. Both the fracture toughness and the fatigue crack growth specimens were oriented in the T-L orientation so that crack growth was in the extrusion direction.

Standard compact specimens 37.75 × 30.48 × 12.7 mm thick (1.25 × 1.20 × 0.50 in.) [designated 1/2 T C(T) specimens] were fabricated for the first set of fracture toughness tests. The second series of tests used small disk compact specimens 12.5 mm in diameter by 4.62 mm thick (0.491 by 0.182 in.) [designated 0.18 T DC(T) specimens]. The DC(T) specimen geometry was chosen to allow the specimens to fit into the High Flux Isotope Reactor target region. Specimens were irradiated as part of a larger experiment which included a variety of austenitic stainless steels [3,4]. The GLIDCOP specimens were irradiated at a nominal irradiation temperature of 250°C to a dose of approximately 2.5 dpa. The calculated fluences were 8.8×10^{17} n/m^2 (total), with a thermal fluence of 3.4×10^{17} n/m^2 (< 0.5 eV) and a fast fluence of 2.6×10^{17} n/m^2 (> 0.1 MeV) [5].

All specimens were fatigue precracked at room temperature and then side-grooved 10% of their thickness on each side prior to testing. Testing was conducted on an 89-kN (20-kip) capacity computer-controlled servohydraulic test machine operating in strain control in the laboratory. Tests in the hot cell used a 445-kN capacity (100-kip) servohydraulic machine with a 22-kN load cell, again operating in strain control. Testing was conducted in general accordance with ASTM E 813-89, Standard Test Method for J_{IC}, A Measure of Fracture Toughness, and ASTM E 1152-87, Standard Test Method for Determining J-R Curves using a computer-controlled data acquisition and analysis system [6]. The J-integral equations from E 1152-87 were used for the calculations. Tensile properties used in the analyses were taken from the literature [7]. Estimated values were used for the irradiated specimens [2].

Crack growth was monitored by the unloading compliance technique for all tests. Displacements were measured on the C(T) specimens with a clip gage seated on knife edges located on the specimen loading line in a notch cutout. For the DC(T) specimens an outboard clip gage was used that was seated in grooves machined on the outer diameter of the disk, above and below the loading holes. The experimental techniques developed for testing the small, irradiated DC(T) specimens have been described elsewhere [8].

After testing, the fracture toughness specimens were heat-tinted by placing them on a hot plate and heating them until a noticeable color change had occurred. The specimens were cooled to room temperature and then broken open to allow the initial and final crack lengths to be measured. Specimens tested in the laboratory were measured with a measuring microscope. The fracture surfaces of the irradiated specimens were photographed, and photographic enlargements were used with a digitizing tablet to measure the crack lengths.

The fatigue crack growth rate specimens had the same overall size as the 1/2 T C(T) specimens [37.75 by 30.48 mm (1.25 by 1.20 in.), but were only 4.95 mm thick (0.195 in.). These specimens were tested in laboratory air in a servohydraulic test machine operating at 20 Hz with a sinusoidal waveform with a minimum-to-maximum load ratio of 0.1. Crack growth was monitored by the direct current potential drop technique. A constant current of 20 A was introduced on the top of the specimen halfway between the loading line and the back face of the specimen (a/W = 0.5). The voltage drop across the specimen was monitored on the front face of the specimen. The crack length determined from the potential drop measurements was compared to the visually measured crack length at the beginning and end of the test as measured from the specimen fracture surface after the test was completed, and the crack lengths determined by the potential drop measurements were within 1.5% of the visual measurements.

Results and Discussion

The results of the fracture toughness testing are shown in Fig. 1 and are summarized in Table 1. At room temperature the unirradiated material had a J_Q value of about 45 kJ/m^2. Similar values were found for the C(T) and smaller DC(T) specimens. This indicates that the small DC(T) specimen can generate useful fracture toughness data in dispersion-strengthened copper alloys. The slope of the J-R curve for the small DC(T) specimens was higher than for the larger C(T) specimen, suggesting that constraint had been lost in the small specimen. These effects of specimen size are similar to those observed for previous tests with a low-toughness austenitic stainless steel [8].

The fracture toughness of the unirradiated material decreases markedly as the test temperature increases, as Fig. 1 shows. At 250°C the toughness is very low (3 kJ/m^2) and the J-R curve has a very low slope. Tearing begins as soon as the specimen is loaded. Irradiation at 250°C to 3 dpa also causes a decrease in the fracture toughness (Fig. 1). At room temperature the toughness drops by about one-half as compared to the unirradiated material, and the slope of the J-R curve decreases also. At 250°C the toughness was so low that the specimen broke as it was being loaded for the first cycle of the test, so no J-R curve could be determined. Based on the peak load that the specimen reached, the fracture toughness value was estimated to be 1 kJ/m^2 (12 MPa$\sqrt{m}$).

The fracture toughness of this material in the unirradiated condition is usefully high. However, there is a significant decrease in the toughness as the test temperature increases. For the unirradiated material, the toughness drops from

about 75 to 20 MPa√m with an increase in test temperature from 20 to 250°C. This is a surprising response, as there is no indication of a significant change in the tensile properties over this same range of temperatures [1,7]. These results are similar to data for the AL-25 alloy [9], which has 0.25 wt % Al. Interestingly, impact tests of notched specimens of AL-25 [9] do not show a decrease in toughness over this temperature range. This suggests that an environmental embrittlement may be responsible for the drop in toughness. The fracture toughness may not be so impaired in a vacuum environment. Further testing at intermediate and higher temperatures and in controlled atmospheres is necessary to confirm these preliminary results.

Irradiation also reduces the fracture toughness. Again, test temperature also has a significant effect. After irradiation at 250°C to 3 dpa, the room temperature fracture toughness is lower than for the unirradiated condition, but is still fairly high, at about 48 MPa√m. However, when the test temperature is increased to 250°C, the toughness is greatly reduced, to about 12 MPa√m. These low toughnesses at higher temperatures, both before and after irradiation, are certainly cause for concern, and need to be verified with further testing.

The results of the fatigue crack propagation (FCP) test are presented in Fig. 2. Typical FCP results for type 316 stainless steel [10] and recent results for V-4Cr-4Ti [11] have been included for comparison to other materials under consideration for ITER applications. The stainless steel offers better resistance to crack propagation than either of the other alloys in air. Both the vanadium alloy and the 316 stainless steel show improved resistance to crack growth in vacuum [11,12], an environment representative of the ITER applications. It is expected that the GLIDCOP AL-15 will also have better resistance to crack growth in vacuum as well.

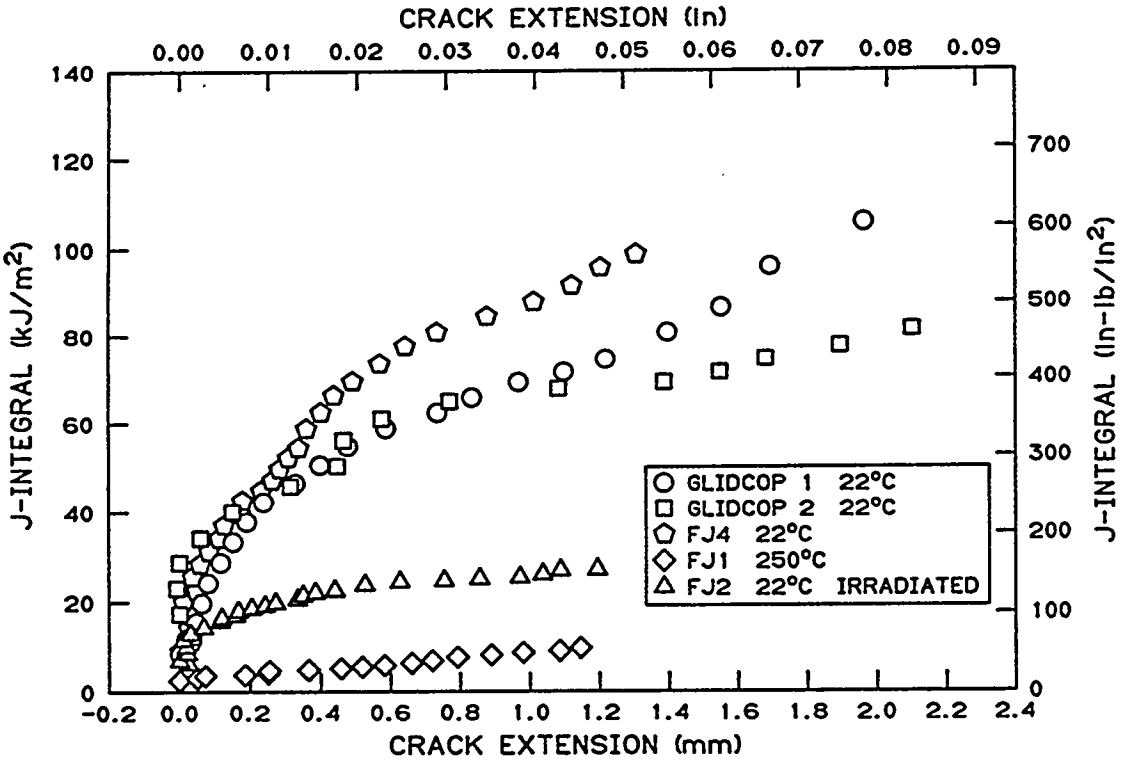

Fig. 1. J-integral-resistance curves for GlidCop AL-15 specimens.

Table 1. Results of fracture toughness testing

Specimen number	Specimen type	Test temperature (°C)	Irradiation temperature (°C)	Irradiation dose (dpa)	J_Q (kJm^2)	K_J[a] (MPa√m)	T	σ_y (MPa)	σ_u (MPa)	E (GPa)
1	0.5T C(T)	22	b	b	43	71	29	330	380	117
2	0.5T C(T)	22	b	b	47	74	18	330	380	117
FJ4	0.18T DC(T)	22	b	b	51	78	42	330	360	117
FJ1	0.18T DC(T)	250	b	b	3	20	9	262	283	112
FJ2	0.18T DC(T)	22	250	2.5	19	48	7	338	372	117
FJ3	0.18T DC(T)	250	250	2.5	1[c]	12[c]	--	290	317	112

[a]$K^2 = JE$.
[b]Unirradiated
[c]Specimen failed during first cycle; value estimated from peak load.

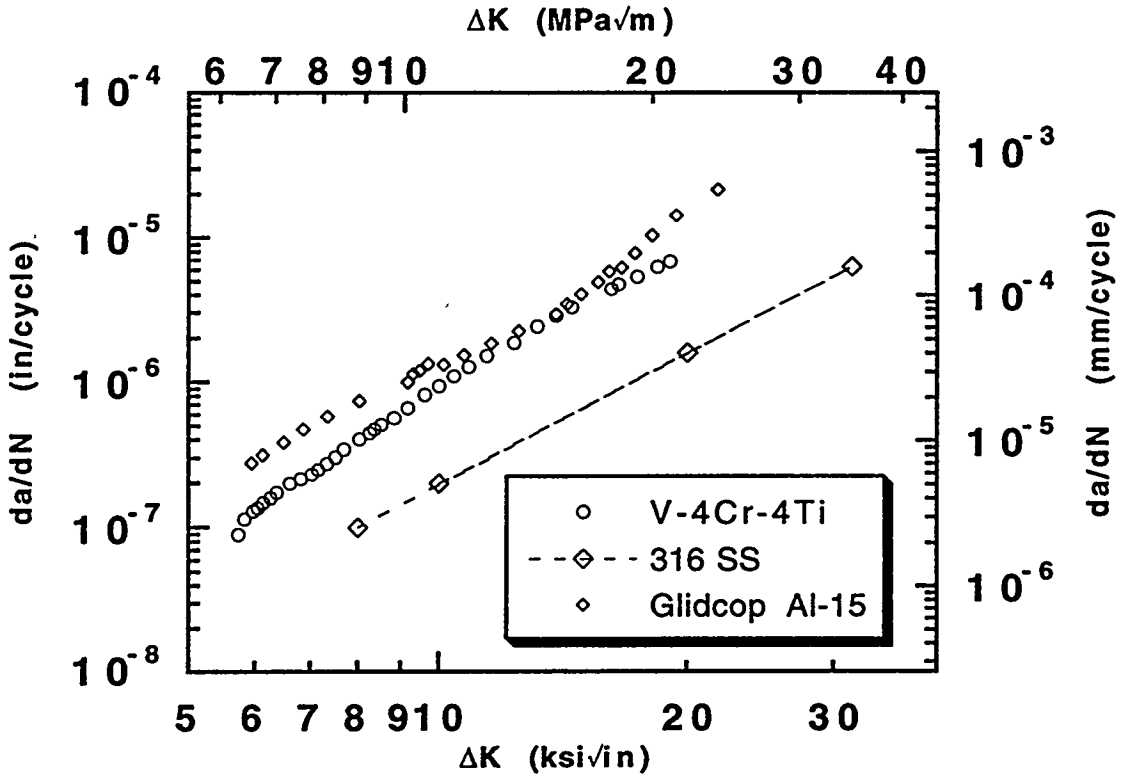

Fig. 2. Fatigue crack growth rate versus applied stress intensity for GlidCop AL-15. Data for V-4Cr-4Ti and type 316 stainless steel are included for comparison.

REFERENCES

1. S. J. Zinkle and S. A. Fabritsiev, "Copper Alloys for High Heat Flux Structure Applications," in *Fusion Materials Semiannual Progress Report for Period Ending March 31, 1994*, DOE/ER-0313/16, 1994, pp. 314-41.

2. S. J. Zinkle, Oak Ridge National Laboratory, personal communication, 1995.

3. J. E. Pawel, D. J. Alexander, M. L. Grossbeck, A. W. Longest, A. F. Rowcliffe, G. E. Lucas, S. Jitsukawa, A. Hishinuma, and K. Shiba, "Fracture Toughness of Candidate Materials for ITER First Wall, Blanket, and Shield Structures," *J. Nucl. Mat.*, 1994, Vol. 212-215, pp. 442-47.

4. D. J. Alexander, J. E. Pawel, M. L. Grossbeck, A. F. Rowcliffe, and K. Shiba, "Fracture Toughness of Irradiated Candidate Materials for ITER First Wall/Blanket Structures," *Effects of Radiation on Materials: 17th International Symposium, ASTM STP 1270*, D. S. Gelles, R. K. Nanstad, A. S. Kumar, and E. A. Little, Editors, American Society for Testing and Materials, Philadelphia, 1995; also published in *Fusion Reactor Materials Semiannual Progress Report for Period Ending March 31, 1994*, DOE/ER-0313/16, pp. 173-93.

5. L. R. Greenwood and C. A. Baldwin, *Fusion Reactor Materials Semiannual Progress Report for Period Ending September 30, 1995*, DOE/ER-0313/19, to be published.

6. R. K. Nanstad, D. J. Alexander, R. L. Swain, J. T. Hutton, and D. L. Thomas, "A Computer-Controlled Automated Test System for Fatigue and Fracture Testing," in *Applications of Automation Technology to Fatigue and Fracture Testing, ASTM STP 1092*, A. A. Braun, N. E. Ashbaugh, and F. M. Smith, Editors, American Society for Testing and Materials, Philadelphia, 1990, pp. 7-20.

7. T. J. Miller, S. J. Zinkle, and B. A. Chin, "Strength and Fatigue of Dispersion-Strengthened Copper," *J. Nucl. Mat.*, 1991, Vol. 179-181, pp. 263-66.

8. D. J. Alexander, "Fracture Toughness Measurements with Subsize Disk Compact Specimens," in *Small Specimen Test Techniques Applied to Nuclear Vessel Thermal Annealing and Plant Life Extension, ASTM STP 1204*, W. R. Corwin, F. M. Haggag, and W. L. Server, Editors, American Society for Testing and Materials, Philadelphia, 1993, pp. 130-42; also published in *Fusion Reactor Materials Semiannual Progress Report for Period Ending March 31, 1992*, DOE/ER-0313/12, pp. 35-45.

9. R. R. Solomon, A. V. Nadkarni, and J. D. Troxell, SCM Metal Products, Inc., unpublished information presented at ITER Workshop, Gatlinburg, Tenn., November 7, 1995

10. *Materials for Fusion Energy Systems*, DOE/TIC-10122, Book 1, Vol. 1, File Code AB02-2431, pp. 1.2-1.3, 1980.

11. B. G. Gieseke, et al., "Fatigue and Crack Growth of V-Cr-Ti Alloys," *J. Nucl. Mater.*, to be published.

12. J. E. Campbell, "Fracture Properties of Wrought Stainless Steels," in *Applications of Fracture Mechanics for Selection of Metallic Structural Materials*, J. E. Campbell, W. W. Gerberich, and J. E. Underwood, Editors, American Society for Metals, Metals Park, Ohio, 1982, p. 135.

FATIGUE BEHAVIOR OF COPPER AND SELECTED COPPER ALLOYS FOR HIGH HEAT FLUX APPLICATIONS - K. D. Leedy, J. F. Stubbins (University of Illinois), B. N. Singh (RISØ National Laboratory), and F. A. Garner (Pacific Northwest National Laboratory)

To be published in J. Nuclear Materials, 1996 proceedings of ICFRM-7

Extended Abstract

The room temperature fatigue behavior of standard and subsize specimens was examined for five copper alloys: OFHC Cu, two CuNiBe alloys, a CuCrZr alloy, and a Cu-Al_2O_3 alloy. Fatigue tests were run in strain control to failure. In addition to establishing failure lives, the stress amplitudes were monitored as a function of numbers of accrued cycles. The results indicate that the alloys with high initial yield strengths provide the best fatigue response over the range of failure lives examined in the present study: $N_f = 10^3$ to 10^6. In fact, the fatigue performance of the best alloys is dominated by the elastic portion of the strain range, as would be expected from the correlation of performance with yield properties. The alumina strengthened alloy and the two CuNiBe alloys show the best overall performance of the group examined here. It was found that the fatigue response is closely related to the uniformity of the material microstructure and particularly the distribution of the finely dispersed strengthening phases. The pre- and post- fatigue microstructures were examined to identify the types and distribution of secondary phases, and their role in fatigue response.

[1] Operated for the US Department of Energy by Battellle memorial Institute under Contract DE-AC06-76RLO 1830.

EVALUATION OF Nb-BASE ALLOYS FOR THE DIVERTOR STRUCTURE IN FUSION REACTORS*

I. M. Purdy (Argonne National Laboratory) and J. A. Todd (Illinois Institute of Technology)

SUMMARY

Niobium-base alloys are candidate materials for the divertor structure in fusion reactors. For this application, an alloy should resist aqueous corrosion, hydrogen embrittlement, and radiation damage and should have high thermal conductivity and low thermal expansion. Results of corrosion and embrittlement screening tests of several binary and ternary Nb alloys in high-temperature water indicated that Nb-1Zr, Nb-5Mo-1Zr, and Nb-5V-1Zr (wt.%) showed sufficient promise for further investigation. These alloys, together with pure Nb and Zircaloy-4, have been exposed to high-purity water containing a low concentration of dissolved oxygen (<12 ppb) at 170, 230, and 300°C for up to ≈3200 h. Weight-change data, microstructural observations, and qualitative mechanical-property evaluations reveal that Nb-5V-1Zr is the most promising alloy at higher temperatures. Below ≈200°C, the alloys exhibit similar corrosion behavior.

INTRODUCTION

The corrosion behavior of several binary and ternary Nb-base alloys was investigated earlier to identify the most promising materials for possible use as the divertor structure in a fusion reactor with an aqueous coolant [1-3]. In this study, corrosion tests were conducted on selected alloys in high-purity deoxygenated water at 170, 230, and 300°C.

EXPERIMENTAL PROCEDURE

Details of the experimental procedures are described in Ref. 4. Thin sheets of pure Nb and several Nb-base alloys were sheared to approximate dimensions of 8 x 20 mm. The Nb-5V-1Zr alloy, formerly designated "Cb 753" by Cabot Corporation, was obtained from two sources. Thickness of the Nb and one lot of Nb-5V-1Zr alloy was 0.5 mm; that of the other materials was 0.8 mm. Impurity levels in the two heats of Nb-5V-1Zr differed by a factor of ≈2. Material compositions are given in Table 1.

Table 1. Composition of Nb and Nb-base alloys[a]

Alloy	wt.%			ppm							
	Mo	V	Zr	O	N	C	H	Si	Al	Fe	Cr
Nb_1	<0.01	--	<0.01	<50	31	<20	<3	<20	--	<40	--
Nb_2	<0.01	<0.01	<0.01	176	42	200	11.4	340	70	65	<20
Nb-1Zr[a]	<0.01	<0.01	0.82	153	57	70	4.0	<100	65	<50	<20
Nb-5Mo-1Zr[a]	4.86	<0.01	0.81	186	56	70	8.5	<100	70	<50	<20
Nb-5V-$1Zr_1$[a]	<0.01	5.76	1.11	720	75	300	10.3	150	155	100	150
Nb-5V-$1Zr_2$[a]	<0.01	5.69	0.84	310	95	130	4.1	260	65	35	25

[a]Concentrations of Hf, W, Ta, and Ti are ≤100 ppm; Mn, Cu, and Ni ≤50 ppm; and Mg ≤5 ppm.

The surface area of each specimen was measured by an image analysis technique. Specimens were annealed in vacuo at 1000°C for 2 h prior to exposure. The exposures were conducted in refreshed autoclave systems at 170, 230, and 300°C (±2°C) with ≈100 psi overpressure (above saturation) at each temperature to maintain liquid-phase water. Corrosion tests at 300°C were performed in a Type 304 stainless steel autoclave; those at 170 and 230°C were conducted in a Hastelloy C276 autoclave (62%Ni-16%Cr-16%Mo). Dissolved-oxygen concentration of the inlet water was maintained at <12 ppb. Each ≈120-day immersion experiment was interrupted at approximately 30, 60, and 90 days for removal of specimens. Weight changes of the specimens were determined to ±1 μg. Ductility changes in the specimens were evaluated by a bend test. Zircaloy-4 (Table 2) was included in later tests at 170 and 230°C to compare its behavior with that of Nb-base alloys.

*Work supported by the U.S. Department of Energy, Office of Fusion Energy Research, under Contract W-31-109-Eng-38.

Table 2. Composition of Zircaloy[a]

Alloy	wt.%			ppm						
	Fe	Cr	Sn	O	N	C	H	Si	Al	Hf
Zircaloy-4	0.23	0.11	1.55	1044	25	145	8.5	54	47	41

[a]Concentrations of Mn, Ti, and W are <25 ppm; Cu and Ni <35 ppm.

EXPERIMENTAL RESULTS

Weight gain versus time of exposure for pure Nb, Nb-base alloys, and Zircaloy-4 is shown in Figs. 1-4. The data were fitted to the expression $W = A \cdot t^n$, where W is the weight gain in $g \cdot m^{-2}$, t is the exposure time in hours, and A and n are empirical fitting parameters. The values of n in the power-law expression range from ≈0.3 to ≈0.7 and are denoted by the slopes of the lines in Figs. 1-4. Most of the materials gained weight at 230 and 300°C; however, weight changes for all specimens at 170°C were relatively small (<0.3 mg) and did not increase with exposure time for Nb and the Nb-base alloys.

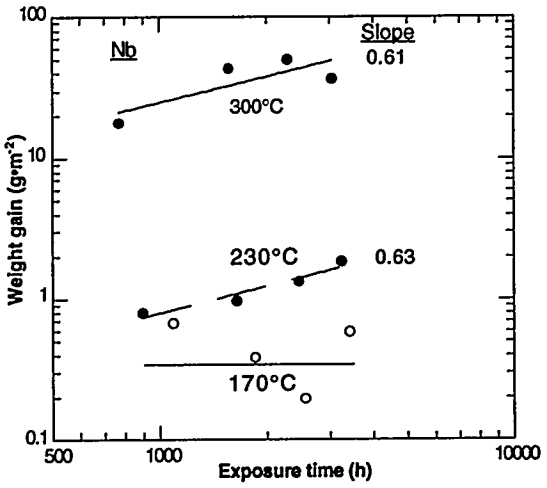

Fig. 1. Weight gain vs. time for Nb in high-purity, low-oxygen water at 170, 230, and 300°C

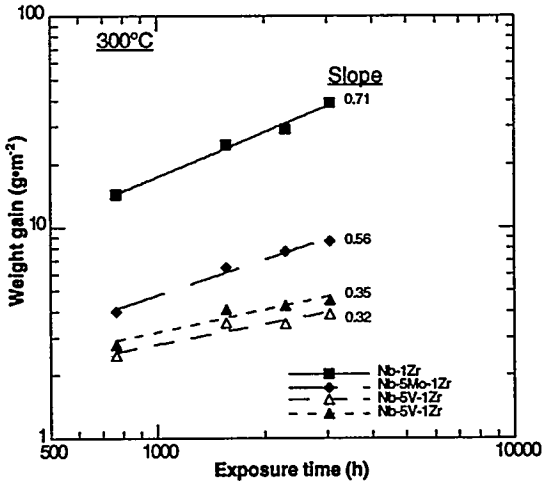

Fig. 2. Weight gain vs. time for Nb-base alloys in high-purity, low-oxygen water at 300°C

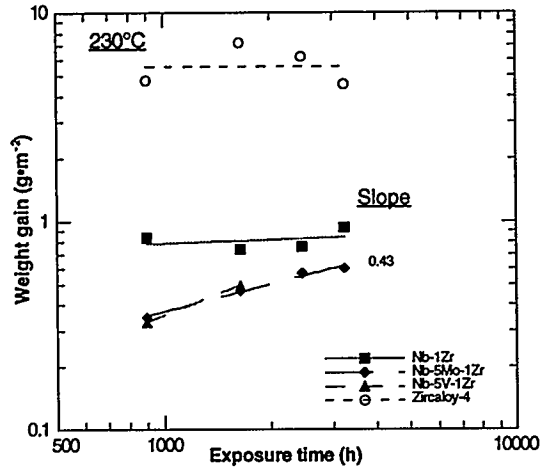

Fig. 3. Weight gain vs. time for Nb-base alloys and Zircaloy-4 in high-purity, low-oxygen water at 230°C

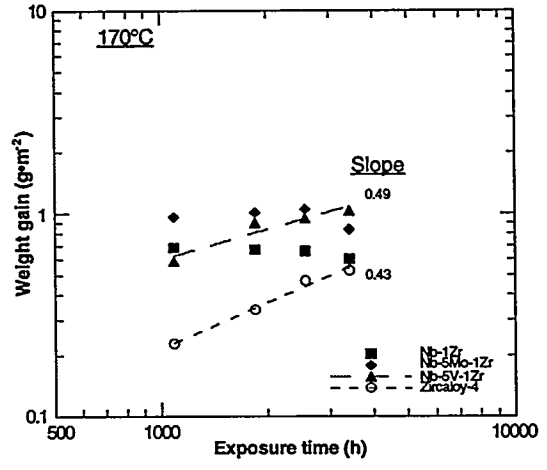

Fig. 4. Weight gain vs. time for Nb-base alloys and Zircaloy-4 in high-purity, low-oxygen water at 170°C

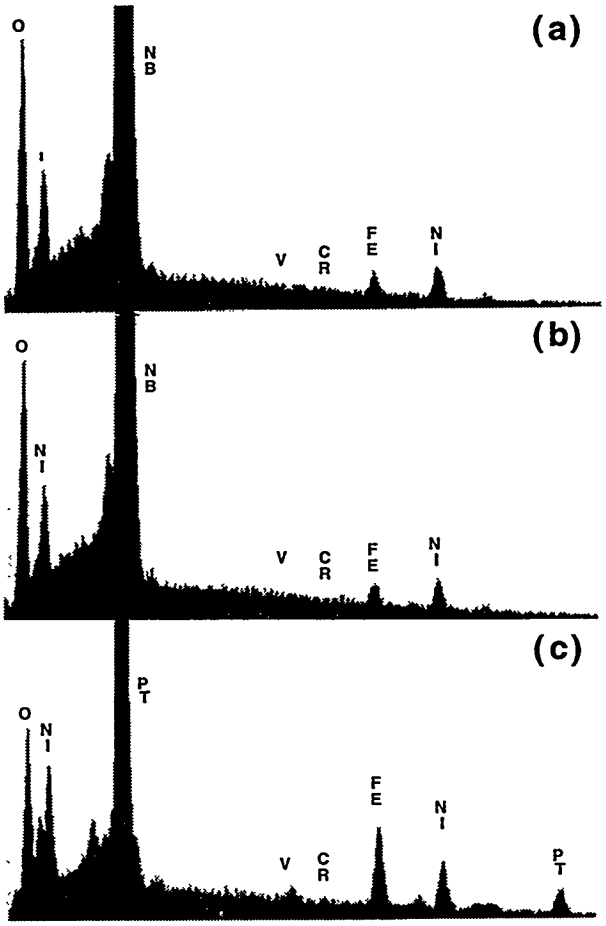

Fig. 5. EDS spectra for Nb, Fe, Cr, Ni, and O on surface of Nb-1Zr specimens after (a) ≈1000 and (b) 3200 h at 170C, and (c) on Pt wire used to suspend specimens in Hastelloy autoclave for ≈3200 h at 230°C

The absence of a time dependence at 230 and 170°C in Figs. 3 and 4 can be attributed primarily to deposition on the specimens of a corrosion product from the Hastelloy autoclave system. The contribution of corrosion-product deposition to weight gain becomes less significant at 300°C (Figs. 1 and 2) because corrosion rates of the Nb-base alloys are higher by one order of magnitude and deposition may be lower in a stainless steel system. Figure 5 shows energy-dispersive-electron spectra (EDS) obtained from the surface of Nb-1Zr specimens after exposure to water at 170°C for ≈1000 and 3200 h, and from a platinum wire used to suspend test specimens in the autoclave for ≈3200 h at 230°C. Heights of the Fe, Ni, and O peaks are similar for all specimens, a qualitative indication that levels of corrosion–product contamination on the surface of all specimens were similar.

Metallographic sections of the specimens were prepared and examined by scanning electron microscopy (SEM). The resulting photomicrographs indicated that corrosion-product films were uniform in thickness across the specimens and tightly adherent to the underlying metal substrates. Cracks were observed in the oxide layer parallel to and just beneath the oxide/water interface in most of the specimens. Cracks in the oxide layer on Nb and Nb-1Zr specimens exposed to water at 300°C for >2000 h penetrated the underlying metal; however, the absence of corrosion on the crack surfaces suggests that the cracks had formed during metallographic preparation of the specimens (Fig. 6). EDS and wavelength–dispersive electron spectroscopy (WDS) were used to determine concentration profiles of (a) Nb, V, and O, and (b) Zr and Mo, respectively, across the specimens. Figure 7 shows line scans for Nb, Mo, Zr, and O in an Nb-5Mo-1Zr specimen after exposure to water at 300°C for ≈3200 h. X-ray diffraction indicated that the corrosion product in this and other specimens is NbO, but Nb_2O_5 also may be present. Alloying elements were incorporated into the corrosion-product layer, as evidenced by no enrichment of Mo and Zr in the Nb-5Mo-1Zr alloy at the metal/oxide interface (Fig. 7). Weight-gain data at 300°C were consistent with measured

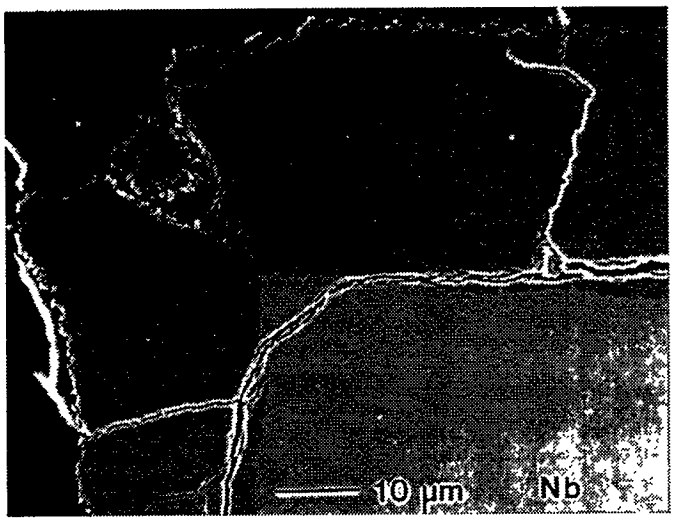

Fig. 6. Cracks formed during specimen preparation in oxide layer on Nb exposed for ≈3000 h at 300°C

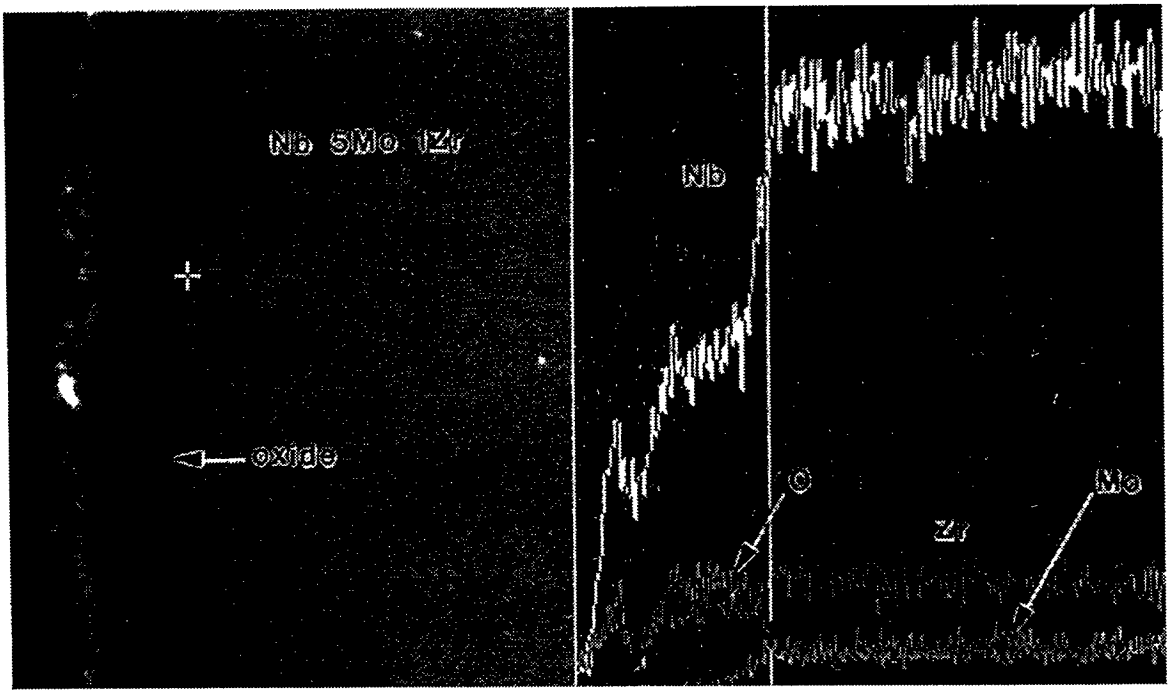

Fig. 7. SEM photomicrograph of cross section of Nb-5Mo-1Zr specimen after ≈3000–h exposure to high-purity deoxygenated water at 300°C (left), and EDS and WDS concentration profiles for Nb, Mo, Zr, and O across the specimen (right)

film thicknesses, based on an NbO corrosion-product layer; this indicates that the corrosion product for the most part was retained on the specimens with minimal dissolution in water under low-flow-rate conditions (4 $mL \cdot min^{-1}$) in these experiments.

Bend tests were performed on the specimens at room temperature to detect changes in ductility after exposure to water. The results were characterized in terms of a fracture index (FI) that qualitatively indicates increasing degrees of embrittlement, i.e., an FI of 1 indicates neither fracture nor surface cracking

at the conclusion of a 180° bend test; 2, fracture was not evident after unfolding of the bend; 3, specimen fractured after unfolding a bend; 4, fracture occurred after 180° of bending; 5, fracture at a ≈90° bend; 6, fracture or cracking was evident prior to the bend test [1].

After a 30-day exposure at 300°C, none of the alloys fractured after a 180° bending and unfolding of a bend (FI = 2); after 60-and 90-day exposures, Nb, Nb-5Mo-1Zr, and Nb-5V-1Zr specimens fractured during 180° bending (FI = 4); and after a 120-day exposure, these materials fractured during a 90° bending (FI = 5). Nb-1Zr specimens fractured during unbending (FI = 3) after 90- and 120-day exposures at 300°C. At 230 and 170°C, weight gains and film thicknesses for the alloys were relatively small and independent of exposure time. Consequently, alloy ductility was independent of exposure time at these temperatures. Nb-1Zr showed the least ductility change, i.e., fracture occurred during unbending of the fold (FI = 3) in specimens exposed to water at 230°C, whereas unbending did not produce fracture in specimens from corrosion tests at 170°C (FI = 2). Nb-5Mo-1Zr and Nb-5V-1Zr specimens exposed to water at 230°C were somewhat less ductile and fractured during 180° bending (FI = 4). Exposures at 170°C led to less embrittlement: the Nb-1Zr, Nb-5V-1Zr, and Nb-5Mo-1Zr specimens exhibited FI values of 2, 3, and 4, respectively, after ≈120 days.

CONCLUSIONS

The Nb-5V-1Zr and Nb-5Mo-1Zr alloys were more resistant to corrosion at 230 and 300°C than were pure Nb and Nb-1Zr. Weight-gain data were consistent with measured thicknesses of NbO on the specimens, which indicates that dissolution of the oxide in water was not significant at a low flow rate in these experiments. At 170°C, corrosion of all materials in deoxygenated high-purity water was relatively low, as indicated by weight-gain data and film thickness measurements. Deposition of corrosion products from the Hastelloy autoclave system contributed significantly to weight gain of the specimens at 170°C. At this temperature, the alloys could survive a 180° bend without fracture at room temperature; this indicates minimal embrittlement due to pickup of hydrogen liberated by the corrosion reaction.

REFERENCES

[1] A. B. Hull, B. A. Loomis, and L. J. Nowicki, *Preliminary Assessment of Aqueous Corrosion of Niobium Alloys for Structural Applications in the ITER Divertor*, Fusion Reactor Materials Semiannual Report for Period Ending March 31, 1991, DOE/ER-0313/10, Oak Ridge National Laboratory, p. 248 (July 1991).

[2] J. A. Todd and I. M. Purdy, *Preliminary Assessment of Candidate Niobium Alloys for the Divertor Structures*, Fusion Reactor Materials Semiannual Report for Period Ending September 30, 1992, DOE/ER-0313/13, Oak Ridge National Laboratory, p. 203 (March 1993).

[3] D. T. Peterson, A. B. Hull, and B. A. Loomis, *Hydrogen Embrittlement of Niobium-Base Alloys for Application in the ITER Divertor*, Fusion Reactor Materials Semiannual Report for Period Ending September 30, 1992, DOE/ER-0313/13, Oak Ridge National Laboratory, p. 182 (March 1993).

[4] I. M. Purdy, *Assessment of Niobium-Base Alloys for Structural Applications in the ITER Divertor,* Fusion Reactor Materials Semiannual Report for Period Ending March 31, 1993, DOE/ER-0313/14, Oak Ridge National Laboratory, p. 294 (July 1993).

ACKNOWLEDGMENTS

B. Tani of the Argonne Analytical Chemistry Laboratory performed X-ray diffraction studies on the oxide films. D. L. Rink obtained the EDS and WDS spectra for the specimens.

5.0 AUSTENITIC STAINLESS STEELS

EFFECTS OF LOW TEMPERATURE NEUTRON IRRADIATION ON DEFORMATION BEHAVIOR OF AUSTENITIC STAINLESS STEELS--J. E. Pawel, A. F. Rowcliffe, D. J. Alexander, M. L. Grossbeck (Oak Ridge National Laboratory), and K. Shiba (Japan Atomic Energy Research Institute)

Presented at the Seventh International Conference on Fusion Reactor Materials, Obninsk, Russia, September 25-29, 1995, and to be published in the Journal of Nuclear Materials, 1996

Extended Abstract

An austenitic stainless steel, designated 316LN-IG, has been chosen for the first wall/shield (FW/S) structure for the International Thermonuclear Experimental Reactor (ITER). The proposed operational temperature range for the structure (100 to 250°C) is below the temperature regimes for void swelling (400-600°C) and for helium embrittlement (500-700°C). However, the proposed neutron dose is such that large changes in yield strength, deformation mode, and strain hardening capacity could be encountered which could significantly affect fracture properties. Definition of the irradiation regimes in which this phenomenon occurs is essential to the establishment of design rules to protect against various modes of failure [1].

Two experiments have been conducted to quantify the effects of neutron irradiation on the deformation and fracture behavior of solution annealed austenitic stainless steels irradiated to doses ranging from 3 to 19 dpa at temperatures from 60 to 400°C. In both experiments the thermal to fast neutron flux ratio was such that the helium generation rate was within the range expected for the ITER first wall and shield, about 10-20 appm He/dpa. Alloys in the study included the European Reference Heat (ERH) which meets the specification for 316LN-IG, J316 and 316F, both Japanese grades of 316 steel, and JPCA, which is a titanium-stabilized austenitic steel.

Large changes in yield strength, deformation mode, strain to failure, and strain hardening capacity were seen in the irradiation experiments described here. For all alloys, yield strength increases rapidly with dose in the 60-300°C regime. For the same dose, a maximum increase in yield strength in the 60-400°C temperature regime is seen after irradiation to 330°C.

Radiation hardening is accompanied by changes in the flow properties with the appearance of an initial yield drop and a significant reduction in strain hardening capacity. The magnitude of the changes is dependent upon both neutron dose and irradiation temperature. Following irradiation at 60 to 90°C, the yield strength is greatly increased and the smooth yielding behavior of the unirradiated material is replaced by the appearance of a small yield drop; subsequently, the irradiated material work hardens at a much lower rate than in the unirradiated condition. The total elongation is progressively reduced with increasing dose. In the range 200 to 250°C, the work hardening rate is decreased still further. Following the yield drop, the work hardening rate is not sufficient to raise the engineering stress above the yield point. Total elongation remains high at 15 to 20%. At around 330°C, a significantly different mode of deformation is observed. Following the yield drop, the J316 stainless steel does not undergo strain hardening and the applied load falls rapidly with failure occurring after only 3 to 4% total elongation.

Each of these stainless steels in the annealed condition had very high values of toughness (K_J > 300 MPa$\sqrt{m}$). Irradiation of ERH at ~90°C to 3 dpa produced a small reduction in K_J. Although irradiation at ~250°C produced a significantly larger decrease, toughness values remained high, in the range 220-280 MPa$\sqrt{m}$. In all tests conducted on the irradiated ERH, the tearing modulus, T_M, which characterizes resistance to crack growth, remained high. The other two steels (J316 and JPCA) also exhibited high values of fracture toughness, a greater reduction in K_J following irradiation at 250°C as compared to 90°C, and a tendency for K_J to decrease with increasing test temperature.

1. G. E. Lucas, M. C. Billone, J. E. Pawel, and M. L. Hamilton, to be published in J. Nucl. Mater.

FRACTURE TOUGHNESS OF IRRADIATED CANDIDATE MATERIALS FOR ITER FIRST WALL/BLANKET STRUCTURES: SUMMARY REPORT

D. J. Alexander, J. E. Pawel, M. L. Grossbeck, and A. F. Rowcliffe, Oak Ridge National Laboratory, Oak Ridge, TN 37831-6151, and K. Shiba, Japan Atomic Energy Research Institute, Tokai-Mura, Japan

OBJECTIVE

The purpose of this work was to determine the effect of irradiation at low temperatures (less than 300°C) and to damage levels of about 3 dpa on the mechanical properties, in particular the fracture toughness, of candidate materials for ITER first wall/blanket structures.

SUMMARY

Disk compact specimens of candidate materials for first wall/blanket structures in ITER have been irradiated to damage levels of about 3 dpa at nominal irradiation temperatures of either 90 or 250°C. These specimens have been tested over a temperature range from 20 to 250°C to determine J-integral values and tearing moduli. The results show that irradiation at these temperatures reduces the fracture toughness of austenitic stainless steels, but the toughness remains quite high. The toughness decreases as the test temperature increases. Irradiation at 250°C is more damaging than at 90°C, causing larger decreases in the fracture toughness. The ferritic-martensitic steels HT-9 and F82H show significantly greater reductions in fracture toughness than the austenitic stainless steels.

PROGRESS AND STATUS

Introduction

The fracture toughnesses of candidate materials for first wall/blanket structure applications in the International Thermonuclear Experimental Reactor (ITER) have been evaluated at Oak Ridge National Laboratory (ORNL). A variety of austenitic stainless steels have been examined, as well as several additional materials. Specimens were fabricated from material in several different conditions, including annealed or cold worked, as well as weldments. These specimens have been irradiated in the High Flux Isotope Reactor (HFIR) at ORNL. Three capsules were designed, fabricated, and irradiated to dose levels of approximately 3 dpa; this approaches the expected accumulated dose at the end of the Basic Performance Phase of operation of ITER. The helium concentration generated as a result of transmutation of nickel was about 50 appm; this is in the range expected for the ITER first wall blanket and shield structure after a neutron exposure of about 3 dpa. These capsules were designed for irradiation temperatures of either 60 to 125°C (capsules HFIR-JP-18 and -19) or 250 to 300°C (HFIR-JP-17) [1-3]. These temperatures covered the expected range of operating temperatures for stainless steel components in different ITER designs. Some of the results of earlier testing have already been reported [4-6]. This report presents the final results for all of the fracture toughness tests, using the best available tensile data for these final analyses.

Experimental Procedure

Four major alloy types were included in this experiment: American and Japanese type 316 steels (designated US316 and J316, respectively), a European type 316L steel (EC316L), and the JPCA alloy. The compositions of the alloys are given in Table 1. Specimens were in solution annealed (SA), cold-worked (CW), or welded conditions. The J316 material was also tested after a thermomechanical treatment in which it was strained, aged, and recrystallized (SAR). There were a total of 12 variants of the austenitic materials in composition and thermomechanical treatment. The EC316L was welded using 16-8-2 filler metal (see Table 1) and gas tungsten arc (GTA) welding with argon cover gas. Both the plate and the filler wire were provided by Joint Research Centre-Ispra from the European Fusion Stockpile. The JPCA and J316 plate material were supplied by the Japan Atomic Energy Research Institute. The JPCA specimens were welded with filler wire with a composition similar

to the base metal (see Table 1) for both the GTA welding. The US316 material was an air-melted heat from the U.S. fusion program, reference heat X15893. Two ferritic-martensitic steels were also included in this experiment, HT-9 and F82H.

A small disk compact specimen 12.5 mm in diameter was selected for the fracture toughness experiments. The techniques developed for generating the J-integral-resistance (J-R) curve using either unloading compliance (UC) or potential drop (PD) to monitor crack extension are described elsewhere [7-9]. The disk compact specimens [designated DC(T)] were 12.5 mm in diameter by 4.63 mm thick. All specimens were fabricated from the middle of the thickness of the parent plates of material, with the notch oriented so that crack growth would occur parallel to the rolling direction (T-L orientation). The specimens were fatigue precracked at room temperature to a crack length to specimen width ratio (a/W) of roughly 0.5 and then side grooved 10% of their thickness on each side, prior to irradiation.

Tests were conducted in general accordance with American Society for Testing and Materials standards E 813-89, Standard Test Method for J_{Ic}, A Measure of Fracture Toughness, and E 1152-87, Standard Test Method for Determining J-R Curves. The equations in E 1152-87 were used for the J calculations. The specimens were tested with a computer-controlled testing and data acquisition system. Tests in the laboratory used an 89-kN capacity servohydraulic test machine. In the hot cell, a 445-kN capacity servohydraulic testing machine with an 22-kN load cell was used. All tests were run in strain control. The displacements were measured with an "outboard" clip gage that seated in grooves machined on the outer edge of the specimen along the load line [7,8]. This arrangement provided very good load-displacement data and so the UC technique was used for all tests. Test temperatures from 90 to 250°C were maintained within ±2°C of the desired temperature with a split-box furnace that enclosed the specimen and the grips during the test. Temperature was monitored throughout the testing with a thermocouple that was held in contact with the specimen by a spring-loaded clip. Tensile data from specimens included in the capsules were used for calculations in the J-R analyses [10]. Estimated values were taken from literature data when necessary.

After testing, the specimens were heat tinted to mark the crack extension. The initial and final crack lengths for the unirradiated specimens were measured with an optical measuring microscope. For the irradiated specimens, photographs of the fracture surfaces were fastened to a digitizing tablet to measure the crack lengths.

Materials with very high toughness and low yield strength, such as the annealed austenitic stainless steels, proved to be more difficult to test than material with lower toughness such as HT-9. The soft, tough materials showed enormous crack-tip blunting before stable crack growth began. This resulted in gross changes in the specimen geometry, and so the crack length predictions were not very accurate. The J-R curve was much steeper than the calculated blunting line. In these cases, the data were used to calculate a blunting line. A straight line was fit by eye through the initial portion of the data points, and a second line was drawn parallel to the first but offset by an amount corresponding to a crack extension of 0.2 mm following ASTM E 813-89. The candidate toughness value J_Q was then determined from the intersection of the data with this offset line. In cases where the data rose very steeply, the test was terminated before there was enough crack growth to cross the second exclusion line (drawn corresponding to a crack extension of 1.5 mm as defined in the ASTM E 813-89). As a result, no tearing modulus value could be calculated. Materials with lower toughness, such as the cold-worked austenitic stainless steels, behaved in a much more conventional manner. For these materials, the data followed the calculated blunting line quite closely, so no additional construction was required. These specimens also showed very good agreement between the measured and predicted final crack lengths.

Results and Discussion

The results of the testing are given in Tables 2 to 6. These tables also includes the tensile values used in the analyses. The tensile data for the specimens included in these experiments are given in Table 7. The toughness of the austenitic steels is very high. In general, the toughness decreases as the test temperature increases, but remains very high. An extended discussion of these results and a comparison to literature data is presented elsewhere [6].

Both before and after irradiation, the fracture toughnesses of the solution annealed materials are very high (K_J> 150 MPa√m) in the test temperature range. The toughness decreases slightly as the temperature increases, but remains very high, even after irradiation and testing at 250°C. Irradiation at 250°C causes a greater decrease in the toughness than irradiation at 90°C. The range of fracture toughness values of these materials is in the upper range of previously reported data from a variety of steels, reactor environments, and test methods [11-16]. The fracture toughness of the cold-worked material is generally lower than that of the annealed material, typically by about 75 to 100 MPa√m, both before and after irradiation.

The fracture toughness of the ferritic materials are also reduced by these irradiations. The F82H alloy is more resistant to damage than the HT-9 material. Both of these alloys show high toughness at high test temperatures (250°C) with lower toughness at 25°C (Table 6). The HT-9 specimen irradiated at 250°C fractured in a brittle manner when tested at room temperature. The load-displacement trace was linear, and the value of the fracture toughness (31 MPa√m) is so low that it satisfies the specimen thickness validity criteria for plane strain fracture toughness, despite the very small specimen size. The F82H specimen irradiated at 250°C and tested at 25°C also shows a lower toughness than when tested at 250°C, but the load-displacement curve showed considerable nonlinearity and the final fracture, although unstable, occurred at a high toughness level of 156 MPa√m.

There is surprisingly little data for comparison with these results. These stainless steel alloys are very tough, and so the fracture toughness is not usually a concern. Odette and Lucas [11,12], Tavassoli [13], and Boutard [14] have recently surveyed the available data for the effects of low temperature irradiation (< 400°C) on the mechanical properties, including the fracture toughness, of austenitic stainless steels. There is very little data that is directly comparable to the present work, but the overall trend of the data shows that irradiation reduces the fracture toughness, but that it still remains high, in agreement with the present results.

A trend line of toughness vs irradiation dose for austenitic stainless steels is shown in Fig. 1, adapted from the review article by Lucas [15]. This represents data for a variety of wrought materials irradiated at temperatures from 290 to 430°C. After a rapid initial decrease, the minimum toughness values (note that K values are shown) approach 50 MPa√m for doses beyond 10 dpa. Also shown are data from Sindelar et al. [16] for a 1950s vintage type 304 stainless steel irradiated at 100 to 155°C to doses up to 2 dpa. The data from the present work fall into two groups. Results from the higher irradiation temperature (250 to 300°C) are consistent with the published data represented by the trend line which indicates toughness values in the range of 200 to 250 MPa√m for doses up to 3 dpa. For the lower irradiation temperature (60 to 125°C) the reduction in fracture toughness is significantly less with the data falling well above the trend line. This is likely the result of a different microstructural response to irradiation, and a reduced level of irradiation hardening for the same dose as compared to higher temperature irradiation. The data of Sindelar et al. [21] fall well below the present data for low temperature irradiation, likely reflecting the greater sensitivity to irradiation damage of the 1950s vintage weldments of type 304 stainless steel.

It should be noted that most of the J-R data generated with this small disk compact specimen do not satisfy all of the validity requirements of the ASTM standards, and so these data are not valid. ASTM standard E 1152-87, "Standard Test Method for Determining J-R Curves," sets three limits based on the specimen size. The maximum J-integral measurement capacity is given by the smaller of

$$J_{max} = b\sigma_f/20 \quad \text{or} \tag{1}$$

$$J_{max} = B\sigma_f/20 \ , \tag{2}$$

where

b = initial ligament size,
B = specimen thickness, and
σ_f = flow stress (average of yield and ultimate tensile stresses).

If the crack length to specimen width ratio (a/W) is 0.5, these are identical, as b will equal B for this specimen, in this case. For nearly all of the data, the measured J-integral values greatly exceed this limit. Only the lowest toughness materials have J-integral values low enough to satisfy these conditions. However, there is another even more limiting condition. The maximum allowable crack extension is limited to 0.1b. For an initial a/W value of 0.5, which was intended, the resultant maximum allowable crack extension is only 0.46 mm, well short of the second exclusion line at 1.5 mm of crack extension. If the initial crack length is longer, as was nearly always the case, even less crack extension is allowed. For tough materials, the limit for crack extension will be reached when the J-R curve data are still on the blunting line, and stable tearing has not even begun to occur. Even for lower toughness conditions, only a few of the data points will be valid, and the bulk of the J-R curve is beyond the limit of validity. The values given in Tables 2 to 6 have been generated by using all the data between the first and second exclusion lines to determine the curve fit for calculation of J_Q, even though this data are not valid according to ASTM E 1152-87.

It must be emphasized that the J-R data, despite being invalid according to ASTM E 1152, are not incorrect. The size limitations imposed are conservative, and the J-integral values are quite likely still true measures of the materials' toughness, as long as the limits are not exceeded by too great a margin. The J-R curves are directly applicable to structures of the same thickness as the specimens.

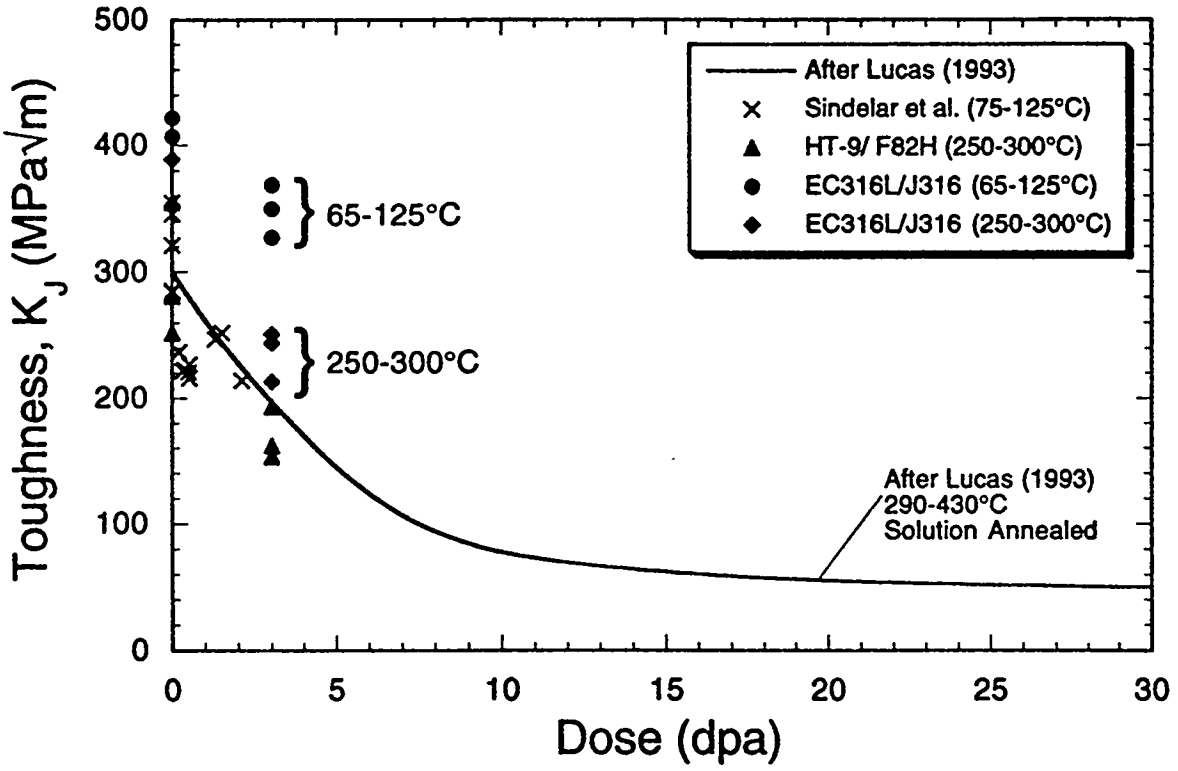

Fig. 1. Trend line of fracture toughness versus irradiation dose in dpa, adapted from Lucas [15], for a range of austenitic stainless steels, irradiation temperatures, and test temperatures. Also shown are data from the present work and the results from Sindelar et al. [16] for comparison.

The J-R curves are of great value in elucidating the materials' responses to irradiation. The J-R curves show how these materials are embrittled by irradiation as a function of irradiation temperature and damage level. They also show which materials are most resistant to embrittlement, and give an indication of the rate at which embrittlement will occur for the present irradiation and material conditions. These are very useful pieces of information for evaluating candidate structural materials for ITER applications.

CONCLUSIONS

Specimens of several austenitic stainless steels and two ferritic-martensitic steels have been irradiated in HFIR to about 3 dpa at nominal irradiation temperatures of 90 or 250°C. For the austenitic stainless steels, irradiation reduces the fracture toughness, and irradiation at 250°C is more damaging than irradiation at 90°C. The fracture toughness decreases with increasing test temperature, for all the austenitic materials. The annealed materials have higher toughnesses than the cold-worked materials. The toughness of the cold-worked materials is still high, with the exception of the US316 material. The welds also have high toughnesses. For the ferritic-martensitic materials, the specimens irradiated at 250°C and tested at room temperature fail in an unstable manner. The F82H has a higher toughness than the HT-9 alloy.

ACKNOWLEDGMENTS

The fracture toughness testing was performed by R. L. Swain. The manuscript was prepared by J. L. Bishop.

REFERENCES

1. A. W. Longest, D. W. Heatherly, K. R. Thoms, and J. E. Corum, "Design and Fabrication of HFIR-MFE-JP Target Irradiation Capsules," *Fusion Reactor Materials Semiannual Progress Report for Period Ending March 31, 1991*, DOE/ER-0313/10, 1991, p. 3.

2. A. W. Longest, D. W. Heatherly, J. E. Wolfe, K. R. Thoms, and J. E. Corum, "Fabrication and Irradiation of HFIR-MFE-JP-17, -18, and -19 Target Irradiation Capsules," *Fusion Reactor Materials Semiannual Progress Report for Period Ending September 30, 1991*, DOE/ER-0313/11, 1992, p. 30.

3. A. W. Longest, D. W. Heatherly, K. R. Thoms, and J. E. Corum, "Fabrication and Irradiation of HFIR-MFE-JP-17, -18, and -19 Target Irradiation Capsules," *Fusion Reactor Materials Semiannual Progress Report for Period Ending March 31, 1992*, DOE/ER-0313/12, 1992, p. 24.

4. D. J. Alexander, J. E. Pawel, M. L. Grossbeck, and A. F. Rowcliffe, "Fracture Toughness of Irradiated Candidate Materials for ITER First Wall/Blanket Structures: Preliminary Results," *Fusion Reactor Materials Semiannual Progress Report for Period Ending March 31, 1992*, DOE/ER-0313/14, 1993, p. 277.

5. J. E. Pawel, D. J. Alexander, M. L. Grossbeck, A. W. Longest, A. F. Rowcliffe, G. E. Lucas, S. Jitsukawa, A. Hishinuma, and K. Shiba, "Fracture Toughness of Candidate Materials for ITER First Wall, Blanket, and Shield Structures," *Fusion Reactor Materials Semiannual Progress Report for Period Ending September 30, 1993*, DOE/ER-0313/15, 1992, p. 173.

6. D. J. Alexander, J. E. Pawel, M. L. Grossbeck, A. F. Rowcliffe, and K. Shiba, "Fracture Toughness of Irradiated Candidate Materials for ITER First Wall/Blanket Structures," *Effects of Radiation on Materials: 17th Volume, ASTM STP 1270*, D. S. Gelles, R. K. Nanstad, A. S. Kumar, and E. A. Little, Editors, American Society for Testing and Materials, Philadelphia, 1996, in press.

7. D. J. Alexander, "Fracture Toughness Measurements with Subsize Disk Compact Specimens," *Fusion Reactor Materials Semiannual Progress Report for Period Ending March 31, 1992*, DOE/ER-0313/12, 1992, p. 35.

8. D. J. Alexander, "Fracture Toughness Measurements with Subsize Disk Compact Specimens," in *Small Specimen Test Techniques Applied to Nuclear Reactor Vessel Thermal Annealing and Plant Life Extension, ASTM STP 1204*, W. R. Corwin, F. M. Haggag, and W. L. Server, Editors, American Society for Testing and Materials, Philadelphia, 1993, p. 130.

9. C. Elliot, M. Enmark, G. E. Lucas, and G. R. Odette, "Development of Disc Compact Specimens and Test Techniques for HFIR Irradiations," *Fusion Reactor Materials Semiannual Progress Report for Period Ending September 30, 1990*, DOE/ER-0313/9, 1991, p. 7.

10. J. E. Pawel, unpublished research, Oak Ridge National Laboratory, 1994.

11. G. R. Odette and G. E. Lucas, *J. Nucl. Mater.*, Vol. 179-181, 1991, p. 572.

12. G. R. Odette and G. E. Lucas, *J. Nucl. Mater.*, Vol. 191-194, 1992, p. 50.

13. A. A. Tavassoli, "Assessment of Austenitic Stainless Steels," N.T. SRMA 94-2061, F.A. 3591-ITER, CEA, CEN-Saclay, 91191 Gif Sur Yvette, France, June 1994.

14. J. L. Boutard, *J. Nucl. Mater.*, Vol. 179-81, 1991, p. 1179.

15. G. E. Lucas, *J. Nucl. Mater.*, Vol. 206, 1993, p. 287.

16. R. L. Sindelar, G. R. Caskey, J. K. Thomas, J. R. Hawthorne, A.. L. Hiser, R. A. Lott, J. A. Begley, and R. P. Shogan, "Mechanical Properties of 195's Vintage Type 304 Stainless Steel Weldment Components, After Low Temperature Irradiation," in *Effects of Radiation on Materials: 16th International Symposium, ASTM STP 1175*, A. S. Kumar, D. S. Gelles, R. K. Nanstad, and E. A. Little, Editors, American Society for Testing and Materials, Philadelphia, 1993, p. 714.

Table 1. Specimen alloy compositions and processing

Alloy	Composition (wt %)											
	Fe	Ni	Cr	Ti	Mo	Mn	Si	C	N	V	W	Ta
JPCA	Bal	15.95	14.3	0.21	2.4	1.6	0.54	0.064	0.003	--	--	--
US316	Bal	12.4	17.3	--	2.1	1.7	0.67	0.061	--	--	--	--
EC316L	Bal	12.3	17.4	--	2.3	1.8	0.46	0.024	0.06	--	--	--
J316	Bal	13.95	16.77	--	2.31	0.23	0.04	0.038	0.011	--	--	--
16-8-2 weld wire	Bal	8.98	16.28	--	2.16	1.82	0.060	0.036	0.029	--	--	--
JPCA weld wire	Bal	16.06	14.39	0.23	2.44	1.77	0.35	0.057	0.0095	--	--	--
HT-9	Bal	0.51	12.1	--	1.04	0.57	0.17	0.20	0.027	0.28	0.45	--
F82H	Bal	0.05	7.65	--	--	0.49	0.09	0.093	0.0018	0.18	1.98	0.038

JPCA Annealed: Solution annealed (1120°C/1 h/water quench).
JPCA Cold Worked: Annealed + cold worked 20%.
J316 Annealed: Solution annealed (1060°C/15 min/water quench).
J316 Cold Worked: Annealed + cold worked 20%.
J316 Strained, Aged, Recrystallized: 1150°C/1 h + 60% cold work + 650°C/15 h +800°C/15 h.
EC316L Annealed: Solution annealed.
US316 Annealed: Cold worked 50% + annealed (1050°C/1 h).
US316 Cold Worked: Annealed + 20% cold work.
HT-9: 1050°C/1 h/air cooled + 780°C/2.5 h/air cooled.
F82H: 1040°C/0.5 h + 740°C/1.5 h/air cooled.

Table 2. Fracture toughness and tensile properties of EC316L

Material	Specimen	Irradiation temperature (°C)	Test temperature (°C)	J_Q (kJ/m²)	K_J[a] (MPa√m)	T	σ_y (MPa)	σ_u (MPa)	E (GPa)
EC316L Annealed	FA14	Unirradiated	22	847	404	NA	296[b]	579	193
	FA22	Unirradiated	100	889	407	NA	283[b]	517	186
	FA5	Unirradiated	200	697	353	NA	214[b]	448	179
EC316L Annealed	FA16	90	25	781	388	107	625	700	193
	FA3	90	25	800	393	93	625	700	193
	FA21	90	25	634	350	135	625	700	193
	FA6	90	100	671	353	129	607[b]	676	186
	FA11	90	100	574	327	92	607[b]	676	186
	FA17	90	200	548	314	221	525	600	179
EC316L Annealed	FA2	250	25	417	284	39	850	860	193
	FA10	250	100	387	268	38	800	810	186
	FA9	250	250	257	214	47	741[b]	748	179
	FA18	250	250	353	252	42	741[b]	748	179
EC316L PERP[c]	FS4	Unirradiated	90	831	393	NA	283	517	186
EC316L PERP[c]	FS1	90	90	512	309	102	607	676	186
EC316L Weld	FB3	Unirradiated	22	772	386	NA	310[b]	614	193
	FB14	Unirradiated	90	710	363	NA	221[b]	476	186
	FB17	Unirradiated	250	610	331	NA	241[b]	448	179
EC316L Weld	FB4	90	90	341	252	109	627[b]	703	186
EC316L Weld	FB5	250	250	160	170	29	741	748	179
	FB13	250	250	152	165	23	741	748	179

[a] $K_J^2 = J_Q E$.
[b] Data from tensile test from these experiments.
[c] PERP = Specimens oriented so that crack growth was perpendicular to the rolling direction.

Table 3. Fracture toughness and tensile properties of J316

Material	Specimen	Irradiation temperature (°C)	Test temperature (°C)	J_Q (kJ/m²)	K_J[a] (MPa√m)	T	σ_y (MPa)	σ_u (MPa)	E (GPa)
J316 Annealed	FC8	Unirradiated	22	790	391	NA	100	450	193
	FC24	Unirradiated	90	959	423	NA	90[b]	427	186
	FC21	Unirradiated	250	843	388	NA	62[b]	372	179
J316 Annealed	FC12	90	90	737	370	100	689[b]	696	186
	FC16	90	250	620	333	99	600	625	179
J316 Annealed	FC10	250	90	453	291	59	825	850	186
	FC2	250	250	333	244	55	750	775	179
J316 SAR[c]	FM5	Unirradiated	22	595	339	103	525	650	193
	FM8	Unirradiated	90	548	319	63	517[b]	634	186
	FM9	Unirradiated	250	392	265	107	455	559	179
J316 SAR[c]	FM11	90	90	263	221	36	690	696	186
J316 SAR[c]	FM2	250	250	170	175	28	750	775	179
J316 CW[d]	FD7	Unirradiated	22	870	410	71	717[b]	765	193
	FD5	Unirradiated	90	591	332	101	593[b]	641	186
	FD1	Unirradiated	250	328	243	89	572[b]	607	179
J316 CW[d]	FD12	90	90	479	299	46	827[b]	841	186
	FD8	90	250	302	233	40	725	750	179
J316 CW[d]	FD10	250	90	271	225	40	889[b]	938	186
	FD11	250	250	138	157	18	821[b]	827	179

[a] $K_J^2 = J_Q E$.
[b] Data from tensile test from this experiment.
[c] SAR = Strained, aged, and recrystallized.
[d] CW = Cold worked 20%.

Table 4. Fracture toughness and tensile properties of JPCA

Material	Specimen	Irradiation temperature (°C)	Test temperature (°C)	J_Q (kJ/m²)	K_J[a] (MPa√m)	T	σ_y (MPa)	σ_u (MPa)	E (GPa)
JPCA Annealed	FF10	Unirradiated	22	616	345	NA	331[b]	600	193
	FF13	Unirradiated	100	706	363	158	269[b]	510	186
	FF20	Unirradiated	200	498	299	82	269[b]	483	179
JPCA Annealed	FF6	90	25	349	260	23	750	770	193
	FF5	90	25	355	262	41	750	770	193
	FF16	90	100	310	240	34	717[b]	738	186
	FF15	90	100	312	241	31	717[b]	738	186
	FF2	90	200	225	201	46	614[b]	634	179
JPCA Annealed	FF3	250	25	271	229	18	900	950	193
	FF11	250	100	133	157	13	862[b]	910	186
	FF18	250	250	123	148	14	779[b]	827	179
JPCA EBW[c]	FR7	Unirradiated	250	619	333	NA	269	483	179
JPCA EBW[c]	FR11	90	90	885	406	101	717	738	186
JPCA EBW[c]	FR12	250	250	315	238	52	779	827	179
JPCA CW[d]	FE6	Unirradiated	22	365	266	45	625	650	193
	FE3	Unirradiated	90	306	239	55	600[b]	627	186
	FE1	Unirradiated	250	181	180	82	524[b]	572	179
JPCA CW[d]	FE8	90	90	167	176	24	931[b]	952	186
JPCA CW[d]	FE7	250	250	124	149	8	868[b]	896	179
JPCA Weld	FG10	Unirradiated	22	655	356	NA	331	600	193
	FG13	Unirradiated	90	1020	436	NA	269	510	186
	FG1	Unirradiated	250	959	415	NA	269	483	179
JPCA Weld	FG8	90	90	316	242	46	717	738	186
JPCA Weld	FG12	250	250	234	205	27	779	827	179

[a] $K_J^2 = J_Q E$.
[b] Data from tensile test from these experiments.
[c] EBW = Electron beam weld.
[d] CW = Cold worked 20%.

Table 5. Fracture toughness and tensile properties of US316

Material	Specimen	Irradiation temperature (°C)	Test temperature (°C)	J_Q (kJ/m²)	K_J[a] (MPa√m)	T	σ_y (MPa)	σ_u (MPa)	E (GPa)
US316 Annealed	FK16	Unirradiated	22	234	213	79	262[b]	607	193
	FK6	Unirradiated	90	235	209	76	186[b]	510	186
	FK8	Unirradiated	250	213	195	88	152[b]	462	179
US316 Annealed	FK7	90	90	156	171	17	500	550	186
US316 Annealed	FK10	250	250	36	80	6	650	700	179
US316 CW[c]	FL13	Unirradiated	22	35	82	4	683[b]	793	193
	FL8	Unirradiated	90	34	80	0	662[b]	724	186
	FL9	Unirradiated	250	28	71	-	572[b]	648	179
US316 CW[c]	FL15	90	90	22	64	0	848[b]	862	186
US316 CW[c]	FL5	250	250	15	52	0	825	850	179

[a] $K_J^2 = J_Q E$.
[b] Data from tensile test from these experiments.
[c] CW = Cold worked 20%.

Table 6. Fracture toughness and tensile properties of ferritic-martensitic alloys

Material	Specimen	Irradiation temperature (°C)	Test temperature (°C)	J_Q (kJ/m²)	K_J[a] (MPa√m)	T	σ_y (MPa)	σ_u (MPa)	E (GPa)
HT-9	FH11	Unirradiated	22	484	316	104	476[b]	696	207
	FH3	Unirradiated	90	470	307	91	414[b]	621	200
	FH4	Unirradiated	250	415	283	131	427[b]	627	193
HT-9	FH1	90	90	283	238	41	903[b]	917	200
HT-9	FH5	250	25	5	31	-	950	1000	207
	FH6	250	250	140	164	17	876[b]	931	193
F82H	FI3	Unirradiated	250	334	254	122	448[b]	531	193
F82H	FI4	250	25	117	156	-	950	975	207
	FI1	250	250	197	195	22	855[b]	855	193

[a]$K_J^2 = J_Q E$.
[b]Data from tensile specimen from these experiments.

Table 7. Tensile Properties of Irradiated and Unirradiated Materials.

Alloy	Specimen I.D.	Dose (dpa)	Helium (appm)	Irrad. Temp (°C)	Test Temp. (°C)	YS (MPa)	UTS (MPa)	Eu (%)	Et (%)	Strain to Necking (%)
JPCA	FF4T	0	0	-	25	331	600	48.8	60.3	51.5
SA	FF3T	0	0	-	90	269	510	40.8	50.2	41.8
	FF6T	0	0	-	250	269	483	32.8	40.1	33.2
	FF7T	2.9	64	83-101	90	717	738	19.3	32.3	23.3
	FF9T	2.9	64	83-101	250	614	634	15.7	22.7	16.7
	FF2T	2.9	69	250-300	250	779	827	2.8	11.8	3.0
	FF5T	2.9	69	250-300	90	862	910	4.9	17.2	7.3
JPCA	FE16T	0	0	-	90	600	627	3.0	17.1	4.4
CW	FE15T	0	0	-	250	524	572	2.5	13.6	3.2
	FE17T	2.9	64	83-101	90	931	952	0.8	10.5	0.9
	FE18T	2.9	69	250-300	250	869	896	1.5	10.9	2.1
	FE19T	2.9	69	250-300	90	979	1020	2.5	15.7	3.3
J316	FC27	0	0	-	90	90	427	69.3	83.5	73.7
SA	FC30	0	0	-	250	62	372	51.6	62.4	53.3
	FC28	2.9	64	83-101	90	690	696	0.3	38.7	29.0
J316	FD2T	0	0	-	25	717	765	2.7	21.0	6.6
CW	FD7T	0	0	-	90	593	641	4.7	23.5	11.0
	FD1T	0	0	-	250	572	607	1.5	16.2	1.8
	FD6T	2.9	64	83-101	90	827	841	0.5	15.7	0.5
	FD3T	2.9	69	250-300	250	821	827	0.3	10.5	0.3
	FD5T	2.9	69	250-300	90	889	938	1.2	13.7	1.4
EU316L	FA27T	0	0	-	25	298	582	59.3	68.5	62.0
SA	FA21T	0	0	-	90	285	516	48.3	57.2	50.2
	FA26T	0	0	-	250	214	451	39.5	51.3	40.8
	FA23T	2.9	64	83-101	90	610	674	34.7	45.0	37.7
	FA24T	2.9	64	83-101	90	605	677	34.7	46.1	37.0
	FA22T	2.9	69	250-300	250	760	764	0.4	18.8	11.7
	FA25T	2.9	69	250-300	250	724	735	0.6	20.8	12.7
EU316L	FB18T	0	0	-	25	308	616	49.6	56.3	50.6
WELD	FB17T	0	0	-	90	224	473	38.3	44.8	39.0
	FB22T	0	0	-	250	242	449	26.5	39.3	27.9
	FB19T	2.9	64	83-101	90	625	707	18.8	26.1	20.3
HT-9	FH6T	0	0	-	25	473	695	14.3	24.1	14.3
	FH5T	0	0	-	90	416	622	14.1	23.7	14.1
	FH4T	0	0	-	250	425	624	12.1	20.8	12.1
	FH1T	2.9	2	83-101	90	903	914	0.4	8.7	0.4
	FH2T	2.9	2	250-300	250	875	932	6.2	13.4	6.2
F82H	FI19	0	0	-	25	573	682	5.4	15.5	5.4
	FI18	0	0	-	90	571	660	4.5	15.3	4.5
	FI17	0	0	-	250	507	577	3.2	13.3	3.2
	FI16	0	0	-	250	451	530	3.4	13.3	3.4
	FI13	2.9	30	250-300	250	852	856	0.3	7.8	0.3
	FI14	2.9	30	250-300	90	723	821	8.2	17.7	8.2

MICROSTRUCTURAL OBSERVATION OF HFIR-IRRADIATED AUSTENITIC STAINLESS STEELS INCLUDING WELDS FROM JP9-16 --- T. Sawai, K. Shiba, A. Hishinuma [Japan Atomic Energy Research Institute)

SUMMARY

Austenitic stainless steels, including specimens taken from various electron beam (EB) welds, have been irradiated in HFIR Phase II capsules, JP 9-16. Fifteen specimens irradiated at 300, 400, and 500°C up to 17 dpa are so far examined by a transmission electron microscope (TEM). In 300°C irradiation, cavities were smaller than 2 nm and different specimens showed little difference in cavity microstructure. At 400°C, cavities were larger but still very small (<8 nm). At 500°C, cavity size reached 30 nm in weld metal specimens of JPCA, while cold worked JPCA contained only small (<5 nm) cavities. Inhomogeneous microstructural evolution was observed in weld-metal specimens irradiated at 500°C.

PROGRESS AND STATUS

To evaluate the performance of weld joint of austenitic stainless steels is one of the major objectives of HFIR Phase II irradiation project in JAERI-ORNL collaborative program. Studies on the microstructural evolution of irradiated weld are extremely limited although the complex blanket structure of fusion reactor requires inevitable welding. High voltage electron microscope (HVEM) irradiation has shown appreciable increase of swelling in welded austenitic stainless steels [1]. Swelling was especially high at the weld metal due to segregation. The objective of this study is to reveal the microstructural evolution of welded austenitic stainless steels irradiated by HFIR neutrons.

Table 1. TEM specimens examined.

JP10, position 4. 400 °C 16.7dpa

ID	description	Negative #
AH25	316F SA BM	J19197-J19215 J19413-J19441
PK03	JPCA SA TIG HAZ	J19216-J19253
AA25	316F SA EB WM	J19254-J19279
PJ16	JPCA SA TIG WM	J19280-J19309
AE15	316F SA EB sHAZ	J19310-J19342 J19385-J19412

ID	description	Negative #
AH33	316F SA BM	J19991-J20040***
PJ19	JPCA SA TIG WM	J20041-J20106***
AA33	316F SA EB WM	J20128-J20166

*** Numbers on negatives read J1????, not J2????.

JP11, position 6, 500 °C 17.3dpa

ID	description	Negative #
BN38	JPCA CW BM	J19480-J19519
BL21	JPCA CW EB sHAZ	J19520-19544
HJ22	JPCA SA 10Ti-EB WM	J19546-J19645
BM09	JPCA CW EB J*	J19646-19725

* TEM foil was obtained at WM

JP10, position 6, 400 °C 17.3dpa

ID	description	Negative #
BN25	JPCA CW BM	J19774-J19848
BL13	JPCA CW EB sHAZ	J19849-J19892
BM06	JPCA CW EB J**	J19893-J19940

** TEM foil was obtained at WM

JP10, position 8 300 °C 16.7dpa

abbreviations;
- SA : solution annealed
- CW : cold worked
- EB : electron beam (weld)
- TIG : tungsten inert gas (weld)
- BM : base metal
- WM : weld metal
- HAZ : heat affected zone
- sHAZ : simulated HAZ
- J : joint (fusion line at the disk center)

EXPERIMENTAL

Two kinds of austenitic stainless steels, JPCA and 316F, were welded by electron beam (EB) welding and tungsten inert gas (TIG) welding. TEM specimens obtained from these welds were loaded in capsules JP9 through 16. Details of specimens were summarized elsewhere [2]. Fifteen TEM specimens from two capsules (four container tubes) were examined as the first batch of these experiments. Table 1 shows the list of these specimens. Damage level given in Table 1 is calculated values for type 316 steel (13Ni, 18Cr) [3]. The analysis of obtained micrographs is now going on. Results so far obtained are as follows.

RESULTS AND DISCUSSIONS

300 °C irradiation

Only three specimens at this irradiation condition were examined. They are 316F BM (AH33), 316F SA EB WM(AA33), and JPCA SA TIG WM (PJ19). Differences in microstructural evolution of these specimens are very small. Cavities are very fine (up to 2nm) and the size of Frank loops is less than 25 nm. In weld metal specimens (AA33, PJ19), cellular structure due to solidification was observed but the microstructural evolution at the cell boundary or cell center region showed no difference. Some microstructural features recognized as tiny black dots in a bright field image showed triangles in a weak beam dark field image with B = <110>. This suggests these features are stacking fault tetrahedra (SFT).

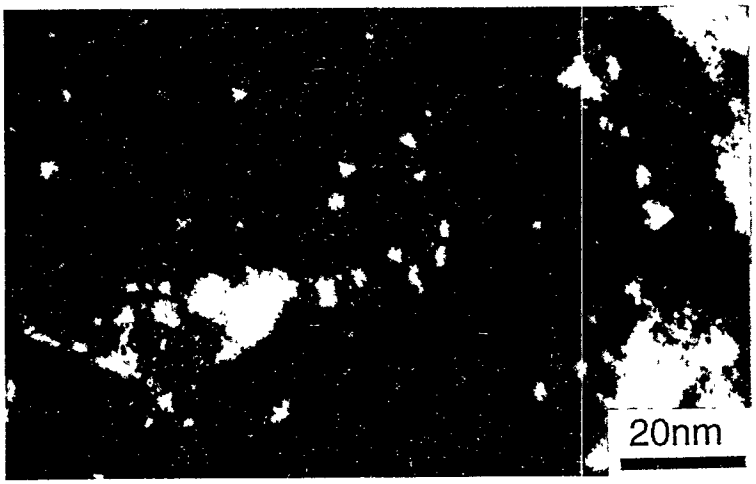

Fig. 1. Stacking fault tetrahedra observed in a JPCA SA TIG WM specimen irradiated in HFIR at 300°C up to 16.9 dpa. This micrograph was taken with B = <110>.

400°C irradiation

Eight specimens were examined at this irradiation condition. For detail, see Table 1. Larger cavities were observed at this irradiation condition compared to that of 300°C. Cavities in 316F specimens are almost the same size (4 nm), but JPCA specimen showed wider size distribution of cavities up to 8nm. This coincides with the results of immersion densitometry where 316F showed less swelling than JPCA [4]. Frank loops were also larger than those of 300°C irradiation. Their size is up to 40 nm. SFTs were also observed. Their size is up to 4 nm (almost similar to 300°C irradiation), and the number density, which is very hard to measure, seems to be less than that of 300°C irradiation.

In specimens obtained from weld metal (AA25, BM06, PJ16), cellular structure due to solidification was observed but the microstructural evolution at the cell boundary or cell core area showed no difference.

500°C irradiation

Only JPCA specimens were observed in this irradiation condition. A cold worked specimen (BN38) showed a good swelling resistance. Its cavity size is less than 5 nm. On the other hand, heat treated cold worked specimen (CW sHAZ, BL21) showed larger swelling. The cavity size is up to 20 nm. The CW EB J specimen (BM09) had its electron transparent foil at the weld metal. This specimen can be regarded as the weld metal specimen of JPCA EB welding. Another weld metal specimen observed is obtained from Ti-foil-insert welding [5]. The Ti concentration at the weld metal is 0.28 wt% [2]. In both weld metal specimens, cellular structure was observed and the microstructural evolution was quite different at the cell boundary and at the cell center region. At the cell boundary, size of cavities are up to 5 nm, showing good swelling resistance. Cavities at the cell center region included much larger ones. The cavity size reached 30 nm and showed bimodal distribution. As for Frank loops, the size and number density were larger at the cell center region than at the cell boundary.

In HFIR phase I experiments of JAERI-ORNL collaboration, the difference in the swelling resistance between solution annealed condition and cold worked condition or 316R and JPCA was clearly observed only at 500°C and higher temperatures [6-8]. In present experiment, different cavity microstructure in various specimens was clearly observed only at 500°C, either. Cavities observed in specimens irradiated at 300 and 400°C were helium bubbles.

Inhomogeneous cavity formation in weld metal was first reported by a HVEM irradiation experiment [1]. A typical cellular microstructure of weld metal is shown in Fig. 2 [1]. HVEM irradiation of weld metal of Type 316 stainless steel containing 0.08 Ti led inhomogeneous cavity formation and growth (Fig. 3 [1]). Present results of weld metals irradiated at 500°C are also shown in Fig. 4. These micrographs were quantified and the results are shown in Fig. 5.

Fig. 2. A typical cellular structure of weld metal [1]. This specimen was taken from EB-welded JPCA.

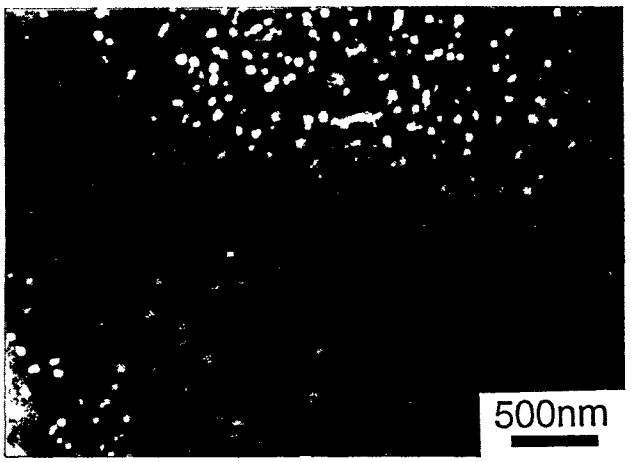

Fig. 3. Inhomogeneous cavity formation and growth in HVEM-irradiated weld metal [1]. This specimen was taken from EB-welded Type 316 stainless steel containing 0.08 Ti.

As shown in Fig. 3, cavity number density is much smaller at the cell boundary than at the cell center region in HVEM-irradiated weld metal. Enriched Ti at the cell boundary reduced the number density of cavities by trapping oxygen and/or nitrogen which will help the cavity nucleation. Cavity growth is also suppressed at the cell boundary. Enriched Ti also reduces the dislocation bias and, therefore, the supply of excess vacancy. In HFIR irradiation, the swelling is larger at the cell center region than at the cell boundary (Fig. 4 and Fig. 5). This result is similar to that of HVEM irradiation. The cavity number density is, however, much larger at the cell boundary than at the cell center region. Enough helium produced in HFIR

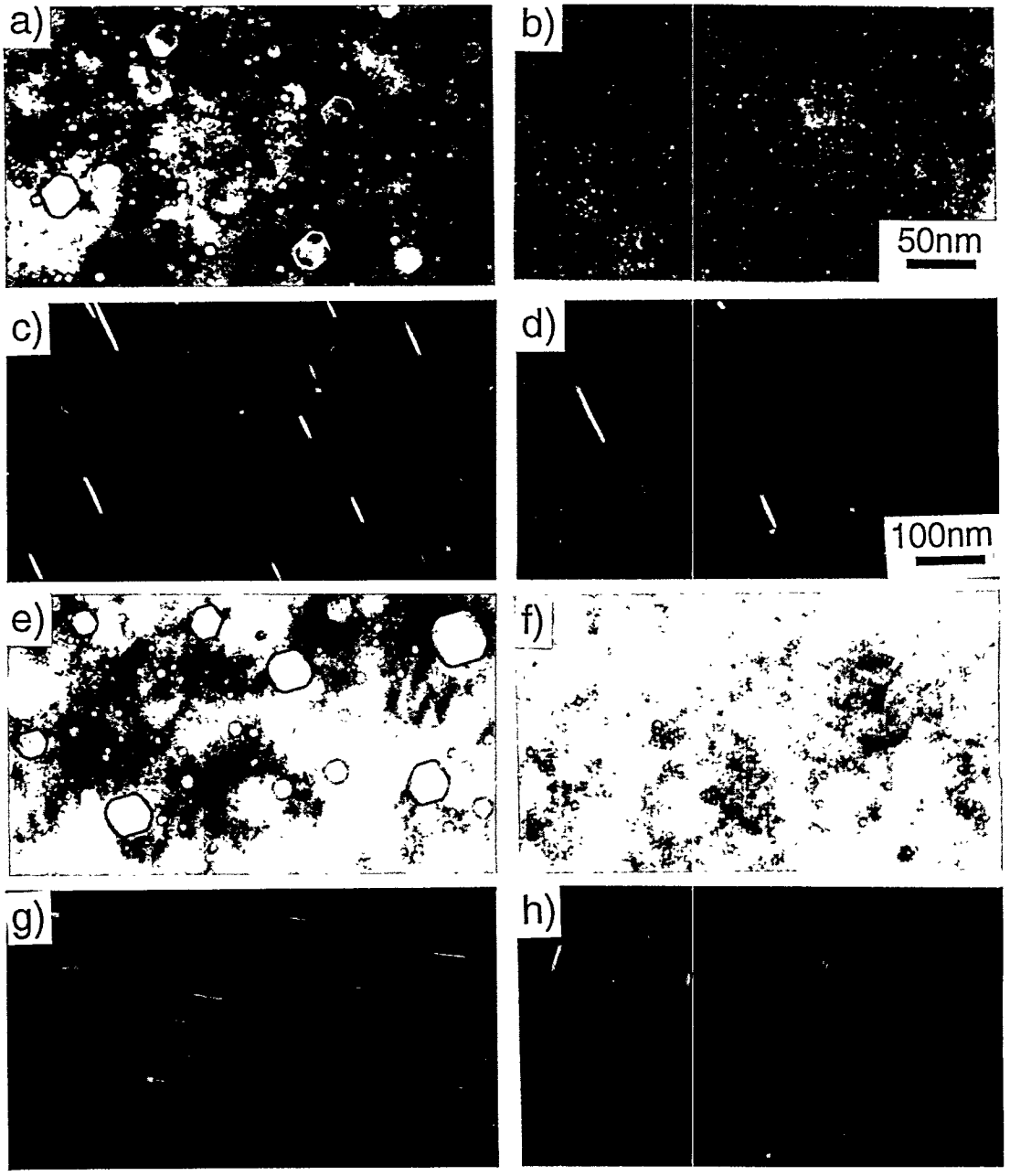

Fig. 4. Microstructure of two JPCA weld metal specimens irradiated at 500°C. Specimens are BM09, EB-welding [(a), (b), (c), (d)], and HJ22, 10micron-Ti-foil insert EB welding [(e), (f), (g), (h)]. Cavities are shown in (a), (b), (e), (f) and Frank loop in (c), (d), (g), and (h). Micrographs were taken at cell center region [(a), (c), (e), (g)], and at cell boundary [(b), (d), (f), (h)].

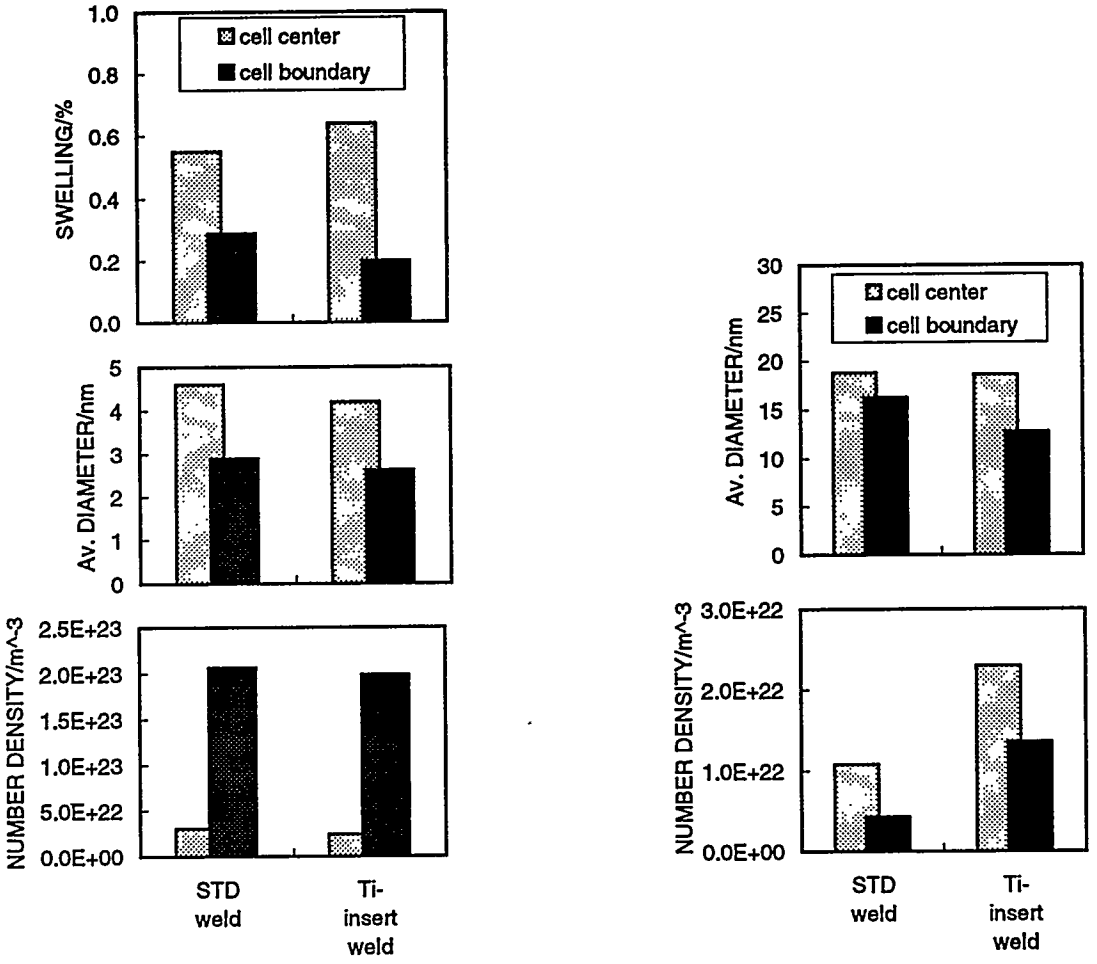

Fig. 5 Cavity and Frank loop data of two JPCA weld metal specimens irradiated at 500°C shown in Fig. 4.

irradiation enhances cavity nucleation. Present results on cavity microstructure at cell boundary and cell center region can be compared with that of 316R and JPCA base metals irradiated in HFIR Phase I capsules. Swelling is 0.25 and 1.09% for JPCA and 316R irradiated at 500°C to 34 dpa in HFIR Phase I capsules. Cavity number density is 1.3×10^{23} and 8.9×10^{21} m^{-3}, respectively. More swelling-resistant JPCA showed higher cavity number density. In HFIR neutron irradiation, swelling is suppressed by suppressing cavity growth, rather than suppressing cavity number density. Although the detailed microstructural evolution is thus different, swelling is enhanced at the cell center region both in HVEM irradiation and HFIR neutron irradiation.

In case of HFIR 500°C irradiation, solution annealed JPCA contained cavities up to 30 nm at 34 dpa [5]. Present results show that the weld metal specimens of standard and It-insert EB weld of JPCA contained cavities up to 30 nm at cell center region only after 17.3 dpa. This suggests the degradation of swelling resistance in austenitic stainless steel by welding. Present results also show that introduced titanium by Ti-insert EB welding could not prevent this degradation.

FUTURE WORK

Quantification of obtained micrographs will be continued.

REFERENCES

[1] T. Sawai et al., J. Nucl. Mater., 141-143(1986), pp.444-447.
[2] JAERI internal data (JAERI-memo 62-328).
[3] L. R. Greenwood and R. T. Ratner, in this FRM Semiannual Prog. Rep.
[4] JAERI internal data.
[5] T. Sawai et al., J. Nucl. Mater., 155-157(1988), pp861-865.
[6] M. P. Tanaka et al., J. Nucl. Mater., 141-143(1986), pp.943-947.
[7] M. P. Tanaka et al., J. Nucl. Mater., 155-157(1988), pp.801-805.
[8] S. Hamada et al., J. Nucl. Mater., 155-157(1988), pp.838-844.

IRRADIATION CREEP IN AUSTENITIC AND FERRITIC STEELS IRRADIATED IN A TAILORED NEUTRON SPECTRUM TO INDUCE FUSION REACTOR LEVELS OF HELIUM – M. L. Grossbeck and L. T. Gibson (Oak Ridge National Laboratory), and S. Jitsukawa (Japan Atomic Energy Research Institute)

Presented at the Seventh International Conference on Fusion Reactor Materials, Obninsk, Russia, September 25-29, 1995, and to be published in the Journal of Nuclear Materials, 1996

Extended Abstract

Six austenitic stainless steels and two ferritic alloys were irradiated sequentially in two research reactors where the neutron spectrum was tailored to produce a He production rate typical of a fusion device. Irradiation began in the Oak Ridge Research Reactor where an atomic displacement level of 7.4 dpa was achieved and was then transferred to the High Flux Isotope Reactor for the remainder of the irradiation to a total displacement level of 19 dpa. Temperatures of 60 and 330°C are reported on. At 330°C irradiation creep was found to be linear in stress and fluence with rates in the range of $1.7 - 5.5 \times 10^{-4}$% MPa^{-1} dpa^{-1}. Annealed and cold-worked materials exhibited similar creep rates. There is some indication that austenitic alloys with TiC or TiO precipitates had a slightly higher irradiation creep rate than those without. The ferritic alloys HT-9 and Fe-16Cr had irradiation creep rates about 0.5×10^{-4}% MPa^{-1} dpa^{-1}. No meaningful data could be obtained from the tubes irradiated at 60°C because of damage to the tubes.

The irradiation creep rates are provided in Table 1. From the table, it can be seen that there is little difference in the average deformation between 7.4 and 19 dpa. This indicates that the observed creep does not result from the initial microstructural transient. Most differences between the two fluence levels are attributed to errors in measurements, especially with the lower exposure values. It is clear that the ferritic alloys have lower levels of irradiation creep by about a factor of 5 to 6. This is consistent with previous determinations of irradiation creep in this class of alloys. It is also apparent from the table that the alloys containing titanium have a higher irradiation creep rate than the other alloys. Both of these alloys have precipitates of TiC or TiO. It is suggested that the interfacial misfit due to the volume expansion upon formation of the precipitates results in a sink for vacancies. The correspondingly higher concentration of interstitials in the matrix could than give rise to higher levels of irradiation creep as predicted by the SIPA or climb-assisted-glide mechanisms.

Several effects observed in the austenitic alloys are illustrated by the PCA data plotted in Fig. 1. The linear dependence of irradiation creep on stress is clear from the graphs. It as also evident that cold-worked material creeps at the same rate as annealed material. Although creep rate is predicted to be linear in dislocation density, in the sink-dominated regime, the interstitial concentration is inversely proportional to the dislocation density which cancels its effect on irradiation creep.

Table 1. Irradiation Creep Rate for 330°C
Normalized with Respect to Stress and Displacements

Alloy	Creep Rate (% MPa^{-1} dpa^{-1} $\times 10^{-4}$	
	7.4 dpa*	19 dpa*
USPCA 25% CW	23 ± .1	2.7 ± .08
JPCA SA	1.6 ± .7	2.7
J316 20% CW	1.3 ± .1	2.1 ± .4
Fe-13.5 Cr-15 Ni	1.4 ± .7	0.8 ± 2**
Fe-13.5 Cr-35 Ni	3.0 ± .2	3.4 ± .4
Fe-13.5 C4-15 Ni--.18 Ti	5.1 ± .8	5.5 ± .6
Ht-9	0.44 ± .09	0.43 ± .08
Fe-16 Cr	0.8 ± .3	0.5 ± .2

*standard errors in curve fitting only
**scatter in data does not permit an accurate creep rate to be determined

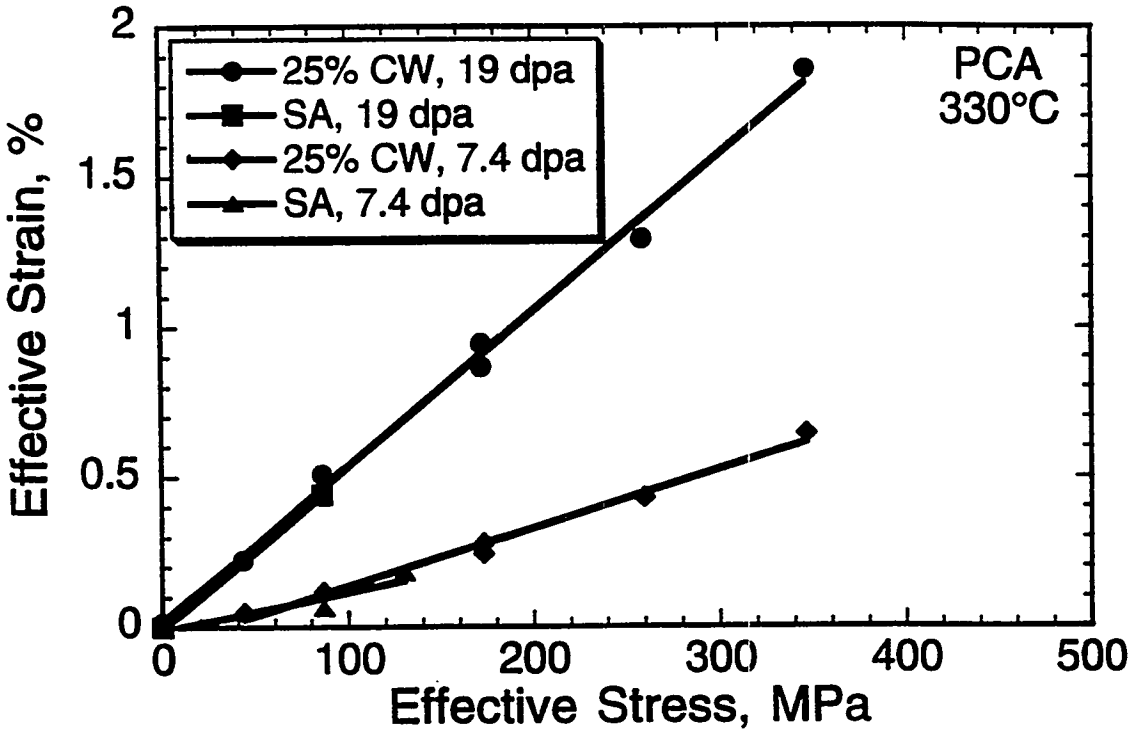

Fig. 1. Effective uniaxial strain vs. effective stress for the austenitic stainless steel PCA in the 25% cold-worked state from the U.S. Fusion Program and annealed PCA from the Japanese Fusion Program.

6.0 INSULATING CERAMICS AND OPTICAL MATERIALS

INFLUENCE OF IRRADIATION SPECTRUM AND IMPLANTED IONS ON THE AMORPHIZATION OF CERAMICS – S. J. Zinkle and L. L. Snead (Oak Ridge National Laboratory)

Invited paper presented at the 8th International Conference on Radiation Effects in Insulators, Catania, Italy, September 11-15, 1995 (accepted for publication in Nucl. Instr. Methods B)

Extended Abstract

Amorphization cannot be tolerated in ceramics proposed for fusion energy applications due to the accompanying large volume change (~15% in SiC) and loss of strength. Ion beam irradiations at temperatures between 200 K and 450 K were used to examine the likelihood of amorphization in ceramics being considered for the structure (SiC) and numerous diagnostic and plasma heating systems ($MgAl_2O_4$, Al_2O_3, MgO, Si_3N_4) in fusion energy systems. The microstructures were examined following irradiation using cross-section transmission electron microscopy. The materials in this study included ceramics with predominantly covalent bonding (SiC, Si_3N_4) and predominantly ionic bonding ($MgAl_2O_4$, Al_2O_3, MgO). The samples were irradiated with a variety of ion beams (including some simultaneous dual ion beam irradiations) in order to investigate possible irradiation spectrum effects. The ion energies were >0.5 MeV in all cases, so that the displacement damage effects could be examined in regions well separated from the implanted ion region.

The amorphization tendencies of the five materials examined is summarized in Table 1 [1-5]. It may be concluded that amorphization does not occur during room temperature irradiation of $MgAl_2O_4$, Al_2O_3 or MgO in the absence of implanted ion chemical effects, at least for doses up to 100 dpa (10 keV/atom damage energy). Amorphization can be induced at room temperature by the implantation of certain ion species, e.g. I^+ in spinel, Zr^+ in alumina, and Ti^+ in magnesia. Silicon nitride cannot be amorphized during room temperature irradiation up to doses of at least 7 dpa (and probably 100 dpa) unless certain implanted ions are present. However, the presence of implanted Fe^{++} ions ($\leq$0.1 at. % Fe) reduced the amorphization threshold dose of Si_3N_4 to <1 dpa. SiC became completely amorphous at room temperature for doses greater than about 0.4 dpa. The amorphization threshold dose was only about 0.1 dpa in Cl-implanted regions of SiC. The effect of irradiation temperature on the amorphization thrshold dose of SiC is shown in Fig. 1.

The effect of the PKA and ionizing radiation spectrum is uncertain in the three oxide ceramics, due to their high resistance to amorphization at room temperature. On the other hand, the amorphous layer in the Fe-implanted region of Si_3N_4 did not appear if the specimen was simultaneously irradiated at room temperature with 1 MeV He^+ ions at an ionizing radiation dose rate of ~1.6 MGy/s (~0.35 eV/atom-s), which suggests that ionization enhanced diffusion may be counteracting the implanted ion effect. There was no apparent effect of PKA spectrum on the amorphization threshold dose in SiC irradiated near room temperature with He, Cl, Si and Fe^{++} ions. However, published data obtained with electrons and Xe ions suggest that the low-temperature amorphization dose increases by about a factor of 5 as the irradiation source is changed from electrons to Xe ions. Ionizing radiation dose rates up to 5 MGy/s (~1 eV/atom-s) did not affect the room temperature amorphization threshold dose in SiC irradiated with Cl^+ ions.

In the absence of implanted ion effects, the ranking of these five materials with regard to increasing resistance to amorphization is SiC, Si_3N_4, Al_2O_3, and $MgAl_2O_4$ and MgO (cf Table 1). There are insufficient data to determine whether spinel or MgO has the highest resistance to amorphization, although it is clear that both of these materials (along with alumina) are very resistant to amorphization at room temperature. This experimentally determined ranking is in good agreement with predictions for amorphization resistance made according to bonding type (ionicity) [6] and available structural freedom [7] models. The present results and previous studies clearly show that implanted ions can have a significant effect on the amorphization threshold dose for ceramics, particularly for "damage-resistant" ceramics such as $MgAl_2O_4$, Al_2O_3 and MgO. The existing data suggest that these three materials cannot be amorphized at room temperature without the aid of implanted ions.

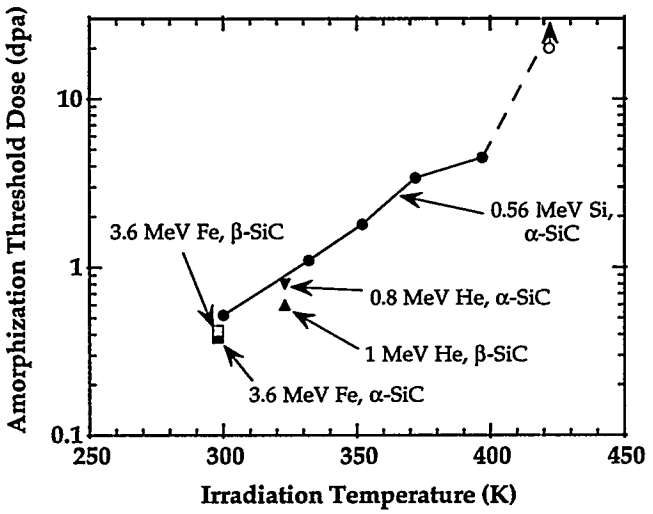

Fig. 1. Summary of temperature-dependent amorphization threshold dose measurements in SiC from this study. The unfilled circle at 423 K, 21 dpa denotes a specimen that did not amorphize.

Table 1. Summary of Amorphization Resistance of Ceramics
(the amorphization dose was obtained from the present study and refs. [1-5])

Material	Pauling's Ionicity	Structural Freedom $(f)^7$	Implanted Ion Effect		Amorphization Dose (dpa)	
			weak effect	accel. amorph.	300 K	77 K
MgO	0.68	-10	Nb	Ti, Cr	>100	??
$MgAl_2O_4$	0.63	–	Al, Mg	I	>100	>20
α-Al_2O_3	0.57	-6.2	Fe, Cr, Nb, Mo, Al	Zr	>100	3
Si_3N_4	0.28	-1.5	Kr	Fe	>100	??
SiC	0.10	<0	H, He, N, Al, Si, Fe, Cr	Cl	0.4	0.2

References

[1] L. Cartz, F. G. Karioris, and R. A. Fournelle, Radiat. Eff. 54 (1981) 57.
[2] C. W. White, C. J. McHargue, P. S. Sklad, L. A. Boatner, and G. C. Farlow, Mater Sci. Rep. 4 (1989) 41.
[3] S.M.M. Ramos, B. Canut, L. Gea, L. Romana, J. LeBrusq, P. Thevenard, and M. Brunel, Nucl. Instr. Meth. B 59/60 (1991) 1201.
[4] W. J. Weber and L. M. Wang, in Proc. 9th Int. Conf. Ion Beam Modification of Materials, Nucl. Instr. Meth. B, in press (1995)
[5] K. E. Sickafus et al., 8th Int. Conf. on Radiation Effects in Insulators, Catania, Italy, to be published in Nucl. Instr. Meth. B.
[6] H. M. Naguib and R. Kelly, Radiat. Effects 25 (1975) 1.
[7] L. W. Hobbs, J. Non-Crystalline Solids 182 (1995) 27.

ELECTRICAL INTEGRITY OF OXIDES IN A RADIATION FIELD – S.J. Zinkle (Oak Ridge National Laboratory) and C. Kinoshita (Kyushu Univ.)

Based on an invited paper entitled, "Potential and Limitations of Ceramics in Terms of Structural and Electrical Integrity in Fusion Environments," by C. Kinoshita and S.J . Zinkle, presented at the 7th International Conference on Fusion Reactor Materials, Obninsk, Russia, to be published in J. Nucl. Mater.

Extended Abstract

In the absence of an applied electric field, irradiation generally produces a decrease in the permanent ("beam-off") electrical conductivity of ceramic insulators. However, in the past 6 years several research groups have reported a phenomenon known as radiation induced electrical degradation (RIED), which produces significant permanent increases in the electrical conductivity of ceramic insulators irradiated with an applied electric field. RIED has been reported to occur at temperatures between 420 and 800 K with applied electric fields as low as 20 V/mm. The RIED phenomenon has become somewhat controversial in the past 3 years, and several research groups have failed to observe evidence for RIED in some grades of alumina. Figure 1 summarizes the existing data base on RIED measurements in single crystal alumina irradiated at temperatures of 670-820 K , which is near the expected peak degradation temperature for RIED. Definitive levels of bulk RIED at low doses ($<10^{-4}$ dpa) have been reported by two different research groups that examined electron-irradiated sapphire. On the other hand, several recent studies on electron- or proton-irradiated sapphire have failed to observe RIED. Three neutron irradiation RIED studies on sapphire have been performed to date, and definitive levels of RIED have not been observed in any of these studies.

As summarized in Fig. 2, the available RIED results on polycrystalline alumina show an even wider range of behavior than the single crystal results. Three different research groups have found that significant levels of RIED are produced in Vitox alumina. Significant amounts of RIED have also been reported for anodized aluminum and in amorphous alumina. On the other hand, RIED was not observed by 5 different research groups in an international round-robin experiment performed on Wesgo AL995. RIED was also not observed in Deranox and Hoechst Rubalit 710 grades of alumina. There was some indication of slight RIED in a Kyocera A479ss grade of alumina irradiated with fission neutrons, although surface leakage currents or gas ionization effects may have been responsible.

It is not clear why different grades of alumina exhibit a different sensitivity to RIED. There is some evidence that RIED may be due to heterogeneous processes occurring in the bulk. Proposed mechanisms include formation of dislocation arrays, radiation enhanced diffusion of electrode metal along grain boundaries, radiation-induced microcracking (in conjunction with radiation enhanced diffusion of electrode metal), and formation of gamma-alumina precipitates. There is evidence that significant charge storage can occur in alumina (which might lead to localized dielectric breakdown and microcracking), in spite of the radiation induced conductivity (RIC) which would help to mitigate charge buildup during irradiation. The localized electric fields produced in ceramic insulators during irradiation would be sensitive to numerous experimental variables such as chemical impurities, dose rate, and the relative amounts of ionizing vs. displacive radiation (i.e., the competition between RIC and charge trapping). This dependence on experimental details might explain the diverse RIED behavior reported by different researchers (cf. Figs. 1, 2).

Considering the puzzling, diverse behavior of RIED observed in different experiments, further study of the RIED phenomenon is recommended. In particular, further work on sapphire is recommended to define the irradiation conditions which lead to RIED. Radiation induced polygonization and radiation enhanced diffusion of metallic electrode material along grain boundaries or microcracks are plausible mechanisms for RIED in ceramic insulators. Wesgo, Rubalit and Deranox appear to be promising grades of polycrystalline alumina in terms of proven resistance to RIED.

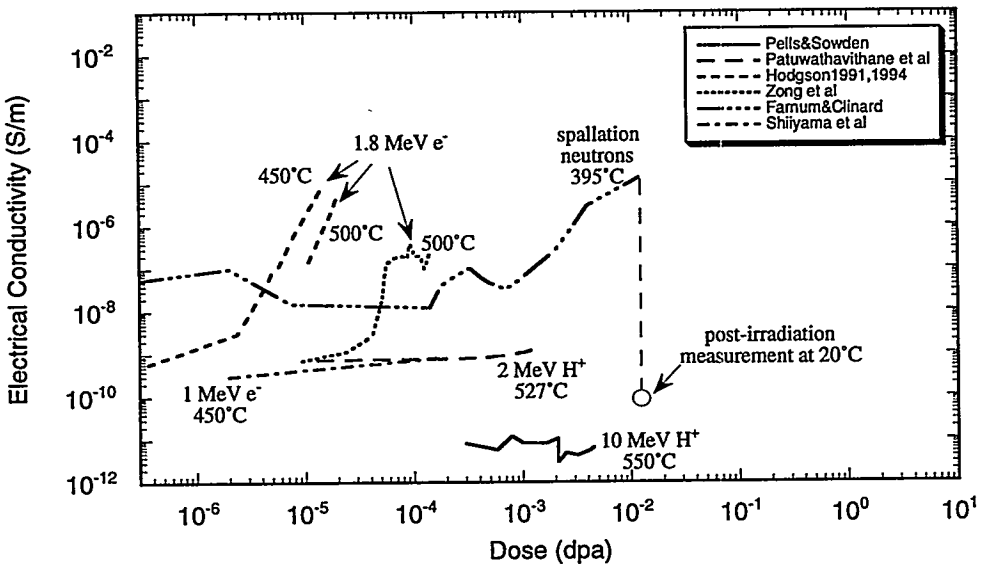

Fig. 1. Summary of RIED measurements on single crystal alumina specimens irradiated at temperatures between 670 and 820 K (please see manuscript for list of references). All of the electrical conductivity measurements were performed at the irradiation temperature with the radiation source turned off.

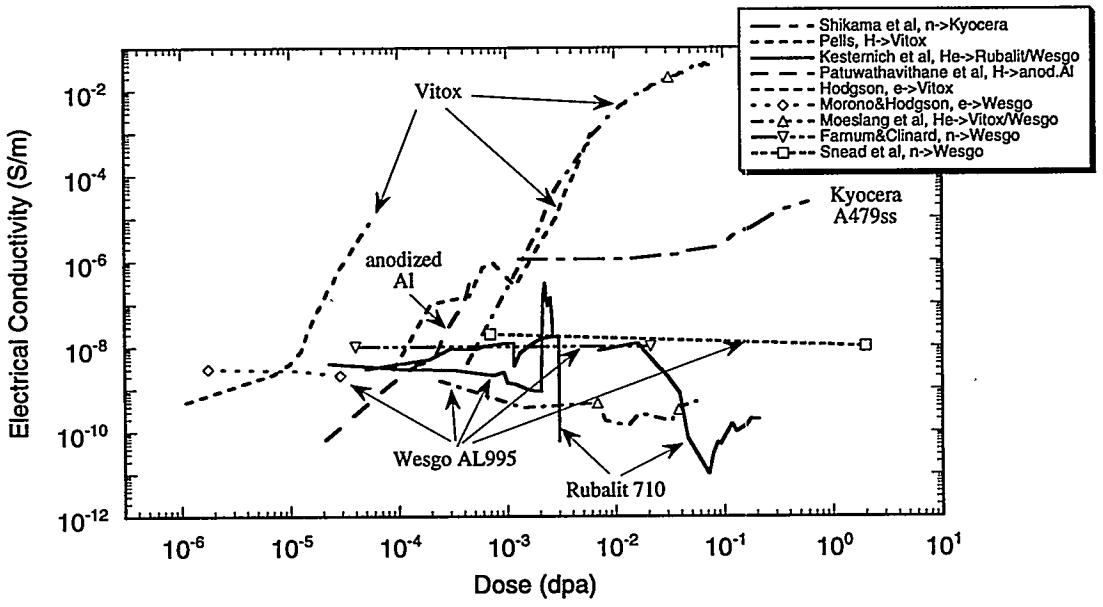

Fig. 2. Summary of RIED measurements on polycrystalline grades of alumina irradiated at temperatures between 670 and 810 K (please see manuscript for list of references). The electrical conductivity was measured at the irradiation temperature with the radiation source turned off, except for the fission reactor irradiations of Wesgo and Kyocera alumina.

LOSS TANGENT MEASUREMENTS ON UNIRRADIATED ALUMINA – S. J. Zinkle and R. H. Goulding (Oak Ridge National Laboratory)

OBJECTIVE

The objective of this report is to summarize some of the available unirradiated room temperature data on the loss tangents of several commercial grades of alumina.

SUMMARY

Unirradiated room temperature loss tangent data for sapphire and several commercial grades of polycrystalline alumina are compiled for frequencies between 10^5 and 4×10^{11} Hz. Sapphire exhibits significantly lower values for the loss tangent at frequencies up to 10^{11} Hz. The loss tangents of 3 different grades of Wesgo alumina (AL300, AL995, AL998) and 2 different grades of Coors alumina (AD94, AD995) have typical values near $\sim 10^{-4}$ at a frequency of 10^8 Hz. On the other hand, the loss tangent of Vitox alumina exhibits a large loss peak ($\tan \delta \sim 5 \times 10^{-3}$) at this frequency.

PROGRESS AND STATUS

Introduction

Ceramic insulators are required for radiofrequency (RF) heating components in magnetic fusion energy systems. The insulator is required to transmit megawatts of RF beam power and therefore must have low amounts of dielectric power loss (i.e., low loss tangent) in addition to good thermal conductivity and mechanical strength [1-4]. In order to avoid overheating of the insulator, the loss tangent must be less than $\sim 10^{-3}$ for ion cyclotron range of frequencies (ICRF, ~50-100 MHz) and less than $\sim 10^{-6}$ for electron cyclotron range of frequencies (ECRF, ~100 GHz). Alumina has been identified as one of the leading candidates for near-term RF systems. A large amount of work has been performed over the past few decades to measure the dielectric properties of alumina in the unirradiated [2-10] and irradiated [2,3,10-12] conditions. Most of the published neutron irradiation results on the loss tangent of alumina are summarized in ref. 13. The present report summarizes some of the published information on the room temperature dielectric loss tangent of unirradiated single crystal and polycrystal alumina at frequencies between 10^5 and 4×10^{11} Hz. This compilation is not intended to be an exhaustive summary of all existing data, but is instead a representative listing of typical results.

Results and Discussion

The room temperature loss tangents of 5 different commercial grades of polycrystalline alumina produced by GTE Wesgo and Coors Ceramics were measured at a frequency near 100 MHz as part of a larger program investigating the effects of gamma ray and pulsed neutron irradiation on prompt dielectric properties of ceramic insulators [14,15]. Some of the unirradiated values were not published in previous reports and are therefore summarized here for completeness. In order to provide a more comprehensive data set, room temperature loss tangent measurements on sapphire [4], Vitox (polycrystalline 99.9% Al_2O_3) [4,11], Wesgo AL995 [8,9], Wesgo AL300, and Coors AD995 [7,9] at frequencies between 10^5 and 4×10^{11} Hz have been compiled from published reports. Details concerning the measurement techniques may be found in the original reports. Some limited data quoted by the manufacturers [16,17] are included for purposes of comparison.

Table 1 summarizes the measured chemical composition of the Wesgo, Coors and Vitox grades of alumina [4,19-21]. It should be noted that the chemical analyses were performed on different heats of material compared to the dielectric measurements. However, heat-to-heat variations in the chemical composition of

Table 1. Chemical analysis (wt. %) for some of the commercial polycrystalline grades of alumina. Chemical analysis performed by Coors Analytical Laboratory [19] unless otherwise noted. Representative uncertainties in the impurity measurements quoted by the analysis laboratories are noted. The alumina concentration was obtained by subtraction of the measured impurity content.

Element	Wesgo AL995	Wesgo AL995 [20]	Wesgo AL300	Coors AD94	Coors AD998	Vitox [4,21]
Al_2O_3	99.3	99.5	97.3	93.4	99.72	99.9
Si	0.22±0.02	0.137±0.006	1.4 ± 0.1	4.0 ± 0.4	0.085±0.009	<0.01
Fe	0.076	0.034	0.081	0.18	0.040	0.0027
Ca	0.095	0.0424	1.1 ± 0.1	0.26	0.042	0.0054
Mg	0.31±0.03	0.249±0.005	0.033	0.68	0.077±0.008	0.038
Zr	0.008	0.007	0.009	0.65	0.006	0.00033
Ba	<0.005	<0.0002	<0.005	0.76	<0.005	
Na	0.027	0.021	0.039	0.045	0.028	0.0013
Ti	0.005	0.01	0.003	0.02	0.003	
K	0.007	<0.002	0.007	0.06	0.004	
Co		<0.005				
Cr		<0.001				<0.00005
Ni		<0.002				
Cu						0.00065
Ga						0.0030
Sr						0.0004
Zn						0.0018

these well-established commercial ceramics are thought to be less than the uncertainty in the chemical measurements. The chemical compositions for two of the materials measured at a frequency of 100 MHz (Coors AD995 and Wesgo AL998) are not yet available, and will be reported in a future progress report. Two independent chemical analyses have been performed on the U.S. fusion heat [18] of Wesgo AL995, which provides some indication of the absolute accuracy of the chemical measurements.

The results of the loss tangent measurements are summarized in Figures 1 and 2. Figure 1 compares the loss tangent for sapphire [4], Vitox [4,11] and Wesgo AL995 [8,9,15,17]. Sapphire exhibits very low values of loss tangent ($<10^{-5}$) for frequencies up to ~10^{10} Hz. The intrinsic loss peak in alumina occurs at a frequency of ~10^{13} Hz [22], which causes the loss tangent of sapphire to increase rapidly with frequency above 10^{10} Hz. The loss tangent of Wesgo AL995 is approximately an order of magnitude larger than that of sapphire over a wide frequency range. The Wesgo AL995 loss tangent converges toward the sapphire value at frequencies above ~10^{11} Hz, due to the intrinsic alumina loss peak at high frequencies. The dielectric loss tangent of Vitox is characterized by a very pronounced loss peak at frequencies near 10^8-10^9 Hz.

A further comparison of the loss tangents of the different Coors and Wesgo grades of alumina is shown in Fig. 2, where the low-loss and high-loss curves associated with sapphire and Vitox, respectively have been omitted for clarity. All five of the Coors and Wesgo grades of alumina have room temperature loss tangent values near 10^{-4} at a frequency of 100 MHz. With the exception of the higher loss tangent for AD995 quoted in the Coors technical literature [16], very good agreement is found between the loss tangent values reported in different studies on a particular grade of alumina. This indicates that heat-to-heat variations in the dielectric properties of these commercial grades of alumina are small.

All five of the Coors and Wesgo grades of polycrystalline alumina appear to be suitable for potential application in ICRF heating systems, since their unirradiated room temperature loss tangents are well below 10^{-3}. Previous work has found that the unirradiated loss tangent of low-loss grades of alumina in the 1 MHz-10 GHz range of frequencies is relatively insensitive to temperature between 20 and ~300°C [4-6].

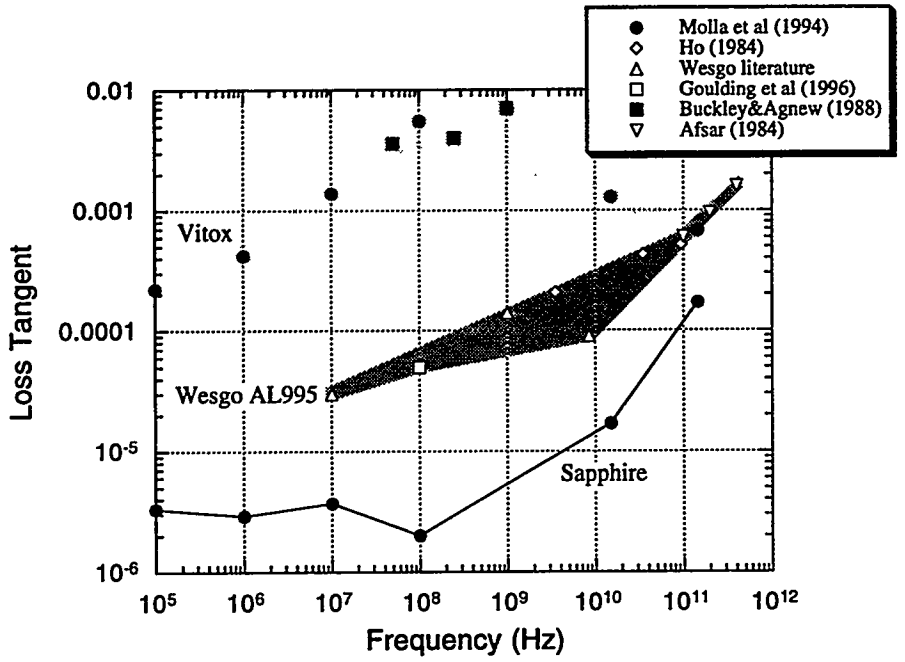

Fig. 1. Room temperature loss tangent vs. frequency for single crystal alumina [4] and two commercial grades of polycrystalline alumina [4,8,9,12,15,17].

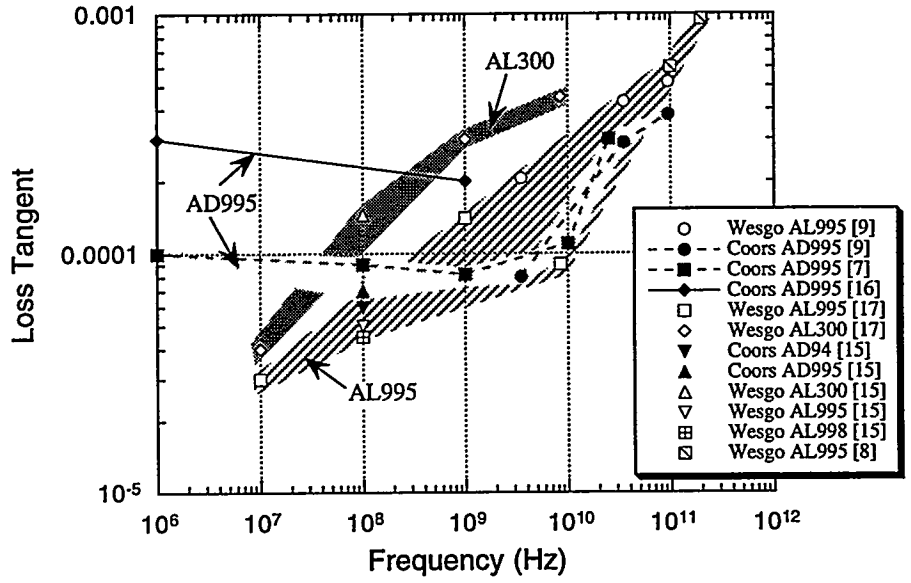

Fig. 2. Room temperature loss tangent vs. frequency for Wesgo AL300, AL995, AL998 [8,9,15,17] and Coors AD94, AD995 [7,9,15,16] grades of polycrystalline alumina.

Neutron irradiation damage would increase the loss tangent. Extrapolation of the available loss tangent data on alumina irradiated with fission neutrons near room temperature [13] suggests that the loss tangent would approach 10^{-3} after a neutron fluence of ~10^{25} n/m^2 (E>0.1 MeV), which corresponds to a damage level of ~1 dpa.

The cause of the large loss peak at ~100-1000 MHz in the Vitox grade of polycrystalline alumina is uncertain. This loss peak does not occur in any of the five Wesgo and Coors grades of alumina investigated in this report. The major impurity in Vitox is 380 ppm Mg. However, both Coors AD998 and Wesgo AL300 grades of alumina have similar Mg levels (Table 1) without the corresponding large loss peak near 100-1000 MHz. Therefore, the loss cannot be strictly associated with a specific concentration of Mg. Previous work has found that impurities such as Mg and Si can have a significant effect on the loss tangent at low frequencies (≤1 MHz), but do not have a noticeable effect at ~9 GHz [5,6]. The low-frequency losses were shown to be associated with increased electrical conductivity in the impurity-doped specimens. The conductivity contribution to the loss tangent becomes insignificant at frequencies above ~10 MHz since it is inversely proportional to frequency. Therefore, this mechanism would not explain the appearance of a loss peak at 100-1000 MHz in Vitox.

Ho [9] noted that the dielectric loss tangent at GHz frequencies in sintered alumina did not correlate with impurity concentration. Instead, the location and chemical form of the impurity (which is dependent on the details of the sintering process) was found to be the most important factor. For example, a laboratory-prepared Al_2O_3 -0.2% MgO specimen was found to have a factor of two higher loss tangent at 35 GHz than any of the Coors or Wesgo grades of alumina [9]. The lowest loss tangents were observed in commercial grades of alumina that were sintered for sufficiently long times to eliminate impurities within the grains and to produce relatively pure secondary phases (located at grain boundaries). The presence of large sintering pores at the grain boundaries did not have a deleterious effect on the millimeter-wave losses, whereas fine porosity apparently produced increases in the loss tangent [9]. The grain size in Vitox (~1.4 μm) [4] is considerably smaller than in the other commercial grades of alumina (~30 μm) investigated in this report. Due to the larger grain boundary surface area per unit volume in fine-grained materials, impurities need to be controlled to much lower concentration levels to achieve the same loss properties as larger-grained materials [9]. Further work is needed to determine if the loss peak at 100-1000 MHz in Vitox can be eliminated by modifying the sintering process.

Conclusions

Sapphire and the five Coors and Wesgo grades of polycrystalline alumina are worthy of further consideration for ICRF insulator applications, whereas Vitox exhibits unacceptably large losses in this frequency range.

Future Work

Room temperature dielectric property measurements at 50 and 100 MHz will be performed on various unirradiated and neutron-irradiated ceramic insulators. The postirradiation measurements will be performed on ceramic insulators irradiated in HFIR at 60-600°C to damage levels of ~1 and ~15 dpa (hydraulic rabbit and CTR60/61 target capsules) and in FFTF MOTA 2B at 420-800°C to damage levels of ~30 to 60 dpa.

Acknowledgements

Research sponsored by the Office of Fusion Energy, U.S. Department of Energy under contract DE-AC05-96OR22464 with Lockheed Martin Energy Research Corp.

REFERENCES

1. J. L. Scott, F. W. Clinard, Jr., and F. W. Wiffen, J. Nucl. Mater. **133&134** (1985) 156.
2. H. M. Frost and F. W. Clinard, Jr., J. Nucl. Mater. **155-157** (1988) 315.
3. R. Heidinger, J. Nucl. Mater. **179-181** (1991) 64.
4. J. Molla, R. Heidinger and A. Ibarra, J. Nucl. Mater. **212-215** (1994) 1029.
5. L. M. Atlas, H. Nagao and H. H. Nakamura, J. Am. Ceram. Soc. **45** (1962) 464; **46** (1962) 196.
6. G. S. Perry, Brit. Ceram Soc. Trans. **69** (1970) 177.
7. W. H. Gitzen, Ed., Alumina as a Ceramic Material (Amer. Cer. Soc., Westerville, OH, 1970).
8. M. N. Afsar, IEEE Trans. Microwave Theory Tech. **MTT-32**, No. 12 (1984) 1598.
9. W. W. Ho, Millimeter Wave Dielectric Property Measurement of Gyrotron Window Materials, ORNL/SUB/83-51926/1 (April 1984); ORNL/SUB/83-51926/2 (April 1985).
10. R. Heidinger, J. Nucl. Mater. **173** (1990) 243.
11. S. N. Buckley and P. Agnew, J. Nucl. Mater. **155-157** (1988) 361.
12. R. Heidinger and A. Hofmann, H-U Nickel and P. Morajitra, Fus. Eng. Des. **18** (1988) 337.
13. L. W. Hobbs, F. W. Clinard, Jr., R. C. Ewing, and S. J. Zinkle, J. Nucl. Mater. **216** (1994) 291
14. R. E. Stoller, R. H. Goulding, and S. J. Zinkle, J. Nucl. Mater. **191-194** (1992) 602; also Fusion Reactor Materials semiann. prog. report for period ending Sept. 30, 1990, DOE/ER/1313/9, p. 317.
15. R. H. Goulding, S. J. Zinkle, D. A. Rasmussen, and R. E. Stoller, Fusion Reactor Materials semiann. prog. report for period ending Sept. 30, 1993, DOE/ER/1313/15, p. 434; also J. Appl. Phys. **79**, No. 5 (1996) in press.
16. Material Properties Chart, Coors Ceramics Co., Structural Division, Golden, Colorado.
17. Technical bulletin, Wesgo Division, GTE Products Corp., Belmont, California.
18. R. E. Stoller, Fusion Reactor Materials semiann. prog. report for period ending March 31, 1990, DOE/ER/1313/8, p. 299.
19. Coors Analytical Laboratory, Golden, Colorado, Lab. analysis #90-04229 (Dec. 21, 1990).
20. Forschungszentrum Karlsruhe, IMF-I chemical analysis 360/94 (October, 1994).
21. G. P. Pells and M. J. Murphy, J. Nucl. Mater. **183** (1991) 137.
22. G. Link and R. Heidinger, in 18th Int. Conf. on Infrared and Millimeter Waves, eds. J. R. Birch and T. J. Parker, proc. SPIE vol. 2104 (1993) 150.

INVESTIGATION OF THE FEASIBILITY OF IN-SITU DIELECTRIC PROPERTY MEASUREMENTS ON NEUTRON-IRRADIATED CERAMIC INSULATORS – R. H. Goulding and S. J. Zinkle (Oak Ridge National Laboratory)

OBJECTIVE

The objective of this task is to determine the dielectric properties of polycrystalline alumina and silicon nitride ceramic insulators at a frequency of ~80 MHz during fission neutron irradiation.

SUMMARY

Computer modeling and experimental benchtop tests have demonstrated that a capacitively loaded resonant coaxial cavity can produce accurate in-situ measurements of the loss tangent and dielectric constant of ceramic insulators at a frequency of ~80 MHz during fission reactor irradiation. The start of the reactor irradiations has been postponed indefinitely due to budgetary constraints.

PROGRESS AND STATUS

Introduction

According to the present design of the International Experimental Thermonuclear Reactor (ITER), the ICRF vacuum transmission lines will contain one or two dielectric supports and a double vacuum window that will be exposed to relatively high neutron fluxes ($>2.5 \times 10^{15}$ n/m^2-s).[1] High neutron fluences are known to cause degradation of the structural and dielectric properties of the ceramic materials.[2] This radiation-induced degradation might be enhanced by the presence of RF fields and is dependent on the operating temperature. At the present time, there are no known in-situ data on the dielectric properties of ceramic insulators obtained during irradiation to ITER-relevant neutron irradiation doses. A research program was initiated under ITER R&D Task T26 to investigate the irradiated dielectric behavior of two candidate ceramic insulators, alumina and silicon nitride.

The objective of this task is to determine the amount of dielectric degradation in two candidate ceramic insulators undergoing long term neutron irradiation, at fluences up to 10 times larger than those expected in ITER operation. The HFBR reactor at Brookhaven National Laboratory was chosen for the neutron irradiations due to the accessibility of large-volume, high-flux irradiation regions in the core thimble positions.[3] Based on previous pulsed neutron irradiation experiments,[4] the in-situ dielectric loss of ceramic insulators should be identical to the loss measured immediately following irradiation. However, room temperature annealing of metastable point defects created by low temperature (~50°C) neutron irradiation is expected to occur. Therefore, post-irradiation measurements of the dielectric properties of ceramics (typically performed several months after the irradiation) might be an underestimate of the loss tangent degradation that would be present during operation in ITER.

A capacitively loaded resonant coaxial cavity was chosen for the in-situ dielectric property measurements. The cavity method is well-suited to measurement of the loss tangent because the power dissipation in the ceramic specimen is maximized relative to that dissipated in the rest of the experimental apparatus. In addition, losses in the feed line can be accounted for without the need for prior calibration.[4] This resonant cavity technique was successfully used in a previous study on the dielectric properties of ceramic insulators during pulsed fission reactor irradiation to low doses.[4]

Results and Discussion

The technique chosen to obtain in-situ dielectric properties involves measuring the resonant cavity Q using swept frequency techniques, with corrections made for external loading.[4] In previous pulsed fission reactor measurements, it was noted that the pressure in an air-filled cavity had to be <0.1 Pa to eliminate errors associated with gas ionization.[4] A solid dielectric cavity design was adopted for the present study to avoid the need to maintain a vacuum between the inner and outer coaxial metal surfaces, greatly simplifying in-reactor measurements. The solid dielectric cavity consisted of a coaxial cylindrical cavity terminated in a disk capacitor. The cavity is fed by a loop coupler which enters through the open end of the cavity, passes through a small hole drilled in the annulus of the ceramic ~25 mm from the open end, and is brazed to the metallic coating on the outer surface. The resonant cavity technique allows a measurement of the internal cavity losses that is fully corrected for external losses, such as those occurring in the ionized air inside the cavity center conductor. Therefore, the measurement does not require a vacuum. The change in loss tangent is calculated from the measured change in the cavity "unloaded Q" (which eliminates effects of the coupling circuit) using the following equations:

$$\tan\delta = \frac{1}{Q_o} - \frac{r_1(Z_o)}{Z_o\beta},$$

$$r_1(Z_o) = 2.61 \times 10^{-7} \frac{\sqrt{f}}{2\pi}\left(\frac{1}{r_o} + \frac{1}{r_i(Z_o)}\right)$$

where Q_o is the unloaded Q, r_o is the outer radius of the cavity, $r_i(Z_o) = r_o\exp(-Z_o(\varepsilon_r/60)$, Z_o is the characteristic impedance, ε_r is the dielectric constant of the ceramic and $b = \omega/c$, where $w = 2\pi f$ is the operating frequency and c is the speed of light. The cavity outer radius was fixed by the requirement that it fit inside the HFBR reactor tube (maximum r_o~11 mm). The cavity Z can be increased somewhat by increasing the characteristic impedance. This requires decreasing the diameter of the central hole, which makes access for metallizing the interior surface and connecting the coupling loop difficult. A compromise value for the inner diameter is 12.5 mm, which gives a calculated characteristic impedance for the cavity of 12 Ω. At an ITER-relevant frequency of 80 MHz, the required resonant cavity length is ~0.32 m and the corresponding optimal capacitor thickness is 3 mm for polycrystalline alumina (assuming ε_r =8.5). A highly conductive metallic coating (e.g., Cu) is required on the surfaces of the ceramic cavity in order to achieve the largest possible Q value. The thickness of the high-conductivity metallic layer should be at least 3 skin depths (~21 μm for pure copper at 100 MHz).

A prototype polycrystalline alumina (99.8% pure) cavity was fabricated by Coors Ceramics Company in the form of an AD998 alumina flat-bottomed tube with one closed end. This geometry was available as a stock item in a limited number of sizes from Coors. The stock size with the closest geometry to the optimal size was purchased in order to test metallizing techniques and to perform initial benchtop verification of computer model. The dielectric properties of the solid Coors AD998 alumina ceramic resonant cavity (1.25 cm inner diam/1.9 cm outer diam × 33 cm long) were measured following the deposition of high-conductivity metallic coating on the alumina tube. A very thin (<0.1 μm) layer of a commercial gold overglaze (organic suspension) was first applied to the alumina tube. A thin layer (~25 μm) of copper was plated onto the gold film after it had been fired in air. Numerous problems were encountered with the gold overglaze. In particular, the copper-gold film flaked off when the alumina cavity was heated to temperatures above ~350°C. Simple heat transfer calculations indicate that the maximum temperature of the ceramic cavity will be less than 200°C during irradiation in the HFBR fission reactor. However, in order to maintain a reliable brazed connection for the feedthrough and coupling loop during irradiation, a brazing temperature ≥300°C is required. The critical parameters for obtaining uniform coverage of the gold overglaze include the firing temperature and maintenance of sufficient air circulation at the sealed end of the tube.

The prototype cavity exhibited a resonance at 74 MHz and an unloaded cavity Q of 269. Since changes in Q of ~50 would be easily detected during neutron irradiation[4], this cavity would be sensitive to increases in the alumina loss tangent above ~10^{-3}. Figure 1 is a graph of measured reflection coefficient vs. frequency for the prototype cavity. The frequency of the first resonance is at 73.8 MHz. The second resonance (not shown) occurs at 219.0 MHz. Figure 2 is a Smith chart showing the reflection coefficient amplitude and phase as the frequency is swept from 68.8 MHz to 78.8 MHz. As can be seen from Figs. 1 and 2, the reflection coefficient magnitude is very near 1 far from resonance, indicating negligible series resistance in the coupling structure. The input resistance of the prototype

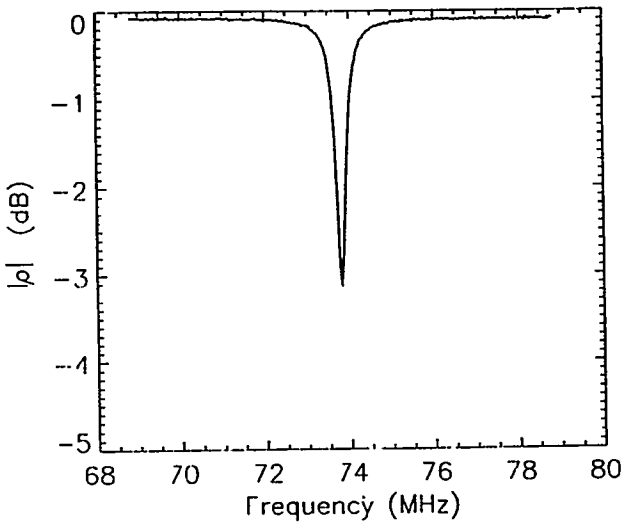

Fig. 1. Measured reflection coefficient vs. frequency for the prototype Coors AD998 alumina cavity.

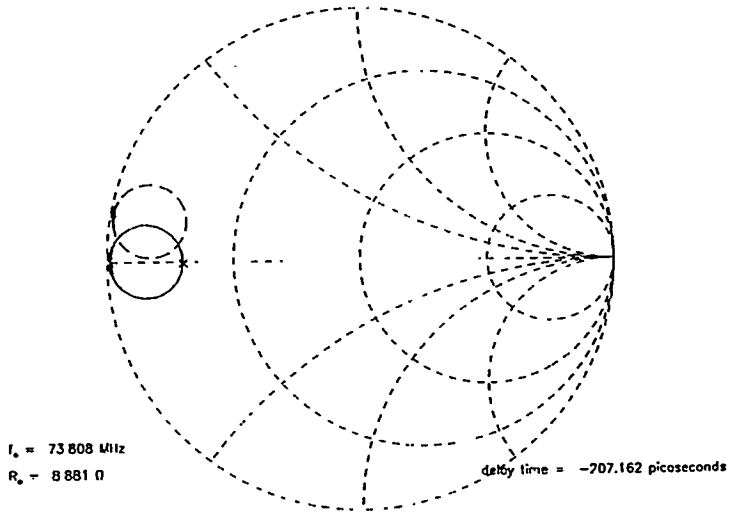

Fig. 2. Smith chart for the prototype alumina cavity at frequencies between 68.8 MHz and 78.8 MHz.

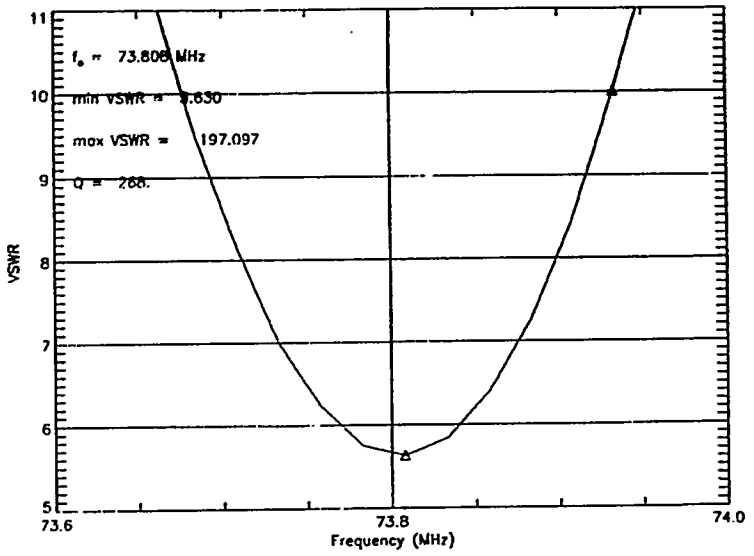

Fig. 3. Measured VSWR vs. frequency near the first resonance of the prototype Coors AD998 alumina cavity.

cavity was only ~9 ohms at resonance. This low input resistance has been increased in subsequent cavities by using a larger coupling loop (~25 mm). Figure 3 is a plot of measured VSWR vs. frequency near resonance, from which the unloaded cavity Q was calculated. The measured value of $Q_0 = 268$ can be compared to the design value of $Q_0 = 311$, which assumes an ideal value of 5.8×10^7 S/m for the conductivity of the copper layer, and that tand=7×10^{-5} for the AD998 alumina at the resonant frequency. Our model reproduces the measured Q_0 value if the electroplated copper conductivity is reduced by only ~15% compared to pure Cu, which is a reasonable conductivity for electroplated copper.

In our initial tests, we used the thickest walled alumina tubing available as a stock item from Coors. A new set of 4 custom-made Coors AD998 alumina cavities with approximately twice the previous wall thickness (new tube inner diameter of 11 mm and wall thickness of ~4.3 mm) were obtained from Coors. According to calculations, these tubes should have an unloaded Q of ~500, which would allow loss tangents as low as ~3×10^{-4} to be accurately measured during neutron irradiation. Due to the delamination problems associated with the commercial gold overglaze in the prototype cavity, an alternative metallization procedure was adopted for the new alumina cavities. A thin (~10 μm) layer of copper was evaporated onto the interior of two alumina tubes using a custom-made tungsten crucible, and the outside of the tubes was coated with a thin layer of copper using a plasma spray technique. The evaporated copper was observed to adhere to the alumina after heating to temperatures as high as 400°C. A thicker (~25 μm) layer of copper was subsequently electroplated onto the surfaces of the alumina tubes to produce a total copper thickness >30 μm on all surfaces of the cavity.

Future Work

Work performed to date has demonstrated the technical feasibility of the solid resonant coaxial cavity technique for measuring the dielectric properties of ceramic insulators at ~80 MHz during fission neutron irradiation. The final bench testing of the new metallized alumina cavities and the start of the HFBR irradiation program have been delayed indefinitely due to a lack of funding. In the event that sufficient funds become available, the loss tangent and dielectric constant of the Coors AD998 alumina cavity will be measured in-situ during low-temperature (~100°C) neutron irradiation up to a dose of ~0.1 dpa (10^{24} n/m^2,

E>0.1 MeV). These irradiations would initially be performed at a low electric field (<500 V/cm). A second irradiation experiment at a high electric field ((~5 kV/cm) may also be performed, along with fabrication and neutron irradiation of a Norton NT154 polycrystalline Si_3N_4 ceramic cavity.

References

1. G. Bosia, ITER JCT (Garching co-center), personal communication, 1994.
2. L. W. Hobbs, F. W. Clinard, Jr., S. J. Zinkle, and R. C. Ewing, J. Nucl. Mater. 216 (1994) 291-321.
3. L. L. Snead, D. P. White, and S. J. Zinkle, J. Nucl. Mater. 226 (1995) 58-66.
4. R. H. Goulding, S. J. Zinkle, D. A. Rasmussen and R. E. Stoller, "Transient Effects of Ionizing and Displacive Radiation on the Dielectric Properties of Ceramics," J. Appl. Phys. 79, No. 5 (March 1996), in press.

CAPSULE FABRICATION FOR IN-SITU MEASUREMENT OF RADIATION INDUCED ELECTRICAL DEGRADATION (RIED) OF CERAMICS IN HFIR – W. S. Eatherly, D. W. Heatherly, M. T. Hurst, A. L. Qualls, D. G. Raby, R. G. Sitterson, L. L. Snead, K. R. Thoms, R. L. Wallace, D. P. White, and S. J. Zinkle (Oak Ridge National Laboratory), E.H. Farnum and K. Scarborough (Los Alamos National Laboratory), K. Shiiyama (Kyushu University), T. Sagawa (JAERI), M. Narui and T. Shikama (Tohoku University)

OBJECTIVE

The objective of this work is to determine the existence or absence of radiation induced electrical degradation (RIED) in Al_2O_3 with and without biasing voltage applied to the sample.

SUMMARY

A collaborative DOE/Monbusho series of irradiation experiments is being implemented to determine, in-situ, the effects of irradiation on the electrical resistivity of ceramic materials. The first experiment, TRIST-ER1, has been designed to irradiate 15 Al_2O_3 test specimens at 450°C in an RB* position of the High Flux Isotope Reactor (HFIR). Each test specimen is located in a sealed vanadium subcapsule with instrumentation provided to each subcapsule to measure temperature and resistance, and to place a biasing voltage across the specimen. Twelve of the specimens will be biased with 200 V/mm across the sample at all times, while three will not be biased, but can be if so desired during the irradiation. The experiment design, component fabrication, and subcapsule assembly have been completed. A three cycle irradiation, to a fast neutron (E>0.1 MeV) fluence of about 3×10^{25} n/m^2 (~3 dpa in Al_2O_3), is expected to begin early in March 1996.

PROGRESS AND STATUS

Introduction

Ceramic insulators are required for the heating, control and diagnostic measurement of magnetically confined plasmas [1]. A potentially serious degradation of the electrical resistance of ceramic insulators, known as radiation induced electrical degradation (RIED), has raised concern about the suitability of ceramic insulators in intense radiation fields [1-5]. Since the original reported observation of RIED by Hodgson in 1989 [4], numerous studies have been performed with conflicting results (see ref. 3 for a recent summary). The main goal of these US-Monbusho collaborative experiments is to understand the fusion-relevant behavior of RIED, including the physical mechanisms responsible for RIED (bulk and surface conductivity effects) and the magnitude of the effect. Previous studies indicate that RIED is most pronounced at temperatures between 300 and 600°C and at applied voltages >100 V/mm, with an apparent maximum degradation rate occurring near 450°C. Therefore, the initial experiment was chosen to be performed at 450°C with an applied potential of 200 V/mm. A guard ring specimen geometry will be used to minimize surface leakage currents. The experiments will be performed in the Temperature-Regulated In-Situ Test (TRIST) facility located in a Removable Beryllium (RB*) position of the HFIR at Oak Ridge National Laboratory (ORNL). The design and assembly of this experiment required a coordinated effort between technical staff at several U.S. and Japanese institutions.

A total of 15 specimens will be irradiated in the in-situ electrical conductivity capsule. The specimen matrix for the first irradiation capsule focusses on various grades of polycrystal and single crystal alumina (Table 1). The rationale for investigating different grades of alumina is based largely on the recent discovery

Table 1. Specimen List for the HFIR TRIST-ER1 RIED Experiment (3 dpa, 450°C)

Specimen position	Material	Appl. Voltage	Vendor and grade
1	Al_2O_3, single crystal	150 V	Crystal Systems (Hemex UV grade) a-axis
2	Al_2O_3, single crystal	150 V	Crystal Systems (Hemex UV grade) c-axis
3	Al_2O_3, single crystal	150 V	Crystal Systems (Hemex regular) c-axis
4	Al_2O_3, single crystal	150 V	Crystal Systems (Hemex regular) a-axis
5	Al_2O_3, polycrystalline	150 V	Vitox (99.9% purity, Morgan Matroc, Anderman Div.)
6	Al_2O_3, polycrystalline	150 V	Kyocera A-480 (99.9% purity)
7	Al_2O_3, polycrystalline	150 V	Wesgo AL300 (97.0% purity)
8	Al_2O_3, polycrystalline	150 V	Kyocera A-479 (99.0% purity)
9	Al_2O_3, polycrystalline	150 V	Coors AD998 (99.8% purity)
10	Al_2O_3, polycrystalline	150 V	Wesgo AL995 (99.5% purity)
11	Al_2O_3, polycrystalline	0 V	Wesgo AL995 (99.5% purity)
12	Al_2O_3, single crystal	0 V	Crystal Systems (Hemex regular) c-axis
13	Al_2O_3+Cr, single crystal	150 V	Union Carbide (UV grade), 60° from c axis
14	Al_2O_3, single crystal	150 V	Kyocera SA100 ($1\bar{1}02$ orientation)
15	Al_2O_3, single crystal	0 V	Kyocera SA100 ($1\bar{1}02$ orientation)

by KfK Karlsruhe researchers [5] that catastrophic RIED was induced in one grade of polycrystalline alumina (Vitox, 99.9% purity), but not in the IEA reference heat of polycrystalline alumina (Wesgo AL995) during ion beam irradiation to damage levels of ~0.02 dpa. Considering the conflicting RIED results reported to date by different researchers that studied different grades of alumina [3], it was deemed prudent in the first experiment to try to identify what factor is responsible for the absence or presence of RIED in a single class of material (i.e., alumina).

Irradiation Capsule Design and Fabrication

The TRIST-ER1 capsule will irradiate 15 Al_2O_3 test specimens 8.5 mm in diameter and 0.75 mm thick. Each specimen is contained in a sealed subcapsule assembly composed of alumina and vanadium as shown in Fig. 1. The subcapsule design is similar to that used in prototype irradiations carried out at the High Flux Beam Reactor (HFBR) [6,7]. The samples were vacuum brazed at 870°C to alumina pedestals using a Ticusil braze foil. This braze material covered the entire bottom surface of the sample and the top of a nickel pin which served as the rear electrode. The alumina pedestal was simultaneously vacuum brazed to a metal heat sink using Ticusil braze foil.

In the original subcapsule design for HFIR, the alumina pedestal was brazed to a dispersion strengthened (GlidCop AL15) copper alloy in order to take advantage of the high thermal conductivity of copper. However, the large difference in thermal expansion coefficients between copper (17×10^{-6}/°C) and alumina (8×10^{-6}/°C), coupled with the relatively high yield strength of GlidCop (~350 MPa) produced cracking in the alumina pedestal during the cooldown following brazing. Scoping tests demonstrated that vanadium did not produce cracking in the alumina pedestals, due to the similar thermal expansion coefficients for vanadium (9×10^{-6}/°C) and alumina. It was therefore decided to use vanadium as the metal heat sink for all of the subcapsules. Unfortunately, the significantly lower thermal conductivity of vanadium (~32 W/m-K) compared to GlidCop AL15 (~330 W/m-K) required extremely small gas gaps (<25 μm) between the subcapsule walls and the aluminum capsule walls for the subcapsules located near the horizontal midplane of the HFIR in order to maintain the specimen design temperature of 450°C. This caused an extended delay in the delivery of the vanadium heat sinks. The outside diameter of each vanadium subcapsule body was sized, based on a thermal analysis, to minimize the axial temperature gradient caused by the HFIR gamma

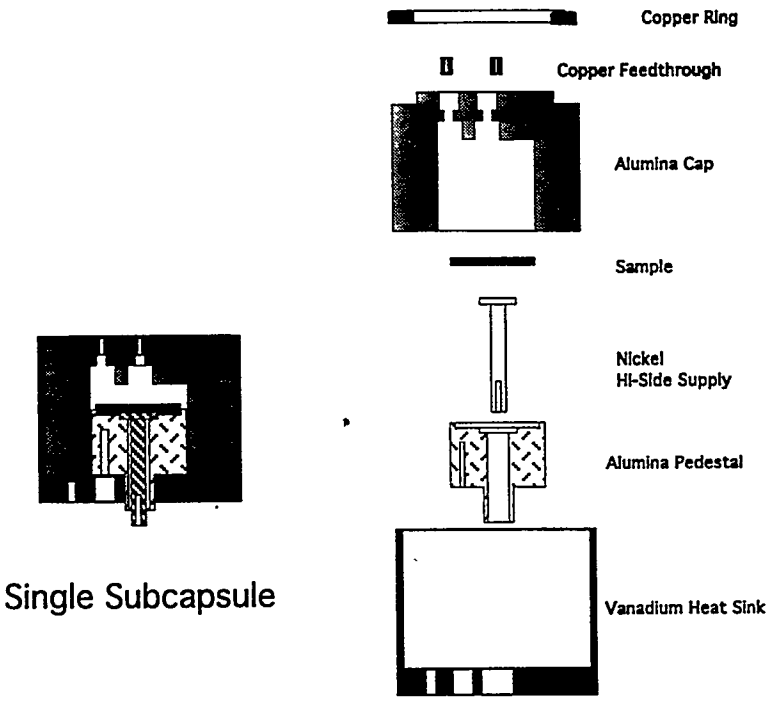

Fig. 1. Subcapsule for HFIR TRIST-ER1 experiment.

heating rate profile. In addition, because the base of the vanadium body will thermally expand more than the top, the outside diameter of the subcapsules was tapered, so that at operating temperatures the gas gap between the subcapsule and the aluminum holder sleeve will be uniform.

Braze pads were applied to the center and guard electrode regions on the top surface of the alumina specimens. Nickel wires were subsequently laser welded to braze pads to provide a secure electrical connection. Initially, the braze pads were applied to the virgin specimens (prior to the Ticusil braze step) using a 96%Ag-4%Ti alloy in an induction vacuum furnace at 1050°C. However, the rapid cooldown following brazing in the induction furnace produced microcracking in a subsurface layer beneath the braze pads in some of the alumina specimens. This caused delamination of the braze pads when the Ni wires were laser welded to the braze pads. Most of the braze pads were attached to the surfaces of the alumina specimens using an Incusil braze alloy at 750°C. The Incusil braze pads were applied after the specimen and alumina pedestal had been brazed to the vanadium heat sink, and the vacuum furnace was slowly cooled to minimize the possibility of specimen cracking.

Platinum electrodes were sputtered onto the sample in a guard ring configuration with a 4 mm central electrode diameter and a 1.0 mm gap between the central electrode and the guard ring. The electrode deposition was performed under high vacuum conditions after the Ni wires had been laser welded to the braze pads. It was determined that Pt did not mechanically adhere sufficiently well to the surfaces of the single crystal alumina specimens, even when the surfaces were mechanically abraded. A thin layer (<0.1 μm) of titanium was applied prior to the ~1 μm Pt layer using a two-gun vacuum deposition system in order to improve the adhesion of the electrodes to the alumina specimens. Ohmic behavior of the Ti + Pt electrodes (in the absence of irradiation) was verified for a Wesgo AL995 and sapphire specimen.

All of the subcapsules were sealed to minimize the amount of surface contamination buildup during irradiation. Subcapsule #15 was sealed using Incusil braze alloy, whereas the remaining subcapsules were sealed using a Cotronics high temperature ceramic paste that can be used at temperatures up to 1500°C.

This paste was successfully used in a recent RIED experiment at the HFBR reactor [7]. Since the effect of irradiation on the adhesive properties of the ceramic paste is not known, wires were laser welded at three locations along the top of the subcapsules sealed with the ceramic paste to ensure that the subcapsules would stay intact during the HFIR irradiation.

Stainless steel sheathed, mineral insulated (MI) cables are used to instrument the sample in each of the subcapsules. A 1.1 mm OD triaxial MI cable is used as the data lead, with the center copper conductor being connected to the nickel wire emanating from the center electrode on top of the sample, and the inner copper sheath connected to the nickel wire coming from the guard ring. A 1.6 mm OD coaxial MI cable is used as the power lead, with the center copper conductor connected to the nickel wire brazed to the nickel pin emanating from the bottom electrode. The line resistances of the coaxial and triaxial cables were all ~1 Ω. A special fixture was used to make a secure electrical connection between the Ni leads from the subcapsule and the MI cables. The leads were twisted several revolutions, and then spot-welded together. Each subcapsule is instrumented with two 0.5 mm OD, stainless steel sheathed, chromel/alumel (type K) thermocouples, one of which is placed in the alumina pedestal, ~1.3 mm from the sample, while the other is embedded in the vanadium base of the subcapsule. The use of two thermocouples, in combination with a 3-dimensional heat transfer analysis code, allows the specimen temperature to be known within an accuracy of ~1°C.

An axial cross section through the in-reactor portion of the irradiation capsule is shown in Fig. 2. An aluminum (6061-T6) subcapsule holder sleeve, fabricated in two halves to permit assembly, surrounds the subcapsules, and the outside surface of this sleeve is grooved to provide a path for the MI cables and thermocouples to be routed to each subcapsule. When assembled, the interior volume is divided into three separate axial regions with independent temperature control gases being supplied to each region. This will permit maintaining uniform axial temperatures as the gamma heating rate profile changes during a reactor cycle. The center region contains 7 subcapsules, and the top and bottom regions each contain 4 subcapsules. To minimize the probability of a power lead interfering with a data lead, every other subcapsule is inverted. This results in the region between subcapsules containing either two data leads or two power leads and two thermocouples.

The capsule containment tube (35.7 mm OD and 31.8 mm ID) is made of 6061-T6 aluminum in the in-reactor region and Type 304 stainless steel in the upper region. The upper and lower sections of the containment tube are joined by a special aluminum-to-stainless-steel transition tube. The capsule is cooled with 49°C reactor coolant water flowing downward at a flow rate of 0.9 l/s with a water temperature rise of 5°C over the length of the capsule. The sample temperatures are controlled by adjusting the composition of a flowing mixture of helium and neon (or possibly argon) in the control gas gap between the subcapsules and the holder sleeve. As stated above, this mixture is controlled independently for the three regions over the length of the capsule to account for the change in gamma heating profile during a reactor cycle. A purge of helium is maintained in the region between the holder sleeve and the capsule containment tube to maintain the holder sleeve and MI cables at as low a temperature as possible.

Instrumentation Facility

The instrumentation facility for the TRIST-ER1 experiment is made up of two separate components. The first component is the capsule temperature monitoring and control system, and the second is the sample biasing and electrical resistivity measuring system.

The capsule temperature monitoring and control system monitors all temperatures and pressures, and supplies all gases to the capsule. The output of the 30 thermocouples is fed into a PC-based μDCS Plus control system. The computer reads and stores all thermocouple information, relates it to specimen temperatures, controls the temperature by adjusting control gas composition, and displays the temperatures,

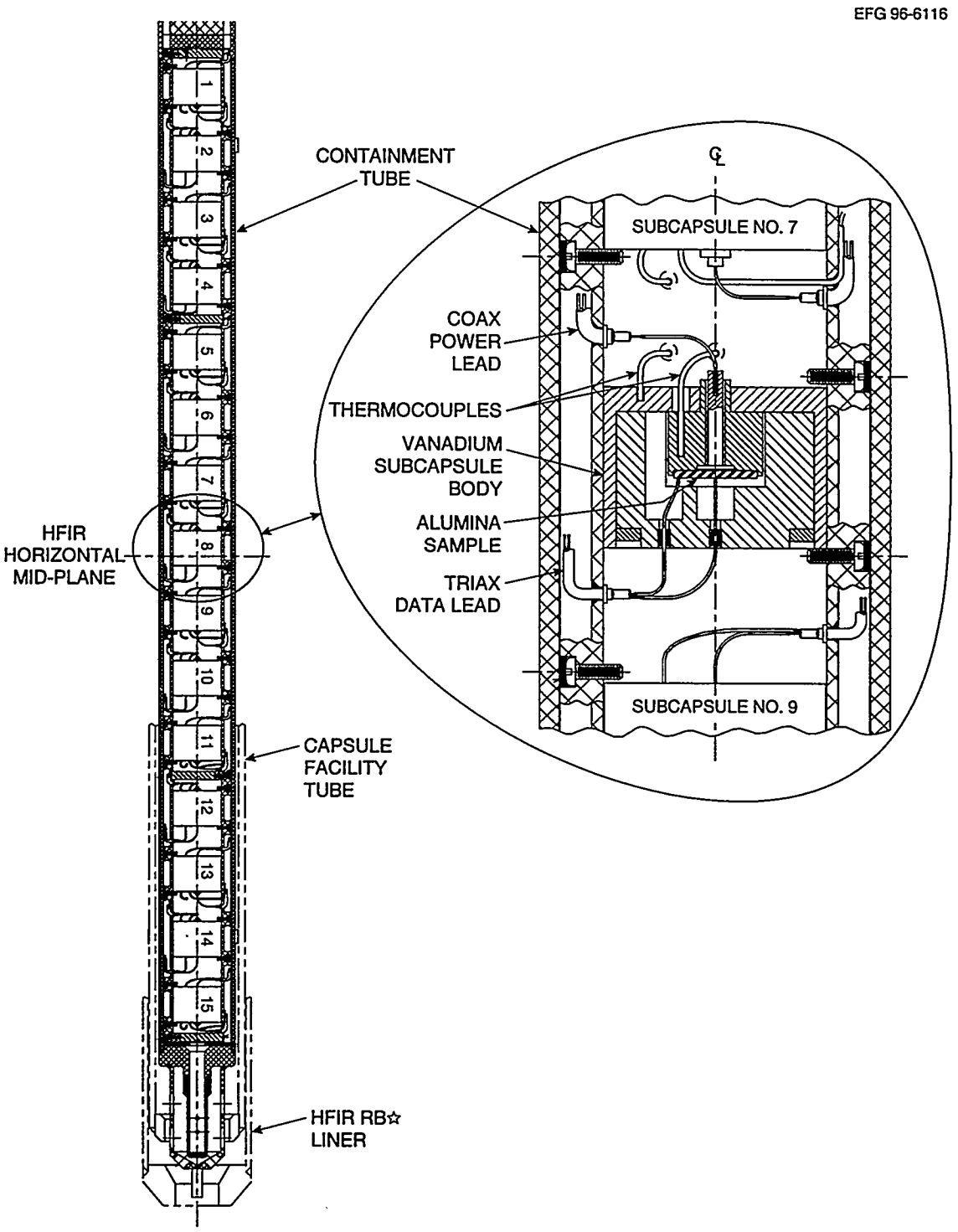

Fig. 2. Axial cross-section of the irradiation capsule.

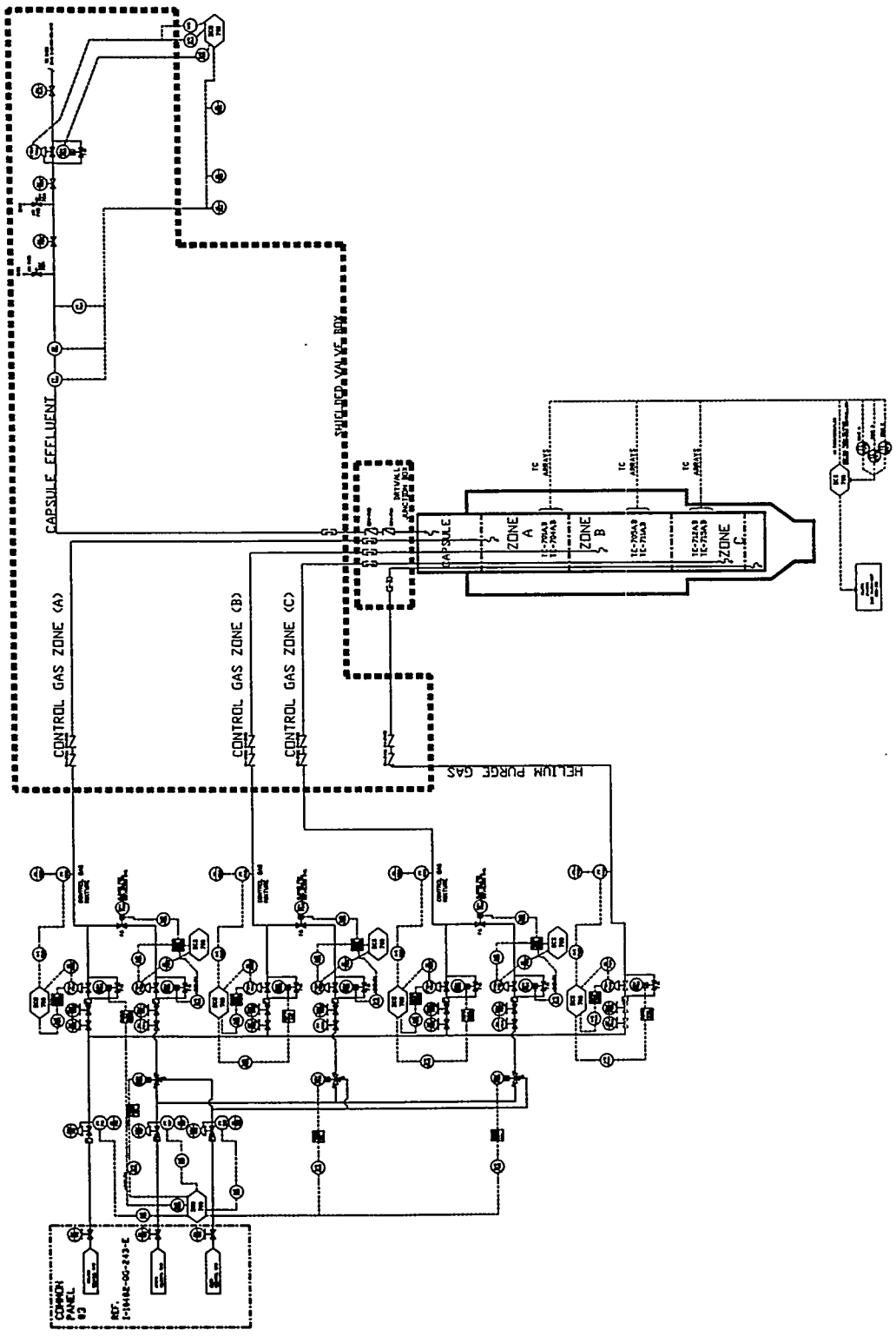

Fig. 3. Diagram of the capsule temperature monitoring and control system.

flow rates, and pressures to an operator. An operator can also manually control the flow rate of the temperature control gases and the helium purge gas. Operating temperatures, pressures, and flow rates will be monitored continuously and trended at a rate of approximately once per 5 to 10 seconds. The trended information will be saved on redundant hard disks. An instrument application diagram of this system is shown in Fig. 3.

The triax and coax cables will terminate in a cabinet containing the sample biasing and electrical resistivity measuring system. Several power supplies will be used to bias the samples. Only one power supply will be used to make the periodic resistance measurements on all 15 samples. A multiplexer will be used to switch sample leads to the appropriate power supply. A PowerMacintosh PC will run a graphical interface program (LabView) to orchestrate the actions of the power supplies and the multiplexer through a GPIB port. The information generated by this system will be passed to the temperature control system computer for redundant database storage using GPIB protocol. Appropriate alarms are incorporated on both systems to alert operators of any abnormal operating conditions or malfunctioning equipment.

It is planned that the dc electrical conductivity of each of the 15 specimens will be periodically measured approximately once every hour during the irradiation (more frequently during the beginning of the irradiation or if a large increase in the conductivity begins to occur). In addition, the ac impedance will be periodically measured. Several diagnostic tests including specimen current vs applied voltage (verification of ohmic behavior) and surface leakage resistance measurements will be performed on approximately a daily basis. The capsule will be irradiated for a total of 3 cycles in the HFIR Removable Beryllium region, which will produce a fast neutron fluence ($E > 0.1$ MeV) of about 3×10^{25} n/m^2 (~3 dpa in Al_2O_3).

Status

During this reporting period the detailed capsule and instrumentation design was completed. In addition, all capsule component fabrication, subcapsule assembly, and instrumentation system assembly was completed. Capsule component fit up and assembly has begun and is expected to be completed by early February 1996 in time for installation in the HFIR during the refueling outage planned to begin on February 19, 1996.

FUTURE WORK

Final assembly and irradiation of the TRIST-ER1 capsule are expected to be completed during the next reporting period. Irradiation is expected to begin in HFIR cycle 344 starting in March 1996. The irradiation is scheduled to last for three cycles, ending in June 1996, after accruing approximately 3 dpa damage dose. Following irradiation the capsule be allowed to decay for a few months in the HFIR pool and will then be taken to a hot cell for disassembly and post-irradiation examination (PIE) of the samples. The extent of PIE will be determined based on the observed performance during irradiation. These measurements may include (a) electrical conductivity, (b) optical absorption, fluorescence and scattering, (c) thermal conductivity, (d) surface chemical analysis, (e) mechanical strength and crack propagation tests, (f) transmission electron microscopy examination of the bulk and surface layers and scanning electron microscopy of the fracture surfaces, and (g) isochronal annealing studies.

REFERENCES

1. S. J. Zinkle and E. R. Hodgson, J. Nucl. Mater. 191-194 (1992) 58.

2. L. W. Hobbs, F. W. Clinard, Jr., S. J. Zinkle, and R. C. Ewing, J. Nucl. Mater. 216 (1994) 291.

3. S. J. Zinkle and C. Kinoshita, this report; also C. Kinoshita and S. J. Zinkle, proc. 7th Int. Conf. on Fusion Reactor Materials, Obninsk, Russia, J. Nucl. Mater. (in press).

4. E. R. Hodgson, Cryst. Latt. Def. Amorph. Mater. 18 (1989) 169.

5. A. Möslang, E. Daum, and R. Lindau, Proc. 18th Symp. of Fusion Technology, Karlsruhe, Germany, August 1994, p. 1313.

6. L. L. Snead, D. P. White, and S. J. Zinkle, in Fusion Materials Semiannual Progress Report for the Period Ending March 31, 1995, DOE/ER-0313/18, pp. 385-396; also J. Nucl. Mater. 226 (1995) 58.

7. L. L. Snead, D. P. White, W. S. Eatherly, and S. J. Zinkle, this report.

ISEC-3: RESULTS FROM THE THIRD IN-SITU ELECTRICAL CONDUCTIVITY TEST ON POLYCRYSTALLINE ALUMINA

L. L. Snead, D. P. White,* W. S. Eatherly, and S. J. Zinkle
(Oak Ridge National Laboratory)

SUMMARY

An experimental investigation of radiation induced electrical degradation (RIED) has been performed at the High Flux Beam Reactor (HFBR) at Brookhaven National Laboratory. In this study (the third in a series of experiments at the HFBR) the effects of neutron irradiation on the electrical conductivity of Wesgo AL995 polycrystalline alumina has been investigated at approximately 450°C. The capsule design used in this study is very similar to a design used in the first two experiments in this series with some improvements made in the cable terminations. A guard ring configuration was used on the disk shaped sample. Triaxial mineral insulated cable was used as the data lead from the sputter deposited guard ring and central electrode of the sample, and coaxial mineral insulated cable was used as the sample power lead. No evidence for RIED was observed in this series of experiments to a dose level of ~1.8 dpa. The effect of neutron irradiation on the electrical properties of two mineral insulated (MgO) cables was also investigated.

Introduction

A considerable amount of interest has been generated in the last few years on a phenomenon known as radiation induced electrical degradation (RIED) in ceramic insulators (see ref. 1 for a recent review). The results from several studies indicate that permanent degradation of the electrical resistivity of ceramic insulators such as alumina can occur if the material is irradiated under an applied electric field >20 V/mm at temperatures between ~200 and 530°C. This report represents the third in a series of in-situ electrical conductivity experiments performed at different temperatures on two different grades of polycrystalline alumina at the High Flux Beam Reactor (HFBR) at Brookhaven National Laboratory.

Experimental Details

The design for the third In-Situ Electrical Conductivity (ISEC-3) capsule was very similar to the design used in the previous two experiments. The data acquisition system is identical to that used in the previous studies and the reader is referred to Refs. 2 and 3 for the details of the system. The design of the subcapsule used in this experiment differs slightly from that used in the previous experiments and is shown in Fig. 1. The primary design difference is that the contacts to the samples were not spring loaded onto the sample electrodes. Instead, a small pad of TiCuSil braze material was vacuum brazed at 870°C onto the sample surface in the center and guard electrode regions, and then nickel lead wires were laser welded to the pads. Following this, platinum center and guard electrodes were sputter deposited onto the sample.

Another difference between the ISEC-3 capsule and previous two is that the termination of the power lead was modified. In the previous capsules the MgO-insulated coaxial power leads were either left unsealed in the case of the first experiment [1] or were sealed using glass as in the second HFBR experiment [2]. In these previous experiments many of the power leads experienced failure. It was felt that the cause of these failures was that the terminations on the power leads were unsatisfactory, leading to contamination of the cable ends and subsequent failure. In an attempt to remedy this problem the power lead was terminated as shown in Fig 2. With this termination, the end of the power lead is completely sealed from the capsule environment. Excellent results were obtained using this method of termination. In addition to using this new termination on the coaxial power lead, an identically terminated coaxial cable was monitored throughout the irradiation (with a continuously applied voltage) to determine what changes occur in the cable itself.

As in the previous experiments, the primary thermal conduction path for this capsule design was radial to the walls of the capsule assembly, which were in contact with the reactor coolant water. The atmosphere in the capsule was ultra-high purity helium and the design temperatures were achieved by selection of the

*Present address: Merrimack College, Department of Physics, North Andover, MA 01845

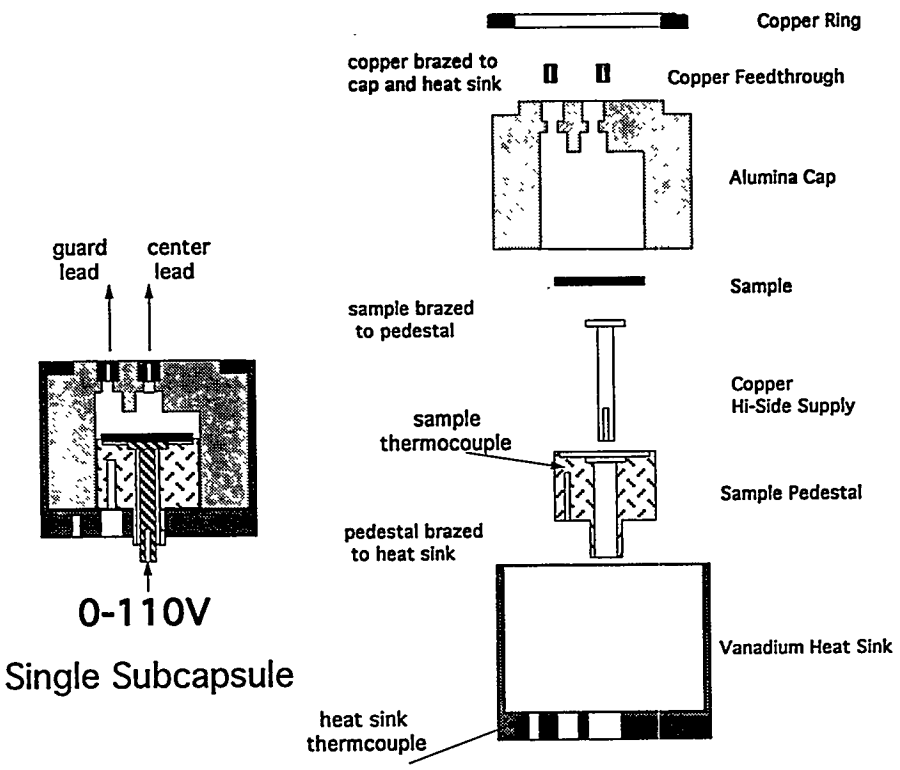

Fig. 1. Schematic of ISEC-3 subcapsule.

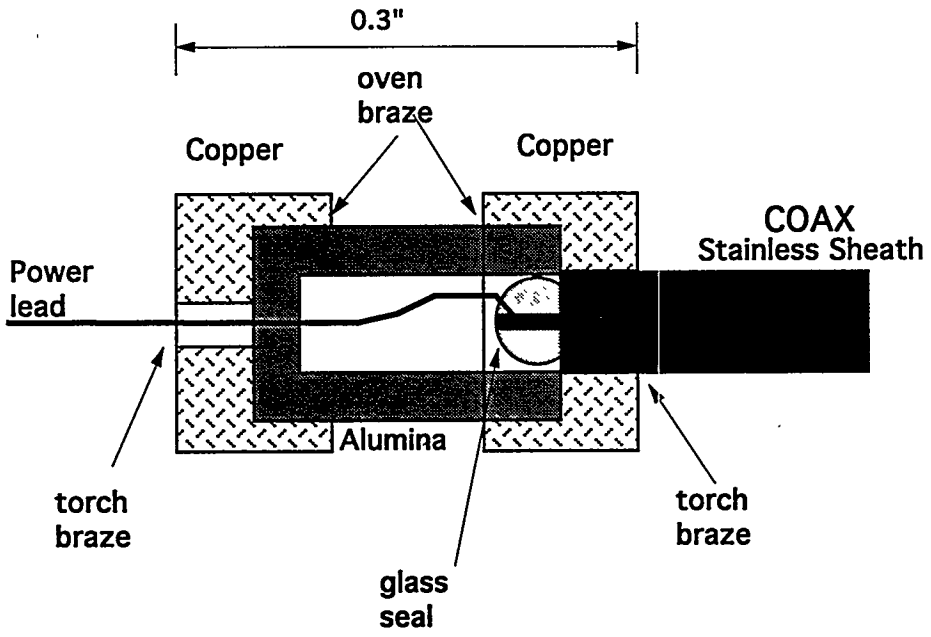

Fig. 2. Schematic of coaxial power lead termination.

helium gas gap thickness between the sample mount and the capsule wall. The sample temperature was monitored during irradiation by two mineral insulated, type K thermocouples in contact with the alumina pedestal and vanadium heat sink.

Considerable care was taken to have the highest purity capsule environment as could be reasonably achieved. The specimen was housed in a sealed subcapsule to minimize possible deposition of electrically conductive surface contaminants. The material facing the exposed surfaces of the specimen in the subcapsule interior was alumina. The atmosphere in both the sealed subcapsule and capsule was helium. As in the previous experiments, the capsule underwent three cycles of evacuation and back filling using a turbomolecular pump and ultra-high purity helium prior to insertion of the capsule into the reactor. The capsule was held at 15 psi over atmosphere of helium during the irradiation.

The data acquisition system used for this experiment was identical to that used in the previous HFBR experiments [2,3]. The material for this study was Wesgo AL995 polycrystalline alumina [4]. The sample was 0.75 mm thick by 8.5 mm diameter, the center electrode diameter was 4 mm, and the gap between the center and guard electrode was 1 mm. A DC electric potential of 110 volts was applied to the sample which corresponds to an applied field strength of 147 V/mm. As mentioned earlier, an MgO insulated coaxial cable of 1.5 mm outer diameter with a copper center conductor of 0.25 mm diameter was identically terminated and placed in the irradiation capsule. A constant potential of 110 volts (which corresponds to a minimum and maximum electric field strength in the insulation of 80 and 490 V/mm, respectively) was also applied to this cable and the leakage current was monitored throughout the experiment to determine if a breakdown in the insulating properties of the cable occurred during the irradiation. In addition, an MgO insulated triaxial cable identical to that used in the data lead from the alumina sample was placed in the capsule and irradiated without an applied voltage. The outer diameter of this cable was 1.06 mm with an inner conductor of 0.15 mm. The center conductor of this cable was periodically sourced with a voltage of from -1 to 1 V, with the guard and shield held at ground. The leakage current was measured to determine if the insulation in this cable underwent breakdown.

The capsule was placed into the V-16 thimble of the HFBR during reactor operation. The capsule was located mid-core, which has approximately 6000 Gy/s (6 W/g) ionizing dose rate and an associated fast neutron flux of 4×10^{18} n/m^2-s (E > 0.1 MeV). The temperature of the sample was continuously recorded as the capsule was inserted into the reactor and the initial specimen current measurements were taken within ten minutes of capsule insertion.

Results

The temperature of the sample is shown in Fig. 3. This plot shows that the sample thermocouple, which was located ~1 mm below the sample in the alumina pedestal, registered a temperature of 440°C for the entire irradiation. The large drop in temperature from about 250 hours to about 525 hours was due to the shutdown of the HFBR for a scheduled refueling. After approximately 24 days of irradiation this thermocouple failed and remained bad throughout the remainder of the experiment. However, a second thermocouple located in the vanadium heat sink, which can be seen from Fig. 3 to track closely with the sample thermocouple (although at a lower temperature due to its location), gave steady temperature readings until just before the second shutdown.

Figure 4 is a plot of the time-dependent low side (triax) alumina sample current for an applied potential of 110 volts. Note that at the very start of the irradiation the current was initially high and almost immediately dropped off to a lower stable value. It is possible that this is due to a self cleaning of the sample surface at the irradiation temperature (e.g., oxidation of conductive contaminants), thereby reducing spurious surface leakage currents. A second possibility is that some of the Pt electrode may have delaminated from the specimen surface--this possibility will be checked during postirradiation examination in the next reporting period. Note that during both reactor shutdowns the sample current decreased dramatically and that it immediately increased upon restart of the reactor.

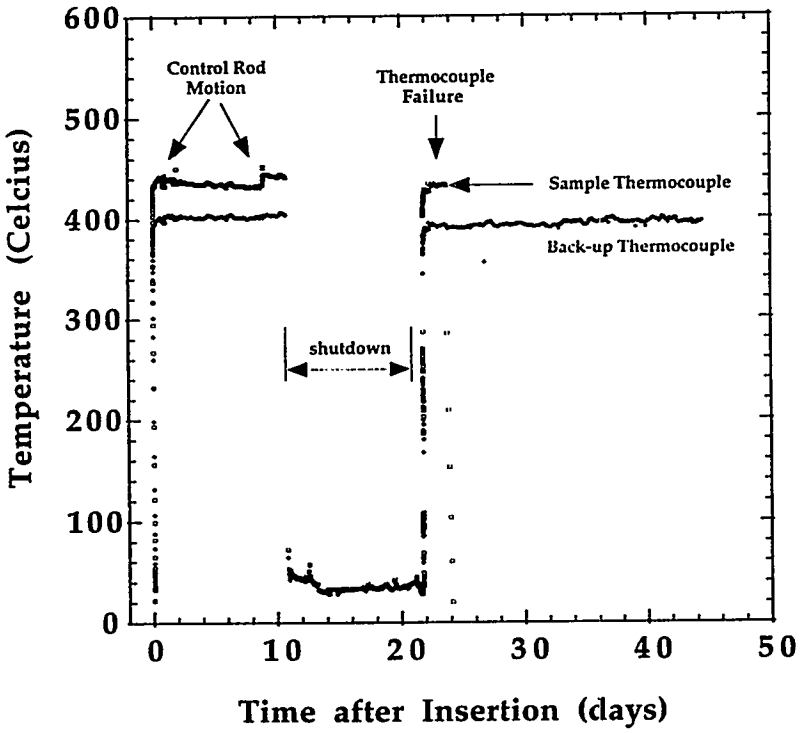

Fig. 3. Temperature history of the ISEC-3 subcapsule. The backup thermocouple was located in the vanadium heat sink.

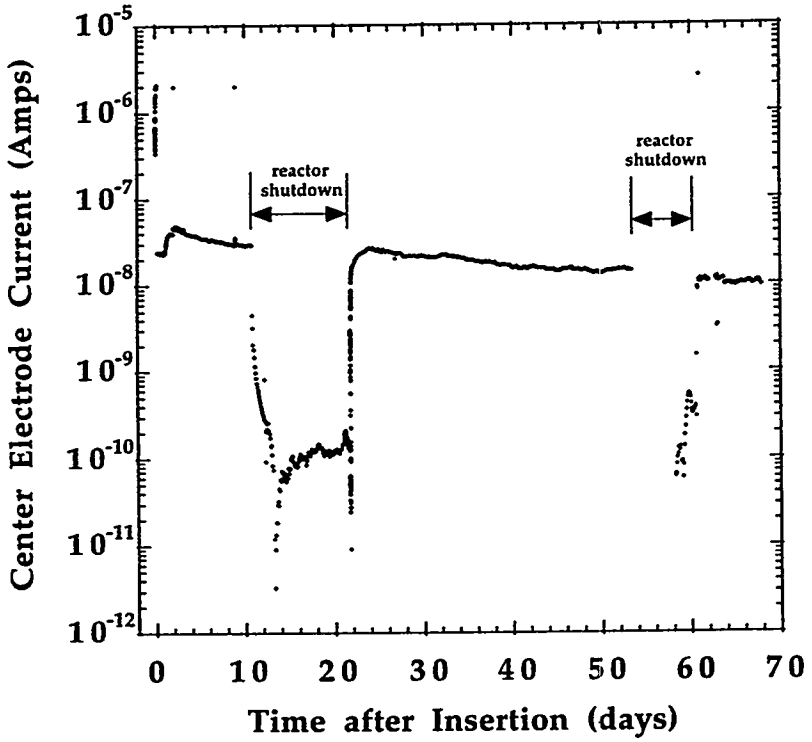

Fig. 4. Measured center electrode current for the ISEC-3 subcapsule (110 V applied potential).

Assuming that Ohm's law is observed, the conductivity of the sample is given by:

$$\sigma_v = \frac{t}{A}\frac{1}{R_v}$$

where A is the effective electrode area, t is the thickness of the disk sample, and R_V is the measured volume resistance. The effective area A is given by [5]:

$$A = \pi\left(\frac{D}{2} + \frac{g}{2} - \delta\right)^2$$

where D is the actual center electrode diameter, g is the gap between the center and outer electrode, and δ is a parameter given by:

$$\delta = t\left(\frac{2}{\pi}\ln\left(\cosh\left[\frac{\pi}{4}\frac{g}{t}\right]\right)\right)$$

which in this case gives an effective area of A = 16.3 mm^2. Taking the data as plotted in Fig. 4 and using the above equation, the calculated radiation induced conductivity (RIC) for most of the irradiation at 450°C is ~10^{-8} S/m, which is at the low end of the scatter band for RIC data on polycrystalline alumina at this dose rate (6000 Gy/s). During the two month irradiation, it is seen from Figure 4 that the current decreased by about a factor of three. Also note that during shutdown the value of the conductivity dropped off rapidly and approached the resolution limit of our equipment (~10^{-11} A) due to the greatly diminished ionizing dose rate and lower specimen temperature when the reactor was shut down. Following the restart of the reactor, the conductivity immediately increased to the level measured immediately prior to shutdown. The damage dose at the end of the irradiation was about 1.8 dpa (1.8×10^{25} n/m^2, E > 0.1 MeV), taking into account the reactor shutdowns. Thus, in this sample RIED has not occurred (at least not above the level of RIC) at damage doses up to 1.8 dpa.

The guard ring leakage current from the sample versus time from insertion is shown in Fig. 5. Note the leakage current decreases by more than an order of magnitude during the irradiation. This may be due to self cleaning of the sample during the irradiation, but postirradiation examination of the specimen is needed to confirm this possibility. Again note the decrease in leakage current during the reactor shutdown.

Figure 6 gives an example of the results of ramping the voltage from zero to a maximum of 110 volts at varied times during the irradiation. This was done primarily to determine the ohmic nature of the contacts as well as provide the conductivity of the sample from the slope of the curve (assuming linearity.) The plots show that the sample was not ohmic and therefore the conductivity cannot be directly obtained from Eq. 1 and Fig. 4. The measured current at a potential of 110 V decreased by about a factor of 3 between an irradiation time of 3 days and 60 days. However, the normalized shapes of the four current vs. voltage curves shown in Fig. 6 were all similar. This suggests that there has not been any significant change in the nature of the electrode for this time period. The measured sample current from the center lead of the triax cable was typically a few nA when the applied bias was 0 V (Fig. 6).

The results of the leakage current measurements on the terminated coaxial cable sample are plotted in Fig. 7. From this plot it is seen that this cable, which was sourced at 110 volts throughout the irradiation, did not experience a breakdown of its insulation despite the presence of a continuously applied electric field of 260 to 1580 V/mm in the MgO insulation.

As mentioned earlier, a triaxial cable which was not connected to a sample was also placed in the capsule. The center electrode of this cable was sourced from -1 to 1 volt and the current measured. Figure 8 is a representative plot of the voltage versus current for this cable measured during neutron irradiation. The triaxial cable did not experience a breakdown of its insulating properties during the irradiation, although it should be noted that voltage was not applied to this cable for most of the irradiation. The cable exhibited a slightly nonohmic behavior, with a positive offset current of ~1 nA when the applied potential was zero.

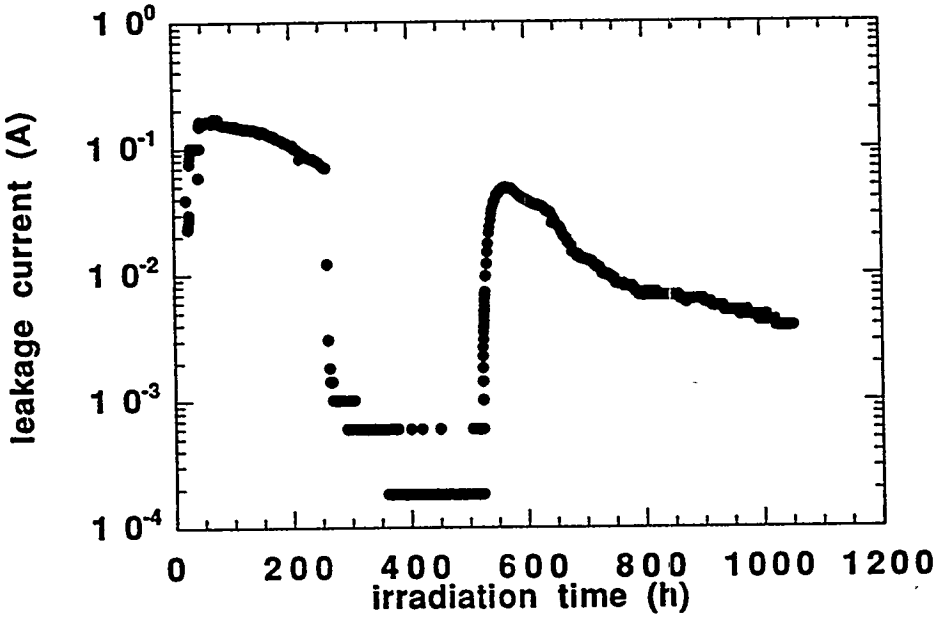

Fig. 5. Measured guard ring leakage current for the ISEC-3 subcapsule.

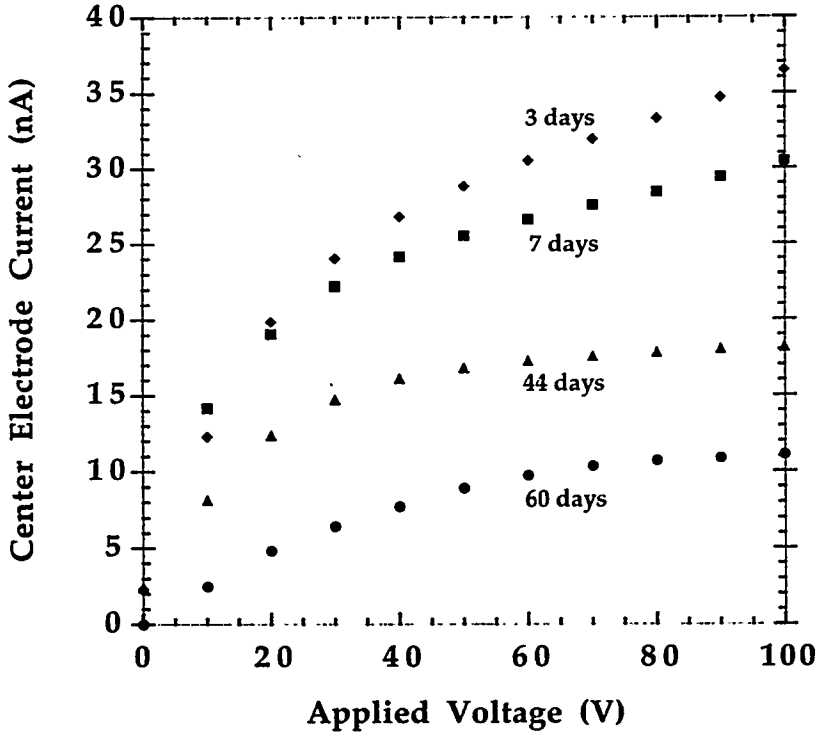

Fig. 6. Measured ohmic checks for the Wesgo alumina sample at different stages of the irradiation.

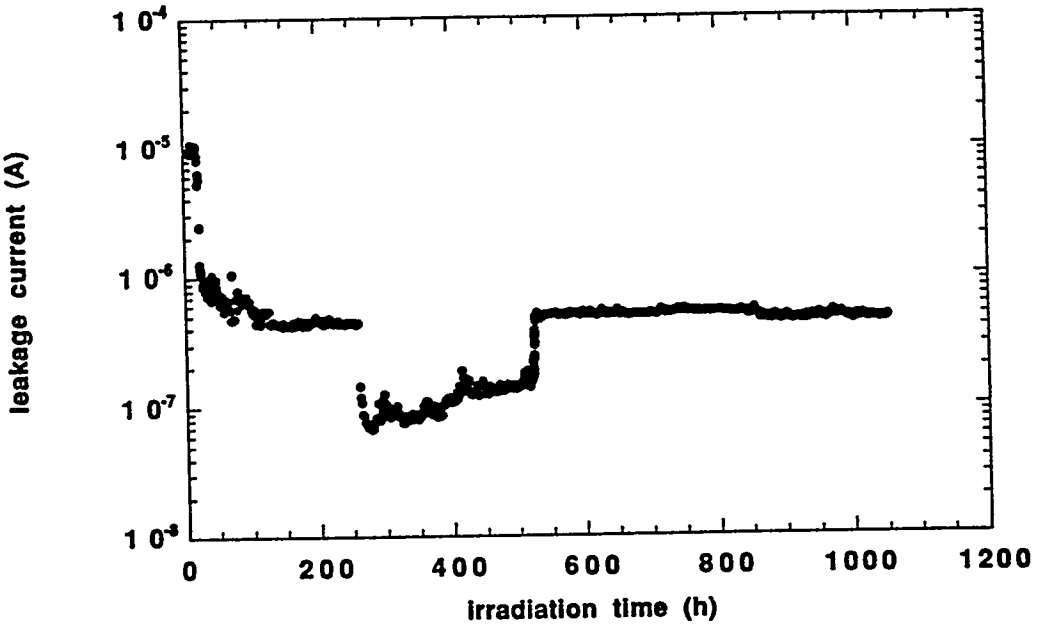

Fig. 7. Measured leakage current from the terminated coaxial cable sample.

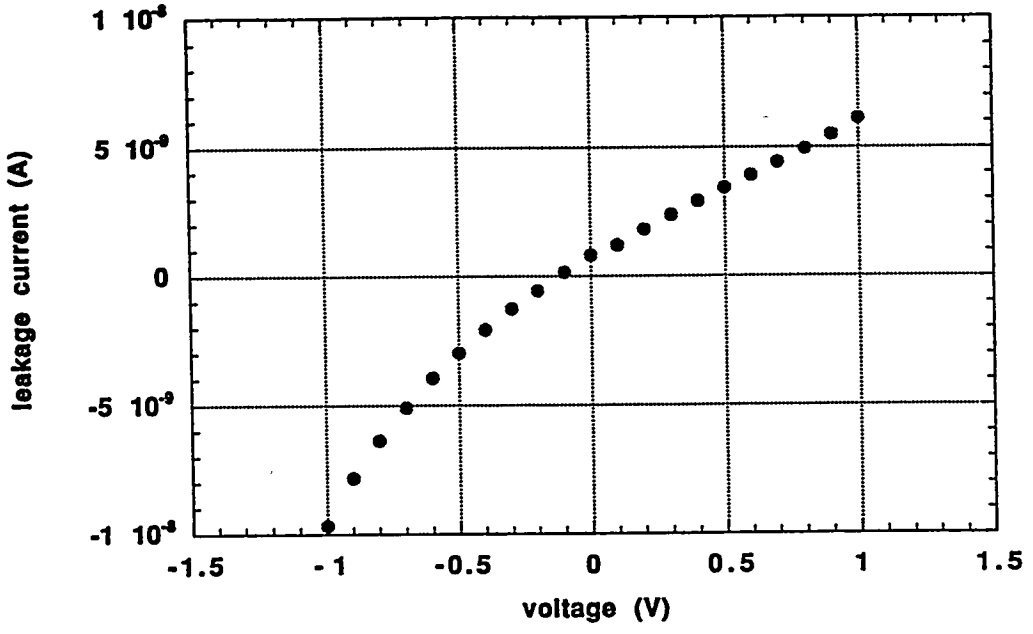

Fig. 8. Ohmic check on the center electrode of the triaxial cable sample after 50 h of irradiation.

Discussion

Polycrystalline Wesgo AL995 alumina has been studied by five different research groups as part of an IEA round robin effort to examine the RIED effect in alumina [6]. To this point there has been no bulk RIED observed in the Wesgo material. The results presented in this paper represent the highest neutron dose level of any RIED study undertaken thus far (~1.8 dpa) and are at the expected optimum temperature for the onset of RIED (450°C). For this reason the data presented here further reinforce the position presented in the previous work [3], that through the selection of the appropriate polycrystalline alumina, e.g. Wesgo AL995, the RIED effect as a bulk phenomenon may not pose a problem for fusion systems such as ITER. Furthermore, it should be noted that RIED was not observed in the coaxial cable which was irradiated with an applied voltage of 110 V (corresponding electric field in the insulation of 80 to 490 V/mm). The irradiation temperature of the coaxial cable is uncertain since it was not directly measured. The temperature was most likely ~100°C since it was in contact with the aluminum capsule wall. Therefore, the absence of RIED in the coaxial cable insulation may be due to an irradiation temperature below the regime where RIED has generally been observed, 200-500°C.

A definitive statement regarding the actual radiation induced conductivity measured in this study is not possible from the data presented here. This is due to the open question of the integrity of the sputter deposited electrodes. Whereas we have tentatively attributed the drop in the sample current shortly after the start of the irradiation (Fig. 4) to cleaning of the specimen surface, it is also possible that some change occurred to the electrodes. In addition, the nonohmic behavior of the sample current requires additional analysis. It is worth noting that another RIED study has also reported non-ohmic behavior of Wesgo AL995 following ion irradiation [7]. It is possible that degradation of the platinum electrode occurred or some other sample/electrical degradation has taken place. However, it is apparent that there was good electrical contact to the sample surface, as demonstrated by the low-side response to applied voltage shown in Fig. 6. Therefore, it may be concluded that an applied field of 147 V/mm was applied to the Wesgo AL995 sample to a cumulative dose of approximately 1.8 dpa without catastrophic RIED occurring. We are planning to cut open the ISEC-3 subcapsule during the next reporting period to inspect the irradiated guard ring and electrode configuration.

Conclusions

The results of this experiment demonstrate that no RIED occurred in a sample irradiated with an applied DC potential of ~150 V/mm to 1.8 dpa at a temperature of 440°C. This temperature is well within the range of temperatures where it has been reported that RIED will occur. The fact that it was not seen in this case implies that at least some grades of ceramic insulators may perform satisfactorily in ITER and other fusion reactors.

The termination used for the mineral-insulated power lead cable worked well and allowed the power lead to operate for the 2-month reactor irradiation without failure. The fact that the separate coaxial cable sample which was also sourced with 110 V (corresponding electric fields of 80 to 490 V/mm) for the duration of the irradiation also did not experience a breakdown of its insulating properties is further evidence that this new method of cable termination helps in increasing the life expectancy of the power cables under irradiation.

Acknowledgments

The authors would like to thank Joe O'Conor, Joel Errante, and Guy Hartsough for their assistance with accessing the HFBR facilities. The AL995 alumina was provided to the U.S. Fusion Materials Program as a reference material by GTE Wesgo. Research sponsored by the Office of Fusion Energy, U.S. Department of Energy under contract DE-AC05-96OR22464 with Lockheed Martin Energy Research Corp.

References

[1] S. J. Zinkle and C. Kinoshita, this report; also C. Kinoshita and S. J. Zinkle, Proc. ICFRM-7, Obninsk, Russia, J. Nucl. Mater. (in press).
[2] L. L. Snead, D. P. White, and S. J. Zinkle, J. Nucl. Mater., 212-215 (1994) 1107.
[3] L. L. Snead, D. P. White and S. J. Zinkle, J. Nucl. Mater., 226 (1995) 58.
[4] R. E. Stoller, Fusion Reactor Materials Semiannual Progress Report DOE/ER-0313/8 (1990) 299.
[5] Standard Test Methods for DC Resistance or Conductance of Insulating Materials, ASTM D257-91.
[6] S. J. Zinkle, "Summary of the IEA Workshop on Radiation Effects in Ceramic Insulators," this report.
[7] W. Kesternich, F. Scheuermann, and S. J. Zinkle, J. Nucl. Mater. 219 (1995) 190.

SUMMARY OF THE IEA WORKSHOP ON RADIATION EFFECTS IN CERAMIC INSULATORS –

S.J. Zinkle (Oak Ridge National Laboratory)

OBJECTIVE

The objective of this report is to provide a written summary of an IEA Workshop on Radiation Effects in Ceramic Insulators that was held in Obninsk, Russia.

SUMMARY

A brief summary is given of research on radiation effects in ceramic insulators for fusion energy applications performed during the last two years in Europe, Canada, Japan, the Russian Federation, the Ukraine and the United States. The IEA round-robin radiation-induced electrical degradation (RIED) experiment on Wesgo AL995 polycrystalline alumina has been completed by 5 research groups, with none of the groups observing clear indications of RIED.

PROGRESS AND STATUS

Introduction

An IEA workshop on Radiation Effects in Ceramic Insulators was organized as an evening session during the 7th International Conference on Fusion Reactor Materials (ICFRM-7) in Obninsk, Russia on September 26, 1995. This workshop was the 8th in its series, and served as a forum to discuss advances in understanding radiation effects in ceramics for fusion energy systems that have been attained since the last workshop held in Stresa, Italy in September, 1993. Approximately 25 scientists from Japan, the European Union, Russian Federation, The Ukraine and the United States attended the workshop. A partial list of attendees is given in Table 1.

Overviews of recent work on ceramic insulators

Eric Hodgson summarized work performed in Europe and Canada (CIEMAT, AEA Technologies/Harwell Lab, Forschungszentrum Karlsruhe, and McMaster University) on electrical, dielectric, mechanical, and optical properties, and tritium diffusion. It was noted that radiation-induced electrical degradation (RIED) has been observed in BeO, and an indication of RIED-like effects has been observed in AlN. Work has proceeded on a model to explain RIED in alumina on the basis of nucleation of gamma-alumina precipitates by colloids. Bulk RIED was not observed in Wesgo AL995 alumina irradiated with electrons or alpha particles, although significant increases in the surface conductivity were observed under some circumstances (see following section on the IEA round-robin RIED experiment on Wesgo AL995 alumina). The importance of the Mg content on dielectric loss of alumina at 100 MHz was noted. Irradiation of sapphire with fission neutrons at room temperature and ~80 K produced comparable increases in the loss tangent measured at electron cyclotron frequencies, indicating that the surviving defect concentrations were similar for these two irradiation temperatures. Important progress has been made with Si and diamond, two alternative ECRH materials. Results for sub-critical crack growth for alumina under gamma irradiation indicate a radiation hardening. Initial results for the effect of RIED on the mechanical properties of alumina show a weakening of the material together with the formation of a complex microstructure. The observed large variation in the diffusivity of hydrogen isotopes for sapphire and aluminas is believed to be related to impurity and grain size effects. An ionizing radiation field of 10^6 Gy/s increased the room temperature tritium diffusion coefficient in alumina by a factor of 10^{20}.

Table 1. Partial list of Attendees at the IEA Workshop on Radiation Effects in Ceramic Insulators

Japan	European Union	Russian Federation/Ukraine
K. Abe (Tohoku Univ.)	E.R. Hodgson (CIEMAT)	V.A. Belyakov (Efremov)
C. Kinoshita (Kyushu Univ.)	R. Vila (CIEMAT)	V.M. Chernov (IPPE)
K. Noda (JAERI)	A. Möslang (FZK-Karlsruhe)	V.A. Stepanov (IPPE)
T. Shikama (Tohoku Univ.)		A.V. Zrodnikov (IPPE)
T. Yano (Tokyo Inst. Tech.)		O. A. Plaksin (IPPE)
	United States	D.V. Orlinski (Kurchatov)
	L.L. Snead (ORNL)	T.A. Bazilevskaya (Kharkov)
ITER-Garching JWS	R.E. Stoller (ORNL)	V.T. Gritsyna (Kharkov)
S. Yamamoto	S.J. Zinkle (ORNL)	V.S. Voitsenya (Kharkov)

Prof. Chiken Kinoshita noted that bulk RIED has not been observed so far in UV-grade sapphire irradiated with 1-MeV electrons at 450°C up to doses of ~2×10^{-4} dpa. Microstructural observations on spinel, MgO and alumina specimens irradiated under a variety of experimental conditions were also summarized.

Kenji Noda reported on radiation induced conductivity measurements performed on sapphire during gamma ray and 14-MeV neutron irradiation at temperatures between 300 and 870 K. The RIC values were in good agreement with previous studies on alumina irradiated with electrons, ions and fission neutrons. Work is in progress on an RIED experiment on alumina and MgO in the JRR-3 reactor (670 K, 50 V/mm, 4×10^{-8} dpa/s, total dose of ~0.3 dpa). The electrical conductivity will be measured following irradiation. An initial set of triple-beam (H, He, O) irradiations on alumina have been performed at the recently-completed triple-beam accelerator facility at Takasaki. The facility is capable of irradiation temperatures from 77 to 1270 K and has accelerator energies of 0.2-0.4 MeV, 0.4-3 MeV, and 0.8-21 MeV, respectively.

Steve Zinkle reported that RIED was not observed in Wesgo AL995 alumina during fission neutron irradiation at 350 and 440°C up to damage levels of ~2 dpa (see following section on the IEA round-robin RIED experiment on Wesgo AL995 alumina). However, bulk RIED was observed in amorphous thin films of alumina irradiated with 2 MeV He ions to doses >10^{-3} dpa. Coaxial cables containing either high-purity alumina or Cr-doped alumina insulation exhibited the lowest RIC values of 8 types of mineral insulated cables during X-ray irradiation at temperatures between 100 and 750°C (synthetic diamond and normal grade alumina insulation exhibited the highest RIC values). The irradiation spectrum was reported to strongly affect the microstructural evolution in ceramic insulators, with dislocation loop formation strongly suppressed in environments with high amounts of ionization and low primary knock-on atom energies.

Prof. V. M. Chernov summarized recent RIC and RIED measurements performed with 7-8 MeV protons at 300 K and in the BR-10 reactor at 850 K. The measured RIC in sapphire was found to be several orders of magnitude smaller than that reported by other investigators, and RIED was not observed (although the irradiation temperatures for these experiments were outside of the envelope were RIED is expected to occur). It was suggested that many of the RIC results reported in the literature may be erroneously high due to experimental artifacts (surface leakage currents, gas ionization, etc.). During the ensuing discussion it was agreed that the sapphire used in these experiments would be supplied to several western laboratories for further RIC studies. It was tentatively agreed that the RIC measurements would be performed by Eric Hodgson at CIEMAT, and chemical analysis of the Russian sapphire would be performed by Anton Möslang of Forschungszentrum Karlsruhe. It was also proposed that a western grade of sapphire should be supplied to the Obninsk researchers for RIC measurements.

V. S. Voitsenya and V. T. Gritsyna discussed recent work in the Ukraine on radiation effects in ceramic insulators. The possibility of radiation-induced voltages occurring between the center wire and outer sheath of mineral insulated cables (due to Compton electrons) was outlined, and optical spectroscopy measurements on electron and neutron irradiated spinel were shown.

Summary of round-robin RIED measurements on Wesgo AL995 alumina

One of the major issues discussed at the preceding IEA Workshop on Radiation Effects in Ceramic Insulators held in Stresa, Italy in September, 1993 was the conflicting data at that time on RIED in alumina. The Stresa workshop participants agreed to perform a round-robin RIED experiment on the IEA reference ceramic, Wesgo AL995 alumina, at a temperature of 450°C with an applied field of >200 V/mm and a damage rate between 10^{-9} and 10^{-8} dpa/s (see Table 2 for a summary of the approved experimental features). Specimens from a single heat of this material were supplied to interested parties by R. E. Stoller (ORNL). A total of 5 different research groups participated in the round-robin experiment [1-5], including one experiment [2] that was performed on this heat of material prior to the Stresa workshop. In some cases, the experimental conditions were slightly different from the standard conditions due to experimental limitations (e.g., minimum flux available in a fission reactor).

The results of the five RIED studies on Wesgo AL995 alumina are summarized in Fig. 1 [1-5]. The spallation [2] and fission [5] neutron data include RIC contributions, whereas the remaining data were obtained in the "beam-off" condition. All five studies are in agreement that significant amounts of bulk RIED were not observed in this grade of alumina for the conditions studied. Furthermore, it should be noted that good agreement was obtained between the different research groups regarding the unirradiated electrical conductivity at 450°C and the magnitude of the RIC. The relatively large increase in the electrical conductivity of the specimen irradiated with 28 MeV He ions at a dose of ~2×10^{-3} dpa was due to a change in the polarity of the applied electric field [1].

A significant amount of radiation-enhanced degradation of the surface conductivity of Wesgo AL995 alumina was reported to occur during irradiation with 1.8 MeV electrons [4]. This surface degradation was not observed in previous experiments on sapphire and Vitox polycrystalline alumina, and the source of the degradation in Wesgo AL995 could not be removed by cleaning in acetone [4]. The surface conductivity could be removed by mechanical polishing, and cross-section scanning electron microscope analysis of one of the specimens suggested that the degradation extended to a depth of 20-100 μm [4]. Heating in air for 20 hours at 500°C eliminated the surface degradation [4]. Further work is needed to identify the source of this increased surface conductivity. Likely candidates include radiation-enhanced reduction of the alumina surface in vacuum, impurity effects, and residual hydrocarbons from cutting and polishing. The other participants in the round-robin experiment did not report degradation of the surface resistance.

Table 2. IEA Round-Robin RIED Experimental Parameters

Material: Wesgo AL995 polycrystalline Al_2O_3 (IEA reference material)
Temperature: 450°C Electric field: >200 V/mm Damage rate: 10^{-9} to 10^{-8} dpa/s

Essential experimental features

1. The temperature of the specimen must be directly measured.
2. A guard ring geometry must be used for the specimen electrodes. The surface conductivities (center-guard and guard-base) must be measured and reported (at least the surface conductivities at the beginning and end of the irradiation, preferably with the beam on). If a spring-loaded electrical contact system is used, then the contact resistance to the guard electrode must be measured.
3. Ohmic behavior should be verified and reported.
4. A detailed description of the experiment should be reported (specimen geometry, electrode dimensions, irradiation atmosphere, apparatus to suppress secondary electron emission, etc.).
5. Detailed postirradiation examination of the specimens (including TEM) is strongly encouraged.

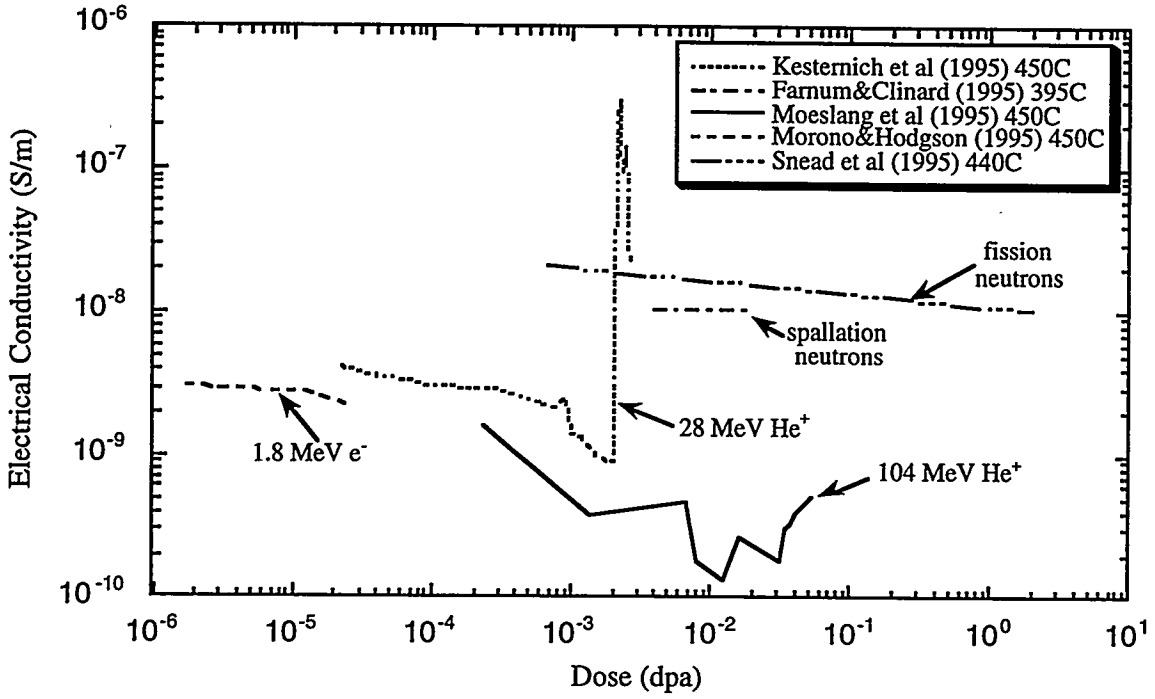

Figure 1. Summary of IEA round-robin RIED measurements on Wesgo AL995 alumina.

Eric Hodgson presented evidence that the threshold electric field to induce high concentrations of F^+ centers and RIED in alumina is higher for polycrystalline grades of alumina (e.g., ~90 V/mm in Vitox) compared to single crystal alumina (~30 V/mm). This implies that the resistance of Wesgo AL995 alumina to bulk RIED may be due to a higher threshold electric field for initiation of RIED.

Future Work

A proposal was made to initiate a new round-robin RIED experiment on an ultra-violet grade of sapphire in order to eliminate possible complicating effects associated with a high threshold electric field for RIED initiation in polycrystalline alumina. The details of this new round-robin experiment need to be determined, in particular who would supply the sapphire. The irradiation conditions would presumably be identical to those summarized in Table 2 (450°C, >200 V/mm, 10^{-9} to 10^{-8} dpa/s). A proposal was made by Voitsenya to investigate electrical degradation effects in mineral insulated cables, but an action plan was not established by the workshop participants.

References

1. W. Kesternich, F. Scheuermann and S.J. Zinkle, J. Nucl. Mater. 219 (1995) 190.
2. E.H. Farnum and F.W. Clinard, Jr., J. Nucl. Mater. 219 (1995) 161.
3. A. Möslang, E. Daum and R. Lindau, Proc. 18th Symp. on Fusion Technology, Karlsruhe, Germany, Aug. 1994, p. 1313.
4. A. Morono and E.R. Hodgson, 7th Intern. Conf. on Fusion Reactor Materials, Obninsk, Russia, proceedings to be published in J. Nucl. Mater.
5. L.L. Snead, D.P. White and S.J. Zinkle, presented at 7th Intern. Conf. on Fusion Reactor Materials, Obninsk, Russia, to be submitted as a regular paper to J. Appl. Phys.

OPTICAL PROPERTIES OF SILICA FIBERS AND LAYERED DIELECTRIC MIRRORS -- D. W. Cooke, E. H. Farnum, F. W. Clinard, Jr., B. L. Bennett (Los Alamos National Laboratory) and A. M. Portis (UC-Berkeley)

SUMMARY

Radioluminescence (RL) from virgin and neutron-irradiated (10^{23} n-m^{-2}) silica fibers has been measured in the temperature interval 4 to 300 K. Unirradiated specimens exhibit a *decrease* in RL intensity with increasing temperature such that the intensity is extremely weak at room temperature. The luminescence is well described by a barrier-limited exciton mechanism. In contrast, the heavily-irradiated samples show an *increase* in RL with elevated temperatures such that the intensity at room temperature is about twice that measured at 4 K. Neutron irradiation presumably produces many luminescence centers that act as radiative sites for exciton decay. Absolute specular reflectance of a series of neutron-irradiated, layered dielectric mirrors was also measured. In addition to structural damage that has already been reported, we typically found approximately 10% reduction in the reflectance following irradiation. These results suggest that neither fibers nor dielectric mirrors are well suited for use near the high radiation area of the ITER plasma.

PROGRESS AND STATUS

Radioluminescence

The use of optical fibers for transmitting diagnostic information on ITER plasma performance is anticipated,[1] and the general consensus is that pure-silica-core/F-doped silica clad fibers are the best candidate materials.[2] However, they are not ideal because they suffer from radiation-induced luminescence (radioluminescence) and attenuation, which complicates measurement of the diagnostic signal.[3] Furthermore, at high γ-flux levels scattered electrons act to produce Cerenkov radiation in the silica fibers thus contributing additional unwanted emission.[4] As part of our ongoing research into the radioluminescence (RL) of silica fibers,[5] we have investigated silica-core/F-doped clad fibers containing low OH (< 1 ppm) as manufactured by Fiberguide Industries, Inc. (the material is referred to commercially as anhydroguide™). A comparison is made of the RL from unirradiated and heavily neutron-irradiated (10^{23} n-m^{-2}) specimens in the temperature interval 4 to 300 K. We also investigated RL from the core material, core+cladding, and fiber separately to see if any differences resulted from fiber processing.

In unirradiated specimens of anhydroguide (core, core+cladding, and fiber) we generally found principal emission near 500 nm. Weaker band emission is also seen near 670 nm as previously reported.[5] From a Gaussian fit of the RL data taken under continuous x-ray exposure (E_{eff}= 25 keV) as a function of temperature we conclude that the principal emission is due to recombination of self-trapped excitons.[6] It is important to note that samples are exposed only during a 15-s interval at each temperature of interest. As shown in Fig. 1, the RL decreases as temperature increases such that at room temperature we cannot resolve the main emission band. The solid circles of Fig. 1 are RL data and the solid line is a fit to Eq. (1) of the temperature dependence based upon our assumption that the reduction in RL intensity arises from quenching of self-trapped exciton luminescence by nonradiative recombination. Assuming a polynomial distribution of exciton barrier energies, a straightforward analysis leads to an equation describing RL as a function of temperature:

$$L_s(T) \approx L_s(0)e^{-T/T_s} = \frac{L_s(0)}{1+(T/T_s)+(1/2)(T/T_s)^2+\cdots(1/n!)(T/T_s)^n+\cdots} \qquad (1)$$

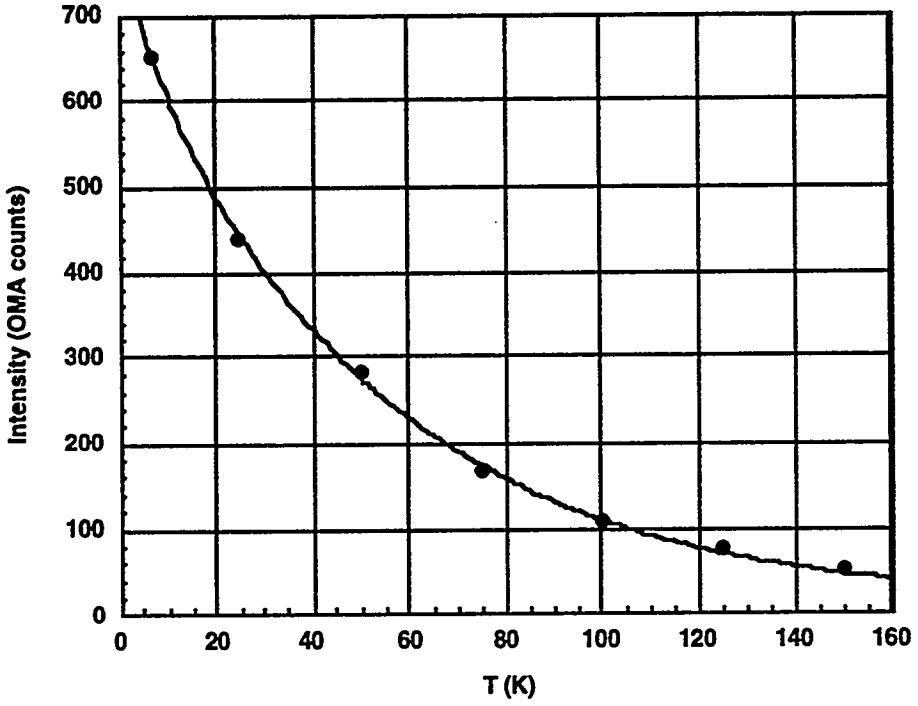

Fig. 1. Temperature dependence of RL from unirradiated anhydroguide. Solid circles are experimental data and the solid line is a fit to Eq. (1). Error bars are smaller than the plot symbols.

Temperature dependence of RL from neutron-irradiated (10^{23} n-m^{-2}) fibers is shown in Fig. 2. First we note that the general trend is an *increase* in intensity as temperature increases, quite unlike the well-behaved *decrease* observed in the unirradiated fibers. Secondly, there is considerable error in the fitting of the spectra to a Gaussian form. Presumably this is due to the plethora of radiation-induced defects that now provide a broad array of recombination sites. Although we do not understand the details of radiation damage suffered by this sample, it is obvious that many sites now exist for exciton recombination as compared to the pristine specimen.

For ITER diagnostic applications the data suggest that RL will indeed be a problem at some level of total dose. Unfortunately we have data only for the two extreme cases, unirradiated and heavily irradiated. It is plausible that some intermediate dose may be acceptable for diagnostic purposes. Nevertheless, the data suggest that RL from silica fibers subjected to heavy neutron doses must be taken into account when used in diagnostic applications. This luminescence is in addition to the Cerenkov radiation that is expected to also interfere with transmission of diagnostic signals. It is important to note that a direct comparison of the intensities given in Figs. 1 and 2 cannot be made because of variations in quality of optical coupling and sample size. However, we note that the weakest signal from the irradiated specimen (Fig. 2) is easily detected and is greater than the weakest signal from the unirradiated sample (Fig. 1). The trends of the data shown in Figs. 1 and 2 are correct and clearly illuminate the problem of RL in heavily irradiated fibers. Further work on RL of neutron-irradiated fibers will be required to quantify the signals and to assess their dependence on total dose.

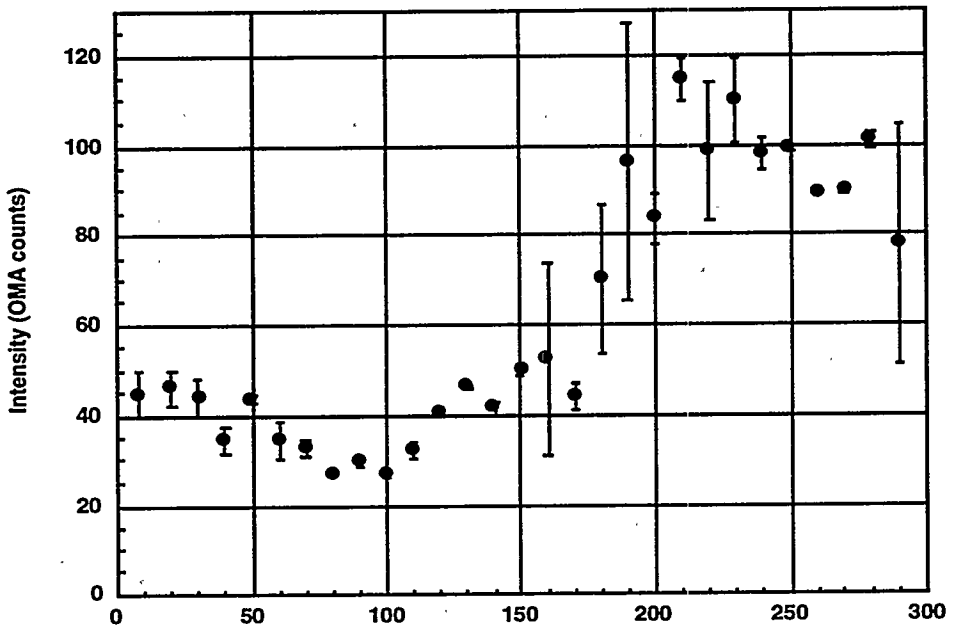

Fig. 2. Temperature dependence of RL from neutron-irradiated anhydroguide.

Neutron-Irradiated Mirrors

A series of multilayered synthetic mirrors, designed for use in the visible/near infrared region, were exposed to a fast neutron fluence of 10^{23} n-m^{-2} near 300°C. Characteristics of these mirrors along with a description of the physical damage incurred due to the neutron exposure has been previously described.[7] Briefly, these mirrors are composed of alternating layers of either HfO_2, ZrO_2, or TiO_2 with SiO_2 deposited onto SiO_2 substrates. The purpose of the high-Z material is to reflect the incident radiation while the low-Z material acts to tune the reflectance to specific wavelengths. Four mirrors and one plate polarizer investigated. The number of bilayers, with comments on the appearance of each after irradiation, are given below:

HfO_2/SiO_2, 37 bilayers – slight crazing
ZrO_2/SiO_2, 121 bilayers – coating almost totally flaked off
ZrO_2/SiO_2, 29 bilayers – moderate crazing and chipping
TiO_2/SiO_2, 39 bilayers – no discernible damage
TiO_2/SiO_2, 39 bilayers (plate polarizer) – no discernible damage

Absolute spectral reflectance measurements on each mirror and plate polarizer were made at room temperature with a specially-equipped Cary 5E spectrophotometer. All measurements were made at an incident angle of 7°and the results are shown in Fig. 3. Unfortunately, pre-irradiation measurements were not made; therefore, direct comparison is not possible. However, data obtained from the manufacturer[8] on similar materials indicate that reflectivity at designated wavelengths is greater than 90%. Mirrors were designed for optimal reflectivity at the following wavelengths; refer to Fig. 3: (a) 248 nm, (b) 400-700 nm, (c) 511 nm, (d) 694 nm, and (e) 1064 nm. In each case there is at least a 10% reduction in reflectance following neutron irradiation. Fig. 3(b) does not represent a reliable measurement because the coating was almost totally flaked off this particular mirror. The cause(s) for reduced reflectivity is not understood at present although it has been suggested[7] that differential swelling between substrates and their layered structures could be a source of physical damage that could also affect the overall reflectivity.

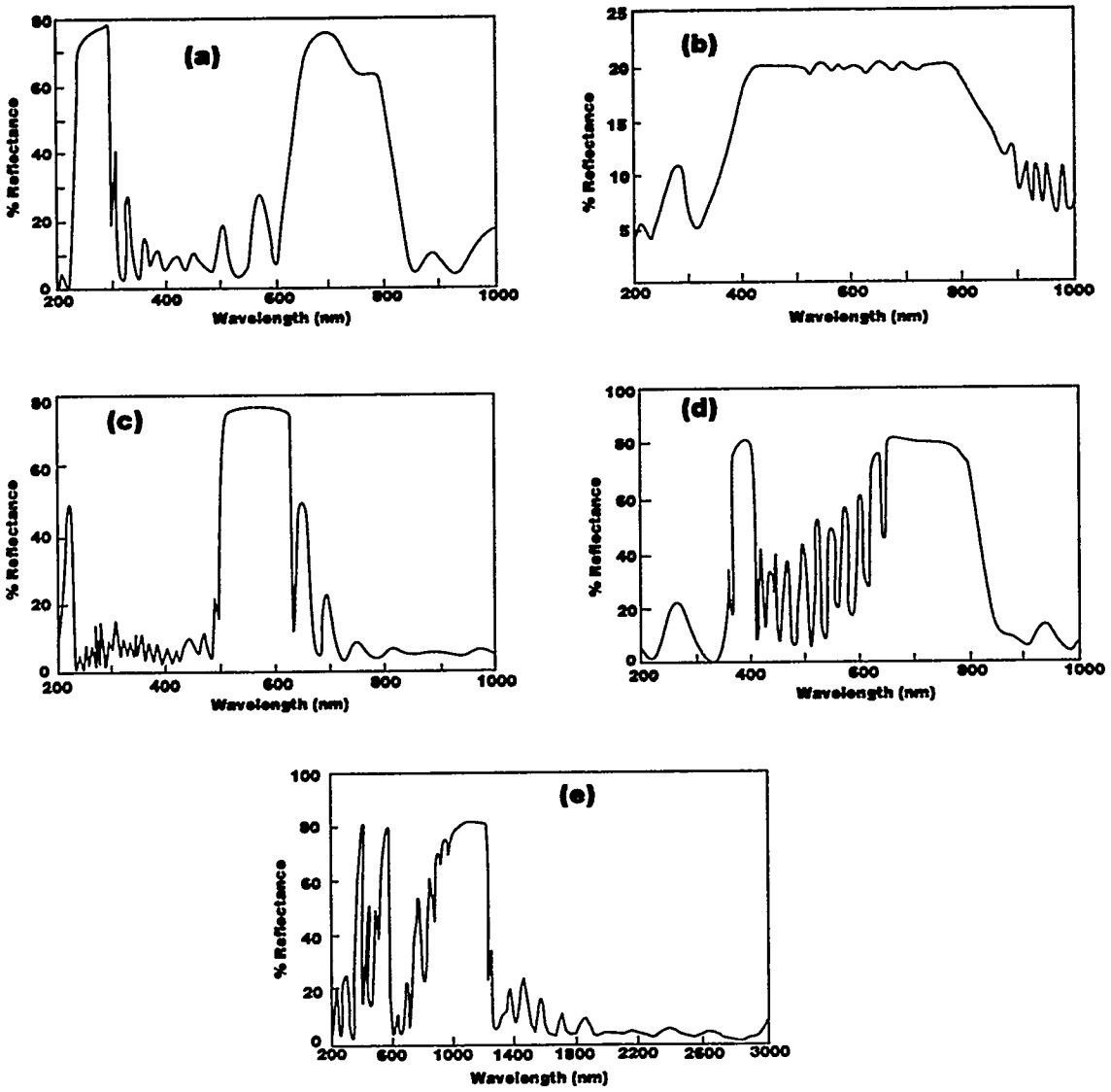

Fig. 3. Absolute specular reflectance of neutron-irradiated mirrors. (a) HfO_2/SiO_2 - 37, (b) ZrO_2/SiO_2 - 121, (c) ZrO_2/SiO_2 - 29, (d) TiO_2/SiO_2 - 39, and (e) TiO_2/SiO_2 - 39.

CONCLUSIONS

Our results suggest that RL from heavily-irradiated silica fibers will be significant at the temperatures anticipated for ITER operation. This emission, in addition to Cerenkov radiation, will certainly interfere with the transmission of ITER diagnostic signals via optical fibers. Dielectric mirrors suffer at least a 10% reduction in reflectivity as a result of high-fluence (10^{23} n-m^{-2}) neutron irradiation and will not likely be good candidates for use in the high-fluence regions of ITER.

REFERENCES

[1] W. Tighe, P. Morgan, H. Adler, D. Cylinder, D. Griscom, D. Johnson, D. Palladino, and A. Ramsey, *Rev. Sci. Instrum.* **66**, 907 (1995).
[2] D. L. Griscom, *J. Appl. Phys*. **77**, 5008 (1995).
[3] D. L. Griscom, *J. Ceram. Soc. Jpn*. **99**, 923 (1991).
[4] S. F. Paul, J. L. Goldstein, R. D. Durst, and R. J. Fonck, *Rev. Sci. Instrum.* **66**, 1252 (1995).
[5] D. W. Cooke, E. H. Farnum, F. W. Clinard, Jr., B. L. Bennett, and A. M. Portis, Fusion Reactor Materials Semiannual Progress Report, DOE/ER-0313/18, Oak Ridge National Laboratory, Oak Ridge, TN. March, 1995.
[6] D. L. Griscom, *Phys. Rev. B* **40**, 4224 (1989).
[7] E. H. Farnum, F. W. Clinard, Jr., S. P. Regan, and B. Schunke, *J. Nucl. Mater*. **219**, 224 (1995).
[8] Technical Optics, Ltd., Second Avenue, Onchan, Isle of Man, British Isles.

7.0 SOLID BREEDING MATERIALS

No contributions.

8.0 RADIATION EFFECTS, MECHANISTIC STUDIES, AND EXPERIMENTAL METHODS

THEORY AND MODELING OF RADIATION EFFECTS IN MATERIALS FOR FUSION ENERGY SYSTEMS- H. L. Heinisch (Pacific Northwest National Laboratory[1])

OBJECTIVE

The objective of this report is to present a brief summary of the recent US/Japan Workshop on Theory and Modeling of Radiation Effects in Materials for Fusion Energy Systems.

SUMMARY

The US/Japan Workshop on Theory and Modeling of Radiation Effects in Materials for Fusion Energy Systems, under Phase III of the DOE/Monbusho Collaboration, convened on July 17-18, 1995, at Lawrence Livermore National Laboratory. A brief summary of the workshop is followed by the workshop program.

PROGRESS AND STATUS

Several very positive trends in fusion materials research emerged from this workshop. Technically, the theory and modeling work is moving toward more technologically relevant problems. We have obtained a quantitative understanding of many of the "generic" fundamental issues of irradiation effects. In gaining that understanding, theories, models, and methodology were developed that can now be applied to more complicated problems. We are now focusing attention on the potential real materials of fusion energy. Atomic-scale modeling is presently under way on defect production in vanadium and silicon carbide. New methods for obtaining reasonable interatomic potentials for treating alloys and impurities look very promising. We can simulate the initial state of damage quite well now, and emphasis is moving toward understanding its influence on microstructure development. Massively parallel computers are available to handle much larger systems, and we are working to exploit this development.

Even as the number of neutron irradiation facilities available for testing and development of fusion materials is decreasing worldwide, the opportunities for advancement in theory and modeling are definitely improving. Using more computing power and better models, the new insights gained from theory and modeling activities can help us extrapolate our limited neutron irradiation information to more fusion-relevant environments.

Nineteen participants attended the workshop, eleven from Japan and eight from the US. An overview of the status of the collaboration and of the theory and modeling task was followed by technical presentations. The workshop concluded with group discussions on cascade simulations, microstructure evolution and mechanical properties, critical experiments and continuing specific collaborations. We were fortunate also to have a presentation on massively parallel computing by Dr. Alice Koniges from the National Energy Research Supercomputer Center at LLNL. A report containing extended abstracts of the presentations and summaries of the group discussions was distributed to participants and collaboration task leaders.

---

[1]*Pacific Northwest National Laboratory is operated for the U.S. Department of Energy by Battelle Memorial Institute under Contract DE-AC06-76RLO 1830.*

PROGRAM

Introduction, H.L. Heinisch (PNL)

Overviews and Projections

Overview of JUPITER Collaboration, A. Kohyama (Kyoto U.)
Objectives for Theory and Modeling in the JUPITER Collaboration, N. Sekimura (U. Tokyo)
Historical Overview of Theory and Modeling of Irradiation Effects in Fusion Materials, S. Ishino (Tokai U.)

Computational Resources

MPP Computing Resources at NERSC, A. Koniges (NERSC, LLNL)
Japanese Computing Resources and Needs, Y. Katoh (NIFS)

MD Simulations of Defect Production

Interatomic Potentials, J.B. Adams (U. Illinois)
Critical Review of Molecular Dynamics Simulations of Cascades, T. Diaz de la Rubia (LLNL)
MD Cascades in BCC Metals, R.E. Stoller (ORNL)
Defect Production in SiC, N.M. Ghoniem (UCLA)
Molecular Dynamic Simulation of Si, M.J. Caturla (LLNL)
Critical Evaluation of Various Interatomic Potentials for Radiation Damage Studies of Vanadium, K. Morishita (U Tokyo)

Simulations of Defect Behavior

Defect Clusters in Irradiated Metals, Y. Shimomura (Hiroshima U.)
MD Simulations of Point Defect Behavior Near a Dislocation, H. Matsui (Tohoku U.)
Stochastic Annealing Simulation, H.L. Heinisch (PNL)
Defect Clusters in SiC, K. Fukumoto (Tohoku U.)

Microstructure Evolution and Mechanical Properties

Modeling Radiation-induced Segregation, S. Watanabe (Hokkaido U.)
Modeling of Radiation Embrittlement of Steels, R.E. Stoller (ORNL)
Development of an Integrated Code for Swelling Evaluation, Y. Katoh (NIFS)
Microstructure-Mechanical Properties Correlations, G.R. Odette (UCSB)
Numerical Analysis of Microstructural Evolution under Applied Stress in Irradiated Fe-Cr-Ni Alloys, H. Tanigawa (U. Tokyo/Kyoto U.)
Application of Various Irradiation Methods for Advanced Modeling of Microstructure Evolution, T. Iwai (U. Tokyo, Tokai-mura)

Group Discussion

Simulating Cascade Damage, Leader, T. Diaz de la Rubia (LLNL)
Microstructure Evolution, Mechanical Properties, Leader, G.R. Odette (UCSB)
Critical Experiments, Leader, N. Sekimura (U. Tokyo)
Specific Collaborations, Leader, A. Kohyama (Kyoto U.)

ACKNOWLEDGEMENTS

On behalf of all the participants, we would like to thank Dr.Tomas Diaz de la Rubia and Lawrence Livermore National Laboratory for providing the workshop facilities. We are indebted to Mrs. Margie Altenbach for artfully coordinating the local arrangements.

DISPLACEMENT RATE DEPENDENCE OF IRRADIATION CREEP AS PREDICTED BY THE PRODUCTION BIAS MODEL - C. H. Woo (Atomic Energy of Canada Limited) and F. A. Garner (Pacific Northwest National Laboratory)

To be published in J. Nuclear Materials, 1996 proceedings of ICFRM-7

Extended Abstract

Recently, it has been shown that the non-swelling component of irradiation creep of austenitic stainless steels is relatively independent of temperature but is sensitive to the displacement rate. An earlier model of Lewthwaite and Mosedale anticipated the sensitivity of displacement rate and attributed it to the flux sensitivity of point defect recombination. The point-defect recombination process does not yield the observed temperature dependence, however, although it does predict an inverse dependence of the creep rate on the square root of the displacement rate that was experimentally observed at relatively low temperatures.

The production bias concept of Woo and Singh provides for an improved irradiation creep model. It predicts the correct temperature and dpa rate dependence of the non-swelling-related component of creep, and also provides a good description of the swelling-enhanced component of creep. The dose-rate dependence of the creep and swelling rates occurs as a result of the generation, during cascade damage, of primary clusters, the sink strengths of which are significant compared with those of sinks visible using electron microscopy. The primary clusters act as recombination centers for the single defects. As the dose rate increases, the number density and hence the sink strength of these primary clusters also increases, thus reducing their efficiency. This model leads to a prediction that the creep rate varies as the displacement rate, in close agreement with the observed square root behavior.

[1] Operated for the US Department of Energy by Battelle Memorial Institute under Contract DE-AC06-76RLO 1830

STOCHASTIC ANNEALING SIMULATION OF CASCADES IN METALS - H. L. Heinisch (Pacific Northwest National Laboratory[1])

OBJECTIVE

The objective of this work is to determine the energy and temperature dependence of defect production and microstructure evolution for the development of fission-fusion correlations.

SUMMARY

The stochastic annealing simulation code ALSOME is used to investigate quantitatively the differential production of mobile vacancy and SIA defects as a function of temperature for isolated 25 keV cascades in copper generated by MD simulations. The ALSOME code and cascade annealing simulations are described. The annealing simulations indicate that above Stage V, where the cascade vacancy clusters are unstable, nearly 80% of the post-quench vacancies escape the cascade volume, while about half of the post-quench SIAs remain in clusters. The results are sensitive to the relative fractions of SIAs that occur in small, highly mobile clusters and large stable clusters, respectively, which may dependent on the cascade energy.

PROGRESS AND STATUS

Recent molecular dynamics (MD) studies have confirmed that significant clustering of both vacancies and self-interstitial atoms (SIAs) takes place by the end of the quenching stage of a cascade, and that small interstitial clusters can form glissile loops with migration energies on the order of 0.1 eV. The segregation of the vacancy and SIA distributions and the clustering give rise to a differential production of mobile vacancies and SIAs that has a strong temperature dependence. At temperatures above recovery Stage V, vacancies can evaporate from clusters, while large SIA clusters produced in the cascade remain stable, leading to a differential increase of mobile vacancies that represents a "production bias" that may be responsible for void swelling.

The creation of defects, their migration through the material, and their influence on microstructure evolution take place over time and distance scales that span up to twenty orders of magnitude. In practice, multiple models are required to study radiation damage over the entire range of scales. Molecular dynamics (MD) is effective in describing the defect creation at the atomic scale in the sub-nanosecond time frame, and reaction rate theory is necessary for describing the microstructure evolution over macroscopic distances and reactor lifetimes. Stochastic annealing simulation helps bridge the gap between MD and rate theory. It preserves the identity and position of individual defects, and it is practical at scales of up to microns and seconds. Stochastic annealing simulation is being used in two primary applications: 1.) to study the short term annealing of defects in the vicinity of an individual cascade, essentially extending the MD description of a cascade through the diffusional phase, and 2.) to study the interactions of defects in a volume of material subjected to a flux of cascades, essentially a molecular scale simulation of microstructure evolution.

Stochastic annealing simulations are being performed with the ALSOME computer code. In ALSOME defects are the interacting entities. Each defect is associated with a lattice site and is characterized as a

---

[1]*Pacific Northwest National Laboratory is operated for the U.S. Department of Energy by Battelle Memorial Institute under Contract DE-AC06-76RLO 1830.*

sphere with a radius determined by the number of point defects it contains. Defects that are mobile (single point defects and small clusters) jump stochastically according to relative jump probabilities based on their type (vacancy or interstitial) and size and weighted by their concentration. Two defects interact, becoming a single defect, when they are within a critical reaction distance that depends on their types and sizes. Defects may dissolve stochastically, one point defect at a time, depending on their relative stability. Defects may also be absorbed at sinks depending on either spatial location or statistical criteria. Input to ALSOME consists of a list of defects with positions, types and sizes; activation energies for migration and dissolution; critical reaction distances; rates of defect production or annihilation at sinks when appropriate; and temperature. In practice, defect distributions are taken from MD simulations and most activation energies are from atomistic simulations or measured values where available.

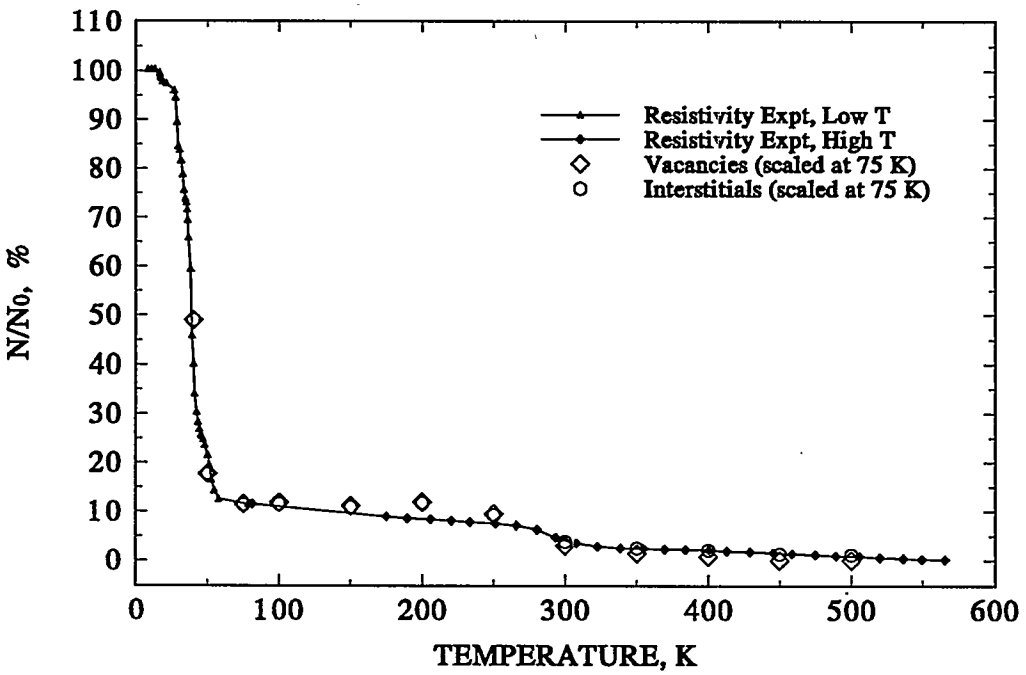

Figure 1. ALSOME Simulations of Isochronal Annealing of Copper Irradiated by Electrons to 100 ppm Frenkel Pairs.

One way to test the annealing model is to simulate the resistivity recovery experiments on material irradiated with electrons at low temperatures. Figure 1 shows the ALSOME results and experimental results[1] for isochronal annealing of electron-irradiated copper. The general shape of the recovery curve is well matched. The ALSOME simulation did not include effects of the sink structure and impurities in the experiments, which are unknown.

Figure 2 shows the results of ALSOME simulations[2] of short-term annealing of two quenched MD cascades in copper[3]. The cascades, both 25 keV, are at the threshold energy of subcascade formation, and they are the most energetic cascades simulated by MD to date. The fractions of initial defects escaping

the cascade region as a function of temperature demonstrate the concept of production bias[4] in cascade-producing irradiations. Above $0.3T_m$, which is the beginning of the void swelling regime, the fraction of escaping vacancies is almost double that of escaping interstitials. The interstitials remaining in the cascade volume reside in large, stable interstitial clusters, and about half of the escaping interstitials are in the form of rapidly moving (in one dimension) small glissile loops.

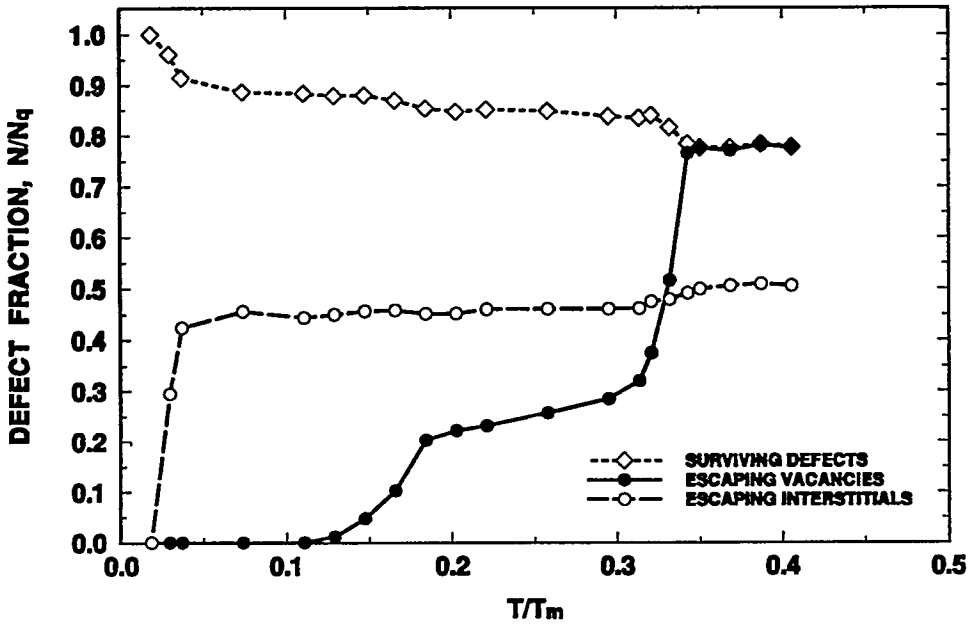

Figure 2. Short-term Annealing of Isolated 25 keV Cascades in Copper. The fractions of total surviving defects and escaping defects are relative to the number of defects present after the quenching of the cascade.

As in rate theory (but unlike MD), stochastic annealing simulations must explicitly contain the provisions for all important phenomena to occur. One should maintain a healthy skepticism of results of these simulations. On the other hand, such simulations by their nature, allow one to explore the effects of various mechanisms, conditions and phenomena in a controlled, totally observable system.

FUTURE WORK

A regular journal article on the work summarized here has been written and will be submitted to the *Journal of Nuclear Materials*. ALSOME simulations of irradiations by both high energy electrons and neutrons are in progress. For these simulations, larger volumes with periodic boundaries are used. Methods of simulating sink distributions are being investigated. Methods for investigating the annealing stage of high

energy cascades that have multiple subcascades are also being studied. A comparison of annealing stage behavior of cascades in fcc and bcc metals is being planned.

REFERENCES

1. J.W. Corbett, R.B. Smith and R.M. Walker, Phys. Rev. 114 (1959) 1452; C.J. Meechan and J.A. Brinkman, Phys. Rev. 103 (1956) 1193.

2. H.L. Heinisch, Nucl. Inst. Meth. B 102 (1995).

3. T. Diaz de la Rubia and M.W. Guinan, Mater. Res. Forum 97-99 (1992) 23.

4. C.H. Woo and B.N. Singh, Phil Mag. A65 (1992) 889.

9.0 DOSIMETRY, DAMAGE PARAMETERS, AND ACTIVATION CALCULATIONS

NEUTRON DOSIMETRY AND DAMAGE CALCULATIONS FOR THE JP-10, 11, 13, and 16 EXPERIMENTS IN HFIR

L.R. Greenwood and R.T. Ratner
Pacific Northwest National Laboratory

OBJECTIVE

To provide dosimetry and damage analysis for fusion materials irradiation experiments.

SUMMARY

Neutron fluence measurements and radiation damage calculations are reported for the joint U.S.-Japanese experiments JP-10, 11, 13, and 16 in the target of the High Flux Isotope Reactor (HFIR) at Oak Ridge National Laboratory (ORNL). These experiments were irradiated at 85 MW for 238.5 EFPD. The maximum fast neutron fluence >0.1MeV was about 2.1E+22 n/cm^2 for all of the experiments resulting in about 17.3 dpa in 316 stainless steel.

PROGRESS AND STATUS

The fabrication and irradiation of the JP-10, 11, 13, and 16 experiments have been described previously.[1-4] The assemblies were irradiated in the target position of HFIR for cycles 289-291, removed during cycle 292, and reinstalled for cycles 293-300. The net exposure was 20279 MWD over the period from July 20, 1990, to September 19, 1991.

Small dosimetry capsules measuring about 0.05"in diameter by 0.25"in length were located at 6 different positions in each assembly. Each dosimetry capsule contained milligram quantities of Fe, Ni, Ti, Nb, 0.1% Co-Al, and 80.2% Mn-Cu. Following the irradiation, selected capsules from each irradiation were sent to PNL for analysis. Each capsule was disassembled in a hot cell and subsequently gamma counted.

The measured activities were converted to activation rates, as listed in Table 1, by correcting for burnup of the reacting and product atoms, gamma self-absorption, decay of the product isotopes during and after irradiation, isotopic abundance, and atomic weight. Burnup corrections are based on an iterative procedure for the thermal/epithermal monitor reactions. The resultant estimates of the thermal/epithermal neutron fluences were then used to calculate burnup corrections for the threshold fast neutron monitor reactions. Due to the relatively long exposure, burnup corrections ranged from 20-40% for the thermal/epithermal reactions and from 10-30% for the threshold reaction rates. The activation rates listed in Table 1 are normalized to full reactor power of 85 MW and have a net absolute uncertainty of about 5%.

The fast neutron reactions, $^{54}Fe(n,p)^{54}Mn$ and $^{55}Mn(n,2n)^{54}Mn$, for all four irradiations appear to fall on a smooth curve when plotted versus the height relative to the HFIR midplane. The thermal neutron activities for the ^{59}Co and ^{93}Nb capture reactions also fall on a very similar curve; however, there is clearly a difference of up to 13% in the thermal/epithermal reaction rates. The thermal flux is highest for JP-16, declining in order as JP-13, JP-11, and JP-10. If these variations are averaged, then the average $^{93}Nb(n,\gamma)$ rate has a standard deviation of 4.0%; however, the $^{59}Co(n,\gamma)$ deviates by 7.5%. The best fit to all four reactions results in a global equation $A(X) = A(0)\ (1 - 9.85E\text{-}4\ X^2)$ where A(0) is the midplane value and X is the height in cm.

Midplane activation rates were used as input to the STAY'SL computer code[5] to adjust the neutron flux spectrum determined previously in HFIR.[6] STAY'SL performs a generalized least-squares adjustment of all measured and calculated values including the measured activities, calculated spectra, and neutron cross sections. Neutron cross sections and their uncertainties were generally taken from ENDF/B-V.[7] The adjusted neutron fluence values are listed in Table 2. The activation rates and the derived neutron spectra and fluences are in excellent agreement with previous measurements in the target position of HFIR.[6,8]

Neutron damage calculations with the SPECTER computer code[9] were performed for the midplane position. Midplane dpa and helium (appm) values are also listed in Table 2. The fluence and damage values at other experimental positions can be calculated by the gradient equation given above. Damage parameters for other elements or compounds have been calculated and are readily available on request.

Helium production in nickel and nickel alloys requires a more complicated non-linear calculation.[10] Helium production in 316 stainless steel is listed as a function of height in Table 3.

FUTURE WORK

Dosimeters have been received from the HFIR-JP-23 irradiation and for the COBRA-1A1 irradiation in the Experimental Breeder Reactor II.

REFERENCES

1. J. E. Pawel and R. L. Senn, Status of US/Japan Collaborative Program Phase II HFIR Target Capsules, Fusion Reactor Materials Semiannual Progress Report, DOE/ER-00313/12, pp. 15-23, March 1992.

2. R. L. Senn, Status of U. S./Japan Collaborative Program Phase II HFIR Target Capsules, Fusion Reactor Materials Semiannual Progress Report, DOE/ER-0313/3, pp. 8-20, March 1987.

3. R. L. Senn, Status of U. S./Japan Collaborative Program Phase II HFIR Target Capsules, Fusion Reactor Materials Semiannual Progress Report, DOE/ER-0313/4, pp. 7-9, March 1988.

4. R. L. Senn, Status of U. S./Japan Collaborative Program Phase II HFIR Target Capsules, Fusion Reactor Materials Semiannual Progress Report, DOE/ER-0313/5, pp. 6-13, September 1988.

5. F. G. Perey, Least Squares Dosimetry Unfolding: The Program STAY'SL, ORNL/TM-6062 (1977).

6. L. R. Greenwood, Neutron Source Characterization for Materials Experiments, Alloy Development for Irradiation Performance Semiannual Progress Report, DOE/ER-0045/10, pp. 12-18, March 1983.

7. Evaluated Nuclear Data File, Version V, Part B, National Neutron Data Center, Brookhaven National Laboratory.

8. L. R. Greenwood and C. A. Seils, Dosimetry and Damage Calculations for the JP-4, -5, and -8 US/Japanese Experiments in HFIR, Fusion Reactor Materials Semiannual Progress Report, DOE-ER-0313/3, pp. 30-32, September 1987.

9. L. R. Greenwood and R. K. Smither, SPECTER: Neutron Damage Calculations for Materials Irradiations, ANL/FPP-TM-197, January 1985.

10. L. R. Greenwood, A New Calculation of Thermal Neutron Damage and Helium Production in Nickel, Journal of Nuclear Materials 116, pp. 137-142 (1983).

TABLE 1 - Activation Rates (at/at-s) - HFIR-MFE-JP-10, 11, 13, 16

Sample	$^{54}Fe(n,p)^{54}Mn$ Ht,cm	$^{93}Nb(n,\gamma)^{94}Nb$ ($x10^{-11}$)	$^{59}Co(n,\gamma)^{60}Co$ ($x10^{-9}$)	$^{55}Mn(n,2n)^{54}Mn$ ($x10^{-8}$)	($x10^{-13}$)
10-8	11.3	4.78	2.15	4.48	1.52
10-9	4.6	5.45	2.51	5.06	1.61
10-10	- 2.1	5.42	2.52	5.30	1.60
10-11	-16.2	4.06	1.84	4.14	1.24
10-12	-20.3	3.22	1.48	3.32	0.98
11-14	11.3	4.80	2.45	4.68	1.50
11-15	4.6	5.53	2.66	5.34	1.62
11-16	- 2.1	5.45	2.62	5.41	1.60
11-49	-16.2	3.63	2.04	3.92	1.18
11-18	-20.3	3.25	1.51	3.50	
13-25	22.7	2.53	1.19	2.73	0.80
13-26	17.4	3.89	1.80	3.95	1.17
13-28	2.1	5.45	2.63	5.11	1.62
13-29	- 9.7	4.87	2.25	4.31	1.46
13-30	-17.4	3.92	1.75	3.87	1.15
16-43	22.6	2.59	1.19	2.69	
16-44	10.0	4.83	2.16	4.58	1.44
16-45	4.6	5.30	2.40	4.70	1.71
16-46	- 4.6	5.47	2.31	4.82	1.66
16-47	-12.8	4.84	2.16	4.40	1.49
16-48	-19.8	3.25	1.41	3.20	1.03

TABLE 2 - Midplane Fluence and Damage Values for HFIR-MFE-JP-10, 11, 13, 16

Neutron Fluence, $x10^{22}$ n/cm2		Element	dpa	He,appm
Total	7.88	C	15.1	35.4
Thermal (<.5eV)	3.12	Al	27.5	13.5
0.5 eV - 0.1 MeV	2.64	V	19.6	45.4
> 0.1 MeV	2.12	Cr	17.2	3.1
> 1 MeV	1.07	Fe	15.3	5.5
		Ni Fast	16.4	72.6
		59-Ni	12.1	6844.6
		Total	28.5	6917.2
		Cu	19.9	4.9

TABLE 3 -DPA and He Values for 316 SS in HFIR-MFE-JP-10, 11, 13, 16
(Includes ^{59}Ni effect)

Ht (±cm)	dpa	He (appm)
0	17.3	903.4
3	17.2	892.2
6	16.7	858.8
9	16.0	803.1
12	14.9	726.0
15	13.5	628.7
18	11.8	513.2
21	9.8	383.9
24	7.5	248.1

316SS = Fe(0.645), Ni(0.13), Cr(0.18), Mn(0.019), Mo(0.026) wt%

NEUTRON DOSIMETRY AND DAMAGE CALCULATIONS FOR THE JP-17, 18, and 19 EXPERIMENTS IN HFIR

L.R. Greenwood[1]
C. A. Baldwin[2]

OBJECTIVE

To provide dosimetry and damage analysis for fusion materials irradiation experiments.

SUMMARY

Neutron fluence measurements and radiation damage calculations are reported for the joint U.S.-Japanese experiments JP-17, 18, and 19 in the target of the High Flux Isotope Reactor (HFIR) at Oak Ridge National Laboratory (ORNL). These experiments were irradiated at 85 MW for two cycles resulting in 43.55 EFPD for JP-17 and 42.06 EFPD for JP-18 and 19. The maximum fast neutron fluence >0.1MeV was about 3.7E+21 n/cm^2 for all three irradiations, resulting in about 3 dpa in 316 stainless steel.

PROGRESS AND STATUS

The fabrication and irradiation of the JP-17, 18, and 19 experiments have been described previously.[1,2] The JP-17 irradiation was conducted from December 31, 1991 to February 27, 1992 for an exposure of 43.553 EFPD at 85 MW. The JP-18 and -19 irradiations were in the reactor for the same exposure of 42.058 EFPD from August 28, 1991 to October 19, 1991.

Small dosimetry capsules measuring about 0.05"in diameter by 0.25"in length were located at 8 different positions in the JP-18 and -19 assemblies and at 7 positions in JP-17. Each dosimetry capsule contained milligram quantities of Fe, Ni, Ti, Nb, 0.1% Co-Al, and 80.2% Mn-Cu. Following the irradiation, selected capsules from each irradiation were disassembled in hot cells and subsequently gamma counted at ORNL.

The gamma-counting results were forwarded to Pacific Northwest Laboratory (PNL) for analysis. The measured activities were converted to activation rates, as listed in Table 1, by correcting for burnup of the reacting and product atoms, gamma self-absorption, decay of the product isotopes during and after irradiation, isotopic abundance, and atomic weight. Burnup corrections are based on an iterative procedure for the thermal/epithermal monitor reactions. The resultant estimates of the thermal/epithermal neutron fluences were then used to calculate burnup corrections for the threshold fast neutron monitor reactions. Burnup corrections averaged 5-10% for the thermal/epithermal reactions and only a few percent for the threshold reaction rates. The activation rates listed in Table 1 are normalized to full reactor power of 85 MW and have a net absolute uncertainty of about 5%.

The fast neutron reactions, $^{54}Fe(n,p)^{54}Mn$ and $^{55}Mn(n,2n)^{54}Mn$, for all three irradiations appear to fall on a smooth curve when plotted versus the height relative to the HFIR midplane. The thermal neutron activities for the ^{59}Co and ^{93}Nb capture reactions also fall on a very similar curve for the JP-18 and -19 reactions. The best fit to all four reactions results in a global equation $A(X) = A(0)\ (1 - 9.31E\text{-}4\ X^2)$ where A(0) is the midplane value and X is the height in cm.

For the JP-17 irradiation, the thermal neutron activities for the ^{59}Co and ^{93}Nb capture reactions were about 25% lower than for the JP-18 and 19 irradiations, although the fast neutron reaction rates were about the same for all three experiments. The reason for this difference is not known but may be due to a thermal neutron flux depression effect due to other materials that were co-irradiated in the target region.

Midplane activation rates were used as input to the STAY'SL computer code[3] to adjust the neutron flux spectrum determined previously in HFIR.[4] STAY'SL performs a generalized least-squares adjustment of all measured and calculated values including the measured activities, calculated spectra, and neutron cross sections. Neutron cross sections and their uncertainties were generally taken from ENDF/B-V.[5] The adjusted neutron fluence values are listed in Table 2. The activation rates and the derived neutron spectra and fluences are in excellent agreement with previous measurements in the target position of HFIR,[4,6] except for the thermal flux depression noted for JP-17.

Neutron damage calculations with the SPECTER computer code[7] were performed for the midplane position. Midplane dpa and helium (appm) values are also listed in Table 2. The fluence and damage values at other experimental positions can be calculated by the gradient equation given above. Damage parameters for other elements or compounds have been calculated and are readily available on request.

Helium production in nickel and nickel alloys requires a more complicated non-linear calculation.[8] Helium production in 316 stainless steel is listed as a function of height in Table 3.

FUTURE WORK

Dosimeters have been received from the HFIR-JP-23 irradiation and for the COBRA-1A1 irradiation in the Experimental Breeder Reactor II.

REFERENCES

1. A. W. Longest, D. W. Heatherly, J. E. Wolfe, and K. R. Thoms, Fabrication and irradiation of HFIR-MFE-JP-17, -18, and -19 Target Irradiation Capsules, Fusion Reactor Materials Semiannual Progress Report, DOE-ER-0313/11, pp. 30-32, September 1991.

2. A. W. Longest, D. W. Heatherly, K. R. Thoms, and J. E. Corum, Fabrication and Irradiation of HFIR-MFE-JP-17, -18, and -19 Target Irradiation Capsules, Fusion Reactor Materials Semiannual Progress Report, DOE-ER-0313/12, pp. 24-28, March 1992.

3. F. G. Perey, Least Squares Dosimetry Unfolding: The Program STAY'SL, ORNL/TM-6062 (1977).

4. L. R. Greenwood, Neutron Source Characterization for Materials Experiments, Alloy Development for Irradiation Performance Semiannual Progress Report, DOE/ER-0045/10, pp. 12-18, March 1983.

5. Evaluated Nuclear Data File, Version V, Part B, National Nuclear Data Center, Brookhaven National Laboratory.

6. L. R. Greenwood and C. A. Seils, Dosimetry and Damage Calculations for the JP-4, -5, and -8 US/Japanese Experiments in HFIR, Fusion Reactor Materials Semiannual Progress Report, DOE-ER-0313/3, pp. 30-32, September 1987.

7. L. R. Greenwood and R. K. Smither, SPECTER: Neutron Damage Calculations for Materials Irradiations, ANL/FPP-TM-197, January 1985.

8. L. R. Greenwood, A New Calculation of Thermal Neutron Damage and Helium Production in Nickel, Journal of Nuclear Materials 116, pp. 137-142 (1983).

TABLE 1 - Activation Rates (at/at-s) - HFIR-MFE-JP-17, 18, 19

Sample Ht,cm	$^{54}Fe(n,p)^{54}Mn$ ($x10^{-11}$)	$^{93}Nb(n,\gamma)^{94}Nb$ ($x10^{-9}$)	$^{59}Co(n,\gamma)^{60}Co$ ($x10^{-8}$)	$55Mn(n,2n)^{54}Mn$ ($x10^{-13}O$
17-23 24.1	2.60	1.03	2.43	0.76
17-50 -0.9	-	-	4.57	1.77
17-54 -10.5	5.12	1.79	4.15	1.47
17-55 -18.2	3.89	1.30	2.76	1.11
17-57 -24.3	2.41	-	2.24	-
18-22 22.9	2.66	1.27	3.05	0.81
18-32 -4.6	5.34	2.40	5.64	1.49
18-34 -16.8	3.87	1.77	4.24	1.11
19-65 3.1	5.41	2.50	6.10	1.56
19-72 -4.6	5.27	2.48	6.07	1.52

TABLE 2 - Midplane Fluence and Damage Values for HFIR-MFE-JP-17, 18, 19

	JP-17	JP-18,19		JP-17		JP-18/19	
	Neutron Fluence $.x10^{21}n/cm2$		Element	dpa	He.appm	dpa	He.appm
Total	12.60	14.78	C	2.65	6.5	2.69	6.2
Therma(<.5eV)	4.78	6.44	Al	4.91	2.5	4.89	2.4
0.5eV - 0.1MeV	4.09	4.60	V	3.50	0.1	3.48	0.1
>0.1MeV	3.73	3.74	Cr	3.11	0.6	3.07	0.5
>1MeV	1.96	1.90	Fe	2.75	1.0	2.71	1.0

Ni Fast	2.93	13.6	2.93	12.7
59-Ni	0.50	283.5	0.85	483.9
Total	3.43	297.1	3.78	496.6
Cu	3.56	0.9	3.53	0.9

TABLE 3 - DPA and He Values for 316 SS in HFIR-MFE-JP-17, 18, 19
(includes ^{59}Ni effect)

JP-17			JP-18/19	
Ht (+cm)	dpa	He (appm)	dpa	He (appm)
0	2.90	39.4	2.91	65.3
3	2.87	38.8	2.89	64.3
6	2.80	37.0	2.82	61.4
9	2.69	34.2	2.70	56.6
12	2.52	30.3	2.53	50.2
15	2.30	25.6	2.30	42.4
18	2.03	20.4	2.03	33.7
21	1.71	14.9	1.71	24.5
24	1.35	9.6	1.35	15.6

316SS = Fe(0.645), Ni(0.13), Cr(0.18), Mn(0.019), Mo(0.026) wt%

HYDROGEN GENERATION ARISING FROM THE ^{59}NI(N,P) REACTION AND ITS IMPACT ON FISSION-FUSION CORRELATIONS

- L. R. Greenwood and F. A. Garner (Pacific Northwest National Laboratory[1]

To be published in J. Nuclear Materials, 1996 proceedings of ICFRM-7

EXTENDED ABSTRACT

While the influence of transmutant helium on radiation-induced microstructural evolution has often been studied, there is a tendency to overlook the influence of concurrently-generated hydrogen. There have been some recent speculation and studies, however, that suggest that the influence of hydrogen may be enhanced in the presence of large amounts of helium, especially at lower irradiation temperatures typical of projected ITER operation.

In nickel-bearing alloys, one of the major sources of helium in some neutron spectra is the two-step ^{58}Ni(n,γ)^{59}Ni(n,)^{56}Fe reaction sequence. It now appears that another previously overlooked (n,p) reaction of ^{59}Ni can dominate the hydrogen production process in these same neutron spectra. Whereas the ^{59}Ni(n,)^{56}Fe reaction has a thermal cross-section of 12.3 barns, the ^{59}Ni(n,p)^{59}Co reaction has a thermal cross-section of 2.0 barns, generating approximately one hydrogen atom for each six helium atoms.

Both the (n,) and (n,p) reactions are highly exothermic, producing 4.76 MeV alpha particles and 1.82 MeV protons, traveling 9.5 and 15.7 m, respectively, in stainless steel. Since these ranges greatly exceed the scales of both radiation-induced segregation and microstructural inter-sink distances, there is essentially no measurable influence of nickel segregation on the distribution of either transmutant. There will be some local enhancement of the displacement damage from recoil of the ^{56}Fe and ^{59}Co atoms, however. Inclusion of the damage energy deposited by the (n,p) reaction in the alloy matrix, however, requires that a ^{59}Ni(n,) damage enhancement formula published earlier be only slightly revised (~4%) to incorporate the concurrent effect of the (n,p) reaction.

The impact of the (n,p) reaction on both hydrogen generation rates and displacement rates are evaluated in this paper for a variety of neutron spectra employed in fission-fusion correlation.

---

1 Operated for the US Department of Energy by Battelle Memorial Institute under Contract DE-AC06-76RLO 1830

10.0 MATERIALS ENGINEERING AND DESIGN REQUIREMENTS

SUMMARY OF RECOMMENDED CORRELATIONS FOR ITER-GRADE TYPE 316L(N) FOR THE ITER MATERIAL PROPERTIES HANDBOOK -- M. C. Billone (Argonne National Laboratory) and J. E. Pawel (Oak Ridge National Laboratory)

OBJECTIVE

The objective of this work is to summarize and recommend design correlations for the tensile properties for inclusion in the International Thermonuclear Experimental Reactor (ITER) Material Properties Handbook.

SUMMARY

The focus of this effort is the effects of irradiation on the ultimate tensile strength (UTS), the yield strength (YS), the uniform elongation (UE), the total elongation (TE) and the reduction in area (RA) in the ITER-relevant temperature range of 100-400°C. For the purposes of this summary, data for European heats of 316 with $0.02 \leq C \leq 0.03$ wt.% and $0.06 \leq N \leq 0.08$ wt.% are referred to as E316L(N) data and grouped together. Other heats of 316 and Ti-modified 316 are also included in the data base. For irradiation and postirradiation-test temperatures in the range of 200-400°C, the common behavior of these heats of stainless steel is a yield strength approaching the ultimate tensile strength, an ultimate tensile strength approaching 800 MPa, a uniform elongation approaching 0.3%, a total elongation approaching 3-9% and a high (about 60%) reduction in area as the neutron damage approaches 10 dpa.

PROGRESS AND STATUS

Introduction

Previous reports and open literature publications[1-4] have dealt in depth with uncertainties in the data base for solution-annealed Type 316L(N) stainless steels, methods for resolving the uncertainties, recommended design correlations for the tensile properties, and recommended material correlations for inclusion in the ITER Material Properties Handbook. Because of the evolving nature of this work and the length of the detailed reports, it is useful to summarize the results. The focus of this effort is the effects of irradiation on the ultimate tensile strength (UTS), the yield strength (YS), the uniform elongation (UE), the total elongation (TE) and the reduction in area (RA) in the ITER-relevant temperature range of 100-400°C.

There are many different grades of 316L(N). The particular grade recommended for ITER design is referred to as Type 316LN-IG and is very close to the SUPER PHENIX heat (SPH) of 316L(N).[5-7] A rather substantial irradiation data base is available for this heat, as well as for other European heats which are close in composition to the SPH heat. However, it is very difficult to determine from the literature the evolution in terminology and chemical composition of the European heats of 316L(N). Experimental samples are referred to as E316 or EC316, E316L, E316LN, E316L(N) and ERH, but the chemistry presented is often not detailed enough -- particularly with regard to the nitrogen content -- to determine whether or not these samples are from the specific SPH heat. With regard to irradiation effects, the distinction is not significant as all of these steels harden in the same manner. For the purposes of this summary, data for European heats of 316 with $0.02 \leq C \leq 0.03$ wt.% and $0.06 \leq N \leq 0.08$ wt.% are referred to as E316L(N) data and grouped together. Data for other heats of 316 have also been collected and are designated as J316 for a particular Japanese heat and US316 for a particular US heat. A Japanese Ti-modified 316 (JPCA) has also been included. These three other heats are not low in carbon (0.05-0.06 wt.%) and have lower nitrogen contents (0 - 0.04 wt.%) than E316L(N). They have been included in this data assessment and correlation development because their behavior under irradiation is indistinguishable from E316L(N). For irradiation and postirradiation-test temperatures in the range of 200-400°C, the common behavior of these heats of stainless steel is a yield strength approaching the ultimate tensile strength, an ultimate tensile strength approaching 800 MPa, a uniform elongation approaching 0.3%, a total elongation approaching 3-9% and a high (about 60%) reduction in area as the neutron damage approaches 10 dpa.

Data are collected for samples with irradiation and postirradiation-test temperatures of 200, 227, 250, 270, 290, 300, 327, 330, 340, and 400°C. As demonstrated by Pawel et al.[8-10], the stress-stain curves for the 200°C and 400°C cases are distinctly different from those in the range of 250-340°C. While the UTS, YS, TE and RA values are similar enough to be grouped together, the UE values are not. In particular, the 200 and 400°C cases exhibit higher UE values. These topics are discussed in some detail in the sections below.

Data Base

Tables 1-4 summarize the tensile data which have been collected for E316L(N) (Table 1), JPCA (Table 2), J316 (Table 3) and US316 (Table 4). Reference numbers are also included in the tables. Reported values for the neutron damage (dpa) and the He content (appm) for experiments vary from pre-test reports to post-test reports to open literature publications. Values for UTS, YS, and UE for the same sample vary from publication to publication. Some of these apparent discrepancies are due to the nature of the engineering stress-strain curve (e.g., near elastic/ perfectly-plastic at 250°C and 5.1 dpa), some are due to the double hump nature of the stress-strain curves for 316 (small peak at about 0.2% plastic strain, followed by a broad peak), some are due to analysts converting to true-stress/true-strain curves before deriving values, and some arise from a confusion in terminology. In the present work, direct interpretation of the engineering stress-strain curves available to this study has been used to derive a consistent set of data from the data base. For cases in which the stress-strain curve is ambiguous, analytical methods, graphical methods and engineering judgment have been used to determine the permanent engineering strain at the onset of necking, which is what the uniform elongation is supposed to represent. These are described below.

For unirradiated material, the engineering stress-strain curves tend to be classical in that there is one broad peak in stress at a large plastic strain. For irradiated material which may exhibit near elastic/perfectly-plastic behavior and/or double-peaked behavior (e.g., sharp peak at about 0.2% plastic strain followed by a broad peak) analytical and graphical onset-of-necking criteria were used to resolve ambiguous values of UE. The onset of necking criterion[1] for stainless steels which exhibit very little strain-rate sensitivity is based on true stress (s_t) and true plastic strain (e_{pt}):

$$(1/e_{pt})\,\partial\,(\ln\ s_t)/\partial\,(\ln\ e_{pt}) = (1/s_t)(\partial\ s_t/\partial\ e_{pt}) = 1 \qquad (1)$$

As the stress-strain data for engineering stress (s) and total engineering strain (e) are in analog form with a particular associated error and digitizing these data points introduces additional error, Eq. 1 was not found to be convenient for the determination of the onset of necking. In addition, for the elastic/perfectly-plastic engineering stress-strain curve, Eq. 1 gives a value of 1 over a broad range of permanent strains. As it can be shown that Eq. 1 reduces approximately to $\partial\ s/\partial\ e = 0$ for low strain-hardening materials, it was found to be sufficient within the uncertainty of the data to note graphically where the slope of the engineering stress-strain curve made a transition from positive to zero to negative. In this work, the transition between a zero slope and a negative slope was used to determine the uniform strain at the onset of localized necking. For the double-peaked cases, the first sharp peak was ignored unless the curve at higher strain values was characterized by a negative slope throughout. If the slope of the curve beyond the first peak made transitions from negative to zero to negative or negative to zero to positive to zero to negative, then the last transition from zero to negative was used. The precision of this approach is about ±1% for UE values greater than 2%.

Summary of Correlations for UTS and YS

The UTS and YS data for unirradiated 316L(N)-SPH are used as the basis for deriving the correlations for irradiated material. Temperature independent hardening parameters have been determined for UTS (f_{hu}) and YS (f_{hy}) by examining the normalized increase in UTS and YS for E316L(N) steels as a function of neutron damage (D in dpa). This approach is only approximate as the hardening is, in fact, temperature dependent. However, the temperature dependence for unirradiated and irradiated properties is relatively mild in the range of 200-400°C. The recommended correlations are:

$$UTS = 580\ f_{hu}\ (1.03914 - 2.07760 \times 10^{-3}\ T + 6.15684 \times 10^{-6}\ T^2 - 6.15298 \times 10^{-9}\ T^3) \qquad (2)$$

and

$$YS = 297\ f_{hy}\ (1.04396 - 2.26091 \times 10^{-3}\ T + 3.17660 \times 10^{-6}\ T^2 - 1.50601 \times 10^{-9}\ T^3) \qquad (3)$$

Table 1. Summary of the yield strength (YS), ultimate tensile strength (UTS), uniform elongation (UE), total elongation (TE) and reduction in area (RA) for unirradiated and irradiated, solution annealed E316L(N) austenitic stainless steel. Irradiation temperature equals test temperature (T). Values for UE in parentheses have been taken from tables in the literature. UE values not in parentheses have been determined directly from the stress-strain curves to represent onset of necking.

Material Composition wt.%	Damage dpa	He appm	T °C	YS MPa	UTS MPa	UE %	TE %	RA %	Reactor	Ref.
17.5–Cr	0	0	200	211±17	479±5	(34±3)	47±3	-		11-15
1.8–Mn			227	186±20	478±9	(23±6)	46±2	-		11-15
12.3–Ni			250	200±21	469±9	(31±4)	42±6	79±11		11-15
2.4–Mo			250	289	481	(28.7)	36.5	-		16
0.18–Co			270	272	512	(25.3)	31.9	-		16
0.21–Cu			290	292	523	(27.7)	35.7	-		16
0.43–Si			300	179±3	463±16	(34±2)	46±2	-		11-15
0–Nb			327	164±19	471±17	(23±6)	42±2	68±4		11-15
<0.15–Ta			340	264	523	(25.5)	32.8	-		16
0–Ti			350	155	466±21	(34±2)	44±2	-		11-15
≤0.0023–B			400	173±15	467±21	(33±4)	42±5	74±4		11-15
0.021–C			400	237	488	(24.4)	30.4	-		16
<0.009–S	3.0	69	250	760	764	11.7	18.8	-	HFIR	9,10
<0.029–P				724	735	12.7	20.8	-		9,10
0.06–N	3.1	17.4	250	647	684	9.8	14.5	73	R2	11
				660	693	12.9	18.7	73		11
				664	693	9.8	15.6	72		11
	5.1	140	250	724	724	13	20.4	-	HFIR	16
	6.8	220	270	807	807	6.8	14.6	-		16
	8.2	290	290	827	827	0.23	9.4	-		16
	9.7	380	400	765	772	0.95	7.0	-		16
	9.9	390	340	821	821	0.33	9.3	-		16
	10	140	227	836	844	3.8	12.1	-	HFR	13
			327	804	806	0.5	9.3	-		13
	10.2	103	250	774	774	(0.20)	7.4	72	R2	11
				774	774	(0.10)	6.7	69		11
	10.9	85	250	853	863	0.37	7.1	55	HFR	16
				802	803	0.29	8.7	65		16
				786	793	0.45	7.1	62		16
				779	779	0.20	8.7	67		16
				747	752	0.49	8.7	65		16
				840	843	0.41	7.6	64		16
				837	837	0.20	7.1	56		16
				831	834	0.14	8.0	57		16
				829	829	0.17	8.1	65		16
				819	821	0.14	8.7	60		16

Table 2. Summary of the yield strength (YS), ultimate tensile strength (UTS), uniform elongation (UE), total elongation (TE) and reduction in area (RA) for unirradiated and irradiated, solution annealed Japanese PCA austenitic stainless steel (JPCA). Irradiation temperature equals test temperature (T). Values for UE in parentheses have been taken from tables in the literature. UE values not in parentheses have been determined directly from the stress-strain curves to represent onset of necking.

Material Composition wt.%	Damage dpa	He appm	T ℃	YS MPa	UTS MPa	UE %	TE %	RA %	Reactor	Ref.
14.2–Cr	0	0	250	269	483	(32.8)	40.1	-		10
1.8–Mn				207	474	(30.7)	38.5	-		16
15.6–Ni			270	215	479	(30.8)	38.0	-		16
2.3–Mo			340	175	453	(31.5)	38.4	-		16
<0.002–Co			400	169	441	(30.7)	37.4	-		16
0–Cu	3.0	69	250	779	827	3.0	11.8	-	HFIR	9,10
0.50–Si	3.1	17.4	250	648	689	9.6	14.9	74	R2	11
<0.08–Nb				655	696	10.1	15.6	73		11
0–Ta	5.3	210	250	703	724	8.6	15.6	-	HFIR	11
0.24–Ti	6.9	86	200	714	717	8.8	11.3	-	ORR	17,18
≤0.0024–B				696	703	8.5	11.1	-		17,18
0.06–C	7.4	118	330	821	821	(0.23)	2.5	-		17,18
0.005–S				800	807	(0.38)	3.2	-		17,18
0.027–P				876	883	0.3	2.7	-		17,18
0.004–N			400	505	652	(10.5)	12.9	-		17,18
				549	667	(8.5)	10.5	-		17,18
	10.0	530	400	800	807	(1.4)	7.2	-	HFIR	16
	10.2	550	340	807	807	(0.38)	8.3	-		16
	10.2	103	250	827	827	(0.2)	6.4	73	R2	11
				788	788	(0.2)	7.0	73		11
	10.9	85	250	815	831	2.0	8.1	63	HFR	16
				828	834	3.4	9.8	57		16
				857	857	0.20	7.1	67		16
				825	827	0.25	8.7	62		16
				789	804	0.30	8.1	61		16
				822	822	0.20	8.7	63		16
				809	811	2.0	8.7	61		16
				887	890	0.20	6.5	61		16
				849	850	0.26	8.0	62		16
				814	814	3.5	9.8	64		16
	14	1064	300	884	889	(0.5)	8.0	-	HFIR	17-19
	21	1585	400	878	888	(0.38)	6.4	-		17-19
				896	910	(0.44)	6.0	-		17-19
	25	1973	300	770	789	(2.43)	9.9	-		17-19
	27	2008	500	650	732	(4.7)	8.2	-		17-19
				631	724	(7.2)	11.7	-		17-19
	36	2817	400	858	872	(0.55)	5.7	-		17-19
	44	3488	430	742	781	(1.8)	5.0	-		17-19

Table 3. Summary of the yield strength (YS), ultimate tensile strength (UTS), uniform elongation (UE), total elongation (TE), and reduction in area (RA) for irradiated, solution annealed Japanese 316 austenitic stainless steel (J-316). Irradiation temperature equals test temperature (T). Values for UE in parentheses have been taken from tables in the literature. UE values not in parentheses have been determined directly from the stress-strain curves to represent onset of necking. All data are from References 8-10.

Material Composition wt.%	Damage dpa	He appm	T °C	YS MPa	UTS MPa	UE %	TE %	Reactor
16.7–Cr	0	0	200	254	492	(32)	36	-
1.8–Mn				263	503	(31)	35	-
13.5–Ni			330	230	484	(29)	31	-
2.46–Mo				262	508	(28)	35	-
0.61–Si			400	252	476	(26)	28	-
0.005–Ti				222	476	(33)	35	-
0.058–C	6.9	75	200	758	765	13.6	16	ORR
0.003–S				733	737	12	15	
0.028–P	7.4	102	330	848	855	0.3	3.1	ORR
				869	869	0.3	2.9	
			400	595	677	5.1	7.0	
				650	717	4.9	6.8	
	19	225	330	903	913	0.4	3.1	ORR/
				909	921	0.4	3.1	HFIR

where UTS and YS are in MPa and T is in °C.

Recommended correlations for f_{hu} and f_{hy} are

$$f_{hu} = (1 + 0.3830\, D^{0.2725}) \quad (4)$$

and

$$f_{hy} = (1 + 2.119\, D^{0.1703}) \quad (5)$$

Figures 1 (a) and (b) are trend curves which show the correlation-predicted values vs. dpa at 250°C and all the data collected in the irradiation/test temperature range of 200-400°C. The irradiation hardening factors give good agreement with the UTS and YS data for E316L(N) steel irradiated to 3.0-10.9 dpa at 227-400°C. The predicted results are also in agreement with data for the other steels considered for fluences up to 21 dpa and temperatures as low as 200°C.

Summary of Correlation for UE

From the data in Tables 1-3 it is clear that the 200°C and 400°C data for these three steels exhibit higher uniform elongation than the 227-340°C data. For the low-ductility temperature range, there is a transition between high UE (~10%) and low UE (~0.3%) at a damage level of about 7 dpa. This transition is subtle as it may occur as a result of a slight shift from positive to near zero to negative slope of the stress-strain curves beyond the first sharp peak. The recommended correlation for the uniform elongation (UE in %) of E316L(N), J316 and JPCA steels in the temperature range of 227-340°C is

$$UE = 45.24\, f_{hue}\, (1.08089 - 3.48419\times10^{-3}\, T + 1.01876\times10^{-5}\, T^2 - 9.75233\times10^{-9}\, T^3) \quad (6)$$

where

$$f_{hue} = 0.311\, [1 + 2.22 \exp(-0.9\, D)] \qquad \text{for } 0 \le D < 7 \text{ dpa}$$

$$f_{hue} = 0.0096 \qquad \text{for } D \ge 7 \text{ dpa} \quad (7)$$

Table 4. Summary of the yield strength (YS), ultimate tensile strength (UTS), uniform elongation (UE), total elongation (TE) and reduction in area (RA) for irradiated, solution annealed US 316 austenitic stainless steel (US-316). Double temperatures are test/irradiation. Values for UE in parentheses have been taken from tables in the literature. All data are from Reference 17.

Material Components wt.%	Damage dpa	He appm	T °C	YS MPa	UTS MPa	UE %	TE %	Reactor
17.8% Cr	8.4	<1	700/710	145	235	(6.5)	7.7	EBR-II
1.72% Mn	9.7	<1	430	605	661	(4.8)	8.0	
13.6% Ni			480/430	605	656	(4.9)	8.0	
2.35% Mo	12	<1	430/400	605	681	(6.9)	9.1	
0.2% Cu			700/710	130	235	(6.0)	6.8	
0.38% Si	13	<1	430/410	679	707	(1.7)	5.0	
0.052% C			430	641	696	(3.1)	6.3	
0.02% S			480/430	607	640	(2.2)	5.1	
0.012%			540/480	308	493	(12.8)	14.0	
0.041% N	17	<5	430/400	758	773	(1.1)	4.2	
	18	<5	430/390	748	756	(0.9)	3.9	
	19	<5	650/670	269	331	(2.8)	3.1	
	23	<5	650/670	288	341	(1.9)	2.1	

Equation 6 is based on the UE data for unirradiated 316L(N)-SPH steel. The irradiation hardening factor (Eq. 7) is based on the behavior of irradiated E316L(N), J316 and JPCA in the temperature range of 227-340°C. It is more of an intuitive fit than a best fit. The nature of the data base is a drop of a factor of about 3 in UE from 0 to 3 dpa with no intermediate data, a near constant UE value of about 11% from 3.0-5.3 dpa and a sharp decrease in UE between 6.9 and 8.2 dpa. This transition is assumed to occur at 7 dpa in Eq. 7. Also, the value of 0.3% UE for $D \geq 7$ dpa represents the average of the E316L(N) data and most of the data for J316 and JPCA.

Equation 6 has been evaluated at 250°C and the combined Eqs. 6 and 7 have been evaluated and compared in Fig. 1 (c) to the data in Tables 1-3. The same type of fit could be used for the 400°C data with the transition between high and low UE occurring more gradually with dpa and at a slightly higher damage level. The data base is not complete enough in the range of 7.4-21 dpa to allow this transition to be determined with reasonable confidence. From a design point of view, Eq. 7 should represent a reasonable description of ITER-grade 316L(N) in the temperature range of 227-340°C and a lower bound for higher and lower temperatures.

Summary of Correlation for Total Elongation

The total elongation (TE in %) of irradiated 316 steel is much less temperature sensitive than the uniform elongation. Based on the unirradiated data for 316L(N)-SPH steel, the temperature dependence is taken as:

$$TE = 66.238\, f_{hte}\, (1.05383 - 2.80202\times10^{-3}\, T + 5.59853\times10^{-6}\, T^2 - 3.09260\times10^{-9}\, T^3) \quad (8)$$

The hardening parameter is determined based on all of the TE data in Tables 1-3 to be

$$f_{hte} = 1 - 0.29593\, D + 3.9148\times10^{-2}\, D^2 - 2.2082\times10^{-3}\, D^3 + 4.3795\times10^{-5}\, D^4 \quad (9)$$

Figure 1 (d) shows a comparison between the recommended correlation evaluated at 250°C and the TE data for E316L(N), J316 and JPCA vs. neutron damage in the temperature range of 200-400°C. The correlation represents a best fit to the combined data sets.

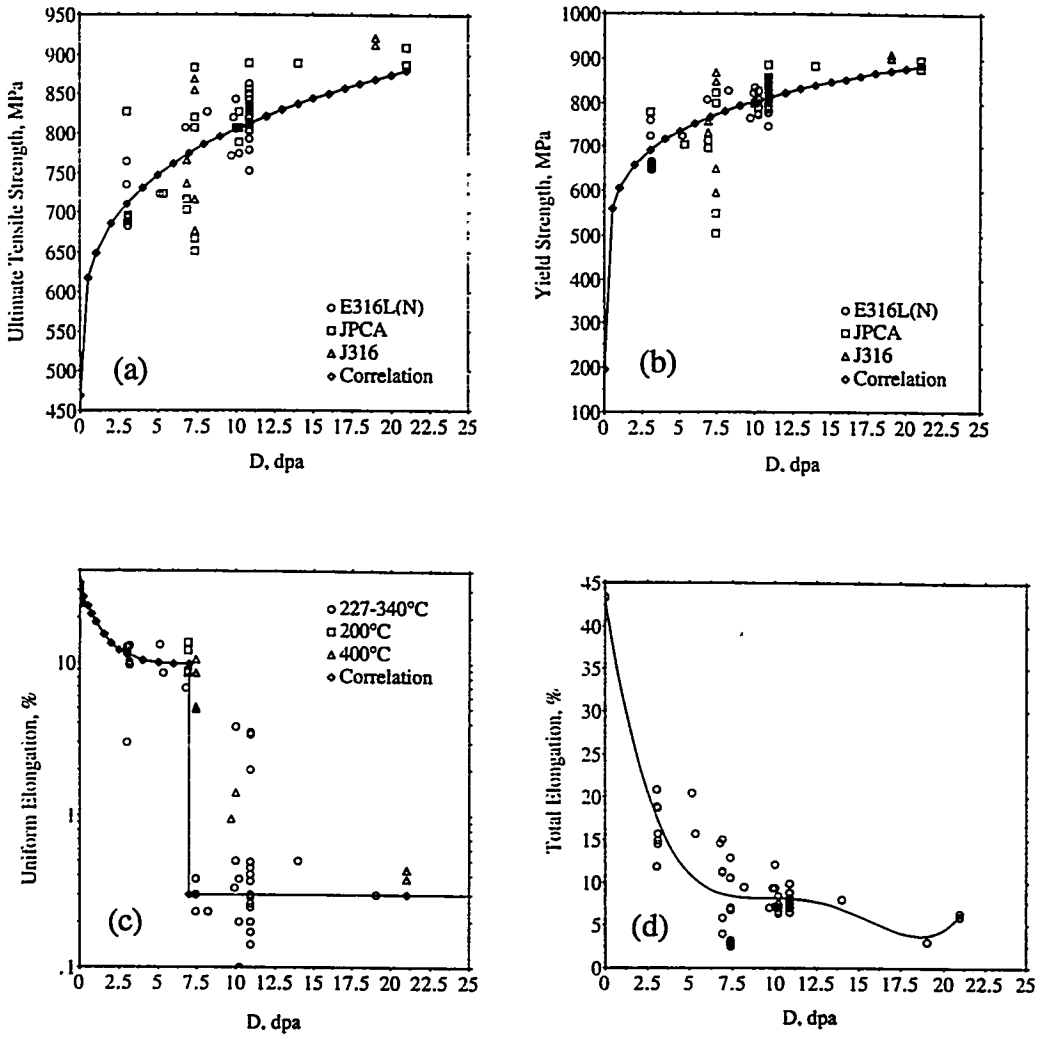

Figure 1. Comparison of correlation values at 250°C of E316L(N) vs. neutron damage (D) in dpa with the data for E316L(N), JPCA, and J316 irradiated at 200-400°C. Test temperature equals irradiation temperature. (a) ultimate tensile strength; (b) yield strength; (c) uniform elongation; (d) total elongation.

Summary of Correlation for Reduction in Area

The recommended reduction in area (RA in %) correlation is based on the correlation for unirradiated 316L(N)-SPH and the data for irradiated E316L(N) and JPCA (see Fig. 2). The irradiation data base includes irradiation/test temperatures of only 250°C and neutron damage levels of 0-10.9 dpa:

$$RA = 94.82\, f_{hra}\, (1.02111 - 1.07266 \times 10^{-3}\, T + 8.61609 \times 10^{-7}\, T^2) \quad (10)$$

$$f_{hra} = 1 - 1.597 \times 10^{-2}\, D \quad (11)$$

The variation in reduction in area with neutron damage level is small at 250°C relative to the other tensile properties. Although no data have been found for samples irradiated/tested at higher or lower temperatures, it is recommended that Eq. 11 be used for the full ITER temperature range of 100-400°C.

Discussion

The correlations for UTS, YS, UE, TE and RA presented in this summary are expressed in a format which is convenient for design criteria analysis. The numerical constant in front of the parenthesis represents the room temperature (20°C) value and the temperature-dependent term in parentheses is normalized to one at 20°C. The standard practice in determining design values for these parameters is to decrease the room temperature value from the average given in the recommended materials correlations to the minimum measured value. The normalized temperature dependence, based on the average of the data, is also used. Thus, for design criteria applications, only the factor in front of Eqs. 2, 3, 6, 8 and 10 needs to be lowered to represent the lower bound of the room temperature values.

While it is difficult to put absolute uncertainty values on the operating conditions and the tensile test parameters for the solution-annealed Type 316 stainless steel data base, several estimates can be made. The neutron damage levels and helium generation listed for each data point in Tables 1-4 are calculated quantities. The accuracy of the calculated results depends on the uncertainties associated with neutron cross-sections, method of analysis, and the details of the neutron flux spectrum for the sample position in the reactor. Based on variations in reported values for the same test specimen, the estimated uncertainty in reported values is about 10%. This order of uncertainty is not large enough to merit a detailed review of the data base to fine tune the reported values of dpa and appm He. The question of the number of data points is an interesting one. In many publications, data are summarized according to temperature, dpa, appm He, UTS, YS, UE and TE. A cross-check for cases in which the sample number is given indicates that the reader cannot determine the number of data points from such summary tables because there is no unique correlation between reported values of dpa, appm He, UTS, YS, UE and TE for an individual sample. With regard to the accuracy of reported tensile properties, two factors are taken into account. The first is the accuracy of the tensile test measurements. The second is a kind of "precision" related to the results of more than one experimenter analyzing the same stress-strain curve. The best consistency and accuracy is in the reported values for TE and RA. The next best consistency and accuracy is in the reported values for UTS. Even for near elastic/perfectly-plastic stress strain curves, the reported values for UTS for the same sample and the spread in the data for a number of samples tested under identical conditions vary by less than 5%. More uncertainty is associated with reported values for YS. Because of the uncertainty in determining the 0.2% off-set stress from the stress strain curves and because of the nature of 316SS which may exhibit an upper and lower yield strength, reported values can vary by as much as ±25%, even though the spread in the data reported by an individual experimenter may be less than 5%. Some of this variation may be due to heat-to-heat variations in chemistry. For example, the JRC heat of E316L(N) reported in Ref. 16 has unirradiated yield strength values which are about 50% higher than the average values reported for the SPH heat. By far, the highest uncertainty is associated with the determination of UE, particularly as the steels harden and lose their work hardening capability. The variation in reported values can span one to two orders of magnitude. This problem in interpretation has been resolved for most of the E316L(N), J316 and JPCA by re-analyzing the engineering stress-strain curves in a consistent manner.

The importance of the accuracy of the data and correlations for the tensile properties varies from property to property. Both the ultimate tensile strength and the yield strength are used to derive design correlations (see Ref. 3), which are then used to determine allowable stress or stress intensity (S_m) values. Confidence in the S_m values increases with the number of data points more than with the

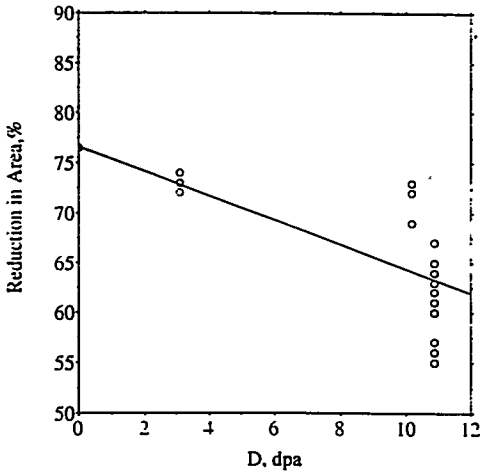

Figure 2. Comparison between the recommended reduction in area (RA) correlation for E316L(N) and the data for E316L(N) and JPCA irradiated and tested at 250°C.

accuracy/precision of individual data points. The uniform elongation is used to classify structural materials (ductile vs. semi-brittle vs. brittle) and to scale certain design limit parameters in the event that a full data set is not available. For stainless steel classification purposes, ductile corresponds to UE ≥ 5%, semi-brittle corresponds to 1 < UE < 5% and brittle corresponds to UE ≤ 1%. In this sense, a high degree of accuracy/precision is not required. Scaling of irradiated/unirradiated UE values is often used when the irradiation data base for certain design limit parameters (e.g., fracture toughness[4]) is incomplete. In the context of the current ITER Interim Structural Design Criteria Guidelines, UE values greater than 1% will result in no additional limit beyond those imposed by parameters for unirradiated material, while UE less than 1% will. In this sense, it matters more whether UE is less than 1% than whether UE = 10 or 13% . Thus, more important to the designer than a very accurate correlation for UE is a map of irradiation temperature and neutron damage level for which UE = 1% (see Fig. 4 of Ref. 9 for a sample plot). The total elongation at room temperature is part of manufacturers' specifications and design code description of materials. As it is dependent on the geometry of the gauge section, it is not really a material property. However, it is sometimes used in design criteria in place of the reduction in area, which is more of a material property. The reason for this is that TE is routinely and easily measured whereas RA is not. The reduction in area can be converted to a true or engineering local failure strain. The ratio of irradiated-to-unirradiated local failure strain (to a power between 1 and 2) is used to scale low-cycle fatigue damage. This is often done if the fatigue data base for irradiated materials is insufficient. While it is certainly important in design guidelines, the data for E316L(N) and JPCA at 250°C and up to 11 dpa indicate very little reduction in RA with neutron damage. Based on average RA values, the fatigue life of 10 dpa steel is predicted to be only 30% less than the fatigue life of unirradiated steel. This is consistent with 227, 327 and 427°C data at 10 dpa which imply an average reduction of only 17%. These small reductions are lost in the very conservative design code practices with regard to fatigue rules.

The focus of this summary is the tensile-test data base for ITER-relevant stainless steels. For mechanistic interpretations of the performance of these steels, the reader is referred to Refs. 4 and 9. With the exception of uniform elongation, the determination of the other tensile properties (UTS, YS, TE and RA) is relatively straightforward. In the case of UE, there is still some question as to how to interpret the zero-slope region of the engineering stress-strain curves, as this region can span about 10% plastic strain. Such behavior may be indicative of diffuse necking followed by localized necking to failure. This issue could be resolved by measuring the reduction in area of the tensile specimens as a function of axial position. Until such measurements are performed, there remains some uncertainty in the interpretation of such regions and the resulting values for UE.

With regard to extrapolating the recommended correlations, which are based on fission-reactor data, to ITER fusion spectra, no indication was found in this study that transmutation helium influences the results in the temperature range of 200-400°C. However, other transmutations which may occur in thermal and mixed neutron spectra, but not in fusion spectra, may influence the hardening. This subject is beyond the scope of the current work.

REFERENCES

1. Billone, M. C., "Recommendations for Annealed Type 316 Stainless Steel Material Properties and Design Criteria," Argonne National Laboratory Technical Report, August 31, 1994.
2. Billone, M. C., "Recommended Properties of Annealed Type 316L(N) Stainless Steel for ITER Design Structural Analyses," Argonne National Laboratory memo to R. F. Mattas, January 7, 1995.
3. Billone, M. C., "Allowable Design Stresses and Design Safety Factors for ITER Type 316L(N) Stainless Steel," Argonne National Laboratory Technical Report, July 31, 1995.
4. Lucas, G. E., M. Billone, J. E. Pawel, M. L. Hamilton, "Implications of Radiation-Induced Loss of Work Hardening to the Design of Austenitic Stainless Steel Structures," presented at ICFRM-7, Obninsk, Russia, September 25-29, 1995. To be published in J. Nucl. Mater.
5. Tavassoli, A. A., "Assessment of Austenitic Stainless Steels," ITER Task BL-URD3, N. T. SRMA 94-2061, F.A. 3591-ITER, June 1994 Revision.
6. A. A. Tavassoli, "Assessment of Austenitic Stainless Steels," Fus. Eng. Des. 29 (1995) 371-390.
7. Tavassoli, A. A. and F. Touboul, "Status of Austenitic Stainless Steels Materials and Design," presented at ICFRM-7, Obninsk, Russia, September 25-29, 1995. To be published in J. Nucl. Mater.
8. Pawel, J. E., Grossbeck, M. L. and Rowcliffe, A. F., "Initial Tensile Results from J316 Stainless Steel Irradiated in the HFIR Spectrally Tailored Experiment," in Fusion Reactor Materials Semiannual Progress Report for the Period Ending September 30, 1994, Report No. DOE/ER-0313/17, pp. 125-133.
9. Pawel, J. E., A. F. Rowcliffe, D. J. Alexander, M. L. Grossbeck and K. Shiba, "Effects of Low Temperature Neutron Irradiation on Deformation of Austenitic Stainless Steel," presented at ICFRM-7, Obninsk, Russia, September 25-29, 1995. To be published in J. Nucl. Mater.
10. Pawel, J. E., A. F. Rowcliffe, D. J. Alexander, M. L. Grossbeck and K. Shiba, "Task T14: Irradiation Testing of Austenitic Stainless Steels," ITER Summary Report for 1994, ITER/US/95/IV MAT 13.
11. Bergenlid, U., Haag, Y., Petterson, K., "The Studsvik Mat 1 Experiment. R2 Irradiations and Post-Irradiation Tensile Tests," Studsvik Nuclear - Report No. Studsvik/NS-90/13, January 1990.
12. Boerman, D. J. and Piatti, G., "Tensile Testing on AISI 316L Reference Steel Plate," Progress Programme Report (No. 4244), Fusion Technology and Safety, CEC - JRC (Ispra, Petten), January - June 1985.
13. Horsten, M. G., Van Hoepen, J., de Vries, M. I., "Tensile Tests on Plate and Electronic-Beam Welded Type 316L(N) Material," ECN, Petten, NL - Report No. ECN-CX--93-112, November 1993.
14. Källstrom, R., Josefsson, B. and Haag, Y., "Results from Tensile Testing of 316L Plate and Weld Material," Studsvik Nuclear - Report No. Studsvik/M-93/45, April 1993.
15. van der Schaaf, B., "Tensile Testing of the European Type 316L Reference Steel for the NET First Wall and Blanket," ECN, Petten, NL, Technical Note 707/01-A/88/90, May 1990.
16. van der Schaaf, B., Grossbeck, M. and Scheurer, H., "Oak Ridge Test Matrix No. 5B and 5C HFR and HFIR Irradiations and Post-Irradiation Tensile Tests in Support of Fusion Reactor First Wall Material Development," EUR 10659 EN (1986).
17. Grossbeck, M. L., "Development of Tensile Property Relations for ITER Data Base," in Fusion Reactor Materials Semiannual Progress Report for the Period Ending March 31, 1989, Report No. DOE/ER-0313/6, pp. 243-252.
18. Hishinuma, A., Jitsukawa, S. and Grossbeck, M. L., "Low Temperature Tensile Behavior of Irradiated Austenitic Stainless Steels," in Fusion Reactor Materials Semiannual Progress Report for the Period Ending September 30, 1991, Report No. DOE/ER-0313/11 (April 1992), pp. 163-164.
19. Jitsukawa, S., Grossbeck, M. L. and Hishinuma, A., "Stress-Strain Relations of Irradiated Stainless Steels Below 673 K," J. Nucl. Mater. 191-194 (1992) 790-794.

11.0 IRRADIATION FACILITIES, TEST MATRICES, AND EXPERIMENTAL METHODS

SCHEDULE AND STATUS OF IRRADIATION EXPERIMENTS – A. F. Rowcliffe and M. L. Grossbeck (Oak Ridge National Laboratory)

OBJECTIVE

To provide an updated summary of the status of irradiation experiments for the neutron-interactive materials program.

SUMMARY

The current status of reactor irradiation experiments is presented in tables summarizing the experimental objectives, conditions, and schedule.

PROGRESS AND STATUS

In the following table, the status of each experiment is shown in the last column with the following legend:

Irradiation complete 

Irradiation in progress 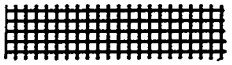

Irradiation planned

Currently, the program has five irradiation experiments in reactor; a further 9 experiments are in the planning or design stages.

Reactor Irradiation Experiments
Summary and Schedule

Experiment	Lead Lab	Collaborators	Responsible Person	Major Objectives	Materials	Temperature °C	Dose (dpa) or fluence	Irrad. Start	Irrad. Finish	Status
EBR-II, Reactor, ANL, Idaho Falls, ID										
COBRA 1A1	PNL	ORNL, ANL, MONBUSHO	M.L. Hamilton	Tensile and fatigue prop., Charpy impact, fracture toughness, TEM	Austenitic and ferritic steels, Fe-alloys, V, Be, low act. materials, Cu alloys, Ti-Al, SiC, C-C comp.	370, 500, 600	9	Nov-92	Apr-93	
COBRA 1A2	PNL	ORNL, ANL, MONBUSHO	M.L. Hamilton	Tensile and fatigue prop., Charpy impact, fracture toughness, TEM	Austenitic and ferritic steels, Fe-alloys, V, Be, low act. materials, Cu alloys, Ti-Al, SiC, C-C comp.	370, 400, 800	33	Nov-92	Sep-94	
X530	ANL		H. Tsai, H.M. Chung	He-effects, swelling, Charpy impact, fracture toughness, tensile prop.	V alloys	370	5	Aug-94	Sep-94	
High Flux Isotope Reactor, ORNL, Oak Ridge, TN										
HFIR-CTR-60	ORNL		S.J. Zinkle	Flexure bars, TEM, indentation disks	Isotopically tailored ceramics	100-600	2.4E+26 n/m2	Dec-94	Aug-95	
HFIR-CTR-61	ORNL		S.J. Zinkle	Similar to HFIR-CTR-60			7.20E+26	Dec-94	Aug-97	
HFIR-JP-9	ORNL	JAERI	P.J. Maziasz/ J.E. Pawel	He effects by isotopic tailoring, tensile prop., TEM	Austenitic and ferritic steels	300-600	57	Jul-90	Apr-94	
HFIR-JP-10	ORNL	JAERI	P.J. Maziasz/ J.E. Pawel	He effects by isotopic tailoring, tensile prop., TEM	Austenitic and ferritic steels	300-600	18	Jul-90	Sep-91	
HFIR-JP-11	ORNL	JAERI	P.J. Maziasz/ J.E. Pawel	Similar to HFIR-JP-10			18	Jul-90	Sep-91	
HFIR-JP-12	ORNL	JAERI	P.J. Maziasz/ J.E. Pawel	Similar to HFIR-JP-9			57	Jul-90	Apr-94	
HFIR-JP-13	ORNL	JAERI	P.J. Maziasz/ J.E. Pawel	Similar to HFIR-JP-10			18	Jul-90	Sep-91	
HFIR-JP-14	ORNL	JAERI	P.J. Maziasz/ J.E. Pawel	He effects by isotopic tailoring, tensile prop., TEM	Austenitic and ferritic steels	300-600	34	Jul-90	Sep-92	

Reactor Irradiation Experiments
Summary and Schedule

Experiment	Lead Lab	Collaborators	Responsible Person	Major Objectives	Materials	Temperature °C	Dose (dpa) or fluence	Irrad. Start	Irrad. Finish	Status
HFIR-JP-15	ORNL	JAERI	P.J. Maziasz/ J.E. Pawel	Similar to HFIR-JP-9			57	Jul-90	Apr-94	
HFIR-JP-16	ORNL	JAERI	P.J. Maziasz/ J.E. Pawel	Similar to HFIR-JP-10			18	Jul-90	Sep-91	
HFIR-JP-17	ORNL	JAERI	M.L. Grossbeck/ J.E. Pawel	Fracture toughness, tensile prop. TEM	Austenitic and ferritic steels	250-300	3	Dec-91	Feb-92	
HFIR-JP-18	ORNL	JAERI	M.L. Grossbeck/ J.E. Pawel	Fracture toughness, tensile prop. TEM	Austenitic and ferritic steels	60-125	3	Aug-91	Oct-91	
HFIR-JP-19	ORNL	JAERI	M.L. Grossbeck/ J.E. Pawel	Similar to HFIR-JP-18		60-125	3	Aug-91	Oct-91	
HFIR-JP-20	ORNL	JAERI	J.E. Pawel	Tensile Prop., TEM, He effects by isotopic tailoring	Austenitic and ferritic steels	300-600	8	Dec-93	Jun-94	
HFIR-JP-21	ORNL	JAERI	J.E. Pawel	Similar to HFIR-JP-20			18	Dec-93	Apr-95	
HFIR-JP-22	ORNL	JAERI	J.E. Pawel	Similar to HFIR -JP-20			34	Dec-93	Jan-96	
HFIR-JP-23	PNL	MONBUSHO	D.S. Gelles	TEM	Austenitic and ferritic steels, Cu, Mo, V alloys, TiAl	300-600	8	Dec-93	Jun-94	
HFIR-MFE-60J	ORNL	JAERI	J.L. Scott/ M.L. Grossbeck	Spectrally tailored for fusion He prod. Began in ORR as ORR-MFE-6J (6.9 dpa). TEM, Charpy, irrad. creep, tensile and crack growth prop.	Austenitic and ferritic steels, and Ni alloys	60	18 (total)	Jul-90	Nov-92	
HFIR-MFE-330J	ORNL	JAERI	J.L. Scott/ M.L. Grossbeck	Similar to HFIR-MFE-60J. Began in ORR as ORR-MFE-7J (7.4 dpa)		330	18 (total)	Jul-90	Nov-92	
HFIR-MFE-200J	ORNL	JAERI	M.L. Grossbeck/ J.E. Pawel	Similar to HFIR-MFE-60J. Began in ORR as ORR-MFE-6J (6.9 dpa)		200	18 (total)	Nov-92	Jan-95	
HFIR-MFE-400J	ORNL	JAERI	M.L. Grossbeck/ J.E. Pawel	Similar to HFIR-MFE-60J. Began as ORR-MFE-7J (7.4 dpa)		400	18 (total)	Nov-92	Jan-95	
HFIR-HT-S1, -S7	ORNL		L.L. Snead	Thermal conductivity	Various insulators	80-350	0.01-1.0	Jun-95	Aug-95	
HFIR-HT-F Series	ORNL		L. L. Snead	Fiber tensile	SiC	80-800	0.001-1.0	Jan-95	Mar-96	

Reactor Irradiation Experiments
Summary and Schedule

Experiment	Lead Lab	Collaborators	Responsible Person	Major Objectives	Materials	Temperature °C	Dose (dpa) or fluence	Irrad. Start	Irrad. Finish	Status
HFIR-TRIST-ER1	ORNL	MONBUSHO/ JAERI	S.J. Zinkle	In-situ electrical conductivity	Al2O3	450	3E+25 n/m2	Apr-96	Jun-96	
HFIR-MFE-RB-10J	ORNL	JAERI	J.E. Pawel	Tensile, fracture	316LN-1G, J316	200, 300	4	Jan-97	Aug-97	
HFIR-MFE-RB-11J	ORNL	MONBUSHO/ JAERI	M. L. Grossbeck	Tensile, fracture, TEM	Low activation ferritics, V alloys, SiC	300	5	Jun-96	May-97	
HFIR-MFE-RB-12J	ORNL	MONBUSHO/ JAERI	M. L. Grossbeck	Tensile, fracture, TEM	Low activation ferritics, V alloys, SiC	500	5	Jun-96	May-97	
HFIR-CTR-62	ORNL	JAERI	R.L. Klueh	Charpy impact and He effects	Reduced act. and conventional ferritic steels	300, 400	10	Feb-95	Dec-95	
HFIR-CTR-63	ORNL	JAERI	R.L. Klueh	Charpy impact and tensile, TEM, He effects	Reduced act. and conventional ferritic steels	300, 400	10	Feb-95	Dec-95	
HFIR-JP25	ORNL	JAERI	R.L. Klueh	Tensile, fracture, TEM	Low activation ferritics	300, 400, 500	20	Jun-97	Sep-98	
HFIR-JP27	ORNL	JAERI	L.L. Snead	Fracture, TEM	Intermetallics, SiC	500-800	10	Oct-97	Jan-98	
HFIR-JP28	ORNL	JAERI	L.L. Snead	Fracture, TEM	SiC	500-800	10	Sep-97	Mar-98	
HFIR-P3-6	ORNL	MONBUSHO	K. R. Thoms	Varying Temperature	TBD	400-600	5	May-97	Apr-98	
High Flux Beam Reactor, Brookhaven National Laboratory										
HFBR-ISEC-3	ORNL		L.L. Snead	In-situ electrical	WESGO Al2O3	450	1.5	Jul-95	Sep-95	
HFBR-V1	ORNL		L.L. Snead	Tensile, fracture	V-4Cr-4Ti	75, 150, 225	0.5	May-95	Jun-95	
HFBR-V2	ORNL		L.L. Snead	Tensile, fracture	V-4Cr-4Ti	75, 225, 300, 375	0.5	Jul-95	Aug-95	
Advanced Test Reactor, Idaho Falls										
ATR-A1	ANL	MONBUSHO	D.L. Smith	Tensile, fracture toughness, TEM, creep	Vanadium alloys	200, 300	5	Dec-95	Apr-96	

Reactor Irradiation Experiments
Summary and Schedule

Experiment	Lead Lab	Collaborators	Responsible Person	Major Objectives	Materials	Temperature °C	Dose (dpa) or fluence	Irrad. Start	Irrad. Finish	Status
BOR-60 Reactor, RIAR, Dimitrovgrad, Russia										
BOR-60-Fusion-1	ORNL, ANL	RDIPE, RIAR	A.F. Rowcliffe, D.L. Smith	Mechanical and microstructural properties	V alloys	350-380	10	Jul-95	Mar-96	
SM-2 Reactor, RIAR, Dimitrovgrad, Russia										
SM-2.1	ORNL, PNL	RIAR	S.J. Zinkle	Tensile, electrical, microstructural, and creep properties	Cu alloys	100, 200, 330	1, 5	Dec-93	Feb-94	
SM-2.2	PNL	SRIAR	D.J. Edwards	Mechanical behavior of bonded materials	Cu alloys/SS, Cu/Be	120, 300	0.2	Jan-96	Mar-96	
SM-2.3	PNL	SRIAR	D.J. Edwards	Mechanical behavior of bonded materials	Cu alloys/SS, Cu/Be	100, 250	0.2	Sep-96	Nov-96	

Irradiation complete

Irradiation in progress

Irradiation planned

STATUS OF DOE/JAERI COLLABORATIVE PROGRAM PHASE II AND PHASE III CAPSULES – J. E. Pawel, K. E. Lenox (Oak Ridge National Laboratory) and I. Ioka (Japan Atomic Energy Research Institute)

OBJECTIVE

The objective of the High Flux Isotope Reactor (HFIR) irradiations is to determine the response of various U.S. and Japanese structural alloys with different pretreatments and alloy compositions to the combined effects of displacement damage and helium generation.

SUMMARY

During this reporting period, the HFIR-MFE-RB-200J-1 and HFIR-MFE-RB-400J-1 spectrally tailored capsules were disassembled and the individual specimens recovered, sorted, and identified. Tensile testing and irradiation creep measurements will be performed during the next reporting period.

PROGRESS AND STATUS

Table 1 summarizes the progress and status of the capsules involved in the DOE/JAERI Phase II and Phase III irradiation programs. Details of the capsule design, assembly, and operation, specimen matrices and testing, and alloy compositions can be found in previous reports in this series. The locations of some of the more detailed reports are shown in the table, but this is not intended to be an exhaustive list.

The JP series HFIR target capsules (JP9-16, 20-22) contain primarily transmission electron microscopy disks (TEM) and SS-3 flat tensile specimens. A wide variety of alloys and thermomechanical conditions are included. Many of the TEM disks were made from isotopically tailored alloys to produce a range of He/dpa ratios (<0.1, 10, 20, 70 appm/dpa). The specimen temperatures are 300, 400, 500, and 600°C and the dose levels are 8, 18, 34, and 57 dpa.

The RB-60J-1, 200J-1, 330J-1, and 400J-1 experiments are a continuation of the Oak Ridge Research Reactor (ORR) spectrally tailored experiments The capsules operated in the RB positions of the HFIR surrounded by a hafnium shield to simulate the expected fusion helium to damage (He/dpa) ratio in steel. The doses shown in the table are in addition to the 7 dpa accumulated during the ORR irradiation, bringing the total for the two-stage irradiation to 16-19 dpa. Dosimetry and helium measurements from specimens from the 60J-1 and 330J-1 capsules indicate that this experiment was successful in producing fusion relevant helium/dpa levels (approximately 11 appm He/dpa). The irradiation temperatures in these experiments were controlled at 60, 200, 330, and 400°C.

The RB-11J and 12J capsules are the first capsules scheduled for assembly in the Phase III program. These capsules will operate in the HFIR RB positions with a thermal neutron shield in place. They will achieve approximately 5 dpa at 300 and 500°C, respectively. The capsules will contain primarily low activation ferritic steel tensile, fracture, and TEM specimens.

The dose levels shown in the table are the peak capsule values achieved at the reactor centerline. The dpa values in the HFIR target are estimated by assuming 0.000873 dpa/MWd. The dpa values in the hafnium-shielded HFIR RB experiments are estimated by assuming 0.000245 dpa/MWd.

While a status of "testing complete" is listed for several of the capsules, it should be noted that data analyses and microscopy examinations are still in progress.

Table 1. Summary of Irradiation Capsule Parameters and Status

Capsule	Primary Research Objectives	Irradiation Start and End; Number of Cycles	Operating Parameters: MWd; dpa; temperature	Status	Most Pertinent Semiannual Report Numbers DOE/ER-0313/*xx*
JP10 JP11 JP13 JP16	isotopically tailored disks; tensile specimens	start: 7/90 end: 9/91 11 cycles	20161 MWd 17.3 dpa 300-600°C	testing complete	Design: 0313/3 Loading: 0313/5 Operation: 0313/16 Dosimetry: 0313/19
JP14	isotopically tailored disks; tensile specimens	start: 7/90 end: 9/92 21 cycles	38786 MWd 33.9 dpa* 300-600°C	testing complete	Design: 0313/3 Loading: 0313/5 Operation: 0313/16
JP9 JP12 JP15	isotopically tailored disks; tensile specimens	start: 7/90 end: 4/94 35 cycles	64904 MWd 56.7 dpa* 300-600°C	disassembly complete	Design: 0313/3 Loading: 0313/5 Operation: 0313/16
JP17	fracture toughness, tensile, TEM specimens	start: 12/91 end: 2/92 2 cycles	3702 MWd 2.9 dpa 250-300 °C	testing complete	Design: 0313/12 Loading: 0313/12 Operation: 0313/19 Dosimetry: 0313/19
JP18 JP19	fracture toughness, tensile, TEM specimens	start: 8/91 end: 10/91 2 cycles	3575 MWd 2.9 dpa 60-125°C	testing complete	Design: 0313/11 Loading: 0313/11 Operation: 0313/19 Dosimetry: 0313/19
JP20	isotopically tailored disks; tensile specimens	start: 12/93 end: 6/94 5 cycles	9367 MWd 8.2 dpa* 300-600°C	disassembly complete	Design: 0313/12 Loading: 0313/15 Operation: 0313/18
JP21	isotopically tailored disks; tensile specimens	start: 12/93 end: 4/95 11 cycles	21337 MWd 18.6 dpa* 300-600°C	irradiation complete	Design: 0313/12 Loading: 0313/15 Operation: 0313/18
JP22	isotopically tailored disks; tensile specimens	start: 12/93 end: 1/96* 18 cycles	38946 MWd* 34 dpa* 300-600°C	irradiation in progress	Design: 0313/12 Loading: 0313/15 Operation: 0313/18
RB-60J-1	spectrally tailored; tensile, creep, TEM specimens	start: 7/90 end: 11/92 24 cycles	44450 MWd 11.6 dpa 60°C	testing in progress	Design: 0313/3, 4 Loading: 0313/4 Operation: 0313/13 Dosimetry: 0313/17
RB-200J-1	spectrally tailored; tensile, creep, TEM specimens	start: 11/92 end: 1/95 20 cycles	37450 MWd 9.2 dpa* 200°C	testing in progress	Design: 0313/3, 6 Loading: 0313/14 Operation: 0313/15, 18
RB-330J-1	spectrally tailored; tensile, creep, TEM specimens	start: 7/90 end: 11/92 24 cycles	44450 MWd 11.6 dpa 330°C	testing in progress	Design: 0313/3, 5 Loading: 0313/5 Operation: 0313/11, 13 Dosimetry: 0313/17
RB-400J-1	spectrally tailored; tensile, creep, TEM specimens	start: 11/92 end: 1/95 20 cycles	37450 MWd 9.2 dpa* 400°C	testing in progress	Design: 0313/3, 6 Loading: 0313/14 Operation: 0313/15, 18
RB-11J RB-12J	spectrally tailored; tensile, fracture, TEM specimens	start: 6/96* end: 4/97* 10 cycles	5 dpa* 300, 500°C	design in progress	

*estimated

ATR-A1 IRRADIATION EXPERIMENT ON VANADIUM ALLOYS AND LOW-ACTIVATION STEELS*

H. Tsai, R. V. Strain, I. Gomes, A. G. Hins, and D. L. Smith (Argonne National Laboratory), H. Matsui (Tohoku University)

SUMMARY

To study the mechanical properties of vanadium alloys under neutron irradiation at low temperatures, an experiment was designed and constructed for irradiation in the Advanced Test Reactor (ATR). The experiment contained Charpy, tensile, compact tension, TEM, and creep specimens of vanadium alloys. It also contained limited low-activation ferritic steel specimens as part of the collaborative agreement with Monbusho of Japan. The design irradiation temperatures for the vanadium alloy specimens in the experiment are ≈200 and 300°C, achieved with passive gas-gap sizing and fill-gas blending. To mitigate vanadium-to-chromium transmutation from the thermal neutron flux, the test specimens are contained inside gadolinium flux filters. All specimens are lithium-bonded. The irradiation started in Cycle 108A (December 3, 1995) and is expected to have a duration of three ATR cycles and a peak fluence of 4.5 dpa.

OBJECTIVE

The principal objective of the ATR-A1 irradiation experiment is to obtain mechanical property data for vanadium alloys irradiated at two low temperatures (≈200 and 300°C). Such data, important for fusion first-wall/blanket applications, are presently lacking.

DESCRIPTION OF EXPERIMENT

Advanced Test Reactor (ATR)

The ATR is a light-water-moderated and -cooled reactor with highly enriched uranium in plate-type fuel. The cooling water enters the reactor core, which is 1.22 m (4 ft) high, from the top at a nominal temperature of ≈52°C. Forty fuel elements are arranged in a serpentine pattern that forms four corner lobes and one central lobe. The ATR-A1 experiment is a drop-in capsule occupying the A-10 irradiation channel in the southeast lobe. Compared to other available irradiation positions, the A-10 channel has among the highest fast neutron fluxes and lowest thermal fluxes in ATR. Although the reactor is water cooled, with double encapsulation and other precautions, lithium can be used as the thermal bond for the specimens in the subcapsules. Lithium bonding ensures a high degree of temperature uniformity and impurity control for the vanadium alloy specimens.

The nuclear power for the southeast lobe where the ATR-A1 experiment resides is 25 MW and is projected to remain at that level for the duration of the experiment. (This power level is somewhat lower than the initial forecast of 27 MW, the design specification for the vehicle. The reduced power would thus have a corresponding effect on the specimen temperature and fluence. All temperature and dpa data reported in this article are based on the actual 25 MW power.)

Irradiation Vehicle

The irradiation vehicle is a drop-in capsule consisting of four segments and a handling fixture. The test specimens are contained in lithium-bonded subcapsules that are placed in the gas-filled capsule segments. Configuration of the capsule segments is shown in Fig. 1. The upper two capsule segments (AC4 and AC3) each contain three subcapsules, the third segment (AC2) contains five subcapsules, and the bottom segment (AC1) contains four subcapsules. With a few exceptions, the capsule segments are constructed to the ASME Boiler & Pressure Vessel Code, Section III. The materials for both the capsule tube and end fittings are Type 304 stainless steel. The tubing for the bottom and top segments has an OD of 0.580 in. and an ID of 0.546 in., and that for the two middle segments has an OD of 0.580 in. and an ID of 0.540 in. The

*Work supported by U.S. Department of Energy, Office of Fusion Energy Research, under Contract W-31-109-Eng-38.

variations of the inside diameter, i.e., gap width, in conjunction with the fill gas selection, provide the test temperature control for the subcapsules. The fill gases are 15%Ar-85%He for segment AC4; pure He for AC3 and AC2; and 5%Ar-95%He for AC1. All gases are purchased pre-blended. The fill gas is pressurized to 130 psig at room temperature to partially counterbalance the ATR system pressure of ≈335 psig.

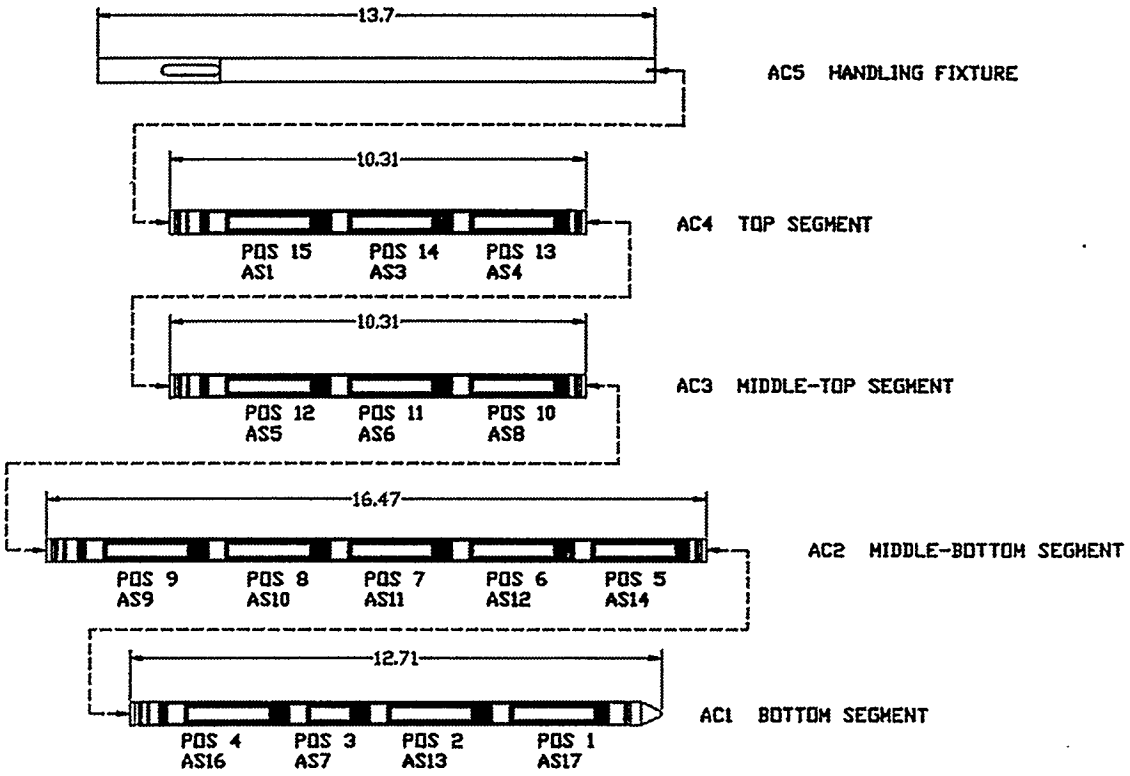

Fig. 1. Schematic of ATR-A1 Showing Capsule Segments and Subcapsule Locations

The test specimens are contained in 15 subcapsules, numbered AS1, AS3 through AS14, AS16 and AS17. Their locations in the capsule segments are shown in Fig. 1. Subcapsules AS4 and AS16 contain only ferritic steel specimens; the remaining subcapsules contain only vanadium alloy specimens. The subcapsule end fittings and tubes are Type 304 stainless steel. The end fittings center the subcapsule in the capsule segments, thereby maintaining the gas gap between the two. The dimensions of all but one subcapsule, are 0.530 in. OD x 0.500 in. ID x 3.07 in. long. The exception is SA7, which has the same diameters but a length of only 2.00 in.

A gadolinium filter set, consisting of a tube, a top end disk and a bottom end disk, is used in each subcapsule to reduce the thermal neutron flux. The filter tubes for all but two subcapsules (SA3 and AS10) are 0.490 in. OD x 0.354 in. ID. For SA3 and SA10, which contain disk compact tension (DCT-A) specimens with an outside diameter of 0.378 in., the filter tube is thinned to produce an inside diameter of 0.390 in. These two subcapsules are located away from the midplane of the reactor (see Fig. 1) to limit their exposure to a level commensurate with the reduced filter thickness. The end disks for all filters are 0.490 in. dia. and 0.075 in. thick. Pretest physics calculations indicate that the filter thicknesses are adequate for the irradiation and will limit vanadium-to-chromium transmutation at discharge to <0.5 wt.%, the compositional tolerance of the as-procured alloy materials.

A predetermined weight of lithium is charged in each subcapsule to provide the heat transfer medium. The lithium, in the form of a solid disk, is loaded into the subcapsules first. After the specimens and filter are loaded, the subcapsule is heated to melt and settle the lithium and wet the surfaces. All operations with exposed lithium are performed in a glovebox with an ultrahigh-purity helium atmosphere.

Dosimeters for determining the spectral and spatial distributions of neutron flux are incorporated in the ATR-A1 experiment. Two spectral/spatial sets and three spatial sets are loaded in selected subcapsules. The monitoring materials are Fe, Ti, Nb, Cu, Mn-20% Cu, and 0.1% Co-Al for the spectral data and Fe and 0.1% Co-Al for the spatial data. All monitoring materials are wires of ≈0.030-in. dia. x 0.15-in length. The wires are individually contained in high-purity vanadium capsules sealed with a laser weld. The placement of the dosimeters in the ATR-A1 subcapsules is shown in Table 1.

Six melt-wire temperature monitors, three for low temperature (≈200°C) and three for high temperature (≈300°C), are included to provide data on the peak temperature experienced during the irradiation. The monitoring materials are Pb/Sn alloy, Se, Sn, and Bi for the low-temperature monitors and Sn, Bi, Pb, and Zn for the high-temperature monitors. All materials are in the form of 0.025 to 0.030-in. dia. wires or particles and sealed in vanadium alloy holders. Locations of the temperature monitors in the capsule are given in Table 1.

Thermal Analysis

Physics calculations were performed by both ATR and ANL personnel to predict the gamma heating rates in test specimens and construction materials in the ATR-A1 experiment. Based on the calculated gamma heating rates (as functions of axial position), the capsule, subcapsule, and specimen temperatures were calculated with the THTB heat transfer code. The predicted specimen temperatures in the subcapsules, based on a 25-MW lobe power, are summarized in Table 2.

Damage Calculation

Damage (displacement per atom, or dpa) in the vanadium alloy specimens was predicted by ATR personnel on the basis of a lobe power of 27 MW. Correcting for the reduced lobe power of 25 MW and using the projected irradiation duration of 133 EFPDs, peak damage is estimated to be 4.54 dpa near the core midplane. The spatial distribution of damage as affected by the axial flux profile is shown in Table 2.

U.S. Vanadium Alloy Test Matrix

The key variables of the U.S. test matrix are

- Material (Heats 832665, T87, T89, T90, T91, T92, BL-47 and the boron-doped BL-70) (see Table 3),
- Heat treatment conditions (final vacuum annealing at 1000°C for 1.0 or 2.0 h),
- Weldment (EB, laser, and resistance),
- Irradiation temperatures (≈200 and 300°C).

The test specimen types are Charpy, tensile, compact tension, transmission-electron-microscope disks, and biaxial creep (pressurized tubes); a summary of the test matrix is presented in Table 4.

Pressurized creep specimens of vanadium alloys are being irradiated for the first time. The creep specimens are 0.180 in. OD x 0.160 in. ID x 1.0 in. long tubes with welded end plugs. The tubing is produced by a repeated drawing/cleaning/annealing process on a piece of V-4wt.%Cr-4wt.%Ti material from the 832665 heat. The circumferential plug-to-tube welds are made with an electron-beam welder in vacuum. The specimen is then pressurized, through a 0.010-in. dia. hole in the top end plug, with high-purity helium in a high-pressure chamber. The final closure weld of the 0.010-in. dia. hole is made with a laser through the quartz window in the chamber. The pressure loadings and calculated hoop stresses in the specimens are shown in Table 5.

JP Vanadium Alloy Test Matrix

The main variables of the JP vanadium test matrix are material and temperature. The major JP vanadium alloys are V-4Cr-4Ti-0.1Si, V-3Fe-4Ti-0.1Si and V-5Cr-5Ti-1YSiAl. A small number of specimens are made from the U.S. V-4Cr-4Ti (Heat 832665) for comparison purposes to check the effects of specimen geometry on measured data. A summary of the JP test matrix is given in Table 6.

Table 1. Loading Diagram of ATR-A1 Specimens and Monitors

Pos.	Subcap. No.	Target Temp.	Test Mat'l	Tier	US DCT	US CVN	US TS	US MT	US Creep	US TEM	US T.Mtr	US F.Mtr	JP DCT	JP CVN	JP TS	JP TEM	JP Creep
15	AS1	200	V	Top	0	0	2	0	A5	--	--	Gr.(2)	0	4	4	--	0
				Bot	0	3	1	0	0	--	--	--	0	2	4	--	0
14	AS3	200	V	--	9	0	0	0	0	--	MW0	--	3	0	0	--	0
13	AS4	200	FS	Top	0	0	0	0	0	--	MW0	--	0	12	12	--	0
				Bot	0	0	0	0	0	--	--	--	0	12	15	126	0
12	AS5	200	V	Top	0	0	2	0	0	--	--	--	0	4	4	--	J3
				Bot	0	3	1	2	0	65	--	--	0	2	2	--	0
11	AS6	200	V	Top	0	0	2	0	A2	--	--	--	0	4	4	--	0
				Bot	0	3	1	4	0	50	--	--	0	2	0	--	0
10	AS8	200	V	Top	0	0	2	0	A3	--	MW0	--	0	4	4	--	0
				Bot	0	3	1	0	0	--	--	--	0	2	4	64	0
9	AS9	300	V	Top	0	0	2	0	A1	--	--	--	0	4	4	--	0
				Bot	0	2+4* *1.5CVN	1	0	0	41	--	--	0	2	4	--	0
8	AS10	300	V	Top	0	0	2	0	A10	--	--	Sp.(6)	0	4	4	--	0
				Bot	0	3	1	0	0	50	--	--	0	2	4	--	0
7	AS11	300	V	Top	0	0	2	0	A7	--	MW0	--	0	4	4	--	0
				Bot	0	3	1	4	0	24	--	--	0	2	0	--	0
6	AS12	300	V	Top	0	0	2	0	A11	--	--	Gr.(2)	0	4	4	--	0
				Bot	0	3	1	0	0	--	--	--	0	2	4	41	0
5	AS14	300	V	Top	0	0	2	0	0	--	MW0	--	0	4	4	--	J2
				Bot	0	3	1	0	0	--	--	--	0	2	3	23	0
4	AS16	300	FS	Top	0	0	0	0	0	--	--	Gr.(2)	0	12	12	--	0
				Bot	0	0	0	0	0	--	--	--	0	12	15	126	0
3	AS7	300	V	Bot	0	3	1	2	0	--	--	--	0	0	0	--	0
2	AS13	300	V	--	10	0	0	0	0	--	MW1	--	3	0	0	--	0
1	AS17	200	V	Top	0	0	2	0	A4	--	--	Sp.(6)	0	4	4	--	0
				Bot	0	3	1	0	0	--	--	--	0	2	4	--	0
Grand Totals			V 300C		10	21	16	6	4	115			3	30	35	64	1
			V 200C		9	15	15	6	4	115			3	30	34	64	1
			FS 300C		0	0	0	0	0	0			0	24	27	126	0
			FS 200C		0	0	0	0	0	0			0	24	27	126	0

Table 2. Predicted Specimen Temperature and DPA in ATR-A1 Subcapsules[1]

Position	Subcap. Number	Test Mat'l	Gas Gap (mils)	Gas Composition	Target Temp. (°C)	Predicted Temp. (°C)2	Predicted dpa
15 (top)	AS1	V	8	He-15%Ar	200	138	0.68
14	AS3	V	8	He-15%Ar	200	185	1.42
13	AS4	FS	8	He-15%Ar	low	261	2.11
12	AS5	V	5	He	200	200	2.92
11	AS6	V	5	He	200	220	3.42
10	AS8	V	5	He	200	244	3.83
9	AS9	V	5	He	300	270	4.14
8	AS10	V	5	He	300	285	4.46
7	AS11	V	5	He	300	282	4.54
6	AS12	V	5	He	300	278	4.38
5	AS14	V	6	He	300	282	3.98
4	AS16	FS	8	He-5%Ar	high	333	3.71
3	AS7	V	8	He-5%Ar	300	284	2.92
2	AS13	V	8	He-5%Ar	300	243	2.25
1	AS17	V	8	He-5%Ar	200	202	1.42

[1]Based on current projection of 25 MW lobe power and 133 EFPDs exposure.
[2]Averaged specimen temperatures in subcapsules, some with two tiers of specimens. In subcapsules with creep specimens, upper-tier temperature may be slightly lower and lower-tier temperature may be slightly higher than indicated, due to reduced gamma heating from low-mass creep specimen in upper tier.

Table 3. Nominal Compositions of the Heats

832665	V-4wt.%Cr-4wt.%Ti.	T87	V-5wt.%Cr-5wt.%Ti.
T89	V-4wt.%Cr-4wt.%Ti.	T90	V-6wt.%Cr-6wt.%Ti.
T91	V-3wt.%Cr-4wt.%Ti.	T92	V-6wt.%Cr-3wt.%Ti.
BL-47	V-4wt.%Cr-4wt.%Ti.	BL-70	V-4wt.%Cr-4wt.%Ti., (250 appmB)

Specimen Loading in Subcapsules

The specimens in all subcapsules except SA3, SA7 and AS13 are loaded in two tiers, with the bottom tier providing a base to support the specimens in the upper tier. Subcapsules SA3 and SA13 contain exclusively DCT-A specimens, which are cylindrical disks stacked on top of one another. Subcapsule 7 is short and contains only one tier of specimens. Loading of the U.S. and Japanese vanadium alloy specimens in the subcapsules are mixed to achieve a high packing density.

A total of 154 tensile specimens, 144 Charpy specimens, 19 DCT-A specimen, 10 creep specimens, and 610 TEM disk are loaded in the ATR-A1 experiment. The locations of these specimens in the subcapsules are shown in Table 1.

IRRADIATION CONDITIONS AND SCHEDULE

The ATR-A1 experiment is scheduled to be in the core for three cycles: 108A, 108B, and 109A. Projected cycle durations are 42, 42, and 49 EFPDs, respectively. Discharge at the end of Cycle 109A is scheduled on May 5, 1996. ATR projects the lobe power to be constant at 25 MW for the three cycles.

Table 4. U.S. Vanadium Alloy Test Matrix

T (°C)	Material[1]	MCVN	PCVN	SS-3	Matron	DCT	Creep	TEM
	832665 (Pri. Anneal)	4	3	3	2	3	4	16
	832665 (Sec. Anneal)	4		2		3		10
	832665, EB Weld			2				
	832665 Lz, TIG Weld	2		1				1
	BL-47	4		2		2		10
	BL-47 TIG Weld	4[2]						
300	T89							10
	T87			2	2	2		16
	T91			2	2			16
	BL-70							10
	T92			2				16
	T90							10
	Total	18	3	16	6	10	4	115
	832665 (Pri. Anneal)	5		3	2	3	4	16
	832665 (Sec. Anneal)	4		2		2		10
	832665, EB Weld							
	832665 Lz, TIG Weld	2		2				1
	BL-47	4		2		2		10
200	T89							10
	T87			2	2	2		16
	T91			2	2			16
	BL-70							10
	T92			2				16
	T90							10
	Total	15	0	15	6	9	4	115

[1]Primary Anneal: 1000°C for 1.0 h.
Secondary Anneal: 1000°C for 2.0 h.
[2]1.5 CVN size specimens.

Table 5. Calculated Hoop Stress in Creep Specimens

Target Temp.(°C)	Specimen No.[1]	Fill Pressure (psi, @24°C)	Predicted Irradiation Temp. (°C)	Midwall Hoop Stress (MPa)
	A1	0	262	0
	A10	950	273	96
300	A7	1421	272	143
	A11	1910	265	189
	J2	1825	272	191
	A5	0	134	0
	A4	1133	196	99
200	A2	1706	214	154
	A3	2284	235	214
	J3	2189	193	197

[1]Prefix A denotes U.S. specimen and prefix J denotes JP specimen.

Table 6. JP Vanadium Alloy Test Matrix

T (°C)	Material	CVN	TS	DCT	Creep	TEM
	V-4Cr-4Ti-0.1Si	7	9		1	6
	V-3Fe-4Ti-0.1Si	5	8	3		3
300	V-5Cr-5Ti-1YiSiAl	14	18			25
	V-4Cr-4Ti (832665)	4				0
	Other V Alloys					30
	Total	30	35	3	1	64
	V-4Cr-4Ti-0.1Si	10	9		1	6
	V-3Fe-4Ti-0.1Si	5	8	3		3
200	V-5Cr-5Ti-1YiSiAl	10	17			25
	V-4Cr-4Ti (832665)	5				0
	Other V Alloys					30
	Total	30	34	3	1	64

FUTURE ACTIVITIES

Details are being discussed with ATR on the optimal method of disconnecting the capsule segments at ATR after the irradiation. The disconnected capsule segments will then be shipped to ANL for disassembly. Opening of the subcapsules to remove the lithium bond and to retrieve the test specimens is expected to be a routine operation, based on past experience. The cleaned specimens will be disseminated to participating U.S. and Japanese laboratories for postirradiation examination and testing.

DISASSEMBLY OF IRRADIATED LITHIUM-BONDED CAPSULES CONTAINING VANADIUM ALLOY SPECIMENS*

H. Tsai and R. V. Strain (Argonne National Laboratory)

SUMMARY

Capsules containing vanadium alloy specimens from irradiation experiments in FFTF and EBR-II are being processed to remove the lithium bond and retrieve the specimens for testing. The work has progressed smoothly.

OBJECTIVE

Vanadium alloy specimens in lithium-bonded capsules were irradiated in FFTF MOTA-2B, and in EBR-II COBRA-1A and X530 experiments. The objective of this task is to disassemble the capsules from these experiments in order to retrieve the irradiated specimens.

OUTLINE OF PROCESSING METHOD

Although the vanadium alloy specimens are low-activation and generally do not pose a significant radiological hazard after irradiation, the capsules holding the specimens often do. Therefore, the work is being conducted remotely in an alpha-gamma hot cell. The ventilated atmosphere of the hot cell also minimizes personnel exposure from the small quantities of tritium generated in the (n,T) reactions with ^{6}Li.

Opening of the capsule is done with a tubing cutter, at one or both ends. Amounts of tritium released are monitored, but have always been well within the allowable exhaust limits of the hot cell. The entire content of the opened capsule is placed in a stainless-steel wire mesh basket and immersed in a beaker containing liquid ammonia. Dissolution of lithium in liquid ammonia takes hours to days, depending mainly on the specimen packing inside. Following the ammonia dissolution, the specimens, still in the wire-mesh basket, are rinsed several times in clean alcohol baths. An ultrasonic cleaner is sometimes used to accelerate the cleaning process. The used ammonia and alcohol are allow to evaporate and the dried residues are disposed of as wastes.

The cleaned specimens are visually inspected and counted through the hot cell window, then sorted and placed in clean vials and removed from the hot cell. A survey is conducted immediately before the vials are removed from the hot cell facility.

STATUS

In this reporting period, all remaining MOTA-2B and COBRA-1A1 capsules were processed. These capsules are V492, V493, V494, V572, V676, and V677 from the MOTA-2B experiment, and V4101 from the COBRA-1A1 experiment. Specimens that belong to Monbusho were packaged and shipped to Japan.

Processing of the capsules removed from the X530 experiment has begun. Thus far, capsules S1, S2, and S3 have been completed.

Future Activities

Work is continuing on processing the remaining nine capsules from the X530 experiment. Capsules from the COBRA-1A2 experiment, which is being disassembled at PNL, will be scheduled when they become available.

Additional specimens are being irradiated in the ATR-A1 experiment in the Advanced Test Reactor and in the Fusion-1 experiment in the BOR-60 reactor. Both experiments are expected to be completed in the second quarter of 1996. A commitment has been made to collaborate with Russian colleagues to process the completed Fusion-1 experiment at RIAR, Russia.

*Work supported by U.S. Department of Energy, Office of Fusion Energy Research, under Contract W-31-109-Eng-38.

MICROSCOPIST'S AIDE: A Computer Program Written to Analyze TEM Micrographs - D.E. Reinhart, (Graduate Research Assistant, University of Missouri, Rolla) and **D. S. Gelles, (Pacific Northwest National Laboratory)***

OBJECTIVE

Microstructural analysis procedures are being upgraded to a modern computer format.

SUMMARY

A computer program has been rewritten in DOS Basic allowing current state-of-the-art computer equipment to be used for quantitative measurement of microstructural features such as voids, dislocations and precipitates.

PROGRESS AND STATUS

Introduction

In the study of radiation damage in materials, transmission electron microscopes are used to observe the microstructure of the materials because they can attain spatial resolutions to the atomic scale. Photos of the microstructure, commonly referred to as micrographs, are taken and analyzed to determine such damage-related variables as dislocation density, void density, and void distribution.[1] By developing a computerized data acquisition system, researchers will be able to save valuable time and increase the accuracy of their calculations.

This program and its accompanying data acquisition system were created to replace a much older and much simpler program and system that had become obsolete. The specially designed void counting table and the stereoviewer were retained, and the new data acquisition system was specifically designed to incorporate these tools. The computer program can perform three functions: measuring foil thickness, calculating void/loop density and size distribution, and determining dislocation density.

The stereoviewer has been additionally equipped with an adjustable light source. The light is focused to a point and connected to a linear voltage displacement transducer (LVDT). This setup allows the user to focus the light to a point at the apparent upper and lower foil surfaces of the material in the micrographs. The program reads the change in voltage resulting from the movement of the LVDT across the foil and calculates a foil thickness, given the micrograph magnification.

The data obtained from the stereoviewer can then be used in determining the void and/or Frank loop density and size distribution from the same micrograph. This time, the micrograph is placed on the void counting table. A pneumatic piston has been mounted on the table. When the user activates the piston by pressing on the switch located under the table with his or her knee, it causes a small pin to puncture the micrograph and signals the computer to add to the count. If a particular direction is measured, such as <110>, sophisticated computational procedures can be used, such as those outlined in Reference 1. At the same time, a beam of light is focused by the operator to the same diameter as the void being counted. The wheel that adjusts the size of the light beam is connected to a voltage source and a variable resistor (rheostat). Any adjustment of the beam size will cause a subsequent change in the rheostat, and therefore the output voltage to the computer will vary. This voltage is converted by the program to the diameter of the beam, and the size of each void is recorded. The pin punctures in the micrograph allow the user to keep track of which voids or loops have been counted within the region of interest. Once the counting has been completed and the diameter of the region of interest on the foil has been entered into

the program, the computer can then calculate the void/loop density as well as the percent swelling of the material. Furthermore, once the user selects the desired size interval, the programs will create a histogram of the size distribution of the voids/loops.

The third primary function of the computer program, dislocation analysis, does not use an external tool to acquire data. Henceforth, all the data is entered by hand into the program. The basic procedure requires the user to place a transparent sheet over the top of the micrograph. This transparency has a square of specific length (usually 7 cm) drawn upon it, and the user strikes a key on the keyboard for every intersection of this square with a dislocation in the micrograph. After all intersections have been counted and an invisibility factor has been entered for the specific crystal orientation depicted in the print, the program calculates the dislocation density of that area of the material.

The entire computer program was written using National Instruments LabWindows BASIC version 2.2.1. Although LabWindows and the compiled stand-alone Microscopist's Aide executable file are both DOS based programs, the programs themselves are menu and mouse driven, providing a user-friendly environment. Data acquisition is made using a National Instruments Lab+ I/O board and 50 pin connector block.

A copy of the basic program is available on request.

FUTURE WORK

This effort is completed.

REFERENCE

1. D. S. Gelles, R. M. Claudson, and L. E. Thomas, DOE/ER-0313/3, 131.

PASSIVE SIC IRRADIATION TEMPERATURE MONITOR

G. E. Youngblood (Pacific Northwest Laboratory)*

OBJECTIVE

The objective of this work is to examine the use of monolithic SiC as a passive irradiation temperature monitor using several methods.

SUMMARY

A new, improved passive irradiation temperature monitoring method was examined after an irradiation test at 627°C. The method is based on the analysis of the thermal diffusivity changes during post-irradiation annealing of polycrystalline SiC. Based on the results from this test, several advantages for using this new method rather than a method based on length or lattice parameter changes are given.

PROGRESS AND STATUS

Introduction

Over the past twenty years, several workers[1-5] have tested monolithic SiC bars for temperature monitoring in uninstrumented reactor experiments. Test methods are based upon the defect annealing behavior of neutron irradiated SiC; therefore they are out-of-reactor or passive determinations of the actual irradiation temperature. Typically after irradiation, small bars (one or two centimeters long) are subjected to an isochronal annealing schedule consisting of increasing temperature steps, each about one hour duration. When the sample is heated above the irradiation temperature, some of the irradiation defects recover and the remaining defects reach a new quasi-stable concentration dependent on the annealing temperature. Generally, changes in the macroscopic length or the lattice parameter are monitored between each temperature step as they recover toward their unirradiated values. Then a simple graphical approach which plots length (or lattice parameter) versus annealing temperature is used to obtain a fairly accurate prediction of the irradiation temperature. Nevertheless, about a 0.02% length change per anneal usually is observed, which for a bar of length 1.0 cm translates to a required precision in a length measurement of about ±0.1 μm - a very formidable task!

In irradiated SiC/SiC composite, 78% and 66% reductions in thermal diffusivity recently were reported for irradiations at 500° and 800°C, respectively.[6] After further heating to 1200°C, recoveries of almost 30% of the thermal diffusivity change then occurred. From these observations, it was apparent that a method for determining the irradiation temperature based on changes in the thermal diffusivity potentially would be more sensitive than when using length change methods.

Point defects are effective phonon scatterers, therefore irradiation defects should reduce the thermal diffusivity somewhat in proportion to their concentration. Following an annealing schedule similar to that used in the length change methods utilizing SiC, the thermal diffusivity should also recover toward its unirradiated values. Thus, a proposed method for predicting the irradiation temperature is patterned after the Isochronal Anneal Length Change (IALC) method and, hereafter, will be called the Isochronal Anneal Thermal Diffusivity (IATD) method.

---

*Pacific Northwest Laboratory is operated for the U. S. Department of Energy by Battelle Memorial Institute under Contract DE-AC06-76RLO 1830.

Initial results examinig the feasibility of using high purity, monolithic SiC and the IATD method for predicting the irradiation temperature is the subject of this report.

Experimental Procedure

Two small discs, either polycrystalline α-or ß-SiC, were received from Monbusho. Each disc was 1.0 cm diameter by about 2 mm thick with a bulk density greater than 97% of theoretical.

As part of the COBRA 1A1 experiment, the discs were irradiated in the EBR II breeder reactor in Idaho Falls over a period of 88.6 EFPD in subcapsule G05, which was a gas-gapped capsule designed to operate at 627°C. The fluence was 1.75 x 10^{22} n/cm^2 (E>0.1 MeV), equivalent to a dose of about 20 dpa-SiC. The samples were discharged from the reactor in April, 1993. The measured sample activity on contact was less than 3mR after a two year storage period.

The irradiated sample discs were mounted at the top of a low inertia, tungsten alignment tube that extended up into a tungsten mesh heating element inside a gas tight, water-cooled furnace wall. Then the samples were subjected to a series of one hour isochronal anneals in argon at temperatures increasing in about 100°C steps. The thermal diffusivity (TD), measured by the laser flash diffusivity technique and described elsewhere,[7] was measured periodically during the anneals and also at the end of each anneal after cooling the sample to a baseline temperature near 320°C. Importantly, the sample temperature could be rapidly changed in this system (at ≈20°C/min.) to the desired anneal temperature and then held constant to ±2°C during the anneals. To arrive at an average baseline TD value, at least five shots were made after the sample temperature had stabilized at 320°C. Otherwise, TD measurements were taken at about five to ten minute intervals during the one hour anneals to monitor the recovery kinetics. A curve was best-fit to this time dependent annealing data and the TD value determined at the end of each anneal was used as the anneal temperature TD value. The 320°C baseline temperature was chosen because the furnace and sample holder design geometry, made to accomodate radioactive samples, limited TD measurements to the 300° to 1500°C temperature range.

Results and Discussion

Figures 1(a-b) show the measured TD values as a function of temperature for the α- and ß-SiC samples, respectively. Initially, TD measurements were made on heating the irradiated samples up to about 600°C (data indicated as filled in circles); then the temperature was reduced back to the baseline temperature where the TD measurement was repeated. After this measurement cycle up to 600°C, which was somewhat below the irradiation temperature of 627°C, the baseline TD values remained unchanged, as expected for SiC with a quasi-stable as irradiated defect concentration. In both figures, open symbols indicate TD values determined at the end of the one hour anneal periods and following the anneals at the baseline temperature. After an intermediate and a final anneal at temperatures of ≈1000° and 1300°C, respectively, TD measurements were again made as a function of increasing temperatures to trace out the temperature dependence for that particular partially recovered state. These data are indicated with closed symbols and are connected with heavy solid lines in each figure. The TD temperature profiles for the other partially recovered states were estimated by tracing in lightly dashed curves roughly parallel to the solid curves. A darkened dot-dash line is shown traced through the anneal temperature TD values which represent the partially recovered states (anneal temperatures listed along the right-hand border in each figure). The intersection of this line with the extension of the "as irrad." curve, which showed no recovery, yields a rough estimate of the irradiation temperature of from 600° to 700°C. However, a more sensitive estimate can be made by comparing the changes in the TD at a low temperature reference where the effect of phonon scattering from point defects dominates the intrinsic phonon-phonon scattering. In our case, 320°C was selected for this reference.

In Figure 2, the 320°C TD values determined after each isochronal anneal are plotted versus the anneal temperature for both the α- and ß-SiC materials. The horizontal straight lines drawn through the initially measured 320°C TD values are characteristic of the fully irradiated defect state for each material. A third

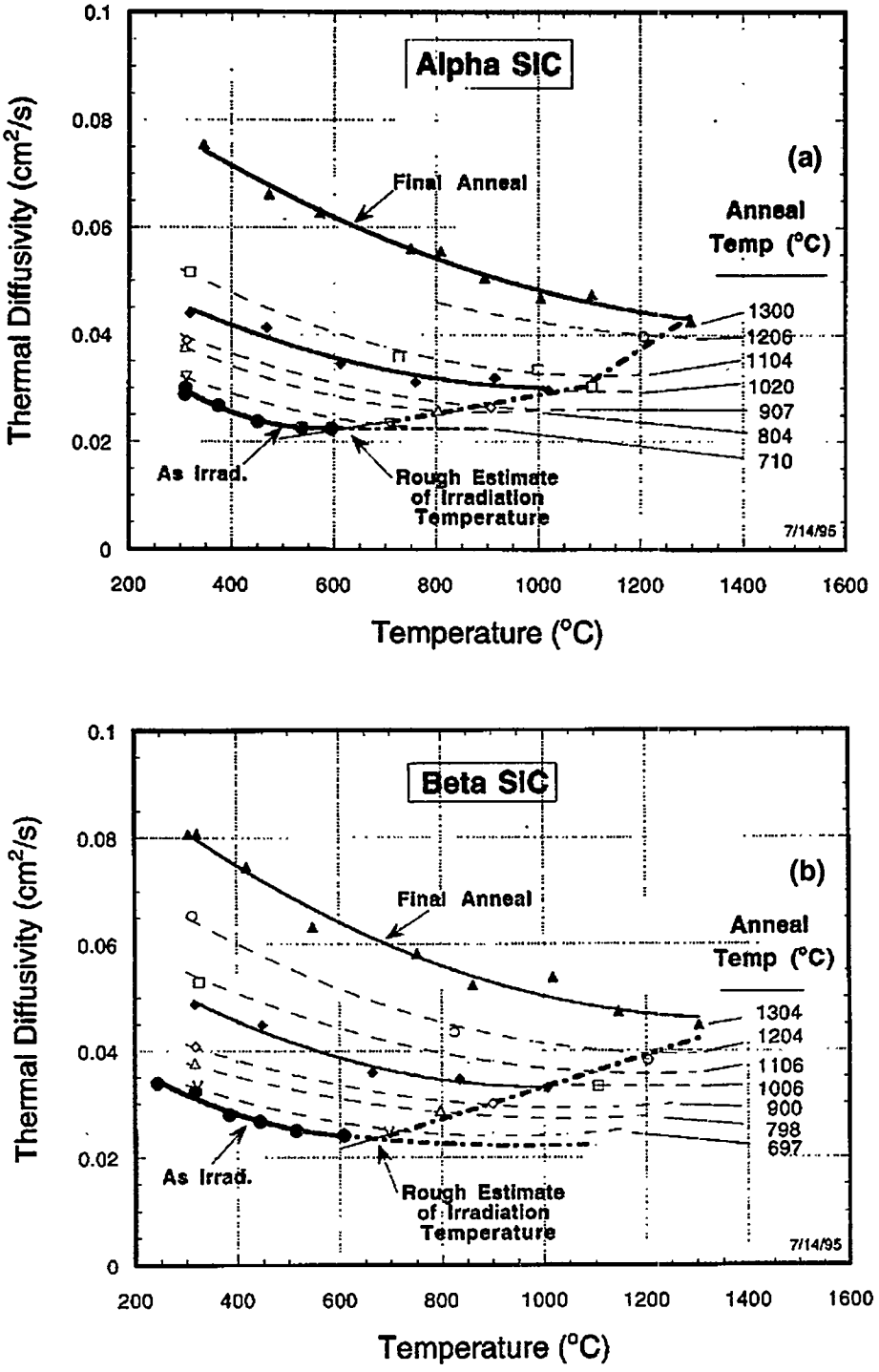

Figure 1(a-b) The thermal diffusivity temperature profiles for **(a)** α-SiC and **(b)** β-SiC after neutron irradiation to a dose of 20 dpa-SiC and after post-irradiation one hour isochronal anneals from 700° to 1300°C in ≈ 100°C steps.

R95120149.5

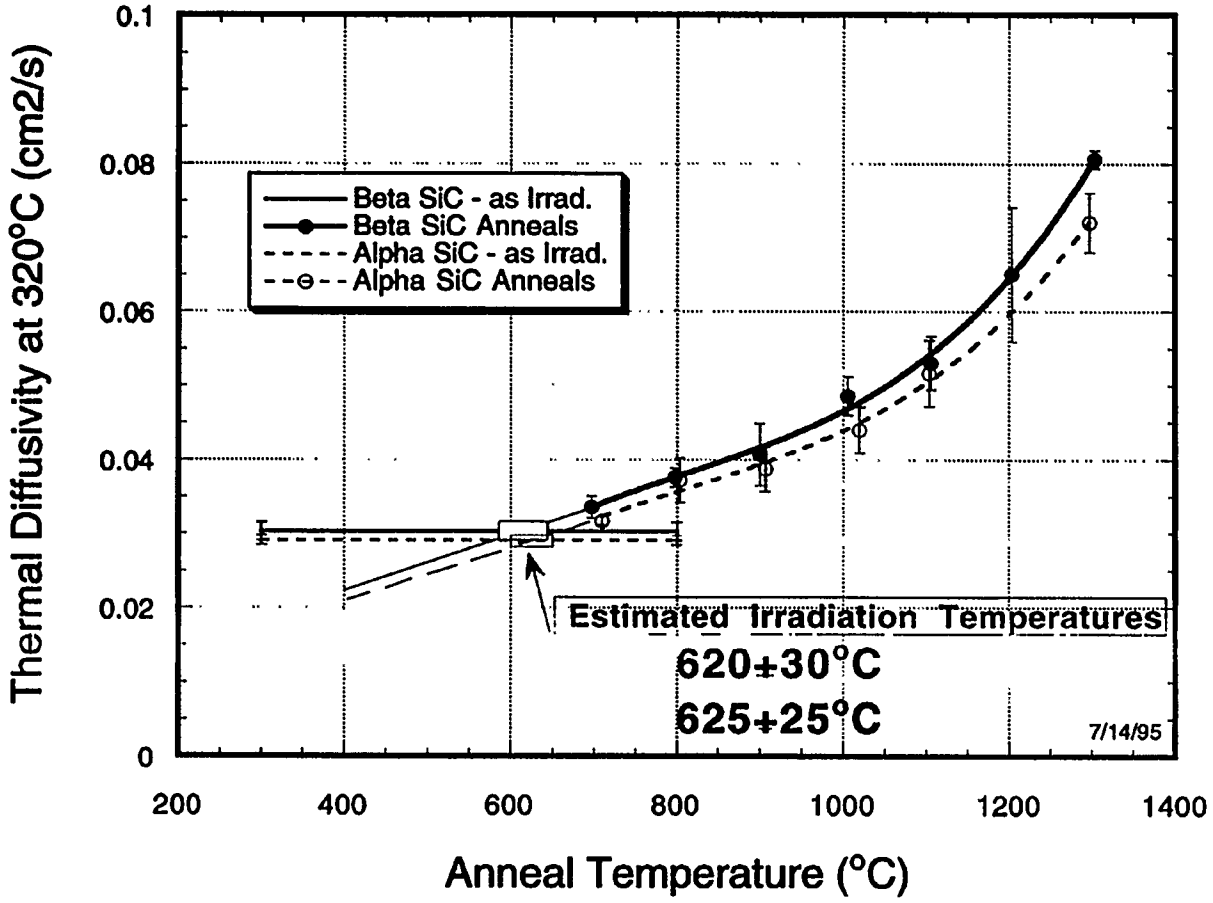

Figure 2 Estimate of the irradiation temperature using passive SiC temperature monitors and the isochronal anneal thermal diffusivity (IATD) method. For comparison of the thermal diffusivity changes due to partial recovery of the irradiation defect states after a series of isochronal anneals, the baseline temperature was taken as 320°C.

R95120149.4

order polynomial curve was best-fit to the 320°C TD values determined after each isochronal anneal. Above the irradiation temperature, these two curves are characteristic of the partially recovered defect states. The irradiation temperature is then estimated by the intersection of the straight line extension of the polynomial curve with its associated the horizontal baseline for the two materials. The two boxes reflect the uncertainties in the intersection points due to the uncertainties in the baselines as well as in the polynomial curve extensions. The irradiation temperatures estimated from the two intersection points are $625\pm25°$ and 620 ± 30°C for the α- and ß-SiC materials, respectively. These predicted irradiation temperatures are in very close agreement with the design irradiation temperature of 627°C within subcapsule G05. Several other observations are worth noting.

First, the 300K TD values, estimated for each type SiC from the extensions of the "as irrad." curves from about 300° down to 27°C, were each about 0.045 cm^2/s. The phonon mean free path[7] estimated from this TD value is about 1 nm, which is a little over x2 lattice constants (l.c. = 0.436 nm for ß-SiC[8]). Therefore, the "as irrad." defect state ($\approx10^4$ appm) is fairly close to saturation after irradiation to a dose of 20 dpa-SiC, even at 627°C.

Second, the magnitudes and shapes of the temperature profiles representing the partially recovered defect states were similar for each SiC phase. For such heavily irradiated SiC, the structural details appear to become dominated by the irradiation defect structures regardless of the original SiC phase structures. Thus, the curves representing the partially recovered or annealed states for the α- and ß-phases (in Figure 2) were almost identical.

Third, the selected isochronal annealing schedule (one hour anneals in 100°C steps) probably was not optimized for precisely determining the irradiation temperature. The TD measurements made as a function of time during the recovery anneals for temperatures up through 900°C indicated that the TD had not reached equilibrium values, but, in fact, was still increasing at the end of the one hour anneal. An annealing schedule designed to allow recovery to approach completion at each step should yield larger changes in the TD, thus a steeper slope in the curve representing the partially recovered states (less uncertainty in the intersection point). Perhaps using one or even two hour anneals with 50°C steps would allow a more accurate prediction of the irradiation temperature. Furthermore, even more sensitivity would be available if the baseline temperature were lower than 320°C, i.e., room temperature, for instance. Of course, neither the annealing kinetics, nor the temperature dependence of the TD values representing the partially recovered states need to be monitored once the optimum annealing schedule has been established.

Fourth, there appears to be a major difference between what is measured with the IALC method and what is measured with the IATD method. Even though vacancies and interstitials are generated in pairs during irradiation, they may have different influences on the observable physical properties. For instance, the associated shrinkage strain field of a vacancy must be smaller than the expansion strain field of an isolated interstitial since net swelling results from the accumulation of simple Frenkel pairs in SiC.[3] After neutron irradiation at intermediate temperatures (T≤900°C), the residual interstitial type defects primarily consist of a relatively high concentration of small interstitial clusters (≈1-5 nm).[9] For irradiations at higher temperatures or to higher fluences ($\geq10^{22}$ n/cm^2), the interstitial defects start to interact and form into more orderly fault or dislocation type loops as required to preserve the covalent Si-C tetrahedral bonding.[10] The interstitial loops have a lower strain energy per defect and therefore contribute little to the macroscopic swelling of SiC. This interpretation is still controversial and other explanations exist, i.e., that of Huang and Ghoneim.[11] Also, the demarcation temperature of 900°C is approximate, as it certainly depends on the irradiation conditions, particularly the neutron fluence. Meanwhile, the mobility of vacancies is much smaller than that of interstitials, so they remain relatively stable and isolated. Thus, the IALC method primarily monitors the decreasing size or concentration of these smaller, cluster type interstitial defects as these defects anneal either by combining into larger loop type interstitial defects (resulting in a smaller expansion strain field per interstitial) or completely disappear by recombination with the residual vacancies. Since the formation of small, cluster type interstitial defects predominates the formation of the larger, loop type interstitial defects only for irradiations below about 900°C, the IALC method is limited in application to this temperature range.

It is likely that the strain fields of relatively isolated point defects, such as impurity atoms or vacancies, are more effective phonon scatterers than are the more extensive strain fields of the clustered interstitial defects, and

certainly more effective than the quite extensive interstitial loop structures. Thus, the IATD method primarily monitors the decreasing concentration of vacancies which only anneal out by recombination with mobile interstitials below about 1300°C.[12] Above 1300°C, vacancy mobility becomes sufficient for the vacancies to anneal out to grain boundaries or other sinks or to combine with other vacancies. In the latter case, vacancy clustering can lead to void or bubble formation, especially if a bubble stabilizing gas such as helium is available within the lattice.[12] Since the TD is primarily sensitive to the vacancy concentration, it appears probable that the IATD method can be used to predict the irradiation temperature to a temperature higher than 900°C. This would be extremely useful for currently planned materials tests of the irradiation performance of SiC or SiC/SiC in the 800° to 1000°C temperature range.

Another significant advantage of an IATD method over IALC methods would be, once the irradiated SiC sample is mounted, all thermal diffusivity measurements and anneals would take place in situ, thus no additional handling of a radioactive sample would be required between anneals. Finally, the use of a high-purity SiC sample, such as one made from Morton CVD/SiC, should further improve the sensitivity of the IATD method since recovery will only involve the induced irradiation defects.

The main disadvantage of either the IATD or the IALC methods is that both methods are sensitive to the temperature during the final period of irradiation due to saturation effects at doses of only a few tenths of a dpa, which may be equivalent to only a few days irradiation in a fast reactor.

CONCLUSIONS

As part of the U.S./Japan collaborative program to study the effects of neutron irradiation on fusion reactor candidate materials (NIMS/ Monbusho), a new improved method for determining the irradiation temperature of an uninstrumented experiment was examined. The new method is called the Isochronal Anneal Thermal Diffusivity (IATD) method. In the IATD method, recovery in irradiated SiC is monitored by measuring the change in the thermal diffusivity (TD) after a series of postirradiation isochronal anneals. The TD is a more sensitive measure of the recovery than length change, so the IATD method is a more sensitive predictor of the irradiation temperature than the Isochronal Anneal Length Change (IALC) method. Other advantages for using the IATD method over the IALC method are its potential for monitoring the annealing kinetics and the reduced handling of a radioactive sample. Finally, the IATD method may be usable to predict irradiation temperatures as high as 1200°C, whereas IALC methods appear to be limited to predicting irradiation temperatures less than about 800°C.

FUTURE WORK

1. Two 20 mm bars made from the same materials as the discs used in the IATD method study were irradiated under identical conditions (≈20 dpa at 627°C) in COBRA 1A1. The bars will be analyzed using the IALC method, and the results will be compared to the IATD results. Also, the defect structures in the SiC's for the as irradiated and for the partially recovered conditions will be analyzed by TEM.

2. Two bars and one disc of very high purity SiC and of theoretical density (Morton CVD/ß-SiC) have been irradiated at about 800°C in the COBRA 1A2 experiment to an extremely high dose of ≈80 dpa-SiC. These samples were discharged from the EBR II reactor after 337 EFPD. Their annealing characteristics as well as their utility as an irradiation temperature monitor (using both the IALC and IATD methods) for such extreme conditions (high dose and temperature) will be examined.

REFERENCES

1. R. J. Price, "Annealing Behavior of Neutron-Irradiated SiC Temperature Monitors," *Nuclear Technology 16, 536-542 (1972).*

2. Hiroshige Suzuki, Takayoshi Iseki and Masahiko Ito, "Annealing Behavior of Neutron Irradiated ß-SiC," *J. of Nucl. Mater. 48, 247-252 (1973).*

3. T. Suzuki, T. Maruyama, T. Iseki, T. Mori and M. Ito, "Recovery Behavior in Neutron Irradiated ß-SiC," *J. of Nucl. Mater. 149, 334-340 (1987).*

4. Hiroyuki Miyazaki, Tetsuya Suzuki, Toyohiko Yano and Takayoshi Iseki, "Effects of Thermal Annealing on the Macroscopic Dimension and Lattice Parameter of Heavily Neutron-Irradiated SiC," *J. Nuclear Science and Technology 29(7), 656-663 (1992).*

5. Toyohiko Yano, Kazunari Sasaki, Tadashi Maruyama, Masahiko Ito and Shoji Onose, "A Step-Heating Dilatometry Method to Measure the Change in Length Due to Annealing of a SiC Temperature Monitor," *Nuclear Technology 93, 12-415 (1991).*

6. G. W. Hollenberg, C. H. Henager, Jr., G. E. Youngblood, D. J. Trimble, S. A. Simonson, G. A. Newsome and E. Lewis, "The Effect of Irradiation on the Stability and Properties of Monolithic SiC and SiC_f/SiC Composites up to 25 dpa," *J. Nucl. Mater. 219, 70-86 (1995).*

7. G. E. Youngblood, "Improvement of the Thermal Conductivity of SiC_f/SiC Composite," this report.

8. Powder Diffraction File Database, 29-1129, JCPDS-ICDD (1994).

9. T. Yano, T. Suzuki, T. Muruyama and T. Iseki, "Microstructure and Annealing Behavior of Heavily Neutron-Irradiated ß-SiC," *J. Nucl. Mater. 155-157, 311-14 (1988).*

10. Tetsuya Suzuki, Toyohiko Yano, Tsutomu Mori, Hiroyuki Miyazaki and Takayoshi Iseki, "Neutron Irradiation Damage of Silicon Carbide," *Fusion Technology 27, 314-25 (1995).*

11. Hanchen Huang and Nasr Ghoniem, "A Phenomenological Model for Swelling of SiC under Neutron Irradiation at Low Temperatures," to be published, April (1995).

12. T. Suzuki, T. Yano, T Maruyama, T. Iseki and T. Mori, "Effects of Sintering Aids on the Length Change of Neutron Irradiated SiC Ceramics During Annealing at High Temperature," *J. Nucl. Mater. 165, 247-51 (1989).*

Distribution

1-15. Argonne National Laboratory, 9700 South Cass Avenue, Argonne, IL 60439

M. C. Billone	A. B. Hull	L. A. Niemark
O. K. Chopra	C. E. Johnson	J. H. Park
H. M. Chung	F. Kassner	D. L. Smith
D. R. Diercks	J. P. Kopasz	S. W. Tam
J. Gazda	R. F. Mattas	H. C. Tsai

16-17. Argonne National Laboratory, EBR-II Division, P.O. Box 2528, Idaho Falls, ID 83403-2528

H. P. Planchon D. L. Porter

18. Auburn University, Department of Mechanical Engineering, 201 Ross Hall, Auburn, AL 36849

B. A. Chin

19-32. Pacific Northwest National Laboratory, P.O. Box 999, Richland, WA 99352

J. L. Ethridge	M. L. Hamilton	R. H. Jones
F. A. Garner (5)	H. L. Heinisch	W. W. Laity
D. S. Gelles	G. W. Hollenberg	O. D. Slagle
L. R. Greenwood		

33. Carnegie Institute of Technology, Carnegie-Mellon University, Schenley Park, Pittsburgh, PA 15213

W. M. Garrison, Jr.

34. Commissariat à l'Energie Atomique, Direction des Technologies Advancées, M2R1/DECM Cen-Saclay, Gif Sur Yvette, Cedex, France

F. Tavassoli

35-38. General Atomics, P.O. Box 85608, San Diego, CA 92138

T. A. Lechtenberg	K. R. Schultz
D. I. Roberts	C. Wong

39. General Dynamics Convair Division, 3302 Pacific Hwy, San Diego, CA 92101-1137

T. L. Cookson

40. Georgia Institute of Technology, Fusion Research Center, 0225, Atlanta, GA 30332

W. M. Stacey

41. Grand Canyon University, Department of Natural Science, 3300 W. Camelback Rd., Phoenix, AZ 85017

W. A. Coghlan

42-44. Idaho National Engineering Laboratory, Fusion Safety Program, P.O. Box 1625, Idaho Falls, ID 83415-3523

G. Longhurst K. McCarthy D. Petti

45. Knolls Atomic Power Laboratory

G. Newsome, P.O. Box 1072, Schenectady, NY 12301

46-47. Lawrence Livermore National Laboratory, P.O. Box 808, Livermore, CA 94550

E.C.N. Dalder J. Perkins

48-56. Los Alamos National Laboratory, P.O. Box 1663, Los Alamos, NM 87545

J. L. Anderson	E. H. Farnum	R. E. Siemon
F. W. Clinard	H. M. Frost	W. F. Sommer
D. W. Cooke	J. C. Kennedy	K. E. Sickafus

57. Manlabs, Inc., 231 Erie Street, Cambridge, MA 02139
D. Tognarelli

58-60. Massachusetts Institute of Technology, Department of Metallurgy and Materials Science, Cambridge, MA 02139
L. W. Hobbs N. J. Grant K. C. Russell

61-62. Massachusette Institute of Technology, Plasma Fusion Center Headquarters, Cambridge, MA 02139
H. D. Becker D. B. Montgomery

63-64. McDonnell-Douglas Aerospace, Mail Code 306 4204, P.O. Box 516, St Louis, MO 63166
J. W. Davis G. W. Wille

65. Merrimack College, Dept. of Physics, 315 Turnpike Street, North Andover, MA 01845
D. P. White

66. M. J. Schiff & Associates, 1291 N. Indian Hill Blvd., Claremont, CA 91711-3897
G.E.C. Bell

67-69. National Institute of Standards and Technology, Boulder, CO 80302
F. R. Fickett H. I. McHenry R. P. Reed

70-71. Naval Research Laboratory, Code 6506, Washington, DC 20375
D. L. Gibson J. A. Sprague

72-112. Oak Ridge National Laboratory, P.O. Box 2008, Oak Ridge, TN 37831

Central Research Library	M. L. Grossbeck	A. F. Rowcliffe (10)
Document Reference Section	A. N. Gubbi	M. J. Saltmarsh
Laboratory Records Department (2)	J. F. King	J. Sheffield
Laboratory Records-RC	E. A. Kenik	L. L. Snead
Patent Section	R. L. Klueh	R. E. Stoller
D. J. Alexander	E. H. Lee	K. R. Thoms
J. Bentley	L. K. Mansur	P. F. Tortorelli
E. E. Bloom	P. J. Maziasz	R. L. Wallace
T. D. Burchell	M. C. Osborne	S. J. Zinkle
G. M. Goodwin	J. E. Pawel	
R. H. Goulding	T. C. Reuther	

113. Oregon Graduate Institute, Dept. of Materials Science & Engineering, 19600 N.W. Von Neumann Drive, Beaverton, OR 97006
J. M. McCarthy

114-116. Princeton University, Princeton Plasma Physics Laboratory, P.O. Box 451, Princeton, NJ 08540
R. C. Davidson Long-Poe Ku D. M. Meade

117-118. Rensselaer Polytechnic Institute, Troy, NY 12181
D. Steiner David Duquette

119. Rockwell International Corporation, NA02, Rocketdyne Division, 6633 Canoga Avenue, Canoga Park, CA 91304
D. W. Kneff

120-122. Sandia National Laboratories, Fusion Technology Dept., Dept. No 6531, P.O. Box 5800, Albuquerque, NM 87185-5800
M. J. Davis M. Ulrickson R. D. Watson

123-125. Sandia National Laboratories, Livermore Division 8316, Livermore, CA 94550
W. Bauer K. Wilson W. G. Wolfer

126. San Diego State University, Mechanical Engineering Dept., San Diego, CA 92182-0191
L. D. Thompson

127. TSI Research, 225 Stevens Ave., #110, Solana Beach, CA 92075
E. T. Cheng

128-129. University of California at San Diego, U.S. ITER Project Office, 9500 Gilman Drive, Bldg. 302, La Jolla, CA 92093-0035
C. C. Baker T. R. James

130-131. University of California, Dept. of Mechanical, Aerospace, and Nuclear Engineering, Santa Barbara, CA 93106
G. E. Lucas G. R. Odette

132-134. University of California, Dept. of Chemical, Nuclear , and Thermal Engineering, Los Angeles, CA 90024
M. A. Abdou N. M. Ghoniem S. Sharafat

135. University of Michigan, Dept. of Nuclear Engineering, Ann Arbor, MI 48109
T. Kammash

136. University of Missouri, Department of Nuclear Engineering, Rolla, MO 65401
A. Kumar

137-138. University of Wisconsin, Nuclear Engineering Dept., 1500 Johnson Drive, Madison, WI 53706
J. B. Blanchard G. L. Kulcinski

139-141. Hokkaido University, Faculty of Engineering, Kita 13, Nishi 8, Kita-ku, Sapporo 060, Japan
Heischichiro Takahashi Somei Ohnuki Akira Okada

142-143. Japan Atomic Energy Research Institute, Tokai Research Establishment, Tokai-mura, Naka-gun, Ibaraki-ken 319-11, Japan
Akimichi Hishinuma K. Noda

144. Kyoto University, Institute of Atomic Energy, Gokasho, Uji, Kyoto 611, Japan
Akira Kohyama

145. Kyushu University, Dept. of Nuclear Engineering, Faculty of Engineering, Kyushu University 36, Hakozaki, Fukuoka 812, Japan
C. Kinoshita

146. Kuyshu University, Research Institute for Applied Mechanics, Kasuga, Fukuoka 816, Japan
Naoaki Yoshida

147-148. Muroran Institute of Technology, Dept. of Metallurgical Engineering, 27-1 Mizumoto-cho, Mororan 050, Japan
Toshihei Misawa Akihiko Kimura

149-150. Nagoya University, Dept. of Nuclear Engineering, Furo-Cho, Chikusa-ku, Nagoya 464-01, Japan
Michio Kiritani Tetuo Tanabe

151-154. National Institute for Fusion Science, Furo-cho, Chikusa-ku, Nagoya 464-01, Japan
Osamu Motojima, Chusei Namba, Takeo Muroga, Nobuaki Noda

155-158. National Research Institute for Metals, Tsukuba Branch, Sengen, Tsukuba-shi, Ibaraki-ken, 305, Japan
Fujio Abe, Tetsuji Noda, Josei Nagakawa, Haruki Shiraishi

159. PNC Oarai, 4002 Narita, Oarai, Ibaraki 311-13, Japan
Itaru Shibahari

160. Science University of Tokyo, Dept. of Materials Science & Technology; 2641 Yamazaki Noda City, Chiba Prefecture 278, Japan
Naohira Igata

161. Teikyo University, Otsuka, Hachioji, Tokyo 192-03, Japan
Akira Miyahara

162-163. Tohoku University, Institute for Materials Research, Katahira 2-2-1, Sendai 980-77, Japan
Akihiko Kimura, Hideki Matsui

164-166. Tohoku University, Institute for Materials Research, Oarai Branch, Oarai, Ibaraki 311-13, Japan
Hideo Kayono, Hiroaki Kurishita, Tatsuo Shikama

167-168. Tohoku University, Dept. of Nuclear Engineering, Tohoku University, Aoba, Aramaki, Sendai 980-77, Japan
Katsunori Abe, Akira Hasegawa

169. Tohoku University, Dept. of Machine Intelligence and Systems Engineering, Aramaki, Aoba-ku, Sendai 980-77, Japan
Tatsuo Kondo

170. Tokai University, Dept. of Nuclear Engineering, 1117 Kitakaname, Hiratsuka-shi, Kanagawa-ken 259-12, Japan
Shiori Ishino

171. University of Tokyo, Dept. of Nuclear Engineering, 3-1, Hongo 7-Chome, Bunkyo-Ku, Tokyo 113, Japan
Naoto Sekimura

172. University of Tokyo, Dept. of Materials Science, 3-1, Hongo 7-Chome, Bunkyo-ku, Tokyo 113, Japan
Yutaka Kohno

173. Commission of European Communities, Directorate-General for Research Science and Education, Fusion Programme RUE De La Loi 200, B-1049 Brussels, Belgium
J. Darvas

174-175. Chalk River Nuclear Laboratories, Atomic Energy of Canada, Ltd., Chalk River, Ontario KOJ 1J0, Canada
I. J. Hastings, D. P. Jackson

176. Southwestern Institute of Physics, P.O. Box 432, Chenedu 610041, Sichuan, P.R. China
J. P. Qian

177. Institute of Atomic Energy, Academia Sinica, P.O. Box 275-51, Beijing, P.R. China
J. Yu

178. Riso National Laboratory, Materials Dept., P.O. Box 49, DK-4000, Roskilde, Denmark
B. N. Singh

179. Centre d'Etudes Nucleaires, Saclay, DLPC/SMCM, Commissariat a l'Energie Atomique, 91191 Gif-Sur-Yvette, Cedex, France
N. Roux

180. Commission for European Communities, Joint Research Centre, I.A.M. Ispra Establishment 21020 Ispra (Varese), Italy
P. Fenici

181. EURATOM/CIEMAT Fusion Association, Avenida Complutense 22, 28040, Madrid, Spain
E. R. Hodgson

182. Paul Scherrer Institute, CH-5232 Villigen, Wuerenlingen PSI, Switzerland
M. Victoria

183. Harwell Laboratory, B393, Radiation Damage Dept., Oxfordshire, OX11 ORA, United Kingdom
C. A. English

184. Metallurgical and Nuclear Consultant, 9A Cumnor Rise Road, Cumnor Hill, Oxford OX2 9HD, United Kingdom
D. R. Harries

185. Hahn-Mietner-Institut fur Kernforschung Berlin, Postfach 390128, Glienicker Str. 100, D-14109, Germany
H. Wollenberger

186. Institut fur Festkorperforschung Forschungszentrum Jülich, Postfach 1913, D-52425 Jülich, Germany
H. Ullmaier

187-190. ITER Garching Joint Work Site, Max-Planck-Institute für Plasmaphysik, Boltzmannstrasse 2, D-85748 Garching bei München, Germany
B. Barabash G. Kalinin
Y. Gohar R. Parker

191-192. ITER Naka Joint Work Site, 801-1 Mukouyama, Naka-machi, Naka-gun, Ibaraki-Ken, 311-01, Japan
M. Huguet (2)

193-196. ITER San Diego Joint Work Site, 11025 N. Torrey Pines Road, La Jolla, CA 92037
V. Chuyanov F. Puhn
S. J. Piet P. Smith

197-198. Kernforschungszentrum Karlsruhe, Postfach 3640, 75 Karlsruhe 1, Germany
M. Dalle-Donne (INR) K. Ehrlich (IMF-II)

199. Max-Planck-Institut für Plasmaphysik, Boltzmannstrasse 2, D-85748 Garching bei München, Germany
Patrick Lorenzetto

200. A. A. Baikov Institute of Metallurgy, USSR Academy of Sciences, Leninsky Prospect 49, Moscow, Russia
L. I. Ivanov

201. CRISM "Prometey," Naberezhnava r. Monastyrick 1, 193167, St. Petersburg, Russia
V. V. Rybin

202. D. V. Efremov Institute of Electro-Physical Apparatus, 189631, St. Petersburg, Russia
S. A. Fabritsiev

203. Kharkov Institute of Physics & Technology, Radiation Damage and Materials Dept., Akademicheskaya 1, 310108 Kharkov, Ukraine
I. M. Neckludov

204-206. V. I. Lenin Research Institute of Atomic Reactors, 433510 Dimitrovgrad-10, Ulyanovsk Region, Russia

V. Kazakov	A. S. Pokrovsky	V. K. Shamardin

207. Korean Atomic Energy Research Institute, P.O. Box 105, Yusung, Taejon, 305-600, Korea
Jun Hwa Hong

208. Department of Energy, DOE Oak Ridge Field Office, P.O. Box 2008, Oak Ridge, TN 37831-6269
Assistant Manager for Energy Research and Development

209. Department of Energy, DOE Oak Ridge Field Office, P.O. Box 2008, Oak Ridge, TN 37831-6269
S. D. Frey

210. Department of Energy, Office of Basic Energy Sciences, Washington, D.C. 20585
R. J. Gottschall

211-218. Department of Energy, Office of Fusion Energy, Germantown, MD 20874

S. E. Berk	W. F. Dove	R. E. Price
M. M. Cohen	R. McKnight	F. W. Wiffen
N. A. Davies	W. Marton	

219. Department of Energy, Richland Operations Office, P.O. Box 550, MS-K850, Richland, WA 99352
J. Turner

220-221. Department of Energy, Office of Scientific and Technical Information, Office of Information Services, P.O. Box 62, Oak Ridge, TN 37831
For distribution by microfiche as shown in DOE/OSTI-4500-R75, Distribution Categories UC-423 (Magnetic Fusion Reactor Materials) and UC-424 (Magnetic Fusion Energy Systems)